ESTIMATION OF LIQUEFACTION-INDUCED LATERAL SPREAD FROM NUMERICAL MODELING AND ITS APPLICATION

by

Xianhong Meng

A dissertation submitted to the faculty of
The University of Utah
in partial fulfillment of the requirements for the degree of

Doctor of Philosophy

Department of Civil and Environmental Engineering

The University of Utah

May 2012

UMI Number: 3504081

All rights reserved

INFORMATION TO ALL USERS
The quality of this reproduction is dependent on the quality of the copy submitted.

In the unlikely event that the author did not send a complete manuscript
and there are missing pages, these will be noted. Also, if material had to be removed,
a note will indicate the deletion.



UMI 3504081

Copyright 2012 by ProQuest LLC.

All rights reserved. This edition of the work is protected against
unauthorized copying under Title 17, United States Code.



ProQuest LLC.
789 East Eisenhower Parkway
P.O. Box 1346
Ann Arbor, MI 48106 - 1346

Copyright © Xianhong Meng 2012

All Rights Reserved

The University of Utah Graduate School

STATEMENT OF DISSERTATION APPROVAL

The dissertation of Xianhong Meng

has been approved by the following supervisory committee members:

Steven Bartlett	, Chair	10/06/2011 Date Approved
Evert Lawton	, Member	10/06/2011 Date Approved
Chris Pantelides	, Member	10/06/2011 Date Approved
Travis Gerber	, Member	10/06/2011 Date Approved
Eunhye Kim	, Member	10/06/2011 Date Approved

and by Paul Tikalsky , Chair of

the Department of Department of Civil & Environmental Engineering

and by Charles A. Wight, Dean of The Graduate School.

ABSTRACT

A noncoupled numerical procedure was developed using a scheme of pore water generation that causes shear modulus degradation and shear strength degradation resulting from earthquake cyclic motion. The designed Fast Lagrangian Analysis of Continua (FLAC) model procedure was tested using the liquefaction-induced lateral spread and ground response for Wildlife and Kobe sites.

Sixteen well-documented case histories of lateral spread were reviewed and modeled using the modeling procedure. The dynamic residual strength ratios were back-calculated by matching the predicted displacement with the measured lateral spread, or with the displacement predicted by the Yound et al. model. Statistical analysis on the modeling results and soil properties show that most significant parameters governing the residual strength of the liquefied soil are the SPT blow count, fine content and soil particle size of the lateral spread layer. A regression equation was developed to express the residual strength values with these soil properties.

Overall, this research demonstrated that a calibrated numerical model can predict the first order effectiveness of liquefaction-induced lateral spread using relatively simple parameters obtained from routine geotechnical investigation. In addition, the model can be used to plan a soil improvement program for cases where liquefaction remediation is needed. This allows the model to be used for design purposes at bridge approaches structured on liquefiable materials.

TABLE OF CONTENTS

ABSTRACT iii

LIST OF TABLES viii

ACKNOWLEDGEMENTS xii

1. INTRODUCTION 1

1.1 General Introduction 1
1.2 Problem Description and Statement 3
1.3 Scope and Approach 5

2. LITERATURE REVIEW 7

2.1 Pseudostatic Analysis 8
2.2 Newmark Sliding Block Analysis 8
2.3 Nonlinear Analysis Approach 9
2.3.1 Uncoupled Pore Water Generation Models 10
2.3.2 Fully Coupled Pore Water Generation Models 12
2.3.3 Advanced Constitutive Models 15
2.4 Summary of Nonlinear Methods 16
2.5 Research Approach 17

3. NUMERICAL MODEL PRECEDURE DESIGN 20

3.1 Introduction 20
3.2 Noncoupled Constitutive Model Design 23
3.2.1 Dynamic Modeling of Behavior B Soils 26
3.2.2 Dynamic Modeling of Behavior A and C Soils 27
3.2.2.1 Initial and Degraded Shear Modulus 29
3.2.2.2 Damping 31
3.2.2.3 Bulk Modulus 32
3.2.2.4 Shear Strength Reduction and Residual Shear Strength 32
3.2.2.5 Shear Stress Tracking 34
3.2.2.6 Modeling of Hysteretic Behavior and Stress Reversals 35
3.2.2.7 Postliquefaction Shear Strength and Shear Modulus 38

3.3 Boundary Condition Considerations 39
3.4 Input Time History Selection and Preparation 42
3.5 Youd's Prediction of Lateral Spread....44
3.6 Summary of Model Design 47

4. PORE WATER GENERATION MECHANISM 49

4.1 Number of Cycles to Liquefaction 49
4.2 Blow Count Adjustment for CSR 54
4.3 Fine Count Adjustment for CSR 55
4.4 Pore Water Generation Calculation 63
4.5 Pore Water Generation Adjustment 64
4.6 Summary of Pore Water Generation....65

5. MODEL VERIFICATION 66

5.1 Model Verification by Simple Cyclic Sinusoidal Input Motion 66
5.1.1 Input Motion 66
5.1.2 Input Soil Parameters 68
5.1.3 Shear Modulus Reduction with Pore Water Generation 69
5.1.4 Hysteretic Behavior of Liquefied Soils 71
5.1.5 Displacement 76
5.1.6 Deamplification of Strong Motion due to Liquefaction 78
5.2 Model Verification Using Real Earthquake Time History 78
5.2.1 Input Motion 80
5.2.2 Input Soil Parameters 80
5.2.3 Shear Modulus Reduction with Pore Water Generation 80
5.2.4 Hysteretic Behavior 80
5.2.5 Displacement 85
5.2.6 Modification of Ground Response due to Liquefaction 88
5.3 Summary....93

6. GROUND RESPONSE CALIBRATION 94

6.1 Calibration with the Wildlife Array 96
6.1.1 Background of Wildlife Superstition Hills Earthquake 96
6.1.2 Model Procedure Development and Execution 98
6.1.3 Model Performance....103
6.1.3.1 Acceleration Time History Comparison 103
6.1.3.2 Response Spectra Comparison....107
6.1.3.3 Pore Water Generation Comparison 109
6.1.3.4 Hysteretic Behavior Comparison....114
6.1.4. Summary of WLA Modeling Comparison 117
6.2 Model Calibration with the Port Island Site, Kobe Japan 119
6.2.1 Background of Kobe Site Earthquake 119

6.2.2 Model Procedure Development and Execution 121
6.2.3 Model Prediction and Comparison 123
6.2.3.1 Motion Comparison 123
6.2.3.2 Response Spectra Comparison.....126
6.2.3.3 Hysteretic Behavior Comparison.....128
6.2.3.4 Pore Water Pressure Generation Comparison.....135
6.2.4 Summary of Kobe FLAC Model Procedure 138
6.3 Summary of Model Calibration 138

7. CASE HISTORY ANALYSIS 139

7.1 Bandai Bridge, Niigata Japan 141
7.2 Niigata Hotel Area 155
7.3 Niigata Railway Station 158
7.4 Niigata Showa Bridge Area 162
7.5 Noshiro Site N-4 Section 168
7.6 Noshiro Site S-7 Section 180
7.7 San Fernando Site Juvenile Hall Section 186
7.8 San Fernando Site Jensen Filtration Plant Section 193
7.9 Imperial Valley Site Heber Road Section 197
7.10 Imperial Valley River Park Site 206
7.11 Turkey Degirmenedere Site 209
7.12 Wildlife Site 214
7.13 Idaho Whiskey Springs Site 218
7.14 Northridge Balboa Site 225
7.15 Turkey Degirmenedere without T_{15} 231
7.16 Turkey Sapanca Hotel Site 232

8. MODEL RESULTS AND ANALYSIS 236

8.1 Model Analysis Results 236
8.2 Regression Analysis of Model Analysis Results 238
8.3 Conclusion 250

9. CONCLUSION AND RECOMMENDATIONS 252
9.1 Conclusions 252
9.2 Recommendations 255

APPENDICES

A NIIGATA BANDAI DATA 257

B NIIGATA HOTEL DATA 276

C NIIGATA SITE RAILWAY SECTION DATA 292

D NIIGATA SHOWA SECTION DATA 308

E NOSHIRO SITE N-4 SECTION DATA 324

F NOSHIRO SITE S-7 SECTION DATA 344

G SAN FERNANDO SITE JUVENILE HALL SECTION DATA 360

H SAN FERNANDO SITE JENSEN FILTRATION PLANT SECTION DATA 379

I IMPERIAL VALLEY SITE HEBER ROAD SECTION DATA 395

J IMPERIAL VALLEY SITE RIVER PARK SECTION DATA 413

K TURKEY DEGIRMENEDERE SITE DATA 421

L WILDLIFE SITE DATA 427

M IDAHO WHISKEY SPRINGS SITE DATA 433

N NORTHRIDGE BALBOA SITE DATA 452

O TURKEY DEGIRMENEDERE WITHOUT T_{15} DATA 456

P TURKEY SAPANCA HOTEL DATA 460

REFERENCE.....467

LIST OF TABLES

Table Page

3.1. Relationship between shear strain and $(N_1)_{60cs}$ for postliquefaction behavior.....39

4.1. Earthquake magnitude and representative cycles at $0.65\tau_{max}$ 52

4.2. Earthquake magnitude, number of representative cycles and CSR 53

4.3. Earthquake magnitude, number of representative cycles and CSR for FC=15% Sand.....57

4.4. Earthquake magnitude, number of representative cycles and CSR for FC=35% Sand.....57

5.1 Selected soil properties for site 1 and site 2.....68

6.1. Soil properties for soils at the WLA (after Bennett et al. 1984) 98

6.2. Blow count and fine content for the T_{15} layer at WLA.....98

6.3. Soil properties for PIDA sediments (after Ishihara et al. 1996) 121

7.1. Selected sites and modeling information 140

7.2. Soil properties of Bandai site, Niigata, Japan 144

7.3. Lateral spread displacements estimated by Youd et al. (2002) model at Bandai site 150

7.4. Lateral spread prediction from FLAC model for residual strength ratio of 0.085 at Niigata Bandai site.....151

7.5. Lateral spread prediction from FLAC model for residual strength ratio of 0.075 at Niigata Bandai site.....152

7.6. Lateral spread prediction from FLAC model for residual strength ratio of 0.065 at Niigata Bandai site 152

7.7. Lateral spread prediction from FLAC model for residual strength ratio of 0.055 at Niigata Bandai site 153

7.8. Soil properties of Niigata Hotel site 157

7.9. Lateral spread prediction by Youd et al. (2002) model at Niigata Hotel site 157

7.10. Lateral spread prediction from FLAC model for different residual strength ratio at Niigata Hotel site 158

7.11. Soil properties of Niigata Railway Station 160

7.12. Prediction of lateral spread from Bartlett's equation 161

7.13 Lateral spread prediction from FLAC model for different residual strength ratio at Niigata Railway Station 161

7.14 soil properties from several boring, Niigata Showa Bridge section 165

7.15. Lateral spread prediction by Youd et al. (2002) model at Niigata Showa site 165

7.16. Lateral spread prediction from FLAC model for residual strength ratio of 0.08 at Niigata Showa section 165

7.17. Lateral spread prediction from FLAC model for residual strength ratio of 0.09 at Niigata Showa section 166

7.18. Lateral spread prediction from FLAC model for residual strength ratio of 0.10 at Niigata Showa section 166

7.19. Lateral spread prediction from FLAC model for residual strength ratio of 0.12 at Niigata Showa section 167

7.20. Soil properties from the available boring at Noshiro site N-4 section 172

7.21. Lateral spread prediction by Youd et al. (2002) model at Norshiro site N-4 section 178

7.22. Lateral spread prediction by FLAC model for residual strength ratio of 0.04 178

7.23. Lateral spread prediction by FLAC model for residual strength ratio of 0.03 179

7.24. Lateral spread prediction by FLAC model for residual strength ratio of 0.02 179

7.25. Soil properties at Noshiro site S-7 section.....182
7.26. Prediction lateral spread from Bartlett's equation 183

7.27. Lateral spread calculation from FLAC model for residual strength ratio of 0.04 .184

7.28. Lateral spread calculation from FLAC model for residual strength ratio of 0.03 .184

7.29. Lateral spread calculation from FLAC model for residual strength ratio of 0.02 .185

7.30. Soil properties at Juvenile Hall section of San Fernando site.....187

7.31. Lateral spread prediction by Youd et al. (2002) model at Juvenile Hall area 192

7.32. Lateral spread calculation from FLAC model with residual strength ratio of 0.15, 0.14 and 0.13 at Juvenile Hall area 192

7.33. Soil properties at Jensen Filtration Plant section of San Fernando site 194

7.34. Lateral spread prediction by Youd et al. (2002) model at Jensen Filtration Plant area.....195

7.35. FLAC model's prediction of the lateral spread with residual strength ratio of 0.06 at Jensen Filtration Plant area 195

7.36. FLAC model's prediction of the lateral spread with residual strength ratio of 0.07 at Jensen Filtration Plant area 196

7.37. FLAC model's prediction of the lateral spread with residual strength ratio of 0.05 at Jensen Filtration Plant area 196

7.38 Average soil properties at Heber Road site.....200

7.39. Lateral spread prediction by Youd et al. (2002) model at Heber Road site.....205

7.40. Lateral spread prediction by FLAC model with residual strength ratio of 0.09 at Heber Road site.....205

7.41. Lateral spread prediction by FLAC model with residual strength ratio of 0.08 at Heber Road site.....205

7.42. Lateral spread prediction by FLAC model with residual strength ratio of 0.07 at Heber Road site.....205

7.43. Lateral spread prediction by FLAC model at Degirmenedere site 214

7.44. Lateral spread prediction by FLAC model at 1987 Superstition Hills site.....218

7.45. Lateral spread calculation from FLAC model for residual strength ratio of 0.16, 0.19, 0.20, 0.22.....225

7.46. Lateral spread prediction by FLAC model at Northridge Balboa site.....230

7.47. Lateral spread prediction by FLAC model at Turkey, Sapanca Hotel site.....235

8.1. Summary of model result, soil and earthquake parameters from case history data set 237

8.2. Residual strength ratio and related soil parameters in regression analysis.....244

8.3. Regression analysis result for residual strength ratio and soil parameters 244

8.4. Residual strength ratio and related soil parameters, including Turkey Sapanca Hotel case, in regression analysis 246

8.5. Regression analysis result for residual strength ratio and soil parameters including Turkey Sapanca Hotel case.....247

8.6. Regression analysis results showing standardized residual values.....249

ACKNOWLEDGEMENTS

This thesis has been made possible through the financial support of the UTAH Department of Transportation. I would like to thank my graduate committee for their expertise, advice, and time. The work presented in this thesis would never have been possible without the guidance and encouragement of my advisor, Dr. Steven Bartlett. The completion of this thesis owes a lot to his relentless efforts, insights and enthusiasm. It was his continued help that has made this thesis complete. I would also like to extend my thanks to Dr. Youd for his help in the selection of earthquake case histories. Finally, I am deeply grateful to my wife and sons for their understanding and support.

CHAPTER 1

INTRODUCTION

1.1 General Introduction

When subjected to earthquake loading, saturated, loose, cohesionless soils have a tendency to densify. This tendency causes the excess pore water pressure to increase as the soil fabric attempts to reach a denser configuration. This in turn results in a decrease in the effective stress of soil. As a consequence, the cohesionless deposit will lose a substantial amount of shear strength and then express a subsequent reduction in void ratio as the excess pore water pressure dissipates into the surrounding soil. The phenomenon of pore pressure build-up resulting in the severe loss of shear strength and stiffness is known as liquefaction. One of the potential types of damage caused by liquefaction is lateral spread, which involves large horizontal displacement of the surficial soil downslope or in the direction of a free face.

Liquefaction-induced ground failure and the subsequent permanent ground deformation are contributors to primary damage during large earthquakes. Lateral spread displacements can range from a few centimeters to as much as 10 m. Lateral spread deformation caused widespread damage during the 1964 Niigata, Japan earthquake (Hamada et al., 1986). During the 1964 Alaska earthquake, lateral spread deformation

caused about $80 million damage to 266 bridges and numerous sections of embankment along the Alaska Railroad and Highway (McCulloch and Bonilla, 1970; Kachadoorian, 1968). Another example of the misery that earthquake disasters bring to humankind is the lateral spread of the 1906 San Francisco earthquake that damaged several buildings, bridges, roads and pipelines (Yond and Hoose, 1978). More recently, liquefaction-induced ground failure during the 1995 Hyogoken-Nanbu earthquake caused substantial damage to lifelines, buildings and bridges along the Kobe, Japan shoreline (Hamada et al., 1996; Tokimatsu et al., 1996).

The severe damage caused by liquefaction-induced ground failure and the continued occurrence of major earthquakes in populated areas present an urgent need for geotechnical engineers to design projects safely with regards to reducing or eliminating liquefaction damage. To design earthquake-resistant systems effectively, it is necessary not only to assess the potential for and estimate the amount of liquefaction-induced ground failure, but it is also necessary to reasonably model the mechanisms that govern the ground response and deformation so that remedial steps can be evaluated. Numerical modeling can be used to understand the mechanism so that the effectiveness of the planned mitigation can be evaluated. However, most numerical methods for estimating liquefaction-induced ground response and lateral spread displacement have the disadvantage of requiring multiple parameters to explain the triggering of liquefaction, liquefaction-induced ground softening and ground response, and the highly nonlinear stress-strain postliquefaction behavior under cyclic loading. Often, the required model input parameters are difficult to obtain from in situ or laboratory testing, so that presently, advanced numerical models are not used widely in geotechnical practice. Thus, models

developed for geotechnical application should be expressed in easily obtained input parameters, yet the model should still reasonably approximate the liquefaction mechanism. There is a balance between the simplified easily-applied models that minimally satisfy the fundamental mechanisms and more complicated models that more truthfully approximate such behavior, but are difficult to apply.

Based upon the above considerations, it is important to have a fundamentally sound, yet easily applied method to predict the liquefaction-induced ground deformation that can be applied in geotechnical practice. In this thesis, the focuses will be on the development of an easily-used, soundly-based, numerical approach to estimate ground response and lateral spread displacement. This method will be calibrated using well-documented case histories from prior earthquakes, and further investigation on the role soil properties play during liquefaction and lateral spread displacement.

1.2 Problem Description and Statement

Earthquakes have a long history of affecting civilizations, yet the increasing cost of liquefaction-induced damage to modern infrastructure has not yet led to a complete understanding of liquefaction and the ground failure mechanism. Important questions are waiting for a more complete solution, of which are mainly those associated with: (1) what are the mechanisms of soil liquefaction, void ratio and pore pressure redistribution, (2) how does this process change the characteristics of the strong motion before and after liquefaction is initiated, (3) when will liquefaction be triggered and how will the subsequent deformation develop, and (4) what type and degree of ground improvement will be required to mitigate the potential for liquefaction-induced ground deformation?

Generally, the methods to predict ground response and liquefaction-induced lateral spread fall in three categories: empirical methods based on statistical analyses of case histories, total stress models based on the equivalent linear (EQL) method and nonlinear numerical analyses. Empirical methods based on statistical analyses of case histories are easily applied and can give reasonable predictions. But these methods do not account for the fundamental mechanics of liquefaction and lateral spread; hence, they have limited application to remedial design.

Total stress models based on the equivalent linear (EQL) method have been used to approximate the ground response of liquefied soils. The EQL method uses an iterative approach to approximate the nonlinear, inelastic behavior of soils. An average shear modulus and damping are used during the analysis. The method is effective for soil response calculation associated with small strain; but because the model is essentially linear and elastic, it cannot be used to model pore water generation and calculate permanent displacements because in an elastic model, the final shear strain returns to zero after cyclic loading is complete. In addition, the linearity of the EQL method can also lead to spurious resonance that would not occur in the field.

Nonlinear numerical analyses can simulate the complex response and stress-strain behavior of liquefied soil. Nonlinear models account for the nonlinear behavior of soil using various constitutive soil relationships. These relationships are implemented in various computer programs and can have different features which may include: (1) updating stress-strain relationships, (2) incorporating pore-pressure generation and flow and (3) accounting for cyclic shear modulus degradation as a function of shear strain or pore pressure generation. These advanced features allow for more realistic modeling of

soil behavior. However, nonlinear models often require soil properties and model parameters that are not readily available, obtainable or estimable in practice (Moriwaki et al., 1998).

To satisfy current geotechnical engineering practice, the present research develops a simple nonlinear numerical modeling method for evaluating liquefaction-induced lateral spread using as few input soil parameters as possible. This strategy will result in an easily implemented and verified method. Fast Lagrangian Analysis of Continua (FLAC, Itasca, 2005) will be used to implement the nonlinear methods. This program was chosen because of its versatility, which includes a custom user programming environment and the ability to adapt custom constitutive relations using either total stress or effective stress analyses.

1.3 Scope and Approach

The scope of this research is to develop a numerical model procedure, calibrate it to case histories of liquefaction-induced lateral spread, and obtain soil liquefaction properties by back analysis. Back analysis using the developed numerical model and calibration to observed deformation will provide soil liquefied properties such as dynamic residual shear strength and residual shear modulus. These values, in turn, will be further correlated with field measurements such as SPT N values, fines content and mean-grain size of the liquefied zone. The developed modeling procedure will be able to estimate the preliquefaction and postliquefaction lateral displacement by reasonably modeling the nonlinear behavior of the liquefied soil using simplified techniques. The required input soil parameters used for the model need to be kept to as few as possible

and must be easily obtained. In order for the model to predict displacement accurately, it should be calibrated using well-documented time histories and measurements.

The approach of this research includes:

1) Literature review of previous studies.
2) Development of nonlinear failure modeling procedure that approximates the liquefaction mechanism.
3) Development of the input parameters and methods for the numerical model including the cyclic stress ratio curves to describe the number of cycles to reach liquefaction, pore-water pressure generation as a function of cycling, shear modulus and shear strength degradation associated with the pore water generation.
4) Implementation of the methods within FLAC, including the set-up of the model, boundary condition considerations, time history development and deconvolution, execution of liquefaction mechanism using FLAC-embedded fish code, etc.
5) Calibration of the developed model with well-documented case histories of ground response that has been modified by liquefaction effects.
6) Application of the numerical model procedure to lateral spread case histories to back calculate the dynamic residual strengths for the various sites that match the observed deformation pattern.
7) Development of a relation to correlate the back calculated residual strengths and in situ soil parameters via regression analyses.
8) Conclusions and recommendations.

CHAPTER 2

LITERATURE REVIEW

A number of techniques for the analysis of ground deformation and slope instability have been proposed. These techniques, which including pseudostatic analysis, Newmark sliding block analysis, and nonlinear analysis approach, differ primarily in their theoretical assumption and thus the accurate prediction of the ground response and deformation.

This research proposes to develop and calibrate a numerical model procedure for predicting horizontal ground displacement generated by liquefaction-induced lateral spread. To perform the model procedure, a commercially available computer program called FLAC (Fast Lagrangian Analysis of Continua Itasca, 2005), and the program language available within FLAC, called FISH, will be used. FLAC is a two-dimensional explicit finite difference program for engineering mechanics computation. This program can simulate the behavior of structures built of soil, rock or other materials that may undergo plastic flow when their yield limit is reached. FLAC can be used to perform either uncoupled or fully coupled pore water generation analyses. In a fully coupled model, the pore water generation is coupled with changes in volumetric strain and shear modulus and strength degradation are calculated using effective stress principles. In an uncoupled model, some other scheme, like counting the number of cycles to reach

liquefaction, is used to approximate pore water pressure generation, and soil properties are reduced accordingly.

2.1 Pseudostatic Analysis

Pseudostatic analysis uses pseudostatic coefficient to present the effect of earthquake. The pseudostatic coefficient are dimensionless horizontal and vertical parameters selected to produce the weight of the failure mass to calculate the inertial force acting on the mass. Factor of safety is calculated by resolving the forces on the potential failure mass in the direction parallel to the failure surface. The limitations of pseudostatic analysis are none information provided associated with the ground failure and in the selection of pseudostatic coefficient, which is mainly closed according to engineering adjudgement. Thus this method can be unreliable for sols that build up large pore pressure or show more than 15% degradation of strength due to earthquake shaking. Based upon its limitation, the usage of this method has been reduced even though it has the advantage of simplicity, due to the development of other complicated approach.

2.2 Newmark Sliding Block Analysis

The Newmark method uses yield coefficient to replace the pseudostatic coefficient used in the pseudostatic analysis. Yield coefficient, corresponding to the yield acceleration, is the acceleration coefficient used to produce the condition in which the dynamic factor of safety equals to one. Ground deformation is accumulated when the failure plane is subjected to an acceleration that exceeds the yield acceleration. Even though this method considers the input of the earthquake motion as the main parameter to

control the accuracy, its assumption of rigid-perfectly plastic stress-strain behavior on the planar failure surface neglects the real soil's strain-softening and strain-hardening behaviors. And the assumption that only the failure planer will produce displacement while the block above and below the failure surface keep rigid also does not simulate what is occurring in the reality. Consequently, the permanently displacement of the ground will be overpredicted or underpredicted. Also neglect of the effects of rate- and displacement-depend strength will affect the accuracy of this method when large displacement has occurred due to liquefaction.

Recently, widely used computer software, QUAKE/W and SLOPE/W, use Newmark techniques to calculate the slope response and deformation. The QUAKE/W first uses equivalent linear analysis to simulate the actual nonlinear behavior and damping ratio under dynamic loading condition in order to calculate the stress time history. The calculated stress history is input to SLOPE/W to be divided by each sliding mass to obtain the acceleration which is finally integrated twice to get the slide deformation.

As discussed above, QUAKE/W and SLOPE/W neglect the soil softening due to the soil degradation in soil sear strength and modulus during large deformation caused by liquefaction. So in the Newmark technique, QUAKE/W and SLOPE/W are not applicable to cases where there is a significant potential for large loss in shear strength due to the generation of excess pore water pressure.

2.3 Nonlinear Analysis Approach

Permanent deformation and ground response can be calculated using finite element and finite difference. The advantage of the nonlinear analysis approach is that it

can consider the soil shear strength and modulus degradation under the earthquake acceleration time history for each element. Especially by applying the finite difference method, the calculation of large deformation during soil softening becomes possible without program crash. Uncoupled and coupled pore water generation techniques can also be executed in this approach.

2.3.1 Uncoupled Pore Water Generation Models

Recently, FLAC has been applied to model liquefaction-induced deformation as reported in the literature. For example, Moriwaki et al. (1998) used FLAC to predict the liquefaction deformation pattern of the Upper San Fernando Dam caused by the 1971 San Fernando earthquake. This study coupled the elastic-perfectly-plastic model in FLAC with initial equivalent linear response, and used the residual strength from case histories (Seed et al., 1988) to model the embankment dam deformation caused by this earthquake. In this study, the shear modulus of the hydraulic fill material was degraded using a FISH model that calculated the excess pore water pressure as a function of the number of earthquake cycles to reach liquefaction. The loss in soil shear strength from excess pore water pressure generation was modeled using the relationships: (1) cyclic stress ratio versus the number of cycles to reach initial liquefaction for a given confining pressure; (2) confining pressure dependency of a relationship using a factor K_σ, as described by Seed and Harder (1990); and (3) increase in pore pressure ratio as a function of the number of cycles applied to the soil elements divided by the number of cycles required to reach initial liquefaction. The input motion used for the evaluation was the modified Pacoima acceleration scaled to 0.6g, applied at the base of the analyzed cross section.

This acceleration record was considered to represent reasonably the shaking at the site without liquefaction. Moriwaki et al. showed that the predicted deformation pattern in the dam from FLAC was consistent with the observed deformation pattern, even though somewhat larger deformations were predicted. The advantage of this model is that it coupled shear modulus degradation with the pore water pressure generation. The post-liquefaction shear strength of the hydraulic fill was based on the work on the Lower San Fernando Dam combined with the evaluation of blow count data for the Upper San Fernando Dam reported in Seed et al. (Moriwaki et al., 1998; Seed et al., 1973).

However, the work of Moriwaki et al. (1998) ignored any shear strength degradation prior to liquefaction induced by the generation of pore water pressure. This is a severe simplification, because shear strength degradation is a primary effect resulting from pore water generation and occurs prior to complete liquefaction and such degradation does produce deformation. Thus, neglecting this effect may cause less accurate predictions of the resulting ground deformation because preliquefaction strain is not addressed by this approach.

Beaty and Byrne (1999) have also used a simplified approach to model pore water generation and its effects on model properties during liquefaction. Like the Moriwaki et al. (1998) model, this approach estimates the degree of pore water pressure generation by counting the number of applied shear stress cycles and comparing this to the total number of cycles required for liquefaction. However, for simplicity's sake, any pore water increase prior to liquefaction was not considered by Beaty and Byrne (1999); there is no reduction of the shear modulus or shear strength prior to liquefaction in their model. Like Moriwaki et al. (1998), postliquefaction strength and stiffness losses are considered by

Beaty and Byrne (1999). The reduced shear modulus and residual strength are used in the model at the instant when liquefaction is initiated. In this approach, a hydrostatic state or isotropic state of stress is imposed in the FLAC model by equating the normal stresses (i.e., setting σ_{xx} equal to σ_{yy}) whenever a soil element undergoes a stress reversal.

Beaty and Byrne (1999) used their approach to estimate the deformation of the Upper San Fernando Dam during the 1971 San Fernando earthquake. Even though the Beaty and Byrne (1999) approach involved several simplifications, such as the immediate reduction of shear modulus and shear strength upon reaching liquefaction, their prediction was reasonable. Thus, it appears that this approach is sufficiently accurate to reproduce the first order effects of liquefaction and deformation. In addition, the method can be easily calibrated with case histories of lateral spread because of its simplicity and relatively few input parameters.

2.3.2 Fully Coupled Pore Water Generation Models

Fully coupled models are effective stress models where the decrease in effective stress is coupled with a pore water generation scheme and with the subsequent loss of shear strength and stiffness. Byrne (1991), Puebla et al. (1997), Beaty and Byrne (1998) and Atigh and Byrne (2004) have applied FLAC to predict the ground deformation resulting from liquefaction using fully coupled models. In these studies, a fully coupled effective stress model with a pore water generation scheme developed by Byrne (1991) is implemented using FLAC via FISH code. In the so-called UBCSAND model, the tangent plastic shear modulus is evaluated using a hyperbolic relationship associated with the stress ratio that develops on the maximum shear stress plane at failure. Yield loci are

assumed to be a radial line of constant stress ratio. These loci and the resulting direction of the plastic strain are consistent with laboratory observations in that at low stress ratios, significant shear-induced plastic compaction occurs; whereas no compaction is predicted at stress ratios corresponding to the constant volume friction angle. For stress ratios greater than this angle, shear-induced plastic expansion or dilation is predicted. Unloading in the model is assumed to be elastic; whereas reloading induces plastic response but with a stiffened plastic shear modulus. This model was first calibrated to cyclic simple shear tests performed on a centrifuge machine using Nevada sand by Byrne and his colleagues. Puebla et al. (1997), Beaty and Byrne (1998), Byrne (1995, 2000) and Atigh and Byrne (2004) used this approach to predict liquefaction-induced ground deformation for specific cases and have obtained reasonable results.

The default fully coupled pore water generation model implemented in FLAC is named the Finn model (Itasca, 2005), which uses a standard Mohr-Coulomb plasticity model; but the user, as required, may modify the constitutive relation. This model, found to be in close agreement with the characteristic behavior of sand observed in laboratory element testing (Itasca, 2005), simulates the stress-strain behavior of soil under cyclic loading for drained or undrained conditions by using an elastic-plastic relationship in which the shear modulus is separated into elastic and plastic components. The plastic volumetric strain increment is computed using plastic shear strain increments and the dilation angle calculated from the constant volume friction angle and the developed friction angle. For undrained conditions, the volumetric strain, which is comprised of elastic and plastic components, is assumed constant. Thus, any elastic volumetric strain decrease will be equal to the plastic volumetric strain increase. The effective stress is

calculated from the decreases in the elastic volumetric strain. As the effective stress decreases to zero, complete liquefaction of the sand is assumed.

The pore water generation scheme used in the Finn model originated from original work by Martin et al. (1975) and was later simplified by Byrne (1991). Martin et al. (1975) presented quantitative data in their landmark paper that showed the amount of compaction per cycle is proportional to the cyclic shear strain amplitude, and that the accumulated volume compaction is independent of the normal effective stress. They also showed that the pore pressure generated per cycle is dependent on the plastic volumetric strain, the rebound modulus of the soil and the stiffness of the pore fluid. Later, Byrne (1991) simplified the 4-parameter Martin et al. (1975) model to two parameters. The Finn model's implementation of the Byrne (1991) model uses constants related to relative density of the sand and correlated with SPT $(N_1)_{60}$ values. This model is appealing for back calculation and calibration, because it only requires one parameter, which could be obtained from back calculation.

Both the Byrne (1991) and Finn models (Itasca, 2005) have been used to predict liquefaction-induced ground deformation for specific cases and have obtained reasonable results; however, like many models, they have not been calibrated to an extensive dataset of cases of liquefaction-induced lateral spread.

Most recently, Cooke (2000) has used FLAC to perform a remedial design of lateral spread at a hypothetical bridge abutment. Cooke performed a nonlinear, coupled effective stress analysis, employing a nonlinear shear stress-strain relation of Pyke (1979) with the pore pressure generation model of Byrne (1991). Pyke's work (1979) showed how to calculate a reduced tangent shear modulus based upon the magnitude of the

incurred shear strain. The reduced shear modulus was evaluated using a hyperbolic type stress-strain formulation that was applicable to the simple shear case. Cooke (2000) used the Byrne (1991) model to estimate the incremental volumetric strain that occurs with each cycle.

In performing his analyses, Cooke (2000) made the following assumptions: (1) any variation of liquefaction resistance with changes in the effective confining stresses was not included; (2) the strength of cohesionless soil was based solely on the initial effective friction angle and the calculated effective stress at each time step (this does not consider the development of residual strength (i.e., friction angle) at large strains, even for a fully liquefied soil) and (3) the effect of initial static shear stress on the pore water pressure generation and liquefaction resistance of the soil was not incorporated.

Cooke (2000) calibrated his model using centrifuge test results and one case study of lateral spreading at the Wildlife, California site from the 1987 Superstition Hills, California earthquake. Cooke found that this coupled nonlinear analysis method generally performed better than results obtained with the other soil models as explained before. However, other than the Wildlife site, the FLAC model parameters used by Cooke (2000) were not verified by an extensive comparison with the case history dataset of lateral spread sites.

2.3.3 Advanced Constitutive Models

Lastly, a bounding surface hypoplasticity model (Wang and Makdisi, 1999; Wang et al., 1990) has been applied to predict the liquefy on performance of the Port of Oakland (Wang et al., 2001). Eight soil parameters are required to perform the fully-

coupled effective stress analyses of a cohesionless soil using this model. The model parameters are determined from basic soil properties used for the equivalent linear analysis and from interpretation of monotonic and cyclic laboratory tests. The cyclic strength parameters are calibrated with empirical liquefaction curves based on standard penetration test (SPT) data. The results of fully coupled analysis provide time histories of pore water pressure, stress, strain and ground displacement during earthquake loading, as well as dissipation and settlement after the end of earthquake shaking. This surface hypoplasticity model attempts to closely replicate the liquefaction mechanism using eight soil parameters; however, some of the parameters are difficult to estimate from standard geotechnical testing. Thus, the application of the bounding surface hypoplasticity model has not been widely used in geotechnical engineering; nor has it been calibrated with cases of lateral spreading at liquefied sites.

2.4 Summary of Nonlinear Methods

Overall, nonlinear analysis methods are capable of modeling liquefaction-caused ground failure to varying degrees of sophistication. They also can, when calibrated, reproduce the observed horizontal ground displacement pattern associated with earthquake-induced liquefaction, as shown by some of the previously discussed research. However, the modeling approaches vary significantly in their complexity and the number of parameters required for completing the analysis; hence from a calibration viewpoint, some models are more preferable than others. Considering the research results by others and current geotechnical engineering requirement, this research is to develop an approach

that models liquefaction and lateral spread, but has sufficiently few parameters, so that it can be calibrated to case histories of liquefaction-induced ground failure.

2.5 Research Approach

The developed model procedure needs to be based on sound modeling principles; but it also needs to be relatively simple, so that it can be calibrated with field data and implemented. In short, the model procedure should be sufficiently developed to capture first order effects and their contribution to liquefaction-induced displacement; yet the back-calculated model parameters must be simple enough so as to be correlated with typical soil and profile factors such as effective vertical stress, soil layer, thickness, mean-grain size and fines content of the liquefied zone, all of which have been shown to influence lateral spread displacement (Bartlett, 1991). Lastly, the calibrated model procedure should be straightforward for application in engineering practice without the requirement of highly specialized geotechnical laboratory testing. Thus, this research will focus on the development of a nonlinear numerical modeling approach and calibrating the model parameters to cases of liquefaction-induced ground failure and their associated geotechnical data.

The scope of this research is to develop and implement a numerical modeling procedure for estimating horizontal displacement from liquefaction and to calibrate the modeling procedure to cases of lateral spread ground failure, so that it can be applied for engineering evaluations. Based on review of the previous approaches, it appears that a noncoupled model has the best chance of meeting the above goals. In a noncoupled model, the pore water pressure generation is usually estimated from the number of cycles

to reach liquefaction and the soil properties (i.e., shear modulus and shear strength) are subsequently degraded as a function of the estimated pore pressure generation.

The nonlinear uncoupled model will be developed within FLAC using FISH code. Calibration of the model procedure and required parameters will be done by matching the FLAC estimated horizontal displacement to the average horizontal displacement for the respective case history site. The calibrated model parameters in turn will be correlated using multiple linear regression analysis with standard geotechnical and soil properties (e.g., SPT $(N_1)_{60}$ values, vertical effective stress, fines content and mean grain size of the liquefied layer) measured at each case history site. Ultimately, it is hoped that the calibrated model and the supporting correlations with geotechnical properties can be used to predict liquefaction-induced lateral spread displacements at potentially liquefiable sites. The modeling procedure can also be used to design the remedial measures at potentially liquefiable sites. To successfully do this, the input soil parameters in the numerical model procedure need to be as few as possible and/or they should be easily obtained from standard tests.

The approach of this research includes:

1) Literature review of previous modeling approaches.

2) Development of nonlinear failure model procedure that approximates the liquefaction mechanism and postliquefaction deformation.

3) Development of input parameters for the numerical model, including the cyclic stress ratio (CSR) curves, and the shear modulus and shear strength decrease associated with the pore water generation.

4) Implementation of the model with FLAC using FISH code, including the set-up of model, boundary condition consideration, time history development and deconvolution, and execution of liquefaction mechanism.

5) Calibration of the developed model procedure and parameters with case histories of liquefaction and lateral spread.

6) Application of the numerical model procedure to case histories to back calculate the residual strengths according to lateral spread deformation.

7) Develop statistical relations between the calibrated model parameters (i.e., residual strength and shear modulus) and case history geotechnical data.

8) Provide conclusions and recommendations for implementation of the modeling approach and the developed statistical relations.

CHAPTER 3

NUMERICAL MODEL PROCEDURE DESIGN

3.1 Introduction

Under loading, an elastic stress-strain relationship governs the deformation of the soil when it experiences initial loading and small strain. For sandy materials, this initial elastic range is very small, e.g., generally less than 0.001 percent (Vucetic et al., 1991). With increased loading, plastic flow dominates the stress-strain relationship, in which stresses would not increase linearly with strain. Some studies have assumed perfect plastic flow after elastic loading, which means that the shear resistance does not change with the increase of effective normal stress. For real soils, the additional strain after peak loading will almost always be associated with either an increase or decrease of effective stress, which is defined as strain-hardening or strain-softening.

For monotonic loading on dense saturated sands, strain hardening resulting from an attempted dilation of the soil fabric greatly limits the amount of postpeak cumulative deformation. Figure 3.1 shows the change of shear strength (q) and extra pore water pressure (Δu) with shear strain (ε). Large damaging deformation seldom happens for dense sands due to their dilative response and the corresponding increase in effective stress that causes an increase in shear strength, as shown by Curve B in Figure 3.1.

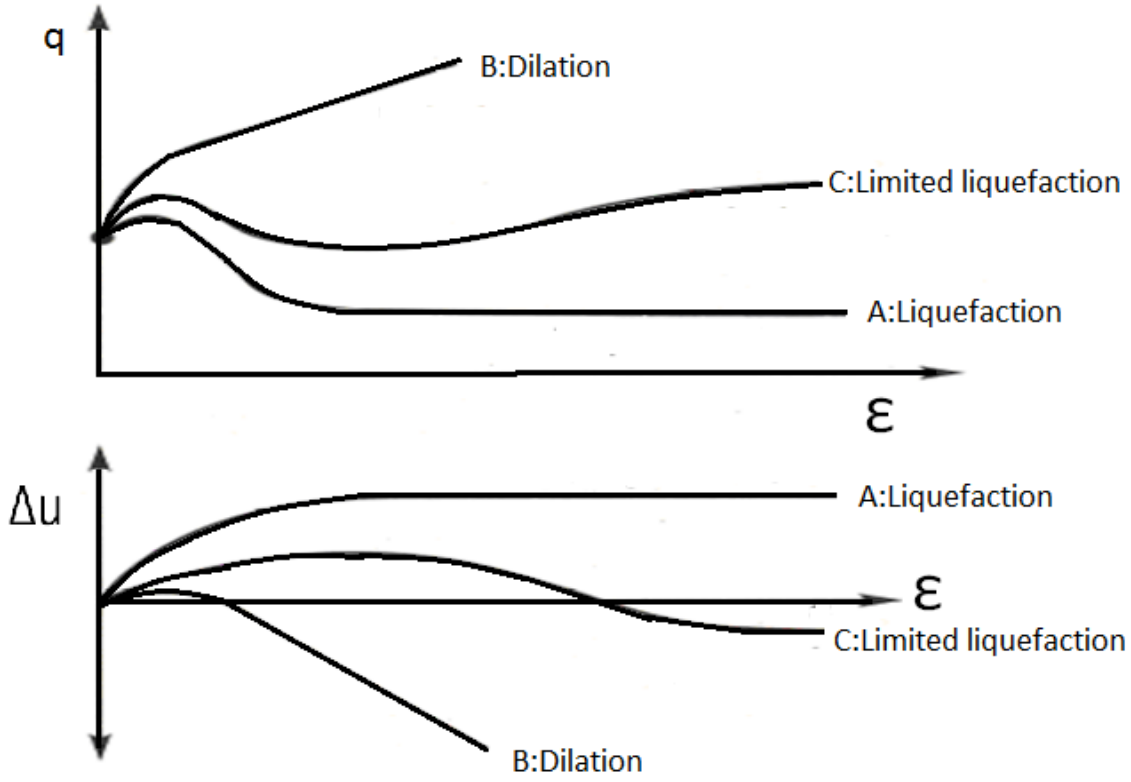


Figure 3.1. Liquefaction, limited liquefaction, and dilation in monotonic loading tests for loose sand (A), dense sand (B), and medium dense sand (C).

In contrast, for the case of monotonic loading on loose, saturated sands, strain softening behavior dominates the postpeak loading behavior as shown by Curve A in Figure 3.1. For these sands, the elastic loading part is only present at the very beginning of the load application. Their postpeak behavior shows a pronounced strain-softening phase. Strain softening is caused by an attempted contraction of the soil fabric that produces a decrease in effective stress and shear strength resulting from the excess pore water generation in undrained conditions. Thus, it is reasonable to assume that complete liquefaction happens at the end of the strain-softening process where the undrained shear strength achieves its lowest value. Such a value is often called the "residual" or "steady

state" shear strength. The residual strength is characterized by continuing shear strain at a constant volume, which implies no further change in the void ratio of the soil or the corresponding state of effective stress.

Most medium dense sands exhibit an intermediate behavior (Figure 3.1. – Curve C), in which initial contraction of the soil fabric is followed by subsequent dilation. This phase transitioning behavior has been termed "limited" liquefaction (Castro, 1969).

For cyclic loading such as earthquake loading, during the loading period, soil experiences the same or similar behavior as monotonic loaded soil. Softening and hardening behavior also depend upon sand relative density, effective confining stress, stress history and other factors. The difference of sand behavior under cyclic loading is its response to unloading with a much higher shear modulus (Beaty and Byrne, 1999). These sites that undergo cyclic loading are also generally restricted to two groups of behaviors: sands with and without significant lateral spread potential. Curves A and C represent the loading behavior of the former and Curve B represents the loading behavior of the latter. For sands with $(N_1)_{60}$ values less than or equal to 15, the stress-strain relation for the loading phase with lateral spread potential soil (curves A and C) is comprised of three phases: (1) an early elastic phase, (2) intermediate strain-softening phase and (3) residual shear strength phase fully including liquefaction and limited liquefaction cases.

It should also be noted that soils with behavior A can also lead to flow failure (i.e., very large displacement), if the initial static shear stress acting on the soil mass is significantly higher than the residual or steady-state strength; such a case may exist in an embankment or a steeper slope.

For sands with $(N_1)_{60}$ values above 15, the behavior B dominates. The loading process of saturated sand without significant lateral spread potential will be assumed to consist of two phases: (1) elastic phase and (2) strain-hardening phase. Thus for these sands, a different constitutive model will be used to represent its stress-strain behavior.

This research, while separating soil into two categories, dense soil without liquefaction potential (soil B) and loose soil with liquefaction potential (soil A and C), will also consider the unloading effect of the liquefaction potential sand under the loading of cyclic motion, as discussed in the following section.

3.2 Noncoupled Constitutive Model Design

Either drained or undrained strength parameters can be used in the FLAC model and the shear strength is calculated from the Mohr-Coulomb model and compared with the current stress state to judge if failure has occurred.

Prior to reaching the Mohr-Coulomb failure state, elastic loading and unloading will govern the soil behavior and deformation. When failure is reached, plastic flow will produce larger deformation whose incremental part will be calculated in FLAC using Hooke's law as expressed in terms of principal stress and strain. A nonassociated flow law is used for the shear flow rule and an associated law for tensile flow. The principal stresses and principal strain directions are evaluated from the stress tensor components corresponding to the principal strain increments. In addition, the loading is kept constant at the failure state for the Mohr-Coulomb model.

For soil without liquefaction potential, Soil Behavior B, the failure state in the Mohr-Coulomb model is reached when the state of stress condition reaches the failure

envelope as defined by equation (3.1) for drained conditions. Drained conditions will be used for soils where there is significant dilation in the soil fabric to relieve any excess pore water pressure.

$$\tau' = c' + \sigma_n' \tan\phi' \qquad (3.1)$$

where: τ' is the drained shear strength, c′ is the drained cohesion intercept, which is nearly zero for most sands, ϕ' is the effective internal angle of friction, and σ_n' is the normal effective stress on the potential failure plane.

For simplicity's sake, the strain-hardening phase for behavior B soils (i.e., soils with $(N_1)_{60}$ values $\geq$ 15) will be taken into account by the combination of linear elastic deformation and any plastic flow deformation using the initial drained friction angle value for the Mohr-Coulomb failure criterion. (Note that the drained friction angle is often used in engineering applications to represent a lower bound for the undrained strength for dilative soils undergoing dilation during cyclic shear.)

Even without liquefaction, there is a reduction in shear modulus and an increase in damping as a function of shear strain during earthquake cycling. This will be accounted for in soil with behavior B using the hysteretic model included in FLAC, as discussed in the next section.

For soils that undergo liquefaction and significant deformation (i.e., soil behaviors represented by curves A and C), undrained conditions will be assumed throughout the entire loading and the shear strength from the Mohr-Coulomb model is:

$$\tau = c = s_{ur} \tag{3.2}$$

where: s_{ur} is the undrained shear strength. For behavior A and C soils, an undrained shear strength, s_{ur}, is incorporated in the model (i.e., σ = 0, c = s_{ur}) to represent the postliquefaction condition. Initially, before pore water pressure has been generated, the soil's s_{ur} value will be set equal to that calculated from the drained friction angle and the initial effective stress in the soil.

In the proposed approach, loss of shear strength and shear stiffness in the liquefied soil will not be coupled with volumetric strain, as is done in a fully-coupled effective stress liquefaction model. Instead, the shear modulus and shear strength of the liquefied soil will be incrementally decreased to represent the softening in the soil fabric associated with the pore water pressure generation function.

As earthquake cycling occurs in the model, pore water generation and liquefaction will be accounted for by using shear modulus degradation and shear strength reduction functions that are related to the pore water generation function. For each time step, the model will track the number of stress cycles, N, and compare it to the number of stress cycles required to reach liquefaction, N_L. The ratio of N/N_L will then be used to calculate the excess pore pressure ratio using a relation published by De Alba et al. (1975).

$$r_u = \frac{1}{2} + \frac{1}{\pi}\sin^{-1}\left[2\left(\frac{N}{N_L}\right)^{1/\alpha} - 1\right] \tag{3.3}$$

where α is a function of the soil properties and test conditions. When r_u equals one, then full liquefaction is assumed. This process is further explained in Chapter 4.

Before complete liquefaction is reached (i.e., r_u=1), the undrained shear strength and shear modulus will be degraded appropriately with pore water generation using relations presented later. Upon reaching liquefaction, s_u will be represented by a residual undrained shear strength s_{ur}, which will be held constant during the subsequent post-liquefaction deformation calculations. However, it is noted that some dilation does occur for behavior C soils (Kramer, 1996), which will be represented by an average s_{ur} in the proposed model.

The dynamic response modeling for soil behaviors B, A and C will be discussed in the following sections, respectively.

3.2.1 Dynamic Modeling of Behavior B Soils

Not all soils found in the subsurface profile will be subjected to liquefaction and lateral spread; thus for these soils, a simplified method is needed to represent their dynamic behavior. For behavior B soils, a reduction in shear modulus and an increase in damping are usually expressed as a function of the cyclic shear strain. This strain-dependent behavior can be represented in FLAC using FLAC's hysteretic model (FLAC v. 5.0; Itasca, 2005). In short, this model incorporates a strain-dependent damping ratio and secant modulus functions to represent the soil's nonlinearity. The application of the hysteretic functions allows for direct comparisons between the fully nonlinear methods formulated in FLAC (Itasca, 2005) and the equivalent-linear (EQL) method of SHAKE91 (Idriss and Sun, 1992). FLAC's hysteretic model can be calibrated to existing laboratory test data, or to published shear modulus reduction and damping curves used in the EQL

method, which formulates the shear modulus and damping as equivalent linear values that are compatible to the average strain level.

The SHAKE91 formulation of damping can be shown to be equivalent to hysteretic damping at the corresponding strain level (Kramer, 1996). The FLAC default hysteretic model uses parameters of L1=-3.325 and L2=0.823, which are the values of logarithmic strain, to produce a reasonable fit with Seed and Idriss data for average sand with low strain (Figure 3.2 and Figure 3.3). For behavior B soils, the earthquake-induced shear strains are often less than 0.3%. Thus, damping is generally about 20% or less. The FLAC default hysteretic model shows good agreement between the FLAC simulations and the SHAKE91 results, as shown in Figure 3.2 and Figure 3.3, for shear strain less than about 0.3% (Itasca, 2005). This research will use FLAC default hysteretic model parameters for behavior B soils.

3.2.2 Dynamic Modeling of Behavior A and C Soils

For soils with lateral spread potential, FLAC's hysteretic model is not appropriate due to the soil's large shear strain and nonlinearity. Thus, FLAC's hysteretic model will not be used for these soils. Instead, the increased softening of A and C soils will be accounted for by adjusting the shear modulus at each time step according to a pre-determined function. This adjustment will be done by calculating r_u at each time step. The cyclic stress ratio (CSR) curve from NCEER (Youd et al., 2001) will be used to calculate the required number of cycles to reach liquefaction, N_L.

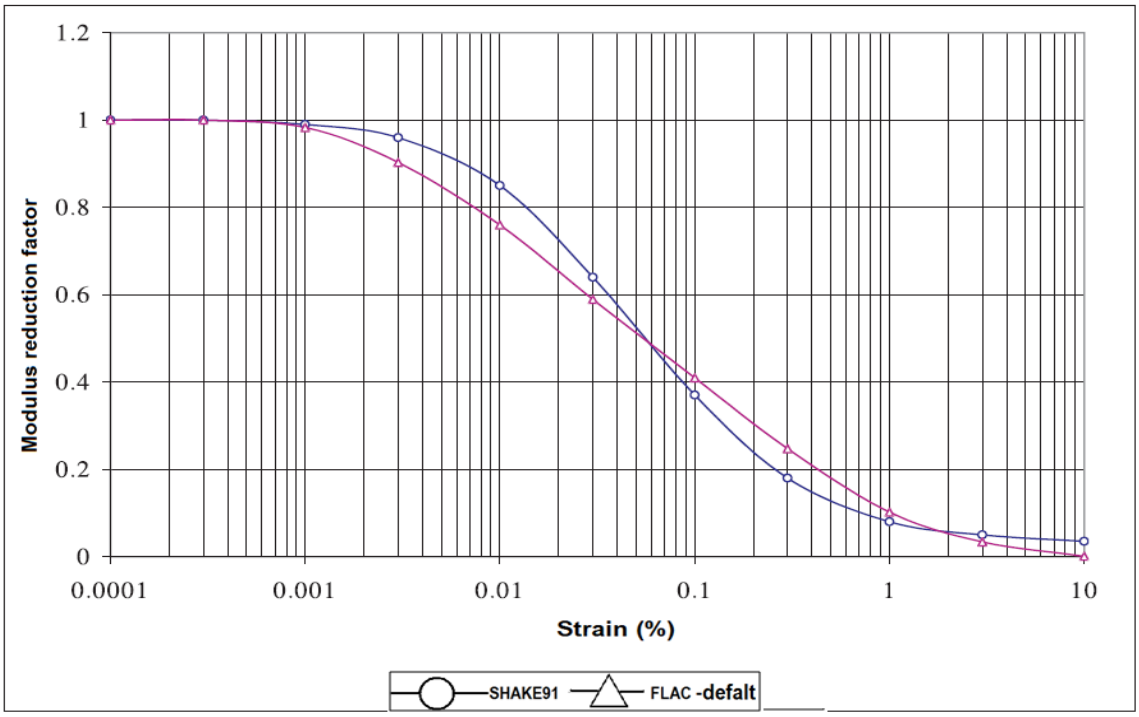


Figure 3.2. Secant modulus values vs. cyclic shear strain
from FLAC and SHAKE91, Seed & Idriss 1971 (after Itasca, 2005)

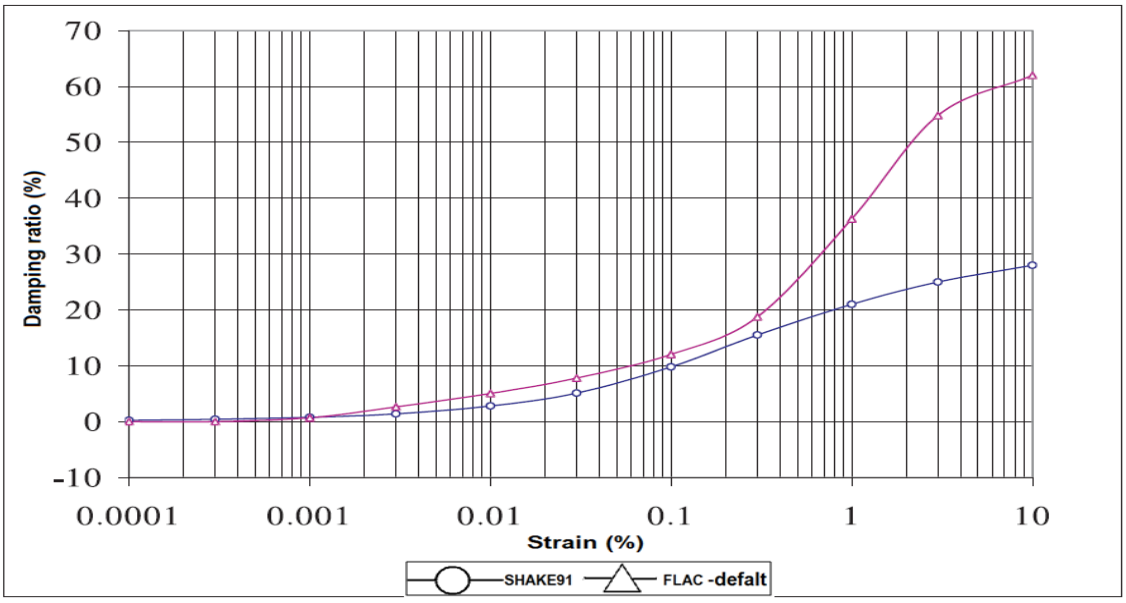


Figure 3.3. Damping values vs. cyclic shear strain
from FLAC and SHAKE91, Seed & Idriss 1971 (after Itasca, 2005)

This curve was developed from case history data and represents the cyclic stress required to initiate liquefaction. The soil's resistance to liquefaction, as expressed by the NCEER curve, is defined by the $(N_1)_{60}$ value and fines content of the potentially liquefiable soil. FISH code has been written to calculate r_u by tracking the stress cycles N and comparing it with the required liquefaction threshold cyclic number N_L. The development of the excess pore water model and the calculation of r_u as a function of N/N_L is explained further in Sections 3.2.2.4 and 3.2.2.5.

3.2.2.1 Initial and Degraded Shear Modulus

Before significant pore water build up is achieved, the traditional relationship among the shear modulus $G_{\max}$, vertical effective stress (σ'_{v0}) and adjusted blow count $(N_1)_{60}$ is used (Seed, 1986) to calculate the shear modulus:

$$G_{\max} = 16500(N_1)_{60}^{1/3}(\sigma'_{v0})^{1/2}\ psf \qquad (3.5)$$

As the pore water pressure builds up with subsequent time steps, as calculated by the FISH code, the soil's behavior is governed by the decrease of the effective stress resulting from excess pore water pressure generation. In reality, this behavior is related to the soil's attempt to change volume during cycling in an undrained loading condition; but such behavior cannot be estimated directly from using a noncoupled model. Thus, the resulting reduction in the soil's shear modulus will be accounted for and estimated using an approach originally proposed by Finn et al. (1978):

$$G = (G_{\max})_0 \left(\frac{\sigma'_{vo} - u_e}{\sigma'_{vo}} \right)^{1/2} \quad (3.6)$$

where: $(G_{\max})_0$ is the initial, low strain shear modulus, σ'_{vo} is the vertical effective stress, and u_e is the generated excess pore water pressure (i.e., pore water pressure above hydrostatic). The value of $(G_{\max})_0$ is a function of the density of the soil and its stiffness, as measured by the soil's shear wave velocity.

However, later Moriwaki et al. (1988) adjusted equation (3.6) to the following format so that the reduction of the shear modulus can be taken into account prior to liquefaction:

$$G = (G_{ini})(1 - r_u)^{1/2} + G_{residual} \quad (3.7)$$

where: G_{ini} is the initial shear modulus before liquefaction occurs, r_u is the excess pore water generation ratio and $G_{residual}$ is the residual shear modulus once complete liquefaction is achieved. Moriwaki et al. (1998) assumed that G_{ini} is approximated by G_{max} divided by 2 to model the initial equivalent linear state of soil and used equation (3.7) to calculate the degree of shear modulus degradation as liquefaction progresses.

However, after conversations with Moriwaki et al. (2004), this research, to model the nonlinear state of soil, modifies equation (3.7) as:

$$G = (G_{\max} - G_{residual})(1 - r_u)^{1/2} + G_{residual} \quad (3.8)$$

where: G_{max} is defined previously. The value of $G_{residual}$ is a large-strain shear modulus that varies about 3% of G_{max} at shear strains ranging from 3 to 10% (Figure 3.2). Thus, equation (3.8) will be used in this research to account for the gradual degradation of shear modulus with the generation of pore water pressure.

Upon reaching complete liquefaction (i.e., $r_u = 1$), a residual shear modulus will be used until the end of the earthquake loading.

3.2.2.2 Damping

No equation is required to calculate damping as a function of r_u. This is because in a nonlinear model, the damping is a function of hysteretic behavior. Hence, as the shear modulus is degraded at each time step, this changes the shape and area of the stress-strain loop, hence increasing hysteretic damping. Thus, damping is automatically accounted for by the shape and area within the hysteresis loop and does not need to be externally imposed on the model. However, Rayleigh damping of 0.5% will also be used in order to satisfy numerical stability. This small amount of Rayleigh damping will not influence the modeling result because even Rayleigh damping of 5% would not make significant change on the motion compared with no Rayleigh damping (Itasca, 2005).

When Rayleigh damping is used, the dominant wave frequency needs to be calculated first using FISH code so that the Rayleigh damping frequency parameter is correctly used to damp the frequency-dominate wave.

3.2.2.3 Bulk Modulus

Generally, it is assumed that liquefaction occurs during undrained loading and the time to achieve the liquefaction state is short, so it is reasonable to use the undrained bulk modulus to deal with liquefaction period for potential liquefiable soils. In the fully coupled model, the bulk modulus of water should be used to represent the soil's undrained bulk modulus to account for the fully undrained condition. However, for this uncoupled model, residual shear strength and shear modulus are degenerated as the function of pore water generation, thus the bulk modulus change is automatically taken into account by the FLAC model with the consideration of shear modulus degradation. The Poisson's ratio of soil is assumed as 0.3 and keeps constant.

3.2.2.4 Shear Strength Reduction and Residual Shear Strength

As r_u increases with earthquake cycling, the soil's shear strength degrades due to a decrease in effective stress. Finn et al. (1978) suggested a linear relationship between shear strength reduction and pore water generation, as shown in the following equation (3.9):

$$\tau = (\tau_{\max})_0 \left(\frac{\sigma'_{vo} - u_e}{\sigma'_{vo}} \right) \tag{3.9}$$

where: $(\tau_{\max})_0$ is the shear strength corresponding to zero excess pore water pressure, σ'_{vo} is the vertical effective stress, and u_e is the earthquake generated excess pore water

pressure. Prior to pore water generation, values of $(\tau_{\max})_0$ can be estimated from equation (3.1) by using the drained friction angle and calculating the vertical effective stress using hydrostatic pore water conditions.

As explained previously, the softening of saturated, loose to medium dense sand under undrained cyclic loading is an important characteristic of liquefaction and induces the subsequent accumulation of permanent strain and displacement. To account for the shear strength reduction prior to liquefaction, this research modifies equation (3.9) to the following equation.

$$\tau = (\tau_{\max} - \tau_{residual})\,(1 - r_u) + \tau_{residual} \tag{3.10}$$

where: $\tau_{resiudal}$ is the fully developed residual shear strength s_{ur}, and r_u is the excess pore water pressure ratio. FISH code has been developed to track the increase in r_u and calculate the corresponding shear strength reduction.

Ultimately, the value of $\tau_{residual}$ for a given case history is unknown and will be estimated by back-calculation using trial and error until a $\tau_{residual}$ value is found that produces the measured horizontal displacement for the respective lateral spread site.

Equations 3.8 and 3.10 are combined and the instantaneous shear strain is calculated using the reduction shear modulus and shear strength. In this example, shear modulus and shear strength are decreased with pore water generation as independent parameters. The calculated shear strain is shown to increase with the increasing pore water generation, as shown in Figure 3.4.

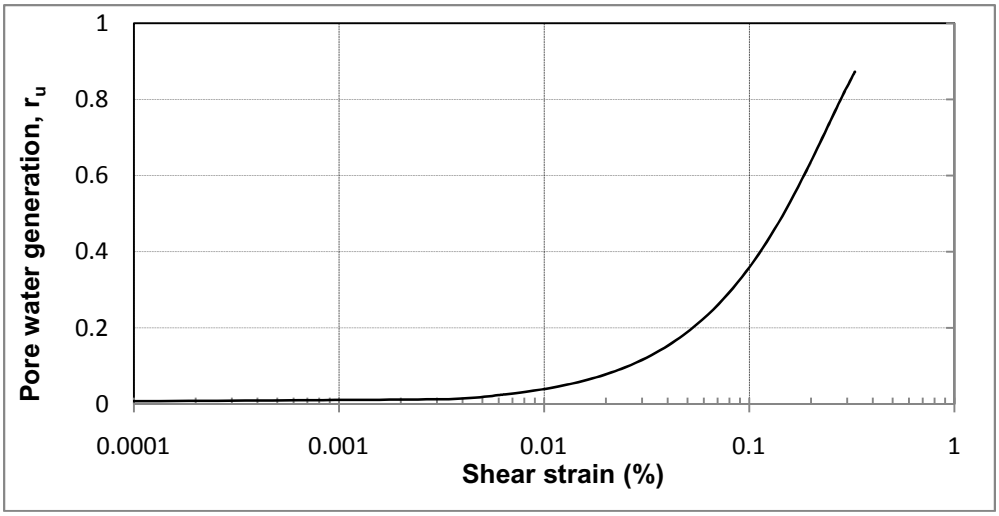


Figure 3.4. Shear strain increase with pore water generation

The trend of Figure 3.4 and its comparison with laboratory data shown in Figure 3.5 (Hazırbaba**,** 2005; Dobry et al., 1982) show the appropriateness of the calculated relationship between shear strain and pore water generation. Because this relationship is derived from the shear modulus and shear strength reduction equations 3.8 and 3.10, this validates that these equations are appropriate.

3.2.2.5 Shear Stress Tracking

In order to calculate pore water generation, the shear stress induced by an acceleration time history needs to be calculated. For sloping ground conditions, a static shear stress exists in the soil profile that moves the loading and unloading threshold from zero shear stress to a nonzero stress level (Figure 3.6). For this case, loading and unloading cycles occur each time when the shear stress reaches its local maximum or minimum value above or below that static shear stress line, respectively.

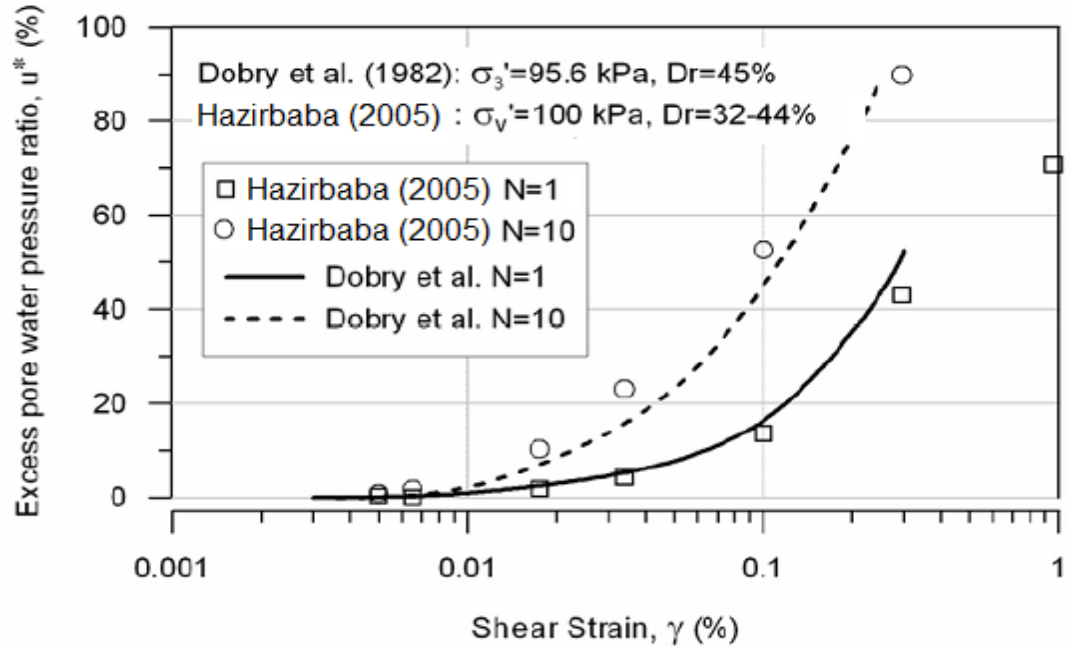


Figure 3.5. Laboratory measurements of pore water generation vs. shear strain by Hazirbaba (2005)

This research uses the Beaty and Byrne (1999) technique (Figure 3.6) to calculate the initial static shear stress and track developing shear stress's maximum and minimum values. To do this, loading and unloading indicator variables are returned when the FISH code finds these maximum and minimum values. Then, the appropriate loading and unloading shear moduli are assigned according to these loading/unloading indicators.

3.2.2.6 Modeling of Hysteretic Behavior and Stress Reversals

In order to track shear stress cycles induced by cyclic loading, the constitutive model should approximately replicate the hysteretic behavior of the soil prior to and after liquefaction. As observed in experimental data (Ishihara and Okada 1982), the amount of strain developing during cyclic unloading depends on the magnitude of stress ratio where the unloading takes place.

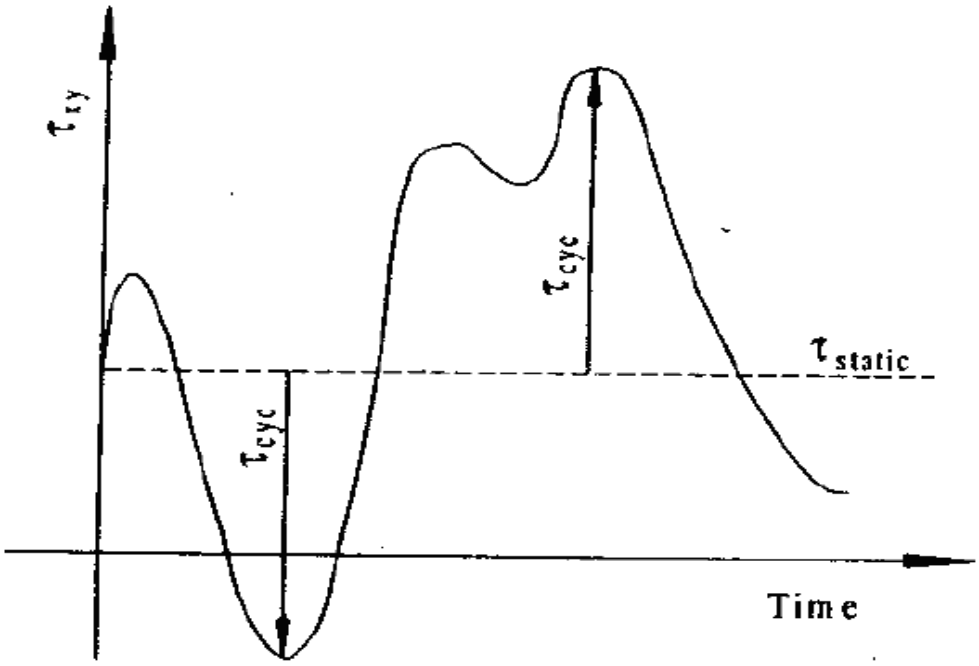


Figure 3.6. Loading and unloading scheme for counting stress cycles

However, in developing a model for hysteretic behavior of the soil, this research will use, for simplicity's sake, a constant unloading shear modulus that does not consider the magnitude of the stress ratio in determining the slope of the unloading curve (Figure 3.7). However, the pre- and postliquefaction loading and unloading moduli will be modified as described below.

Prior to liquefaction ($r_u < 1$), the unloading shear modulus will be set equal to G_{max} and the loading modulus will be calculated from equation (3.7). This is a variation from the approach used by Beaty and Byrne (1999), as shown in Figure 3.7, who set the pre-liquefaction unloading modulus equal to the preliquefaction loading modulus.

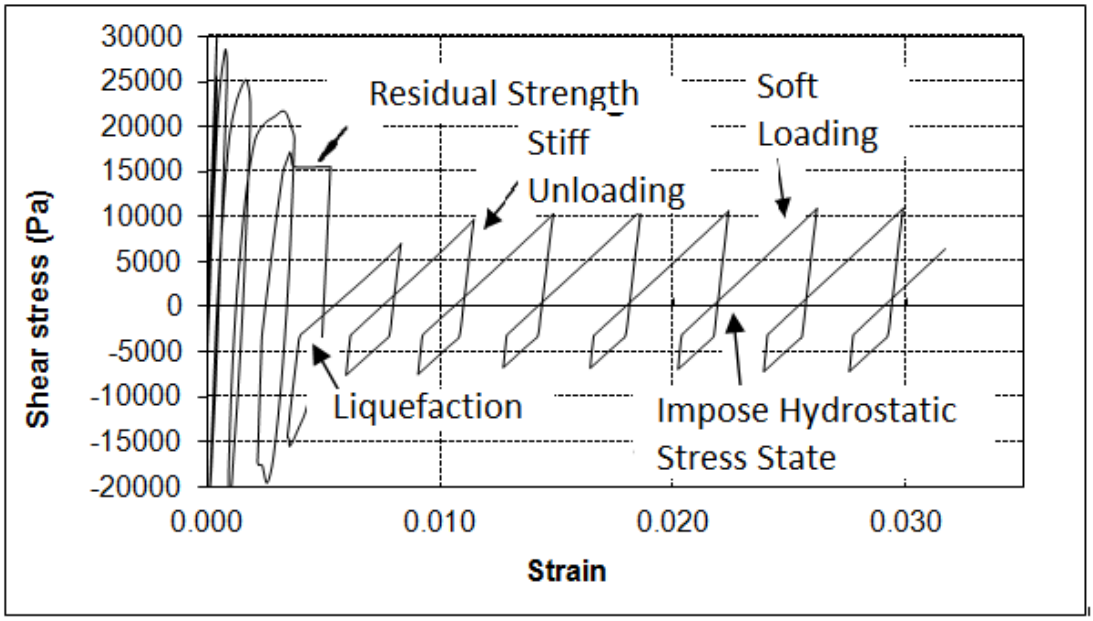


Figure 3.7. Simplified postliquefaction stress-strain behavior

However, this research allows for hysteretic behavior prior to liquefaction, which more closely models the true preliquefaction behavior because: (1) shear modulus is degraded and not kept constant, as done by Beaty and Byrne (1999) and (2) the loading and unloading moduli are different, which produces hysteretic behavior and damping.

For sands that have achieved liquefaction (i.e., $r_u = 1$), the slope of the softened reloading curve is significantly less than the stiffer unloading curve and this in turn produces permanent strain that occurs below the yield strength (i.e., residual strength) (Figure 3. 7). Upon reaching liquefaction, the unloading shear modulus will be set to a value that is ten times the value of the soft loading shear modulus (i.e., residual shear modulus), as recommended by Beaty and Byrne (1999). In addition, if the stress cycle is sufficiently large prior to liquefaction, the yield strength (i.e., residual strength) will be reached and additional plastic deformation will occur, as the soil deforms plastically (see horizontal line labeled “residual strength” in Figure 3.7).

Finally, Beaty and Byrne (1999) recommended that whenever a liquefied soil element experiences a shear stress reversal (i.e., crosses the $\sigma = 0$ line), the occurrence of $r_u = 1$ requires that a hydrostatic state of stress be imposed on the model (Figure 3.7). At this point, the horizontal stress (σ_{xx}) is set equal to the vertical stress (σ_{yy}) and the shear stress (σ_{xy}) is removed (i.e., set equal to zero). FISH code will implement this feature.

3.2.2.7 Postliquefaction Shear Strength and Shear Modulus

Both postliquefaction residual strength and postliquefaction shear modulus are required for the Mohr-Coulomb model. It is desirable that the postliquefaction shear modulus be related to the residual strength to keep the number of required model parameters to a minimum. Beaty and Byrne (1999) suggested that for the case of unidirectional deformation, as shown by postliquefaction stress-strain behavior, the shear strain ranges from a lower value of approximately 2% for sands with $(N_1)_{60cs}$ of about 15, to about 6%, or more, for loose sands with $(N_1)_{60cs}$ equal to 5. ($(N_1)_{60cs}$ is the SPT standard penetration blow count adjusted to 1 ton per square foot and a hammer energy ratio of 60% of the theoretical maximum and for a clean sand.) Thus, this suggests that S_{ur}/G_r is approximately 0.02 for sands with $(N_1)_{60cs} = 15$ and 0.06 for loose sands (i.e., $(N_1)_{60cs} = 5$). The proposed ratio of postliquefaction residual strength to postliquefaction shear modulus (S_{ur}/G_r), decreasing with the increase of $(N_1)_{60cs}$, is shown in Figure 3.8. Thus, for any site with a known $(N_1)_{60cs}$ in the liquefied zone, the postliquefaction residual strength and residual shear modulus ratio can be decided beforehand. This relationship will be used during the back-calculation of the residual strength. The S_{ur}/G_r value selected for the Kobe and Wildlife sites are also shown in Figure 3.8 and Table 3.1.

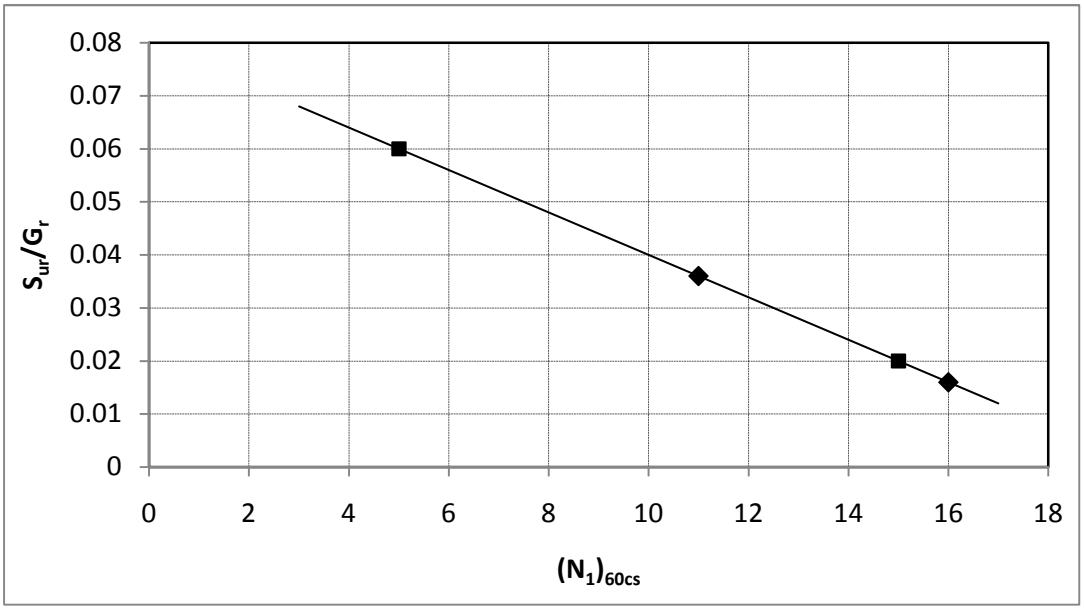


Figure 3.8. Relationship between $(N_1)_{60cs}$ and S_{ur}/G_r for postliquefaction

Table 3.1. Relationship between shear strain and $(N_1)_{60cs}$ for postliquefaction behavior

Site	S_{ur}/G_r	$(N_1)_{60CS}$	Γ(%)
From Beaty (1999)	0.06	5	6
From Beaty (1999)	0.02	15	2
Kobe	0.036	11	3.6
Wildlife	0.016	16	1.6

Chapter 6 will use the S_{ur}/G_r relation listed in Figure 3.8 for the appropriate $(N_1)_{60cs}$ and examine the model's performance in predicting the measured ground response for Kobe, Wildlife and Niigata.

3.3 Boundary Condition Considerations

Numerical analysis of the seismic response of geotechnical structures requires the discretization of a region of the model representing the material adjacent to the

foundation soils underneath the structures. The seismic input is normally represented by vertically propagating horizontal shear waves that excite the foundation and overlying materials. The boundary conditions at the sides of the model must account for the free-field motion that would exist in the absence of the structure or model boundary. In some cases, elementary horizontal boundaries may be sufficient. For example, if only a shear wave were applied on the horizontal boundary, AC, shown in Figure 3.9, it would be possible to fix the boundary along AB and CD in the vertical direction. These boundaries should be placed at sufficient distances to minimize wave reflections and achieve free-field conditions. For soils with high material damping, this condition can be obtained with a relatively small distance (Seed et al., 1975). However, when the material damping is low, the required distance may lead to an impractically large model. An alternative procedure is to "enforce" the free-field motion in such a way that boundaries retain their nonreflecting properties — i.e., outward waves originating from the structure are properly absorbed. A technique of this type was developed for FLAC, involving the execution of a one-dimensional free-field calculation in parallel with the main-grid analysis (Itasca, 2005). The lateral boundaries of the main grid are coupled to the free-field grid by viscous dashpots to simulate a quiet boundary (see Figure 3.9), and the unbalanced forces from the free-field grid are applied to the main-grid boundary. In this way, plane waves propagating upward suffer no distortion at the boundary because the free-field grid supplies conditions that are identical to those in an infinite model. A compliant base, or a quiet boundary, is used at the base of the FLAC mesh to absorb download propagating waves so that they are not reflected back into the model.

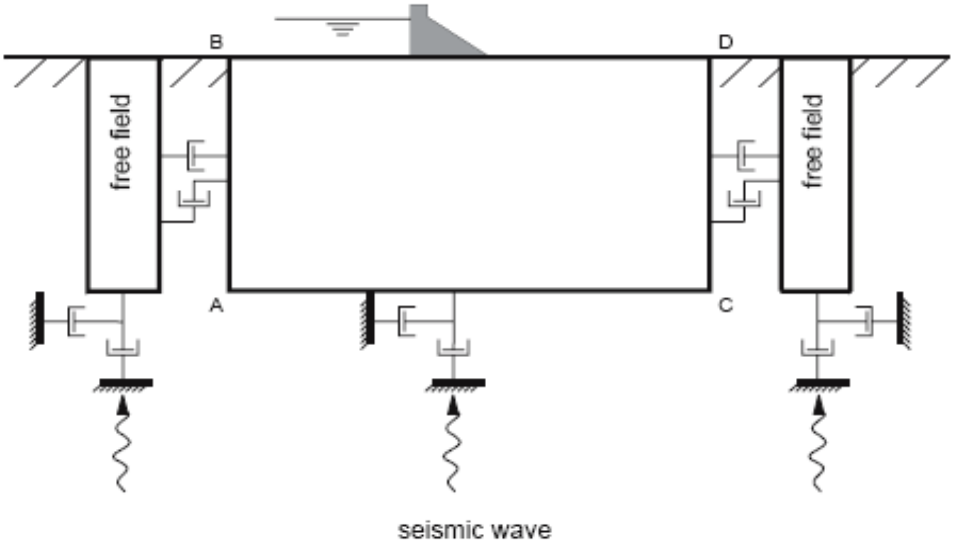


Figure 3.9. Model for seismic analysis of surface structures and free-field mesh (FLAC manual)

For this kind of boundary condition, the acceleration-time history is transformed into a stress-time history for input (Itasca, 2005). First the acceleration is integrated to obtain velocity and then the proportionality of stress to velocity in an elastic wave is used.

The input motion prepared for the FLAC model is obtained using the Proshake model. ProShake (EduPro Civil Systems, Inc., 1998) input and output is not in terms of the upward and downward propagating wave trains, but in terms of the motions at: a) the boundary between two layers, referred to as a 'within' motion; or b) at a free surface, referred to as an 'outcrop' motion. The 'within' motion is the superposition of the upward and downward propagating wave trains. The outcrop motion is the motion that would occur at a free surface at that location. Hence, due to the free surface effect, the outcrop motion is simply twice the upward propagating wave train motion. Thus, the

upward propagating motion within the FLAC model can be computed by taking half the outcrop motion from the ProShake results for the layer that corresponds to the base of the FLAC model (Mejia, 2006). Additionally, viscious dashpots of the FLAC quiet boundary, which absorb downward propagating waves so that they are not reflected back into the model, requires that this base motion be multiplied by a factor of 2 because ½ of the stress is absorbed by the viscous dishpots. To check the reasonableness of the developed stress time history for the quiet boundary, the X-velocity at the base of the model during the dynamic run is monitored and compared to the input velocity. Some adjustment to the input stress wave may be required in order to produce a velocity at the base that approximately corresponds to the input velocity.

3.4 Input Time History Selection and Preparation

Nonlinear analyses require that the time history be inputted at the base of the model. In reality, earthquake time histories are usually recorded on the ground surface. But the FLAC model requires input time history at a certain depth, where the model's base is. Deconvolution techniques were used to transfer the recorded time history on the ground surface to the model's base. ProShake was used to deconvolve the free-field surface motion to the base of the FLAC model (Mejia, 2006). However, for some case history sites, there was no time history recorded. For these sites, a time history will be selected from a suitable nearby site. However, if this is not possible, then a synthetic time history will be generated to represent the strong motion at the candidate site. Thus, in this research, three kinds of time histories are used, in order of preference:

(1) Recorded time history at site

(2) Selected time history from a suitable nearby site for the same earthquake

(3) Synthetic time histories

In a few cases (e.g., Wildlife and Kobe sites), there are recorded downhole time histories below the liquefied zone that will be used directly in the FLAC modeling, verification and calibration. However, in most cases, the time histories used for the analyses will come from nearby sites, or from synthetic time histories.

The main considerations for selecting time histories using cases (2) and (3) above are: appropriate earthquake magnitude, faulting mechanism, source-to-site distance and geological structure. The candidate time histories were selected from earthquake events that have similar conditions, when possible. Also, because time histories for cases (2) and (3) will require deconvolution, as described earlier, the selected time histories are for surface free-field conditions and for a nonliquefied state.

For the analyses using synthetic time histories, seven time histories will be generated using the Strong Ground Motion Simulation code (SGMS) and used for the nonlinear analysis to represent some of the potential stochastic variability in the ground motion. The Strong Ground Motion Simulation code (Papageorgiou et al., 2004) uses the specific barrier model to describe the earthquake source in the stochastic modeling approach as introduced in the reference. Ultimately, the calibrations that use synthetic time histories will be averaged for a given site and the predicted displacement compared to actual measurements or the Bartlett Youd equation predictions (Bartlett et al., 1992).

For each site, the seven generated time histories are selected from a set of 30 generated synthetic time histories using SGMS. The strategy is to select a set of seven time histories from the 30 whose spectral acceleration is close to mean value (1 record), maximum value (1 record), minimum value (1 record), value at +1/2 standard deviation

(1 record), value at –1/2 standard deviation (1 record), value at +1 standard deviation (1 record), and value at –1 standard deviation (1 record). These comparisons were done at the fundamental period of the fully degraded (i.e., liquefied) soil column. In this way, the selection process takes into account the potential variation in strong motion and the dominant period of the soil column including liquefaction effects. The assumption for calculating the soil liquefaction predominant period is that the soil's shear modulus decreases to 1% of the maximum shear modulus for more than 2 to 3% shear strain during the liquefaction process.

For FLAC analyses, the strong motion time history seismic input must be applied at the base of the model rather than at the ground surface. The appropriate input motion at depth can be computed through a 'deconvolution' analysis using a 1-D wave propagation such as ProShake. For the deconvolution analyses, the strong motion was input at the surface and deconvolved to an appropriate depth using strain-compatible soil properties. However, reduced (i.e., liquefied) shear modulus and damping properties were not used in the deconvolution analyses because the deconvolved time histories were selected from cases where liquefaction effects are not included in the recorded time history.

3.5 Youd's Prediction of Lateral Spread

For the sites without numerous lateral spread measurements, there is a need to calculate the average lateral spread displacement using Youd's Multilinear Regression (MLR) model (Youd et al., 2002). This model will be used to calibrate the FLAC procedure. The Youd's MLR model for free-face and ground-slope conditions are shown in equation (3.15) and (3.16), in which R* and R0 are expressed in equation (3.17).

$$\begin{aligned}\log D_H = &-16.713 + 1.532M - 1.406\log R^* - 0.012R \\ &+ 0.592\log W + 0.54\log T_{15} + 3.413\log(100 - F_{15}) \\ &- 0.795\log(D50_{15} + 0.1\,\text{mm})\end{aligned} \tag{3.15}$$

$$\begin{aligned}\log D_H = &-16.213 + 1.532M - 1.406\log R^* - 0.012R \\ &+ 0.338\log S + 0.54\log T_{15} + 3.413\log(100 - F_{15}) \\ &- 0.795\log(D50_{15} + 0.1\,mm)\end{aligned} \tag{3.16}$$

$$R^* = R + 10^{(0.89M - 5.64)} \tag{3.17}$$

where D_H = the estimated lateral ground displacement, in meters; M = the moment magnitude of the earthquake; R = the nearest horizontal or map distance from the site to the seismic energy source, in kilometers; T_{15} = the cumulative thickness of saturated granular layers with corrected blow counts, $(N_1)_{60}$, less than 15, in meters; F_{15} = the average fines content (fraction of sediment sample passing a No. 200 sieve) for granular materials included within T_{15} , in percent; $D50_{15}$ = the average mean grain size for granular materials within T_{15} , in millimeters; S = the ground slope, in percent; and W = the free-face ratio defined as the height (H) of the free face divided by the distance (L) from the base of the free face to the point in question, in percent (Youd et al., 2002). The lateral spreads for the regular free-face and ground-slope conditions will be predicted directly by the above equations. For ground-slope conditions, the contribution from the natural slope part of the topography and its influence on the lateral spread displacement is important. This effect will be taken into account in applying the Youd et al. model, as explained by Figure 3.10 (Bartlett, 1991).

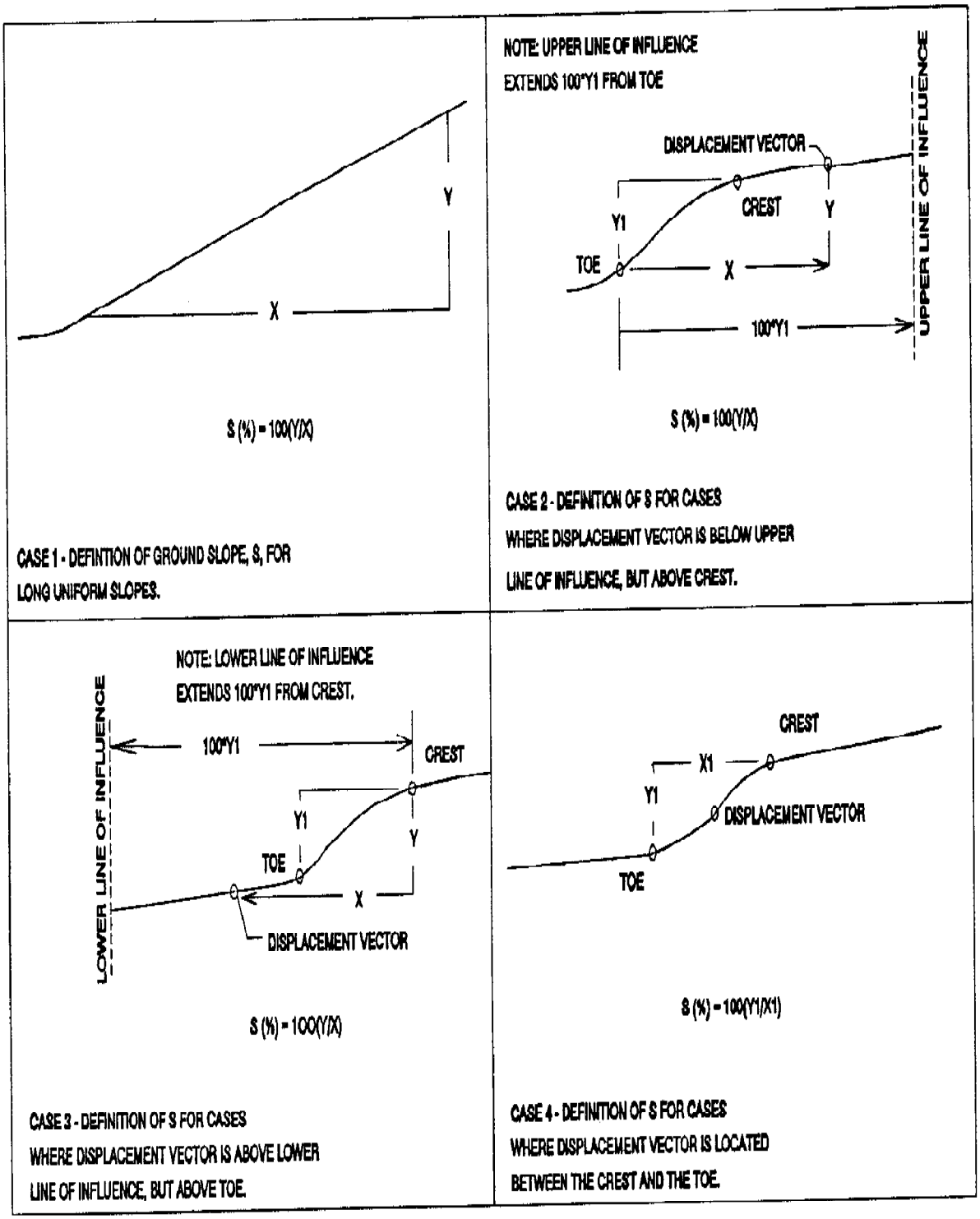


Figure 3.10. Definition of ground slope for long uniform/nonuniform slopes (from Bartlett, 1991).

For the FLAC modeling, the ground slope or free face conditions measured at the case history site will be used in producing the FLAC mesh.

3.6 Summary of Model Design

A noncoupled FLAC mode was designed using the generation of pore water pressure based on the number of cycles to reach liquefaction as an indicator of the degradation of shear modulus and shear strength in the preliquefied soil. The decrease of shear modulus and shear strength as a function of the generation of pore water generation is coupled in the FLAC model using FISH code. Damping is automatically accounted for by the shape and area of the hysteresis loop for the T_{15} layer, while FLAC coupled hysteresis damping is used for layers with $(N_1)_{60} \geq 15$.

For layers with $(N_1)_{60} \leq 15$ (i.e., T_{15} layer), shear stress and the number of stress cycles in the liquefied zone is tracked, so that the progression and number of cycles to reach liquefaction can be calculated to estimate the generation of pore water pressure.

Upon reaching liquefaction, a residual strength and shear modulus is used in the model. In addition, loading and unloading moduli are considered differently, so that the unloading shear modulus is 10 times stiffer than the loading modulus. Also the relation between the residual shear strength and residual shear modulus is predetermined based on the research by Beaty and Byrne (1999). The ultimate goal of the modeling is to calculate a residual strength in the FLAC model that matches the observed displacement pattern at the case history site. Ultimately, the back-calculated residual strength will be correlated with the measured in situ properties at the site, so that this relation can be used to predict the proper residual strength for engineer analyses and design.

The input time histories used in this study are recorded or will be synthetically generated, depending on what was recorded or available at the site. The synthetic times histories take into account potential variability and the response of the soil column at the fundamental period after liquefaction. The time histories are deconvoluted and appropriately assigned to the FLAC model according to where the motion is required and how it should be propagated through the liquefied soil.

CHAPTER 4

PORE WATER GENERATION MODELING

As discussed in the previous chapter, the FLAC model needs to track pore water generation so that the degradation of shear modulus and shear strength can be calculated prior to liquefaction. The track of pore water generation uses the strategy of required uniform earthquake cycles to trigger liquefaction. Earthquake-induced liquefaction, also pore water pressure generation, is related to the cyclic stress ratio (CSR), which is defined as the ratio of shear stress to initial vertical effective stress, and soil cyclic resistance ratio (CRR), which is the function of standard penetration test (SPT) or the cone penetration test (CPT). In this chapter, using the NCEER summary (Youd, et al., 2001) on CSR and CRR, equations are developed to express the required uniform cycles to trigger liquefaction in terms of CSR and CRR (expressed by SPT $(N_1)_{60CS}$), so that this equation can be incorporated in the FLAC model using FISH functions.

4.1 Number of Cycles to Liquefaction

The most widely accept relation between CSR and triggering of liquefaction is found in NCEER's summary about liquefaction resistance (Youd et al., 2001). Equation 4.1 (Youd et al., 2001) is the expression for a M7.5 earthquake, for clean sands with a $(N_1)_{60}$ value less than 30 and a fine content of 5% or less.

$$CRR_{7.5} = \frac{1}{34-(N_1)_{60}} + \frac{(N_1)_{60}}{135} + \frac{50}{\left[10(N_1)_{60}+45\right]^2} - \frac{1}{200} \quad (4.1)$$

where, $CRR_{7.5}$ is the cyclic resistance ratio required to trigger liquefaction for a M7.5 earthquake.

Equation 4.1 is only valid for M7.5 earthquakes and must be adjusted by a magnitude-scaling factor for earthquakes of differing magnitude.

The factor of safety (FS) against liquefaction is calculated as equation (4.2),

$$FS = (CRR_{7.5} / CSR)MSF \bullet K\sigma \bullet K\alpha \quad (4.2)$$

where $K\sigma$ accounts for effective overburden stress greater than 1atm, $K\alpha$ accounts for static driving shear stress due to sloping ground, CSR is the cyclic stress ratio for the earthquake under consideration, and MSF equals to $10^{2.24}/M^{2.56}$ as recommended by NCEER (Youd et al., 2001).

At liquefaction (FS=1), and setting $K\alpha$ and $K\sigma$ equal to 1.0 due to generally shallow and gently sloping T_{15} layer represented in the case histories, equation (4.2) is derived as equation (4.3) and the CSR (cyclic stress ratio) can be expressed as:

$$CSR = CRR_{7.5} \times MSF = \frac{10^{2.24}}{M^{2.56}}\left[\frac{1}{34-(N_1)_{60}} + \frac{(N_1)_{60}}{135} + \frac{50}{\left[10(N_1)_{60}+45\right]^2} - \frac{1}{200}\right] \quad (4.3)$$

Equation (4.3) is the FS=1 curve which differentiates the liquefaction and un-liquefaction zones. This curve shows the required CSR curve to trigger liquefaction. The parameters in equation (4.3), $(N_1)_{60}$ and earthquake magnitude, define the shape of the FS=1 curve. When plotted, the zone below the FS=1 curve means the induced CSR within soil is lower than the required CSR to trigger liquefaction, while the zone above the FS=1 curve means the induced CSR within soil is higher than the required CSR to trigger liquefaction. Thus below the FS=1 curve, no liquefaction occurs, while above the FS=1 curve, liquefaction is predicted. Equation (4.3) is valid for clean sands with the $(N_1)_{60}$ value less than 30. Figure 4.1 shows the relation between the required cyclic stress ratio to trigger liquefaction and the corrected blow count for earthquake magnitudes of 5.5, 6, 6.75, 7, 7.5, 8, and 8.5, arranged from the top curve to the bottom curve, respectively, as expressed in equation (4.3). According to the definition of CRR and CSR (Youd et al., 2001), which implies separation between liquefaction and nonliquefaction area in the coordinate system, each curve in Figure 4.1 defines the required CSR value to achieve liquefaction for earthquake magnitudes of 5.5, 6, 6.75, 7, 7.5, 8, and 8.5, respectively.

To determine the relationship between CSR and the number of cycles to trigger liquefaction, the representative number of stress cycles is needed as a function of earthquake magnitude. Statistical studies by Seed et al. (1975) show the number of representative stress cycles present in differing earthquake magnitudes, as shown in Table 4.1. The information in Table 4.1 and in Figure 4.1 can be combined to determine the number of cycles to reach liquefaction for various earthquake magnitudes and $(N_1)_{60CS}$ values.

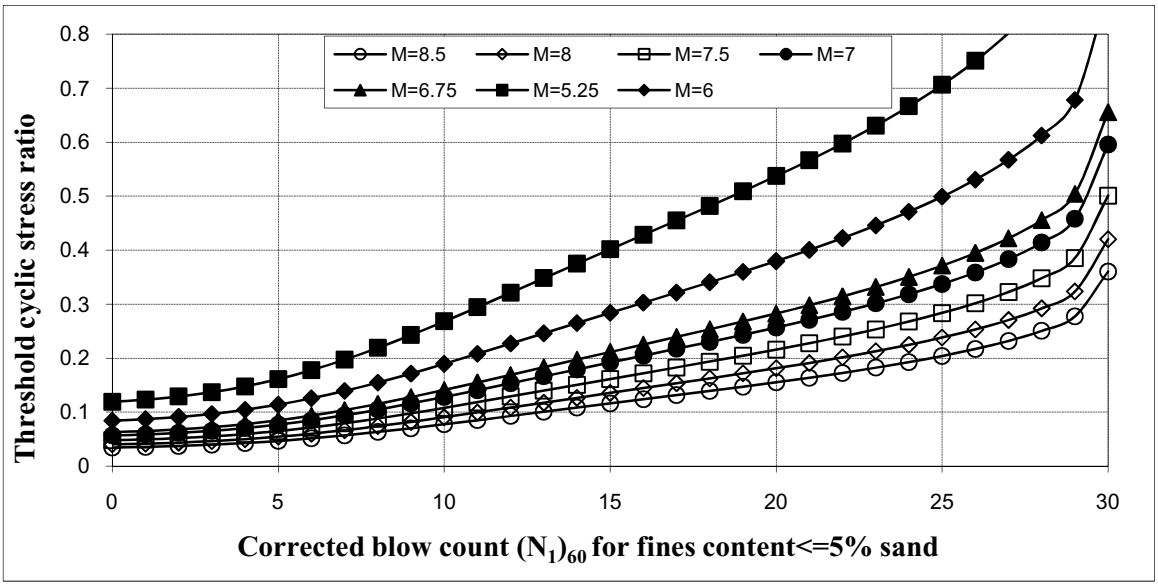


Figure 4.1. CSR vs. $(N_1)_{60}$ values for clean sand

Table 4.1. Earthquake magnitude and representative cycles at $0.65\tau_{max}$

Earthquake magnitude, M	Number of representative uniform cycles at $0.65\tau_{max}$
$8\frac{1}{2}$	26
$7\frac{1}{2}$	15
$6\frac{3}{4}$	10
6	5-6
$5\frac{1}{4}$	2-3

The earthquake magnitude, number of representative cycles, and CSR required to trigger liquefaction is listed in Table 4.2. The relation showed in Figure 4.1 is used to determine the relation between cyclic stress ratio and number of cycles to liquefaction, as shown in Figure 4.2. In Figure 4.2, the curves represent the number of cycles required to reach liquefaction for soil with $(N_1)_{60}$ equal to 5, 10, 15, 20, and 25, respectively. The regression equations for these curves are given in equation (4.4) to (4.8), respectively.

Table 4.2. Earthquake magnitude, number of representative cycles and CSR

Earthquake magnitude	Representative uniform cycles	CSR required to trigger liquefaction				
		$(N_1)_{60}$=5	$(N_1)_{60}$=10	$(N_1)_{60}$=15	$(N_1)_{60}$=20	$(N_1)_{60}$=25
5.25	2.5	0.160	0.290	0.400	0.540	0.710
6	5.5	0.118	0.190	0.283	0.380	0.500
6.75	10	0.085	0.140	0.210	0.280	0.370
7.5	15	0.063	0.110	0.160	0.218	0.285
8.5	26	0.045	0.078	0.115	0.155	0.205

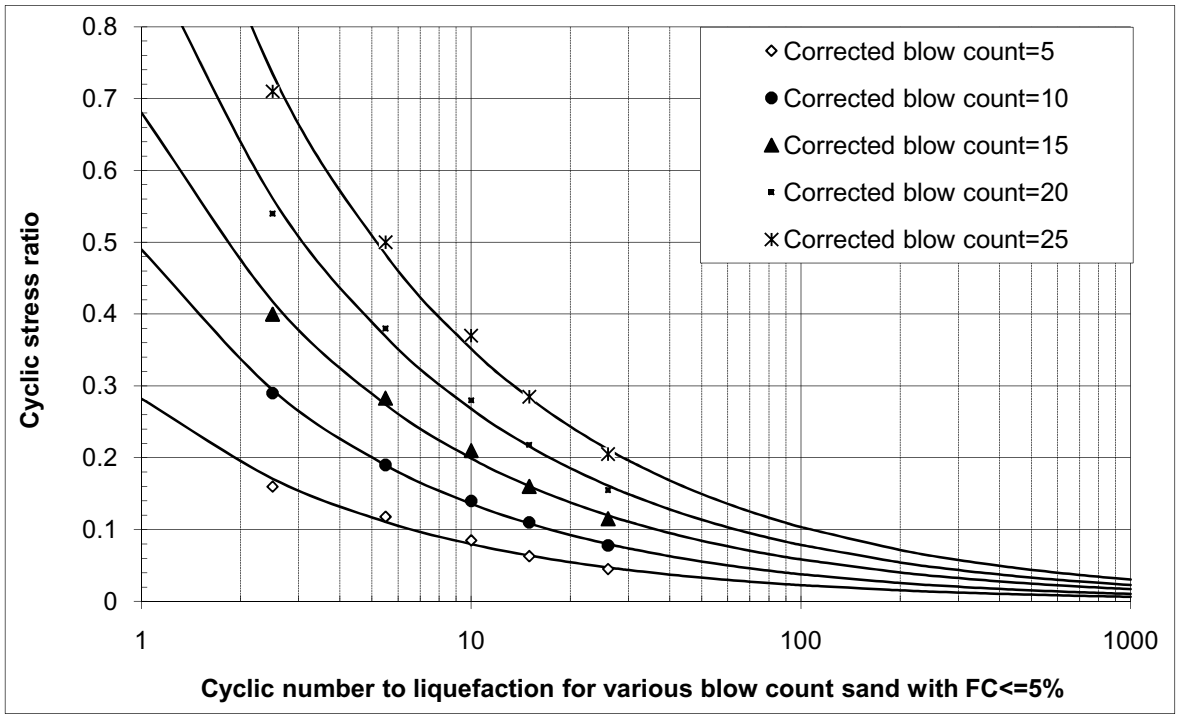


Figure 4.2. CSR vs. number of uniform cycles to liquefaction for FC<=5% sand with various blow count

$$CSR_{(N_1)_{60}=5} = 0.2822 N_{EL}^{-0.5343} \quad (4.4)$$

$$CSR_{(N_1)_{60}=10} = 0.4898 N_{EL}^{-0.5560} \quad (4.5)$$

$$CSR_{(N_1)_{60}=15} = 0.6802 N_{EL}^{-0.5333} \quad (4.6)$$

$$CSR_{(N_1)_{60}=20} = 0.9139 N_{EL}^{-0.5321} \quad (4.7)$$

$$CSR_{(N_1)_{60}=25} = 1.2001 N_{EL}^{-0.5310} \quad (4.8)$$

N_{EL} in the equations is the number of uniformed cycles required to trigger liquefaction.

4.2 Blow Count Adjustment for CSR

Examination of the obtained relation shows that the exponent of the number of cycles to liquefaction for different blow counts is essentially the same, and the regression coefficients increase with the increases in the corrected SPT blow count. Thus, the general equation expressing the relation of CSR and N_{EL} as a function of corrected blow count is:

$$CSR = f((N_1)_{60}) N_{EL}^{-0.5402} \quad (4.9)$$

where $f((N_1)_{60})$ is the coefficient function related with the corrected blow count. The regression analysis gives $f((N_1)_{60})$ as:

$$f((N_1)_{60}) = 0.0006 (N_1)_{60}^{\ 2} + 0.0280 (N_1)_{60} + 0.1355 \quad (4.10)$$

Thus, for clean sand with fines content equal to or less than 5%, the CSR can be expressed using corrected blow count and the number of cycles to liquefaction as shown by the following equation (4.11):

$$CSR = \left\{0.0006(N_1)_{60}{}^2 + 0.0280(N_1)_{60} + 0.1355\right\} N_{EL}^{-0.5402} \quad (4.11)$$

4.3 Fine Count Adjustment for CSR

Seed et al. (1985) found that for a given $(N_1)_{60}$ value, values of CSR increase with the increased fine content. NCEER (Youd et al., 2001) gives the following equation (4.12) for the correction of silty sands to account for the influence of the fines content. This is done by increasing the blow count to a "clean sand" equivalent $(N_1)_{60cs}$ as shown below:

$$(N_1)_{60\,cs} = \alpha + \beta (N_1)_{60} \quad (4.12)$$

where,

$\alpha = 0$ for FC<=5%

$\alpha = \exp\left[1.76 - (190 / FC^2)\right]$ for 5%<FC<35%

$\alpha = 5.0$ for FC>=35%

$\beta = 0$ for FC<=5%

$\beta = \left[0.99 + (FC^{1.5} / 1000)\right]$ for 5%<FC<35%

$\beta = 5.0$ for FC>=35%

If these equations are applied to a sand having a 15% fines content, the relation between the cyclic stress ratio and the corrected blow count for earthquake magnitude 5.5, 6, 6.75, 7, 7.5, 8, and 8.5, arranged from the top curve to the bottom curve, respectively, is shown in Figure 4.3.

Similarly, Figure 4.4 shows the relation for the sand with 35% fines content.

The earthquake magnitude, number of representative cycles to trigger liquefaction and required cyclic stress ratio to trigger liquefaction for 15 and 35% fines are shown in Figure 4.3 and Figure 4.4, respectively, and listed in Table 4.3 and Table 4.4, respectively.

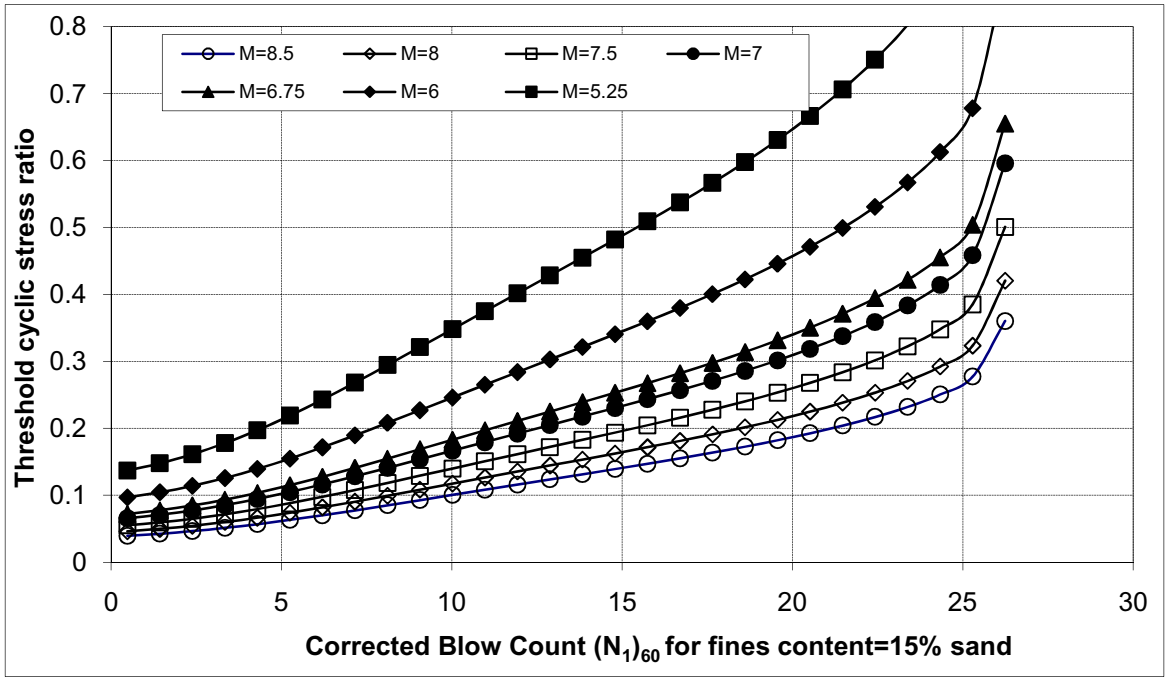


Figure 4.3. CSR vs. $(N_1)_{60}$ values for fines content equal to 15% corresponding to occurrence of liquefaction

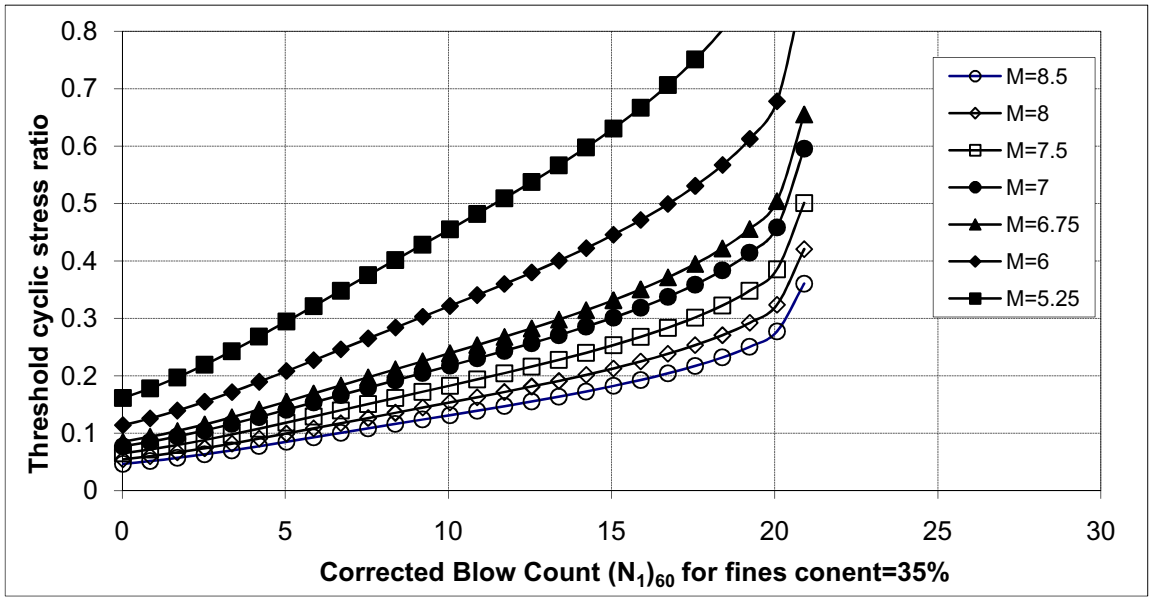


Figure 4.4 CSR vs. $(N_1)_{60}$ values for fines content equal to 35% corresponding to occurrence of liquefaction

Table 4.3. Earthquake magnitude, number of representative cycles and CSR for FC=15% Sand

Earthquake magnitude	Representative uniform cycles	CSR				
		$(N_1)_{60}$=5	$(N_1)_{60}$=10	$(N_1)_{60}$=15	$(N_1)_{60}$=20	$(N_1)_{60}$=25
5.25	2.5	0.219	0.345	0.485	0.643	0.930
6	5.5	0.145	0.250	0.340	0.456	0.650
6.75	10	0.110	0.180	0.257	0.340	0.480
7.5	15	0.084	0.140	0.199	0.260	0.365
8.5	26	0.060	0.100	0.140	0.185	0.265

Table 4.4. Earthquake magnitude, number of representative cycles and CSR for FC=35% Sand

Earthquake magnitude	Representative uniform cycles	CSR			
		$(N_1)_{60}$=5	$(N_1)_{60}$=10	$(N_1)_{60}$=15	$(N_1)_{60}$=20
5.25	2.5	0.300	0.450	0.630	0.940
6	5.5	0.210	0.320	0.445	0.670
6.75	10	0.153	0.240	0.330	0.500
7.5	15	0.120	0.180	0.250	0.380
8.5	26	0.088	0.130	0.185	0.280

From Table 4.3, the relation between cyclic stress ratio and number of uniform cycles to liquefaction for 15% fines content is obtained and shown in Figure 4.5. The regression relation between the CSR and the number of uniform cycles to liquefaction for differing corrected blow counts is obtained for 15% fines content.

The regression relations for various values of corrected blow count and sands with 15% fines are represented by equation (4.13) to equation (4.17):

$$CSR_{(N_1)_{60}=5} = 0.3694 N_{EL}^{-0.5481} \tag{4.13}$$

$$CSR_{(N_1)_{60}=10} = 0.5897 N_{EL}^{-0.5320} \tag{4.14}$$

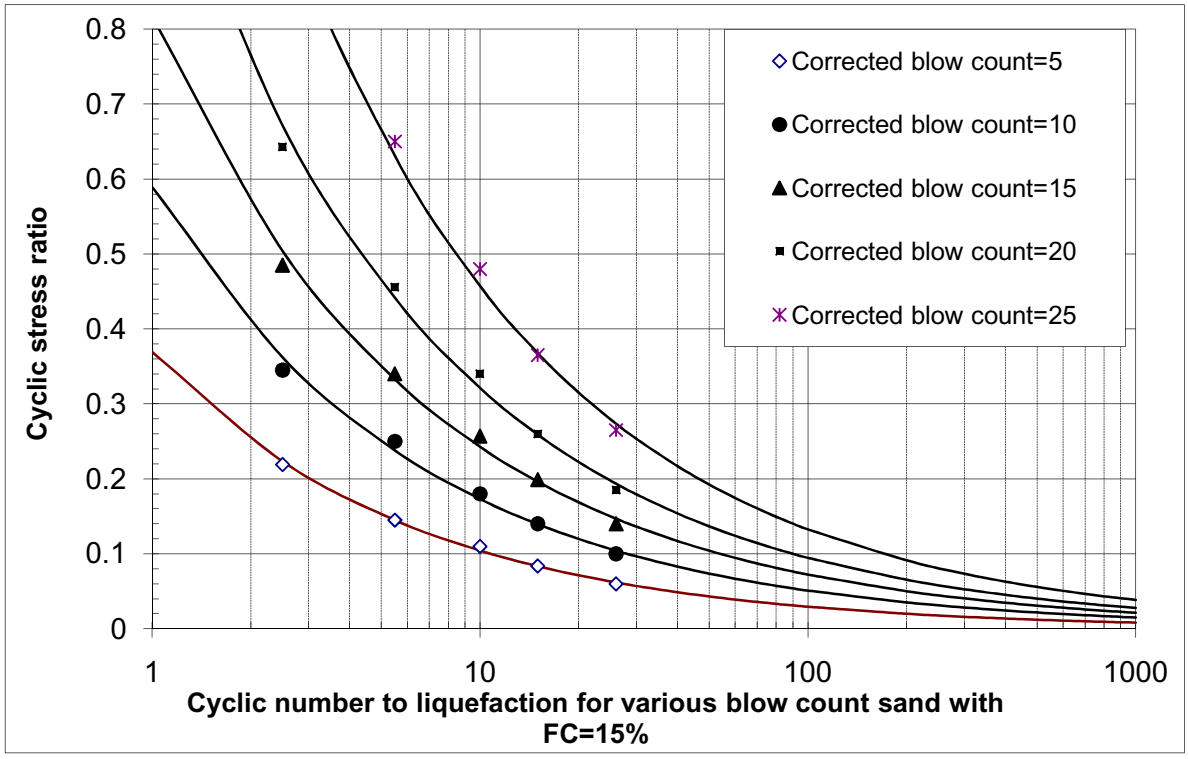


Figure 4.5. CSR vs. number of uniform cycles to liquefaction for FC<=15% sand with various blow count

$$CSR_{(N_1)_{60}=15} = 0.8169 N_{EL}^{-0.5263} \quad (4.15)$$

$$CSR_{(N_1)_{60}=20} = 1.0934 N_{EL}^{-0.5314} \quad (4.16)$$

$$CSR_{(N_1)_{60}=25} = 1.5802 N_{EL}^{0.5382} \quad (4.17)$$

where, N_{EL} is the number of cycles to liquefaction.

Examination of these relations shows that the exponent of the number of cycles to liquefaction for different blow counts is almost the same, and the regression coefficients increase with increasing corrected blow count. Thus, the general equation expressing the relation of CSR and N_{EL} for various corrected blow counts is:

$$CSR = f((N_1)_{60}) N_{EL}^{-0.5352} \quad (4.18)$$

where, $f((N_1)_{60})$ is the coefficient function for the corrected blow count. The regression analysis gives $f((N_1)_{60})$:

$$f((N_1)_{60}) = 0.0017 (N_1)_{60}{}^2 + 0.0086 (N_1)_{60} + 0.3036 \quad (4.19)$$

Thus, for silty sands with fines content equal to 15% fines, the CSR can be calculated using corrected blow count and the number of cycles to liquefaction as shown by the following equation (4.20).

$$CSR = \left\{0.0017 (N_1)_{60}{}^2 + 0.0086 (N_1)_{60} + 0.3036\right\} N_{EL}^{-0.5352} \quad (4.20)$$

The relation between cyclic stress ratio and number of cycles to liquefaction for sands with 35% fines content is obtained from Table 4.4 and shown in Figure 4.6. Also, shown in Figure 4.6 is the regression relation between the CSR and the number of cycles to liquefaction for differing corrected blow counts.

The regression relations for different corrected blow count sand are represented by equation (4.21) to equation (4.24):

$$CSR_{(N_1)_{60}=5} = 0.5004 N_{EL}^{-0.5263} \tag{4.21}$$

$$CSR_{(N_1)_{60}=10} = 0.7667 N_{EL}^{-0.5319} \tag{4.22}$$

$$CSR_{(N_1)_{60}=15} = 1.0597 N_{EL}^{-0.5275} \tag{4.23}$$

$$CSR_{(N_1)_{60}=20} = 1.5753 N_{EL}^{-0.5205} \tag{4.24}$$

where N_{EL} is the number of cycles to liquefaction.

Examining these relations shows that the exponent of the number of cycles to liquefaction for different blow counts is almost the same, and the coefficient increases with the increase of the corrected blow counts. Thus, the general equation expressing the relation of CSR and N_{EL} considering the different blow counts can be written as:

$$CSR = f((N_1)_{60}) N_{EL}^{-0.5266} \tag{4.25}$$

where $f((N_1)_{60})$ is the coefficient function for the corrected blow count. The regression analysis gives $f((N_1)_{60})$ expressed in equation (4.26):

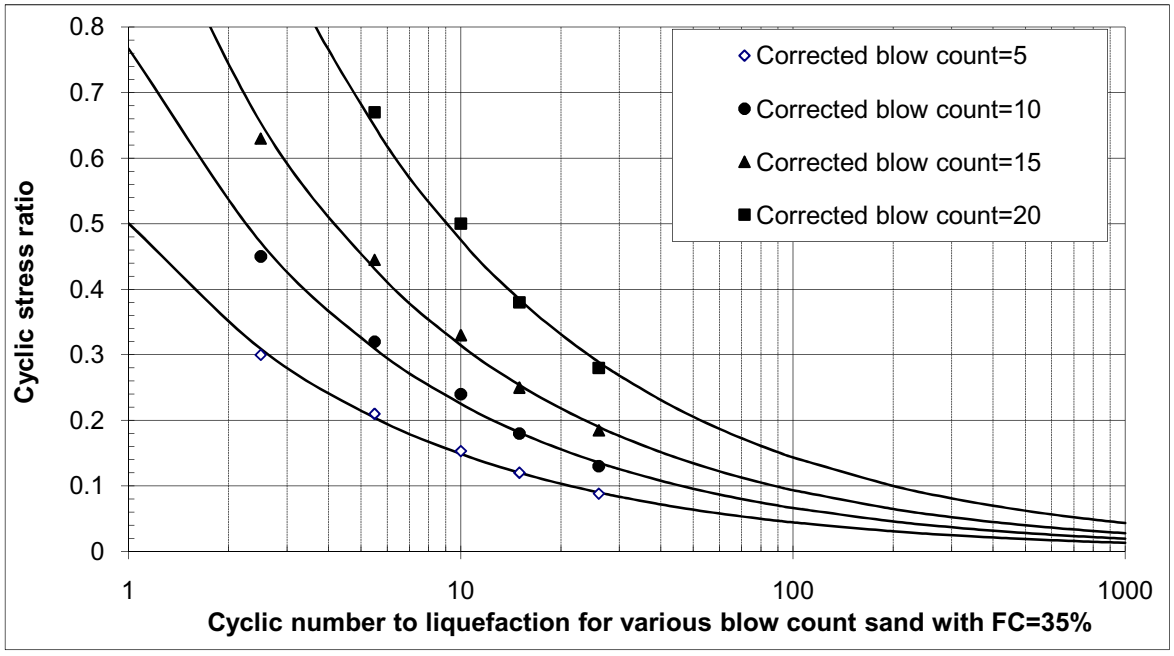


Figure 4.6. CSR vs. number of uniform cycles to liquefaction for FC<=35% sand with various blow count

$$f((N_1)_{60}) = 0.0025(N_1)_{60}{}^2 + 0.0080(N_1)_{60} + 0.4077 \tag{4.26}$$

Thus, for silty sands with fines content equal to 35%, the CSR can be calculated using corrected blow count and the number of cycles to liquefaction as shown by the following equation:

$$CSR = \left\{0.0025(N_1)_{60}{}^2 + 0.0080(N_1)_{60} + 0.4077\right\} N_{EL}^{-0.5266} \tag{4.27}$$

Based upon the above analysis, the relationships between N_{EL} and CSR for the three groups of sands can be expressed using equation (4.28) to equation (4.30).

For FC<=5%,

$$CSR = \left\{0.0006(N_1)_{60}{}^2 + 0.0280(N_1)_{60} + 0.1355\right\} N_{EL}^{-0.5402}$$

$$N_{EL} = \left[\frac{0.0006(N_1)_{60}{}^2 + 0.0280(N_1)_{60} + 0.1355}{CSR}\right]^{1.85} \tag{4.28}$$

For FC=15%,

$$CSR = \left\{0.0017(N_1)_{60}{}^2 + 0.0086(N_1)_{60} + 0.3036\right\} N_{EL}^{-0.5352}$$

$$N_{EL} = \left[\frac{0.0017(N_1)_{60}{}^2 + 0.0086(N_1)_{60} + 0.3036}{CSR}\right]^{1.87} \tag{4.29}$$

For FC=35%,

$$CSR = \left\{0.0025(N_1)_{60}{}^2 + 0.0080(N_1)_{60} + 0.4077\right\} N_{EL}^{-0.5266}$$

$$N_{EL} = \left[\frac{0.0025(N_1)_{60}{}^2 + 0.0080(N_1)_{60} + 0.4077}{CSR}\right]^{1.90} \tag{4.30}$$

For the sand with fines content other than 5, 15 and 35 %, N_{EL} values can be calculated by interpolation. For the sand with fines content more than 35%, the effects of fines on liquefaction resistance is less understood. In order for the FISH program to deal with this case, 35% is used to execute the calculation for fines content greater than 35%.

Equations (4.28), (4.29) and (4.30) represent the relationship between uniformed earthquake cycles and required CSR to achieve liquefaction. They also represent the relationship between induced CSR and required uniform earthquake cycles to achieve liquefaction, or how many required uniform earthquakes are need to achieve liquefaction

under the current induced CSR. Thus, the current induced CSR contribute $1/N_{EL}$ to achieve liquefaction. This relationship is fully expressed both in terms of corrected blow counts and fines content.

4.4 Pore Water Generation Calculation

In order to calculate the pore water generation, the induced CSR value is calculated first by the FLAC FISH code. In every element for each cyclic motion, the shear stress induced is calculated and normalized to a CSR value. According to previously developed equations (4.28), (4.29) and (4.30), this current CSR situation requires a certain number of uniform cycles N_{EL} to achieve liquefaction $(r_u = 1)$. Thus, the calculated CSR contributes $\Delta r_u = 1/N_{EL}$ to pore water generation within the element.

The developed FLAC FISH code will calculate the current CSR, which is the ratio of cyclic shear stress to initial effective vertical stress (Dawson, 2001) within each model mesh, and then interpolates the required number of uniform cycles for liquefaction according to the previously imbedded equations. Because the current CSR is induced by a half seismic cycle, $0.5/N_{EL}$ is contributed to pore water generation as expressed in equation (4.31).

$$\Delta r_u = 0.5/N_{EL}^{i} \tag{4.31}$$

Values of Δr_u will continue accumulating for each element until the total accumulated pore water pressure r_u equals one. At that point, the soil element is fully liquefied and residual shear strength and modulus properties are used.

4.5 Pore Water Generation Adjustment

Laboratory tests reveal the manner in which excess pore water pressure is generated. For stress-controlled cyclic tests with uniform loading, Lee and Albaisa (1974) and DeAlba et al. (1975) found that the pore water pressure ratio, r_u, is related to the number of loading cycles by equation (4.32):

$$r_u = \frac{1}{2} + \frac{1}{\pi}\sin^{-1}\left[2\left(\frac{N}{N_{EL}}\right)^{1/\alpha} - 1\right] \tag{4.32}$$

where N is the number of cycles at the current time and α is a function of the soil properties and test conditions. This equation can be used to estimate how excess pore water pressure is generated as a function of N/N_{EL}.

However, the FLAC model uses equation (4.32) with $\alpha = 0.7$ to adjust the pore water generation predicted by equation (4.31). The purpose of the adjustment with $\alpha = 0.7$ (DeAlba et al., 1975) is to produce a more rapid increase of r_u in the beginning and the final loading cycles, and to produce a more linear increase in the intervening cycles. Such an adjustment is necessary so that pore water generation is more consistent with laboratory test results (DeAlba et al., 1975; Albaisa, 1974).

4.6 Summary of Pore Water Generation

The relationship between CSR and the cyclic number required for fully mobilizing liquefaction was obtained. This developed relationship combined with the calculated CSR by the model's FISH code at the current time for each mesh was used to decide the cyclic number required for full liquefaction for the model. Finally the obtained cyclic number required for full liquefaction is converted to incremental pore water pressure ratio, which was then accumulated to compute the present pore water generation at the current time for each mesh of the FLAC model.

CHAPTER 5

MODEL VERIFICATION

To verify that the FLAC model and its FISH code properly implement the modeling approach, uniform cyclic and irregular motions are used as the input time history for two hypothetical site soils, one with very low residual strength of 5 kPa and the other with 30 kPa residual strength, respectively. The selected input motions are a simple sinuous wave and the Taft Record for the 1952 Kern County Earthquake (ProShake User's Manual, 1998).

5.1 Model Verification by Simple Cyclic Sinusoidal Input Motion

5.1.1 Input Motion

To trigger liquefaction at a reasonable time during the cyclic motion, a sinusoidal motion with an amplitude of 0.26 g and a frequency of 2.75 Hz was selected. The input motion for site 1 is shown in Figure 5.1.

The 2.75 Hz input motion frequency corresponds to the dominant soil column frequency, which is the ratio of soil shear wave velocity to four times of the soil column length. The 0.26 g motion corresponds to the recorded amplitude of the 1995 Kobe earthquake. A 4-m by 4-m mesh is used for the FLAC model with 7.5 percent slope T15 layer. The model scheme is show in Figure 5.2.

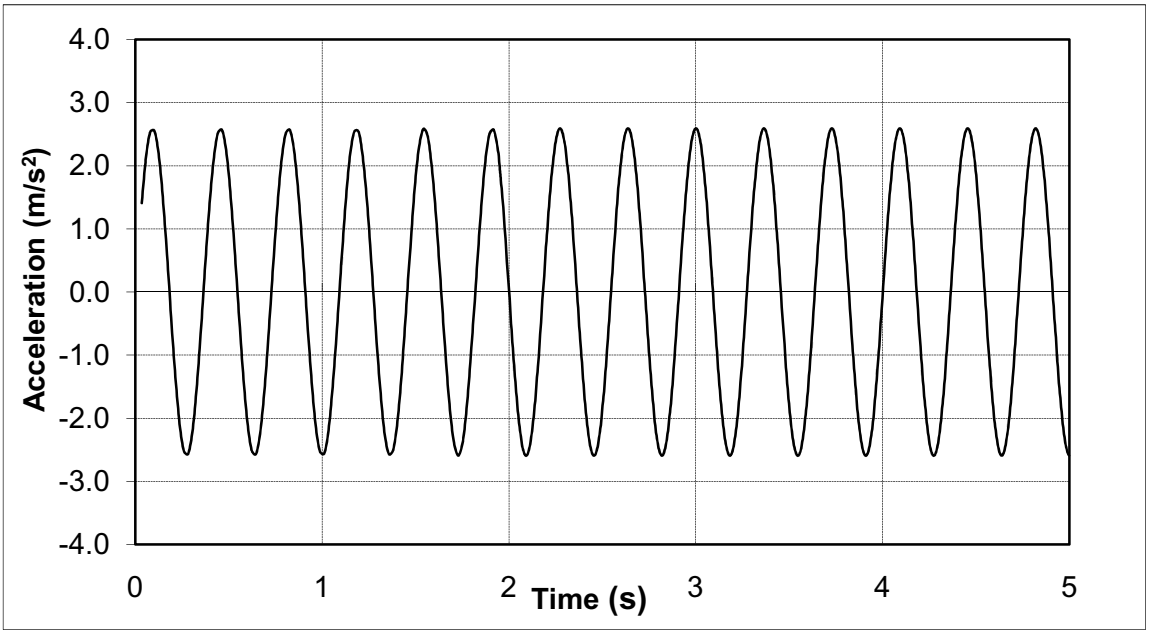


Figure 5.1. Input motion for site 1

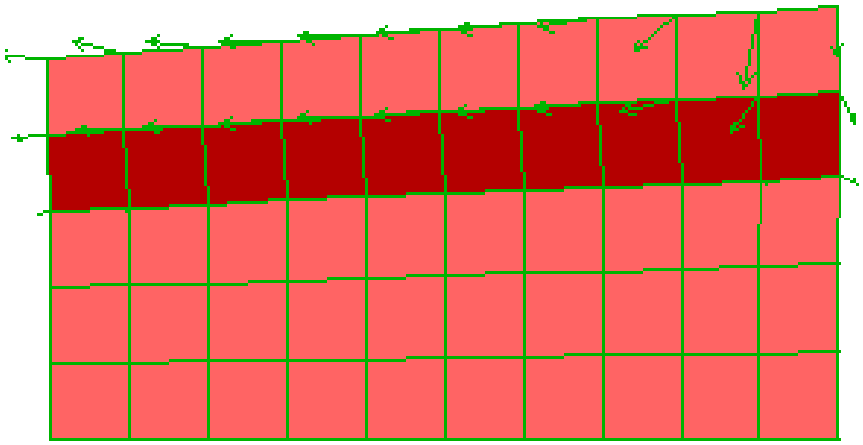


Figure 5.2. Sinusoidal input motion model scheme

5.1.2 Input Soil Parameters

Two sites are selected with different blow count and residual strength as the initial input parameters. In this verification case, equation (5.1) by Seed et al. (1986) is used to calculate the initial shear modulus according to the predetermined soil blow count.

$$G = 1000K_2\left(\sigma_m^{'}\right)^{1/2} \tag{5.1}$$

where $\left(\sigma_m^{'}\right)$ is the effective mean principal stress in the unit of psf and K_2 is shear modulus coefficient which is defined as $K_2 = 20(N_1)_{60}^{1/3}$ in which $(N_1)_{60}$ is the blow count.

The soil properties for the two sites are calculated using the average depth of liquefiable soil layer and listed in Table 5.1.

Bulk modulus is calculated from shear modulus using equation (5.2).

$$K = \frac{2G(1+\upsilon)}{3(1-2\upsilon)} \tag{5.2}$$

The Poisson's ratio for sand is selected as 0.33.

Table 5.1 Selected soil properties for site 1 and site 2.

Soil Types	Shear Modulus	Bulk modulus	$(N_1)_{60}$	Residual strength	Friction angle	Cohesion	Tension	Density
	(MPa)	(MPa)		(KPa)	(degree)	(Pa)	(Pa)	(kg/m^3)
Site 1	59	180	5	5	32	0	0	2150
Site 2	89	280	15	30	32	0	0	2200

As an example and due to the difference in stiffness of the two soils, the residual shear strength is decreased to 2 to 6 percent of the soil residual shear modulus, respectively, for site 1 and site 2.

5.1.3 Shear Modulus Reduction with Pore Water Generation

The corresponding CSR curve is used to calculate the number of cycles to reach liquefaction and further to calculate r_u, the excess pore water generation. For the lower blow count soil, increasing values of r_u and the shear stress history on the bottom of the liquefying soil layer are shown in Figures 5.3 and 5.4. In addition, as r_u increases, the shear modulus is correspondingly reduced to 0.08 Mpa, as shown in Figure 5.5. From Figures 5.3 and 5.4, it is shown that the liquefaction is fully triggered at about 0.5s. After the triggering of liquefaction, the model has a constant pore water ratio r_u=1 and uses residual shear modulus for the subsequent calculation.

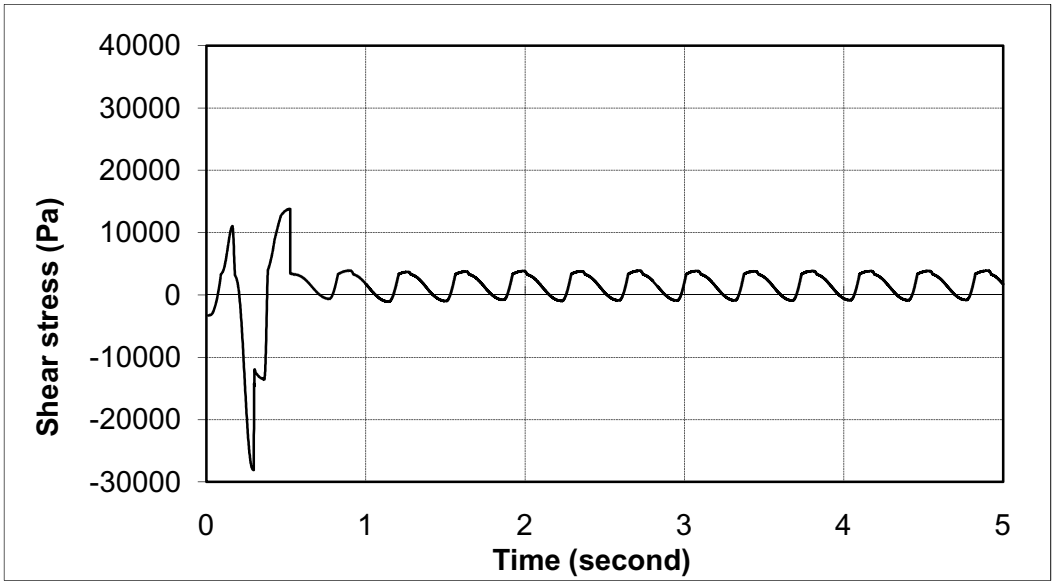


Figure 5.3. Shear stress vs. time within liquefaction layer of site 1.

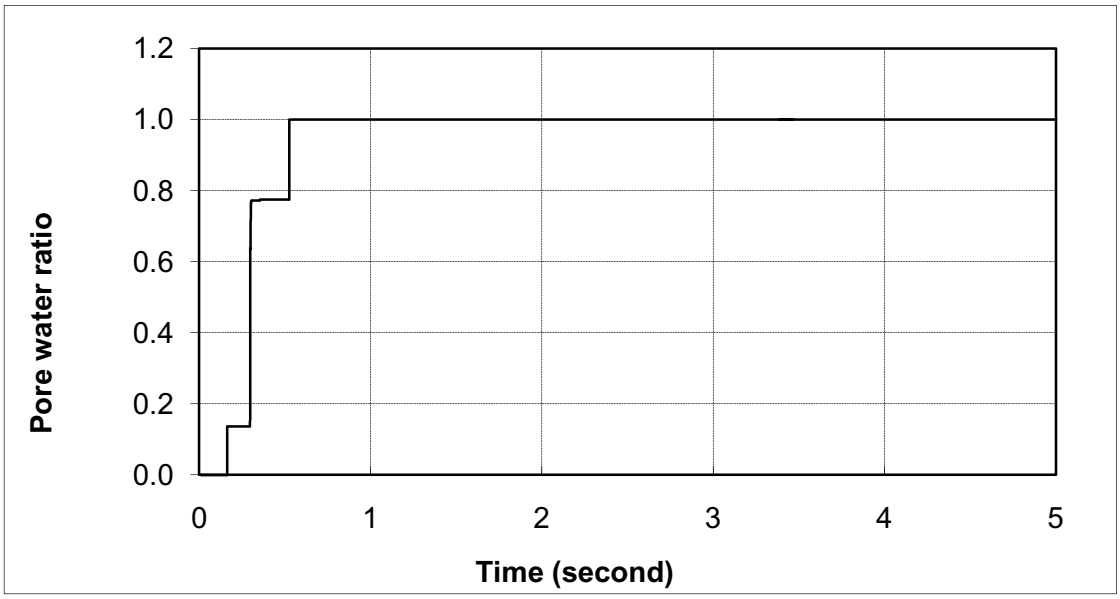


Figure 5.4. Pore water generation vs. time within liquefaction layer of site 1.

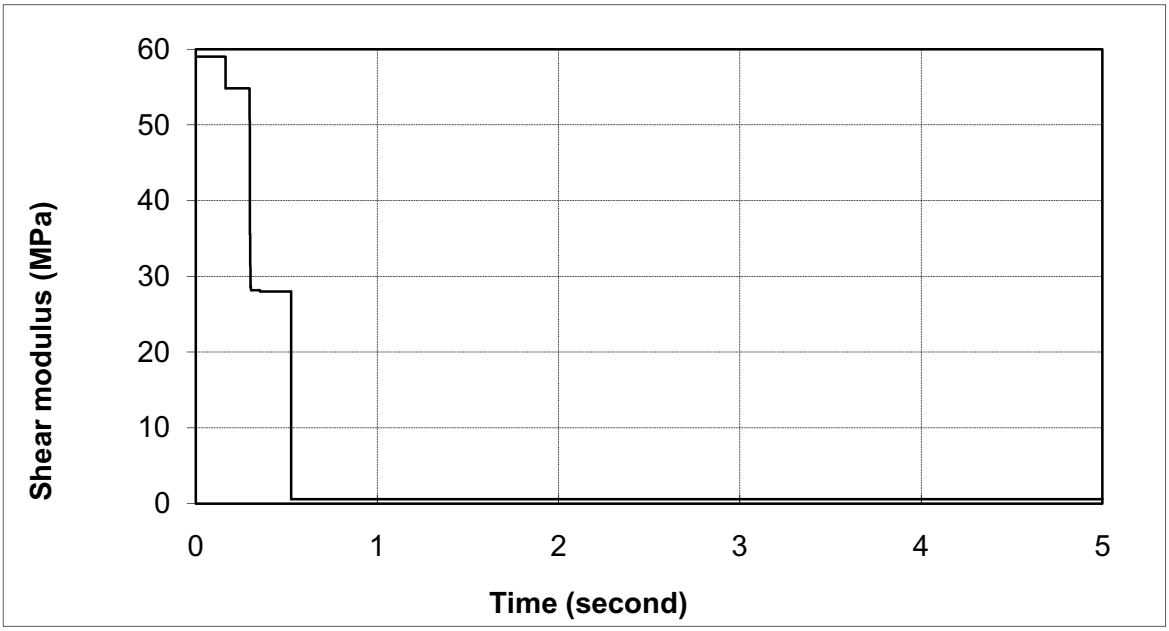


Figure 5.5. Shear modulus degradation for site 1.

For site 2 with a higher blow count, r_u and the shear stress used to generate the pore water pressure are shown in Figures 5.6 and 5.7. The corresponding reduction of shear modulus to 1.90 Mpa is shown in Figure 5.8. Figures 5.6 and 5.7 show that full liquefaction is triggered at about 1.7 s, which is longer than the time required to trigger liquefaction for site 1. This is expected because of the lower blow count used in site 1; hence, the shorter time to reach liquefaction. Note also that the model will also use r_u=1.0 as the pore water ratio cap and keeps the residual shear modulus constant once this condition is reached.

Because of the selection of the idealized cyclic input motion, the increase in r_u and the reduction of the shear modulus follow gradual paths. However, for real earthquake strong motion, this kind of phenomenon seldom happens because of the irregular shape of the input motion, as shown in the next section. For irregular earthquake input motion, the triggering of liquefaction can progress rapidly, especially if high amplitude cycles are present in the early part of the earthquake record.

5.1.4 Hysteretic Behavior of Liquefied Soils

The hysteretic loop of liquefied soils 1 and 2 undergoing uniform cyclic loading are shown in Figure 5.9 and Figure 5.10. Figures 5.9 and 5.10 show that the loading and unloading paths experience different slopes because the model is designed to use different shear modulus for the loading and unloading parts of the cycle. In addition, the model is also designed in a manner that loading and unloading reversals happen when the initial static shear stress level is encounted.

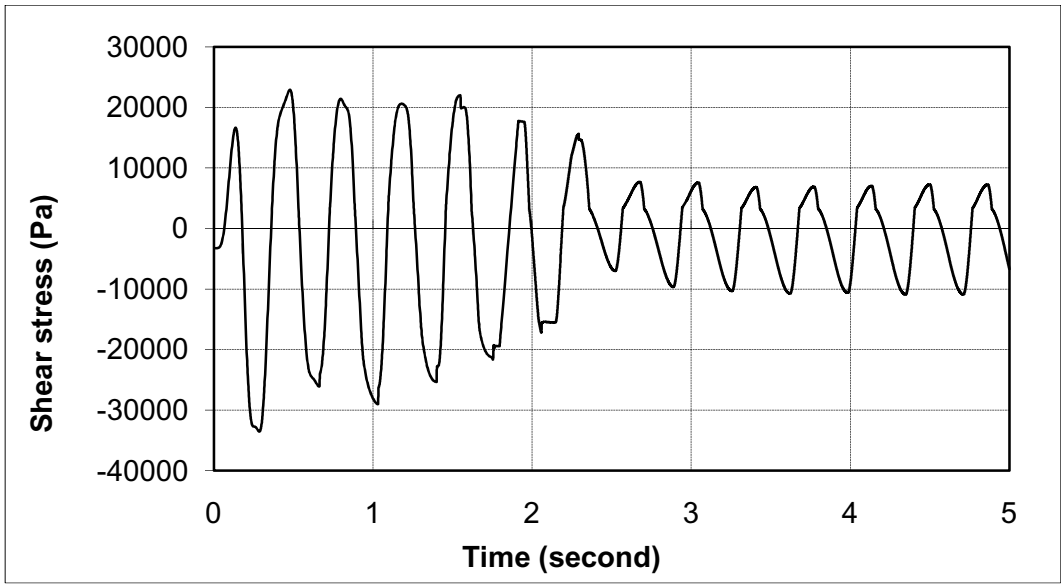


Figure 5.6. Shear stress development vs. time within liquefaction layer of site 2.

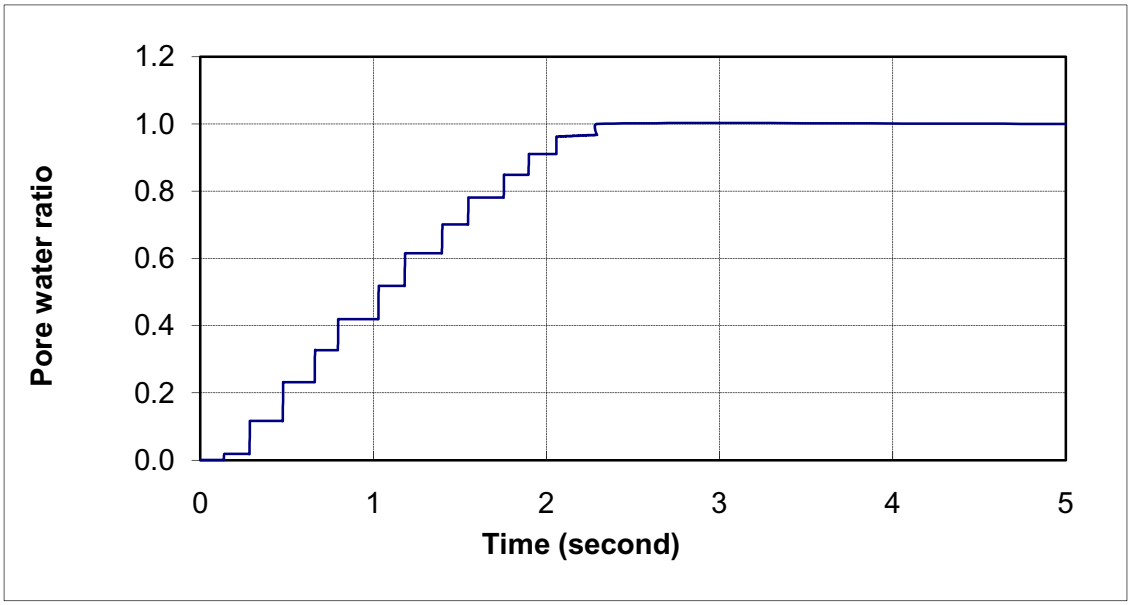


Figure 5.7. Pore water r_u development vs. time within liquefaction layer of site 2.

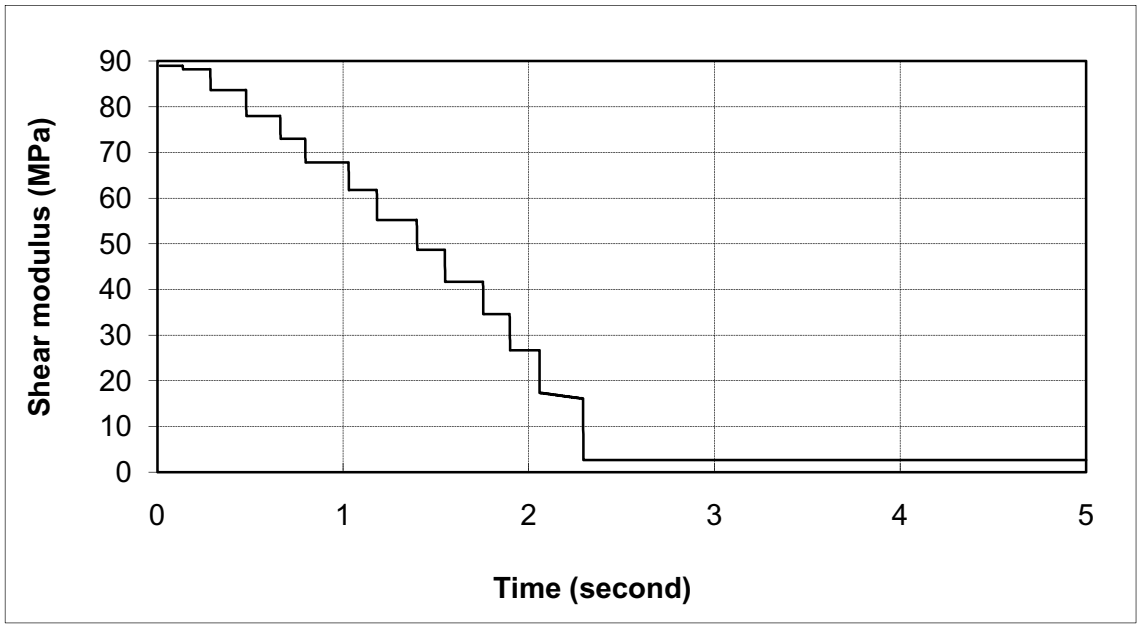


Figure 5.8. Shear modulus degradations vs. time for site 2.

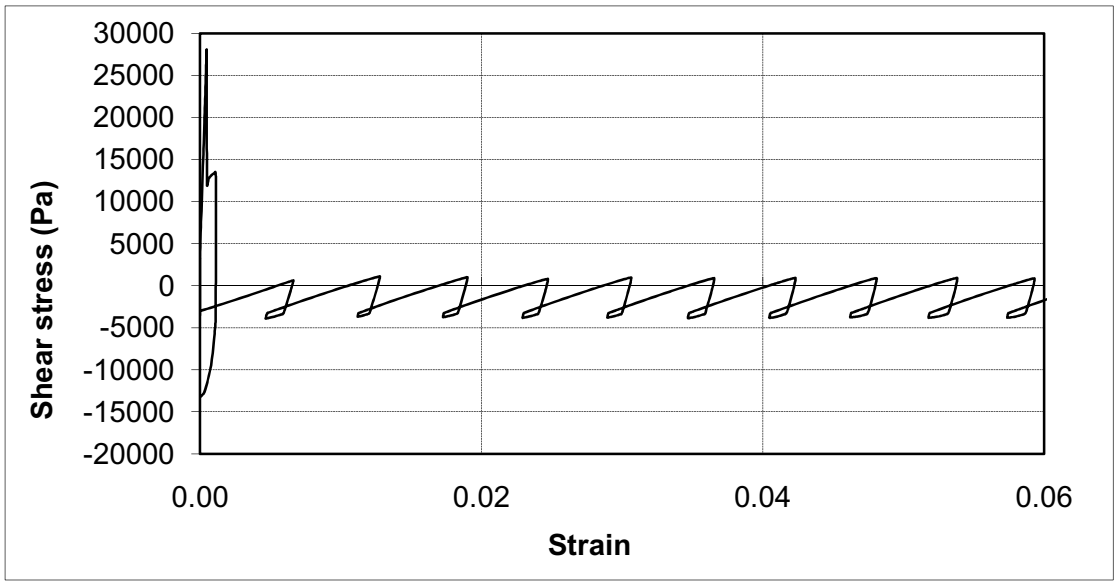


Figure 5.9. Hysteretic loop for site soil 1

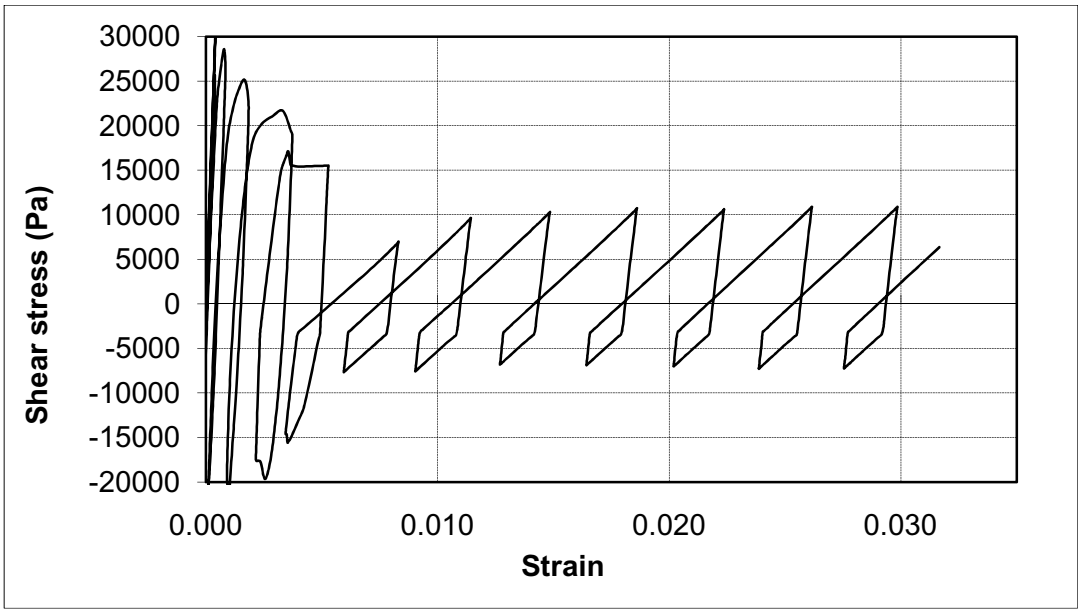


Figure 5.10. Hysteretic loop for site soil 2

The asymmetry in loading about the x-axis is a result of the initial static shear stress level due to the 7.5 percent slope with ground water level on the surface.

Based on the sharp reversal paths shown in Figures 5.9 and 5.10, it is clear that no failure (i.e., yield) happens due to the input motion. Hence, any deformation is accumulated only as a result of the reduced loading shear modulus and the downslope bias of the static shear stress present in the slope. No permanent deformation has occurred due to plastic yielding by exceeding the residual strength.

After the liquefaction, the model shows the following loading and unloading behavior:

(1) The soil block experiences upslope loading using a residual shear modulus (soft modulus) until this loading period ends.

(2) Then the block experiences unloading using an unloading shear modulus (stiff modulus) until this unloading period ends and the initial static shear stress is also reached.

(3) At the initial static shear stress level, the block experiences soft loading again in the downslope direction until this loading period ends.

(4) Then the block experiences stiff unloading until the initial static shear stress is reached. At this point, the block will once again experience a soft loading and the above step (1) will be repeated.

Rerunning the model using a residual strength of 5 kPa for site 2, and if no other soil properties are changed, the hysteretic loop given by the model is shown in Figure 5.11. This figure shows that plastic yielding is occurring both during loading and unloading (note the flat tops and bottom parts of the hysteresis loops). The plastic yielding happens not only before but also after liquefaction.

Overall, the occurrence of the failure (plastic yielding) depends not only on the soil properties (e.g., loading and unloading moduli and shear strength) and earthquake motion, but also the magnitude of static shear stress that has developed in the slope.

Regarding shear strength, loose sands, upon reaching liquefaction, may develop residual strength values that are lower than the static shear stress in the slope and hence experience large deformation, resulting from both the softer loading modulus and plastic yielding in the downslope direction (Figure 5.9). In contrast, dense sands may have sufficiently high residual strengths to prevent yielding, but still undergo some limited deformation due to the softening of the loading modulus (Figure 5.10).

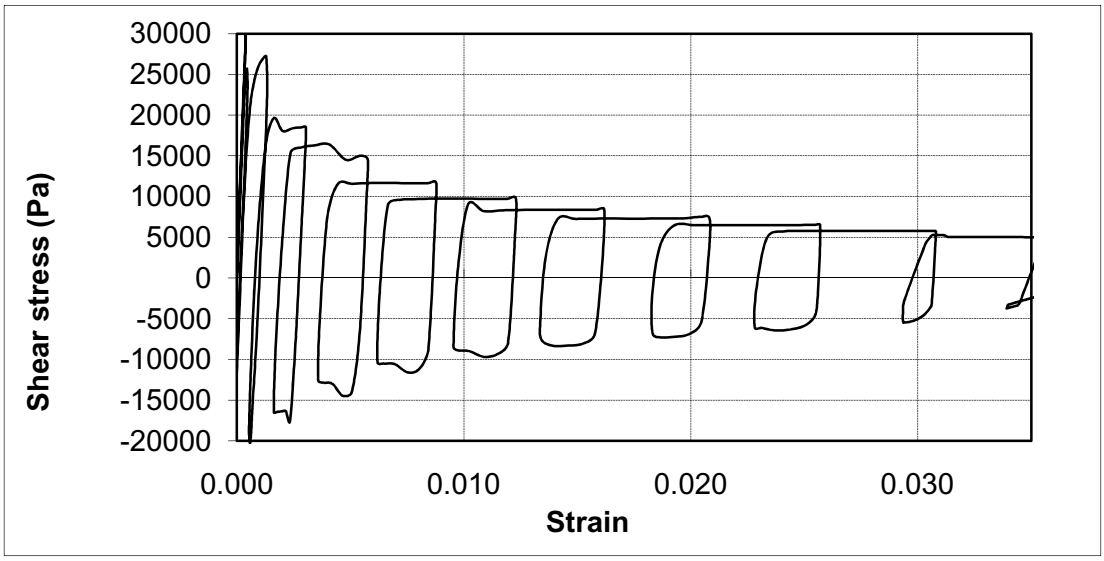


Figure 5.11. Hysteretic loop for site soil 2 with 5 kPa residual strength

Thus, it is concluded that the deformation caused by soil softening and liquefaction depends upon both the degradation of the shear modulus and the reduction of the strength to a residual strength. The combination of the two factors determines the amount of permanent downslope deformation. This is the basic concept developed in this research and the obtained modeling result verifies that this concept is satisfied for the simple test cases with harmonic input motion.

5.1.5 Displacement

Figures 5.12 and 5.13 show the deformation for a 5 s period of uniform cyclic loading, as previously used. At the end of the time interval, the deformation for site soil 1 with a $(N_1)_{60}$ value of 5 is about 2.5 times greater than the deformation for site 2 with a $(N_1)_{60}$ value of 15. The deformation histories increase rapidly after 0.5 s and 1.5 s for sites 1 and 2, respectively, when liquefaction time is reached.

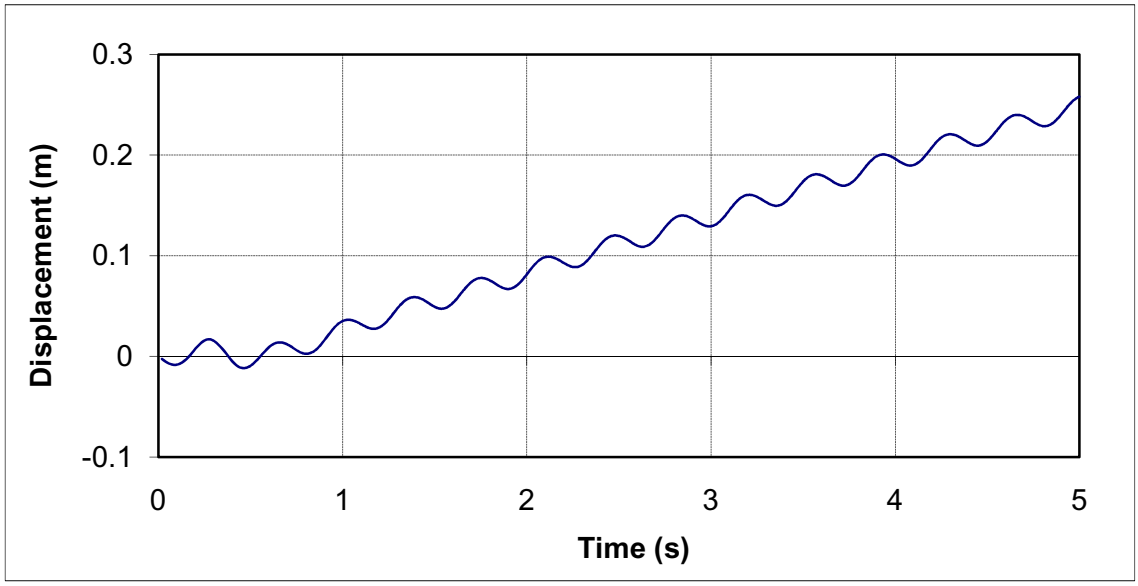


Figure 5.12. Deformation vs. time for site 1 on the middle of the ground surface

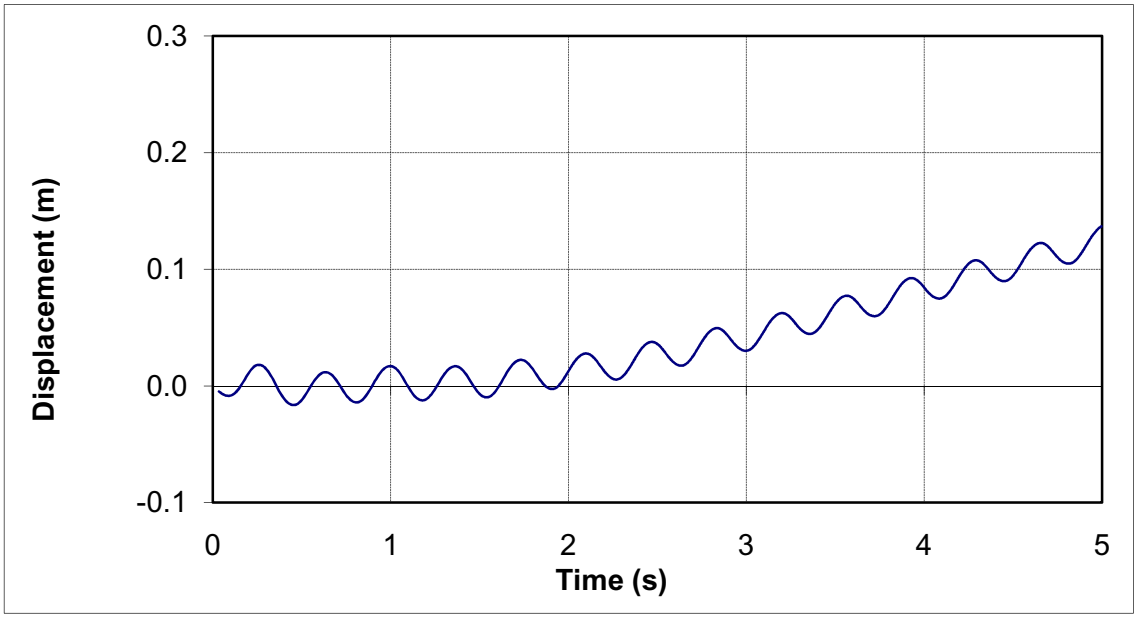


Figure 5.13. Deformation vs. time for site 2 on the middle of the ground surface

5.1.6 Deamplification of Strong Motion due to Liquefaction

Figures 5.14 and 5.15 show the input motion at the base of the model, the base of the liquefied layer and at the top of the liquefied layer, for sites 1 and 2, respectively.

Figure 5.14 shows that the amplitude of the acceleration response at the top of the liquefied layer decreases sharply when full liquefaction is reached. Figure 5.15 also shows that the amplitude of the acceleration response decreases at the same location, but is not as significant. For the latter case, it takes about 1.5 s for the soil to be fully liquefied. A comparison of Figures 5.14 and 5.15 suggests that the deamplification of the input motion is more significant for the lower blow count sand. Figures 5.14 and 5.15 illustrate this reduction in stiffness and its effects on the acceleration response. At about the liquefaction time, both figures show the travel time increase for the wave from the bottom of the liquefaction layer to the top of the liquefaction layer. The decrease of the shear wave velocity indicates the soil softening and the phase transition to liquefaction.

The deamplification caused by the softening soil not only decreases the acceleration amplitude but it also changes the fundamental period of the soil system. The effects on the soil column period and the acceleration response spectrum are explored in Section 5.2.6.

5.2 Model Verification Using a Real Earthquake Time History

The testing of the model using the idealized harmonic input motion and soil properties shows that it can reasonably approximate idealized pre- and postliquefaction behavior. A real earthquake history will now be tested to verify the model's effectiveness as a practical tool to model liquefaction response and ground deformation.

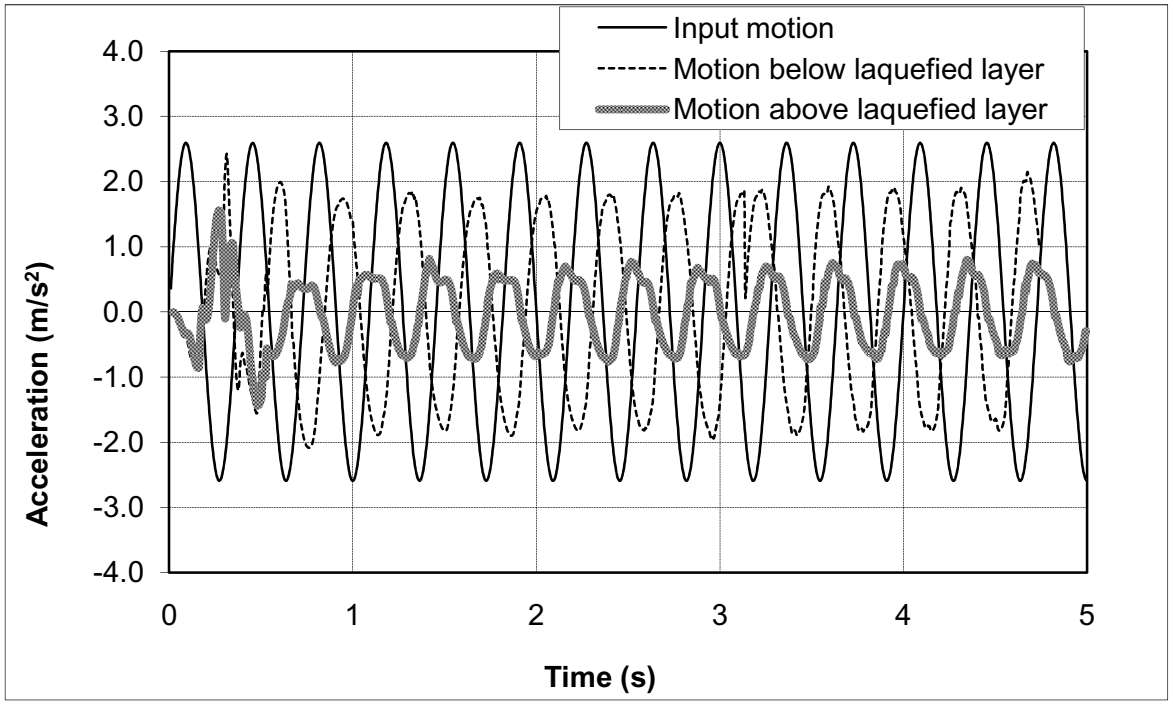


Figure 5.14. Predicted acceleration time histories for hypothetical site 1

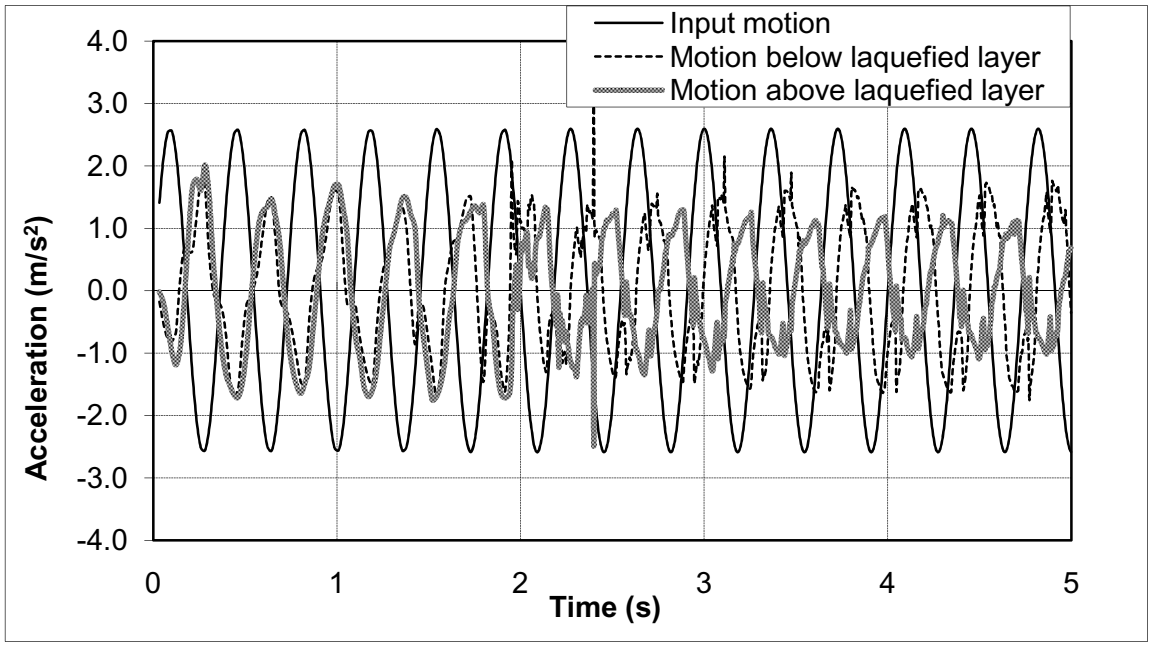


Figure 5.15. Predicted acceleration time histories for hypothetical site 2

5.2.1 Input Motion

The input motion selected for this evaluation is the Taft history, as shown in Figure 5.16. This earthquake time history lasted about 70 s with a peak ground acceleration of 0.15 g. The FLAC program removed the first 15 s, in order to save computational time.

5.2.2 Input Soil Parameters

The soil properties used are the same as those presented in the previous sections.

5.2.3 Shear Modulus Reduction With Pore Water Generation

Figures 5.17 to 5.19 show the shear stress and excess pore water ratio r_u development in the liquefied soil layer, and the degradation of shear modulus for soil 1. Figures 5.20 to 5.22 show the shear stress and associated pore water ratio r_u development in the liquefied soil layer and the degradation of shear modulus for site 2. Since peak acceleration amplitude occurs near 19s, both of the two sands achieve liquefaction almost at the same time, even though site 2 takes slightly more time to reach liquefaction than site 1.

5.2.4 Hysteretic Behavior

Figure 5.23 and Figure 5.24 show the hysteretic loops for sites 1 and 2, respectively. Because the peak ground acceleration (pga) value of the input earthquake motion is low, there is no yielding of the soil (i.e., the assigned residual strength is not reached) for both soils (i.e., the hysteresis loops do not have a flat top).

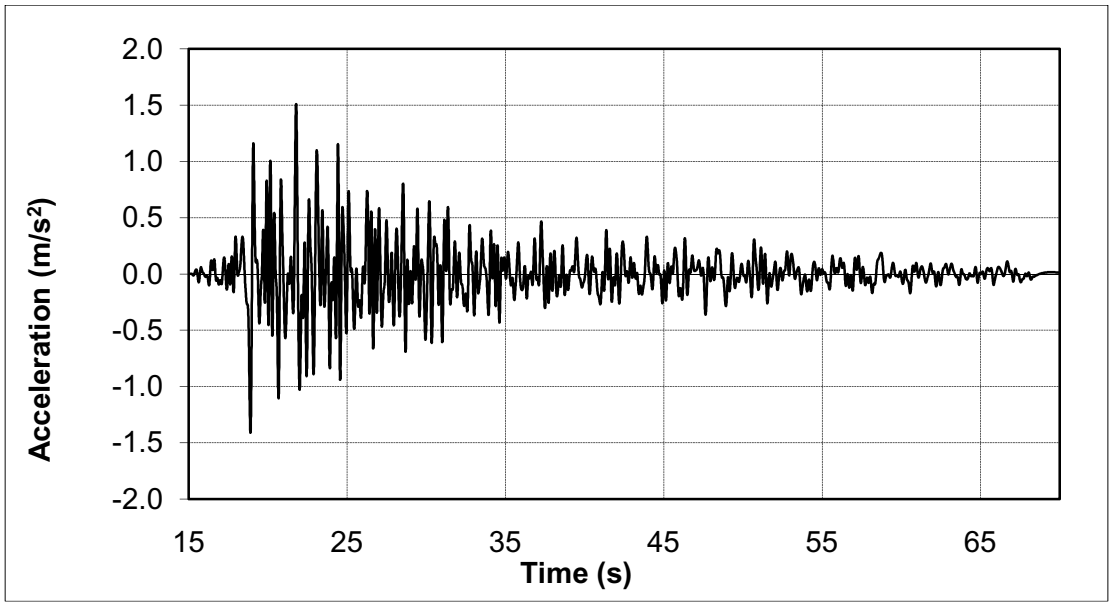


Figure 5.16. Tine history of Taft earthquake

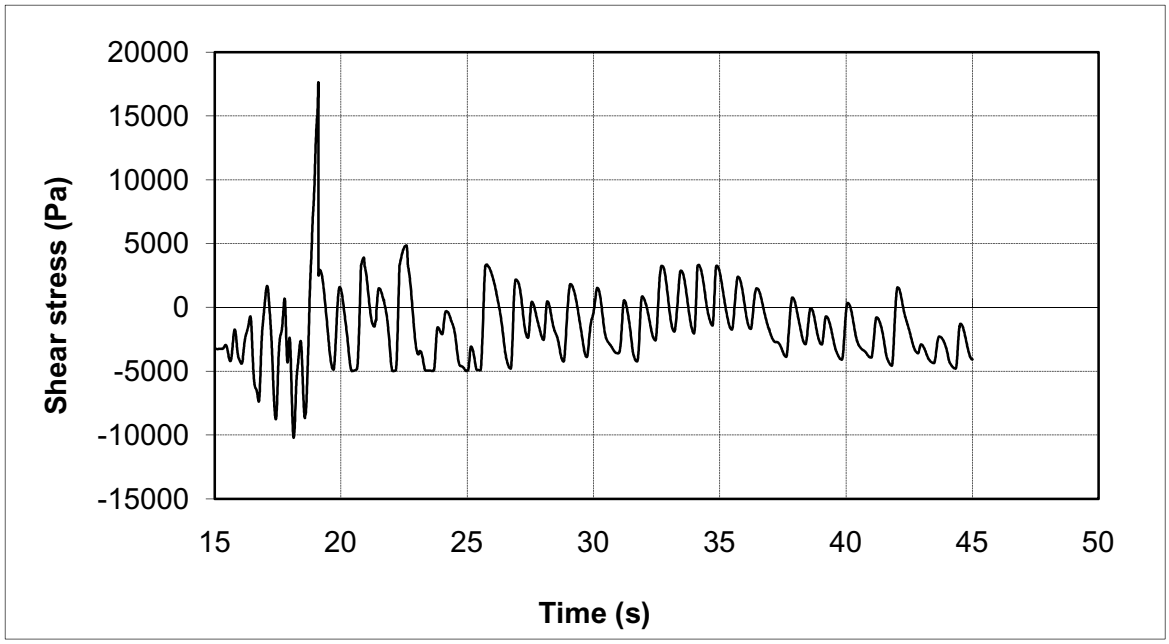


Figure 5.17. Shear stress development vs. time within site 1.

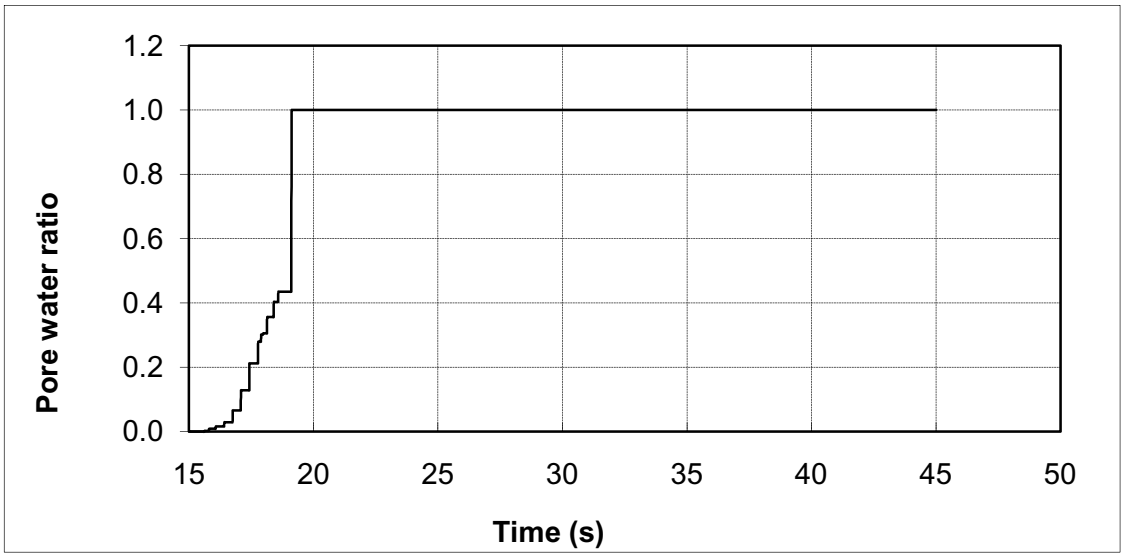


Figure 5.18. Pore water generation r_u development vs. time within site 1.

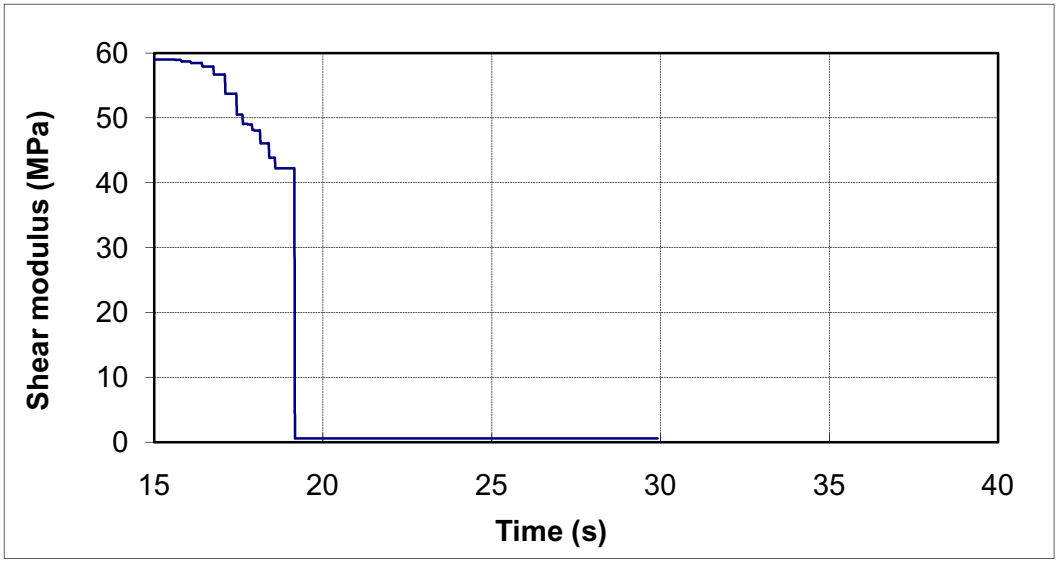


Figure 5.19. Shear modulus degradation for site 1.

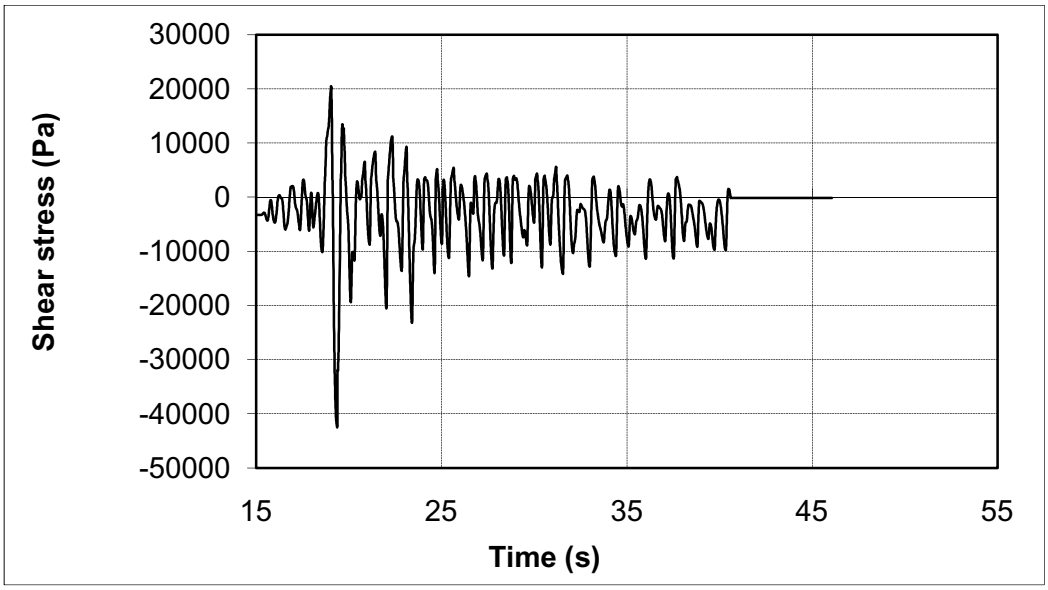


Figure 5.20. Shear stress development vs. time within site 2

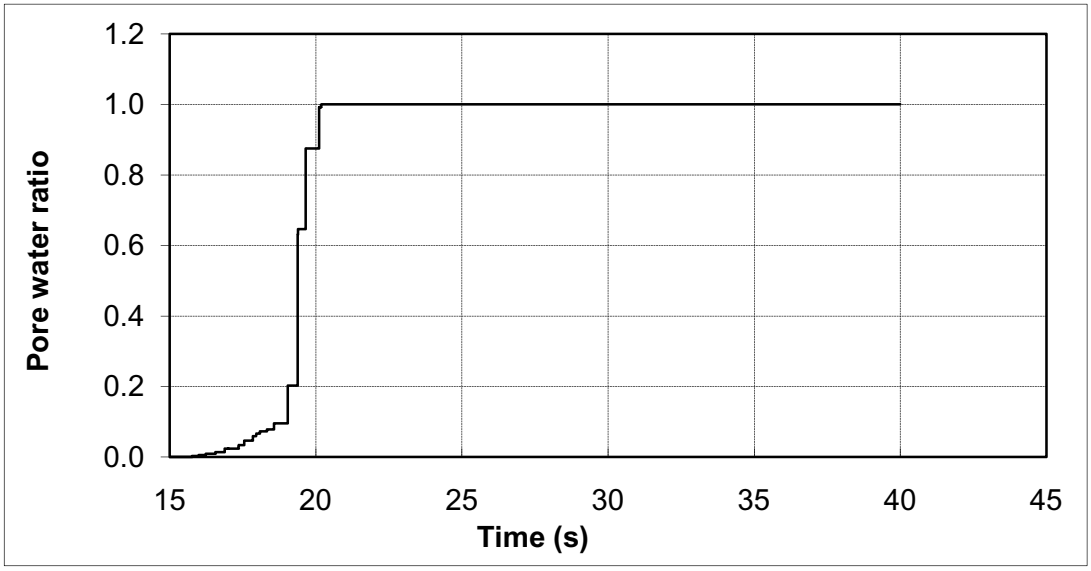


Figure 5.21. Pore water generation r_u development vs. time within site 2

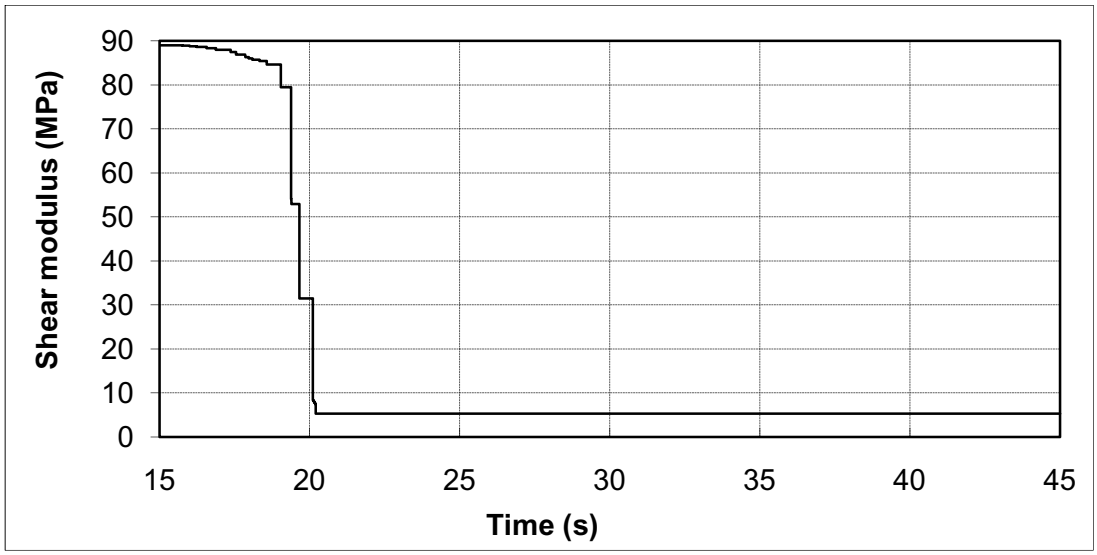


Figure 5.22. Shear modulus degradation for site 2.

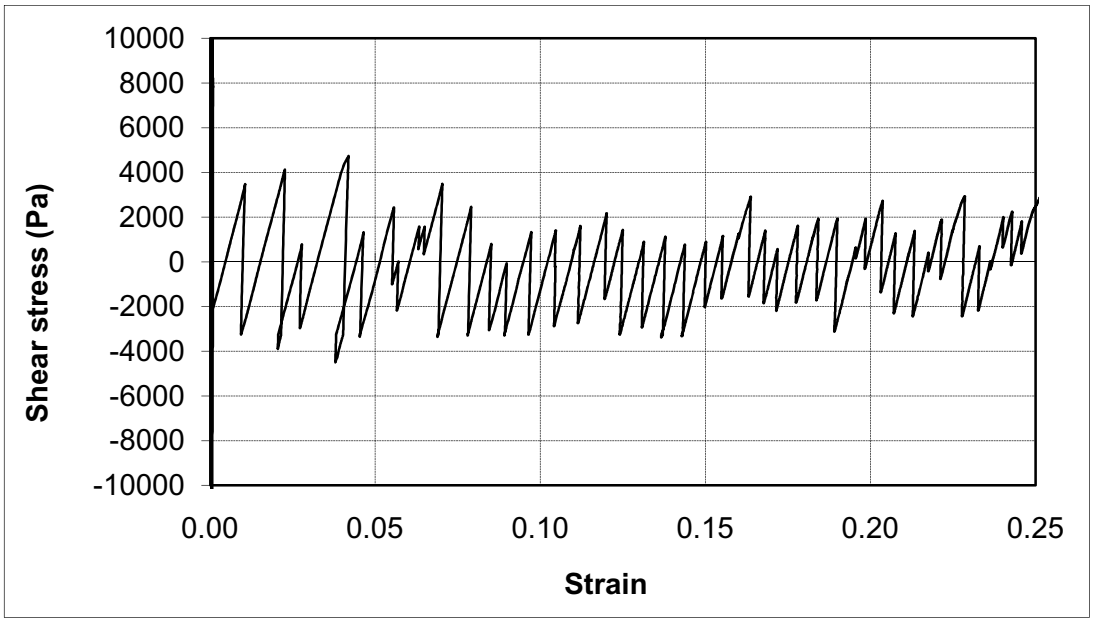


Figure 5.23. Hysteretic loops for site 1

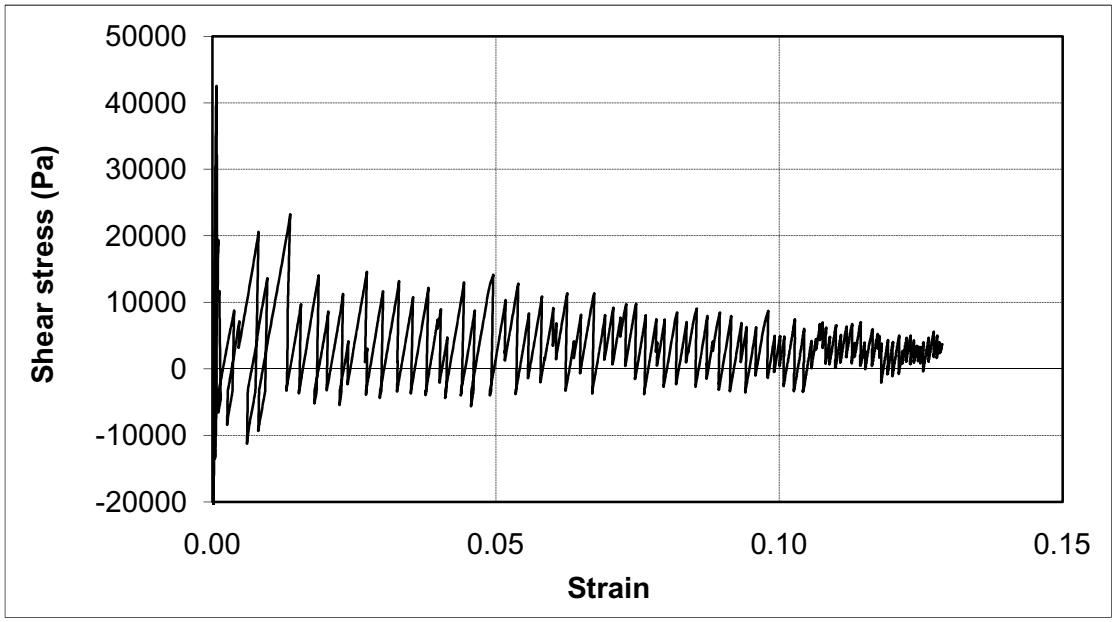


Figure 5.24. Hysteretic loops for site 2

However, permanent downslope deformation has accumulated due to the degradation of the shear modulus and the presence of the bias in static shear stress in the downslope direction. Also, Figures 5.23 and 5.24 show an indication of the loading and unloading inflection points that occur at the initial static shear stress.

5.2.5 Displacement

Figures 5.25 and 5.26 show the deformation history and deformation vectors for site 1, while Figures 5.27 and 5.28 show the deformation history and deformation vectors for site 2. The curves shown in Figure 5.25 and Figure 5.27 represent deformation time histories for the nodes located on the top of the model. From these figures, it can be seen that the deformation of site 1 is approximately 2 times greater than that of site 2 (1.2 m versus 0.6 m, respectively). Because site 1 is softer than site 2, the nodes on the top of site 1 show a much larger shift downslope when compared with that of site 2.

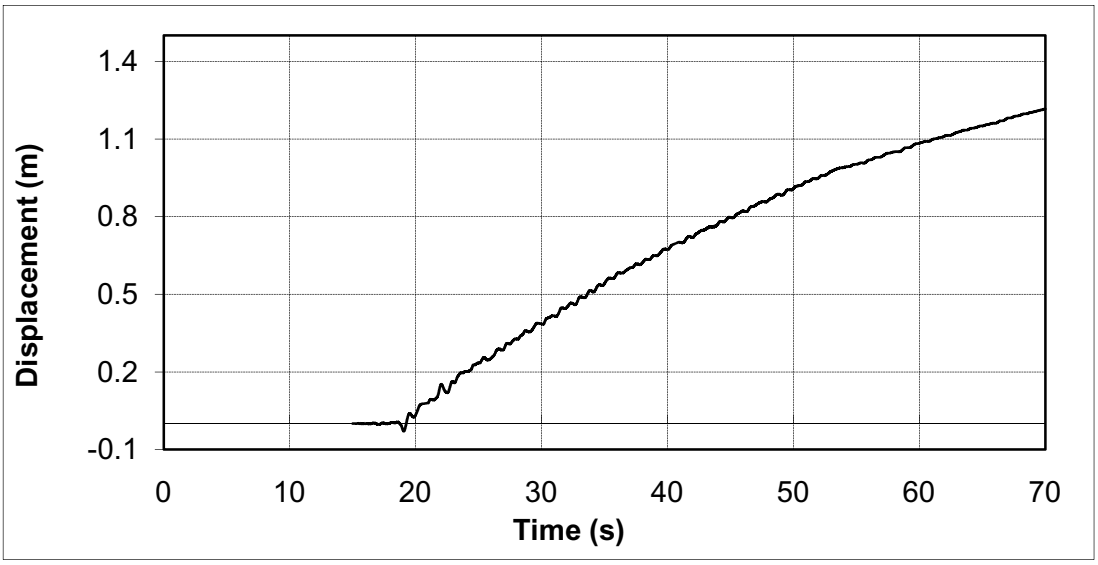


Figure 5.25. Deformation vs. time for site 1

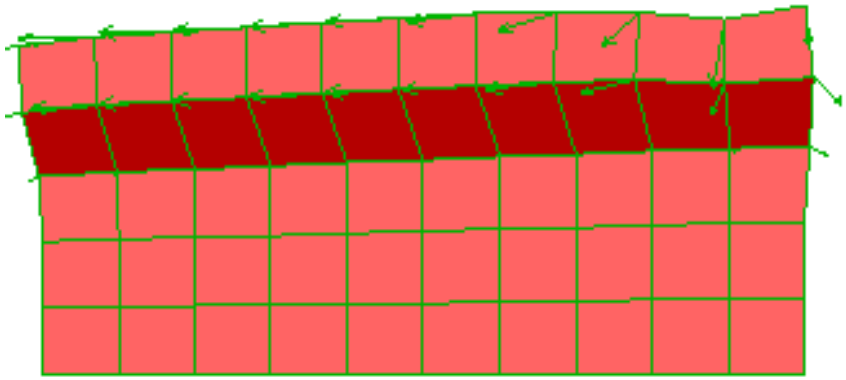


Figure 5.26. Deformation vector for site 1

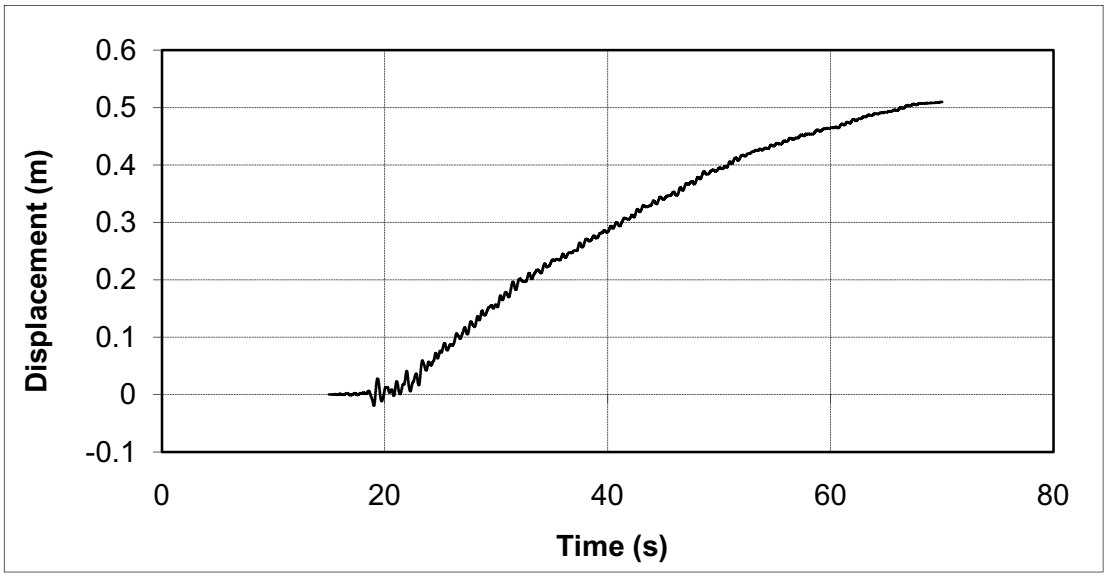


Figure 5.27. Deformation vs. time for hypothetical site 2

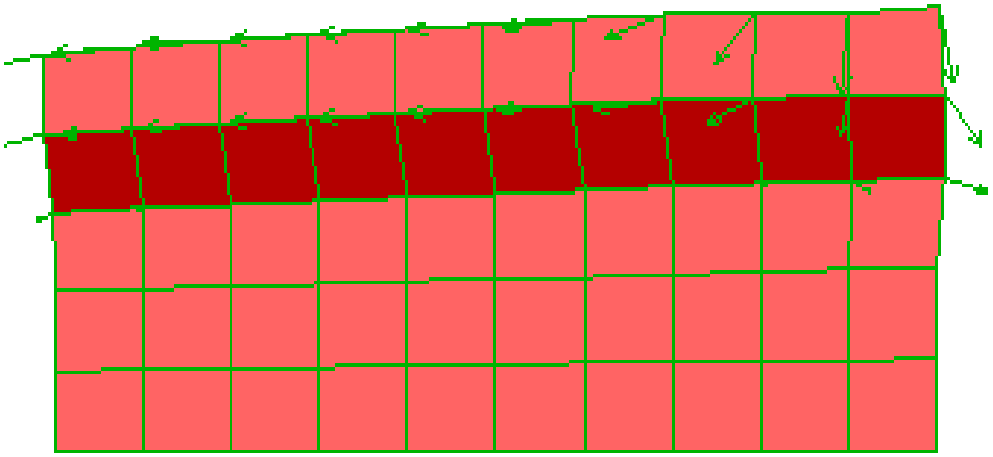


Figure 5.28. Deformation vector for site 2

In addition, for both soils, the deformation below the liquefied soil layer is much smaller than that above the liquefied layer. In Figure 5.26, the vector near the upper right corner is due to the boundary condition effect and would be neglected if the model were larger.

5.2.6 Modification of Ground Response due to Liquefaction

Figures 5.29 to 5.31 show the acceleration time history at the base of the liquefied layer, at the top of the liquefied layer, and the comparison between them for site 1. Figure 5.31 shows that the acceleration amplitude at the top of the liquefied layer decreases at the moment full liquefaction is reached (i.e., at about 19 s).

Figures 5.32 to 5.34 show the acceleration time history at the base of the liquefied layer, at the top of the liquefied layer, and the comparison between them for site 2. Figure 5.34 show that the accelerations at the top of the liquefied layer do not decrease significantly for the denser sand case.

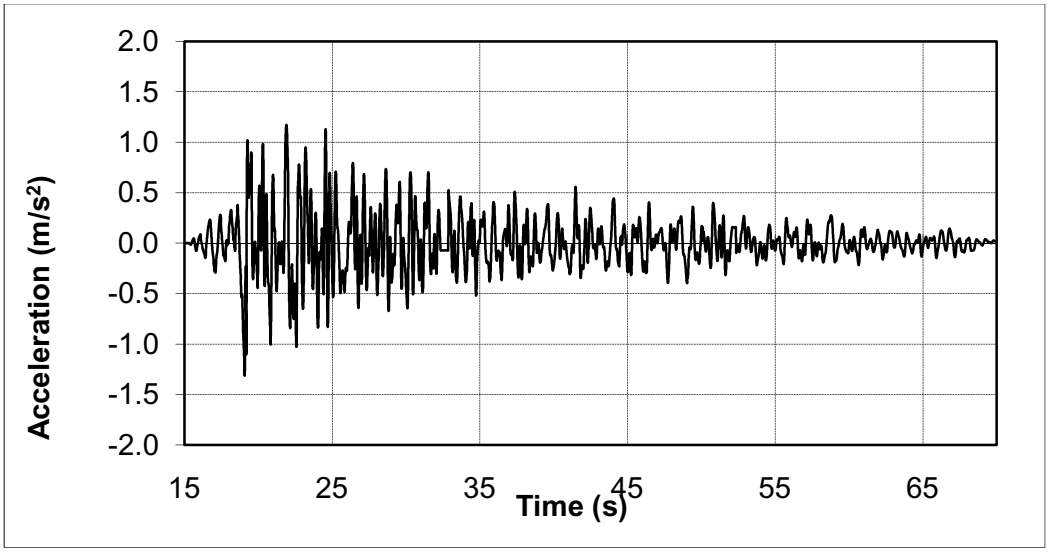


Figure 5.29. Predicted acceleration time history for site 1 on the base of liquefied layer

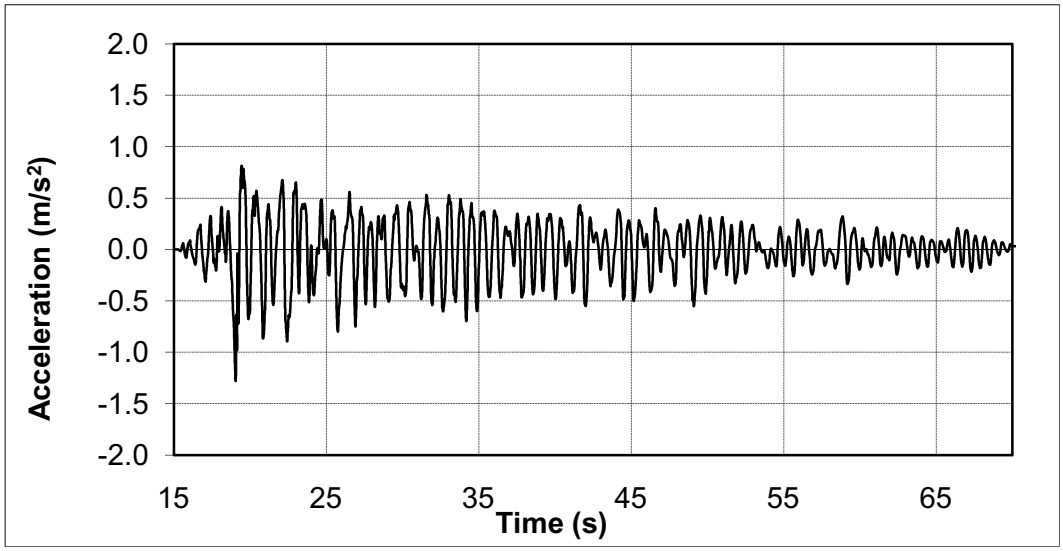


Figure 5.30. Predicted acceleration time history for site 1 on the top of liquefied layer

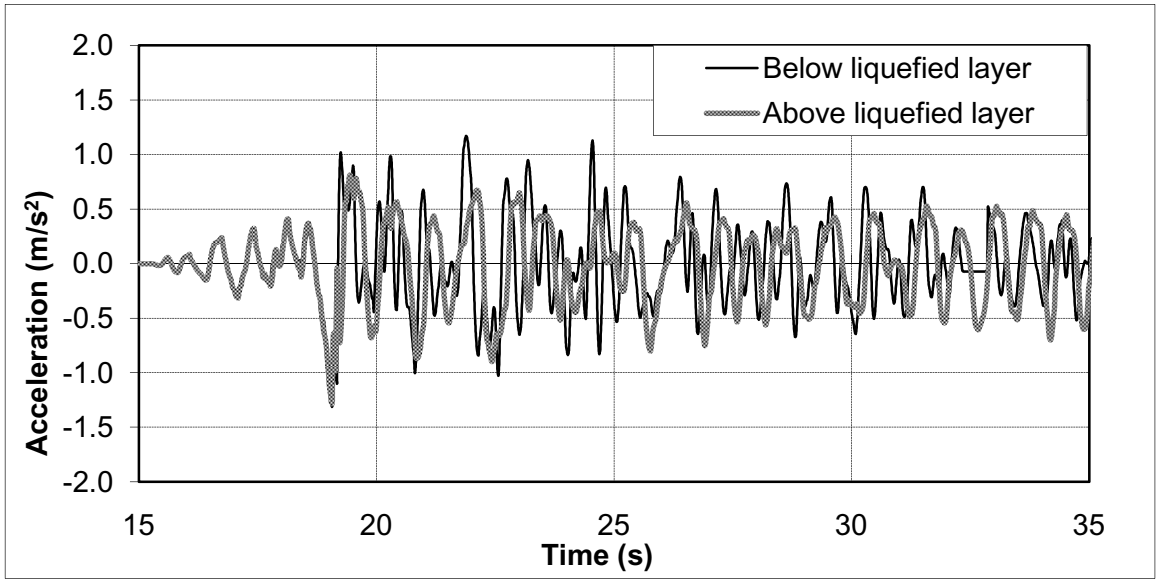


Figure 5.31. Enlargement of Figure 5.29 and 5.30 showing effect of soil softening on wave amplitude and period for site 1

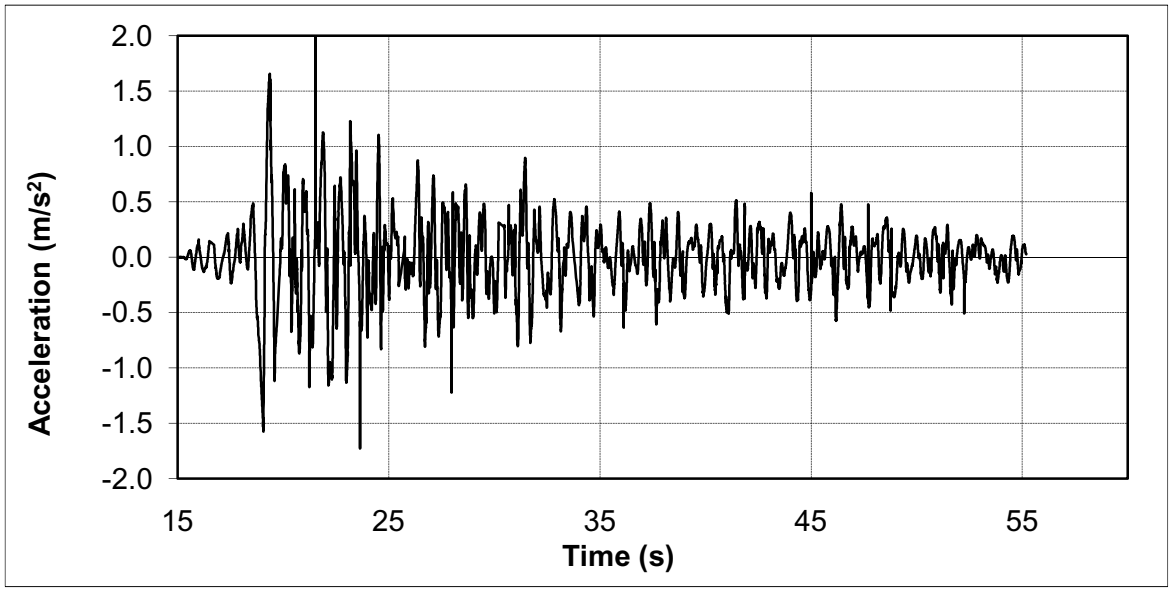


Figure 5.32. Predicted acceleration history for site 2 on the base of of T15 layer

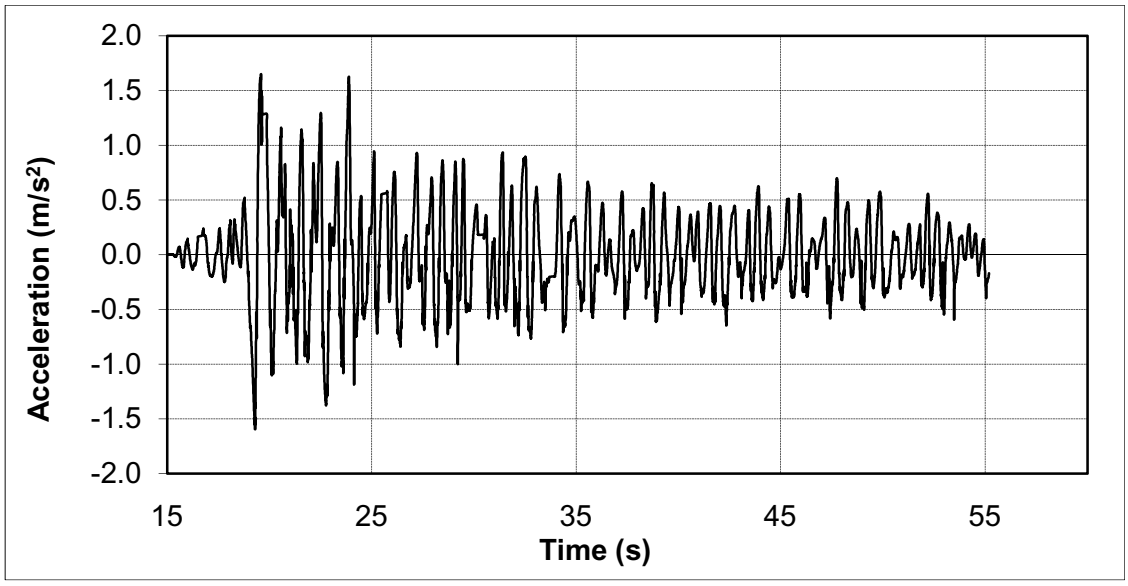


Figure 5.33. Predicted acceleration history for site 2 on the top of the T15 layer

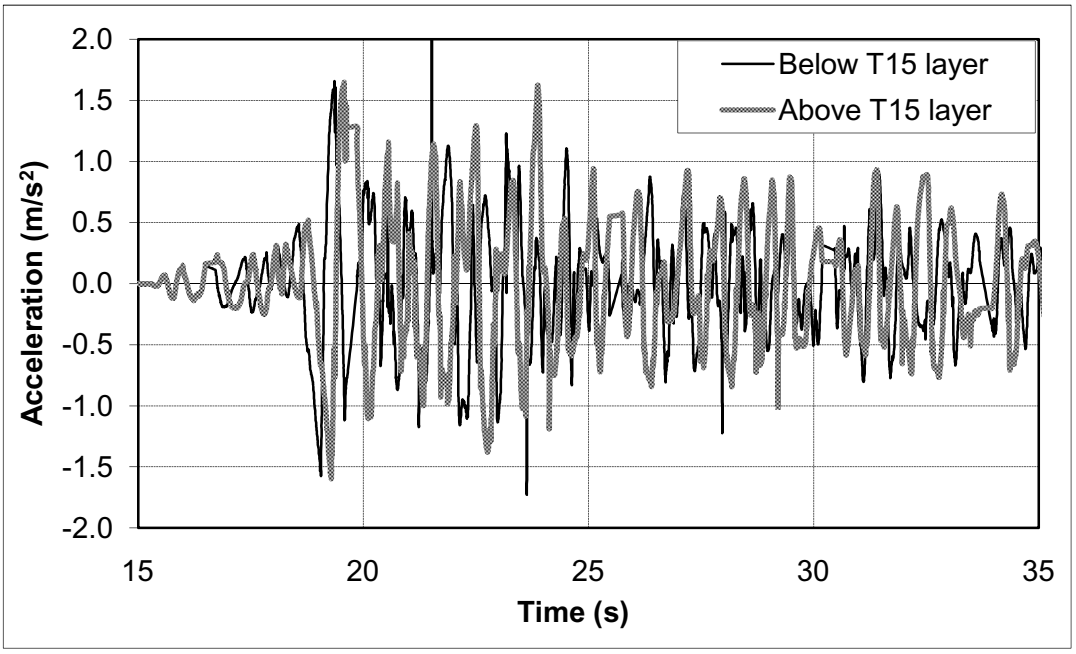


Figure 5.34. Enlargement of Figure 5.32 and 5.33 showing effect of soil softening on wave amplitude and period for site 2

The FLAC models indicate that deamplification of strong motion resulting from liquefaction of the looser sand is much more significant than that for the denser sand. For example, Figures 5.32 and 5.34 show a more detailed view of the acceleration time histories and an increase in wave length calculated at the top of the liquefied layer.

Figure 5.32, in particular, indicates that liquefied sand not only decrease the amplitude of the strong motion, but it also decreases the wave's frequency by filtering out the higher frequency components going through the softening soil.

Lastly, the response spectra obtained from the FLAC models are shown in Figure 5.35 and Figure 5.36 for sites 1 and 2, respectively.

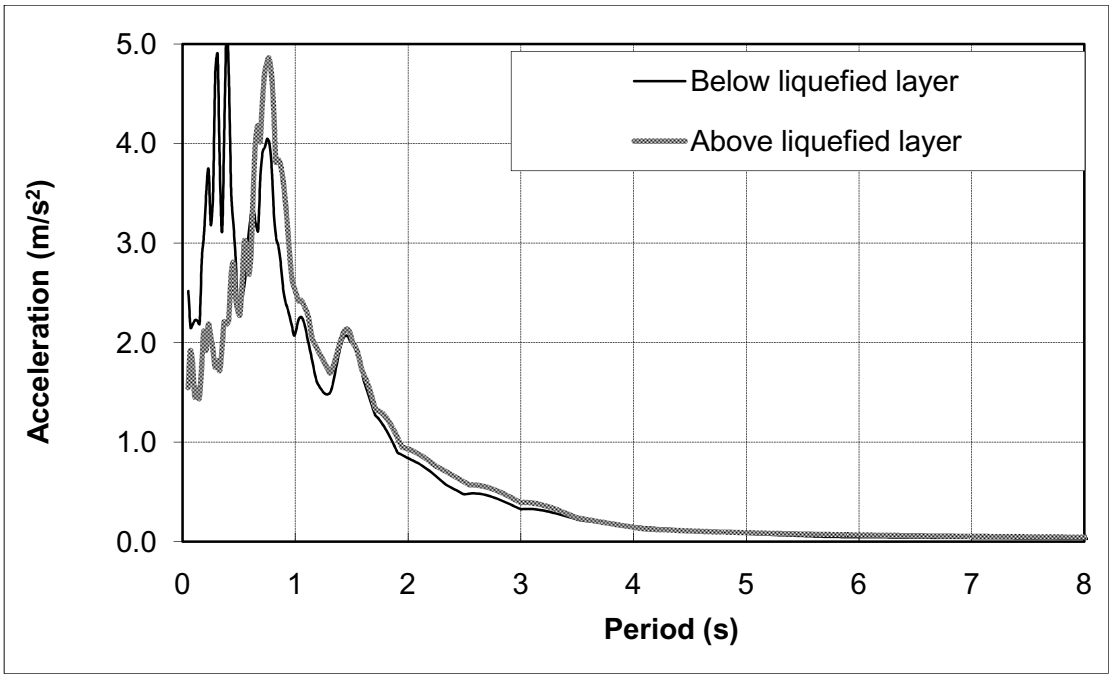


Figure 5.35. Response spectrum for site 1 on the base and top of the liquefied layer

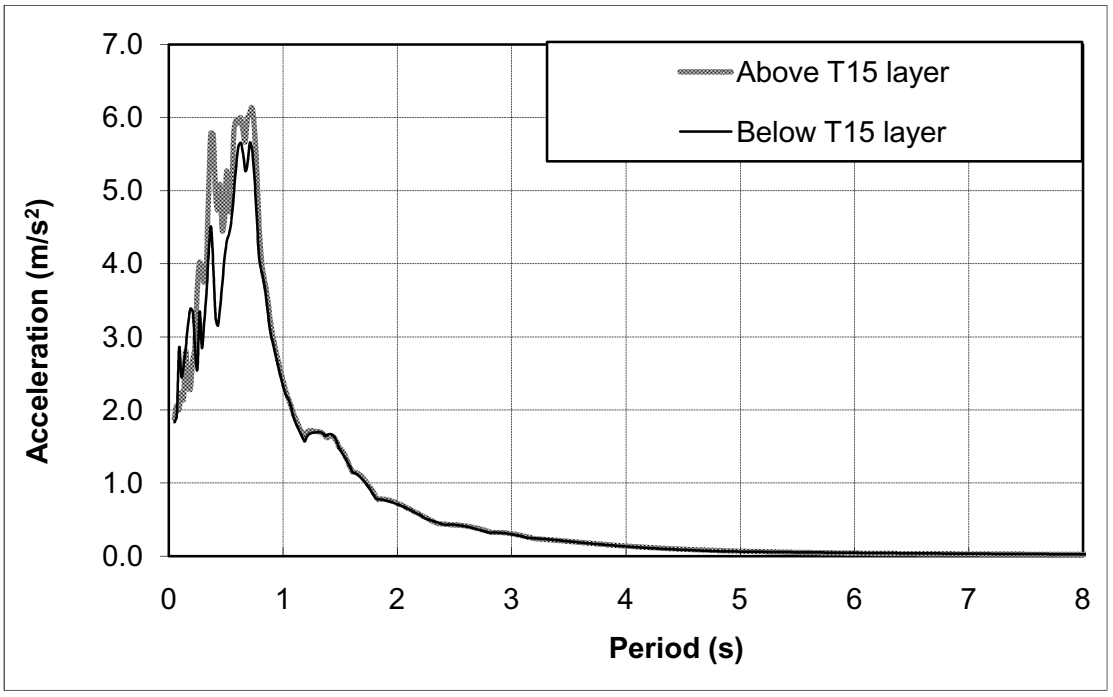


Figure 5.36. Response spectrum for site 2 on the base and top of T15 layer

The response spectrum of site 1 (Figure 5.32) indicates that loose sand decreases the spectral amplitude near the soil pre-liquefied predominated period, and liquefaction also shifts this predominated period to the right, or to increasing period. The response spectrum of site 2 indicates that higher blow count sand does not decrease the response spectrum amplitude as dramatically near the predominated period, but a slight lengthening of the period still occurs.

5.3 Summary

The proposed FLAC model takes into account shear modulus degradation and strength reduction as their effects of excess pore water generation. The model predictions suggest that the model approximates the mechanism of shear modulus degradation and shear strength reduction as a function of pore water generation. The simplified cases evaluated in this chapter also produce a reasonable deformation pattern; however, the magnitude of the deformation may not be accurate because the residual strength of the model has not been calibrated. Further, the ground response predictions show the effects of soil softening due to liquefaction and its effects on the strong motion amplitude near the predominate period of the soil column. The subsequent chapters further discuss verification and calibration of the modeling approach.

CHAPTER 6

GROUND RESPONSE CALIBRATION

As discussed in the previous chapter, it is important that the FLAC model be able to reasonably reproduce the primary effects of liquefaction and its influence on the strong motion as it is propagated through the liquefied layer. The main liquefaction effects are: (1) marked decrease in the amplitude of the high frequency component of the strong motion, (2) increase in the fundamental period of the soil system due to soil softening and (3) potential increase in the strong motion amplitude at longer periods. These effects are caused by liquefaction-induced softening and the soil behaving in an extremely nonlinear and increased damped fashion. From an implementation standpoint, it is important that the developed FLAC algorithms capture these effects so as to represent the transitory (i.e., nonstationary) nature of liquefaction and its impact on the strength, stiffness and inertial forces acting on the potential lateral spread mass.

To judge the performance of the FLAC model in estimating liquefaction effects and their impact on wave propagation, a series of ground response analyses are performed in this chapter using select case histories where strong motion was recorded below and above the liquefied zone. For most cases used in this study, it is impossible to observe the effects of wave propagation through the liquefied layer, because strong motion records are unavailable, or the strong motion was recorded at only the surface.

However, two sites offer a unique opportunity of studying wave propagation through the liquefied zone; the Wildlife site (1987 Superstition Hills, California Earthquake) and the Kobe site (1995 Kobe, Japan Earthquake). At these sites, the strong motion was recorded both below and above the liquefied zone using downhole and surface instrumentation, and these sites have been well documented and studied by other investigators.

The objective of this chapter is to verify that the FLAC model can reproduce, on average, liquefaction effects and their impact on the ground response measured at the ground surface. This is not an easy task because of the strong nonlinearity and transitory (i.e., nonstationary) nature of the problem under consideration and the many uncertainties in the soil properties. The goal of this modeling performed in this chapter is not to exactly replicate the surface acceleration time history that has been influenced by liquefaction, but to show that the model, in general, can produce the softening effects associated with liquefaction in a reasonable manner. The efficacy of the model in capturing liquefaction softening will be judged by comparing the acceleration time histories, corresponding response spectra, pore water generation time histories and stress-strain (i.e., hysteresis) loops with those recorded at, or estimated by other researchers, for the Wildlife and Kobe sites. Once the model has been used for these two sites, a more extensive calibration will be done by using 16 additional case histories. This more extensive calibration will be done by back-calculating the model properties that match the measured displacement pattern at the case history sites, as further discussed in Chapter 7.

6.1 Calibration with Wildlife Array

6.1.1 Background of Wildlife Superstition Hills Earthquake

About 11 hours after the Elmore Ranch earthquake, at local time of 5:15AM on November 24, 1987, the M6.6 Superstition Hills earthquake shook the Wildlife Liquefaction Array **(**WLA) and generated excess pore water pressures as great as 100 percent of the overburden pressure. A plan and cross-sectional views of the Wildlife Array are shown in Figure 6.1 (Bennett et al., 1984). This rise of excess pore pressure in the liquefied sand stratum (layer B) is shown in Figure 6.1. This generated sand boils, ground fissures and horizontal ground displacement toward the adjacent Alamo River (Youd and Holzer, 1994; Bartlett and Youd, 1992; Holzer et al., 1989).

Instruments at the WLA included: two 3-component accelerometers, one placed at the ground surface and one placed at a depth of 7.5 m (immediately below the granular layer) and six electrical transducer pore pressure piezometers. The soil profile (Figure 6.1; Table 6.1) consists of approximately 3 m of silty and clayey nonliquefiable flood plain sediment, overlying 4 m of sand and silty sands (some of which are liquefiable), which in turn overlie thick layers of overconsolidated clay, silt and sand to a depth of several hundred meters (Bennett et al., 1984).

The average SPT N values and fines content for soils at the WLF array (Table 6.2) were calculated from the boreholes and geotechnical investigations. A SPT N value of 9 and average fines content of 36% were used to calculate the soil properties for the FLAC model. (The developed FISH code converts the SPT N value to an equivalent $(N_1)_{60CS}$ automatically. From this value, which is 16, the ratio of residual strength to residual shear modulus, which is 0.016 for this case, is selected, as previously discussed).

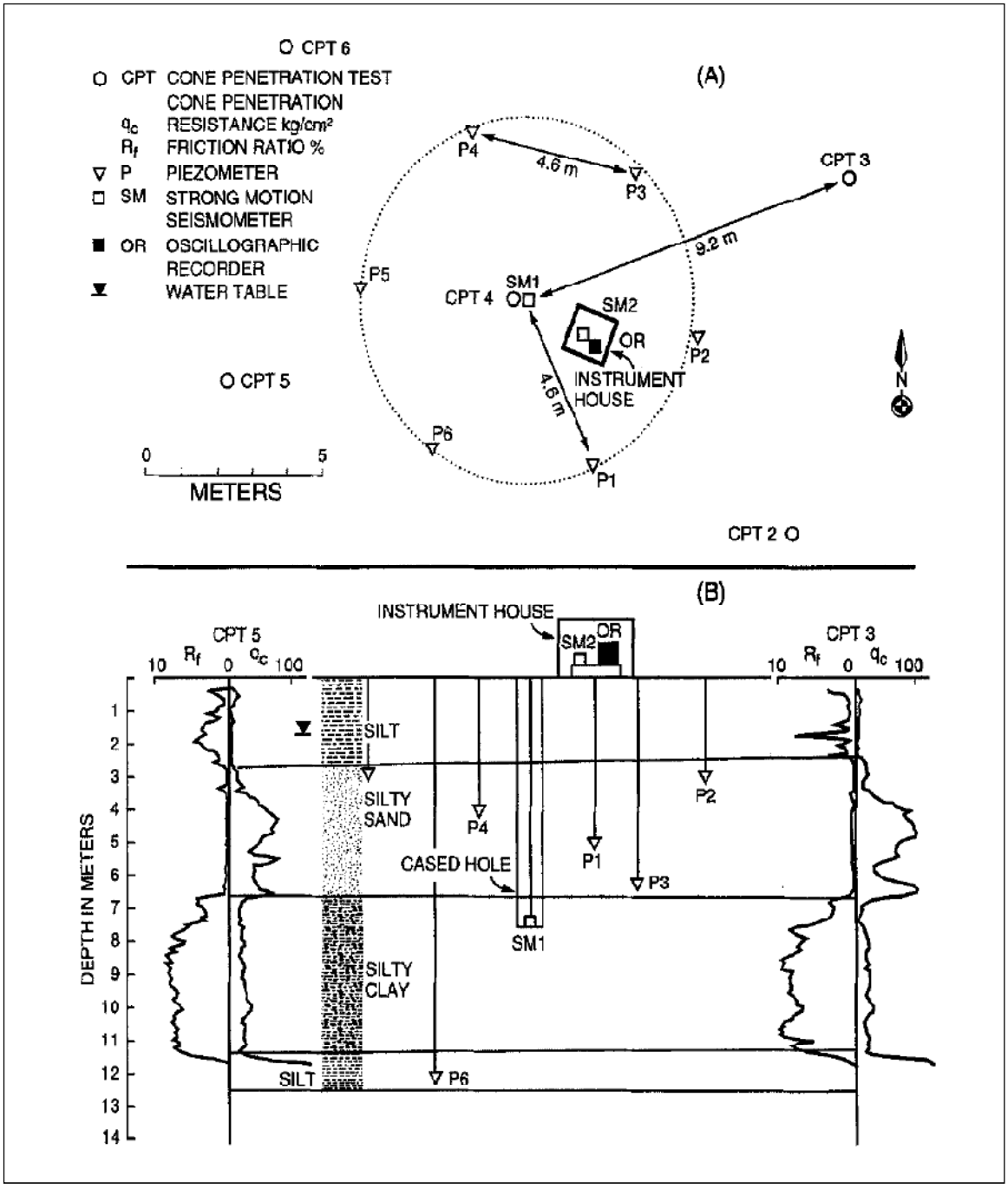


Figure 6.1. Liquefaction array site plan (a) and cross section (b) showing sediment layers and instrument locations at WLA (after Bennett et al. 1984)

Table 6.1. Soil properties for soils at the WLA (after Bennett et al. 1984).

Layer	Material type	Thickness (m)	Dry unit weight (kN/m^3)	Shear velocity (m/s)	Shear modulus (kPa)
A	Silt to clayey silt	~ 3.0	15.7	120	23046
B	Silty sand to sandy silt	~ 4.0	17.3	140	34565
C	Silty clay	~ 8.0	20.4	190	75070

Table 6.2. Blow count and fine content for the T_{15} layer at WLA

Borehole location	$(N_1)_{60}$	Fine content (%)
$5N_g$	7.4	44
$N_{c1,2,3}$	8.2	42
$3N_s$	13.9	39
$2N_{g1,2,3}$	8.6	31
$1N_s$	7.5	22
Average Value	9.0	36

6.1.2 Model Procedure Development and Execution

Using the previously discussed soil properties and the location of the liquefied layer, the dimension of the FLAC model was developed as shown in Figure 6.2. A 4-m wide by 2-m thick mesh size was used for the model (Figure 6.2).

Only acceleration time histories at a 6-m depth and at the ground surface were recorded at the WLF site. Because the 6-m depth was at the bottom of the liquefied layer, a Proshake model was used to deconvolved the 6-m depth motion (Figure 6.3) to the base of the FLAC model (Figure 6.4), which is at 20 m. Subsequently, SeismoSignal™ (2006), Version 3.2 was used to baseline correct the deconvolved motion and it was converted to FLAC input format.

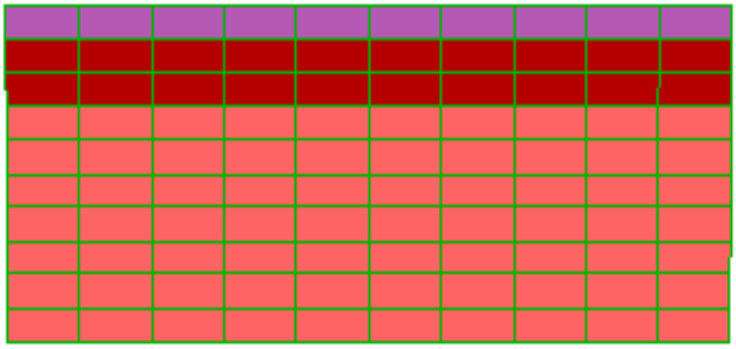


Figure 6.2. FLAC model for Wildlife site

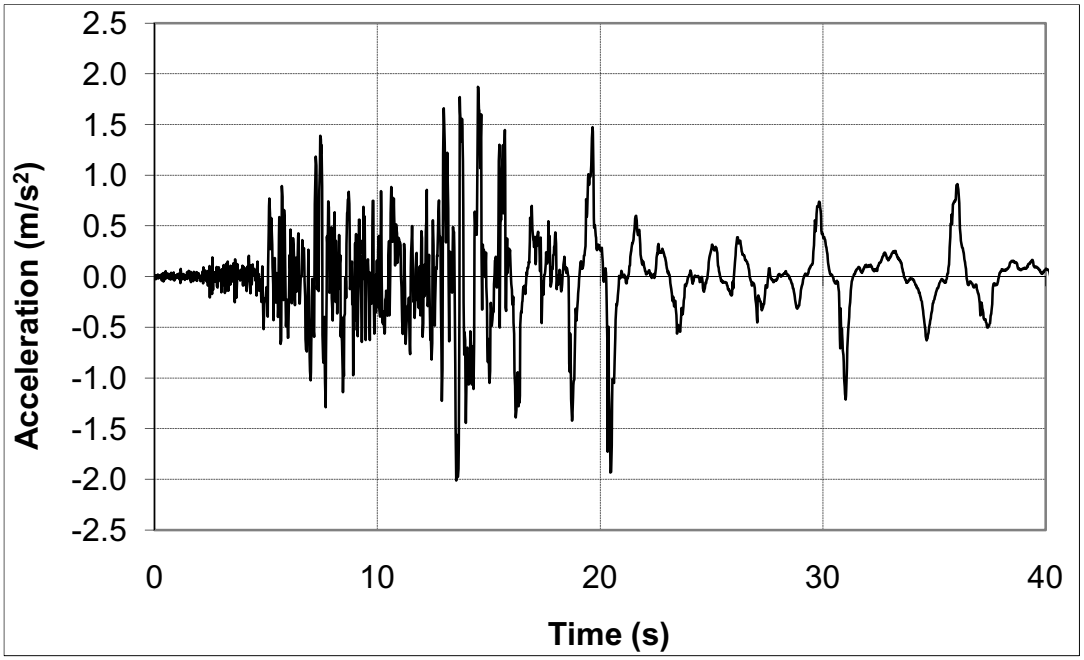


Figure 6.3. Recorded time history at 6-m depth for the WLA

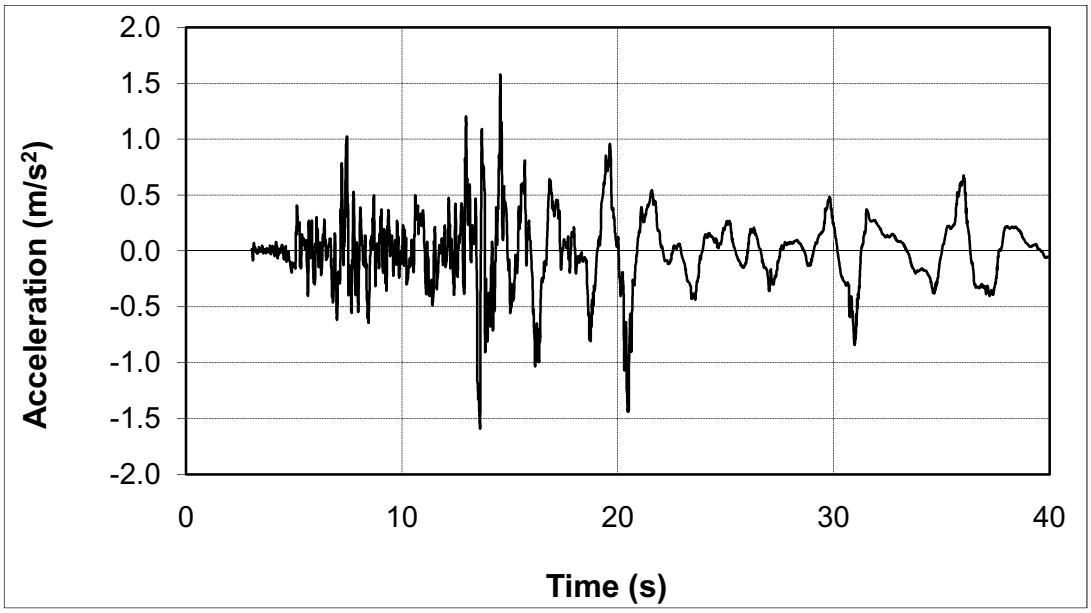


Figure 6.4. Deconvolved acceleration time history at a 20-m depth (i.e., FLAC model base) for the WLA

In addition, for modeling expediency, the earthquake motion after 40 s of elapsed time was not used due to its relatively low amplitude and negligible impact on the modeling.

Lastly, an acceleration time history cannot be used directly at the base of the FLAC model due to the specified boundary condition. Because a compliant base (i.e., quiet boundary) was used at the model's base, this condition requires a stress time history as input for the subsequent convolution analysis (Itasca, 2005). The steps to do this are: (1) The acceleration time history calculated at the base of the Proshake model (Figure 6.4) must be requested as an "outcropping" motion to ensure that only the upward propagating wave is used in the FLAC model (Mejia, 2006). However, because the amplitude of the "outcropping" motion is twice that of an interlayer motion, due to the free surface effect, the "outcropping" acceleration time history values must be divided by

two to convert it to an interlayer upward motion (Mejia, 2006). (2) The interlayer acceleration time from step (1) is then converted to a stress time history. To do this part, the baseline corrected acceleration time history is integrated to obtain a velocity time history and then the proportionality of stress to velocity in an elastic wave is used to calculate the amplitude of the stress wave (Mejia, 2006; Itasca, 2005).

The stress time history was then assigned to the base of the FLAC model in the subsequent convolution analysis and acceleration time histories were obtained at the 6-m depth and ground surface. To check the reasonableness of the developed stress time history for the quiet boundary, the X-velocity at the base of the model during the dynamic run is monitored and compared to the input velocity. Some minor adjustment to the input stress wave may be required in order to produce a velocity at the base that corresponds to the input velocity.

Figures 6.5 and 6.6 show the input and measured velocity histories from convolution analysis and FLAC model, respectively, for the case where the shear stress is used as the base input. This comparison shows that the calculated x velocity from the FLAC model during dynamic time stepping (i.e., running the FLAC model) is similar to the input velocity; however, some differences are expected in the FLAC results due to the presence of reflected waves in this model. (The differences arise from the fact that the inputted motion in this layer has no reflected wave component; whereas the FLAC model results for the basal layer contains reflected waves from the free surface and other overlying layers.)

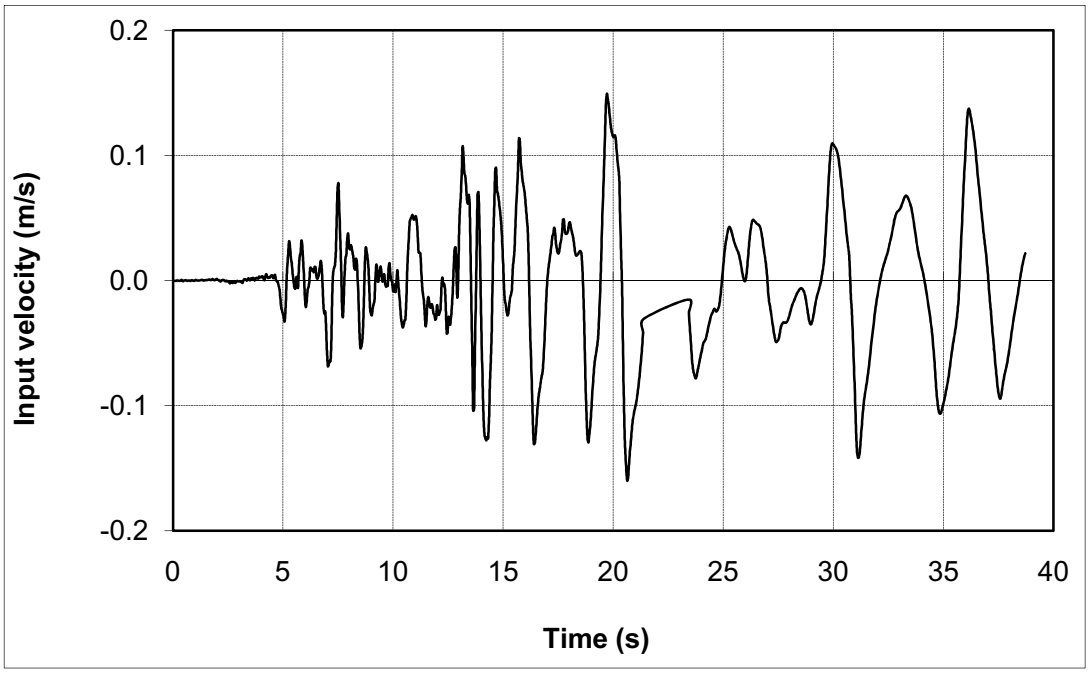


Figure 6.5. Input velocity time history at base of FLAC model (20 m) for the WLA

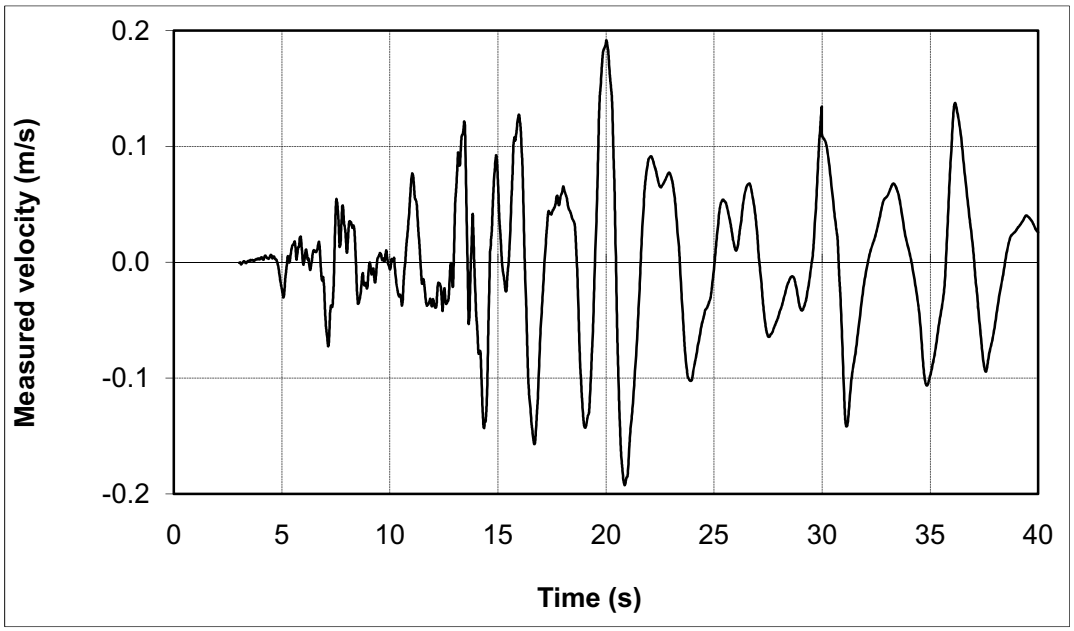


Figure 6.6. Calculated velocity time history at base of FLAC model (20 m) for the WLA

Lastly, all FLAC models used in this study have a small amount of Rayleigh damping (0.5%) for numerical stability to help reduced high frequency noise caused by the numerical algorithm. The use of Rayleigh damping in FLAC requires that the user specify the frequency associated with the Rayleigh damping (Itasca, 2005). To this end, Figure 6.7 shows the power spectrum (i.e., a plot of the portion of a signal's power energy per unit time falling within given frequency bins) of the x velocity time history in the liquefied layer. This curve shows that the predominant frequency for the liquefied soil profile is approximately 0.5 Hz (i.e., T = 2 s). This frequency was used as the Rayleigh damping parameter in the FLAC model (Itasca, 2005).

6.1.3 Model Performance

6.1.3.1 Acceleration Time History Comparison

Figures 6.8 shows the estimated acceleration time history from the FLAC model produced by convolving the motion from 20-m to the 6-m depth.

In addition, a comparison between Figure 6.8 (from FLAC) and Figure 6.3 (recorded) is plotted in Figure 6.9. This figure shows very good agreement between the recorded motion and the motion obtained from the FLAC model. This agreement demonstrates the appropriateness of the deconvolution process and ensures that input motion (Figure 6.5) has been properly calculated and convolved from the base of the model to the base of the liquefied zone. Good agreement was expected for this part of the process because strong nonlinearity (i.e., liquefaction) is not present in the soils at this depth interval making the analyses much easier to perform.

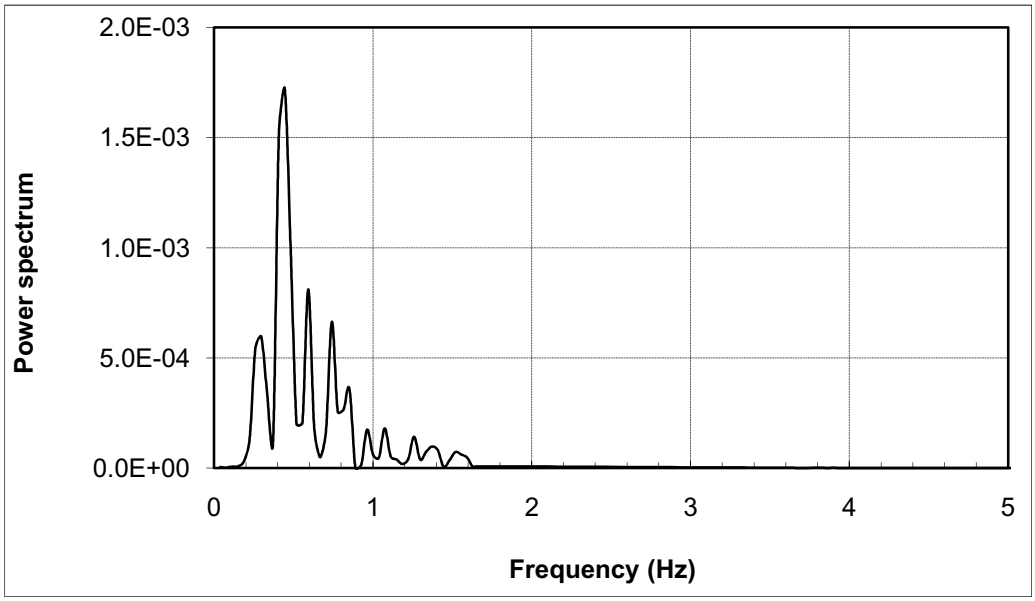


Figure 6.7. Power spectrum of x velocity time history in the liquefied layer for the WLA

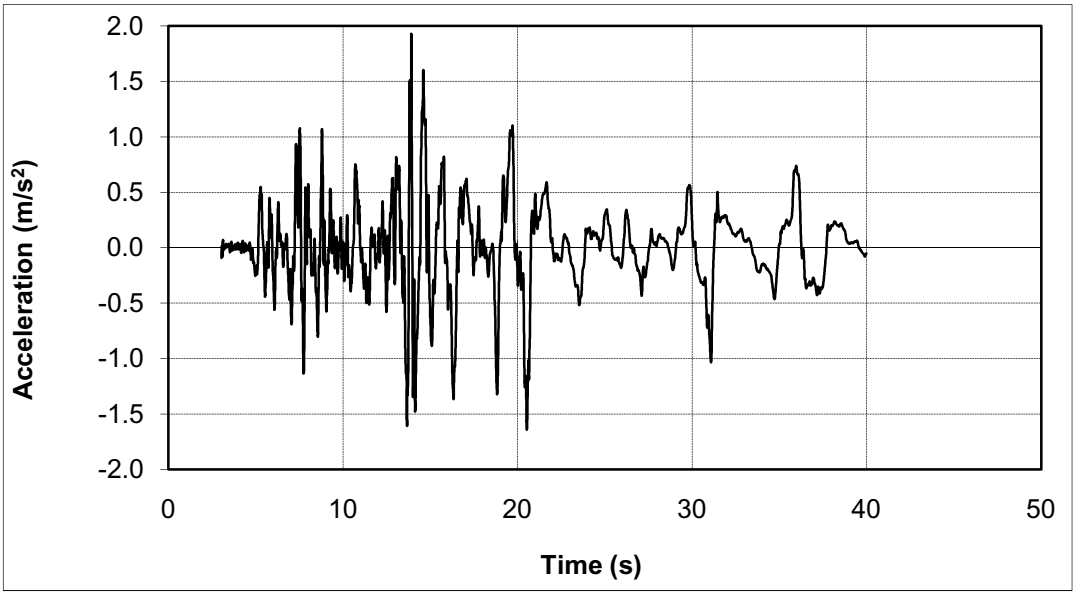


Figure 6.8. Wildlife predicted motion just below liquefied layer at 6 m depth

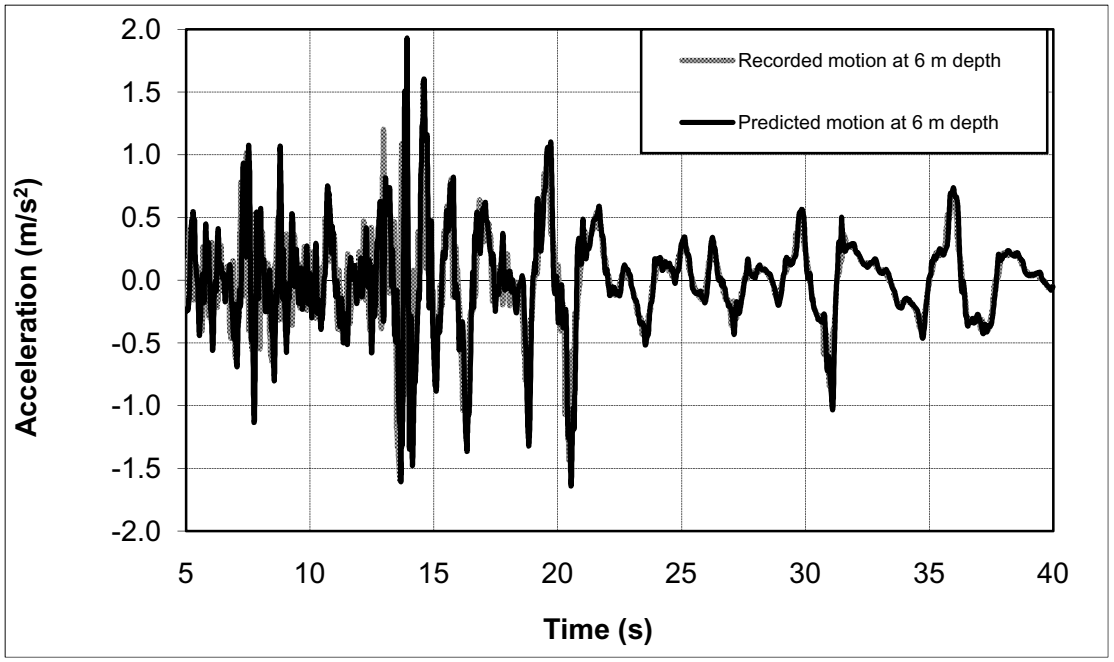


Figure 6.9. Comparison between estimated and recorded motions just below the liquefied layer at a 6 m depth for the WLA.

Figures 6.10 and 6.11 show the FLAC estimated and field recorded motions on the ground surface, respectively, including liquefaction effects. A comparison between the estimated and recorded motions is shown in Figure 6.12. Based on this figure, it can be seen that the FLAC model begins to deviate significantly from the recorded motion at about 13 s. The FLAC model underpredicts the acceleration spike at about 13 s and beginning at about that same time, the period of the predicted motion is somewhat longer. By 18 s, when the FLAC model predicts full liquefaction, the subsequent predicted ground motion has a longer period and somewhat higher amplitude than the recorded motion. (This is because the FLAC model has reached full liquefaction by this time; whereas the WLA may not have reached full liquefaction (see discussion in next section).

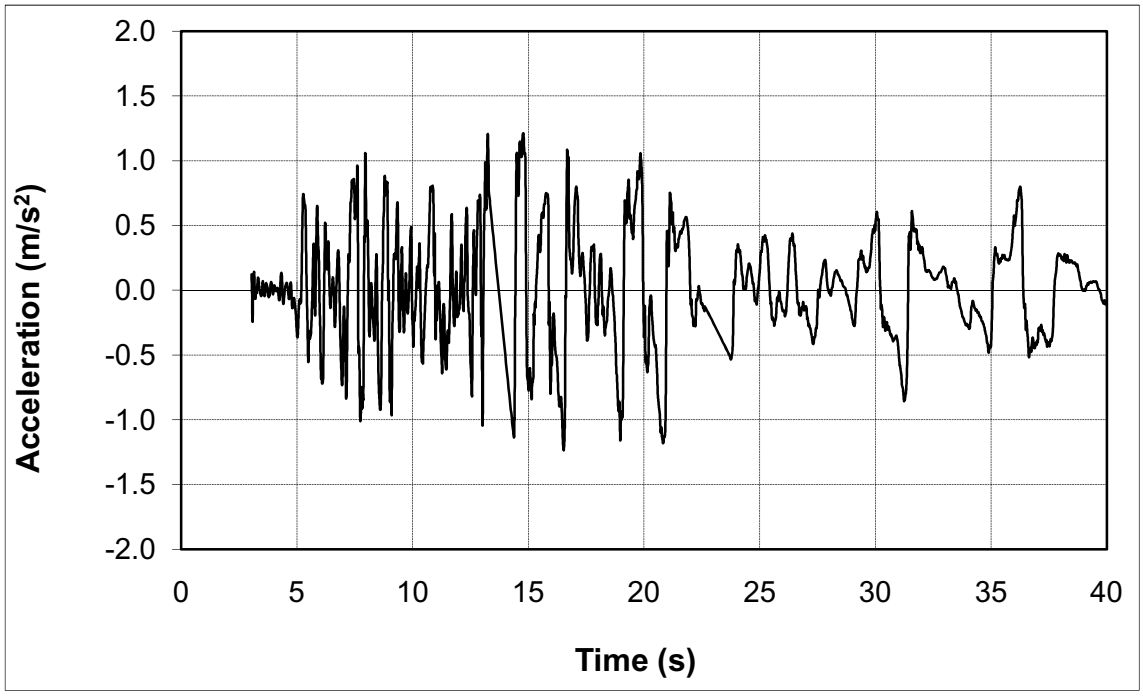


Figure 6.10. Estimated motion at the ground surface for the WLA

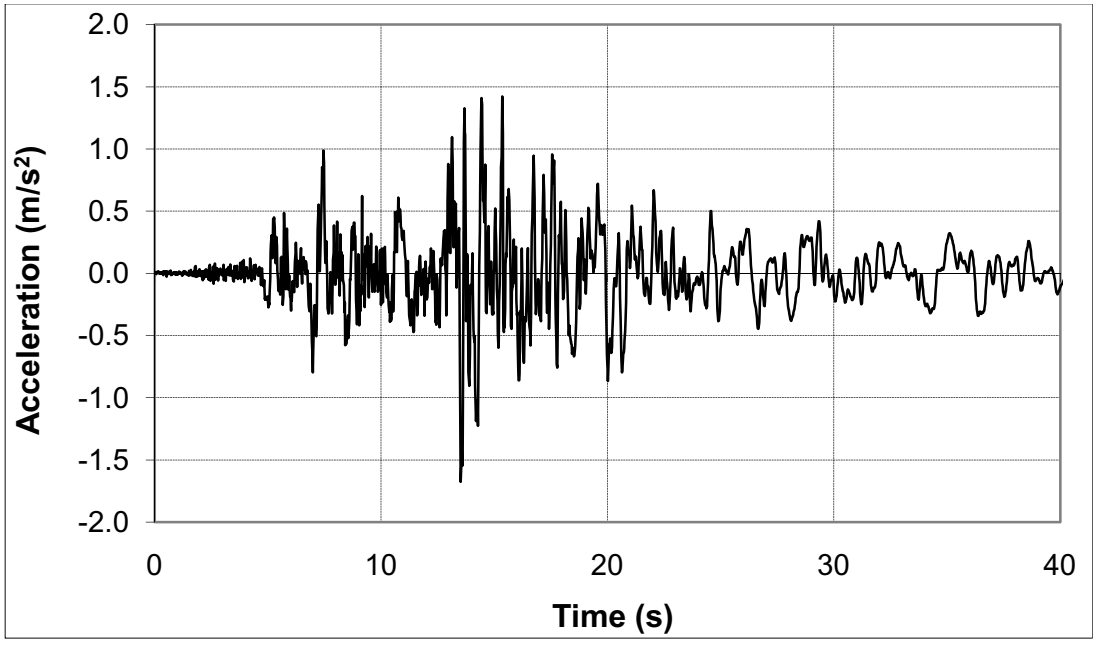


Figure 6.11. Recorded motion at the ground surface for the WLA

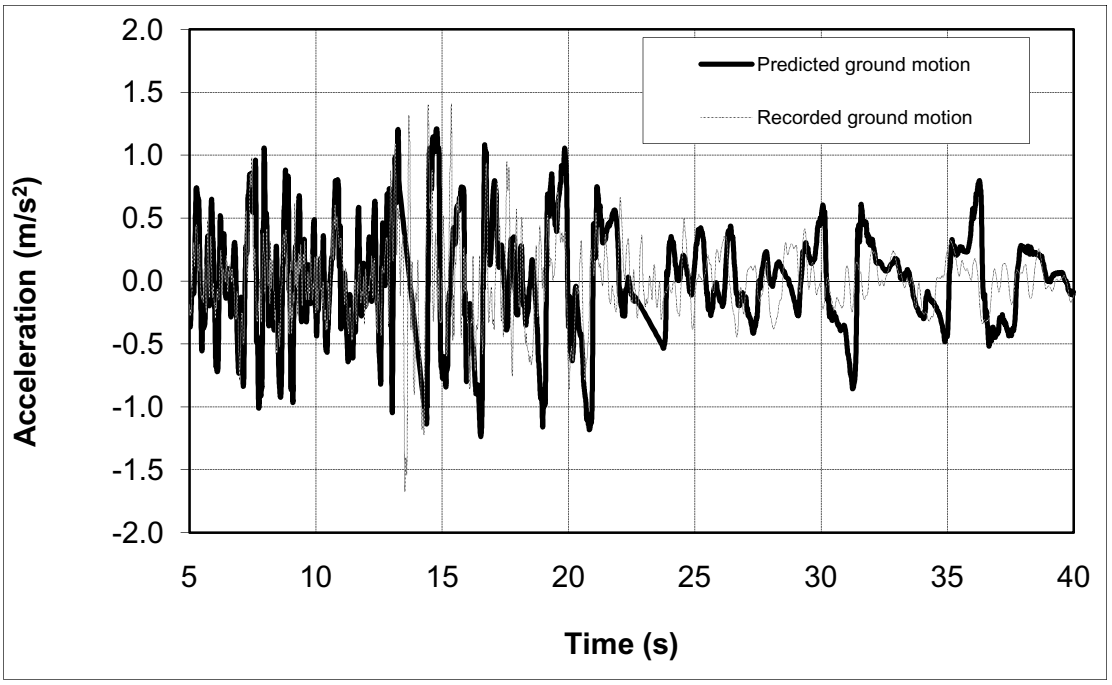


Figure 6.12. Comparison between estimated and recorded motions at the ground surface for the WLA

6.1.3.2 Response Spectra Comparison

The predicted and recorded response spectra at the ground surface are shown in Figure 6.13.

Although the predicted and recorded response spectra have the same shape and trends, the FLAC estimated response spectrum shows higher amplitude at longer periods (i.e., greater than 0.5 s) when compared with the recorded motion. In addition, an overestimation of the longer period spectral response by the FLAC model suggests that the FLAC model may be somewhat underdamped.

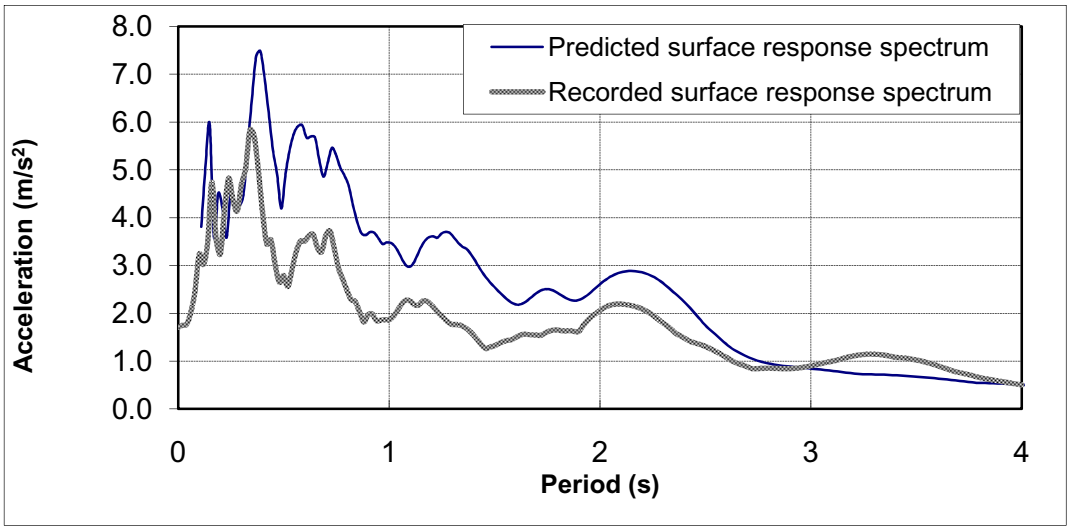


Figure 6.13. Comparison between recorded and estimate spectra for the N-S component of ground motion at WLA

The deviation of the predicted and recorded surface motion at the Wildlife site, starting at about 13 s, may be due to: (1) the FLAC modeling approach is predicting complete liquefaction at an earlier time in the acceleration time history than what may have occurred, (2) natural heterogeneity of the real soil profile versus the homogeneous assumption of soil properties by FLAC model, (3) the selection of soil properties for the modeling is based on averages, which may impact the prediction, and (4) differences in the constitutive relations used in the FLAC model versus the real soil behavior.

Despite the differences, the FLAC model does appear to capture first order effects resulting from liquefaction softening, although it predicts an earlier onset of full liquefaction than is suggested by the pore pressure transducer data recorded for this site. Further evaluations of the FLAC model's performance in terms of pore pressure generation and stress-strain behavior are discussed in the following sections.

6.1.3.3 Pore Water Generation Comparison

The FLAC cyclic shear stress and predicted pore water generation history in the liquefaction layer is shown in Figure 6.14 and Figure 6.15 for the WLA site. The FLAC model uses stress cycles to determine the rise in excess pore water pressure, as previously described. The model predicts that pore water generation begins at 4 s and is fully developed ($r_u = 1$) at about 18 seconds of elapsed time (Figure 6.15).

At 4 s, the earthquake motion acting on the site is about 0.05 g. During the time between 4 and 18 s, the strong motion has several peaks of about 0.2 g, as shown in Figure 6.9. After about 20 s, the amplitude of the strong motion has markedly decreased (Figure 6.9). Thus, from a cyclic stress point of view, the majority of the largest stress cycles have occurred before 20 s. Because pore pressure generation in the FLAC model is calculated from cyclic stress cycles, the FLAC prediction of full liquefaction at about 18 s is reasonable based on the modeling approach implemented in FLAC.

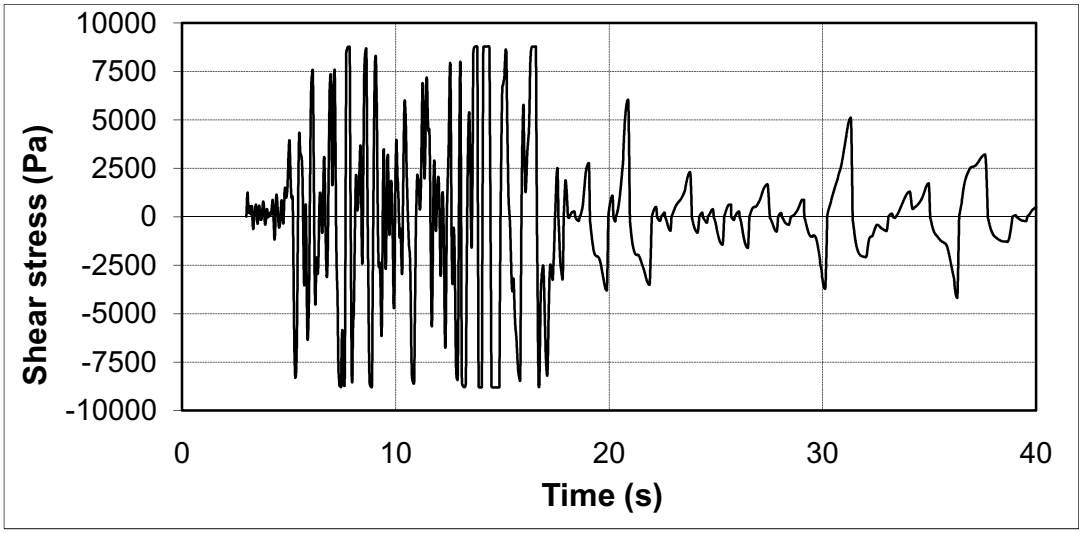


Figure 6.14. FLAC predicted shear stress in liquefaction layer at WLA

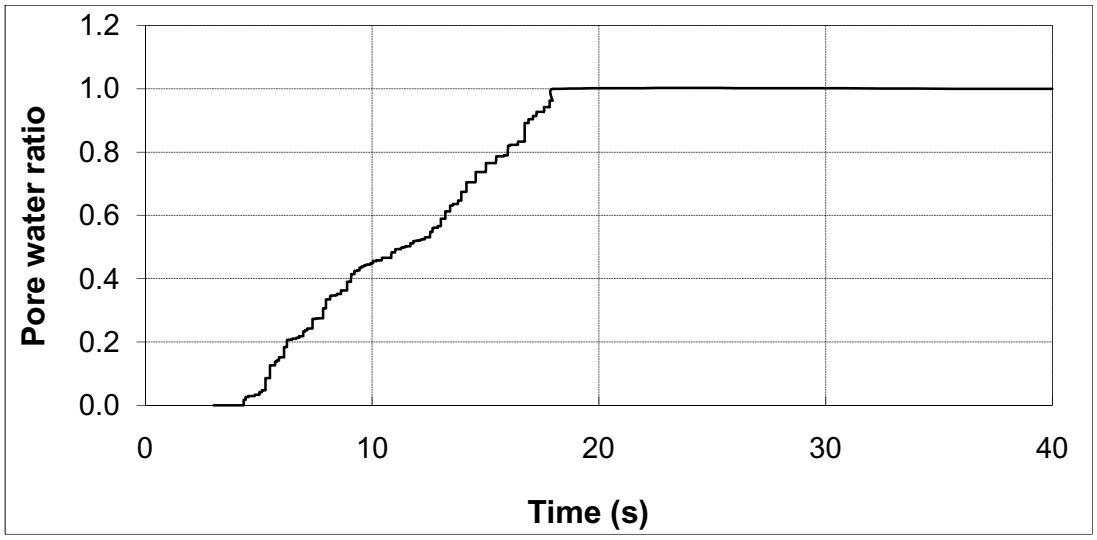


Figure 6.15. FLAC predicted pore water generation history for WLA

However, piezometer P5, which is near the top of the liquefied layer (Figure 6.1) and is considered one of the most reliable records (Youd and Holzer, 1994), did not reach r_u equals 1 until a considerable time after the most intense strong motion peaks (Figure 6.16). This apparent delay in reaching r_u equals 1 has surprised a considerable number of geotechnical experts, who expected the r_u equals 1 should have been reached much earlier in the record (Youd and Holzer, 1994). Continued pore pressure rise in the absence of strong earthquake shaking had not been foreseen (Holzer et al., 1989). Piezometer P5 shows that significant pore pressure generation began at about 14 s and continued to increase significantly to about r_u equals 50 to 70 % during about 27 seconds (Figure 6.16). After this, pore pressures continue to rise at a diminishing rate until r_u equals 100 % was obtained approximately 80 s after the initial triggering of the array (Youd and Holzer, 1994).

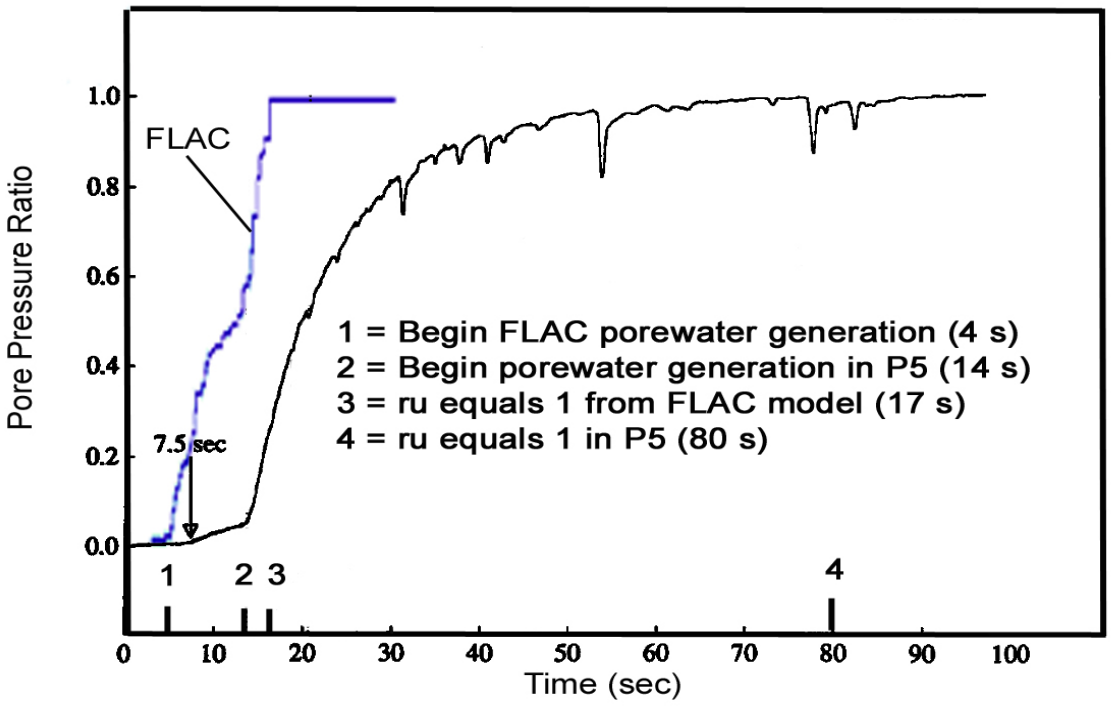


Figure 6.16. Comparison of the FLAC predicted and recorded pore pressure generation versus time at WLA during 1987 Superstition Hills earthquake (M=6.6) for piezometer P5 (after Dobry et al. 1989)

It is possible that the relatively low permeability of the liquefied silty sand (SM) at the WLA may have caused a time delay between when elevated pore pressures were reached in the liquefied zone and when liquefaction (i.e., $r_u = 1$) was recorded by the piezometer (Youd and Holzer, 1994). This time delay is probably a consequence of pore pressure migration and the time required for that migration to reach the piezometers. The FLAC model, as constituted, is not able to predict pore pressure migration; instead, it treats the layer as instantaneously reaching the $r_u = 1$ condition when the appropriate number of stress cycles have been achieved.

If piezometer P5 is not located in the critical zone, there may be some delay in the time when $r_u = 1$ is manifest in this instrument. Possible causes of the pore pressure delay pore water redistribution are: (1) migration of high pore pressure from outside the instrumented silty sand layer; (2) liquefaction of only small pockets of sediment, attributable to natural heterogeneity in the deposit; and (3) migration of high pore pressures through the nonliquefied zone around each transducer that resulted from compaction of a small zone around the transducer as it was pushed into place (Holzer et al. 1989).

The surface strong motion recorded at the WLA offers additional evidence that significant softening from high pore pressures occurred relatively earlier in the record. The softening is strongly evident at about 13 to 14 s where the surface motion begins to be out-of-phase with the downhole record (Figure 6.17). Holzer et al. (1989) believe that a progressive loss of rigidity of the silty sand layer continued at least through 16 s elapsed time (Figure 6.17). This reduction clearly coincided with the phase of sharpest pore water rise predicted by the FLAC model (Figure 6.16). Thus, Holzer et al. (1989) conclude that the period of time between 14 to 30 s may better represent when liquefaction, or at least when very elevated pore pressures were reached in the critical zone. Therefore, it is possible to conclude that using the pore pressure history from P5 and directly comparing it with the FLAC generated pore pressure, as is done in Figure 6.16, is potentially misleading because of these uncertainties.

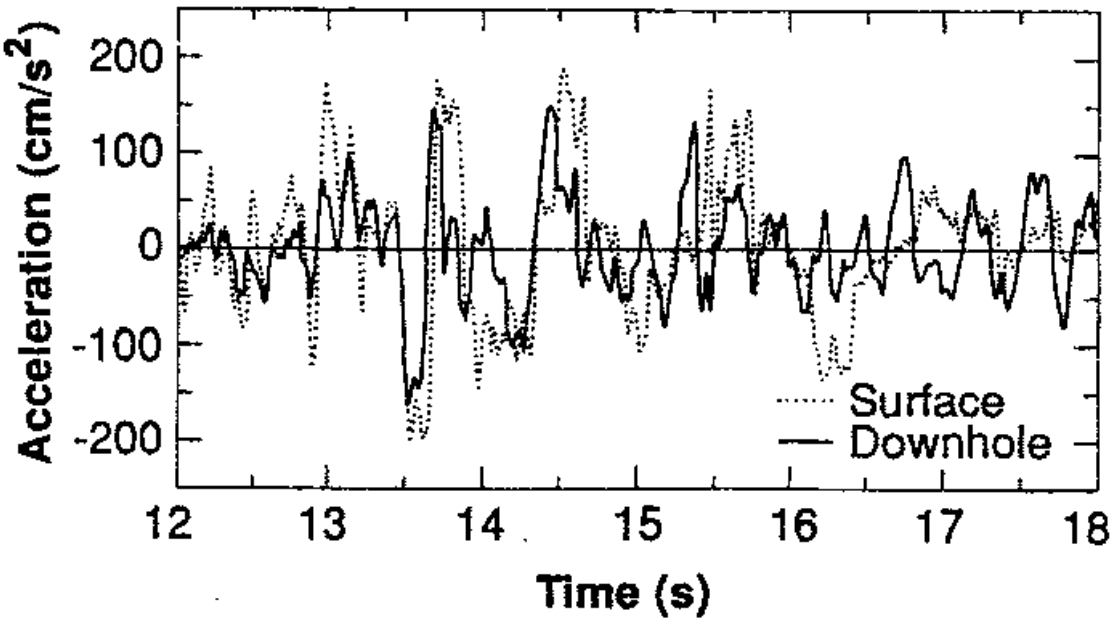


Figure 6.17. Wildlife Superstition hills earthquake N-S record comparison surface to downhole (after Holzer T. L., et al. 1989)

The 16 s duration of soil softening from about 14 s to 30 s indicated by Holzer et al. (1989) is approximately equal to the 14 s period of softening time predicted by the FLAC model. However, as stated before, the FLAC model predicts that this softening begins at about 4 seconds, which is earlier than the starting time suggested by Holzer et al. (1989). This is most likely happening for the following reasons. (1) The selected FLAC modeling approach does not consider pore pressure redistribution in the liquefied layer; thus, incremental pore pressure increases are considered to be instantaneous in the FLAC model and occur uniformly throughout the critical layer. (2) It is possible that the WLA reached the liquefied state later, on average, than typical liquefied sites. This is possible because the FLAC modeling approach is based on using "average" behavior for numerous sites that comprise the case history dataset. The modeling approach proposed

mean values to predict the number of stress cycles to reach liquefaction and mean values from laboratory testing to predict the subsequent rise in pore pressures. Thus, it is possible that the liquefied state was reached more slowly at the WLA when compared to "average" behavior predicted by the cyclic stress and pore water generation relations that were implemented in Chapter 3 and 4.

6.1.3.4 Hysteretic Behavior Comparison

Another indicator of the model performance is its ability to develop hysteresis loops similar to those calculated by others for the WLF site as shown in Figure 6.18.

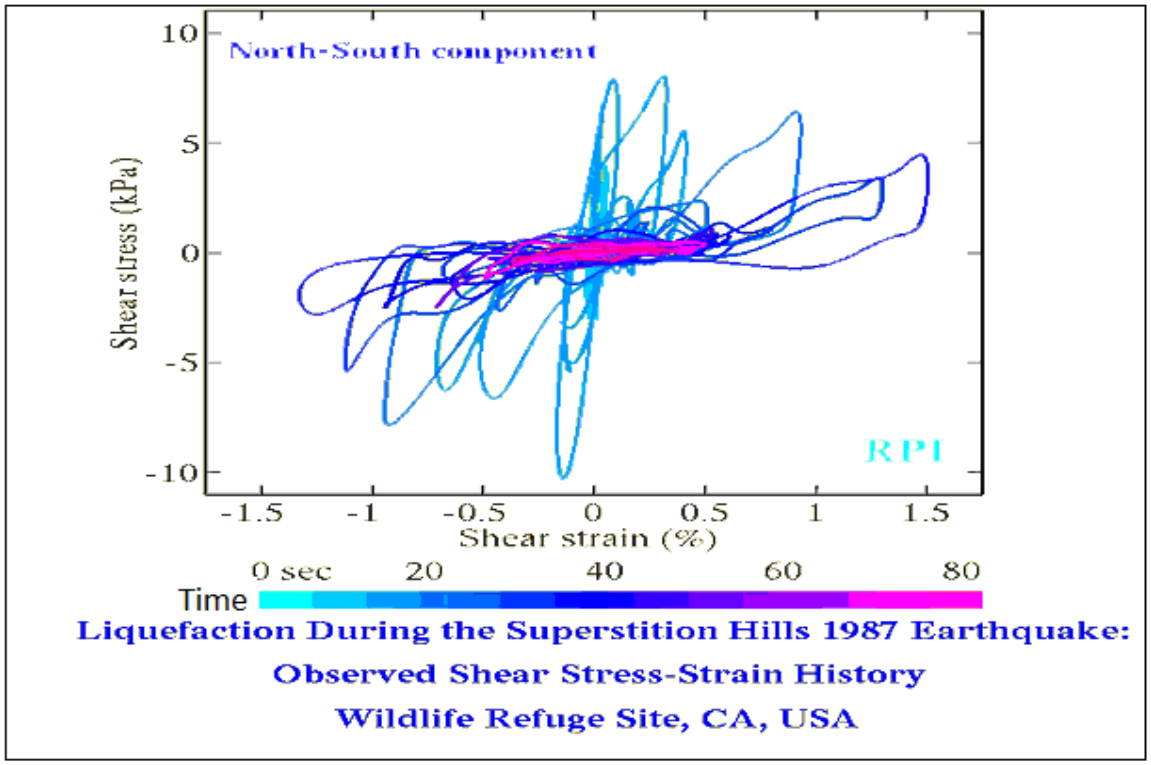


Figure 6.18. The Wildlife stress-strain history during the Superstition Hills 1987 earthquake (after Mourad Zeghal and Ahmed-W. Elgamal, 1994)

The predicted hysteresis loops for the WLF site from the FLAC model are shown in Figure 6.19. It can be seen that the FLAC predicted hysteresis loops have about the same general shear strain amplitude as those calculated by Zeghal and Elgamal (1995). These results were obtained using the residual strength to residual shear modulus ratio of 0.19 (Figure 6.19). This value was selected because it most closely matched the results of Zeghal and Elgamal (1995) (Figure 6.18).

Another way to compare this information is to inspect the stress-strain loops for various time intervals. The plots of shear stress verses shear strain for selected time increments for the 1987 Wildlife site as calculated by Zeghal and Elgamal are shown in Figure 6.20. The FLAC predicted average shear stress versus average shear strain for the corresponding time increments are shown in Figure 6.21.

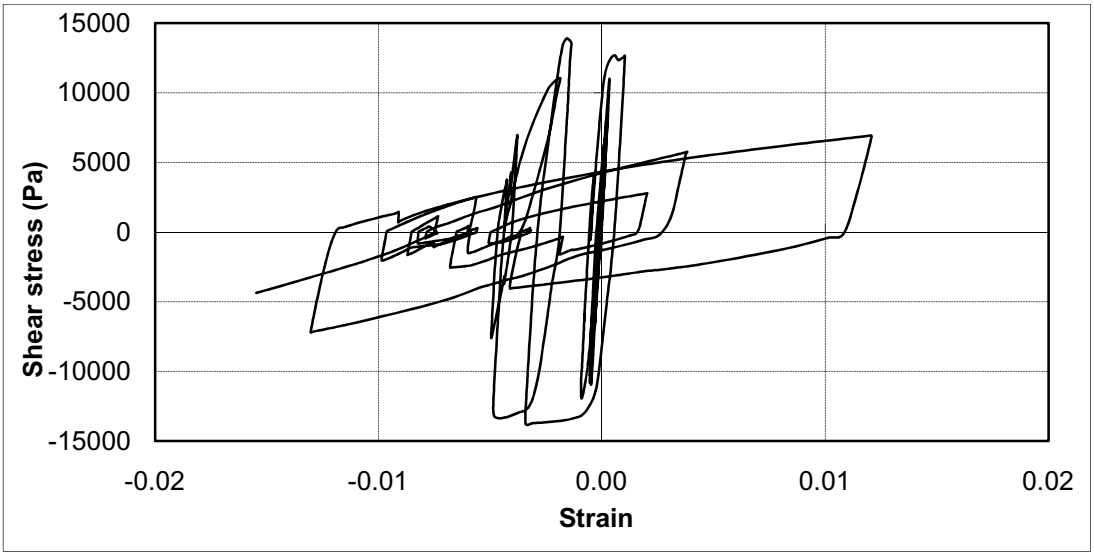


Figure 6.19. Wildlife model predicted hysteretic loop within the liquefaction layer

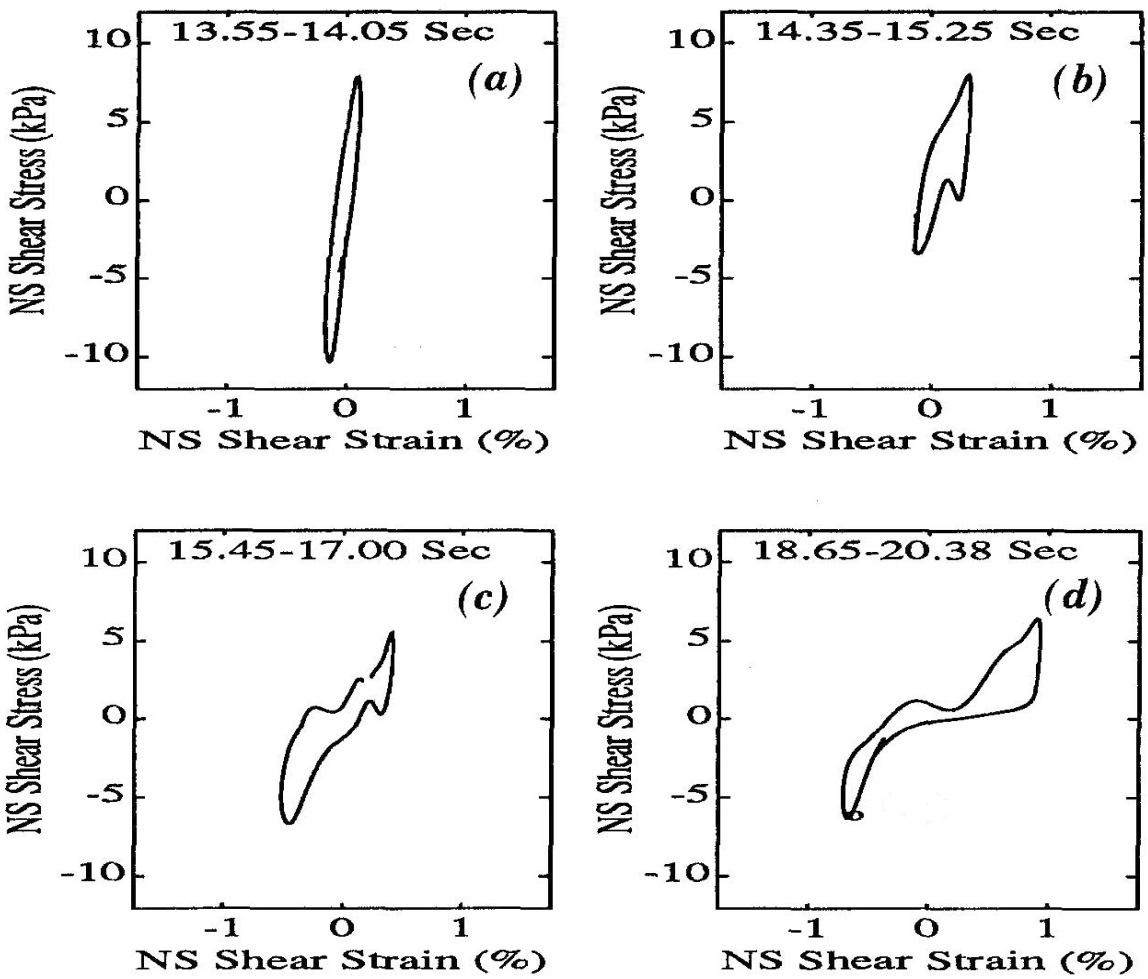


Figure 6.20. Average shear stress vs. average shear strain for selected time increment for 1987 Wildlife site (after Mourad Zeghal and and Ahmed-W. Elgamal, 1994)

In general, the predicted hysteretic loops agree reasonably well with the average trends in Figure 6.20. However, strong dilation is suggested in the WLA record as seen by the loop ends which sharply upward showing a significant strain hardening (Figure 6.18). This dilation effect is not considered in the FLAC modeling approach (Figures 6.19). Thus, in the proposed approach, any soil dilation at larger strain will be accounted for by using a somewhat higher residual strength value in the subsequent calibration process discussed in Chapter 7.

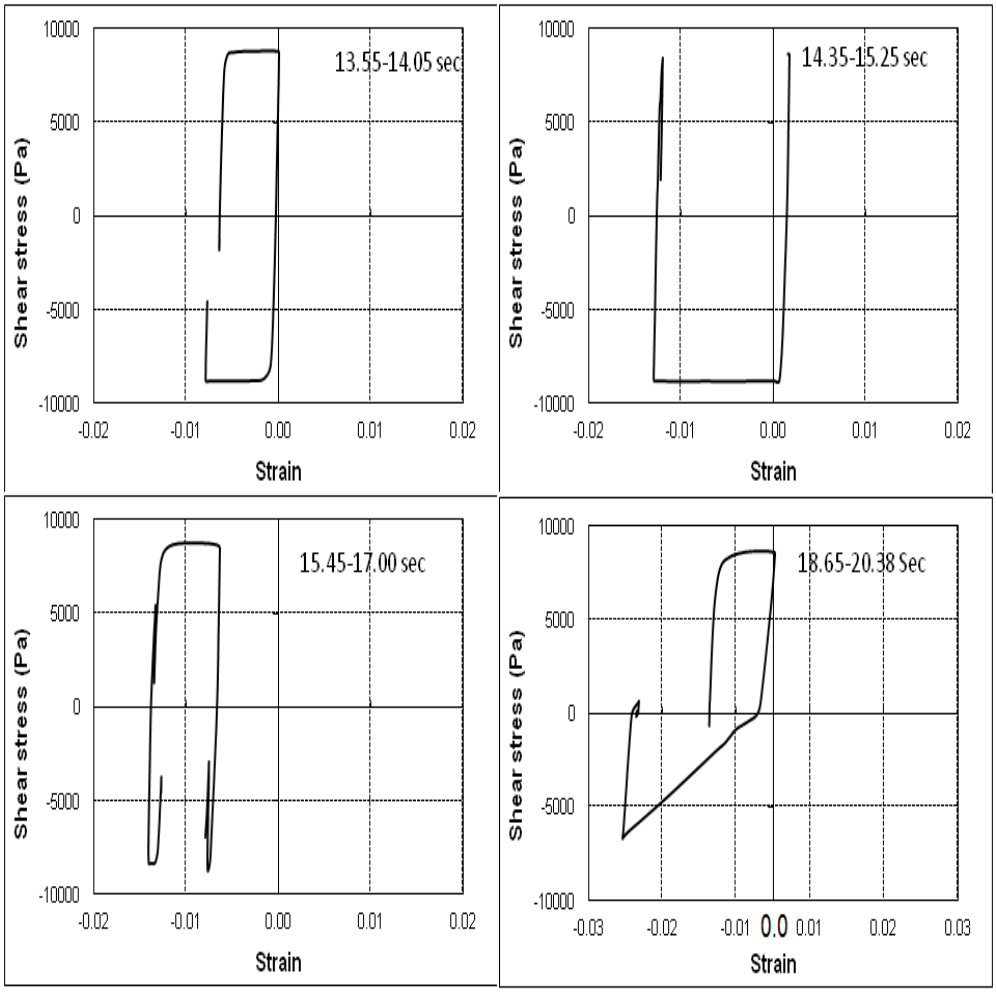


Figure 6.21. Wildlife predicted shear stress vs. shear strain for selected time period

6.1.4 Summary of WLA Modeling Comparison

The comparison performed in this chapter shows that the FLAC modeling approach captures "first order" liquefaction effects manifested in the soil column at the WLA (i.e., softening, increased shear strain, change in fundamental period and decrease in amplitude of the high frequency content). Because the proposed modeling approach is a total stress approach, it does not directly predict pore pressure generation and its subsequent redistribution in the liquefied layer. Hence, when comparing measured

piezometer data (i.e., P5) with the FLAC results, there will be no time delay in the FLAC prediction, because all points in the critical layer will reach the liquefied state at the same time. Nonetheless, this may not be the actual behavior at the WLA, where some lag time was required for the generation and redistribution of pore pressure in the silty sand layer. From the discussion of Holzer et al. (1989), it appears that the initial excess pore water pressure was nonuniform and redistribution of pore water pressure probably occurred. Thus, some sensors, like piezometer P5 (Holzer et al., 1989), may not have recorded r_u equals 1 until a considerable time after the onset of liquefaction in other zones.

Nonetheless, a careful comparison of the recorded downhole and surface accelerometers shows that a significant softening occurred in the soil profile relatively early in the record. Based on Figure 6.17, it appears that the onset of significant softening and out-of-phase behavior occurs at about 13 to 14 s and is well developed by about 16 s. This interval of significant softening (Figure 6.17) is reasonably consistent with the interval of pronounced softening estimated by the FLAC model (Figures 6.12 and 6.15). (Note that in Figure 6.12, a significant softening occurs at about 13 s in the FLAC estimated record and this continues throughout the remainder of the record. In addition, the interval from about 13 to 18 s corresponds to the time when the FLAC model estimates the greatest increase in r_u. During this interval, r_u increases from 0.5 to 1.0 (Figure 6.15).)

For this comparison, it is concluded that the FLAC model generally captures the main mechanisms of liquefaction softening for the WLA; however, the model predicts that complete liquefaction (i.e., $r_u = 1$) may have occurred somewhat earlier than what

was recorded. The FLAC model will be further tested using the downhole and surface records from the Kobe, Japan earthquake.

6.2 Model Calibration with the Port Island Site, Kobe Japan

The ground response and liquefaction recorded at Port Island Downhole Array (PIDA) from the 1995 Kobe, Japan earthquake offers another chance to evaluate the modeling approach.

6.2.1 Background of Kobe Site Earthquake

The January 17, 1995, Hyogoken-Nanbu, Kobe earthquake (M=7.2) shook Port Island with pga values in excess of 0.5 g measured at the PIDA site. Liquefaction was generated in the man-made fill that produced large sand boils and accompanying ground settlements of about 0.5 m to 0.75 m. Figure 6.22 shows the PIDA subsurface stratigraphy, subsurface geotechnical data and downhole instrument locations (after Ishihara et al., 1996). Appropriate soil properties are given in Table 6.3. This array has strong motion accelerometers placed at 0, 16, 32 and 83 m below the ground surface (Figure 6.22). This array did not have any downhole piezometers.

An inspection of the acceleration time histories at the surface and from the 16 m depth (Figure 6.23) shows that liquefaction occurred within the poorly compacted, man-made fill. These records show an initial 8.5 seconds of in-phase motion; after that time, out-of-phase motion begins which suggests significant softening has occurred. The beginning of softening coincides with the acceleration spike of 0.32 g at about 8.5 s (Figure 6.23).

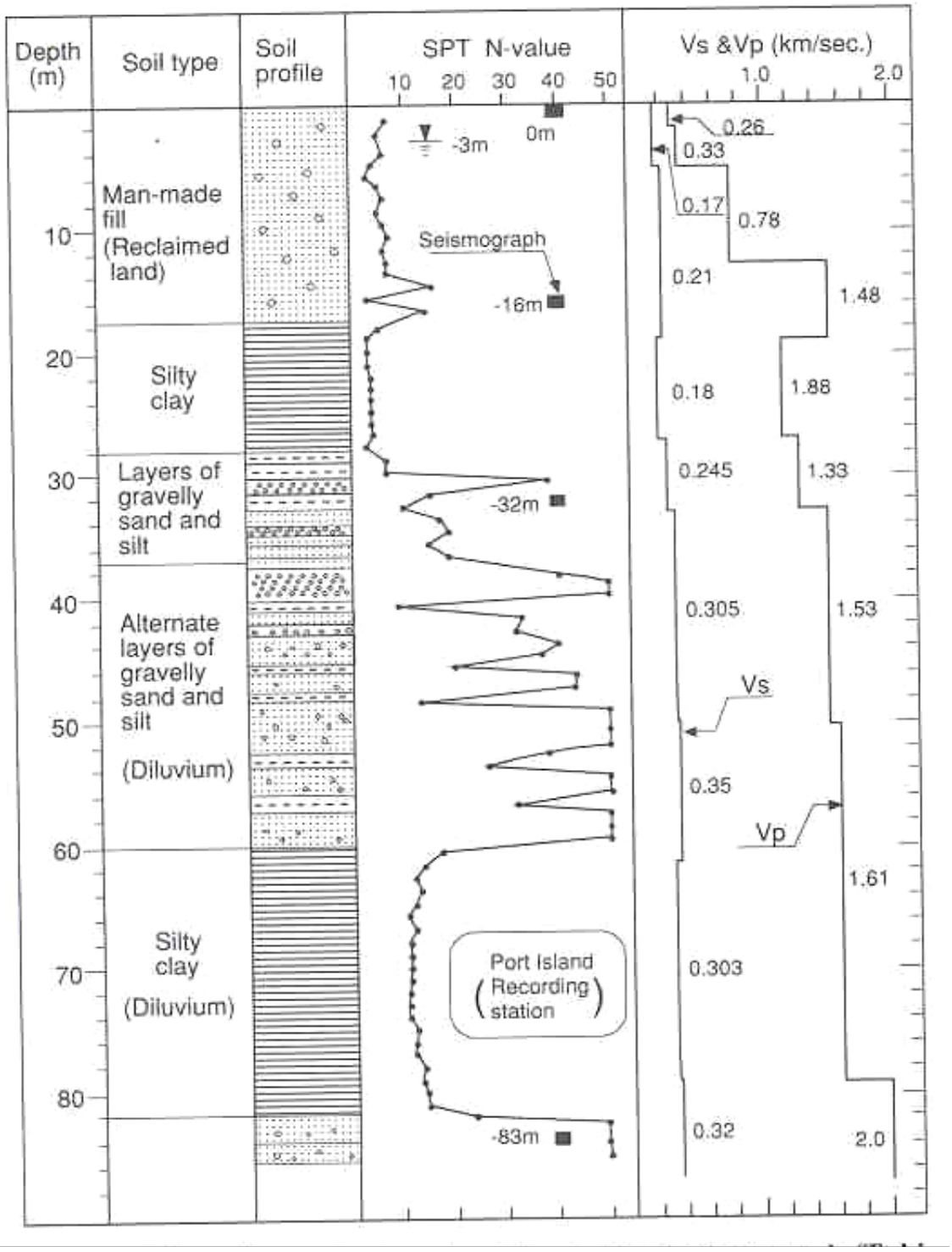


Figure 6.22. PIDA site stratigraphy, cross section and instrument locations (after Hamada et al., 1996)

Table 6.3. Soil properties for PIDA sediments (after Ishihara et al., 1996)

Layer	Material type	Thickness (m)	Dry unit weight (kN/m3)	Shear velocity (m/s)	Shear modulus (kPa)
A	Compact granular fill	~ 4.0	17.0	170	50082
B	Loose granular fill	~ 15.0	16.0	200	65240
C	Alluvial clay	~ 8.0	18.0	240	105688

A comparison of the response for these time histories indicates that the liquefaction causes the peak spectral value to decrease from about 1.9 g (16 m depth) to 1.0 g (ground surface). In addition, the predominant period increased from 0.35 s to 1.2 s, respectively, due to liquefaction, as shown in Figure 6.24.

6.2.2 Model Procedure Development and Execution

Using the soil properties in Table 6.3 and the location of the liquefaction layer as estimated from the SPT data, the FLAC model was designed and dimensioned as shown in Figure 6.25. Ultimately, a 4-m wide by 2-m thick nodal spacing size was used for the PIDA model.

The record at 16 m depth is located at the bottom of the liquefied layer. Thus, as was done for the WLA site, a Proshake model was used to deconvolve the 16 m deep motion to a depth of 28 m to obtain the base input motion for the FLAC modeling. The base motion was requested as an “outcropping” motion in ProShake (Figure 6.26) and changed to a stress wave, as previously discussed.

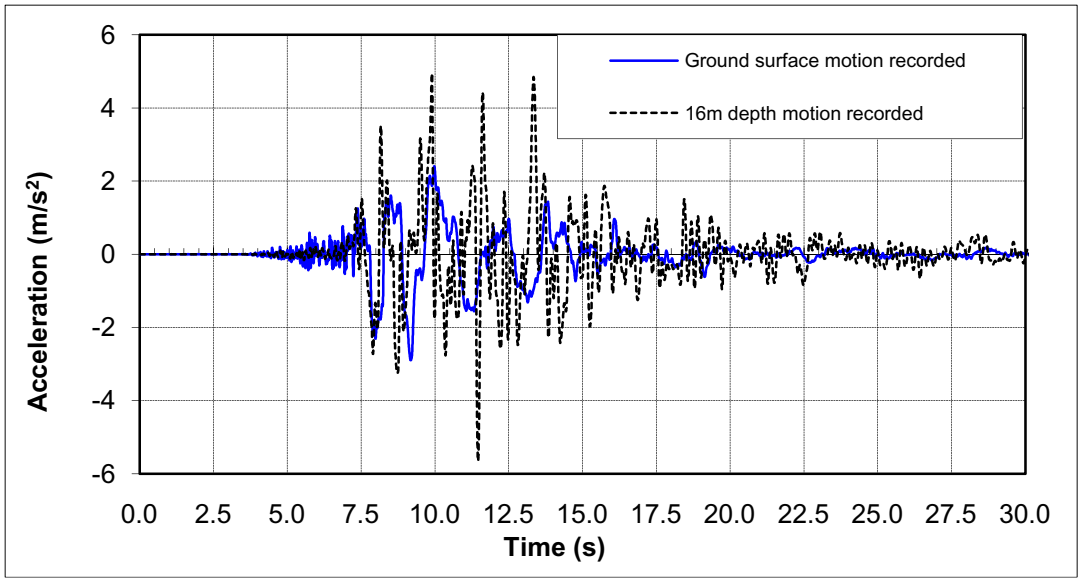


Figure 6.23. PIDA recorded motion for Kobe earthquake at ground surface and 16 m depth (Hamada et al., 1996)

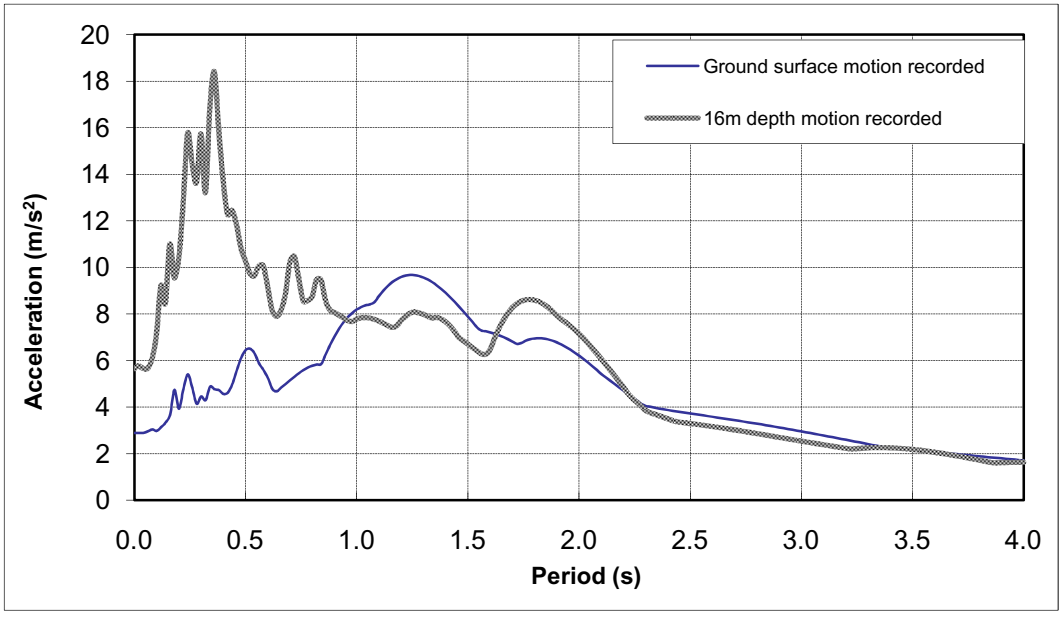


Figure 6.24. PIDA response spectra for the surface motion and 16 m depth.

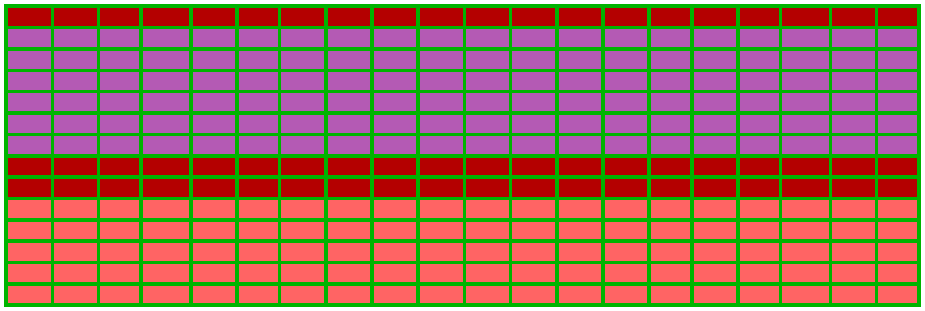


Figure 6.25. Designed FLAC model for Kobe site

In addition, only the first 25 s of the time history was used in the FLAC because the amplitude of the subsequent motion was relatively small and does not significantly affect the results.

Figure 6.27 shows the power spectrum of x velocity time history in the liquefied layer. This curve indicates that the predominant natural frequency is approximately at 0.4 Hz. This predominant natural frequency was used with 0.5% Rayleigh damping in the FLAC to dampen artificial numerical vibration, as previously discussed.

In addition, the input shear stress history was slightly adjusted, so that the monitored x velocity output at the base of the model was comparable to the input velocity, as previously discussed for the WLA site.

6.2.3 Model Prediction and Comparison

6.2.3.1 Motion Comparison

Figure 6.28 and Figure 6.29 show the FLAC predicted motion just below the liquefied layer (i.e., 16 m depth) and at the ground surface, respectively.

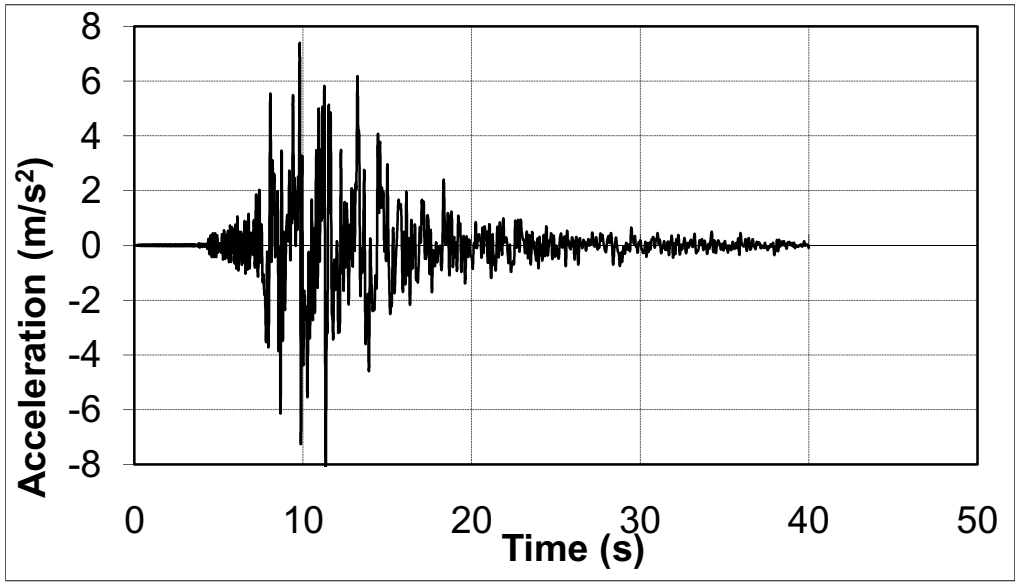
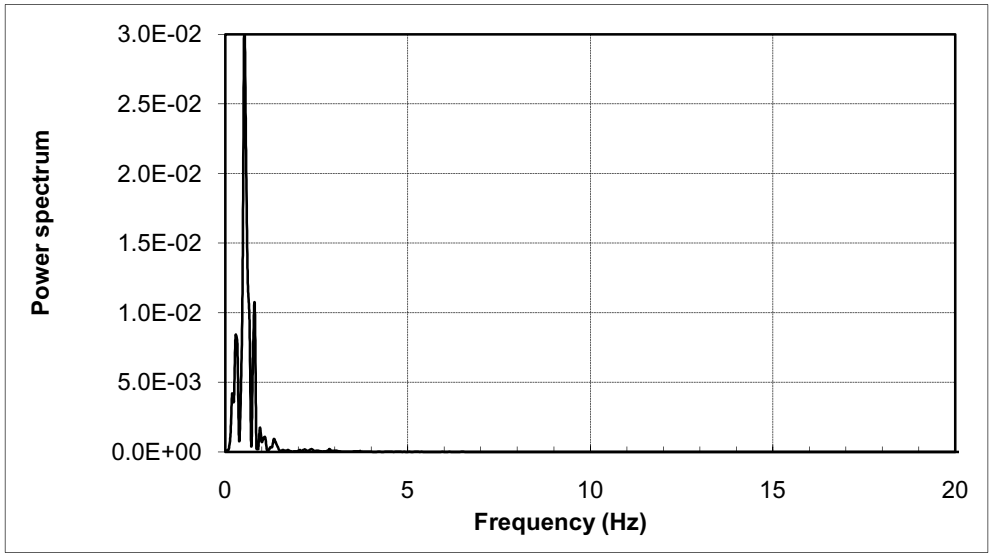


Figure 6.26. PIDA input acceleration time history for the base of the FLAC model



Figures 6.27. Kobe FLAC calculated power spectrum of x velocity time history in liquefaction layer, Kobe site

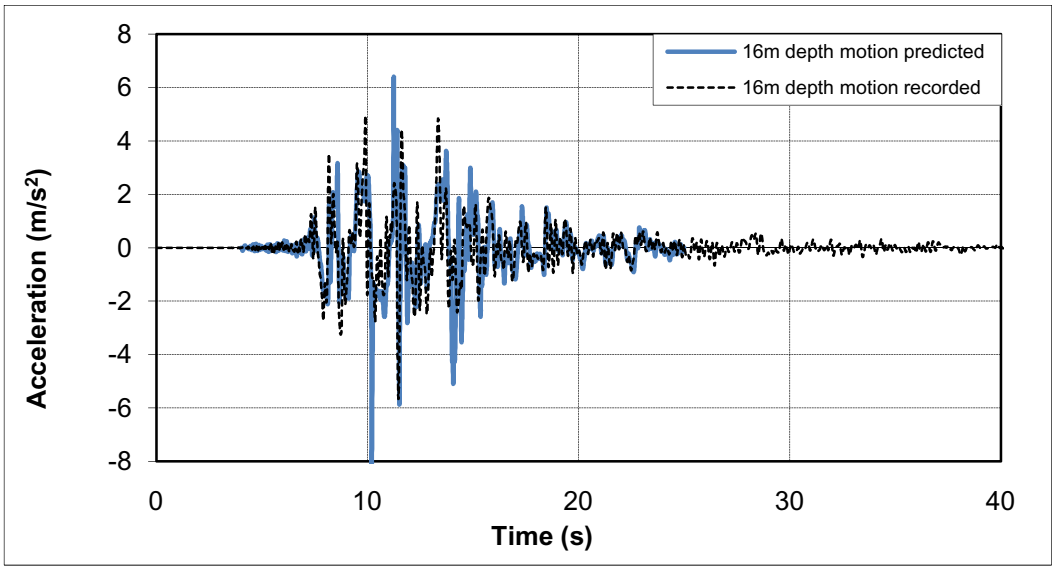


Figure 6.28. Predicted and recorded motion beneath liquefaction layer at 16 m depth, PIDA site

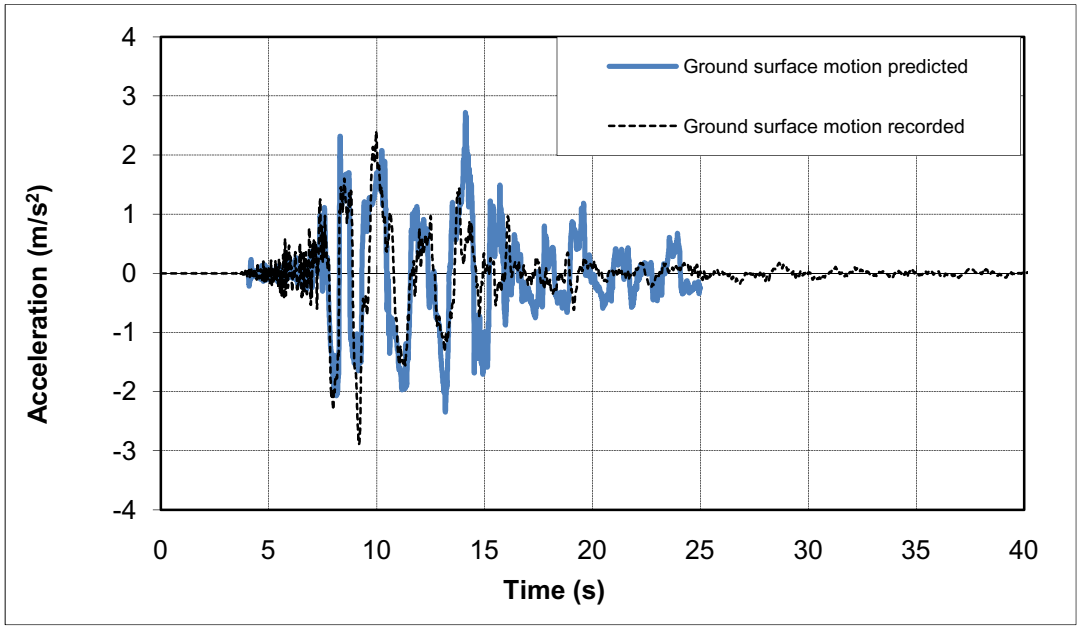


Figure 6.29. Predicted and recorded motion at the ground surface, PIDA site

A comparison of the predicted motions and the recorded motions at the 16 m depth shows reasonably good agreement, as shown in Figure 6.28. This agreement implies that the deconvolution and convolution process used to estimate the transmitted wave motion at the bottom of the liquefaction has been done in a reasonable manner.

More importantly, a comparison of the predicted surface motion and the recorded surface motion also show good agreement for much of the record prior to 17 s, as shown in Figure 6.29. This agreement demonstrates that the modeling procedure explains the softening effects cause by liquefaction. The modeling procedure somewhat overestimates the surface acceleration for the time interval later than about 17 s, indicating that the model is probably underdamped during this time interval.

6.2.3.2 Response Spectra Comparison

The response spectra of predicted and recorded motions just below the liquefaction layer (16 m depth) and on the ground surface are shown in Figures 6.30 and 6.31, respectively.

Some minor discrepancies between the predicted and recorded soil response may be due to: (1) natural heterogeneities in the soil versus the homogeneous assumption of soil properties used by the FLAC model in each layer, (2) pore water redistribution not directly considered by the FLAC model, (3) soil dilative behavior during liquefaction that is not explicitly considered by the FLAC model, and (4) the minor discrepancy in the predicted 16 m depth motion will definitely produce the discrepancy for the prediction of ground motion.

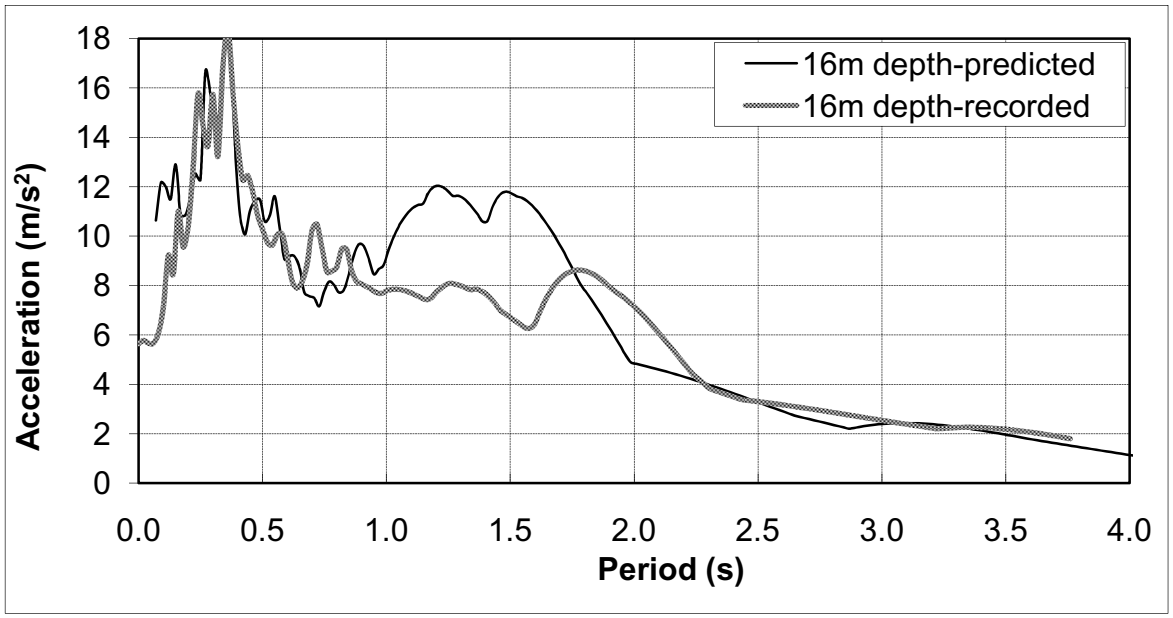


Figure 6.30. PIDA predicted response spectrum just below liquefaction layer at 16-m depth

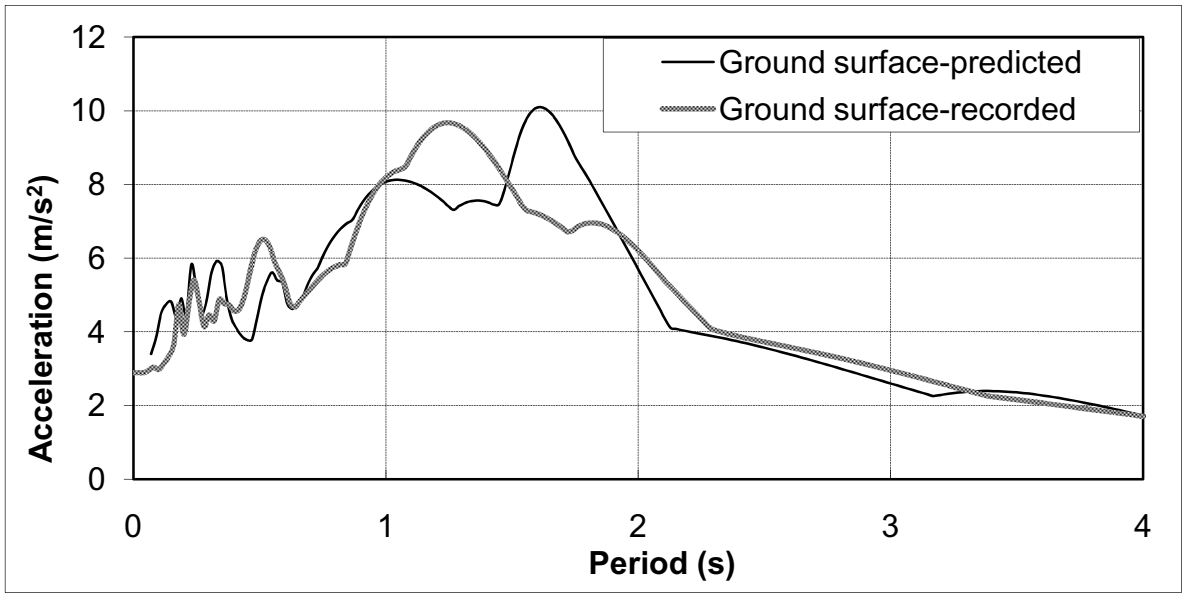


Figure 6.31. PIDA predicted response spectrum at ground surface

Nonetheless, the predicted response spectrum not only shows a decrease in the strong motion amplitude, but also a corresponding increase in the predominate period, as expected, when liquefaction is triggered. In summary, the general agreement of the FLAC model with the PIDA recorded strong motions demonstrates that the proposed FLAC modeling procedure can reasonably capture the primary effects of liquefaction and its softening influence on the ground response.

6.2.3.3 Hysteretic Behavior Comparison

Elgamal et al. (1996) and Olsen (2008) have processed the downhole acceleration time history records for the PIDA using shear beam theory to calculate the hysteresis loops from the processed acceleration time histories above and below the liquefied zones. The results of these studies can also be used to evaluate the performance of the FLAC modeling approach.

The original PIDA data was processed by Elgamal et al. (1996) to remove extraneous frequencies and to correct for drift; then, the time history was rotated into minimum and maximum components. This paper also shows the estimated shear stress-strain time histories at 8, 24 and 57.5 m depths and the estimated excess pore pressure ratio time history at 8 m depth. More recently, Olsen (2008) also used a shear beam model to calculate the hysteretic behavior for the liquefied layer. The Olsen (2008) formulation used only the acceleration at the top of the soil layer. In addition, Olsen (2008) predicted the hysteretic shear stress behavior in the NS direction using a layer thickness of 12 m thickness. Even though there is some difference in the Elgamal et al. (1996) and Olsen (2008) studies, the stresses and ground accelerations computed from

Olsen's model (2008) roughly matches those estimated at the Port Island Downhole Array (PIDA) site by Elgamal et al. (1996).

Figure 6.32 and Figure 6.33 show the hysteretic behavior from Olsen's model (2008) and from the FLAC model, respectively. A comparison of these two results shows that the maximum shear stress amplitude is about 25 KPa and the maximum strain amplitude is about 3%. The trends of these response histories match reasonably well, although the FLAC modeling appears to have some higher stress response at the beginning of the record.

Figures 6.34 to 6.37 show the hysteretic behavior for individual time intervals from Olsen (2008). These corresponding intervals are shown in Figures 6.38 to 6.41 for the FLAC modeling. Detail examination of the results from the two methods shows that the trends and magnitude of the peak stress and strain amplitudes are similar, but some differences still exist. These differences in the individual time interval behaviors are attributable to the calculation scheme used. The Olsen (2008) model, rather than using soil properties and a base motion as inputs to find accelerations at different depths in the soil strata, used the known PIDA accelerations to determine the stress-strain behavior of the soil by defining shear stress as uniquely a function of the acceleration of the ground surface as well as the thickness and unit density of the layer. The shear strain is found by double integrating the recorded acceleration time histories at the top and bottom of the layer to obtain displacement. In contrast, the hystertic behavior for the FLAC model is calculated from the stiffness-strength relations defined in the model developed and is a natural output of the modeling process.

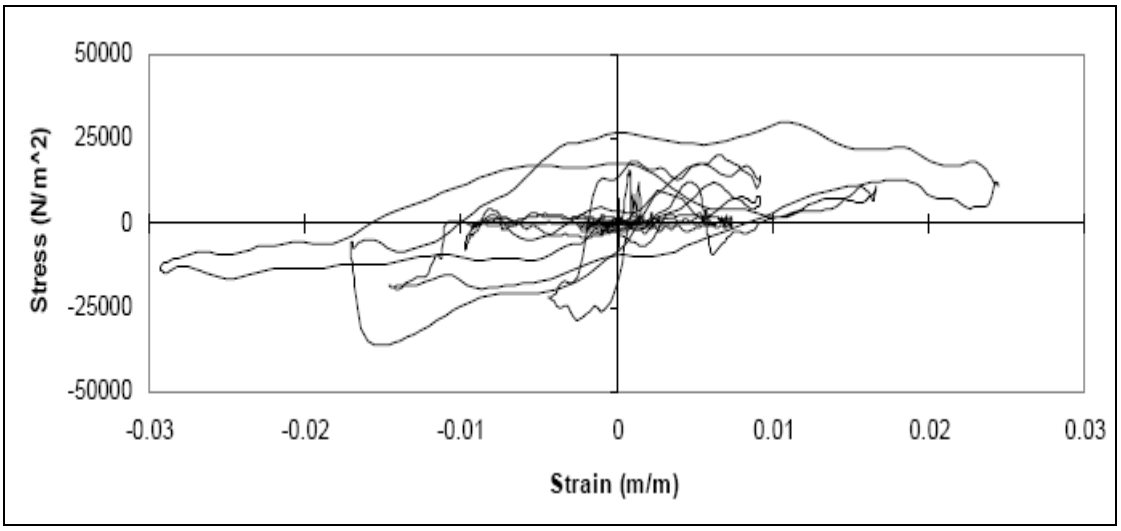


Figure 6.32. Kobe site shear stress-strain plot for the liquefiable soil layer, NS (Olsen, 2008)

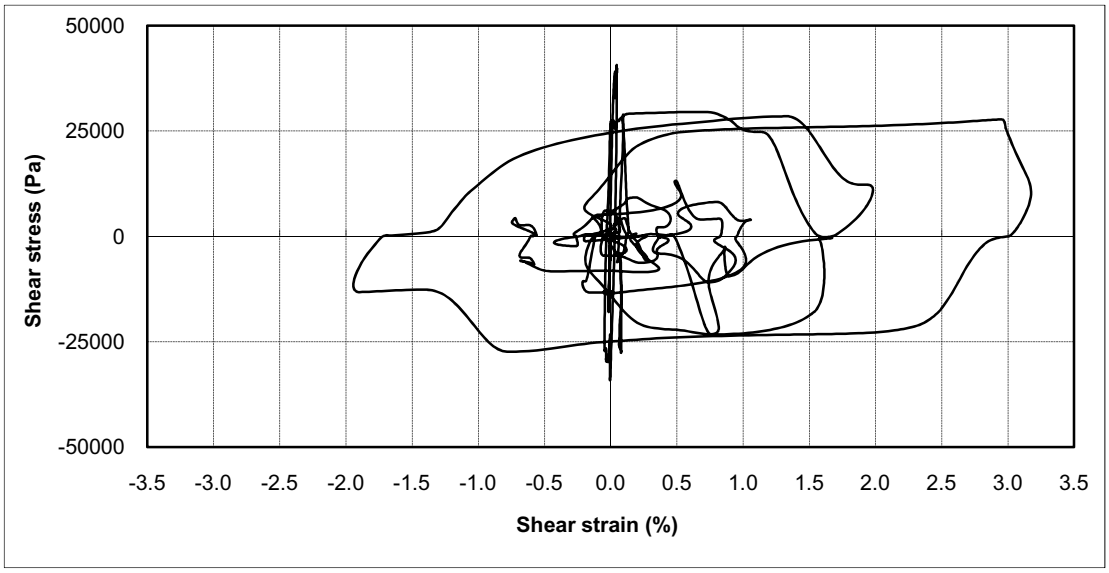


Figure 6.33. Kobe site full stress-strain plots at 8 m depth from FLAC model

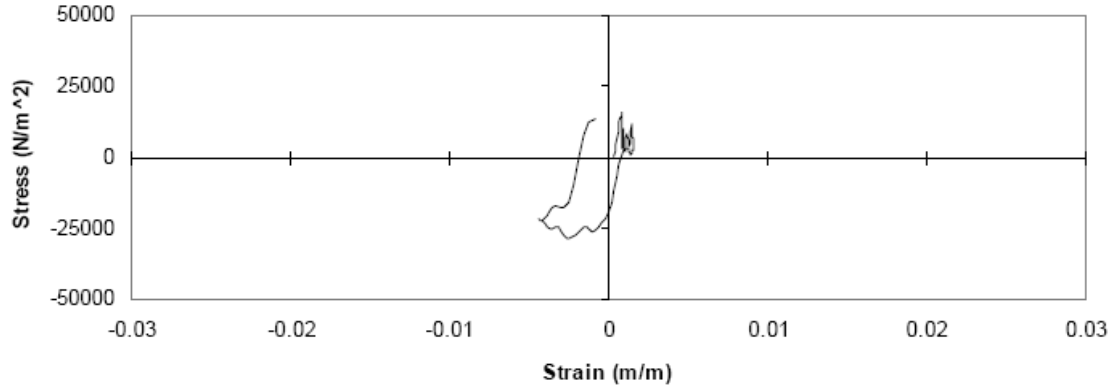


Figure 6.34. Kobe site stress-strain hysteretic loop from 7.3 to 8.3 seconds, NS (Olsen, 2008)

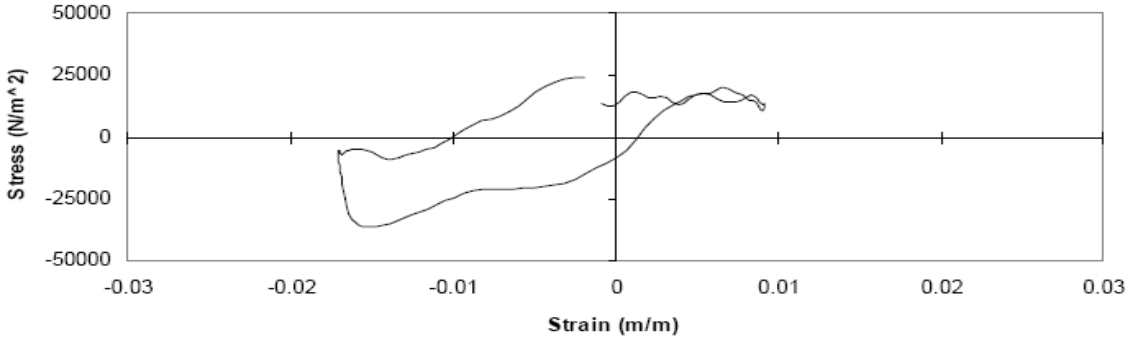


Figure 6.35. Kobe site stress-strain hysteretic loop from 8.3 to 9.8 seconds, NS (Olsen, 2008)

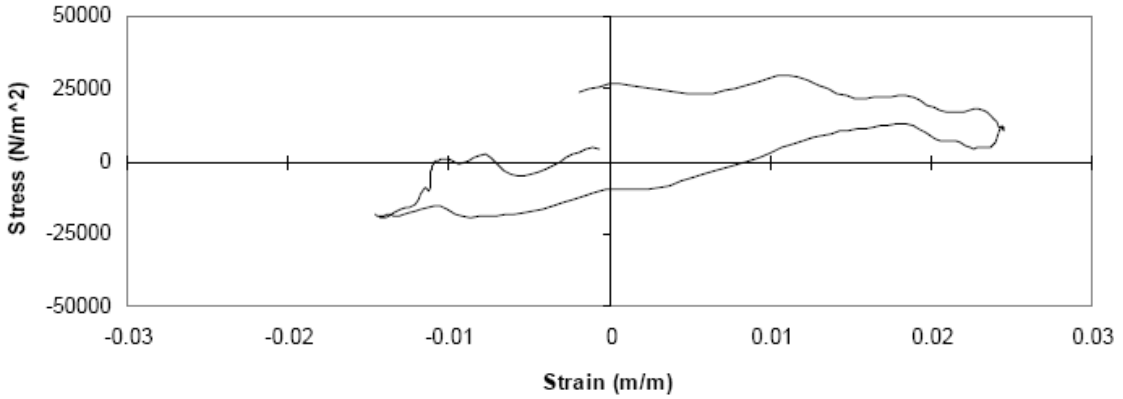


Figure 6.36. Kobe site stress-strain hysteretic loop from 9.8 to 11.9 seconds, NS (Olsen, 2008)

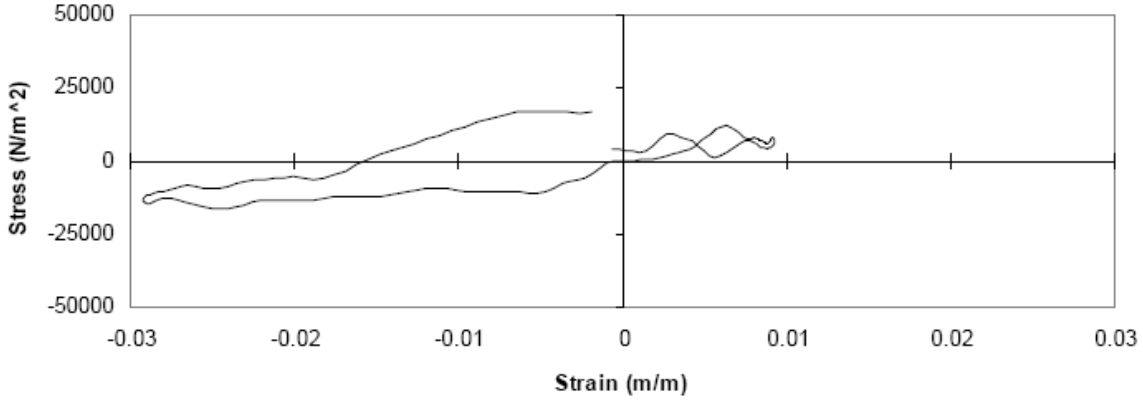


Figure 6.37. Kobe site stress-strain hysteretic loop from 11.9 to 13.8 seconds, NS (Olsen, 2008)

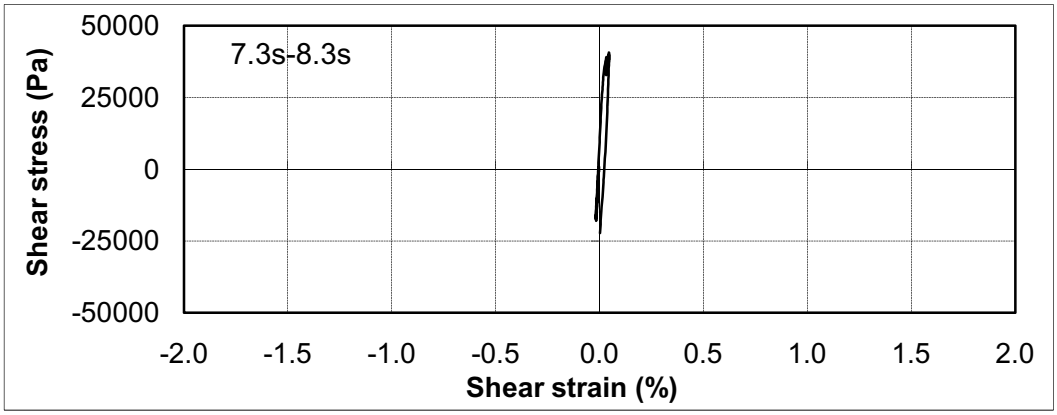


Figure 6.38. Kobe site incremental (7.3s-8.3s) stress-strain plots at 8 m depth from FLAC model

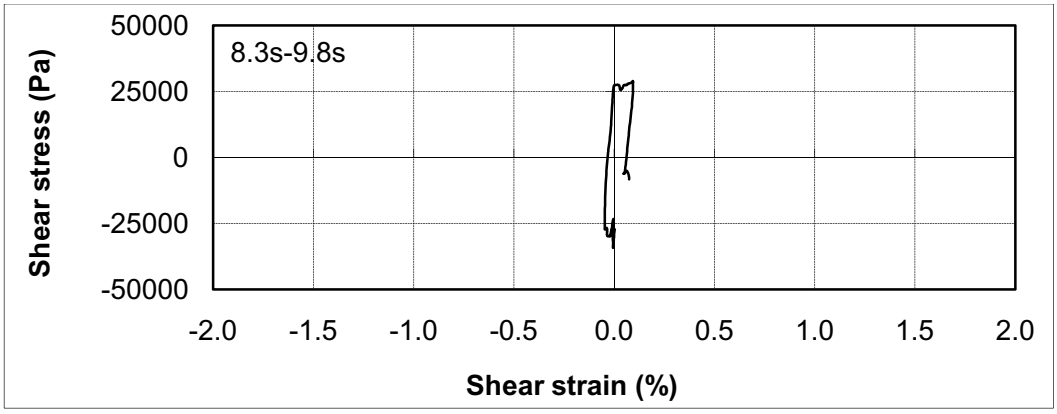


Figure 6.39. Kobe site incremental (8.3s-9.8s) stress-strain plots at 8 m depth from FLAC model

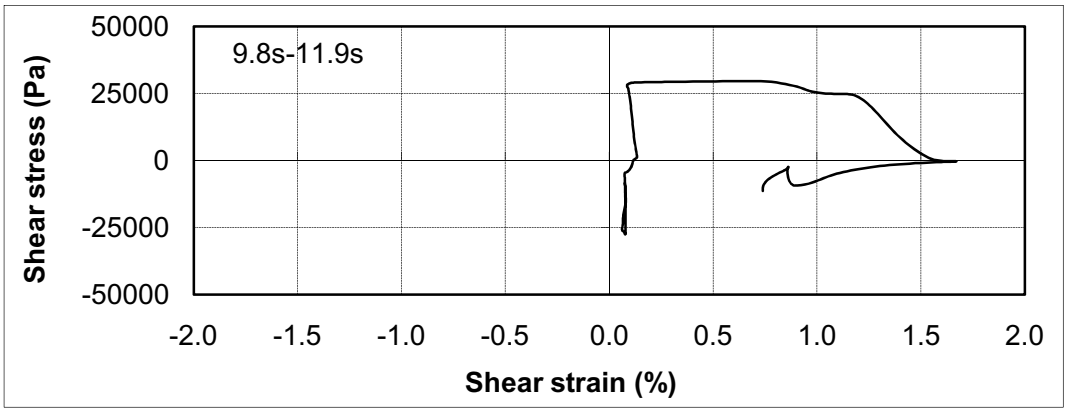


Figure 6.40. Kobe site incremental (9.8s-11.9s) stress-strain plots at 8 m depth from FLAC model

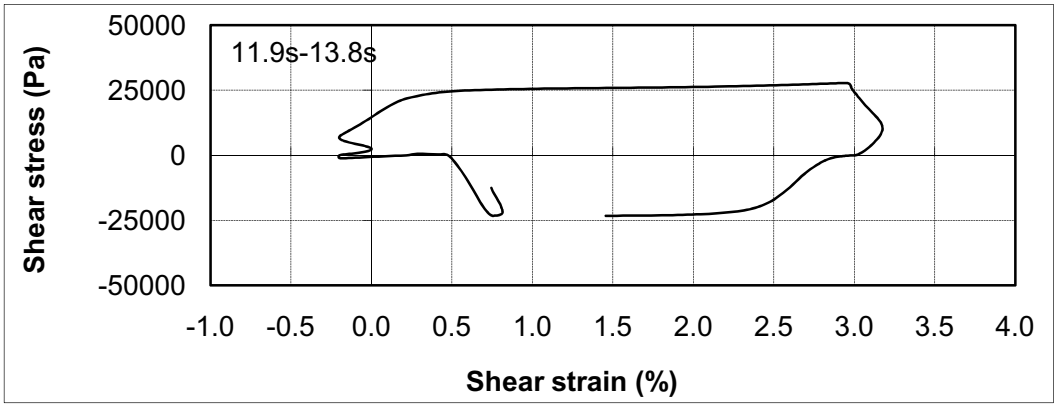


Figure 6.41. Kobe site incremental (11.9s-13.8s) stress-strain plots at 8 m depth from FLAC model

The differences in the stress-strain behavior also contribute to differences in the predicted pore water generation. Complete soil liquefaction estimated by the FLAC procedure occurs at about 10 s, as discussed in the next section. Thus, Figure 6.40 shows a marked softening at about 10 s due to liquefaction. After this, the sand begins to develop substantially more strain than the previous intervals as shown in Figure 6.39.

The Olsen (2008) approach shows about 80 percent pore water pressure generation at about 10 s. Complete liquefaction is predicted at about 15 s, as discussed in the next section. However, even though the Olsen (2008) approach predicts complete

liquefaction at about 15 s, the stress-strain behavior from this method shows that the soil begins to significantly soften at about 10 s. Thus, the FLAC modeling approach reasonably predicts the hysteretic behavior and shows good agreement between pore water generation and its affect on hysteretic behavior.

Further, comparing the stress-strain loops obtained from the FLAC model with those of Elgamal et al. (1996) as shown in Figure 6.42, certain differences are also noted. These differences are mainly due to: (1) Elgamal et al. removed extraneous frequencies for drift correction, (2) Elgamal et al. rotated the orientation of the measured components of motion into minimum and maximum axes, (3) Elgamal et al. used a shear beam model to calculate shear stress (a shear beam model uses accelerations from the top and bottom of the beam or soil layer to compute stresses), and (4) the FLAC model uses recorded motion and lets it propagate through the liquefied layer, the behavior of which is governed by the designed FLAC modeling approach and is associated with pore water generation.

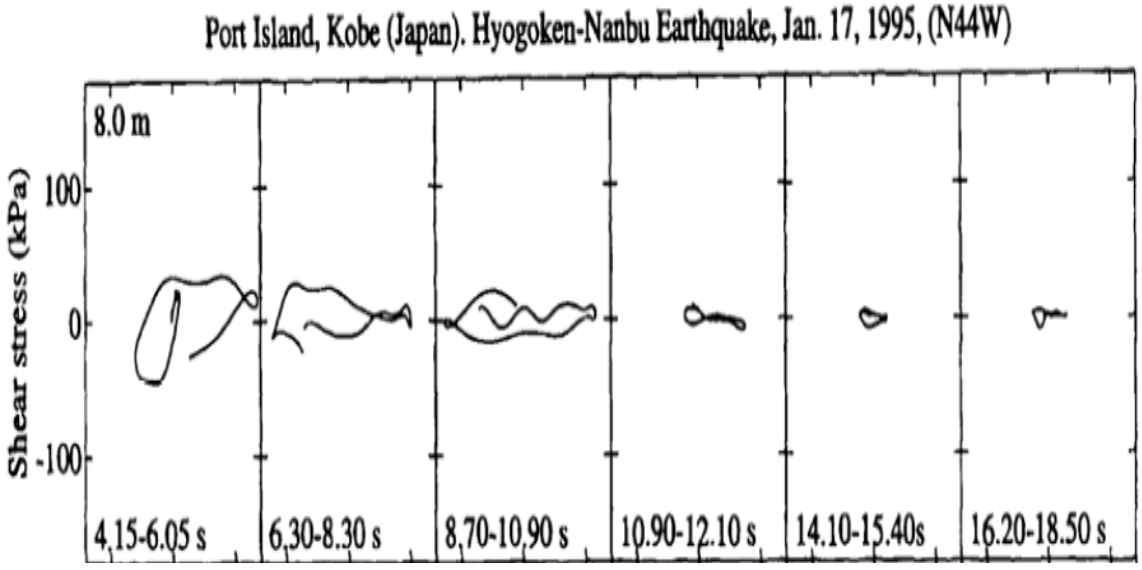


Figure 6.42. Incremental stress-strain plots at various depths (Elgamal et al., 1996)

6.2.3.4 Pore Water Pressure Generation Comparison

There was no recorded pore water record at the PIDA. However, in this section, the pore water pressure generation behavior from the FLAC model is compared with those estimated by the Olsen (2008) and Elgamal et al. (1996) models. The estimation of excess pore water generation from Olsen et al. (2008), Elgamal et al. (1996) and from the FLAC model are shown in Figure 6.43. The estimated cyclic shear stress, which caused the excess pore water pressure generation, is shown in Figure 6.44.

Difference exists between the calculated pore water pressure generation patterns estimated by Olsen (2008) and the FLAC model. The Olsen (2008) and FLAC model both predict that initiation of pore water generation begins at about 7.0 s.

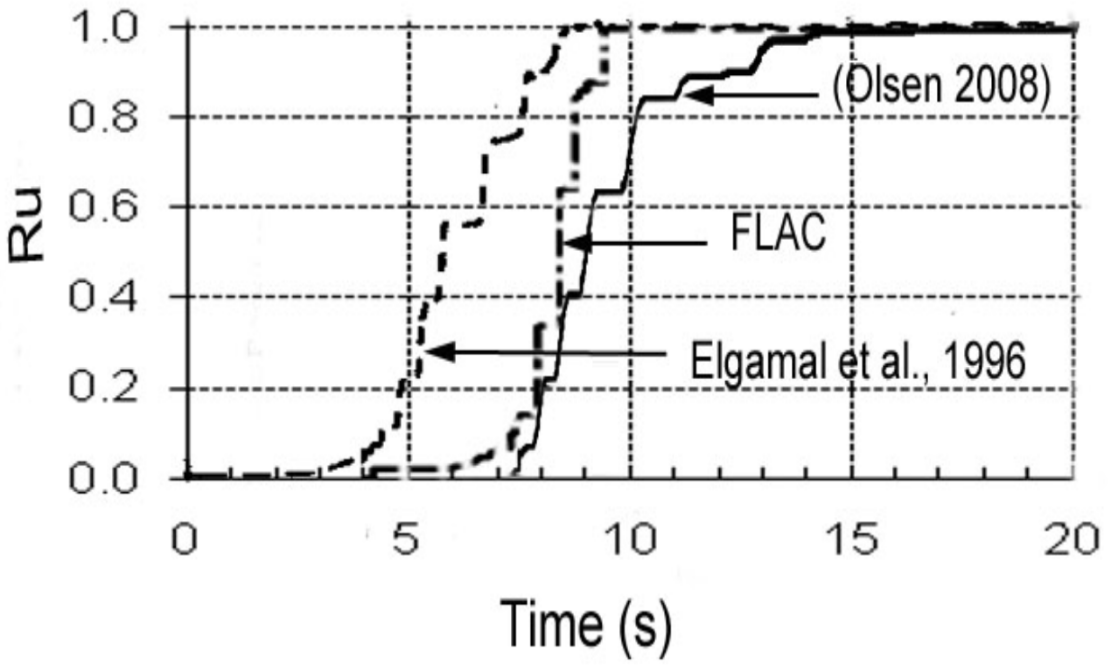


Figure 6.43. Kobe site excess pore water pressure ratio time history from FLAC model, Olsen, and Elgamal et al.

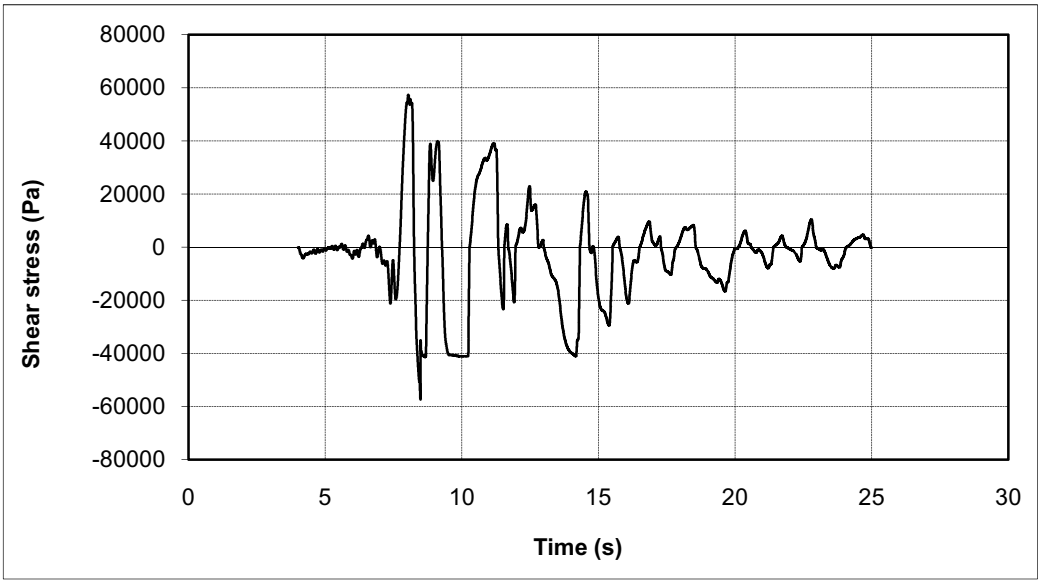


Figure 6.44. Kobe site earthquake generated shear stress from the FLAC model

The FLAC model predicts full liquefaction at about 10 s. For the Olsen (2008) model's prediction, the soil layer is about 80 % liquefied at this time and does not reach full liquefaction until 14.5 s. A closer examination of the recorded earthquake time history at the 16 m depth and at the ground surface indicates that Olsen's (2008) model predicts that the soil reaches full liquefaction only after it experiences the shaking from the complete earthquake time history; whereas, the FLAC model predicts that the soil is fully liquefied just after it experiences the largest peaks in the time history.

The reason for these differences in the predicted pore water pressure time histories can be attributed to the pore water pressure generation methods used by Olsen (2008) and FLAC. Olsen (2008) used measured strain, based upon the adjusted relationship between excess pore pressure and strain developed from the laboratory direct simple shear test, to calculate the pore water generation. In contrast, the FLAC modeling

procedure attempts to account for the effects of the input time history, soil properties and their degradation of stiffness and the soil failure model in a comprehensive, unified fashion using averages from published relations. Thus, considering this, the FLAC model appears to be a reasonable approximation of the process. For example, an examination of the recorded time history at 16 m depth and at the ground surface shows the time history has a significant change in the period of the waves at about 10 s. This substantial increase in wavelength indicates significant soil softening due to very elevated pore pressures. This corresponds to the time of complete liquefaction predicted by the FLAC model.

In addition, Elgamal et al. (1996) indicate that response of the liquefied upper layer is manifest by cycles of large shear strain and small shear stress. Both Elgamal et al. (1996) and Olsen's (2008) modeling of the PIDA suggest that large shear strain and small shear stress occurs at about 10 s, which supports the fact that substantial pore water generation and softening has occurred by this time.

Finally, the estimated pore water pressure generation time history calculated by Elgamal et al. (1996) is shown in Figure 6.43. This prediction is a very close match to that estimated by the FLAC approach. In addition, Elgamal et al. (1996) state that the two predominate acceleration peaks just prior to 10 s caused the soil layer to liquefy. The discrepancy in the calculation by Elgamal et al. (1996) is its prediction of pore water generation before about 6 s from the action of the motion. In fact, the motion is so small before 6 s that it should induce very small excess pore water but the calculation of Elgamal et al. (1996) predicted about 25% excess pore water generation.

Thus, the FLAC results appear to be a reasonable prediction of the pore water pressure generation and softening caused by liquefaction. The pore water pressure generation estimated from the FLAC approach matches sufficiently well with the calculations of Elgamal et al. (1996) and Olsen (2008) to make the model useful for additional calibration.

6.2.4 Summary of Kobe FLAC Model Procedure

Overall, the FLAC model for the PIDA shows that the predicted soil response at the 16 m depth and on the ground surface are, on average, in reasonable agreement with the recorded motions and the corresponding response spectra. In addition, the predicted pore water pressure generation and hysteretic behavior are generally in reasonable agreement with prior studies (Elgmal et al., 1996; Olsen, 2008).

6.3 Summary of Model Calibration

Based upon the modeling results for both the WLA and PIDA sites, it is concluded that the designed FLAC procedures, on average, capture the first order effects that result from elevated pore pressures and the subsequent softening caused by liquefaction. However, the FLAC model needs to be calibrated to a more extensive case history data set prior to possible application in engineering practice. This additional calibration will be done in the subsequent chapter using a more extensive dataset.

CHAPTER 7

CASE HISTORY ANALYSIS

In order to obtain the relationships between the liquefied soil's residual strength ratio (S_r/σ_v') and the soil properties (e.g., F_{15}, $D50_{15}$, Avg. $(N_1)_{60}$, $(N_1)_{60CS}$) at the liquefied sites, as many case histories as possible will be modeled and calibrated in this research. In total, sixteen cases of liquefaction-induced lateral spreading were collected and used in the analyses and calibration. Of these cases, some have recorded acceleration time histories and others do not. For the cases without recorded acceleration time histories, the strong motion was estimated using the techniques described in Chapter 3. In short, seven candidate time histories were selected from 30 synthetically generated time histories. The program SGMSV5 (Papagorgiou, 2004) was used to generate the synthetic time histories. The candidate time histories were further prepared for FLAC modeling, as described in Chapter 3.

All case histories used in the calibration process had measured lateral spread displacements at their respective sites. However, these displacements had various degrees of accuracy and spatial distribution along the longitudinal axis of the failure. For cases where the measured lateral spread displacements were somewhat sparse and where synthetic time histories were used for calibration, the measured displacements were augmented by estimates from the Youd et al. (2002) lateral spread equations to develop a

smoothed displacement profile for FLAC modeling and calibration. The Youd et al. (2002) equation was useful in interpolating how the displacement pattern varied along the length of the lateral spread. This was done only for cases where the strong motion had been synthetically generated at the site. Thus, the calibration for such sites consisted of estimating a smoothed displacement pattern from the Youd et al. (2002) equation and calibrating the FLAC model using the synthetic strong motion estimated by SGMSV5 (Papagorgiou, 2004).

The selected lateral spread cases for the FLAC model calibration are from Niigata and Noshiro, Japan; San Fernando and Imperial Valley, California; Degirmenedere and Sapanca Hotel, Turkey; Whiskey Springs, Idaho; Northridge, California and Wildlife, California. The associated failure type, method of obtaining the acceleration time history for the analyses and notes regarding the lateral spread displacement are listed in Table 7.1. The modeling results for the individual cases are further reviewed in this chapter.

Table 7.1. Selected sites and modeling information

Site	**Failure Type**	**Acceleration Record**	**Lateral Spread Displacements**
Niigata Bandai	Free face	Synthetic	Recorded - Smoothed with Youd's (2002) model
Niigata Hotel	Ground slope	Synthetic	Recorded - Smoothed with Youd's (2002) model
Niigata Railway	Ground slope	Synthetic	Recorded - Smoothed with Youd's (2002) model
Niigata Showa	Free face	Synthetic	Recorded - Smoothed with Youd's (2002) model
Noshiro N-4 Section	Ground slope	Synthetic	Recorded - Smoothed with Youd's (2002) model
Noshiro S-7 Section	Ground slope	Synthetic	Recorded - Smoothed with Youd's (2002) model
Juvenile Hall, California	Ground slope	Synthetic	Recorded - Smoothed with Youd's (2002) model
Jensen Filtration Plant	Free face	Synthetic	Recorded - Smoothed with Youd's (2002) model
Heber Road, California	Free face	Synthetic	Recorded - Smoothed with Youd's (2002) model
River Park, California	Ground slope	Recorded	Recorded
Degirmenedere, Turkey	Ground slope	Recorded	Recorded
Wildlife, California	Free face	Recorded	Recorded
Whiskey Springs, Calif.	Ground slope	Synthetic	Recorded
Balboa Ave., Calif.	Ground slope	Recorded	Recorded
Degirmenedere, Turkey without T_{15} layer	Ground slope	Recorded	Recorded
Sapanca Hotel, Turkey	Ground slope	Recorded	Recorded

7.1 Bandai Bridge, Niigata Japan

The Niigata earthquake, M7.5, occurred on June 16, 1964 and caused extensive soil liquefaction in Niigata City and surrounding areas. The earthquake affected the Japan Sea coast from Niigata through Yamagata and Akita Prefectures. Many buildings, bridges, quay walls and lifeline systems (e.g., electrical, gas, water and telecommunications) suffered severe damage (Hamada et al., 1992).

In Niigata City, which is about 50 km from the epicenter, buildings, bridges, oil storage tanks, lifeline facilities, etc. were extensively damaged. The epicenter was near Awa Island at coordinates 38°21'N, 139°11'E in the Japan Sea, 22 km off the coast, as shown in Figure 7.1. The focus of the earthquake was about 40 km deep. Figure 7.2 shows the location of the Bandai Bridge in Niigata and the associated lateral spread displacement vectors. Figure 7.3 shows the soil conditions at this location.

Liquefaction occurred in the riverbed and in both river banks. The maximum thickness of the liquefied soil is estimated to be about 10 m at the center of the riverbed. The lower boundary of the liquefied layer was inclined toward the center of the river from both banks. It is likely that the depth and slope of the base of the liquefied zone had some effect on the magnitude and distribution of ground displacements toward the river. Also, the free face on the south side of the river had a significant effect.

The FLAC model developed for the Bandai cross section accounts for the geometry of the river channel (i.e., the free face) shown on the south side of the Bandai Bridge. The displacements on the north side of the bridge were not modeled. The model uses the actual river depth and a channel with a width of approximately 180 m. The soil properties used for the model design are shown in Table 7.2.

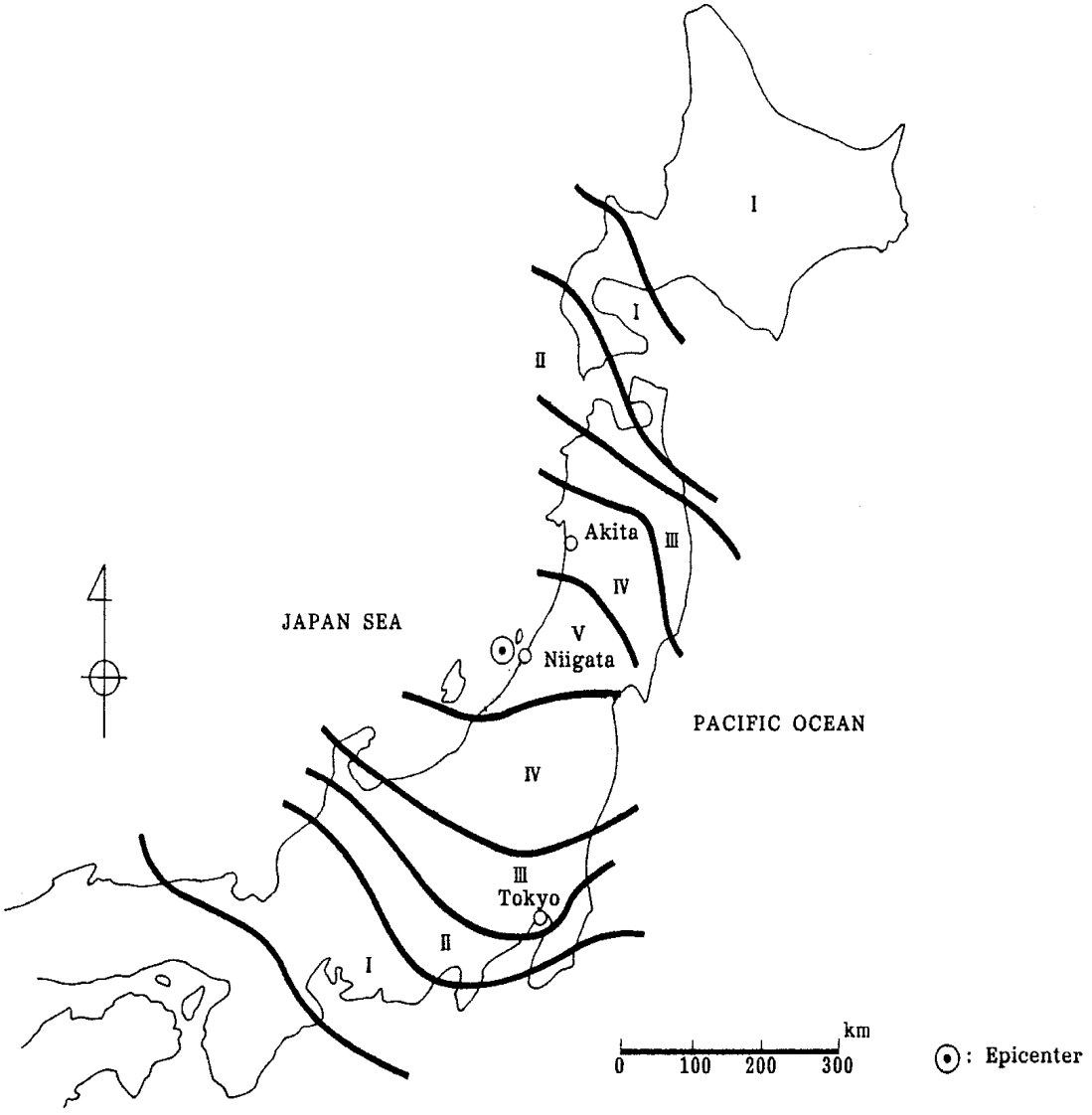


Figure 7.1. Epicenter and Seismic Intensity of the 1964 Niigata Earthquake (after Hamada et al., 1992).

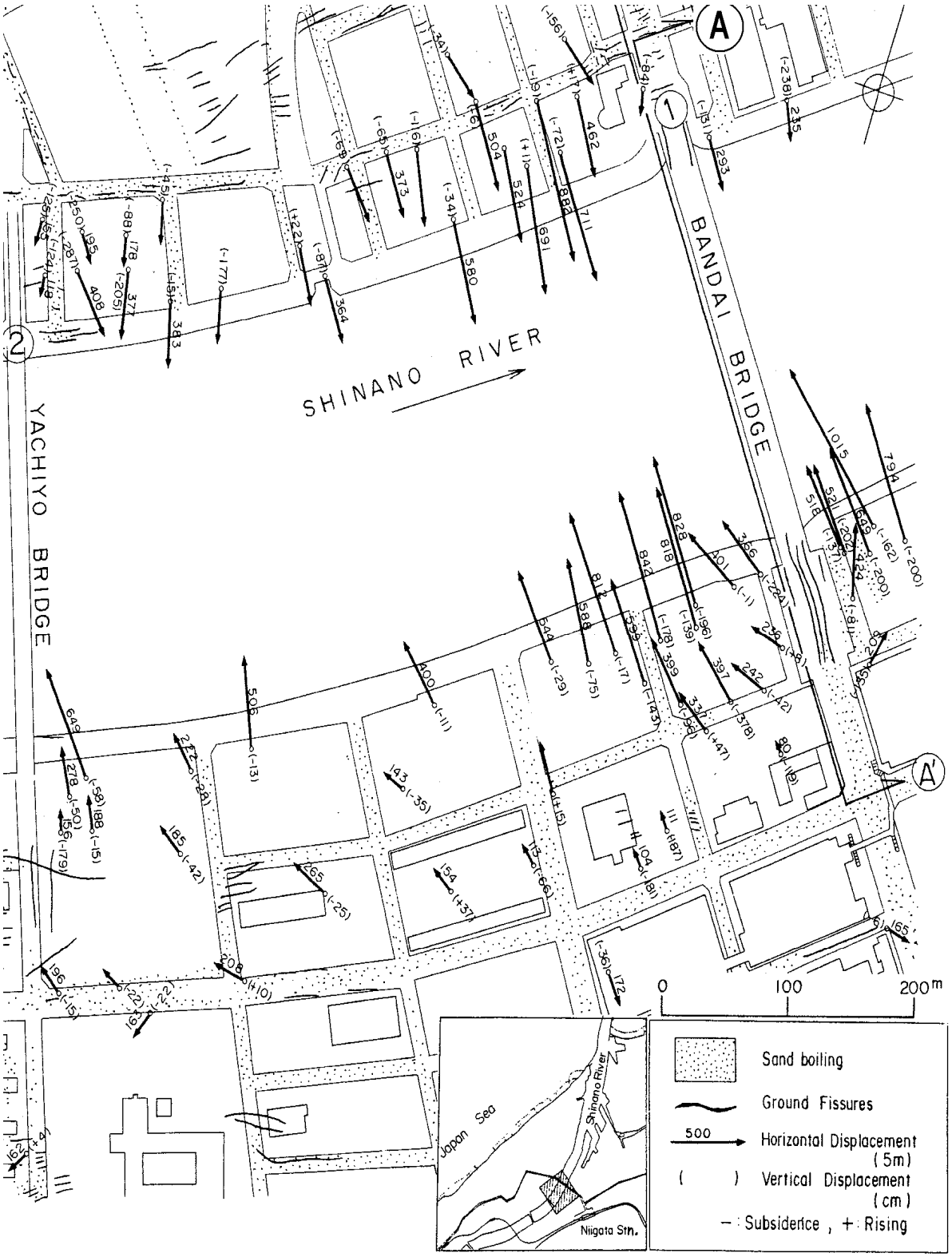


Figure 7.2 Location of the Bandai section in Niigata site and displacement vector (after Hamada et al., 1992).

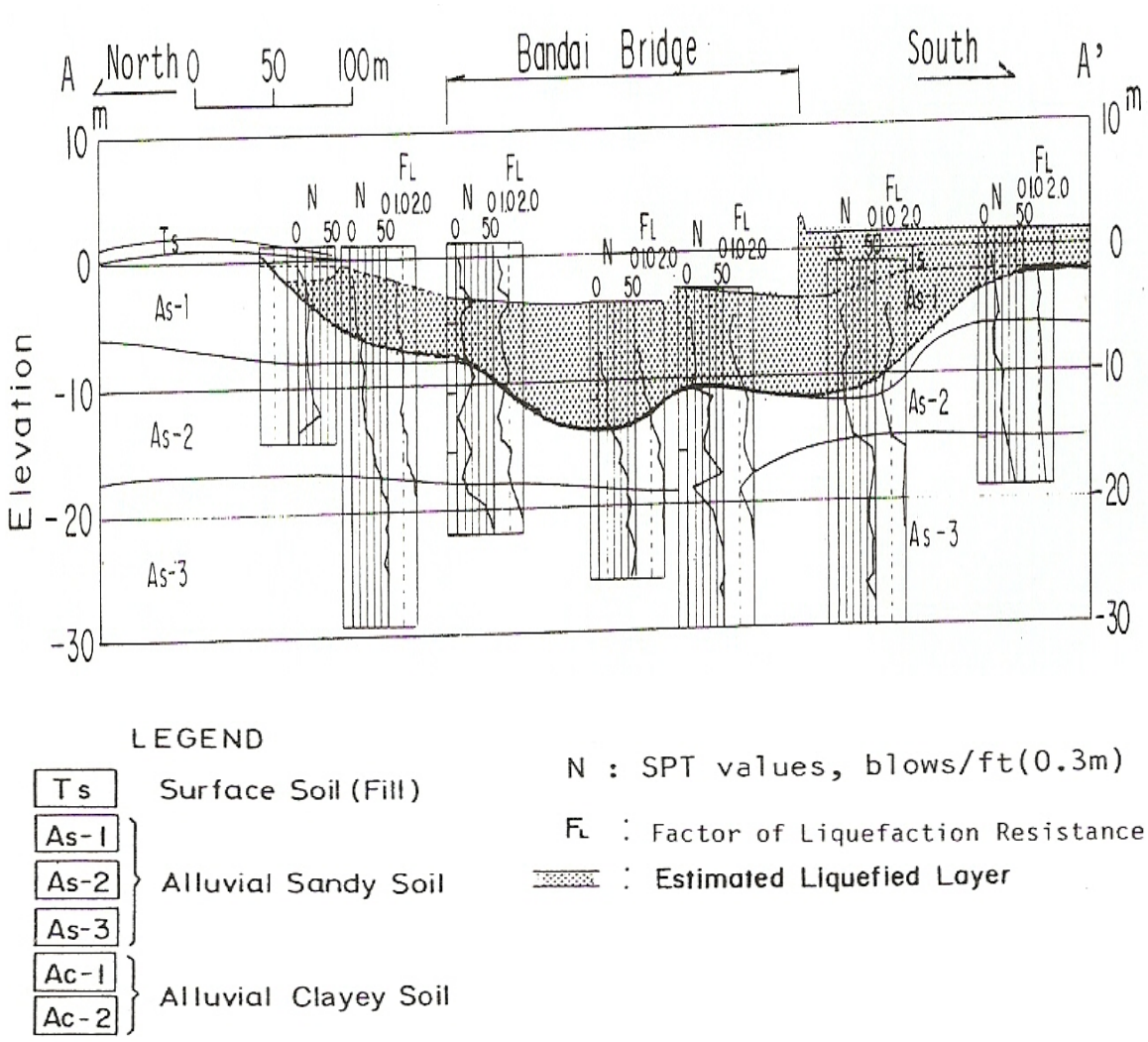


Figure 7.3. Soil conditions near the Bandai Bridge crossing the Shinano River (after Hamada et al., 1992).

Table 7.2. Soil properties of Bandai site, Niigata, Japan

Boring location	Ground water level (m)	Depth of Liq. layer (m)	T_{15}(m)	D_{50}(mm)	F_{15}(%)	Average $(N_1)_{60}$
AF-29	0.9	0.9	13.3	0.248	9.0	8.5
H10-8	1.0	1.0	10.3	0.350	5.0	10.2
8-6	0.7	0.8	6.9	0.225	14.0	6.8
Average	0.9	0.9	10.2	0.300	9.3	8.5

The FLAC model was developed using the average soil properties and depth obtained for this site, as shown in Appendix A. The soil column's predominant period, before and after liquefaction, are calculated to be 0.4 s and 1.9 s, respectively. The assumption for calculating the soil predominant period, as explained in the previous section, is that the soil's shear modulus decreases to 1% of the maximum shear modulus for more than 2 to 3% shear strain during the liquefaction process.

Taking into account the soil's predominant period after liquefaction, the response spectra of the seven time histories generated for the FLAC model is shown in Figure 7.4. The seed number shown in this figure is the number used to randomly generate the realizations of the Gaussian white noise (Papageorgiou, 2004).

These response spectra for the motions shown in Figure 7.4 are shown in Figures 7.5 to Figure 7.11. These acceleration time histories are applied to the PROSHAKE model and deconvolved to the base of the model (i.e., 20 m depth). The requested motion from PROSHAKE was an outcrop motion. This was later adjusted to a stress wave and input at the base of the FLAC model, as discussed in Chapter 3.

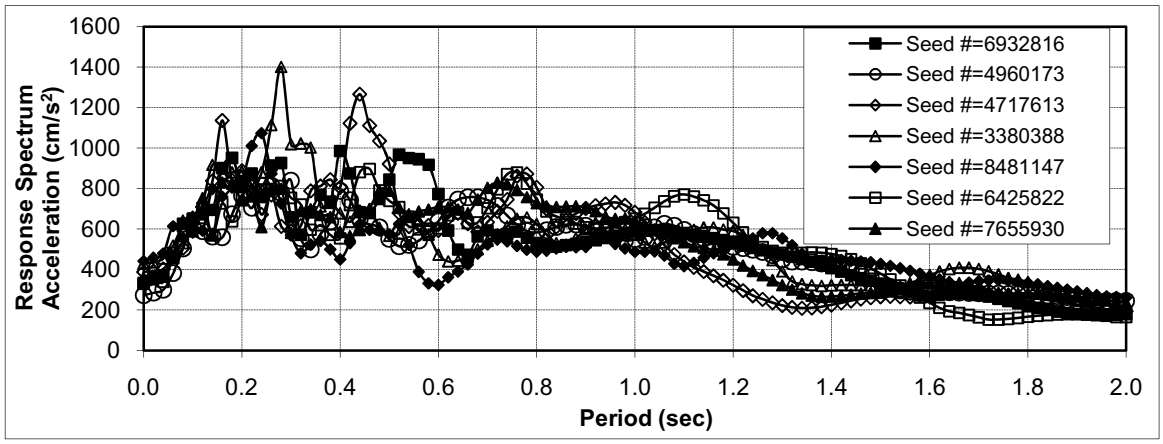


Figure 7.4. Response spectra of seven time histories generated from SMGS for Niigata Bandai section

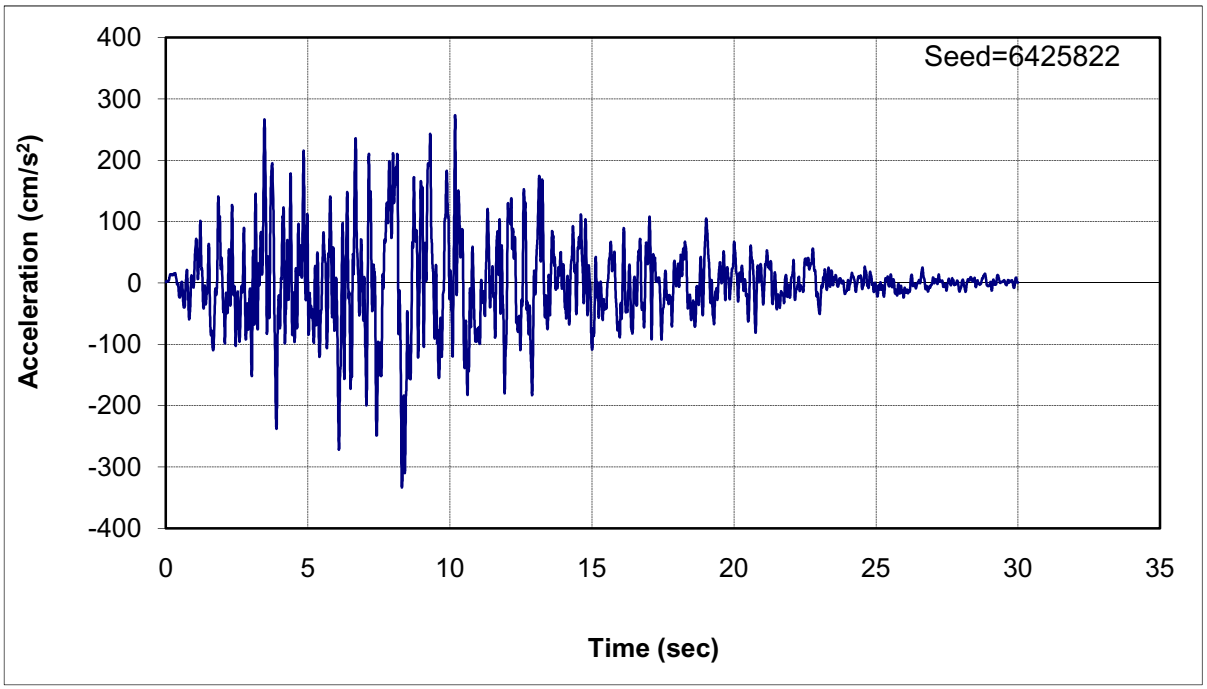


Figure 7.5. Niigata Bandai section model selected motion 1

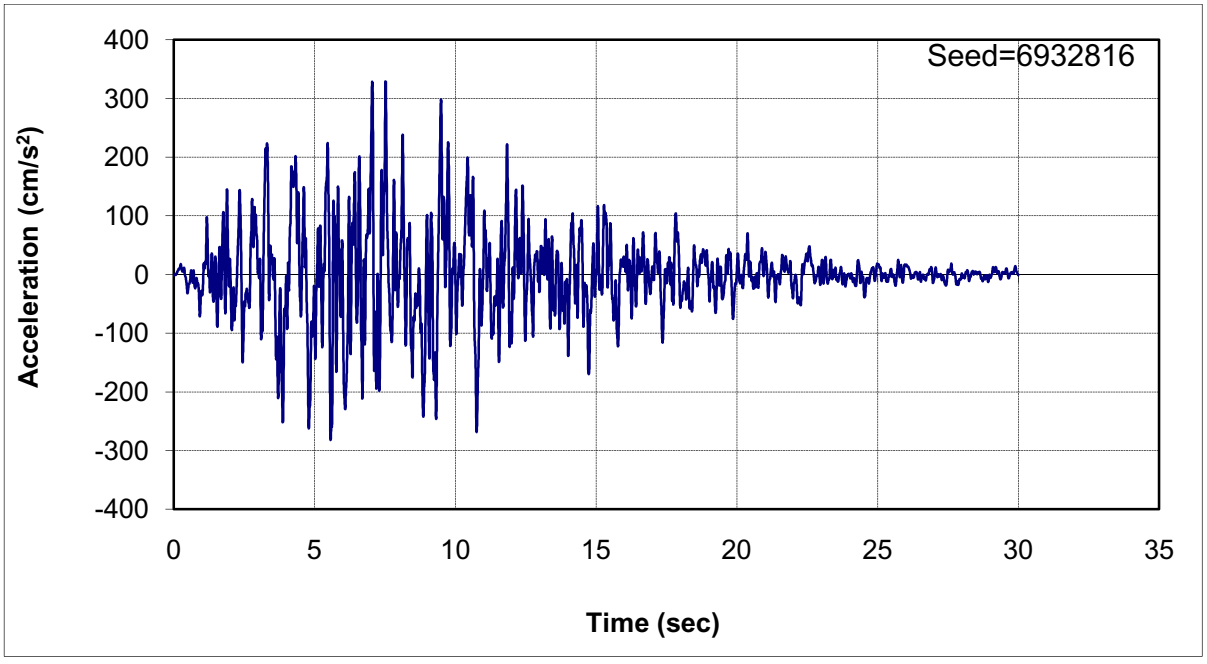


Figure 7.6. Niigata Bandai section model selected motion 2

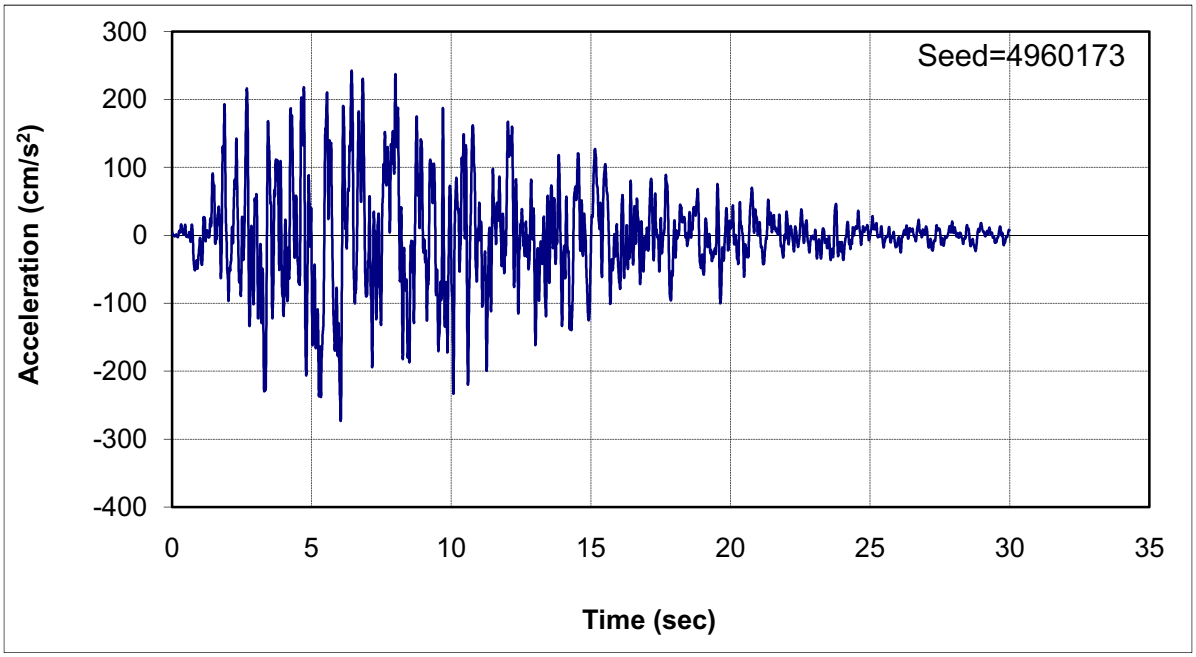


Figure 7.7. Niigata Bandai section model selected motion 3

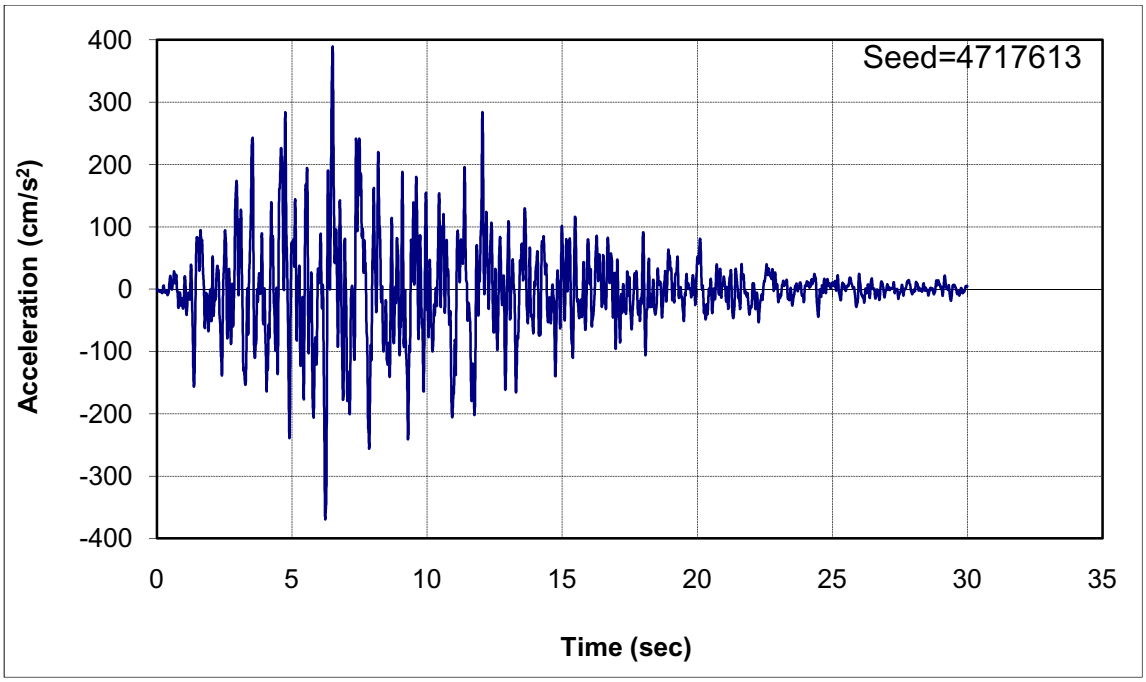


Figure 7.8. Niigata Bandai section model selected motion 4

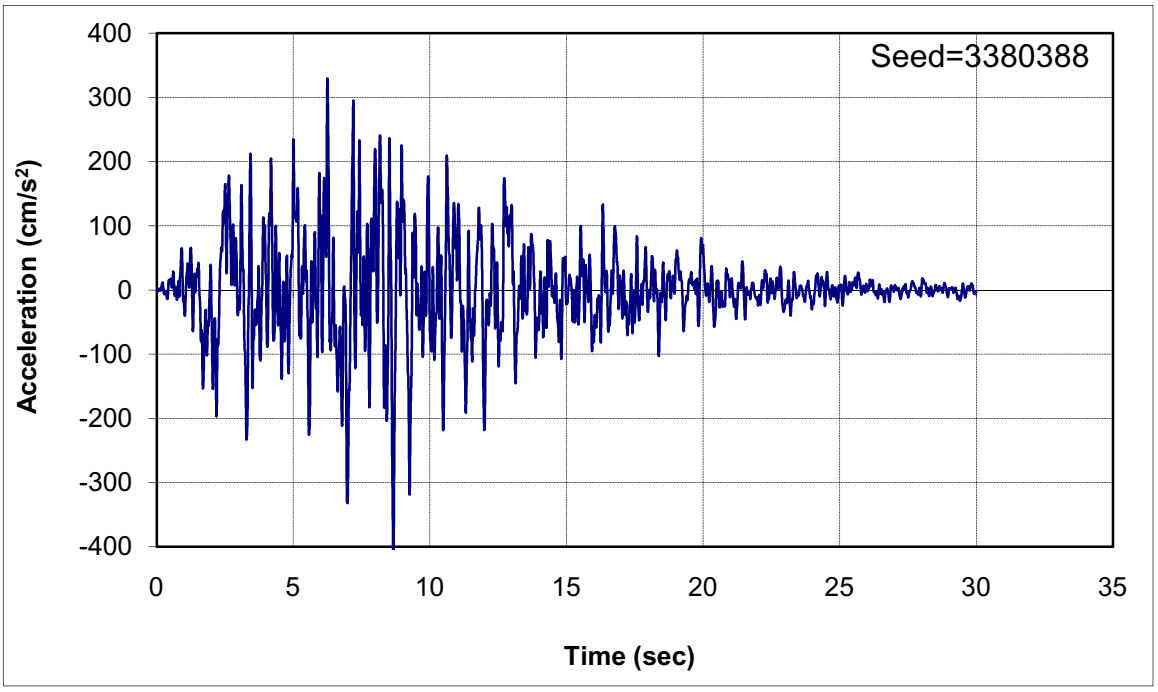


Figure 7.9. Niigata Bandai section model selected motion 5

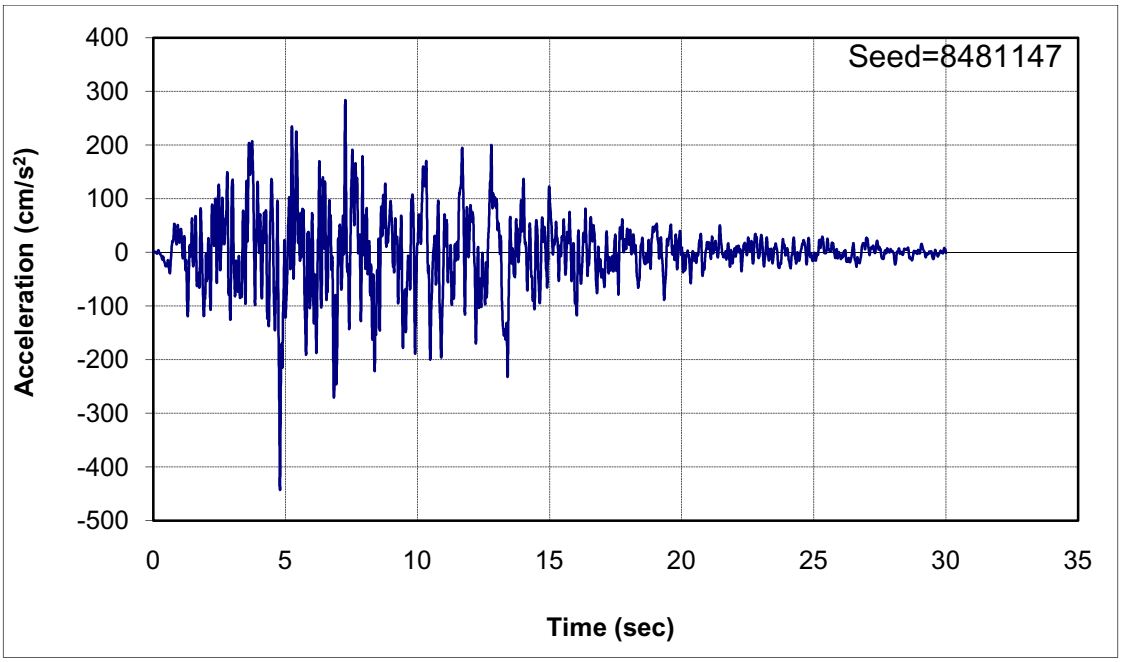


Figure 7.10. Niigata Bandai section model selected motion 6

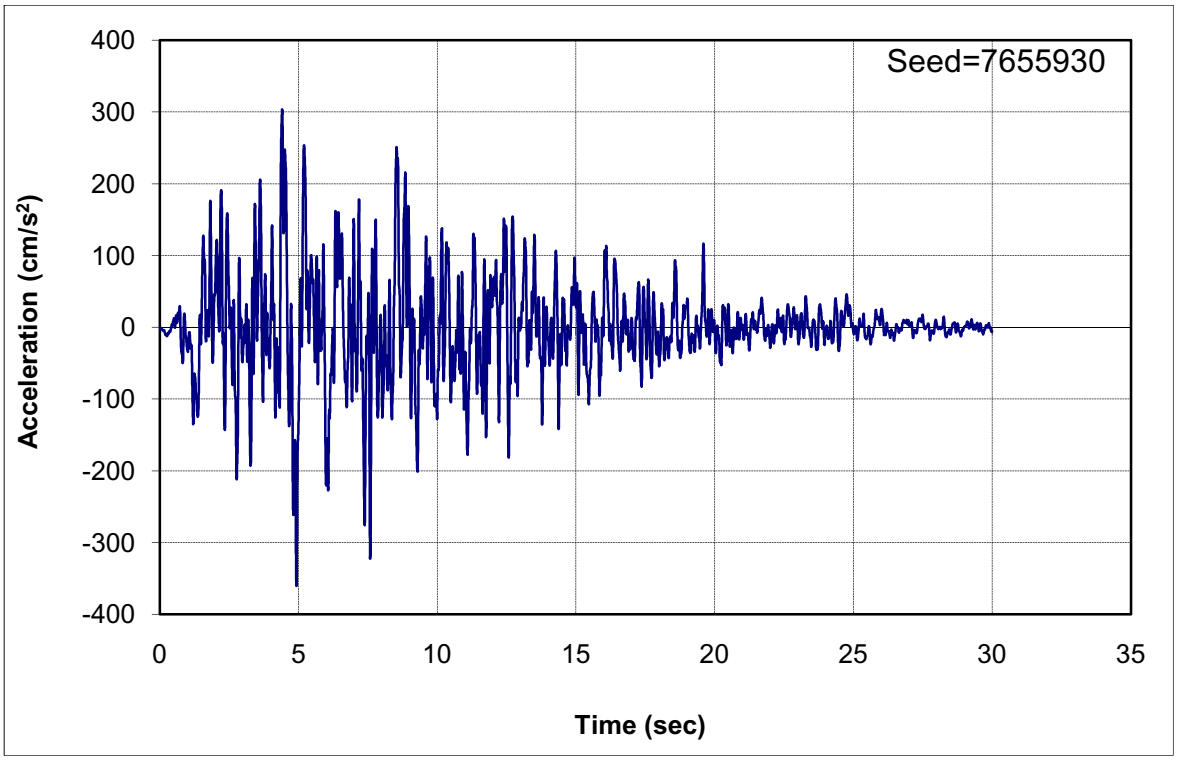


Figure 7.11. Niigata Bandai section model selected motion 7

Based on the Youd et al. (2002) equation for free face failure, the amount of lateral spread displacement is a function of the height of and distance from the free face. The predicted displacement from the Youd et al. (2002) model as a function of distance from the free face is listed in Table 7.3 for the Bandai Bridge site. This distance is the horizontal distance from the vertical river bank that was retained by a quay wall.

A trial and error method was used so that the predicted lateral spread displacement pattern from the FLAC model reasonably matched the record displacements and those values interpolated by the Youd et al. (2002) model. In modeling this case, the FLAC model procedure and time history generation procedure developed in previous chapters of this thesis were strictly followed.

Table 7.3. Lateral spread displacements estimated by Youd et al. (2002) model at Bandai site

M	R(km)	W(%)	S	T_{15} (m)	F_{15} (%)	$D50_{15}$ (mm)	Distance from free face (m)	Lateral spread (m)
7.5	21	18.75	1	6	9	0.27	24	4.12
7.5	21	16.07	1	6	9	0.27	28	3.76
7.5	21	14.06	1	6	9	0.27	32	3.48
7.5	21	12.50	1	6	9	0.27	36	3.24
7.5	21	11.25	1	6	9	0.27	40	3.05
7.5	21	10.23	1	6	9	0.27	44	2.88
7.5	21	9.38	1	6	9	0.27	48	2.73
7.5	21	8.65	1	6	9	0.27	52	2.61
7.5	21	8.04	1	6	9	0.27	56	2.50
7.5	21	7.50	1	6	9	0.27	60	2.40
7.5	21	7.03	1	6	9	0.27	64	2.31
7.5	21	6.62	1	6	9	0.27	68	2.23

The developed FLAC model, input motion and output curves are listed in Appendix A. The output data from the FLAC model output curves are given in the following sections.

The FLAC model best matched the lateral spread displacement pattern using a Su/σv` ratio of 0.065, as discussed later. However, various values of Su/σv` were used and the sum of the square of the errors (i.e., deviation index) was checked, until it reached a minimum value. Then the Su/σv` value corresponding to this minimum variance case was selected for the regression analyses described in Chapter 8.

Table 7.4 shows the process for the first modeled value of Su/σv` of 0.085. This estimate is later refined in the subsequent paragraphs.

The deviation index was used to judge and minimize the difference between the FLAC predictions and those estimated by the Youd (2002) model.

Table 7.4. Lateral spread prediction from FLAC model for residual strength ratio of 0.085 at Niigata Bandai site

Distance from free face (m)	Motion_1	Motion_2	Motion_3	Motion_4	Motion_5	Motion_6	Motion_7	Average	Deviation
24	3.50	3.21	3.28	3.26	3.54	4.04	3.57	3.49	3.32
28	2.94	2.75	2.71	2.75	3.01	3.47	3.95	3.08	4.52
32	2.55	2.43	2.35	2.42	2.65	3.04	2.25	2.53	6.72
36	2.20	2.12	2.08	2.15	2.32	2.61	2.18	2.24	7.27
40	1.97	1.94	1.86	1.96	2.09	2.29	1.96	2.01	7.64
44	1.78	1.72	1.67	1.82	1.89	2.04	1.73	1.81	8.14
48	1.68	1.59	1.54	1.69	1.80	1.85	1.63	1.68	7.82
52	1.57	1.49	1.43	1.58	1.66	1.70	1.52	1.56	7.68
56	1.47	1.43	1.38	1.48	1.57	1.58	1.38	1.47	7.41
60	1.42	1.34	1.31	1.40	1.47	1.48	1.34	1.39	7.06
64	1.37	1.28	1.26	1.31	1.37	1.37	1.25	1.32	6.89
68	1.30	1.24	1.21	1.23	1.29	1.30	1.17	1.25	6.69

The deviation index was calculated as the sum of the square of the error and was defined as $S\sigma\left(X_i - \overline{X_i} \right)^2$, where X_i is the actual displacement or that interpolated by the Youd et al. (2002) equation and $\overline{X_i}$ represent the average FLAC model prediction at the corresponding location for the seven candidate time histories. The deviation index is also shown in Table 7.4. For the residual strength ratio of 0.085; the sum of deviation is 81.2.

The process was repeated using a lower Su/σv`=0.075 ratio and the deviation index was recalculated (Table 7.5). For this case, the deviation index is 48.7.

Subsequently, the FLAC model predicted lateral spread using Su/σv`=0.065 and the derivation of the FLAC predicted lateral spread from that predicted by the Youd et al. (2002) model are shown in Table 7.6. For this case, the deviation index is 43.9.

Table 7.5. Lateral spread prediction from FLAC model for residual strength ratio of 0.075 at Niigata Bandai site

Distance from free face (m)	Motion_1	Motion_2	Motion_3	Motion_4	Motion_5	Motion_6	Motion_7	Average	Deviation
24	4.15	4.32	4.31	4.13	4.22	4.66	4.31	4.30	0.41
28	3.45	3.64	3.55	3.37	3.52	4.93	3.58	3.72	1.77
32	3.00	3.10	3.06	2.90	3.06	3.46	3.01	3.08	1.27
36	2.54	2.59	2.58	2.49	2.65	3.01	2.48	2.62	2.91
40	2.25	2.25	2.24	2.18	2.41	2.65	2.16	2.31	4.02
44	1.99	1.92	1.96	1.92	2.17	2.32	1.92	2.03	5.21
48	1.85	1.75	1.79	1.82	1.99	2.09	1.75	1.86	5.42
52	1.73	1.59	1.62	1.70	1.84	1.90	1.61	1.71	5.70
56	1.64	1.48	1.50	1.58	1.71	1.78	1.49	1.60	5.75
60	1.55	1.40	1.42	1.49	1.60	1.67	1.40	1.50	5.64
64	1.48	1.35	1.34	1.43	1.52	1.57	1.32	1.43	5.44
68	1.43	1.31	1.29	1.38	1.44	1.52	1.22	1.37	5.18

Table 7.6. Lateral spread prediction from FLAC model for residual strength ratio of 0.065 at Niigata Bandai site

Distance from free face (m)	Motion_1	Motion_2	Motion_3	Motion_4	Motion_5	Motion_6	Motion_7	Average	Deviation
24	5.47	5.10	5.59	5.21	5.57	6.00	5.41	5.48	13.39
28	4.61	4.44	4.77	4.44	4.65	5.14	4.56	4.66	5.98
32	3.95	3.76	4.03	3.70	4.06	4.46	3.97	3.99	2.21
36	3.53	3.07	3.51	3.06	3.50	3.76	3.21	3.38	0.55
40	2.83	2.60	3.03	2.65	2.87	3.29	2.66	2.85	0.64
44	2.48	2.29	2.63	2.31	2.55	2.77	2.27	2.47	1.39
48	2.10	1.96	2.21	2.23	2.32	2.53	2.00	2.19	2.29
52	2.00	1.89	2.05	1.07	2.08	2.27	1.90	1.89	4.46
56	1.80	1.68	1.97	1.87	1.84	2.17	1.62	1.85	3.13
60	1.66	1.59	1.84	1.72	1.73	1.97	1.46	1.71	3.46
64	1.63	1.55	1.79	1.69	1.65	1.86	1.41	1.65	3.11
68	1.53	1.41	1.70	1.50	1.60	1.75	1.35	1.55	3.33

Lastly, the FLAC model predicted lateral spread using $Su/\sigma v`=0.055$ and the derivation of the FLAC predicted lateral spread from that predicted by the Youd et al. (2002) model is shown in the Table 7.7. For this case, the deviation index is 176.0. Because the deviation index for the residual strength ratio of 0.065 is at a minimum value, this ratio was used at the calibrated value for the subsequent regression analyses described in Chapter 8.

Table 7.7. Lateral spread prediction from FLAC model for residual strength ratio of 0.055 at Niigata Bandai site

Distance from free face (m)	Motion_1	Motion_2*	Motion_3	Motion_4	Motion_5	Motion_6	Motion_7	Average	Deviation
24	7.23	crash	7.51	7.54	7.82	7.97	7.39	6.49	71.97
28	6.23	crash	6.6	6.48	6.67	6.95	6.29	5.60	46.52
32	5.33	crash	5.71	5.6	5.85	6.12	5.3	4.84	28.87
36	4.41	crash	4.86	4.86	4.82	5.21	4.44	4.09	14.39
40	3.62	crash	4.01	4.08	4.22	4.4	3.75	3.44	6.03
44	3.03	crash	3.56	3.56	3.54	3.87	3.26	2.97	2.51
48	2.57	crash	3.05	3.05	3.22	3.38	2.67	2.56	0.88
52	2.33	crash	2.67	2.74	2.8	2.97	2.33	2.26	0.34
56	2.00	crash	2.28	2.34	2.55	2.55	2.06	1.97	0.51
60	1.76	crash	2.16	2.02	2.23	2.3	1.78	1.75	1.02
64	1.65	crash	1.86	1.94	2.01	2.16	1.63	1.61	1.33
68	1.50	crash	1.62	1.85	1.9	2	1.55	1.49	1.65

Note: *--Motion_2 is not taken into account due to the crash.

Although the residual strength ratio of 0.065 produced the results with the lowest deviation index (i.e., error), the match between the FLAC estimated values and those predicted by Youd et al. (2002) showed some spatial bias.

The FLAC model tended to underestimate, on average, the displacement pattern at the free face. It also tended to overestimate, on average, the displacement pattern at greater distances for a residual strength ratio of 0.065 (Figure 7.12) at the Bandai Bridge site. This same bias was observed for the free face failure at the Showa River site (Section 7.4) even though deviation index was minimized for all cases modeled herein.

Efforts were made to reduce this bias, but it could not be eliminated due to the difference between Youd et al. simplified approach and the FLAC modeling approach.

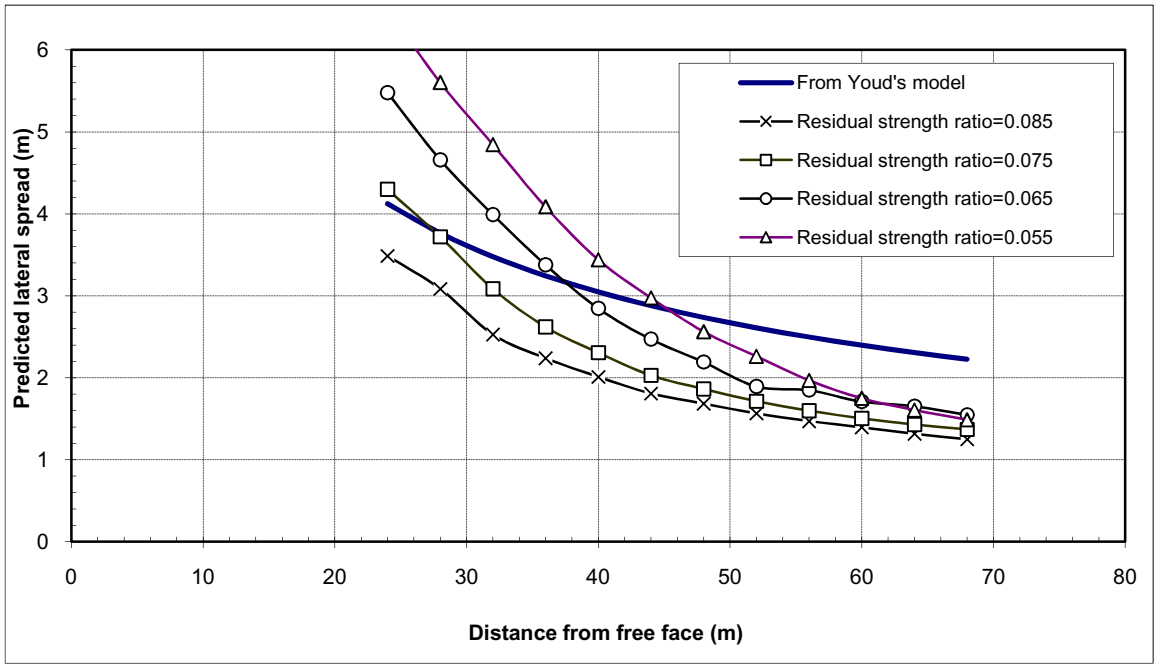


Figure 7.12. Comparison of lateral spread displacements from Youd et al. (2002) free face model and the FLAC model results at Bandai Bridge site, Niigata, Japan.

It was concluded that the Youd et al. (2002) regression equation with its simplified approach of modeling the free face ratio may not completely explain the mechanisms of shear stress distribution and progressive lateral spread failure that may develop for free face failures. In addition, it should be noted that the FLAC modeling approach as implemented is undoubtedly a simplification of the real subsurface conditions, in that the T_{15} layer thickness and depth were not varied along the longitudinal profile. In addition, an average residual strength ratio was used along the length of the profile. These additional simplifications could be contributing to the observed bias.

7.2 Niigata Hotel Area

The location and displacement vector pattern around the Niigata Hotel is shown in Figure 7.13. For the area along the section between the riverbank and the Niigata Hotel as shown in Figure 7.13, the estimated liquefied layer is very thick, at about 10 to 12 m. Its thickness gradually decreases towards the east, shown in Figure 7.14. Around the hotel and to its west, the boundary is inclined toward the east, coinciding with the direction of ground displacements. But the gradient is very small, less than 0.5% (Hamada et al., 1992). Thus for this section, the measured displacements and the Youd et al. (2002) ground slope model were used to calibrate the FLAC model near the Niigata Hotel.

The soil's predominant period, before and after liquefaction, is calculated to be 0.4 s and 2.2 s, respectively. Because of the similarity in the soil predominant period after liquefaction compared to the Bandai Bridge site, the same synthetic motions used in Section 7.1 were selected and deconvolved to the model base as the FLAC input motions.

The Youd et al. (2002) model for ground slope was used to help calibrate the FLAC model. The soil properties used for the ground slope model and the FLAC model are shown in Table 7.8. The input parameters to the Youd et al. (2002) model and its prediction are shown in Table 7.9. The surface profile has a slope of 0.35 percent from the riverbank to Niigata Hotel (Figure 7.14).

Following the developed FLAC model procedure, the FLAC model was constructed and executed. The detailed FLAC model results are in Appendix B. The modeled results for residual strength ratio of 0.105, 0.095, 0.085, 0.075, average of the seven modeling results and the deviation from the Youd et al. (2002) model prediction are shown in the Table 7.10.

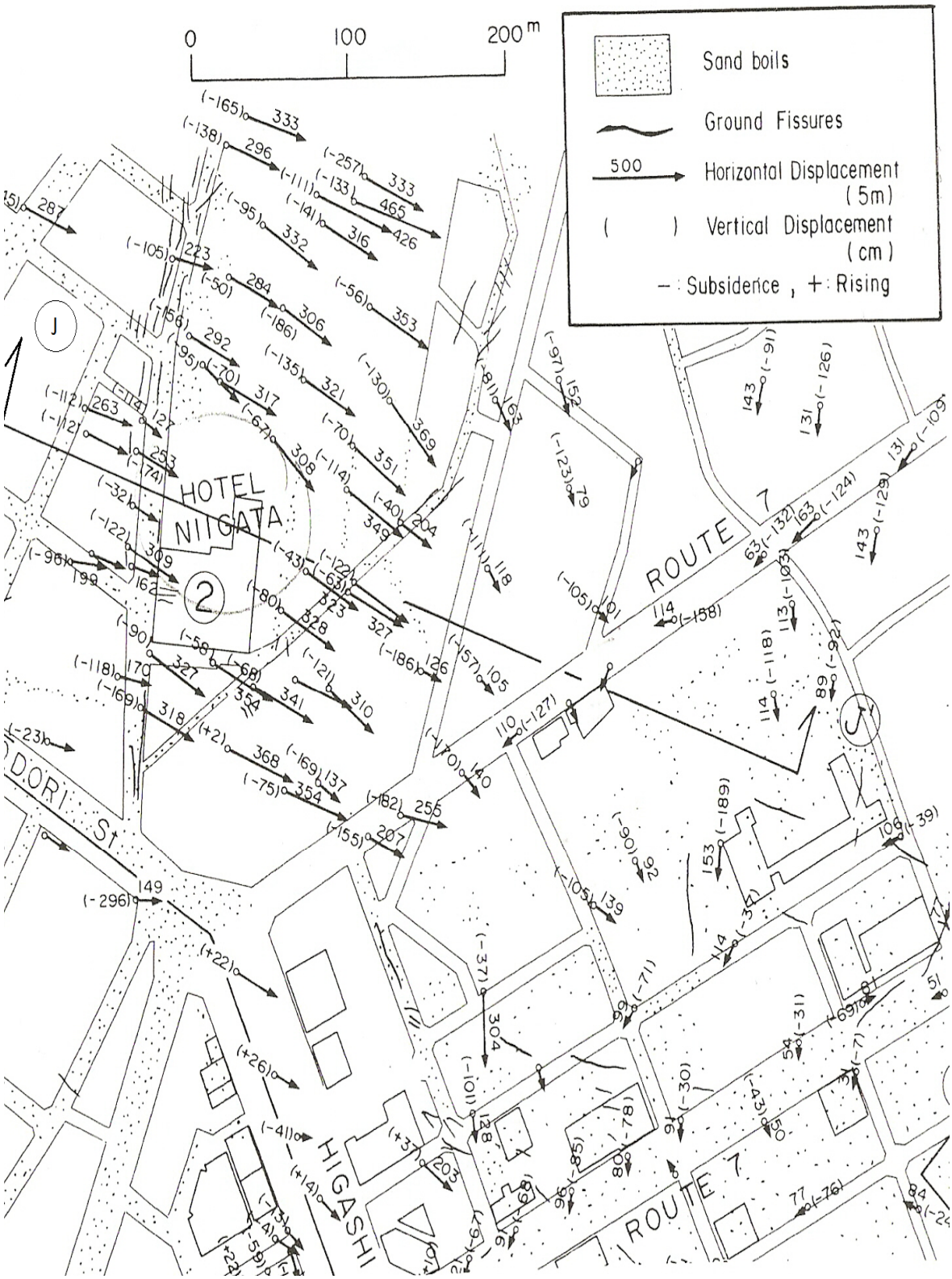


Figure 7.13. Permanent displacement near Niigata Hotel (after Hamada et al., 1992).

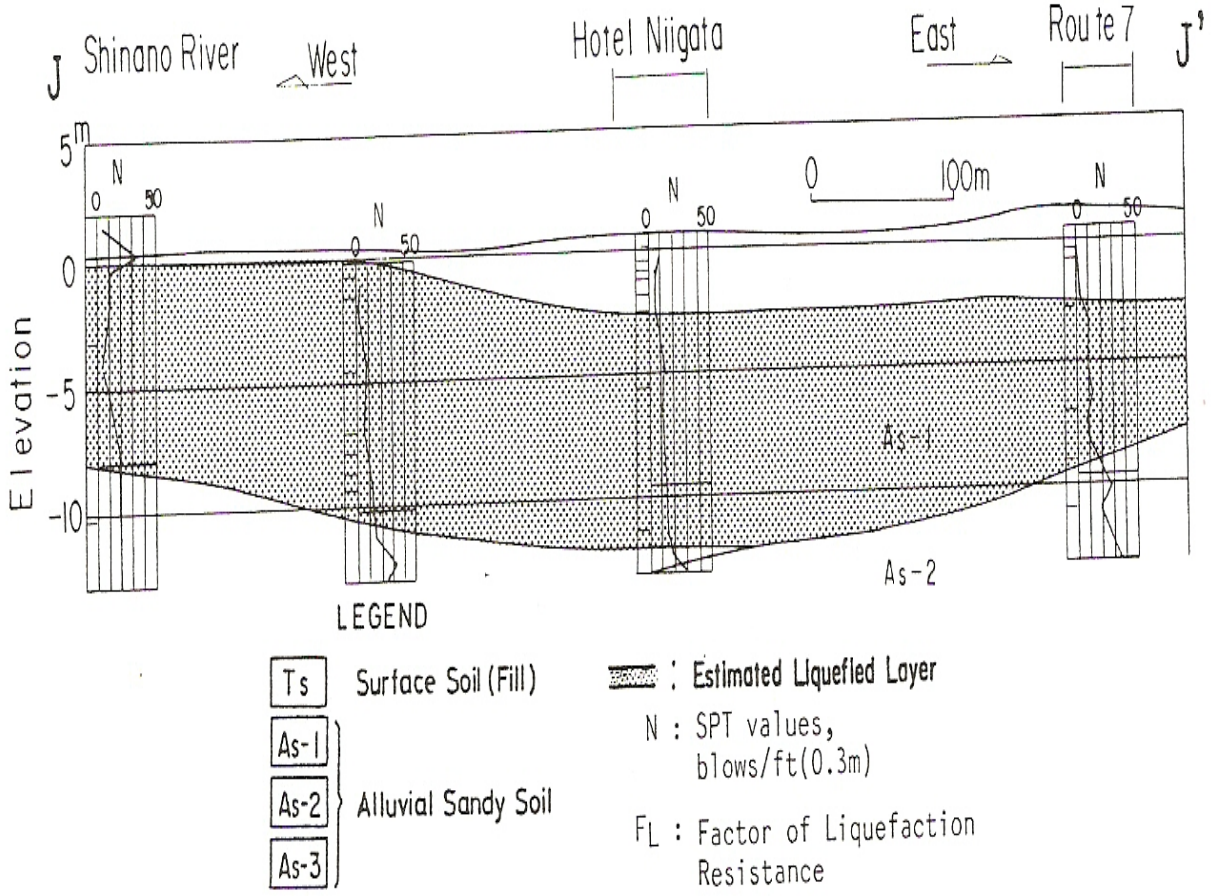


Figure 7.14. Soil conditions and estimated liquefied layer (after Hamada et al., 1992).

Table 7.8. Soil properties of Niigata Hotel site

Boring location		Ground water level (m)	Depth of Liq. layer (m)	T_{15}(m)	D_{50}(mm)	F_{15}(%)	Average $(N_1)_{60}$
8-3	194	2.3	2.3	10.2	0.283	8.0	8.0
8-4	195	0.9	2.0	18.8	0.254	6.0	9.1
Average		1.2	2.2	14.5	0.300	7.0	8.6

Table 7.9. Lateral spread prediction by Youd et al. (2002) model at Niigata Hotel site

M	R (KM)	W	S (%)	T_{15} (m)	F_{15} (%)	$D50_{15}$ (mm)	Lateral spread (m)
7.5	21	1	0.35	12	7	0.3	2.37

Table 7.10. Lateral spread prediction from FLAC model for different residual strength ratio at Niigata Hotel site

Residual strength ratio	Motion 1	Motion 2	Motion 3	Motion 4	Motion 5	Motion 6	Motion 7	Average	Deviation
0.105	1.94	1.84	1.57	1.65	1.85	1.62	1.27	1.68	3.70
0.095	2.43	2.12	1.71	1.78	1.88	2.45	1.41	1.97	2.03
0.085	2.45	2.49	2.14	2.29	2.56	2.65	1.66	2.32	0.70
0.075	2.5	2.85	2.31	2.57	2.64	3.32	2.37	2.65	1.25

Because the deviation for the residual strength ratio of 0.085 is the least of all the cases modeled, 0.085 will be used for further statistical analysis in the next section.

7.3 Niigata Railway Station

The displacement vector pattern near Niigata railway is shown in Figure 7.15. From the Shinano River to the Niigata Railway Station, the vectors represent horizontal ground displacements each with a number indicating the magnitude of displacement in centimeters.

The soil conditions and liquefied soil layers, which were estimated from the bank of the Shinano River at the Bandai Bridge to the Niigata Railway Station, are shown in Figure 7.16. As shown in this figure, the ground surface is slightly inclined from the riverbank toward the station, with the slope of about 0.4%. Along this section, the estimated liquefied layer increases in thickness toward the station.

The boundary between the liquefied layer and the lower nonliquefied layer is inclined toward the station with a gradient of 2 to 3 %. The soil properties used in the FLAC modeling are shown in Table 7.11.

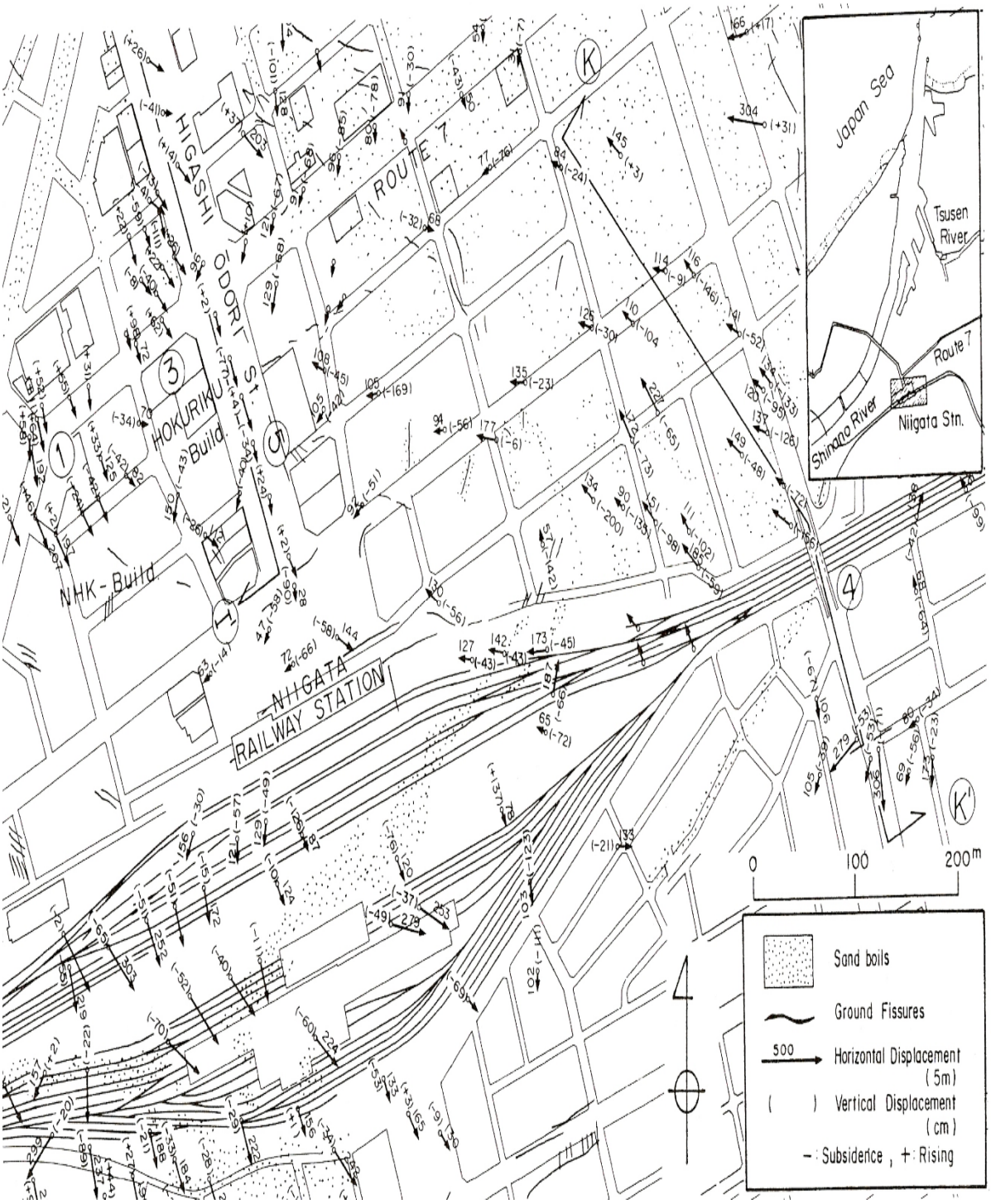


Figure 7.15. Permanent displacement near Niigata Railway Station (after Hamada et al., 1992).

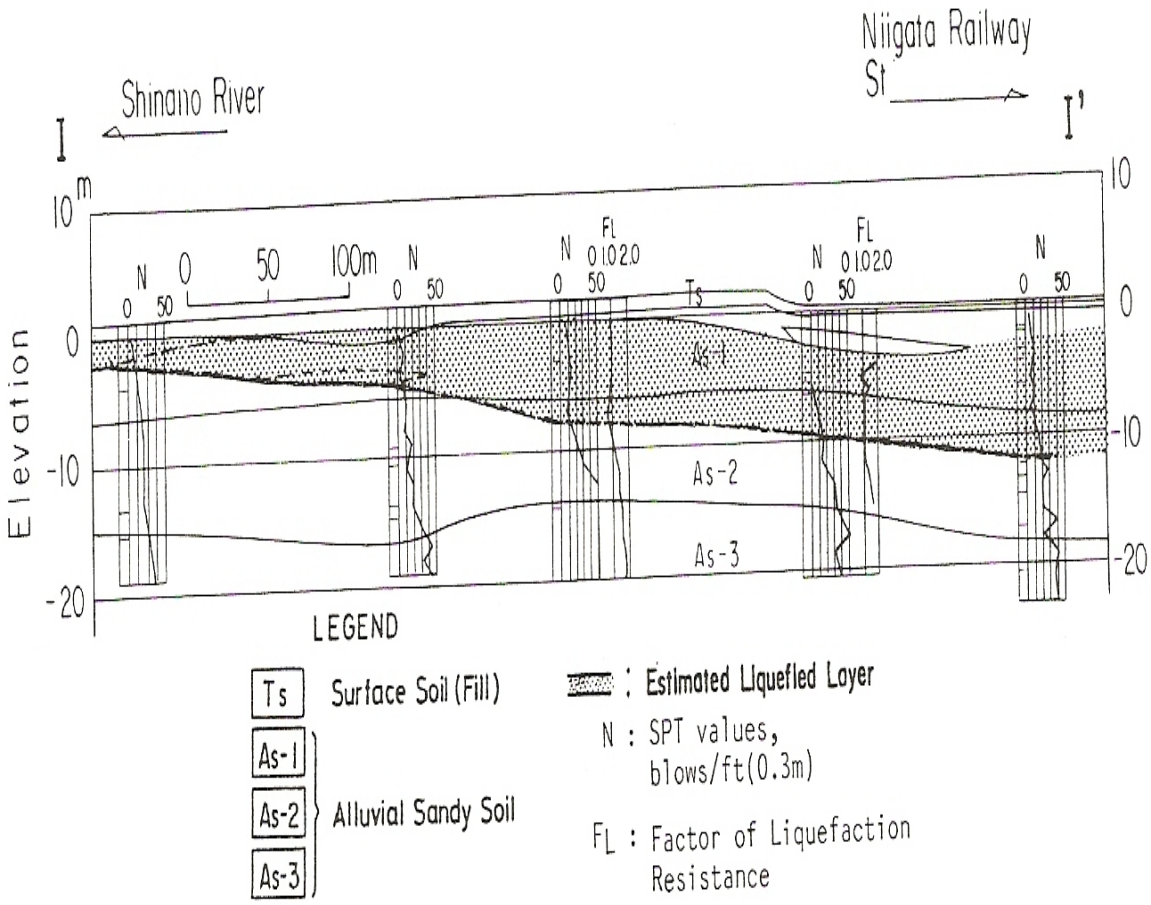


Figure 7.16 . Soil Conditions, Estimated Liquefied Layer, and Horizontal Ground Displacements at Niigata Railway Station (after Hamada et al., 1992).

Table 7.11. Soil properties of Niigata Railway Station

Boring location		Ground water level (m)	Depth of Liq. layer (m)	T_{15} (m)	D_{50} (mm)	F_{15} (%)	Average $(N_1)_{60}$
H10-44	236	2.5	2.5	7.2	0.600	6	11.1
8-37	240	2.5	2.7	15.6	0.281	14	8.5
H10-43	235	2.5	2.5	4.2	0.193	7	10.9
H10-45	237	2.5	2.7	16.1	0.311	6	10.0
Average		2.5	2.6	10.8	0.3000	8	10.1

The Youd et al. (2002) ground slope model was used to aid in the calibration of the measured displacement with those predicted by the FLAC modeling procedure. Both the FLAC model and Youd et al. (2002) model used a T_{15} layer thickness of 12 m to represent the liquefied zone. The calculated predominant period, before and after liquefaction, are calculated to be 0.35 s and 2.2 s, respectively, according to which, the selected seven motions are the same as those used in the Niigata Bandai site analyses. The developed motions are deconvolved by PROSHAKE for use in the FLAC modeling.

Based on the soil properties listed above, the predicted displacement from the Youd et al. (2002) model is listed in Table 7.12 and is about 2.4 m. This is in reasonable agreement with some of the larger displacements measured at this site (Figure 7.15).

The FLAC model results using residual strength ratios of 0.095, 0.085, 0.075, average of the seven modeling results and the deviation from Bartlett's model prediction are shown in Table 7.13. Details of the FLAC model results are listed in Appendix C.

Table 7.12. Prediction of lateral spread from Bartlett's equation

M	R (KM)	W	S (%)	T_{15} (m)	F_{15} (%)	$D50_{15}$ (mm)	Lateral spread (m)
7.5	21	1	0.4	12	8.3	0.3	2.37

Table 7.13 Lateral spread prediction from FLAC model for different residual strength ratio at Niigata Railway Station.

Residual strength ratio	Motion 1	Motion 2	Motion 3	Motion 4	Motion 5	Motion 6	Motion 7	Average	Deviation
0.095	1.77	2.04	1.57	1.92	1.90	2.10	1.46	1.82	2.40
0.085	2.00	2.16	1.81	2.38	2.31	2.15	1.89	2.10	0.76
0.075	2.39	2.59	2.10	2.66	3.15	2.51	2.96	2.62	1.20

Because the deviation of the model results using a residual strength ratio of 0.085 is the least of all cases modeled, 0.085 was used for the regression analyses in Chapter 8 for this case.

7.4 Niigata Showa Bridge Area

Figure 7.17 and 7.18 show the displacement pattern along the Showa Bridge. In the neighborhood of the bridge, the ground moved only on the left (i.e., north) bank with a maximum displacement of about 4 m. The liquefied layers appear to be well developed in the riverbed on this side, but not as well developed under the right (i.e., south) bank.

The permanent ground displacement near the Niigata railway is shown in Figure 7.18. Because of the influence of the river channel, the free face model of the Youd et al. (2002) model was used for this case. The soil properties from several borings are shown in Table 7.14.

The average T_{15} for larger lateral spread is 2.7 m. However, the minimum mesh size used in the FLAC model for this site is 4 m. Thus, this site was calibrated to a T_{15} layer of 4 m and this value was also used in the Youd et al. (2002) model to slightly adjust the measured displacements. With this T_{15} value and considering liquefaction, the soil column's dominant period, before and after liquefaction, are calculated to be 0.35 s and 2.1 s, respectively. Because the dominant period after liquefaction is approximately the same as that for the Niigata Bandai site, the same seven motions used for the Bandai Bridge site were used for this site.

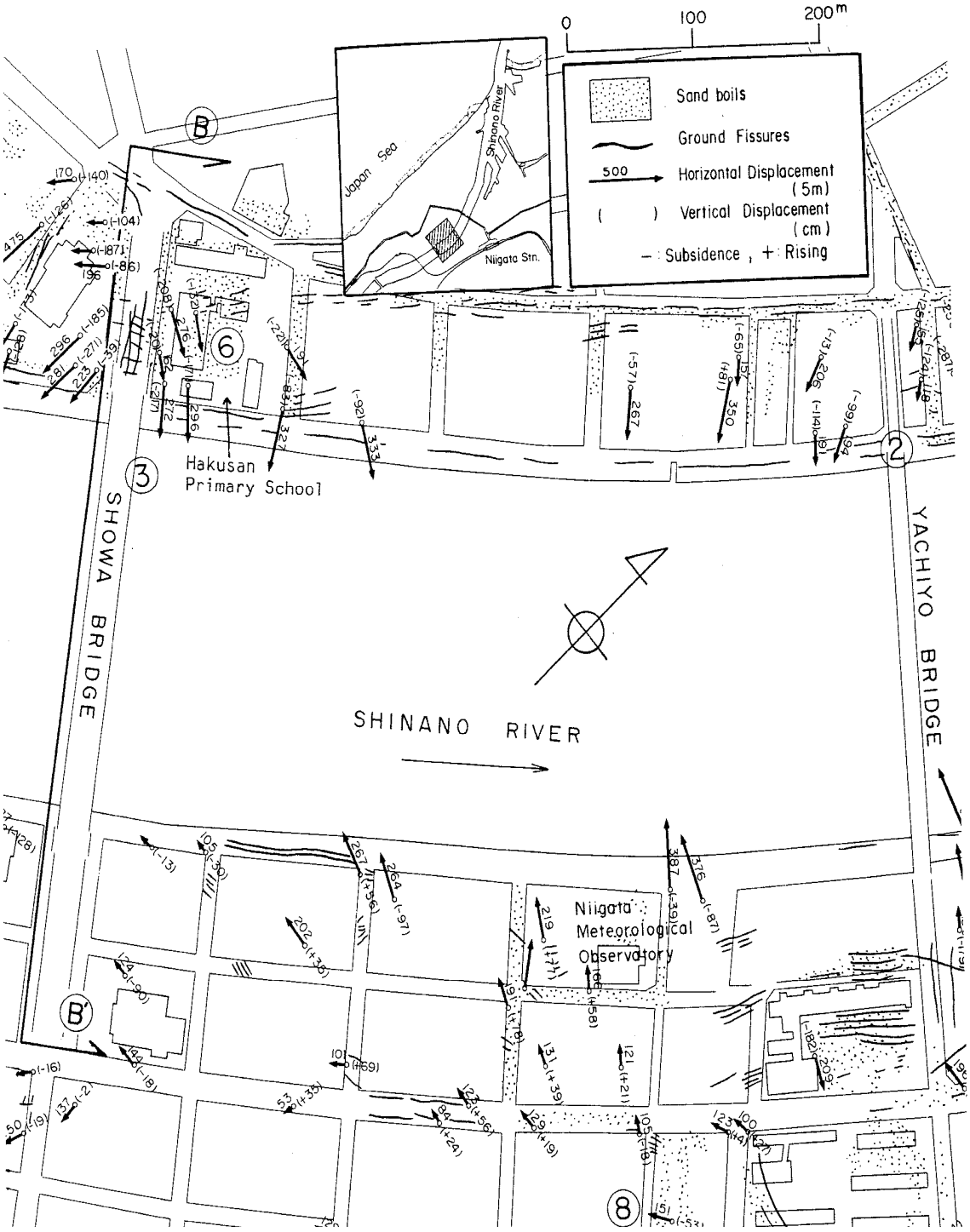


Figure 7.17. Permanent Ground Displacements at the Shinano River near the Showa Bridge (after Hamada et al., 1992).

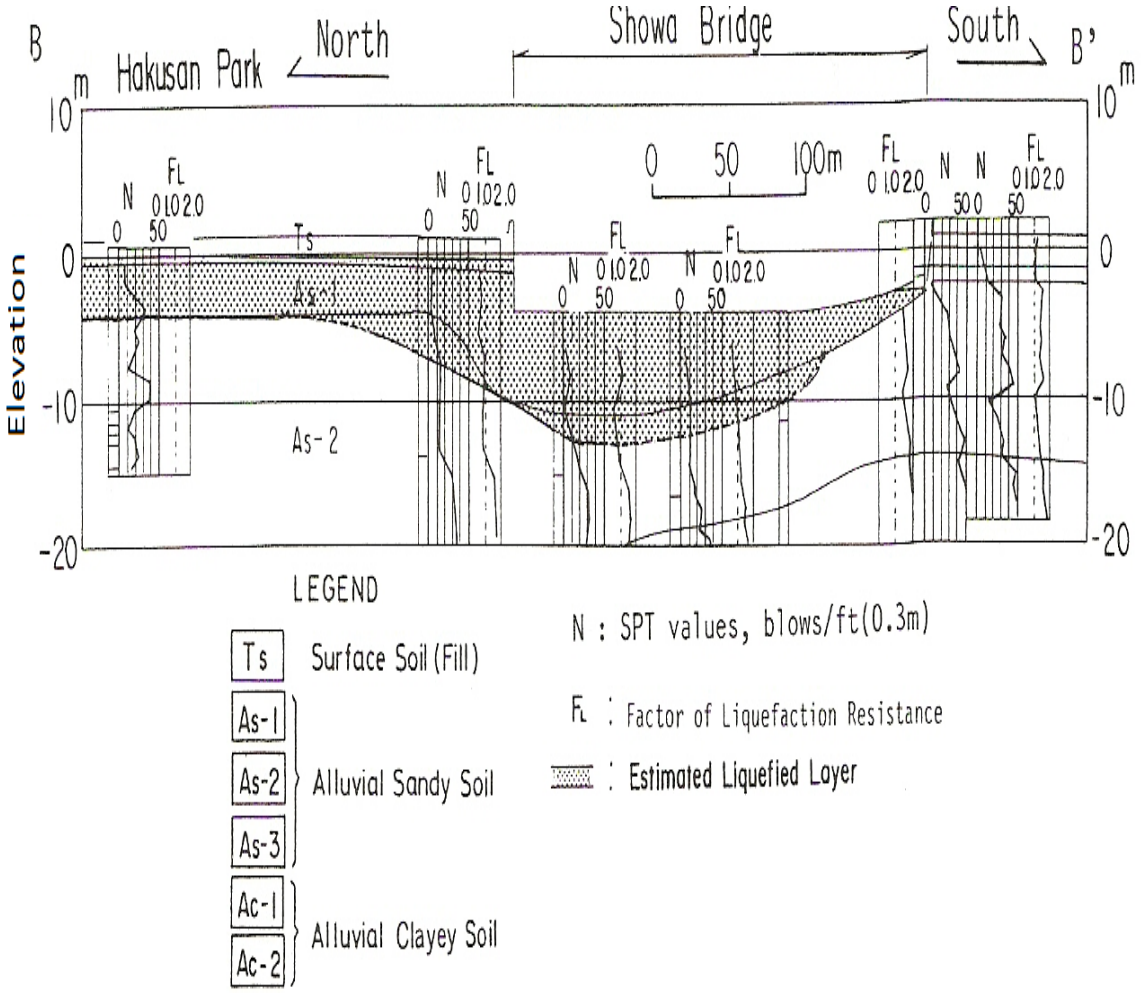


Figure 7.18. Soil properties and permanent deformation at Niigata Showa Bridge section (after Hamada et al., 1992).

Based on the soil properties listed above, the predicted displacements from the Youd et al. (2002) model are listed in Table 7.15. Because this is a free face failure, the lateral spread predictions decrease with increasing distance from the free face.

The FLAC model results with residual strength ratios of 0.08, 0.09, 0.10, and 0.12 are shown in Tables 7.16 to Table 7.19, respectively. More details concerning the FLAC model results are given in Appendix D.

Table 7.14 soil properties from several borings, Niigata Showa Bridge section

Boring location		Ground water level (m)	Depth of Liq. layer (m)	T_{15}(m)	D_{50}(mm)	F_{15}(%)	Average $(N_1)_{60}$
4	178	0.9	0.9	2.9	0.185	17	10.4
11-6	180	0.9	1.0	2.5	0.060	45	2.6
Average		0.9	0.95	2.7	0.120	31	6.5

Table 7.15. Lateral spread prediction by Youd et al. (2002) model at Niigata Showa site

M	R(KM)	W(%)	S	T_{15} (m)	F_{15} (%)	$D50_{15}$ (mm)	Distance from free face (m)	Lateral spread (m)
7.5	21	20.44	1	4	31	0.123	16	2.03
7.5	21	16.35	1	4	31	0.123	20	1.78
7.5	21	13.63	1	4	31	0.123	24	1.59
7.5	21	11.68	1	4	31	0.123	28	1.46
7.5	21	10.22	1	4	31	0.123	32	1.34
7.5	21	9.08	1	4	31	0.123	36	1.25
7.5	21	8.18	1	4	31	0.123	40	1.18
7.5	21	7.43	1	4	31	0.123	44	1.11
7.5	21	6.81	1	4	31	0.123	48	1.06
7.5	21	6.29	1	4	31	0.123	52	1.01
7.5	21	5.84	1	4	31	0.123	56	0.97
7.5	21	5.45	1	4	31	0.123	60	0.93
7.5	21	5.11	1	4	31	0.123	64	0.89
7.5	21	4.81	1	4	31	0.123	68	0.86

Table 7.16. Lateral spread prediction from FLAC model for residual strength ratio of 0.08 at Niigata Showa section

Distance from free face (m)	Motion 1	Motion 2	Motion 3	Motion 4	Motion 5	Motion 6	Motion 7	Average	Deviation
16	2.73	3.62	3.25	2.87	3.19	3.24	3.12	3.15	9.26
20	1.98	2.73	2.44	2.07	2.31	2.36	2.29	2.31	2.37
24	1.37	1.99	1.76	1.53	1.69	1.90	1.91	1.74	0.44
28	0.88	1.50	1.28	1.14	1.27	1.49	1.50	1.29	0.50
32	0.53	1.17	1.00	0.96	0.99	1.17	1.15	1.00	1.16
36	0.31	0.95	0.82	0.81	0.76	1.00	1.00	0.81	1.74
40	0.15	0.77	0.68	0.70	0.58	0.86	0.85	0.66	2.27
44	0.14	0.67	0.58	0.61	0.44	0.79	0.76	0.57	2.37
48	0.14	0.56	0.51	0.52	0.29	0.71	0.67	0.49	2.54
52	0.14	0.46	0.44	0.46	0.17	0.66	0.61	0.42	2.66
56	0.14	0.38	0.37	0.42	0.10	0.58	0.56	0.36	2.74
60	0.14	0.34	0.32	0.38	0.10	0.54	0.51	0.33	2.64
64	0.14	0.30	0.29	0.37	0.10	0.49	0.46	0.31	2.53
68	0.14	0.30	0.29	0.37	0.10	0.49	0.46	0.31	2.28

Table 7.17. Lateral spread prediction from FLAC model for residual strength ratio of 0.09 at Niigata Showa section

Distance from free face (m)	Motion_1	Motion_2	Motion_3	Motion_4	Motion_5	Motion_6	Motion_7	Average	Deviation
16	2.59	2.57	2.71	2.57	2.88	3.11	3.12	2.79	4.47
20	1.8	2.24	1.92	1.86	2.02	2.27	2.28	2.06	0.80
24	1.39	1.60	1.50	1.43	1.47	1.67	1.67	1.53	0.10
28	1.10	1.22	1.03	1.13	1.12	1.30	1.27	1.17	0.64
32	0.82	0.99	0.86	0.95	0.88	1.10	1.04	0.95	1.16
36	0.67	0.82	0.72	0.82	0.69	0.89	0.88	0.78	1.59
40	0.58	0.71	0.59	0.71	0.56	0.75	0.75	0.66	1.89
44	0.47	0.63	0.51	0.63	0.46	0.67	0.67	0.58	2.07
48	0.38	0.56	0.46	0.58	0.35	0.59	0.58	0.50	2.24
52	0.29	0.51	0.41	0.53	0.26	0.51	0.51	0.43	2.41
56	0.19	0.45	0.37	0.48	0.18	0.48	0.47	0.37	2.56
60	0.13	0.41	0.32	0.44	0.12	0.43	0.44	0.33	2.64
64	0.10	0.37	0.29	0.41	0.10	0.39	0.40	0.29	2.62
68	0.10	0.31	0.24	0.38	0.10	0.37	0.37	0.27	2.56

Table 7.18. Lateral spread prediction from FLAC model for residual strength ratio of 0.10 at Niigata Showa section

Distance from free face (m)	Motion 1	Motion 2	Motion 3	Motion 4	Motion 5	Motion 6	Motion 7	Average	Deviation
16	2.4	2.71	2.62	2.12	2.22	2.81	2.46	2.48	1.81
20	1.61	1.86	1.77	1.47	1.57	2.01	1.7	1.71	0.23
24	1.10	1.35	1.28	1.19	1.18	1.45	1.32	1.27	0.83
28	0.74	1.04	0.97	0.96	0.87	1.13	1.03	0.96	1.79
32	0.52	0.89	0.79	0.81	0.70	0.91	0.87	0.78	2.31
36	0.36	0.72	0.67	0.70	0.57	0.81	0.75	0.65	2.65
40	0.23	0.63	0.56	0.60	0.46	0.70	0.65	0.55	2.94
44	0.15	0.53	0.48	0.53	0.37	0.62	0.61	0.47	3.06
48	0.14	0.45	0.41	0.49	0.27	0.57	0.54	0.41	3.08
52	0.14	0.41	0.35	0.43	0.20	0.52	0.49	0.36	3.04
56	0.09	0.35	0.29	0.39	0.14	0.47	0.44	0.31	3.14
60	0.08	0.33	0.25	0.36	0.11	0.43	0.41	0.28	3.03
64	0.08	0.28	0.23	0.34	0.08	0.39	0.36	0.25	2.97
68	0.08	0.22	0.21	0.31	0.06	0.34	0.32	0.22	2.95

Table 7.19. Lateral spread prediction from FLAC model for residual strength ratio of 0.12 at Niigata Showa section

Distance from free face (m)	Motion 1	Motion 2	Motion 3	Motion 4	Motion 5	Motion 6	Motion 7	Average	Deviation
16	1.73	2.31	1.95	2.22	2.2	2.44	1.91	1.78	0.35
20	1.18	1.51	1.29	1.37	1.46	1.68	1.32	1.19	1.07
24	0.88	1.12	1.00	1.02	1.09	1.23	1.07	0.90	1.85
28	0.71	0.87	0.77	0.8	0.83	0.98	0.86	0.71	2.42
32	0.59	0.75	0.64	0.68	0.70	0.79	0.74	0.59	2.60
36	0.49	0.65	0.54	0.59	0.56	0.67	0.65	0.50	2.72
40	0.43	0.57	0.46	0.51	0.47	0.59	0.55	0.43	2.76
44	0.37	0.51	0.40	0.46	0.40	0.52	0.50	0.38	2.73
48	0.30	0.45	0.35	0.42	0.34	0.47	0.46	0.33	2.70
52	0.26	0.39	0.31	0.37	0.30	0.42	0.42	0.30	2.65
56	0.12	0.35	0.28	0.35	0.27	0.37	0.40	0.26	2.72
60	0.12	0.32	0.24	0.32	0.24	0.34	0.37	0.23	2.62
64	0.08	0.30	0.21	0.29	0.21	0.30	0.34	0.20	2.61
68	0.05	0.26	0.19	0.26	0.19	0.26	0.30	0.18	2.59

For the case with residual strength ratio of 0.12, the sum of deviation is 33.2.

For the case with residual strength ratio of 0.08, the sum of deviation is 26.3. For the case with residual strength ratio of 0.09, the sum of deviation is 22.5. For the case with residual strength ratio of 0.10, the sum of deviation is 31.8. For the case with residual strength ratio of 0.12, the sum of deviation is 33.2.

The lateral spread comparison between the Youd et al. (2002) model and the FLAC model is shown in Figure 7.19.

Because the total deviation for the residual strength ratio of 0.09 is the least in all the cases modeled, 0.09 is the residual strength ratio for which the Youd et al. (2002) model and the FLAC model give the prediction with the least error. The residual strength ratio of 0.09 for the Niigata Showa section will be used later for further statistical analysis.

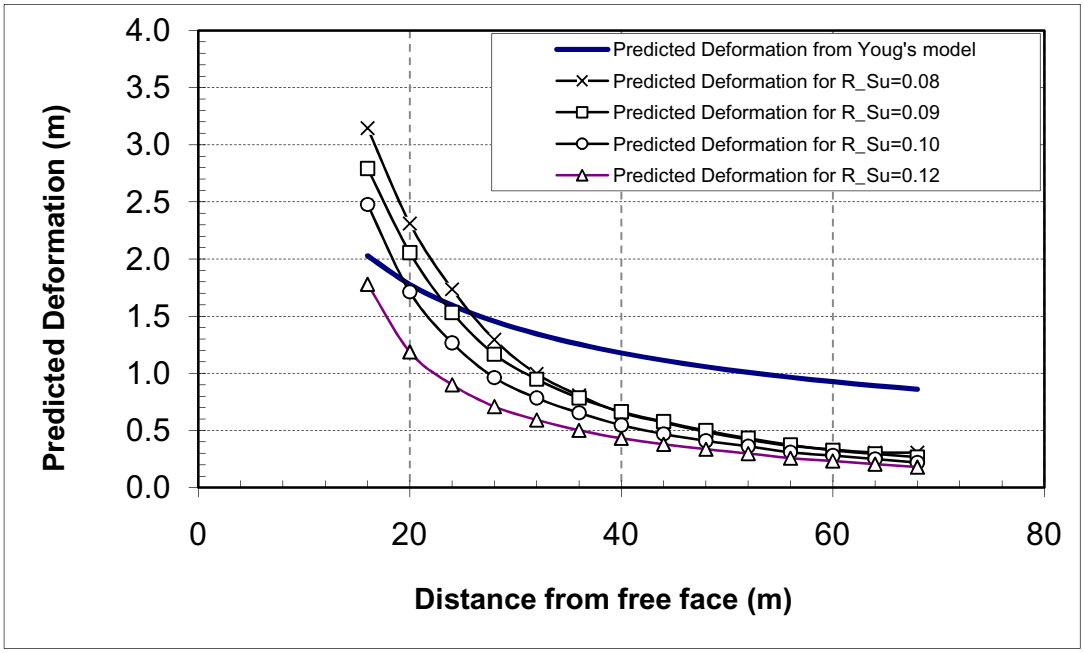


Figure 7.19. Prediction comparison between Youd et al. (2002) model and FLAC model for the Niigata Showa section.

7.5 Noshiro Site N-4 Section

The 1983 M7.7 Nihonkai-Chubu, Japan earthquake occurred in the Japan Sea about 90 km west of the Aomori Prefecture on May 26, 1983 causing severe damage to the coastal areas of the Tohoku region. In particular, liquefaction resulted in severe damage to houses, buildings, and lifeline facilities in cities such as Noshiro and Akita along the Japan Sea.

The epicenter of the main shock was located on the bed of the Japan Sea, 100 km from the main island of Japan, as shown in Figure 7.20 (Hamada et al., 1992). Area of permanent ground displacement was subdivided into the following sections as shown in Figure 7.21.

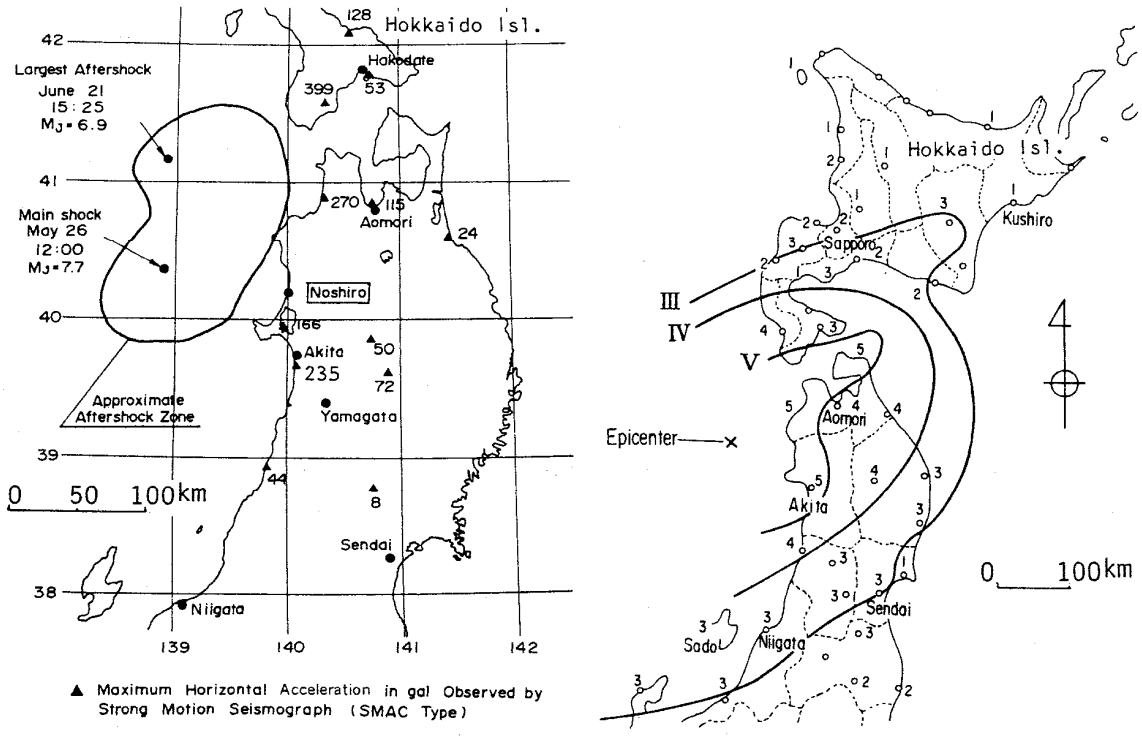


Figure 7.20. Epicenter, Fault Zone and Seismic Intensity of Noshiro case (after Hamada et al., 1992).

Along section N-4 of Zone II, the maximum ground displacement occurred halfway up the slope at the location where the liquefied layer is relatively thick and the ground surface gradient increases abruptly. The displacement vectors are shown in Figure 7.22.

Soil profiles along the N-4 cross section are shown in Figure 7.23. The Youd et al. (2002) model for ground slope conditions was used to calibrate the FLAC model for this location. The thickness of the liquefied layer increases from about 1 to 5 m. The surface gradient in the northern area of the city, which is about 1%, is much less than that in the southern area. Table 7.20 gives the soil properties from the available borings.

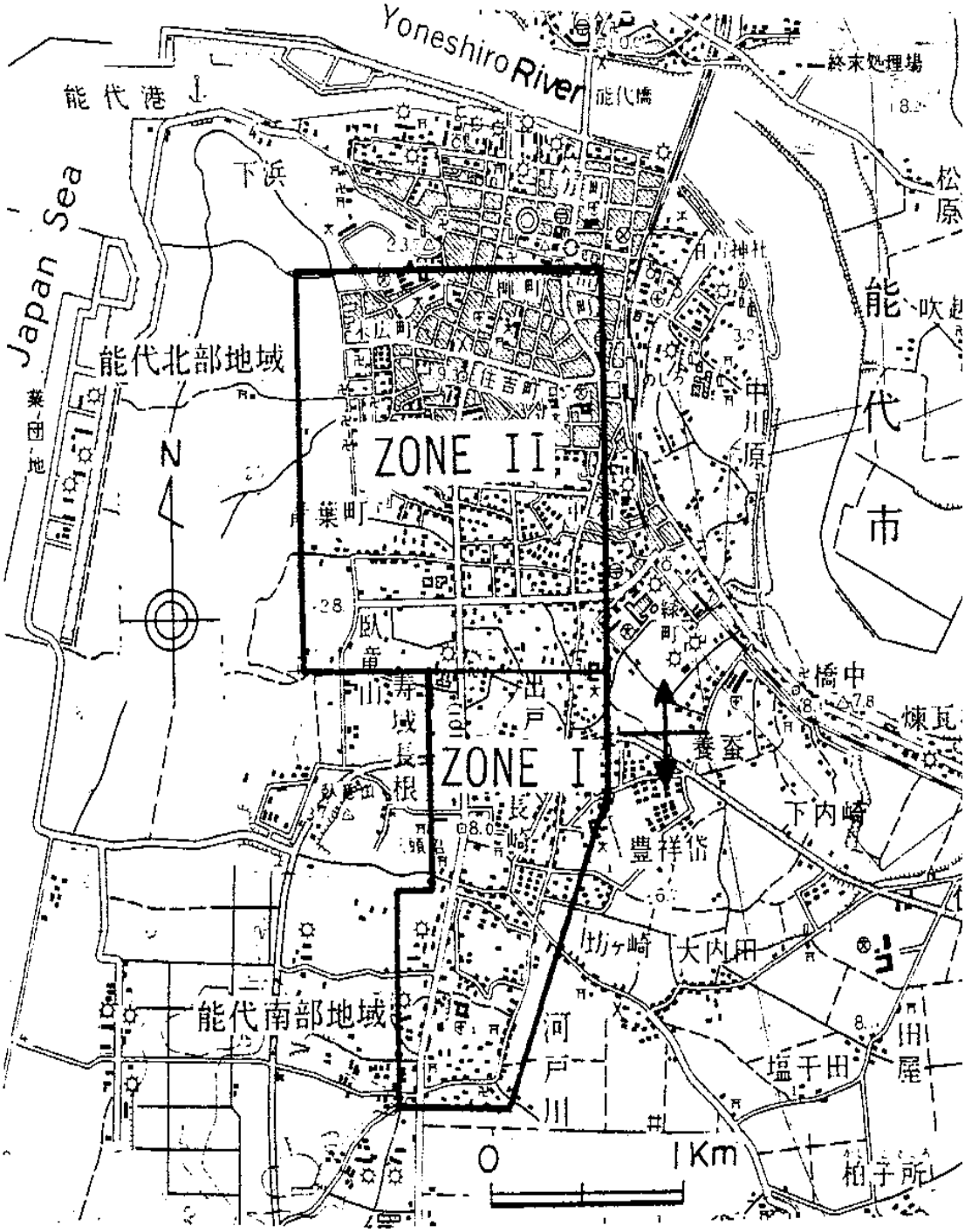


Figure 7.21. Southern and Northern area of Noshiro, Japan (1) Zone I: Southern area of Noshiro City; (2) Zone II: Northern area of Noshiro City (after Hamada et al., 1992).



Figure 7.22. Northern area of Noshiro case (after Hamada et al., 1992).

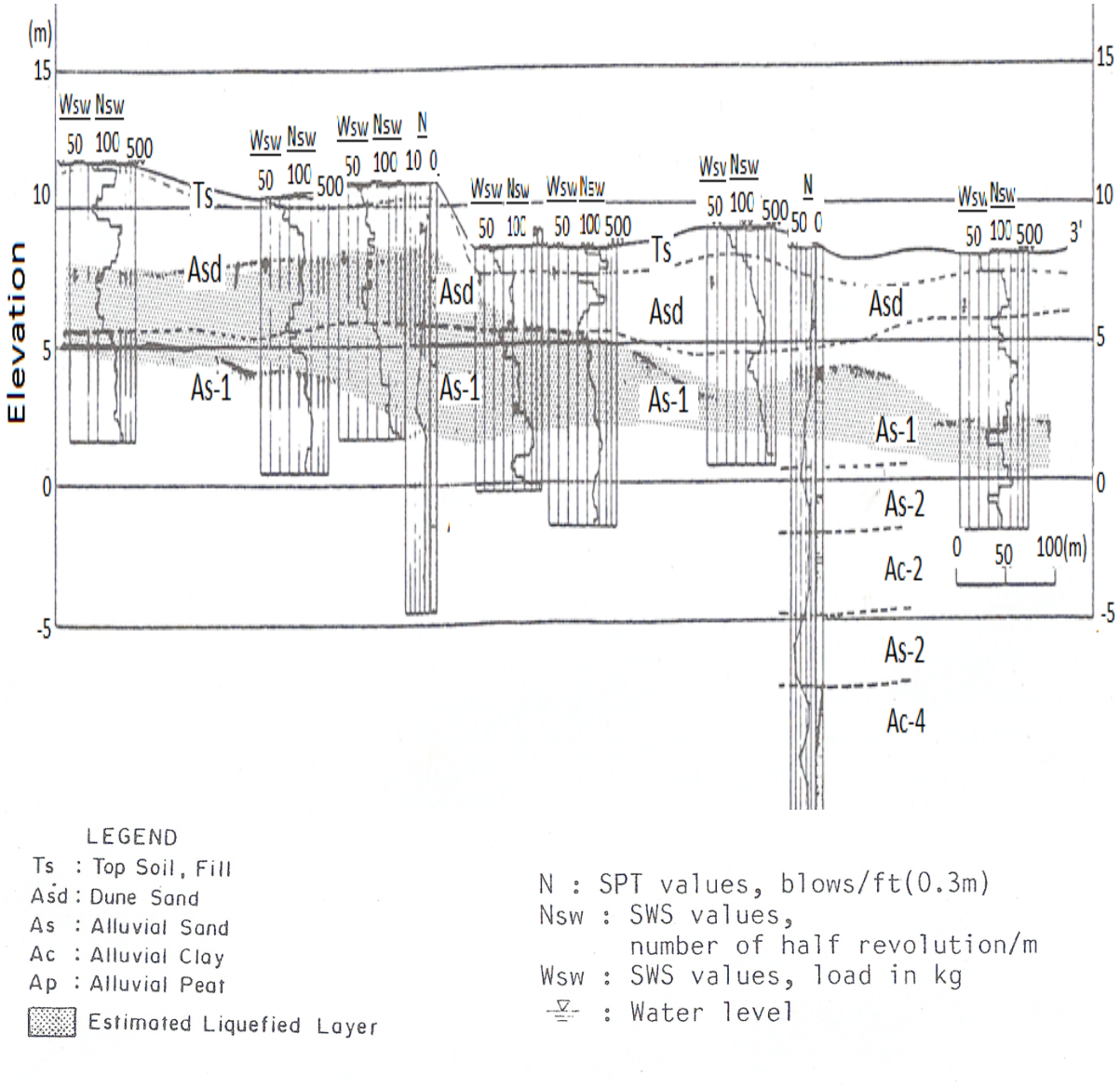


Figure 7.23. Soil profiles of Noshiro N-4 case (after Hamada et al., 1992).

Table 7.20. Soil properties from the available borings at Noshiro site N-4 section

Boring location	Ground water level (m)	Depth of Liq. layer (m)	T_{15}(m)	D_{50}(mm)	F_{15}(%)	Average $(N_1)_{60}$
1L	2.9	5.1	4.6	0.350	4	10.5
2L	2.9	3.0	9.3	0.350	0	7.9
3L	1.3	1.4	5.9	0.350	0	13.4
4L	1.4	1.5	3.0	0.350	0	13.4
5L	2.9	3.0	5.5	0.350	5	14.0
AVERAGE	2.3	2.8	5.7	0.350	2	11.8

A T_{15} layer thickness of 4 m is used in the models to approximately represent the actual layer thickness. Based on this thickness, the predominant postliquefaction soil period was calculated as 0.83 s. Using this estimate, the seven-selected motions from the 30 generated motions were selected. The response spectra of the seven time histories generated for the FLAC model are shown in Figure 7.24.

These acceleration time histories corresponding to these response spectra are shown from Figure 7.25 to Figure 7.31.

PROSHAKE was used to deconvolute the selected seven motions to the model bottom considered as outcrop motion. The developed motions for the FLAC input at the model bottom were taken as one-half of the output motion from the base of the Proshake model and converted to a FLAC compatible file format. The developed FLAC model, input motions and FLAC modeling results are given in Appendix E.

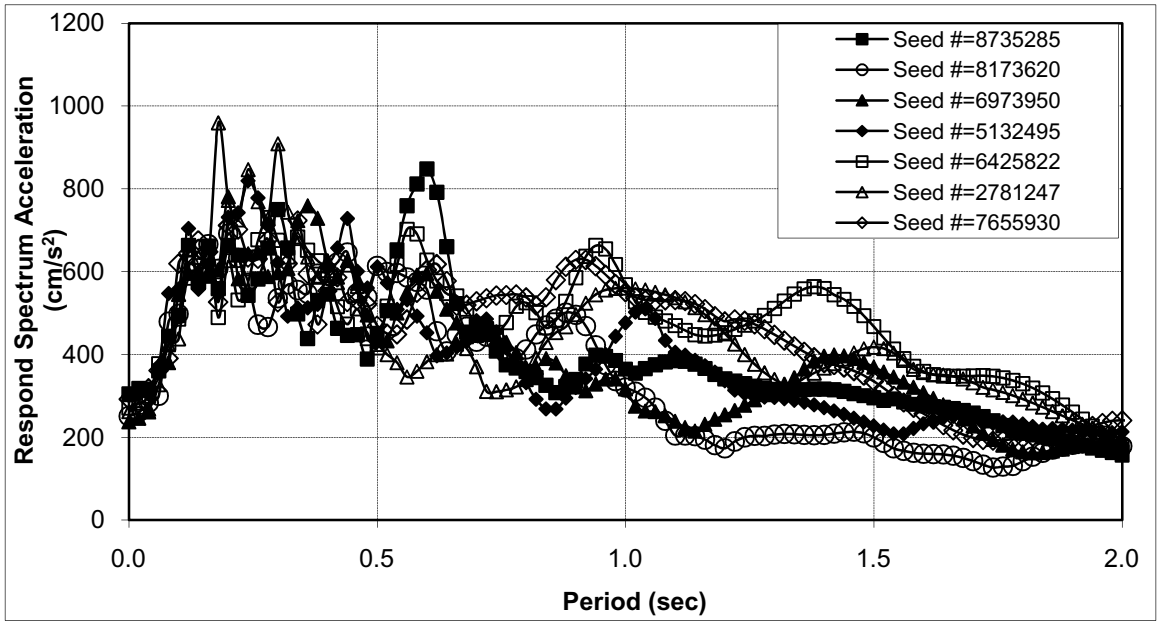


Figure 7.24. Response spectra of seven time histories generated from SMGS for Noshiro N-4 section

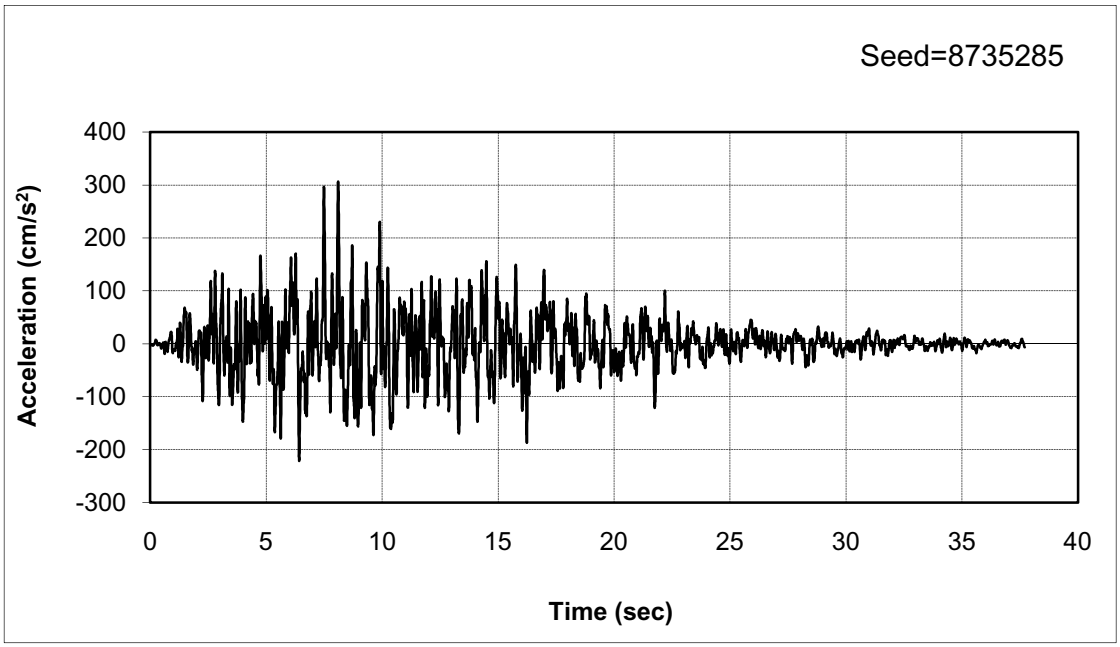


Figure 7.25. Noshiro N-4 section model selected motion 1

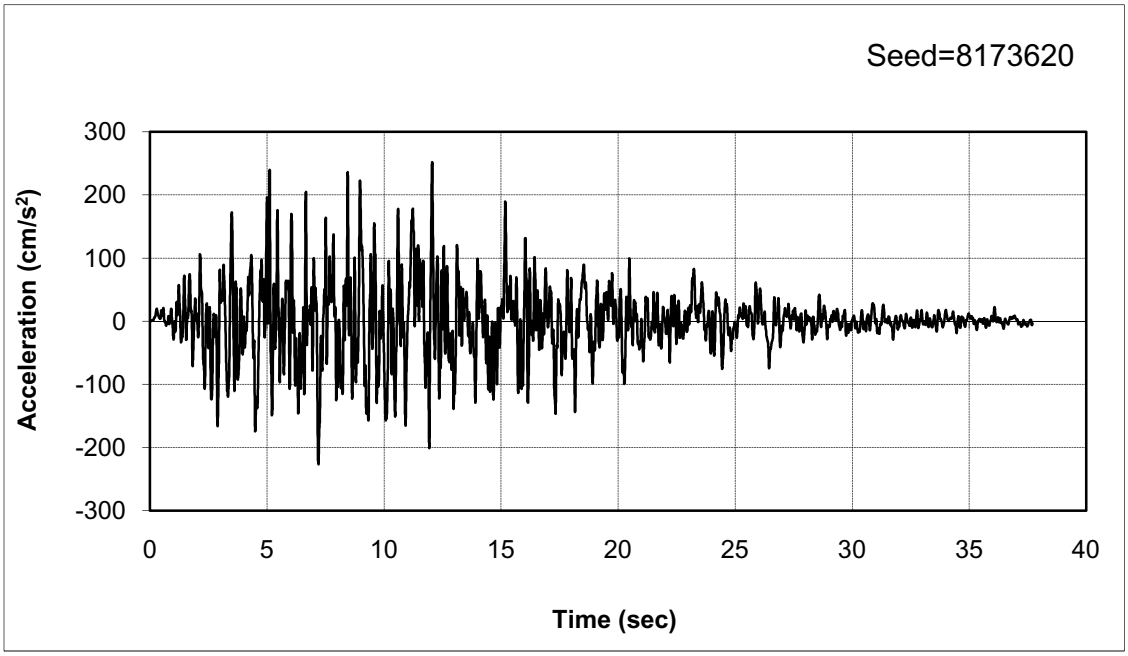


Figure 7.26. Noshiro N-4 section model selected motion 2

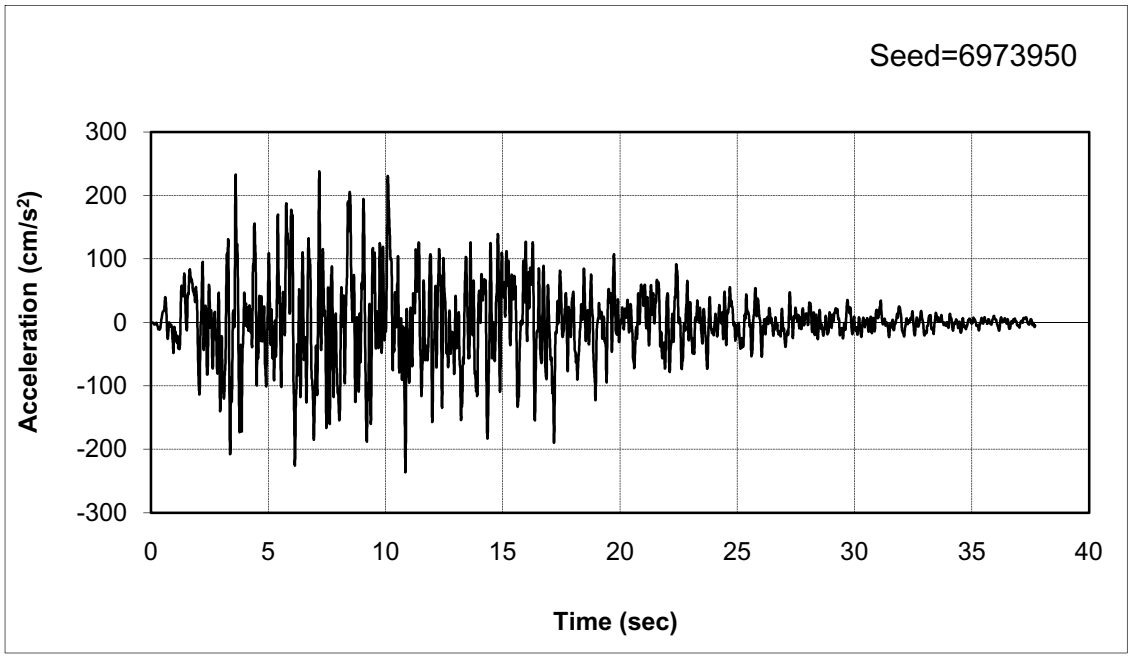


Figure 7.27. Noshiro N-4 section model selected motion 3

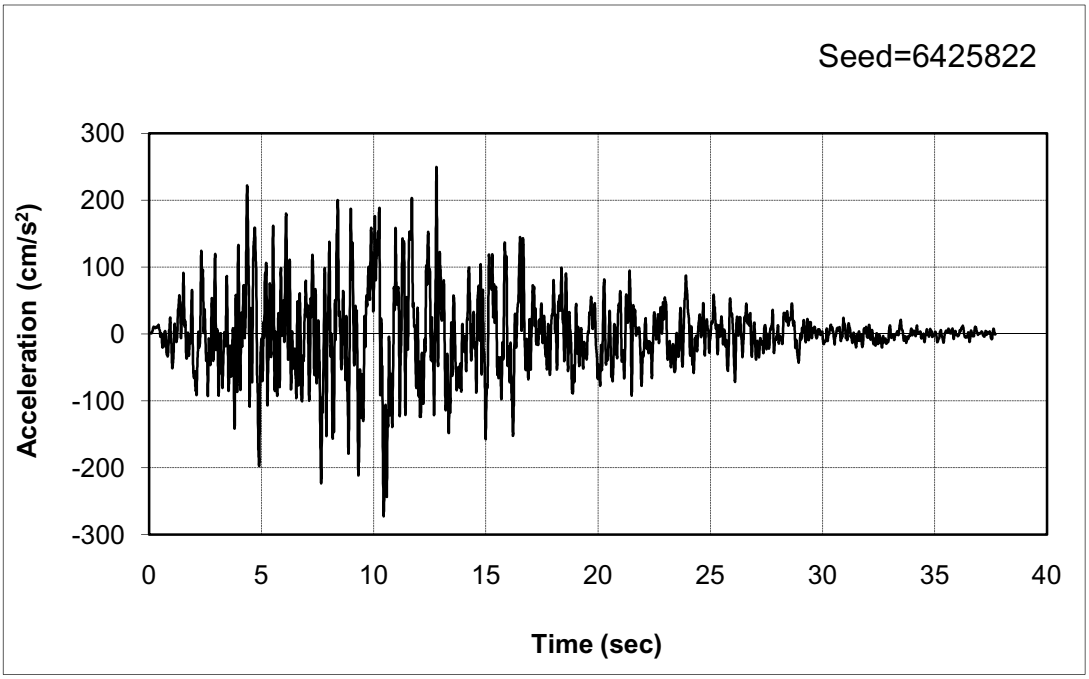


Figure 7.28. Noshiro N-4 section model selected motion 4

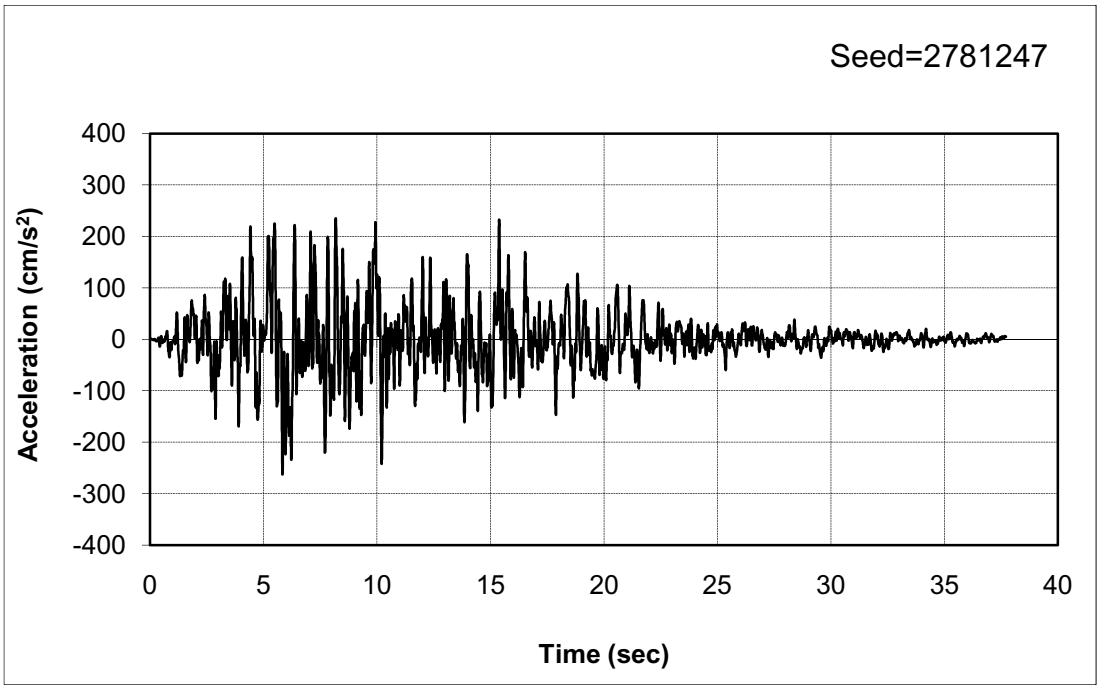


Figure 7.29. Noshiro N-4 section model selected motion 5

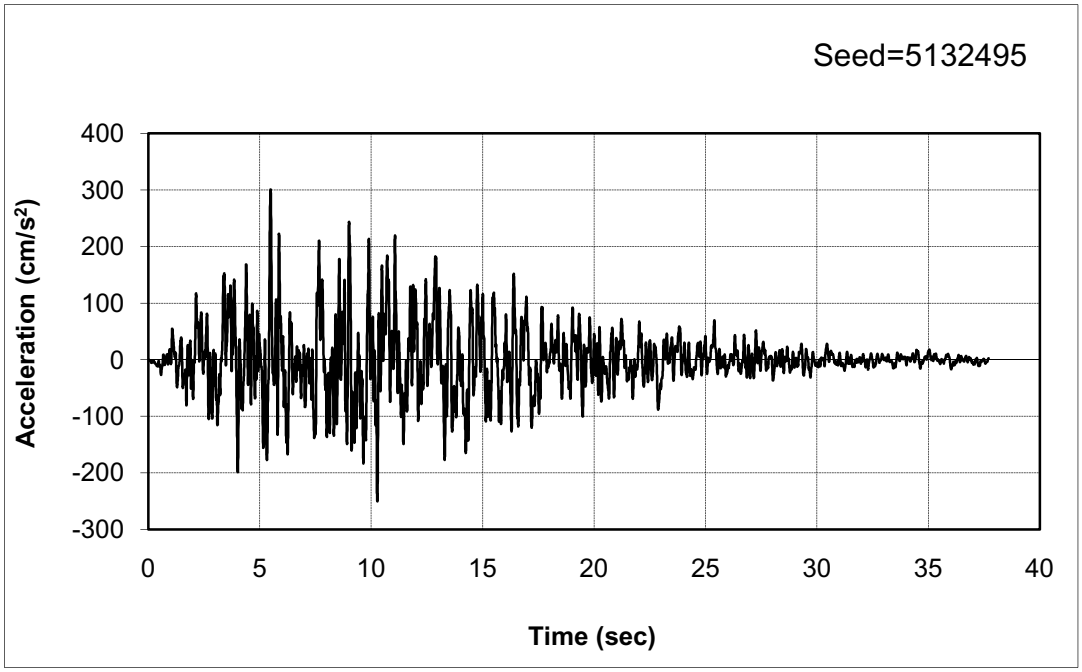


Figure 7.30. Noshiro N-4 section model selected motion 6

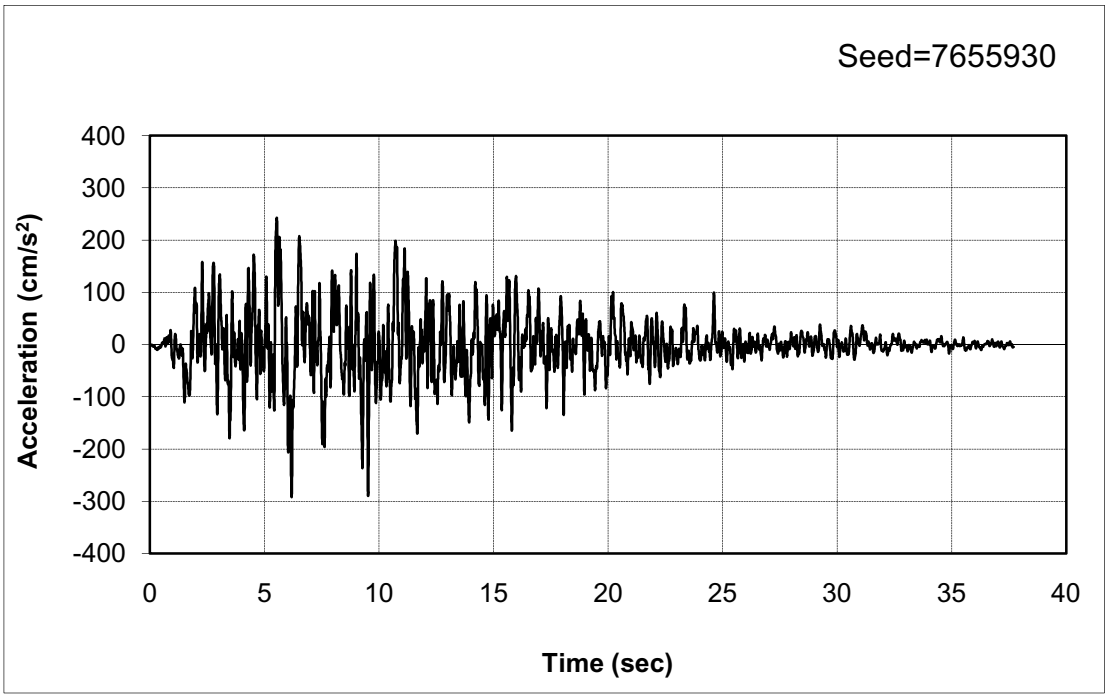


Figure 7.31. Noshiro N-4 section model selected motion 7

As shown in Figures 7.22 and 7.23, the influence of the topography immediately above and below the steepest part of the slope is important. This is taken into account in the Youd et al. (2002) model, as explained by Bartlett (1991). The actual topography and its variation are considered in the 1000 meter-length FLAC model. Thus, the prediction from the Youd et al. (2002) model shows that the lateral spread displacements vary at different points along the ground surface with changing slope, as shown in the Table 7.19.

The FLAC model results with residual strength ratio of 0.04, 0.03, 0.02, average of the seven modeling results and the deviations from the Youd et al. (2002) model predictions are shown in Tables 7.21 to Table 7.24, respectively. The lateral spread comparison between the Youd et al. (2002) model and FLAC model is shown in Figure 7.32.

Table 7.21. Lateral spread prediction by Youd et al. (2002) model at Norshiro site N-4 section

M	R(KM)	W(%)	S	T_{15} (m)	F_{15} (%)	$D50_{15}$ (mm)	Distance from reference* (m)	Lateral spread (m)
7.7	27	1	1.50	4	2	0.35	135	2.15
7.7	27	1	1.50	4	2	0.35	180	2.15
7.7	27	1	1.50	4	2	0.35	200	2.15
7.7	27	1	1.50	4	2	0.35	240	2.15
7.7	27	1	1.50	4	2	0.35	270	2.15
7.7	27	1	0.91	4	2	0.35	300	1.82
7.7	27	1	0.70	4	2	0.35	350	1.66
7.7	27	1	1.69	4	2	0.35	400	2.24
7.7	27	1	4.50	4	2	0.35	450	3.12
7.7	27	1	4.50	4	2	0.35	490	3.12
7.7	27	1	2.57	4	2	0.35	520	2.58
7.7	27	1	1.64	4	2	0.35	560	2.22
7.7	27	1	1.20	4	2	0.35	600	1.99
7.7	27	1	0.13	4	2	0.35	710	0.93
7.7	27	1	0.31	4	2	0.35	800	1.27
7.7	27	1	0.63	4	2	0.35	842	1.60
7.7	27	1	0.63	4	2	0.35	862	1.60
7.7	27	1	0.63	4	2	0.35	882	1.60
7.7	27	1	0.43	4	2	0.35	900	1.41

* The distance is measured from the reference location, which is the left side of the corresponding FLAC model, also the left side of Figure 7.24.

Table 7.22. Lateral spread prediction by FLAC model for residual strength ratio of 0.04

Distance from reference location (m)	Motion_1	Motion_2	Motion_3	Motion_4	Motion_5	Motion_6	Motion_7	Average	Deviation
180	1.75	1.33	1.33	1.55	1.38	1.48	1.2	1.43	3.82
200	1.65	1.3	1.25	1.55	1.38	1.46	1.19	1.40	4.14
240	1.62	1.22	1.1	1.43	1.31	1.34	1.14	1.31	5.16
270	1	0.75	0.75	0.87	0.78	0.87	0.72	0.82	12.46
300	0.83	0.55	0.59	0.66	0.6	0.62	0.55	0.63	9.93
350	0.76	0.51	0.54	0.66	0.53	0.61	0.54	0.59	8.03
400	0.76	0.51	0.54	0.65	0.53	0.61	0.54	0.59	19.05
450	2.3	2.56	2	2.07	2.42	2.39	2.42	2.31	4.84
490	2.3	2.55	1.97	2.05	2.37	2.34	2.39	2.28	5.15
520	2.94	2.13	1.71	1.84	2.02	1.97	2.06	2.10	2.60
560	1.53	1.6	1.42	1.49	1.53	1.47	1.53	1.51	3.50
600	1.17	1.13	1.1	1.21	1.12	1.02	1.03	1.11	5.49
710	1.1	1.04	1.02	1.14	1.03	0.97	0.94	1.03	0.11
800	0.98	0.92	0.91	1.02	0.96	0.88	0.84	0.93	0.81
842	0.96	0.9	0.86	1	0.89	0.86	0.82	0.90	3.47
862	0.94	0.89	0.85	0.97	0.88	0.83	0.8	0.88	3.65
882	0.94	0.87	0.82	0.97	0.84	0.82	0.75	0.86	3.88
900	0.93	0.71	0.67	0.82	0.81	0.71	0.71	0.77	2.97

Table 7.23. Lateral spread prediction by FLAC model for residual strength ratio of 0.03

Distance from reference location (m)	Motion_1	Motion_2	Motion_3	Motion_4	Motion_5	Motion_6	Motion_7	Average	Deviation
135	1.37	1.48	1.5	1.65	1.47	1.56	1.32	1.48	3.24
180	1.37	1.47	1.5	1.64	1.47	1.52	1.28	1.46	3.38
200	1.37	1.47	1.49	1.64	1.47	1.5	1.27	1.46	3.44
240	1.28	1.37	1.42	1.54	1.41	1.38	1.21	1.37	4.31
270	0.77	0.84	0.87	0.94	0.84	0.92	0.79	0.85	11.82
300	0.65	0.64	0.71	0.74	0.65	0.71	0.62	0.67	9.14
350	0.61	0.63	0.69	0.74	0.57	0.63	0.57	0.63	7.40
400	0.61	0.63	0.68	2.54	3	2.96	3.04	1.92	9.50
450	2.64	3	3.2	2.51	2.97	2.88	2.97	2.88	0.72
490	2.56	2.96	3.14	2.19	2.51	2.46	2.55	2.62	2.32
520	2.28	2.51	2.76	1.72	1.99	1.97	2.05	2.18	1.87
560	1.73	2.04	2.35	1.23	1.33	1.36	1.37	1.63	3.48
600	1.23	1.34	1.66	1.15	1.2	1.27	1.24	1.30	3.57
710	1.14	1.21	1.46	1.07	1.08	1.17	1.06	1.17	0.52
800	1.01	1.07	1.24	1.07	1.04	1.14	1.01	1.08	0.28
842	0.96	1.07	1.15	1.02	1.01	1.12	1.01	1.05	2.16
862	0.91	1.01	1.13	1.02	0.97	1.1	0.99	1.02	2.40
882	0.79	0.84	1.06	0.87	0.81	0.95	0.84	0.88	3.68

Table 7.24. Lateral spread prediction by FLAC model for residual strength ratio of 0.02

Distance from reference location (m)	Motion_1	Motion_2	Motion_3	Motion_4	Motion_5	Motion_6	Motion_7	Average	Deviation
135	1.63	1.81	1.62	1.66	1.74	1.63	1.71	1.69	1.55
180	1.63	1.8	1.61	1.66	1.74	1.59	1.68	1.67	1.63
200	1.62	1.79	1.61	1.66	1.74	1.58	1.65	1.66	1.69
240	1.54	1.67	1.52	1.56	1.65	1.48	1.59	1.57	2.37
270	0.95	1.04	0.98	1	1.02	1.02	1.02	1.00	9.21
300	0.87	0.88	0.97	0.93	0.8	0.97	0.84	0.89	5.97
350	0.73	0.78	0.75	0.77	0.76	0.72	0.76	0.75	5.77
400	4.83	4.74	5.04	4.89	4.68	4.86	4.73	4.82	46.87
450	4.73	4.65	4.91	4.83	4.67	4.77	4.65	4.74	18.57
490	4.25	4.09	4.43	4.26	4.05	4.07	4.05	4.17	7.89
520	3.54	3.55	3.78	3.63	3.61	3.63	3.52	3.61	7.44
560	2.22	2.25	2.66	2.31	2.43	2.36	2.28	2.36	0.28
600	1.68	1.78	2.2	1.72	1.85	1.72	1.72	1.81	0.43
710	1.67	1.53	1.82	1.39	1.47	1.39	1.42	1.53	2.67
800	1.29	1.5	1.7	1.34	1.4	1.33	1.35	1.42	0.28
842	1.24	1.48	1.7	1.32	1.38	1.3	1.35	1.40	0.43
862	1.14	1.42	1.61	1.31	1.35	1.28	1.34	1.35	0.56
882	0.98	1.16	1.27	1.12	1.06	1.12	1.07	1.11	1.72

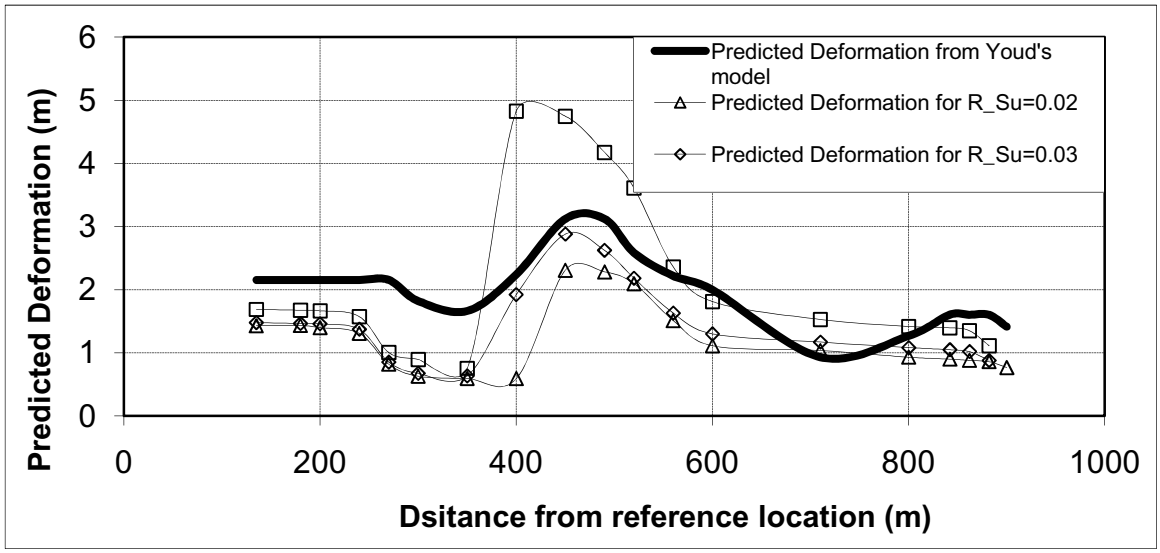


Figure 7.32. Comparison between Youd et al. (2002) model and FLAC model

For the case with residual strength ratio of 0.04, the sum of deviation is 102.9. For the case with residual strength ratio of 0.03, the sum of deviation is 73.2. For the case with residual strength ratio of 0.02, the sum of deviation is 115.3.

Because the total deviation of the model for the residual strength ratio of 0.03 is the least of all the cases modeled, this residual strength ratio will be used later for the statistical analyses performed in Chapter 8.

7.6 Noshiro Site S-7 Section

Figure 7.33 shows the displacement vectors for the Noshiro site S-7 cross section. Figure 7.34 shows the subsurface soil conditions and the estimated liquefied layer along this section line. The subsurface soil consists of sandy fill, natural levee, sand dune, alluvial sand and alluvial clay. Generally speaking, the magnitude of the permanent ground displacement is larger where the surface gradient is large and/or the liquefied soil layer is thick.

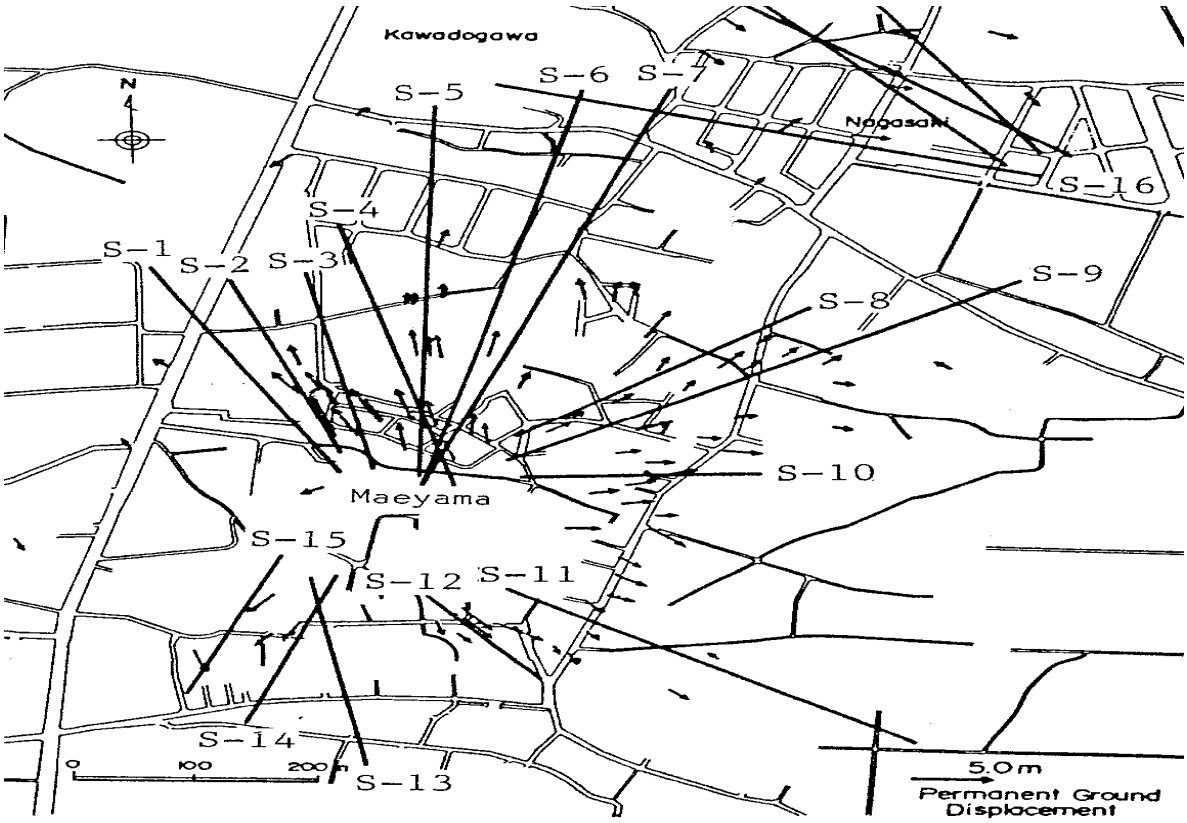


Figure 7.33. Displacement vector of Noshiro site S-7 section (after Hamada et al., 1992).

The gradient of the ground surface and the thickness of the liquefied layer are important factors affecting the magnitude of the displacement.

Because the S-7 section is very near to the N-4 section, and a detailed examination of the soil profile shows that both of the two sections have similar soil properties, the same time histories developed for the N-4 sections were used for the analysis of the S-7 section. The soil properties used for the analysis are shown in Table 7.25. The prediction from the Youd et al. (2002) model, considering the topographical variation along the section, is shown in Table 7.26.

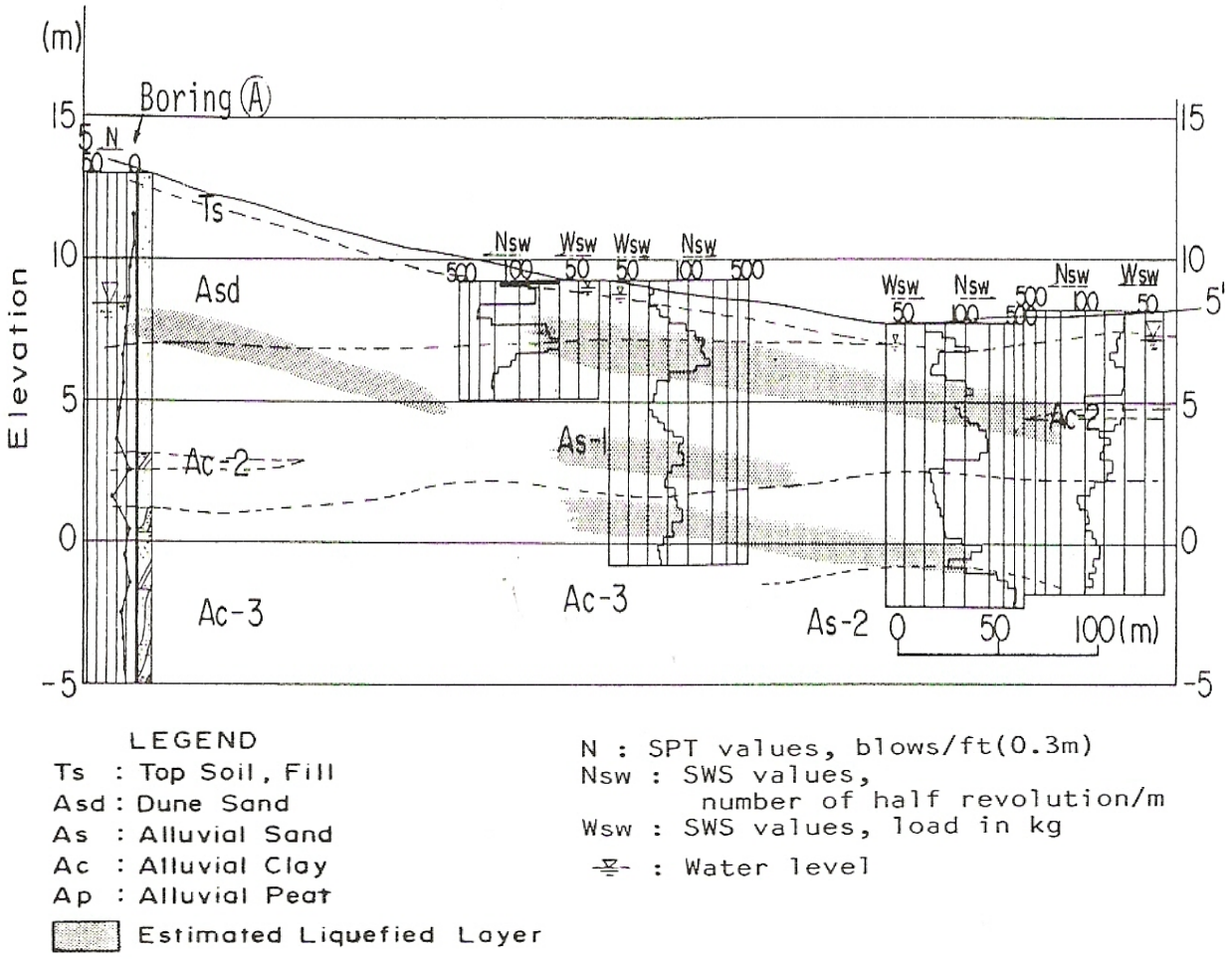


Figure 7.34. Subsurface soil condition and the estimated liquefied layer at Noshiro site S-7 section (after Hamada et al., 1992).

Table 7.25. Soil properties at Noshiro site S-7 section

Boring location	Ground water level (m)	Depth of Liq. layer (m)	T_{15}(m)	D_{50}(mm)	F_{15}(%)	Average $(N_1)_{60}$
1L	4.4	4.5	5.8	0.350	3	12.2
2L	2.0	2.1	5.4	0.350	4	5.7
3L	0.7	0.9	2.3	0.350	4	5.2
4L	0.7	0.8	3.6	0.350	4	7.9
5L	0.6	0.7	6.2	0.350	4	6.9
AVERAGE	1.7	1.8	4.7	0.350	4	7.6

Table 7.26. Prediction lateral spread from Bartlett's equation

M	R(KM)	W(%)	S	T_{15} (m)	F_{15} (%)	$D50_{15}$ (mm)	Distance from reference* (m)	Lateral spread (m)
7.7	27	1	6.00	4	4	0.35	140	3.87
7.7	27	1	5.00	4	4	0.35	150	3.64
7.7	27	1	3.75	4	4	0.35	170	3.30
7.7	27	1	3.33	4	4	0.35	180	3.17
7.7	27	1	2.73	4	4	0.35	190	2.96
7.7	27	1	1.88	4	4	0.35	300	2.61
7.7	27	1	2.00	4	4	0.35	440	2.67
7.7	27	1	1.96	4	4	0.35	470	2.65
7.7	27	1	1.32	4	4	0.35	520	2.32
7.7	27	1	1.14	4	4	0.35	570	2.20
7.7	27	1	1.00	4	4	0.35	600	2.11
7.7	27	1	0.94	4	4	0.35	620	2.07
7.7	27	1	0.89	4	4	0.35	640	2.03
7.7	27	1	0.86	4	4	0.35	680	2.01

* The distance is measured from the reference location, which is the left side of the corresponding FLAC model, also the left side of Figure 7.34.

Deconvolution of the candidate time histories followed the procedures previously described and are listed in Appendix F.

The FLAC model results for residual strength ratio of 0.04, 0.03, 0.02, average of the seven modeling results and the deviation from the Youd et al. (2002) model predictions are shown in Table 7.27 to Table 7.29, respectively. Details of FLAC model results are given in Appendix F.

For the case with residual strength ratio of 0.04, the sum of deviation is 60.8. For the case with residual strength ratio of 0.03, the sum of deviation is 29.5. For the case with residual strength ratio of 0.02, the sum of deviation is 3917.2.

The lateral spread comparison between the Youd et al. (2002) model and FLAC model is shown in Figure 7.35.

Table 7.27. Lateral spread calculation from FLAC model for residual strength ratio of 0.04

Distance from reference (m)	Motion_1	Motion_2	Motion_3	Motion_4	Motion_5	Motion_6	Motion_7	Average	Deviation
140	2.41	2.96	2.59	2.42	2.33	2.52	2.64	2.55	12.35
150	2.41	2.96	2.59	2.41	2.33	2.52	2.64	2.55	8.50
170	2.37	2.94	2.59	2.41	2.33	2.5	2.6	2.53	4.35
180	2.33	2.92	2.55	2.39	2.33	2.49	2.6	2.52	3.26
190	2.31	2.91	2.55	2.27	2.22	2.48	2.56	2.47	2.02
300	2.31	2.86	2.29	2.21	2.22	2.4	2.52	2.40	0.62
440	2.28	2.62	2.29	2.18	2.22	2.29	2.45	2.33	0.92
470	1.81	2.6	2.19	2.17	2.18	2.27	2.45	2.24	1.56
520	1.43	2.59	1.76	1.48	1.63	1.67	1.91	1.78	2.92
570	1.36	1.86	1.41	1.1	1.3	1.41	1.41	1.41	4.75
600	1.33	1.34	1.35	1.03	1.24	1.34	1.31	1.28	4.94
620	1.29	1.23	1.31	1.01	1.23	1.3	1.27	1.23	4.95
640	1.27	1.2	1.3	1.01	1.22	1.28	1.23	1.22	4.71
680	1.10	1.18	1.29	1	1.21	1.23	1.2	1.17	4.93

Table 7.28. Lateral spread calculation from FLAC model for residual strength ratio of 0.03

Distance from reference (m)	Motion_1	Motion_2	Motion_3	Motion_4	Motion_5	Motion_6	Motion_7	Average	Deviation
140	2.67	3.33	3.45	2.95	3.39	2.82	3.04	3.09	4.74
150	2.61	3.33	3.45	2.95	3.39	2.82	3.04	3.08	2.73
170	2.58	3.32	3.44	2.94	3.39	2.82	3.03	3.07	0.98
180	2.57	3.32	3.44	2.93	3.37	2.8	3.02	3.06	0.71
190	2.57	3.31	3.43	2.93	3.29	2.78	2.98	3.04	0.64
300	2.53	3.3	3.42	1.71	3.28	2.75	2.95	2.85	2.53
440	2.52	3.15	3.41	2.71	3.22	2.7	2.93	2.95	1.18
470	2.52	3.15	3.41	2.7	3.22	2.69	2.83	2.93	1.20
520	2.5	3.1	3.4	2.69	3.21	2.68	2.8	2.91	3.13
570	1.92	2.33	2.65	1.94	2.3	1.96	2.09	2.17	0.45
600	1.46	1.68	2.03	1.4	1.61	1.38	1.48	1.58	2.30
620	1.39	1.56	1.85	1.29	1.49	1.27	1.37	1.46	2.84
640	1.33	1.51	1.78	1.22	1.43	1.24	1.33	1.41	2.96
680	1.28	1.51	1.69	1.18	1.38	1.21	1.28	1.36	3.12

Table 7.29. Lateral spread calculation from FLAC model for residual strength ratio of 0.02

Distance from reference (m)	Motion_1	Motion_2	Motion_3	Motion_4	Motion_5	Motion_6	Motion_7	Average	Deviation
140	10.1	11.1	11.5	10.3	10.8	10.1	10.4	10.61	320.40
150	10.1	11.1	11.5	10.3	10.8	10	10.3	10.59	339.98
170	10	11.1	11.5	10.2	10.7	10	10.2	10.53	367.93
180	10	11.1	11.4	10.2	10.7	9.8	10.1	10.47	375.34
190	9.8	10.9	11.3	10.1	10.6	9.8	9.9	10.34	383.43
300	9.7	10.9	11.2	10	10.5	9.7	9.8	10.26	411.61
440	9.7	10.9	11.2	9.9	10.4	9.7	9.8	10.23	402.46
470	9.7	10.9	11.2	9.9	10.3	9.8	9.8	10.23	404.05
520	9.7	10.9	11.2	9.9	10.3	9.7	9.8	10.21	438.98
570	7.96	8.72	9.14	8.22	8.56	7.885	8.13	8.37	267.71
600	5.69	6.46	7	5.95	6.33	5.68	5.94	6.15	115.60
620	4.47	5.28	5.62	4.87	5.15	4.47	4.89	4.96	59.74
640	3.66	4.17	4.6	3.86	4.13	3.63	3.83	3.98	27.37
680	2.29	2.63	2.95	2.59	2.67	2.28	2.5	2.56	2.45

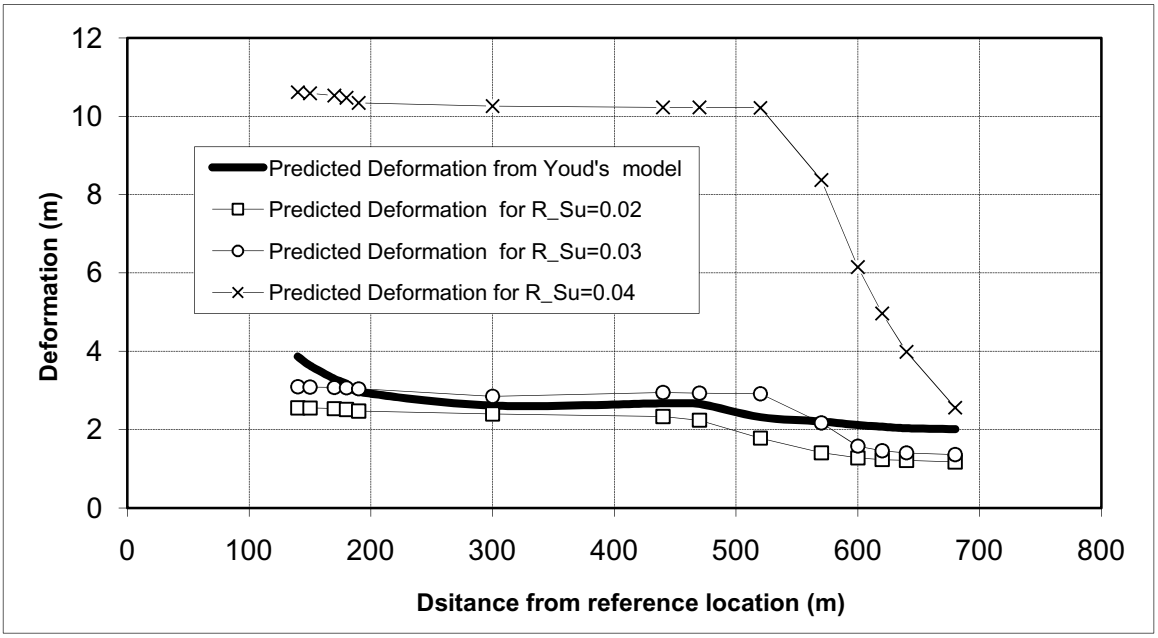


Figure 7.35. Comparison between Youd et al. (2002) model and FLAC model

Because the total deviation of the model result for the residual strength ratio of 0.03 is the least of all the cases modeled, this ratio was used for the statistical analysis in Chapter 8.

7.7 San Fernando Site Juvenile Hall Section

The 1971 San Fernando, California earthquake occurred on February 9, 1971. It was registered as a M6.4 event and the epicenter was located about 13 km north-northeast of San Fernando in the western San Gabriel Mountains (O'Rourke et al., 1992).

Liquefaction-induced ground movements and slope failures caused substantial structural damage and left the lower San Fernando Dam precariously close to catastrophic failure. Liquefaction-induced soil movements also affected bypass pipelines, channels, pump stations, and filtration facilities within and adjacent to the complex. The Joseph Jensen Filtration Plant and Juvenile Hall section are the two well-documented cases with lateral spread due to liquefaction.

The inclination of the ground surface throughout the Juvenile Hall area was about 1.5°, with a maximum slope of about 3°. The boring locations, as well as a legend indicating the soil types, are shown in Figure 7.36. Table 7.30 gives the soil properties at Juvenile Hall.

The calculated soil predominant period after liquefaction is 0.88 s. Accordingly, seven generated time histories were selected for the FLAC modeling from the 30 generated time histories produced by SGMSV5. The response spectra for the seven time histories are shown in the Figure 7.37. The selected seven selected motions are shown in Figures 38 to Figure 44.

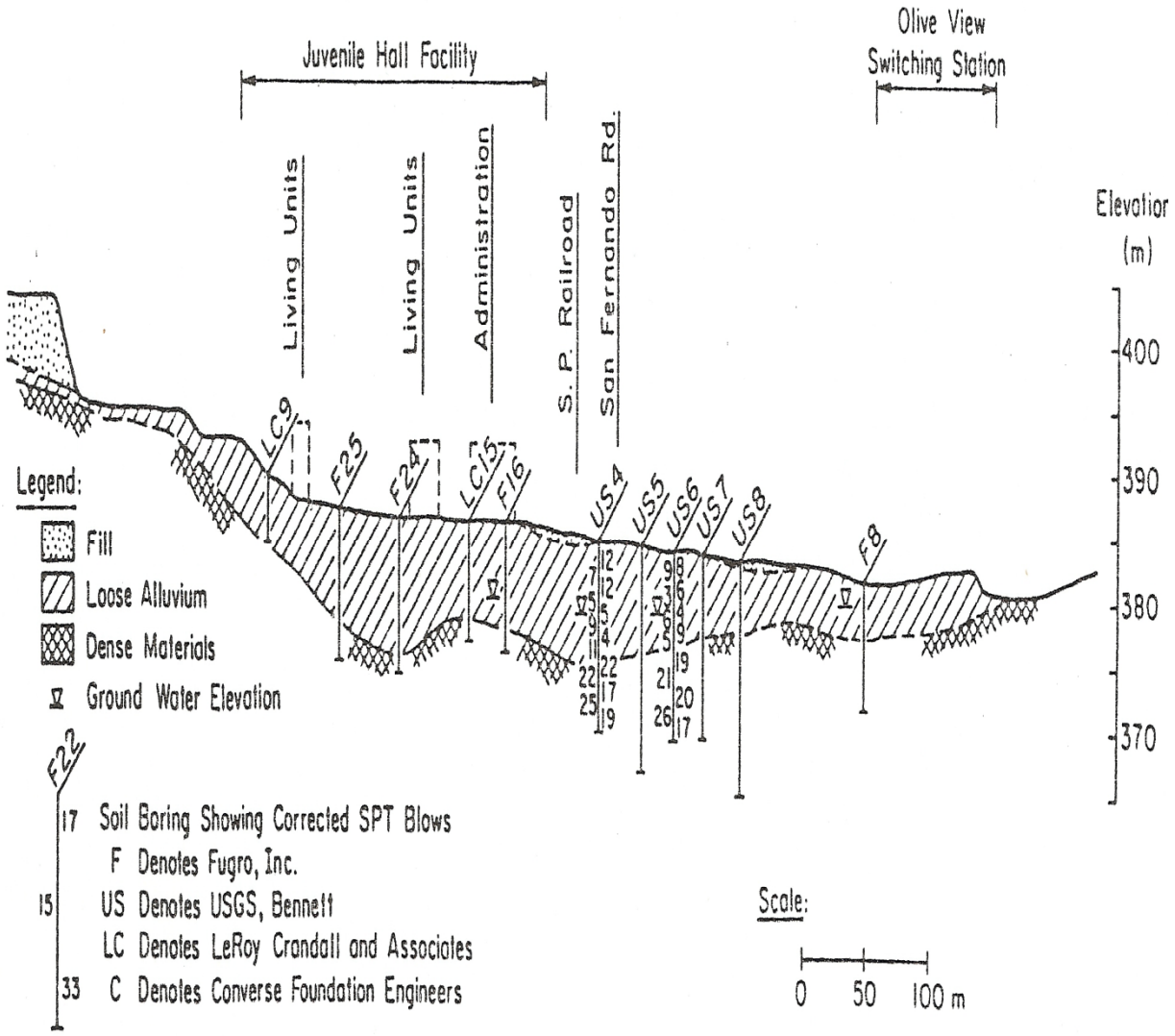


Figure 7.36. Soil Profile at Juvenile Hall of San Fernando site (after O'Rourke et al., 1992).

Table 7.30. Soil properties at Juvenile Hall section of San Fernando site.

Boring location	Ground water level (m)	Depth of Liq. layer (m)	T_{15}(m)	D_{50}(mm)	F_{15}(%)	Average $(N_1)_{60}$
DH13	8.0	7.6	6.4	0.080	47	13.0
DH15	2.0	2.8	3.8	0.080	47	5.3
AVERAGE	5.0	5.2	5.1	0.080	47	9.2

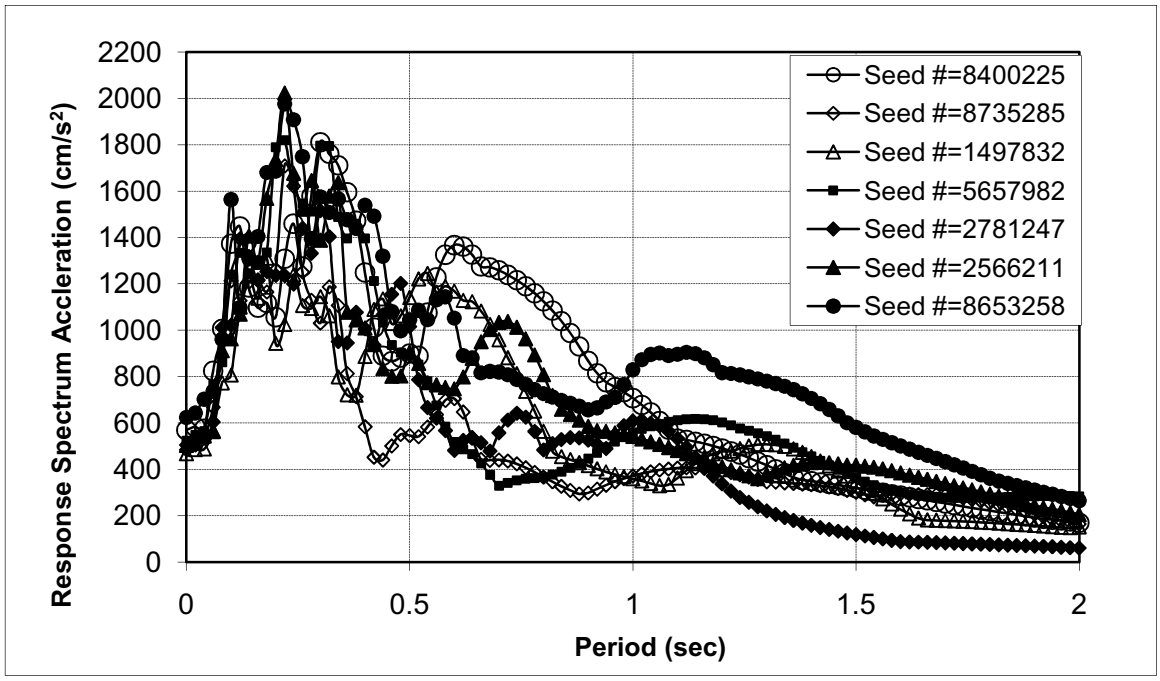


Figure 7.37. Response spectra of seven time histories generated from SMGS for San Fernando Juvenile Hall section

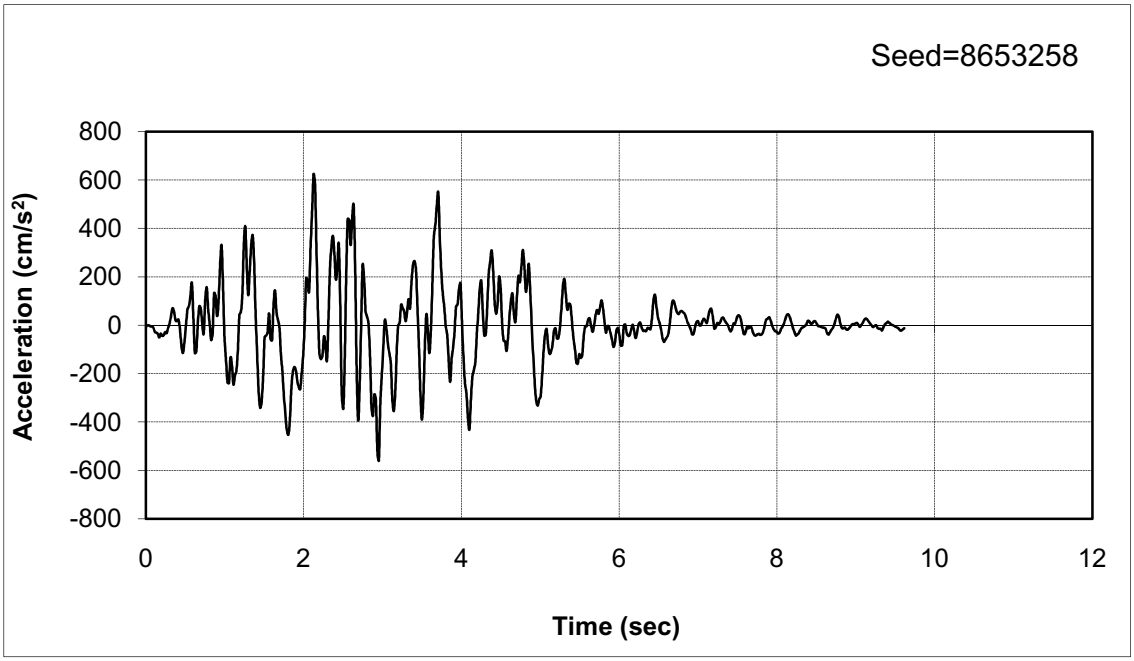


Figure 7.38. San Fernando Juvenile Hall section model selected motion 1

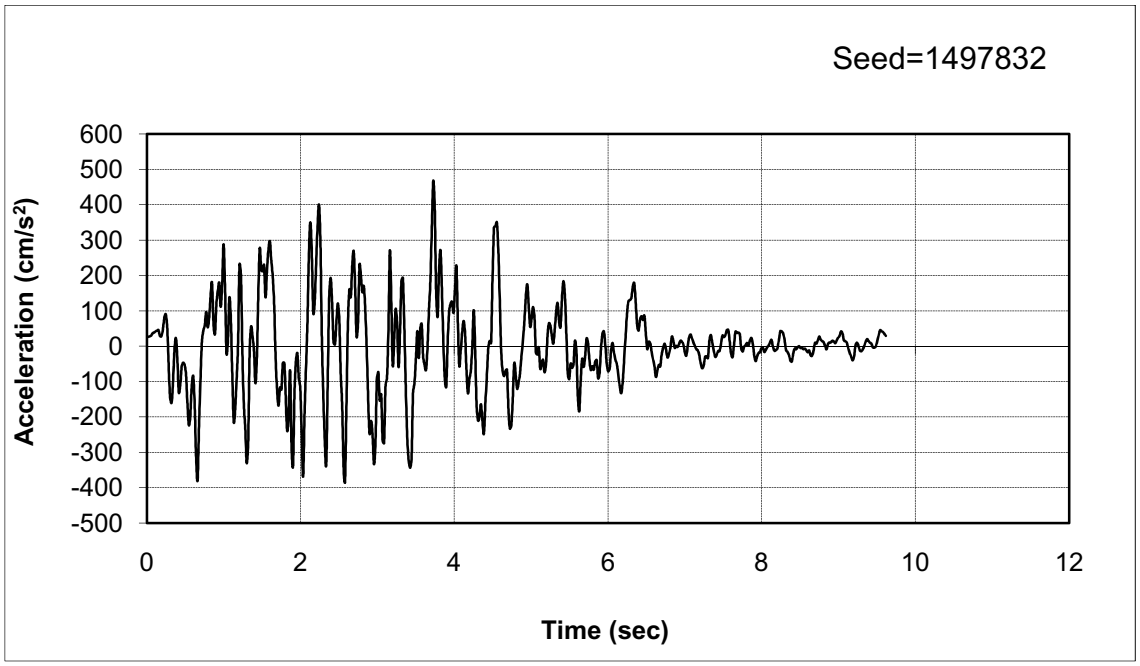


Figure 7.39. San Fernando Juvenile Hall section model selected motion 2

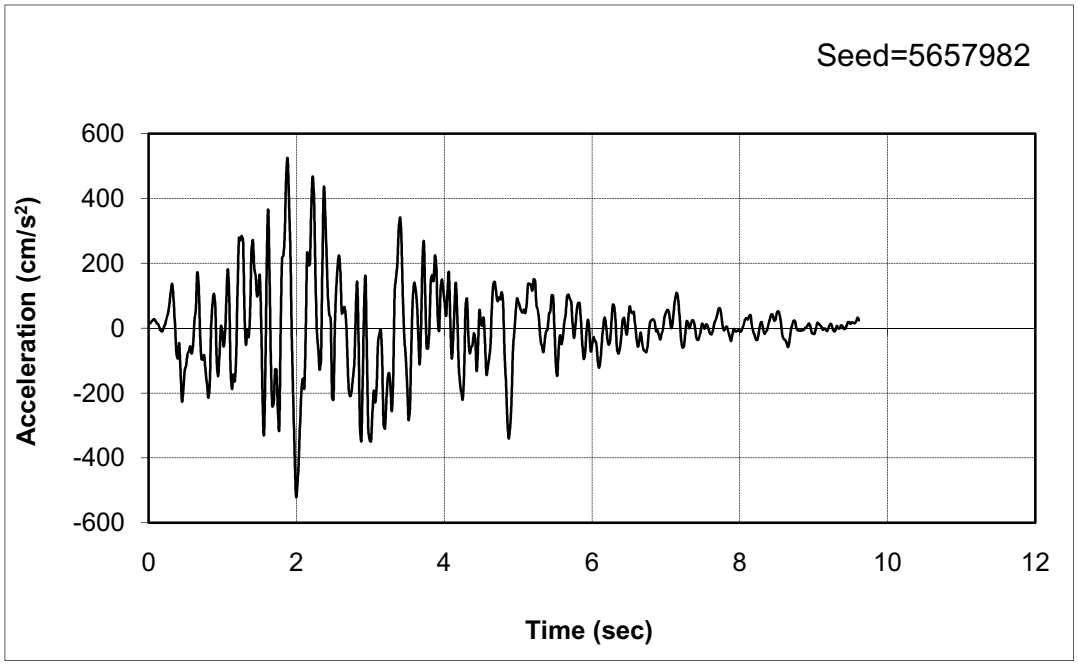


Figure 7.40. San Fernando Juvenile Hall section model selected motion 3

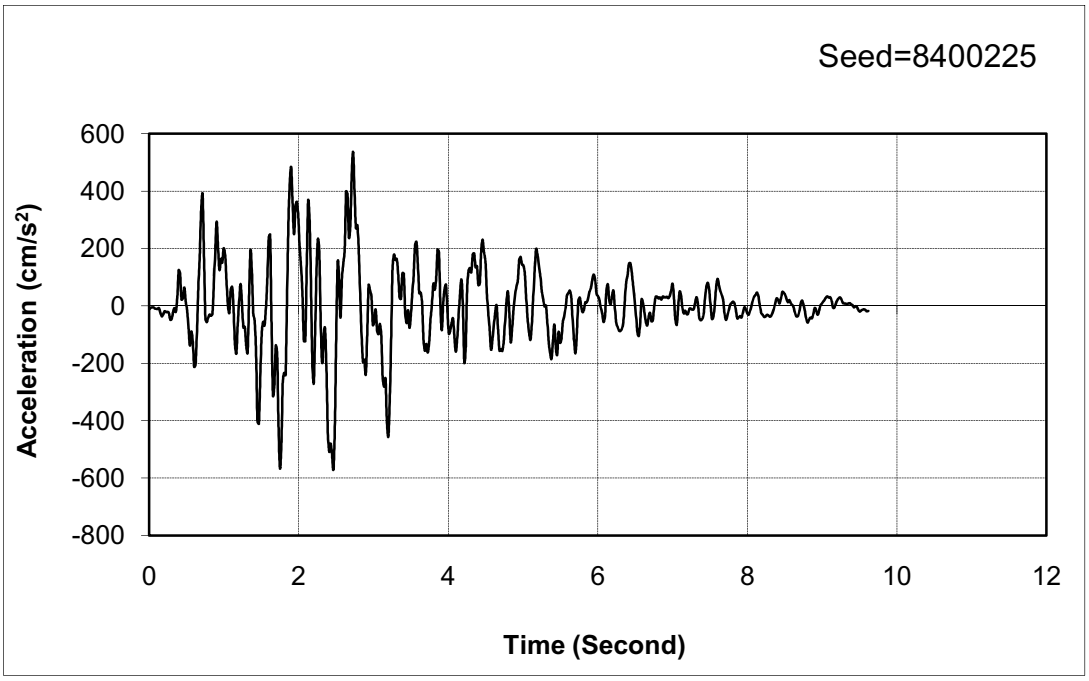


Figure 7.41. San Fernando Juvenile Hall section model selected motion 4

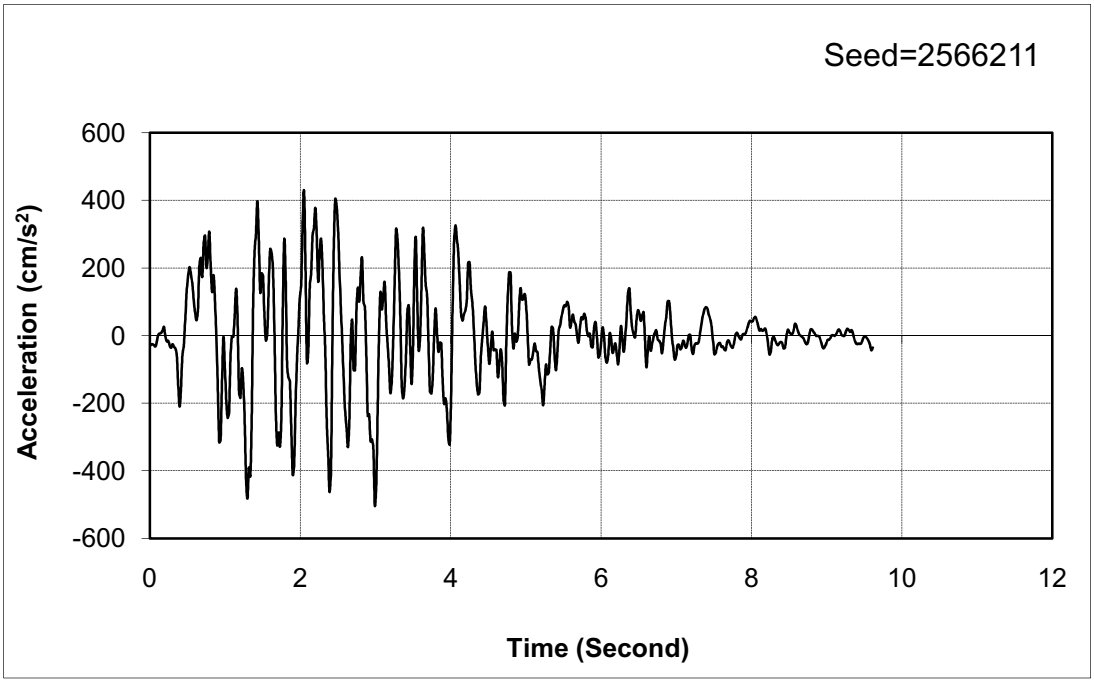


Figure 7.42. San Fernando Juvenile Hall section model selected motion 5

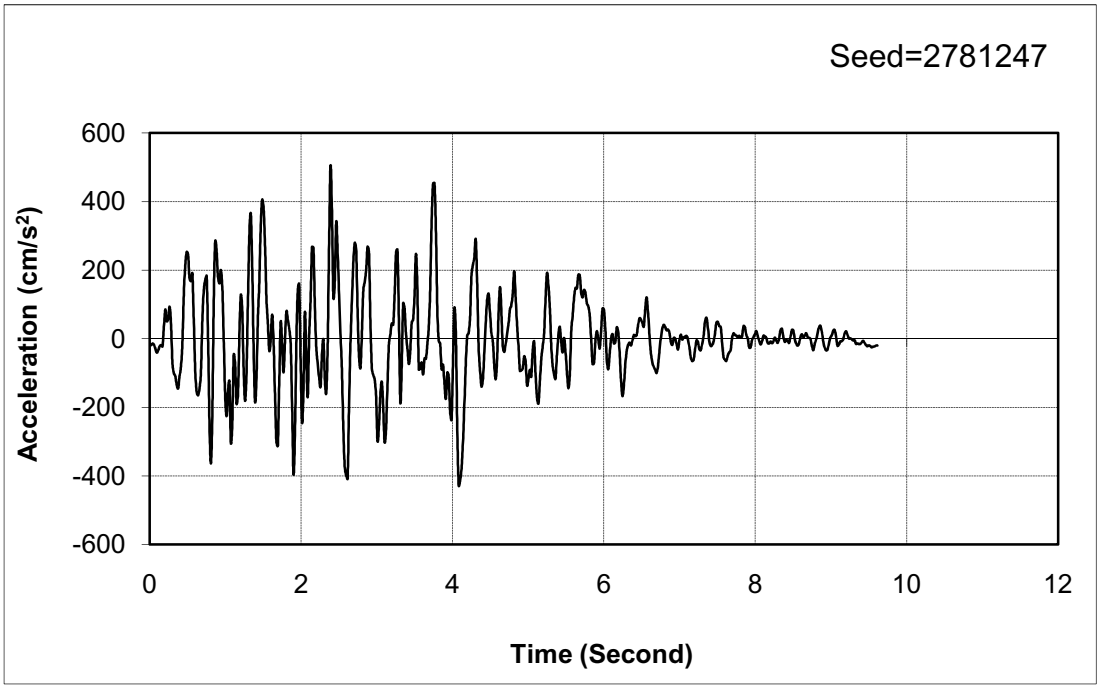


Figure 7.43. San Fernando Juvenile Hall section model selected motion 6

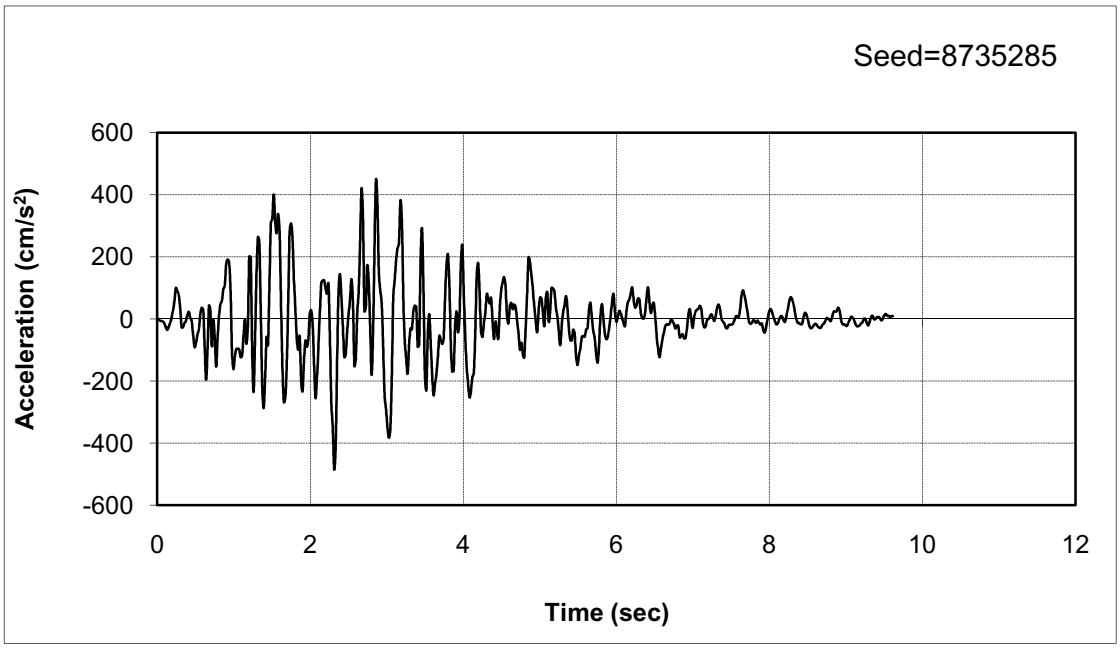


Figure 7.44. San Fernando Juvenile Hall section model selected motion 7

Detailed examination of the soil profile shows the average slope of the section is about 1.2. The prediction from the Youd et al. (2002) ground slope model is shown in Table. 7.31.

PROSHAKE is used to deconvolve the selected seven motions, as previously discussed. The developed FLAC model input motions and FLAC results are listed in Appendix G.

The FLAC model results with residual strength ratio of 0.15, 0.14, 0.13 are given in Table 7.32.

Because the total deviation of the model results with the residual strength ratio of 0.14 is the least of all the cases modeled, this was used in the subsequent statistical analyses (Chapter 8).

Table. 7.31. Lateral spread prediction by Youd et al. (2002) model at Juvenile Hall area

M	R(KM)	W(%)	S	T_{15} (m)	F_{15} (%)	$D50_{15}$ (mm)	Lateral spread (m)
6.4	0.2	1	1.23	4	64	0.06	0.29

Table 7.32. Lateral spread calculation from FLAC model with residual strength ratio of 0.15, 0.14 and 0.13 at Juvenile Hall area.

Distance from reference (m)	Motion_1	Motion_2	Motion_3	Motion_4	Motion_5	Motion_6	Motion_7	Average	Derivation
0.15	0.26	0.25	0.28	0.27	0.26	0.29	0.23	0.263	0.009
0.14	0.32	0.3	0.33	0.29	0.27	0.34	0.26	0.301	0.006
0.13	0.36	0.32	0.34	0.33	0.29	0.36	0.29	0.327	0.013

7.8 San Fernando Site Jensen Filtration Plant Section

Figure 7.45 shows a plan view of the Jensen Filtration Plant areas at the San Fernando site**.** The soil profile at the A-A' section for this site is shown in Figure 7.46.

The soil profile of the A-A' section was developed from the available borings, as shown in Table 7.33. From this, the dominate period was calculated as 0.88 s after liquefaction. Seven acceleration time histories were chosen according to this period. It turns out that the selected seven time histories are the same as those used in the Juvenile Hall analyses due to the similar soil profiles.

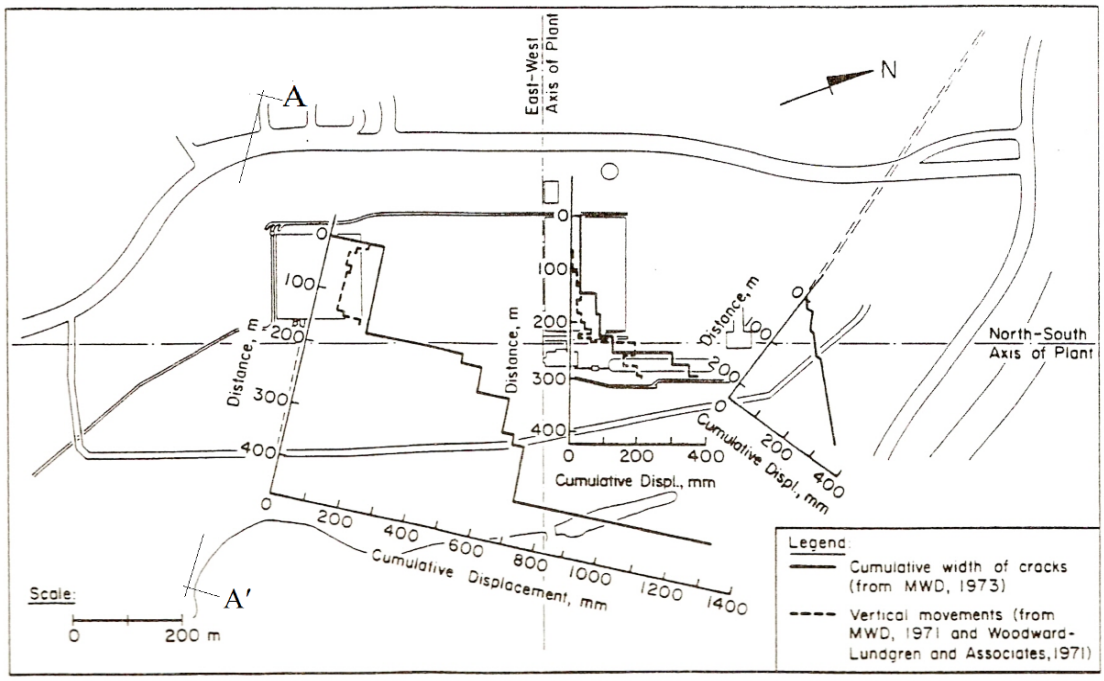


Figure 7.45. Plan View of Joseph Jensen Filtration Plant of San Fernando site (after O'Rourke et al., 1992)

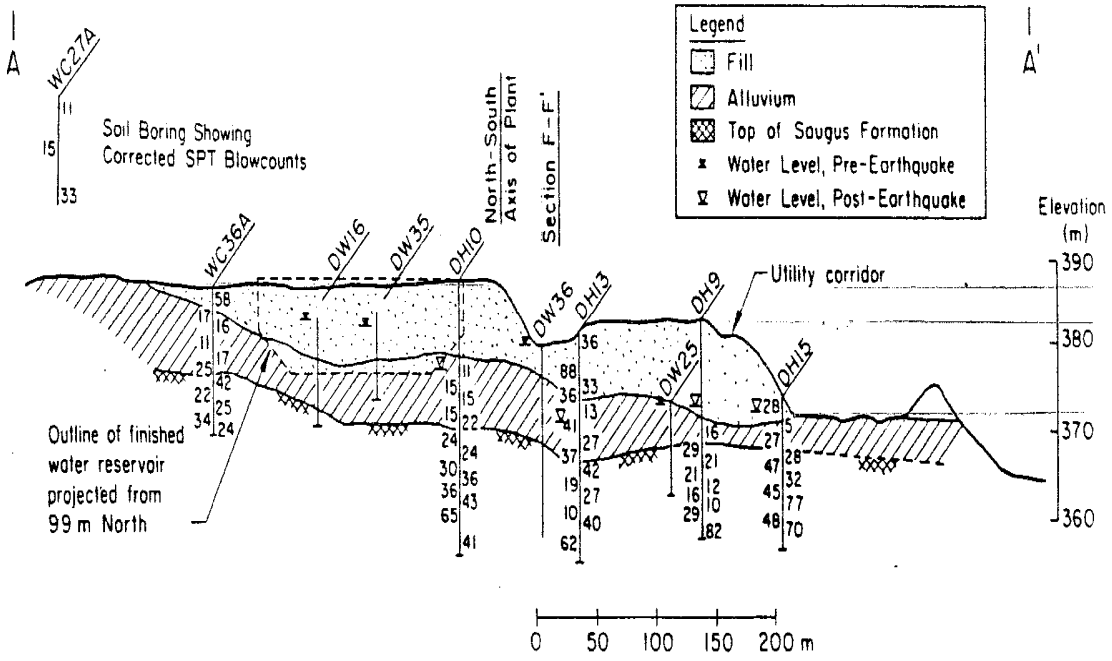


Figure 7.46. Soil Profile at A-A' section, Jensen Filtration Plant of San Fernando site (after O'Rourke et al., 1992).

Table 7.33. Soil properties at Jensen Filtration Plant section of San Fernando site.

Boring location	Ground water level (m)	Depth of Liq. layer (m)	T_{15}(m)	D_{50}(mm)	F_{15}(%)	Average $(N_1)_{60}$
DH13	8.0	7.6	6.4	0.080	47	13.0
DH15	2.0	2.8	3.8	0.080	47	5.3
AVERAGE	5.0	5.2	5.1	0.080	47	9.2

For this site section, the free face effect from the slope near Section F-F' in Figure 7.46 was accounted for in the lateral spread modeling. The height of the free face is about 9 m. The reference location for both the FLAC model and Youd et al. (2002) model is the crest of the free face near section F-F'.

The prediction from the Youd et al. (2002) model for the various points along this cross section is shown in Table 7.34.

Table 7.34. Lateral spread prediction by Youd et al. (2002) model at Jensen Filtration Plant area.

M	R(KM)	W(%)	S	T_{15} (m)	F_{15} (%)	$D50_{15}$ (mm)	Distance from reference(m)	Lateral spread (m)
6.4	0.5	18.00	1	4	47	0.08	50	1.95
6.4	0.5	16.67	1	4	47	0.08	54	1.86
6.4	0.5	15.52	1	4	47	0.08	58	1.79
6.4	0.5	14.52	1	4	47	0.08	62	1.72
6.4	0.5	13.64	1	4	47	0.08	66	1.66
6.4	0.5	12.86	1	4	47	0.08	70	1.60
6.4	0.5	10.98	1	4	47	0.08	82	1.46
6.4	0.5	10.47	1	4	47	0.08	86	1.42
6.4	0.5	10.00	1	4	47	0.08	90	1.38
6.4	0.5	9.57	1	4	47	0.08	94	1.34
6.4	0.5	9.18	1	4	47	0.08	98	1.31

As previously discussed, PROSHAKE was used to deconvolve the seven motions to the model bottom of the FLAC model. The developed FLAC model input motion and FLAC results are given in Appendix H.

The predicted FLAC results for various locations, as referenced to the reference location, for a residual strength ratio of 0.06 is listed in Table 7.35. The sum of the derivation for this calculation is 22.3.

Table 7.35. FLAC model's prediction of the lateral spread with residual strength ratio of 0.06 at Jensen Filtration Plant area.

Distance from reference (m)	Motion 1	Motion 2	Motion 3	Motion 4	Motion 5	Motion 6	Motion 7	Average	Derivation
50	2.95	2.95	3.3	3.12	2.72	3.02	2.95	3.00	7.92
54	2.35	2.33	2.61	2.47	2.13	2.36	2.35	2.37	1.93
58	1.87	1.87	2.05	1.96	1.66	1.88	1.87	1.88	0.14
62	1.52	1.53	1.64	1.59	1.30	1.49	1.52	1.51	0.36
66	1.30	1.30	1.34	1.28	1.07	1.21	1.30	1.26	1.16
70	1.13	1.14	1.12	1.10	0.93	1.03	1.13	1.08	1.90
82	1.03	1.05	0.98	0.89	0.80	0.92	1.03	0.96	1.79
86	0.93	0.94	0.82	0.88	0.69	0.80	0.93	0.86	2.24
90	0.90	0.92	0.81	0.87	0.68	0.76	0.90	0.83	2.11
94	0.88	0.91	0.81	0.83	0.67	0.74	0.88	0.82	1.98
98	0.88	0.91	0.81	0.83	0.67	0.74	0.88	0.82	1.74

The FLAC model's prediction of the lateral spread for different locations from the reference point with residual strength ratio of 0.07 is listed in Table 3.36. The sum of the derivation for this calculation is 26.5.

The FLAC model's prediction of the lateral spread for different locations from the reference point with residual strength ratio of 0.05 is list in Table 7.37. The sum of the derivation for this calculation is 82.5.

Table 7.36. FLAC model's prediction of the lateral spread with residual strength ratio of 0.07 at Jensen Filtration Plant area.

Distance from reference (m)	Motion_1	Motion_2	Motion_3	Motion_4	Motion_5	Motion_6	Motion_7	Average	Derivation
50	1.96	2.14	2.07	1.83	1.82	1.9	1.96	1.95	0.08
54	1.55	1.76	1.63	1.39	1.43	1.49	1.55	1.54	0.82
58	1.29	1.51	1.28	1.07	1.18	1.21	1.29	1.26	2.04
62	1.12	1.25	1.05	0.87	0.99	1.02	1.12	1.06	3.11
66	1.01	1.26	0.91	0.73	0.87	0.93	1.01	0.96	3.54
70	0.96	1.21	0.81	0.67	0.81	0.84	0.96	0.89	3.65
82	0.93	1.15	0.74	0.61	0.76	0.80	0.93	0.85	2.79
86	0.91	1.12	0.69	0.58	0.68	0.76	0.91	0.81	2.79
90	0.87	1.09	0.65	0.56	0.63	0.74	0.87	0.77	2.76
94	0.85	1.07	0.63	0.56	0.62	0.73	0.85	0.76	2.58
98	0.85	1.06	0.62	0.56	0.62	0.73	0.85	0.76	2.34

Table 7.37. FLAC model's prediction of the lateral spread with residual strength ratio of 0.05 at Jensen Filtration Plant area.

Distance from reference (m)	Motion_1	Motion_2	Motion_3	Motion_4	Motion_5	Motion_6	Motion_7	Average	Derivation
50	4.2	4.26	4.87	4.65	4.18	4.67	4.2	4.43	43.62
54	3.40	3.42	3.99	3.79	3.31	3.83	3.40	3.59	21.32
58	2.76	2.74	3.22	3.07	2.64	3.04	2.76	2.89	8.80
62	2.18	2.24	2.57	2.44	2.07	2.48	2.18	2.31	2.65
66	1.79	1.86	2.06	1.99	1.68	2.00	1.79	1.88	0.47
70	1.44	1.57	1.71	1.61	1.33	1.66	1.44	1.54	0.14
82	1.25	1.33	1.42	1.39	1.10	1.38	1.25	1.30	0.24
86	0.95	1.10	1.04	1.03	0.81	1.05	0.95	0.99	1.32
90	0.94	0.99	0.94	0.92	0.74	0.94	0.94	0.92	1.53
94	0.94	0.98	0.94	0.92	0.74	0.93	0.94	0.91	1.33
98	0.94	0.98	0.94	0.92	0.74	0.93	0.94	0.91	1.14

Because the total deviation of the model result with the residual strength ratio of 0.06 is the least of all the cases modeled, this residual strength ratio of 0.06 was used for the statistical analysis described in Chapter 8 for the Jensen Filtration Plant.

7.9 Imperial Valley Site Heber Road Section

On October 15, 1979, a M6.6 earthquake struck the Imperial Valley near El Centro, California. The River Park and Heber Road sites, located in the Imperial Valley of California as shown in Figure 7.47, are important case histories from a liquefaction perspective. These sites have experienced several seismic events, liquefaction has been observed after strong ground shaking, and the liquefiable layers have reasonably high fines content.

A maximum of 4.24 m lateral spread is observed on the southern edge of the unlined canal adjacent to the Heber road. The northern edge of the canal, closer to the road, moved laterally up to 2.29 m. The soil layer is mainly a 0.9 m to 1.5 m thick layer of sandy fill caps in the Heber Road site. Beneath the fill, the cross section contains a 3.4 m to 4 m thick layer composed of silt and fine sand with three distinct subunits. A dense fine sand of point-bar origin lies beneath the fill in the western part of the section. This sand is characterized by SPT values of 29 to 36 blows per foot (safety hammer) or 32 to 35 blows per foot (donut hammer). The central part of the section contains loose, very fine sand and silty sand that is natural channel fill deposited by the ancient stream. This sand is characterized by SPT-values of 1 to 7 blows per foot (safety hammer) or 2 to 4 blows per foot (donut hammer).

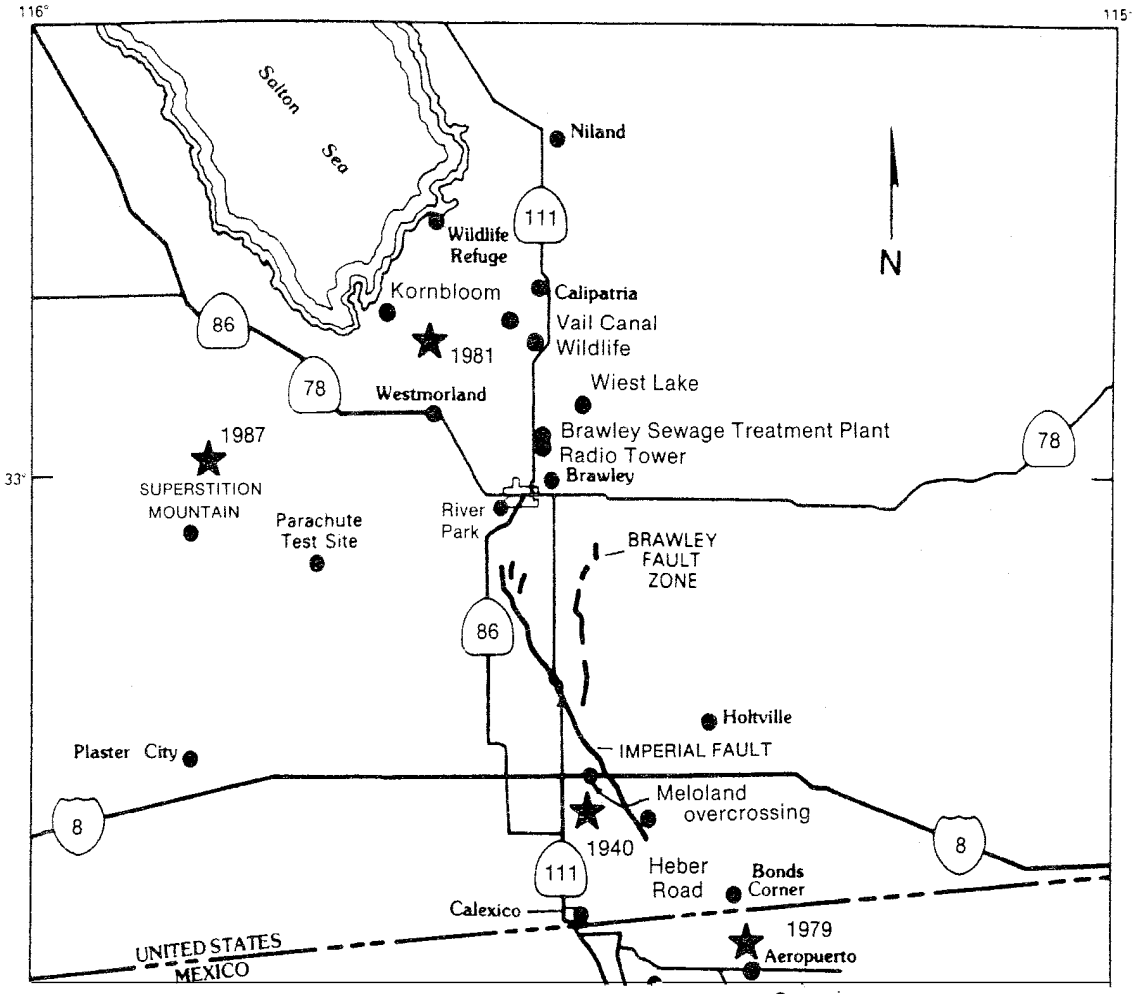


Figure 7.47. Regional map of sites and epicentral locations Imperial Valley site (after O'Rourke et al., 1992)

The eastern part of the section contains moderately dense sand and silty sandy overbank deposits characterized by SPT-values of 9 to 13 blows per foot (safety hammer) and 17 to 19 blows per foot (donut hammer). The water table depth was at about 1.6 m during the tests in December 1979 and January 1981 and was at about 2.6 m during the tests in May 1982 (O'Rourke et al., 1992). Figure 7.48 shows the soil profile of Heber Road Site.

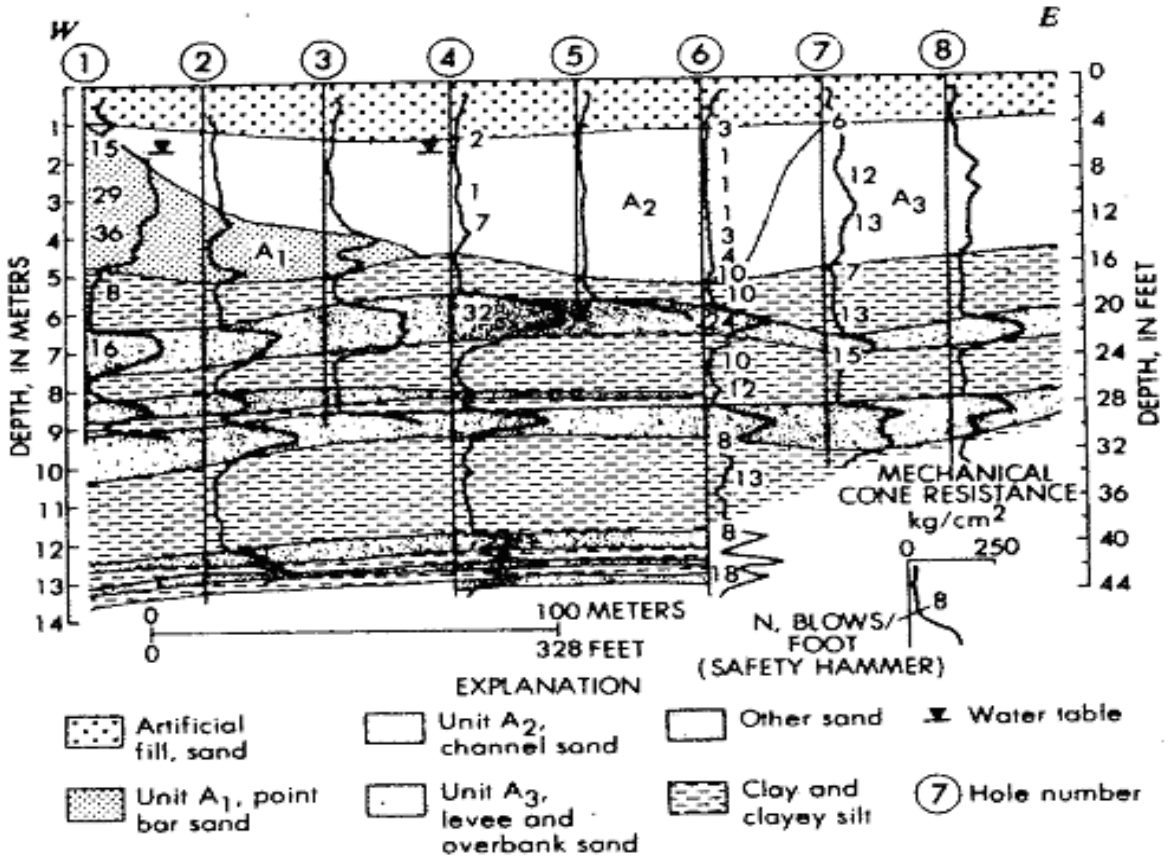


Figure 7.48. Soil Profile of Heber Road Site, Imperial Valley (Youd and Bennett, 1983)

The 1979 Imperial Valley earthquake caused liquefaction and a large lateral spread to occur at the Heber Road site. The contour of the deformation for the Heber Road site is shown in Figure 7.49. Table 7.38 shows the summary of soil parameters from available borings.

The soil's dominate period following liquefaction is 1.36 second, according to which the seven generated time histories were selected from the 30 generated time histories using SGMSV5. The response spectra for the seven selected motions are shown in Figure 7.50., and the individual acceleration time histories are given in Figures 7.51 to 7.57.

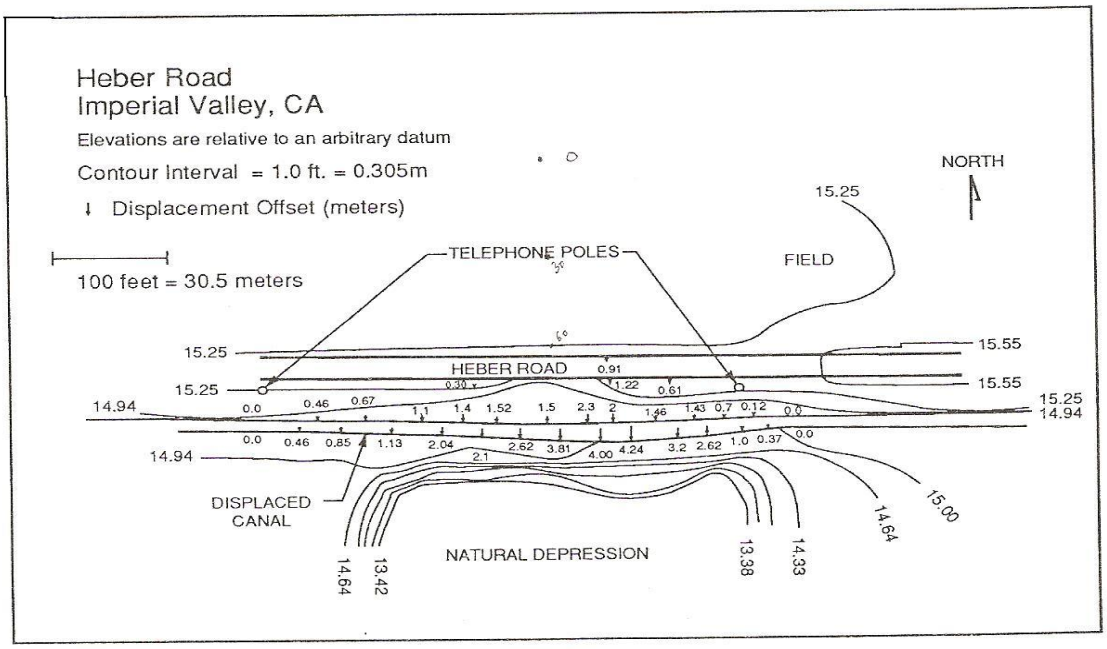


Figure 7.49. Heber Road site deformation due to the earthquake (Measurements and mapping by S. F. Bartlett and T. L. Youd)

Table 7.38 Average soil properties at Heber Road site

Boring location	Groundwater level (m)	Depth of Liq. layer (m)	T_{15}(m)	D_{50}(mm)	F_{15}(%)	Average $(N_1)_{60}$
4	1.6	1.7	4.0	0.120	25	5.7

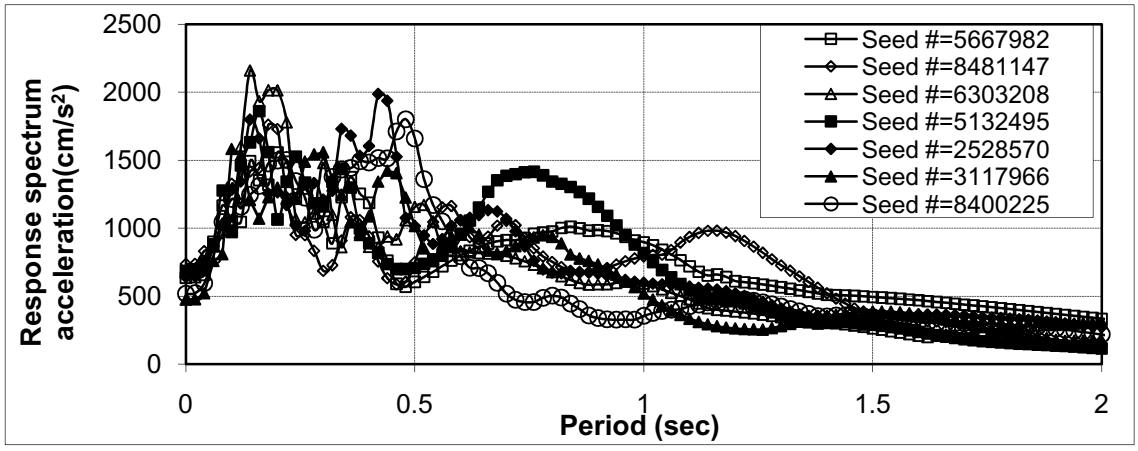


Figure 7.50. Response spectra of seven time histories generated from SMGSV5 for Heber Road site

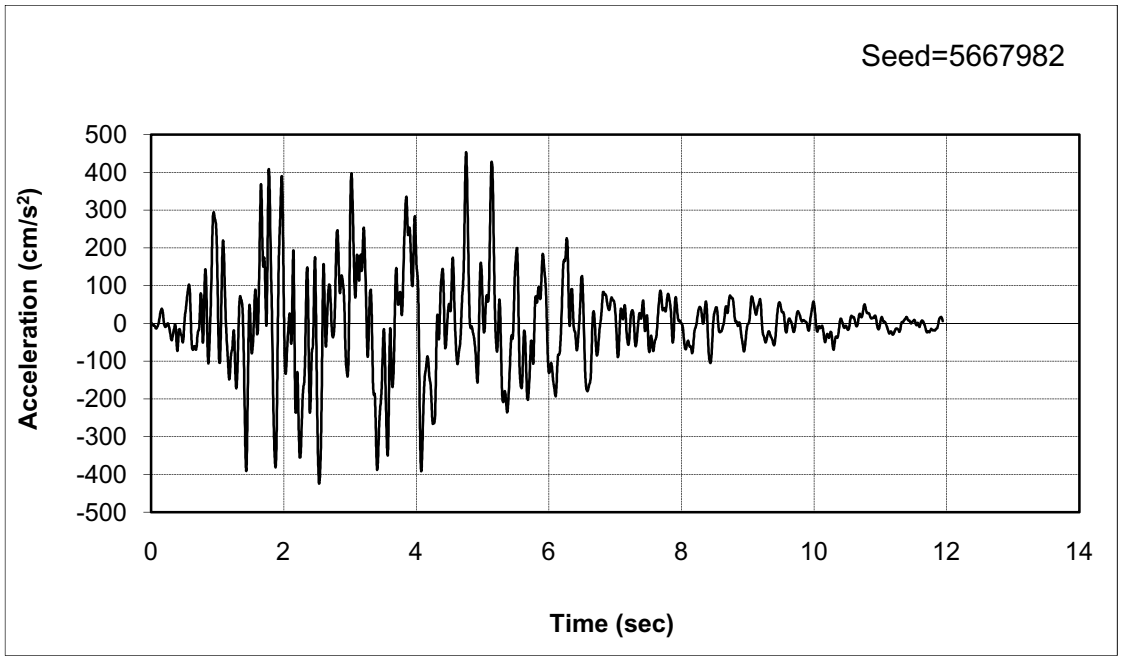


Figure 7.51. Heber Road site model selected motion 1

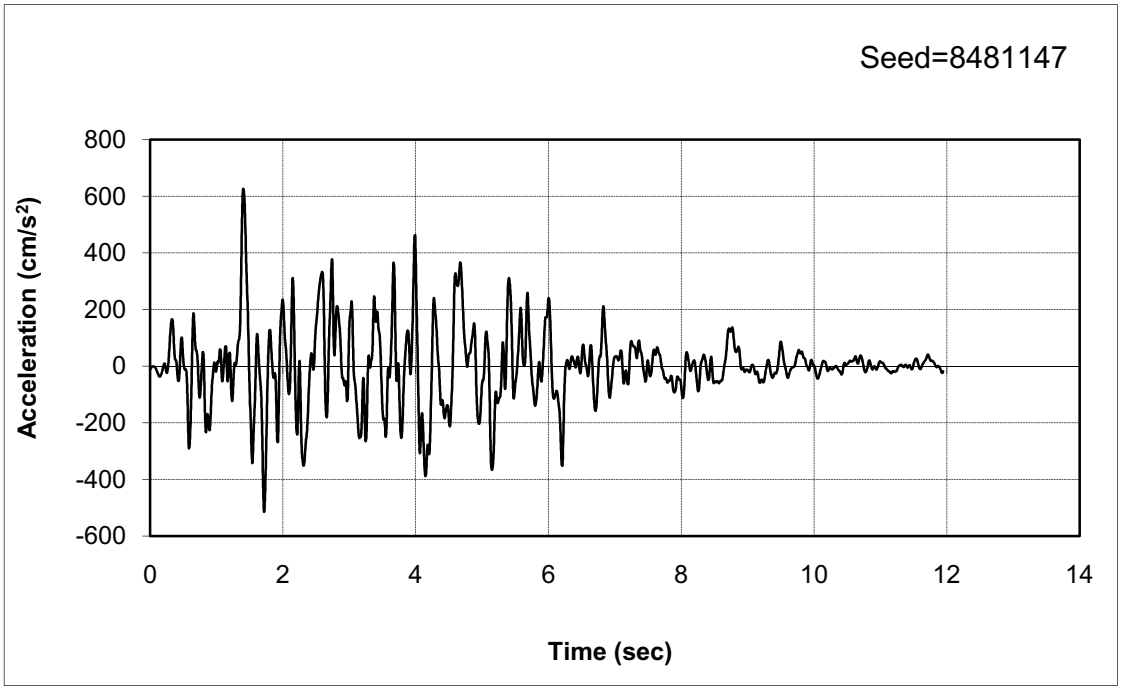


Figure 7.52. Heber Road site model selected motion 2

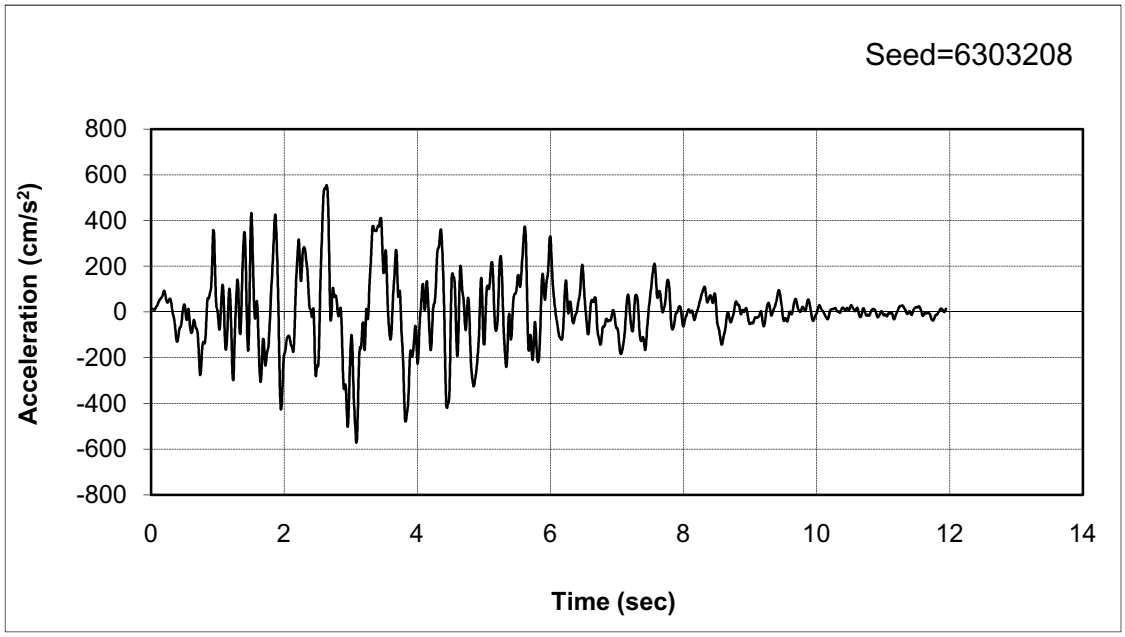


Figure 7.53. Heber Road site model selected motion 3

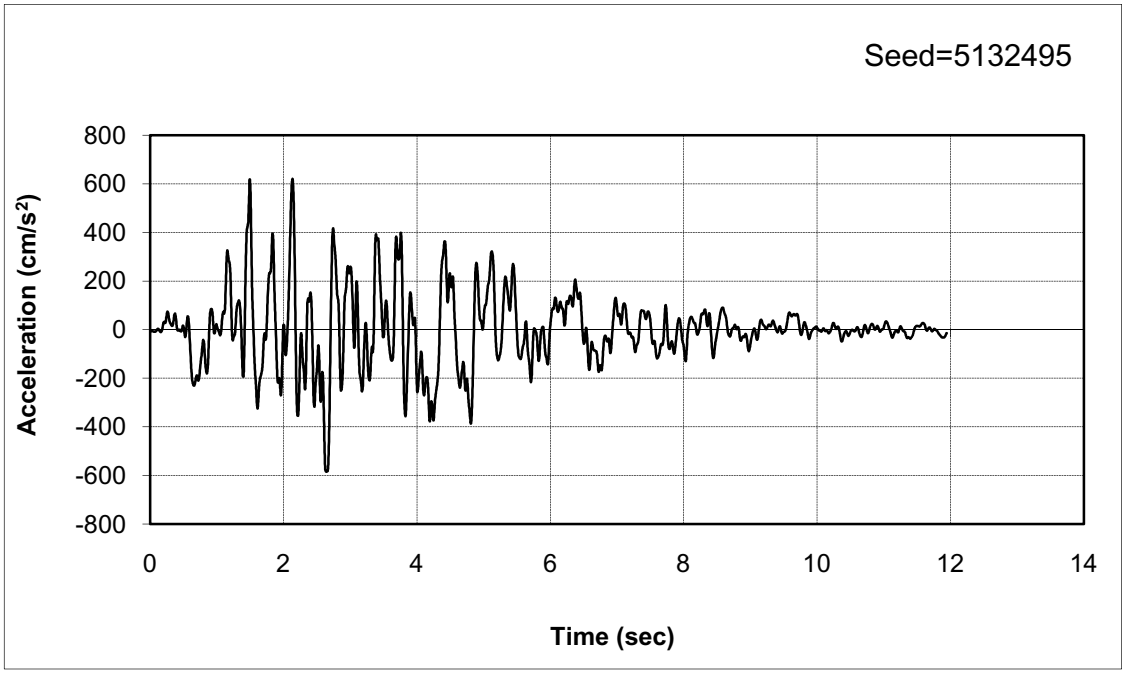


Figure 7.54. Heber Road site model selected motion 4

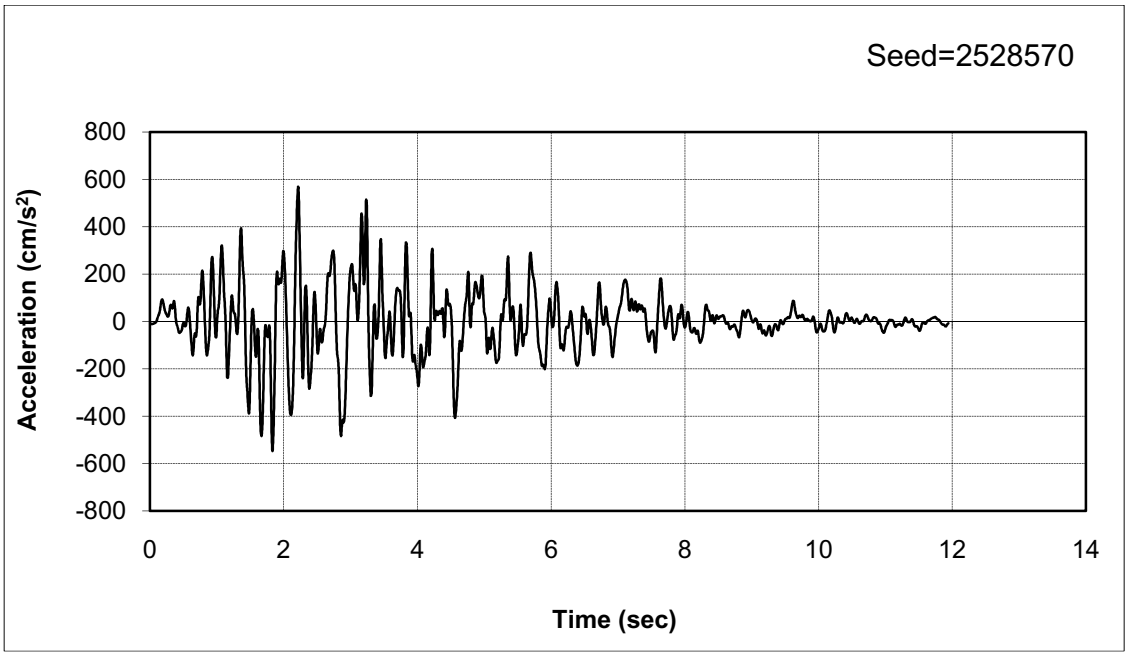


Figure 7.55. Heber Road site model selected motion 5

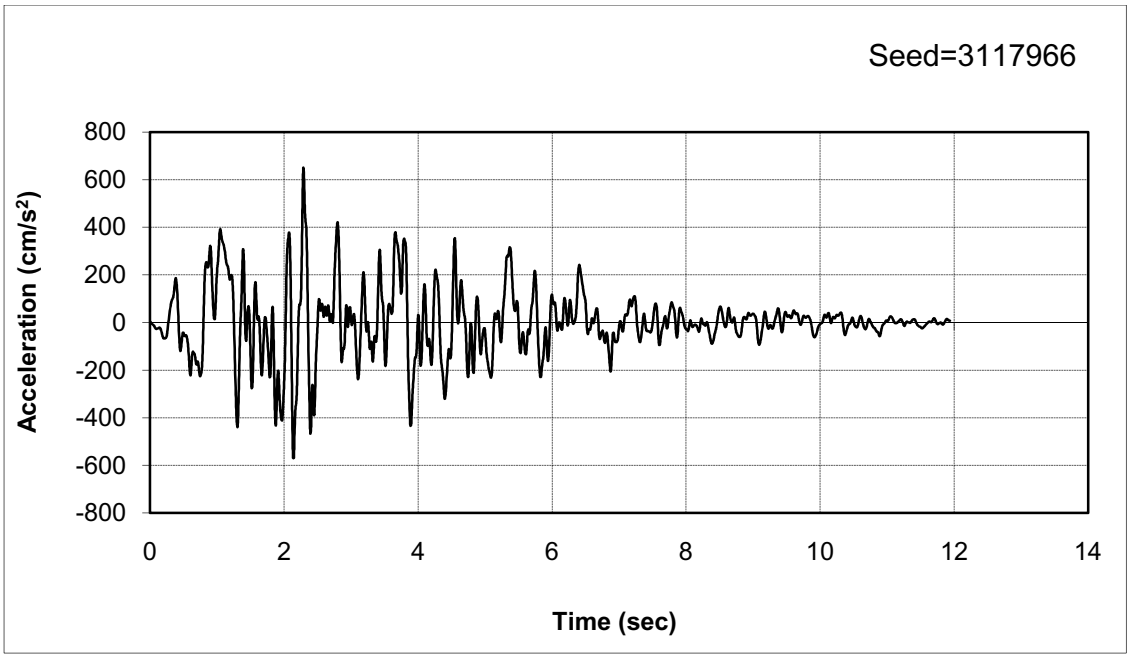


Figure 7.56. Heber Road site model selected motion 6

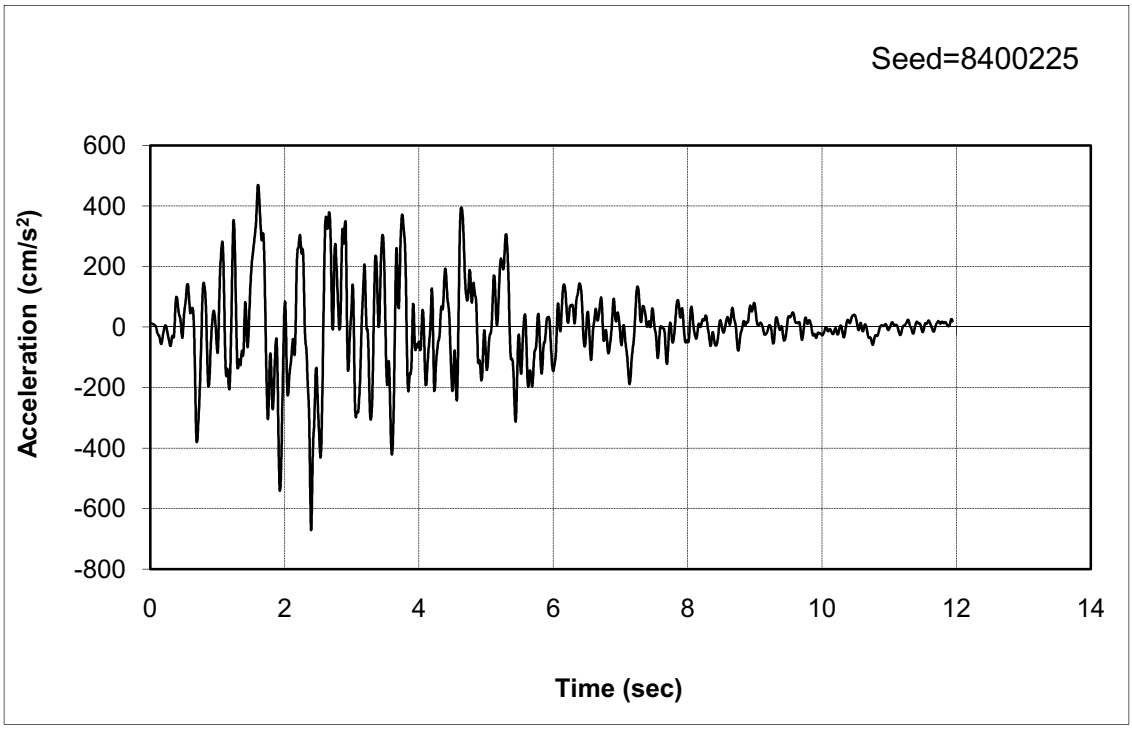


Figure 7.57. Heber Road site model selected motion 7

The Youd et al. (2002) model for a free face condition was used to predict the lateral spread due to the steepness of the natural depression at the Heber Road site. Using the soil properties listed in Table 7.39, the predicted lateral spread displacement from the Youd et al. (2002) model is also shown in Table 7.39.

PROSHAKE is used to deconvolve the selected seven motions to the base of the FLAC model bottom, as previously described. The input motions developed for the FLAC model and the results are given in Appendix I.

The predicted lateral spread values change depending upon their location from the free face. The prediction from the FLAC model for residual strength ratios of 0.09, 0.08 and 0.07 are given in Tables 7.40 through 7.42, respectively.

Table 7.39. Lateral spread prediction by Youd et al. (2002) model at Heber Road site.

M	R(KM)	W(%)	S	T_{15} (m)	F_{15} (%)	$D50_{15}$ (mm)	Distance from free face (m)	Lateral spread (m)
6.6	1.6	15.00	1	4	25	0.12	10	3.03
6.6	1.6	10.71	1	4	25	0.12	14	2.48
6.6	1.6	8.33	1	4	25	0.12	18	2.14
6.6	1.6	6.25	1	4	25	0.12	24	1.80
6.6	1.6	5.36	1	4	25	0.12	28	1.65
6.6	1.6	4.69	1	4	25	0.12	32	1.52

Table 7.40. Lateral spread prediction by FLAC model with residual strength ratio of 0.09 at Heber Road site.

Distance from free face (m)	Motion 1	Motion 2	Motion 3	Motion 4	Motion 5	Motion 6	Motion 7	Average	Derivation
10	1.47	2.55	2.02	2.55	2.69	1.89	1.54	2.10	1.94
14	1.36	2.5	1.95	2.47	2.62	1.83	1.5	2.03	1.94
18	1.29	2.38	1.89	2.41	2.55	1.73	1.42	1.95	1.94
24	1.21	2.32	1.82	2.34	2.49	1.69	1.32	1.88	1.94
28	1.15	2.26	1.78	2.29	2.44	1.64	1.27	1.83	1.94
32	1.11	2.20	1.66	2.21	2.38	1.56	1.24	1.77	1.94

Table 7.41. . Lateral spread prediction by FLAC model with residual strength ratio of 0.08 at Heber Road site.

Distance from reference (m)	Motion 1	Motion 2	Motion 3	Motion 4	Motion 5	Motion 6	Motion 7	Average	Derivation
10	1.7	2.69	2.22	2.67	2.93	2.21	1.72	2.31	5.07
14	1.61	2.58	2.05	2.57	2.9	2.04	1.7	2.21	1.95
18	1.52	2.5	1.94	2.5	2.82	1.96	1.6	2.12	1.47
24	1.31	2.44	1.88	2.45	2.75	1.88	1.52	2.03	2.05
28	1.26	2.38	1.83	2.39	2.70	1.84	1.40	1.97	2.48
32	1.22	2.33	1.76	2.33	2.64	1.81	1.33	1.92	2.82

Table 7.42. . Lateral spread prediction by FLAC model with residual strength ratio of 0.07 at Heber Road site.

Distance from reference (m)	Motion 1	Motion 2	Motion 3	Motion 4	Motion 5	Motion 6	Motion 7	Average	Derivation
10	2.1	2.79	2.23	2.77	2.84	2.12	1.79	2.38	4.03
14	2.04	2.69	2.17	2.69	2.79	2.07	1.73	2.31	1.21
18	1.9	2.63	2.08	2.63	2.7	2.01	1.69	2.23	1.07
24	1.84	2.55	2.02	2.57	2.65	1.93	1.62	2.17	1.95
28	1.82	2.50	1.99	2.52	2.61	1.89	1.57	2.13	2.63
32	1.80	2.43	1.90	2.44	2.53	1.81	1.49	2.06	2.99

The sum of deviation for the residual strength of 0.09, 0.08 and 0.07 is 17.7, 15.8 and 18.4, respectively.

Because residual strength ratio of 0.08 gave the best results for all of the cases modeled, this will be used in the statistical analyses described in Chapter 8.

7.10 Imperial Valley River Park Site

The soil profile for the Imperial Valley River Park, California site is shown in Figure 7.58. The upper soil layer consists of loose, brown, sandy silts grading to clayey silts. The sandy silts are interpreted as flood plain deposits. The middle soil layer is predominantly fine-grained silty clay and clay. The lower unit is generally dense, well-sorted fine sand. The sand appears to be massive with a slight change in color with depth. The upper part of this unit is noticeably less dense than the lower part.

The upper layer soil of sand and silt and the third layer soil of sand are the candidates for liquefaction. During the earthquake, a lot of sand boils were found because the loose zone at the top of the sand layer was likely produced by upward migration of pore water as a consequence of compaction of sand in the underlying layer. The N value for the site soil is shown in Figure 7.58, with N value in the range of 4 to 10 for liquefaction layers (Youd et al., 1983).

The earthquake-induced lateral spread at this site was very small. Because an acceleration time history was recorded and was obtained (http://peer.berkeley.edu/), it was not necessary to develop synthetic time histories.

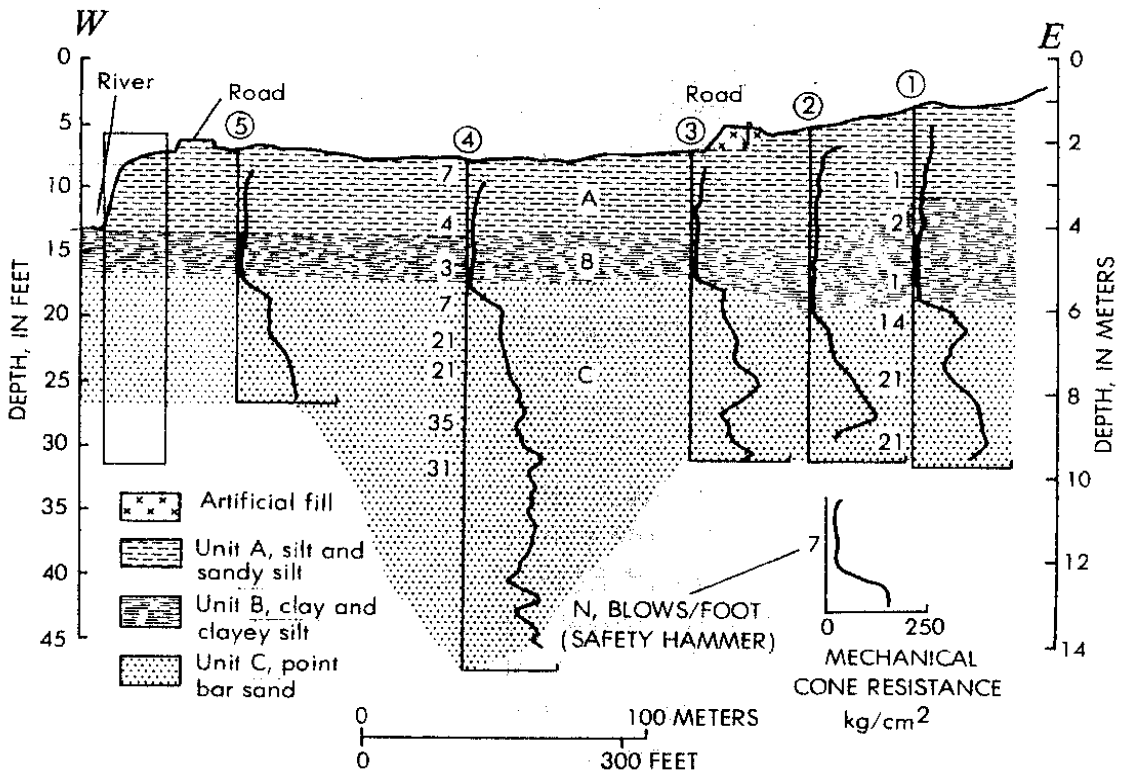


Figure 7.58. River Park soil profile and SPT value (after Youd et al., 1983)

Two 1979-earthquake time histories were downloaded with one in the 225° direction and one in the 315° direction, as shown in Figures 7.59 and 7.60, respectively.

PROSHAKE is used to deconvolve the two record motions to the base of the FLAC model, as previously discussed. The input motion developed for the FLAC model and the modeling results are given in Appendix J.

As discussed previously, the input motion to FLAC takes the form of shear stress input, thus the input shear stress time history needs to be checked and slightly adjusted so that input motion is approximately the same as the recorded motion at the base of the FLAC model. This check can be executed by comparing the velocity time histories.

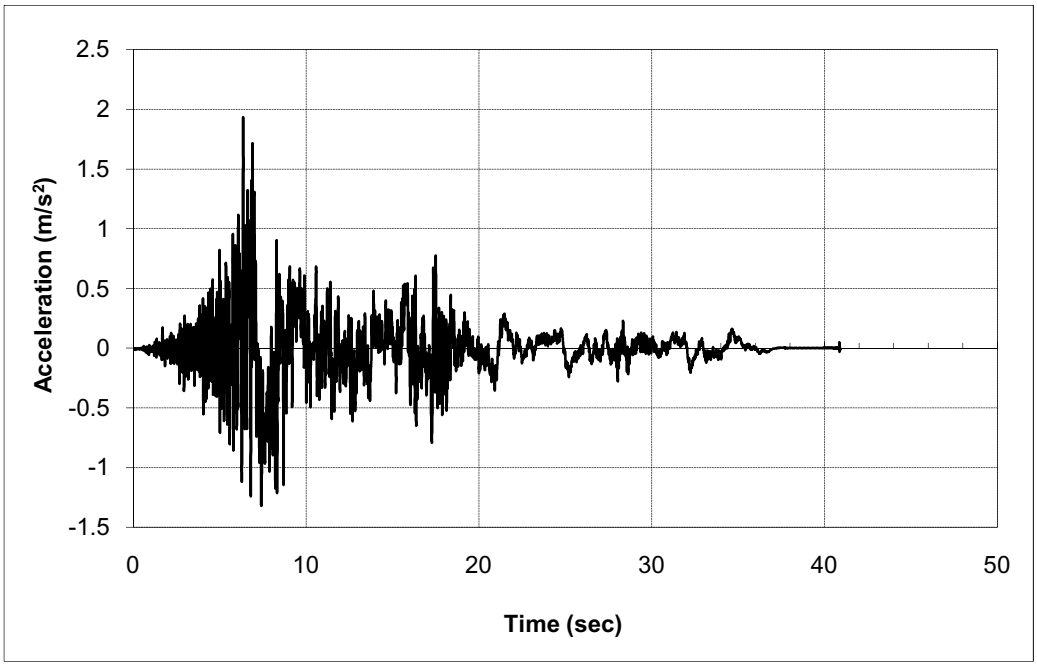


Figure 7.59 River Park site downloaded motion in 225° direction

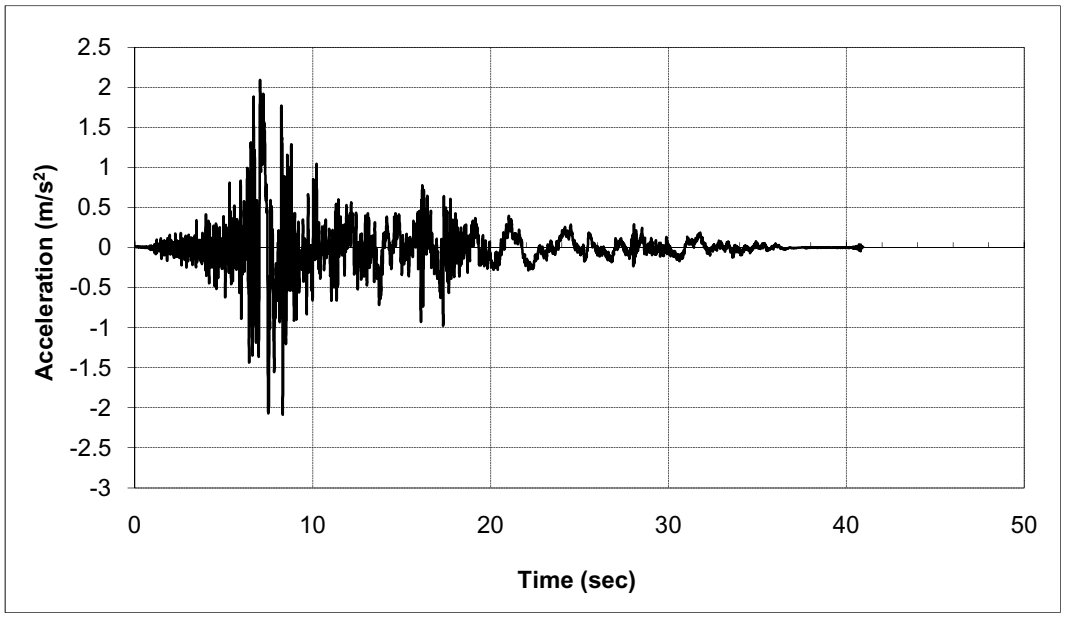


Figure 7.60 River Park site downloaded motion in 315° directions

The comparison between the input velocity time history and the record at the FLAC bottom is checked to ensure a reasonable input motion.

Using a trial and error method, when the residual strength ratio is set to 0.15, the predicted lateral spread from the recorded motions in both the directions gives very small values of lateral spread. The details of the FLAC results for this site is listed in Appendix J. Thus the residual strength of 0.15 will be used in the subsequent statistical analysis.

7.11 Turkey Degirmenedere Site

The August 17th, 1999 Kocaeli-Turkey earthquake was a M7.4 event that caused extensive liquefaction-induced ground displacements along the coast of Izmit Bay. It happened along a 125 km segment along the North Anatolian Fault, as shown in Figure 7.61. The earthquake generated a large number of ground-motion recordings within 20 km of the fault rupture. Estimates from event-specific attenuation relationships suggest that the peak horizontal ground acceleration (pga) on a hypothetical "rock outcrop" and on soft soil at the police station, soccer field, Degirmedere Nose, and Yalova Harbor sites, located within a maximum of 2 to 3 km from the fault rupture, were about 0.3g to 0.45*g*, respectively (Cetin et al., 2004).

The Degirmendere Nose site is located at the north edge of the town of Degirmendere, on a small peninsular intrusion into the Bay of Izmit. The failure mechanism was attributed to fault-induced slope instability and/or liquefaction of underlying fill materials (Cetin et al., 2004). The ground surface slope is approximately at an average angle of 10 to 15° towards the bay, as shown in Figure 7.62.

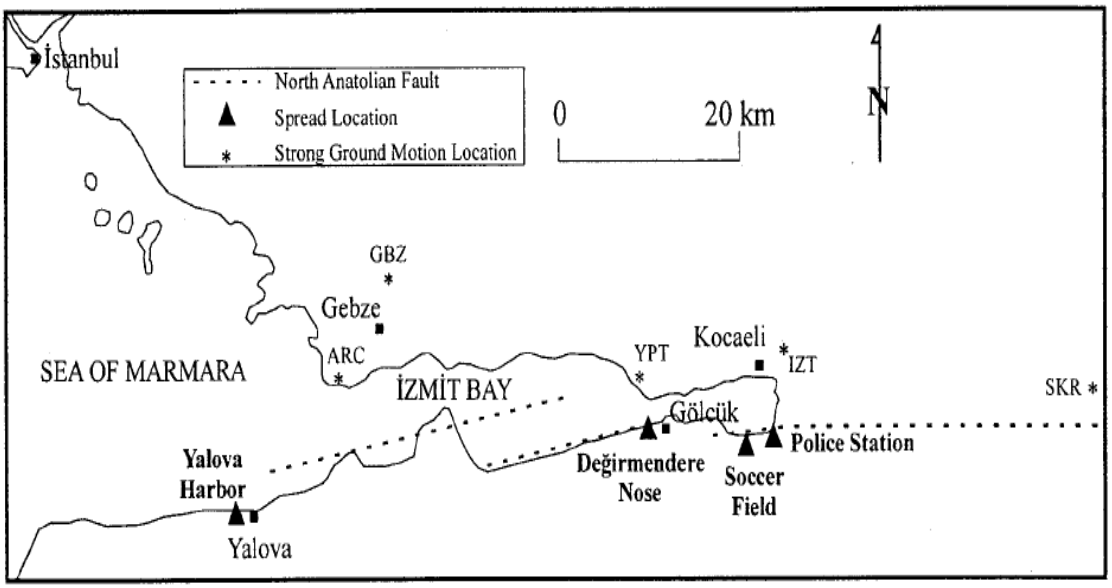


Figure 7.61. Case history of Turkey Degirmenedere site (after Cetin et al., 2004)

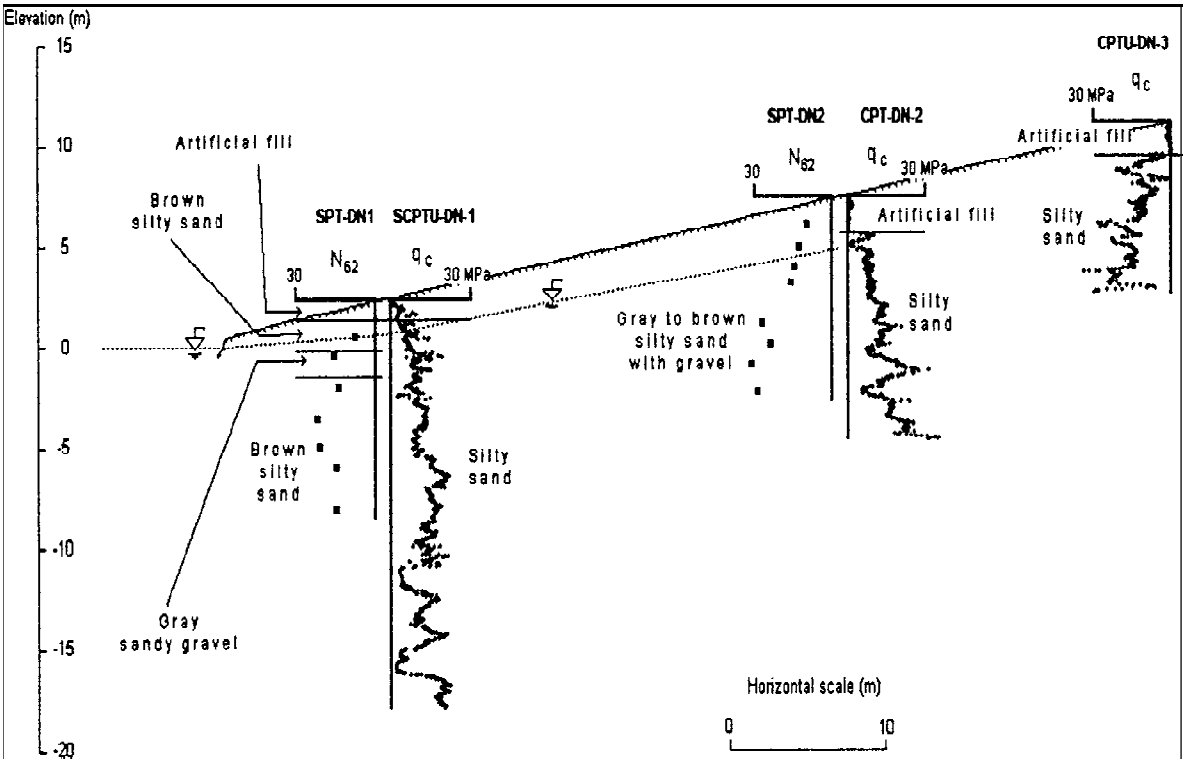


Figure 7.62. Turkey Degirmenedere site cross section and soil profile (after Cetin et al., 2004)

Soil conditions across the site are represented by one interpreted cross section largely perpendicular to the shoreline and parallel to the direction of lateral ground displacements. Surfacial soils consist of artificial fill comprised of gravel, brown gravelly sand to red silty clay ranging in thickness from 0.5 to 1 m. This fill layer is underlain by a thick silty sand layer with occasional gravelly sand and silty clay mixtures. Energy corrected SPT blow counts are in the range of 15 to 20 blows per foot in this silty sand layer. Considering the artificial fill on the top layer of the site, a blow count of 11 is used in the modeling for the liquefaction layer to take into account the fill effect. The fines content of the material is generally in the range of 10 to 30%, for which the average of 20% is used for the modeling.

At the Degirmendere Nose site, three major lines of ground cracks were surveyed parallel to the shoreline, located between the park area and the residential buildings to the east. The crack widths were measured approximately as 9, 50, and 28 cm, respectively, summing to a total of 87 cm along the survey section perpendicular to the shoreline.

The recorded time history at the YPT site was used for the FLAC model because the YPT site is approximately the same distance from the North Anatolian Fault as the Degirmenedere Nose site. The YPT histories in 60° and 330° directions are downloaded from http://peer.berkeley.edu/, as shown in Figure 7.63 and Figure 7.64.

The recorded components of the time history were rotated to the North direction, in which the lateral spread is measured. The rotated time history is shown in Figure 7.65.

The time history is then adjusted to 0.4g, as shown in Figure 7.66, according to event-specific attenuation relationships.

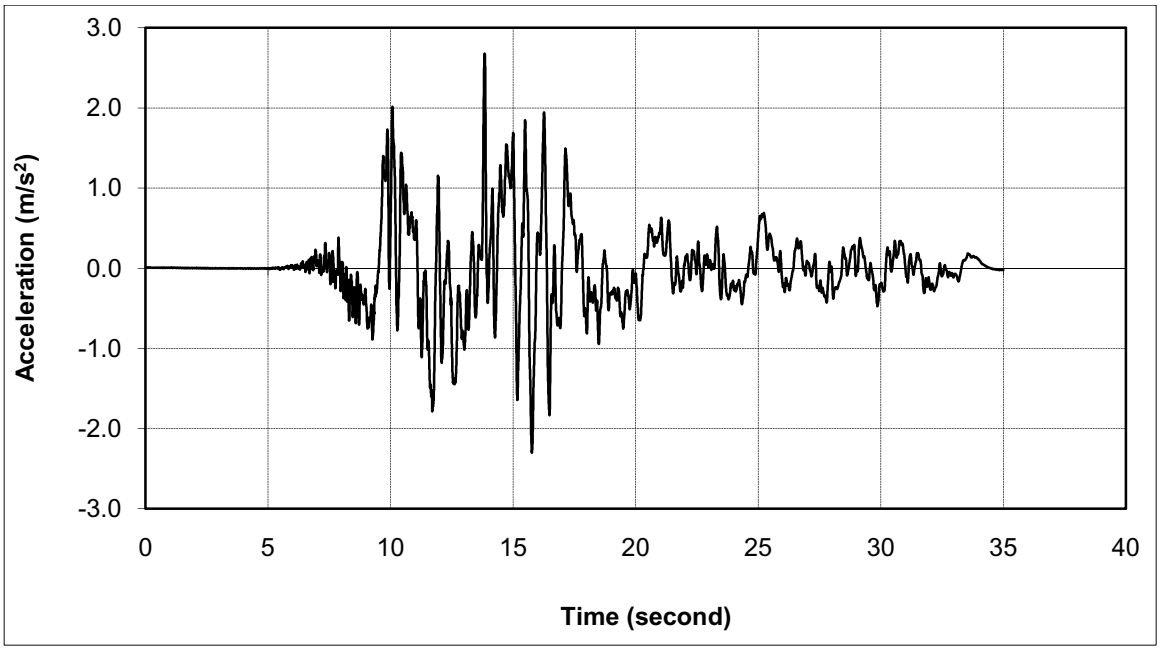


Figure 7.63. Time history at YPT in 60° directions

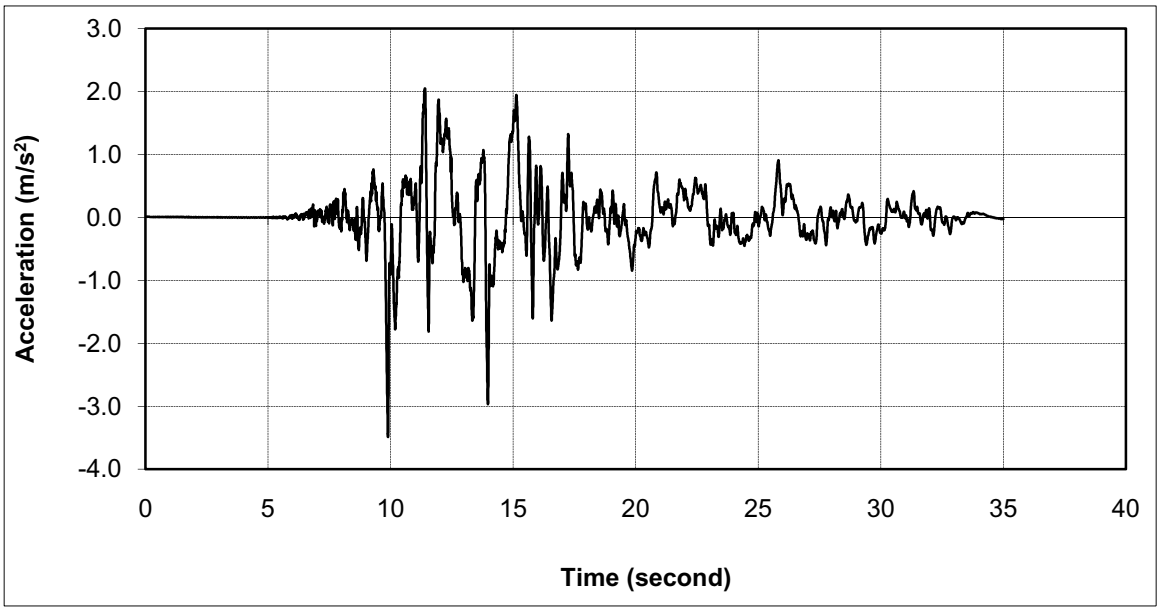


Figure 7.64. Time history at YPT in 330° directions

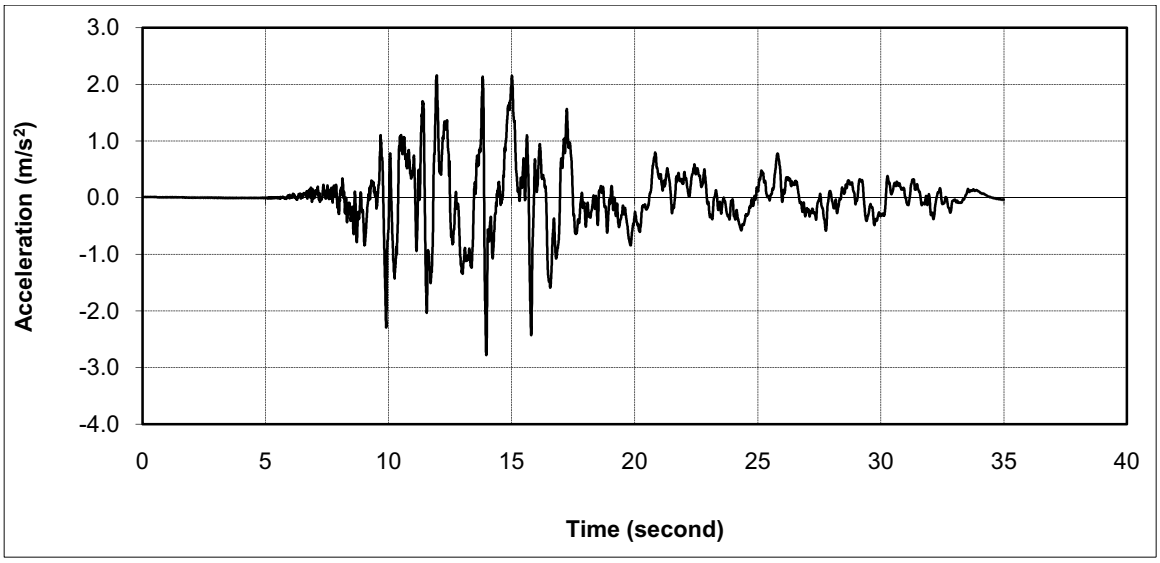


Figure 7.65. Rotated time history in the lateral spread direction for Degirmenedere site

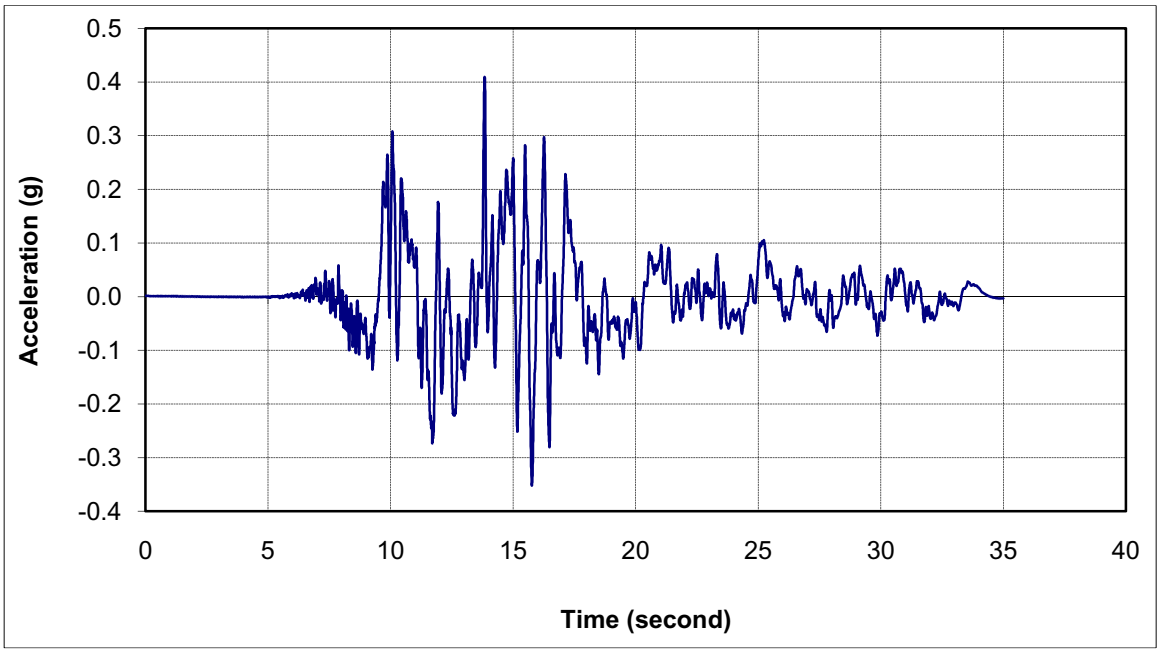


Figure 7.66. Time history adjusted to 0.4g at Degirmenedere site

PROSHAKE is used to deconvolve the motion to the base of the FLAC model, as previously discussed. The developed FLAC model input motion and results are given in Appendix K.

Using the actual soil profile and a trial and error method, the FLAC model was executed in order to achieve the same measured lateral spread of 87 cm. The simulation results from the FLAC model are given in Appendix K. Table 7.43 lists the predicted lateral spread displacements from the FLAC model with different residual strength ratios. Because the prediction by the FLAC model with residual strength ratio of 0.16 gives the best results, the residual strength ratio of 0.16 was used in the statistical analysis (Chapter 8).

7.12 Wildlife Site

The Wildlife, California case has been discussed in Chapter 6 regarding the calibration of the FLAC model in terms of the recorded downhole and surface ground response. During the calibration process, the matching of the lateral spread displacement pattern of the 1987 Superstition Hills earthquake was not considered. This section calibrates the FLAC model to the measured lateral spread during the earthquake in order to obtain the residual strength ratio. The cross section developed for the lateral spread at this site is shown in Figure 7.67.

Table 7.43. Lateral spread prediction by FLAC model at Degirmenedere site.

Residual strength radio	Predicted lateral spread (m)
0.15	1.12
0.16	0.90
0.17	0.80

The cross section with 0.59 ft (0.18 m) displacement vector at 2Ig slope inclinometer location, as shown in Figure 7.67, will be modeled using FLAC. This site is a free face failure because of the Alamo River channel, which is located on the eastern edge of the array. The 2Ig slope inclinometer is located about 50 feet away from the Alamo River free face.

The Wildlife acceleration time histories for the 1987 Superstition Hills Earthquake were recorded in 0° and 90° directions. These records were downloaded from http://peer.berkeley.edu/ and rotated to the direction of the modeled cross section in the direction of the measured lateral spread, which is about 15° to the north. The same soil profile is used as presented in Chapter 6 for this site.

The downloaded time histories in 0°, 90° and rotated time histories in 15° are shown in Figures 7.68 through 7.70, respectively.

PROSHAKE was used to deconvolve the rotated motion to the base of the FLAC model, as previously discussed. The developed motion for the FLAC model and the modeling results are given in Appendix L.

Using the actual soil profile and a trial and error method, the FLAC model was executed in order to achieve the same measured lateral spread of 18 cm. The simulation results from the FLAC model are given in Appendix L. Table 7.44 lists the predicted lateral spread by the FLAC model with different residual strength ratios. Because the prediction by the FLAC model with a residual strength ratio of 0.21 gives the best results in terms of displacement, this value was used for the statistics analysis performed in Chapter 8.

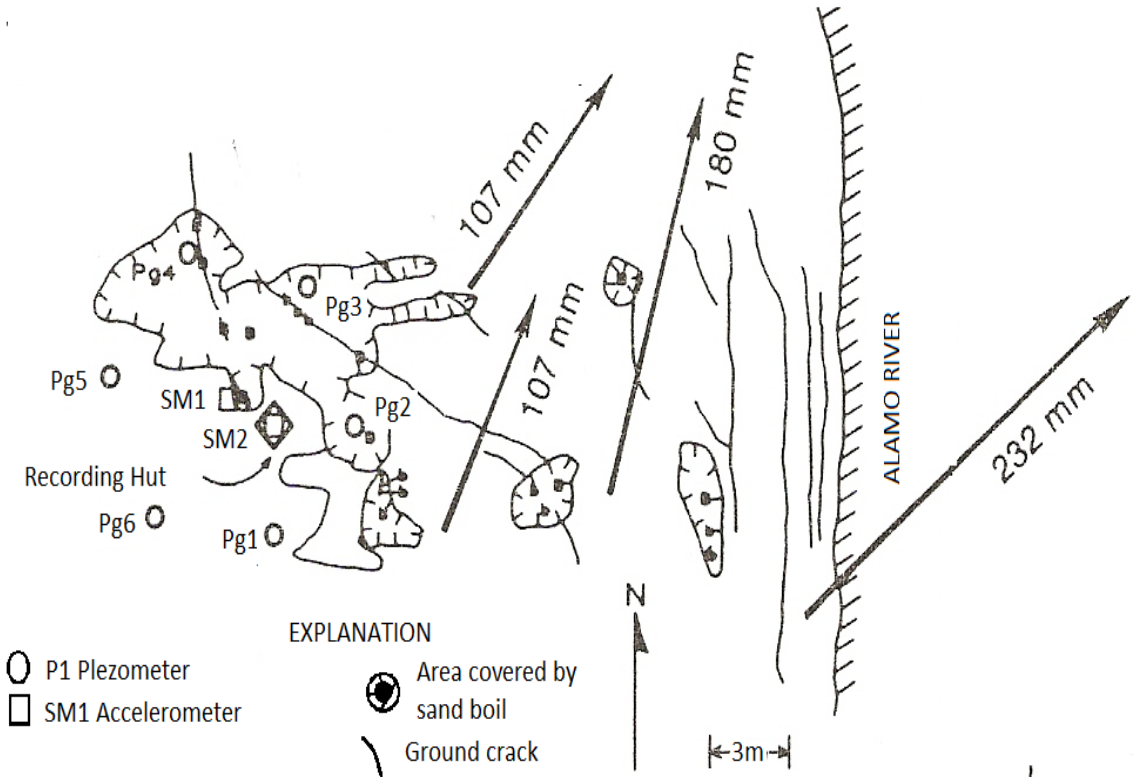


Figure 7.67. Displacement of survey points at Wildlife site during 1987 Superstition Hills Earthquake (after Youd et al., 1988)

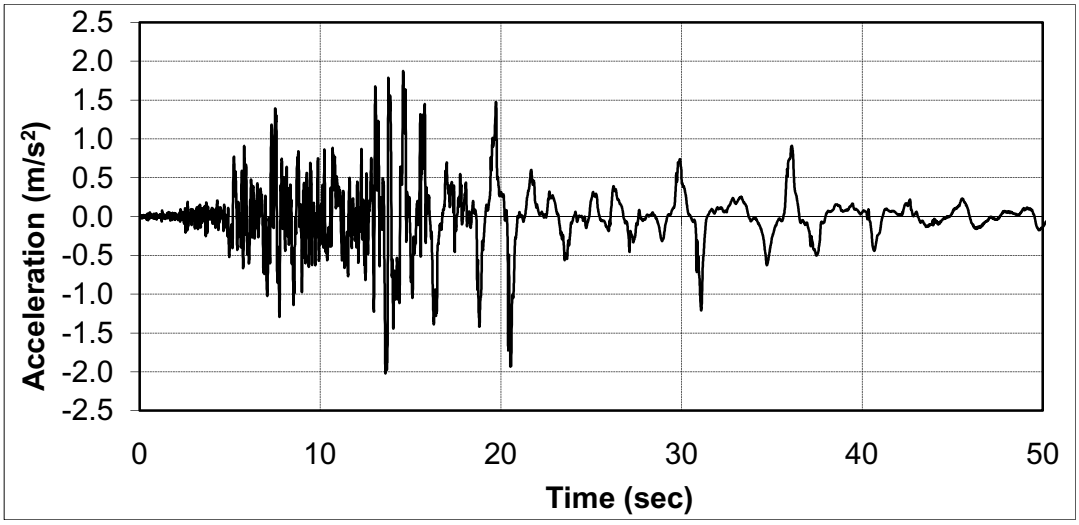


Figure 7.68. Time history in 0° direction for 1987 Superstition Hills Earthquake

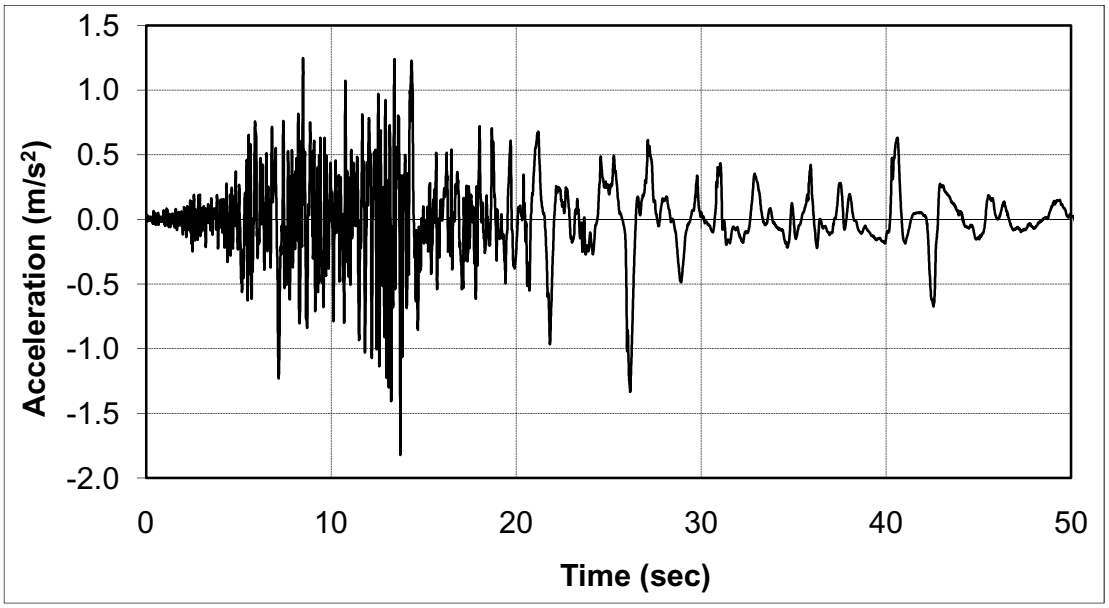


Figure 7.69. Time history in 90° direction to North for 1987 Superstition Hills Earthquake

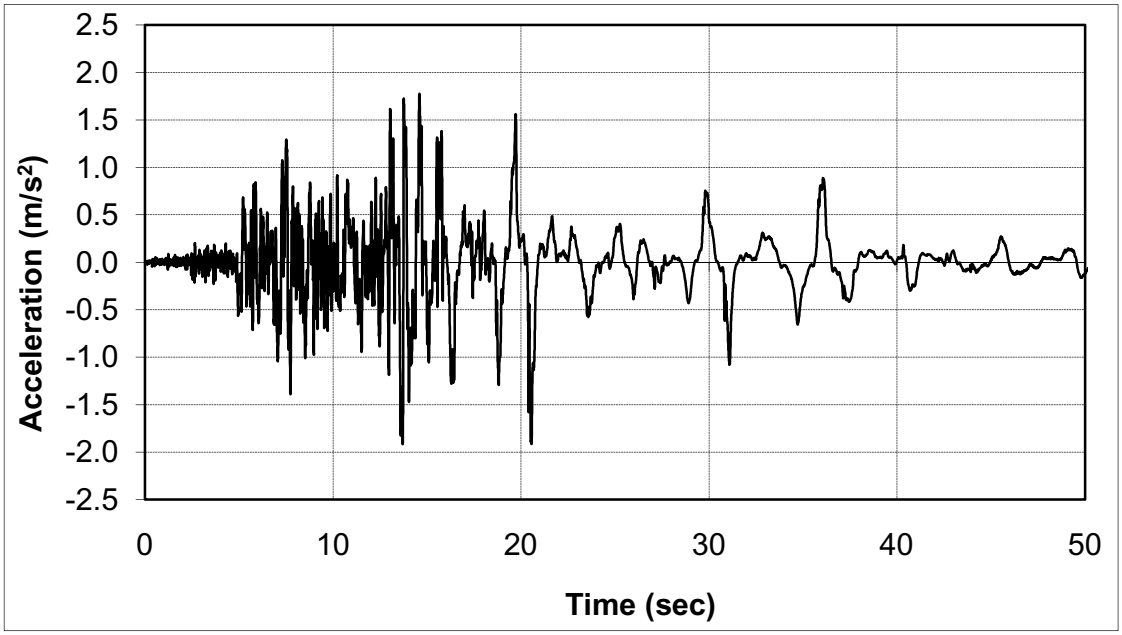


Figure 7.70. Time history in 15° direction to North for 1987 Superstition Hills Earthquake

Table 7.44. Lateral spread prediction by FLAC model at 1987 Superstition Hills site

Residual strength radio	Predicted lateral spread (m)
0.20	0.10
0.21	0.15
0.22	0.23

7.13 Idaho Whiskey Springs Site

On October 28, 1983, the M7.3 Borah Peak Earthquake struck central Idaho. Earthquake effects included a 38 km (23 mi) long surface rupture, landslides, disruption of ground water and several liquefaction effects (Youd et al., 1985). A topographical map of the liquefaction effect site at Whiskey Springs, Idaho is shown in Figure 7.71.

Figure 7.71 shows a zone of fissures generated by lateral spreading of the distal ends of an alluvial fan and the location of the Whiskey Springs investigation site. The zone of lateral spreading in the Thousand Springs Valley was 2.1 km long and 75 m wide. Maximum lateral movement was estimated to be 0.8 m to 1.0 m (Youd et al., 1985).

Figure 7.72 is a generalized A-A' cross section showing the sediment layers beneath the Whiskey Springs site.

Nearly all of the sediment is poorly sorted, gap-graded, subangular gravel. The area is capped by a dense to very dense silty gravel. At the top of unit A, a caliche soil horizon has formed. Unit A thins down slope from 5.5 m to 0.8 m. Unit B is characterized by a penetration resistance about twice as high as in unit A. Unit B thins down slope from 3 m to 0.6 m. A looser and finer-grained gravelly sediment, unit C, lies below unit B.

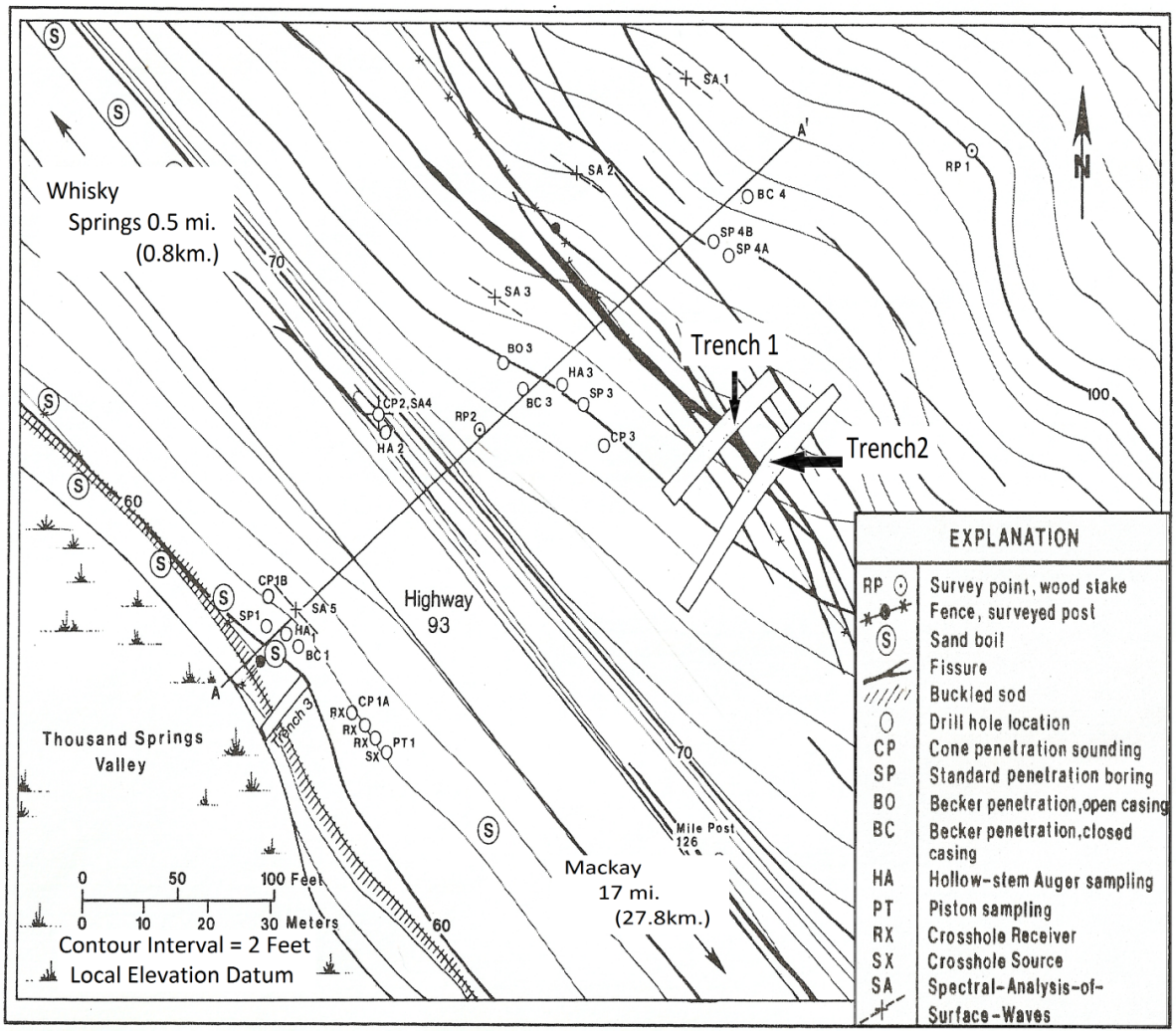


Figure 7.71. Location of Whiskey Springs, Idaho site (after Andrus et al., 1987)

Unit C1 is classified as silty gravel with appreciable sand content. Unit C1 thickens down slope from 1.2 m to cover 2 m. The lower half of unit C1 appears to be coarser. N-values for unit C1 range between 5 and 14; CPT tip resistances range from 1 to 120 kg_f/cm^2.

Based on the sediment cross section for the site and relative penetration resistances, liquefaction and shear deformation occurred in the loose silty gravel in unit C1.

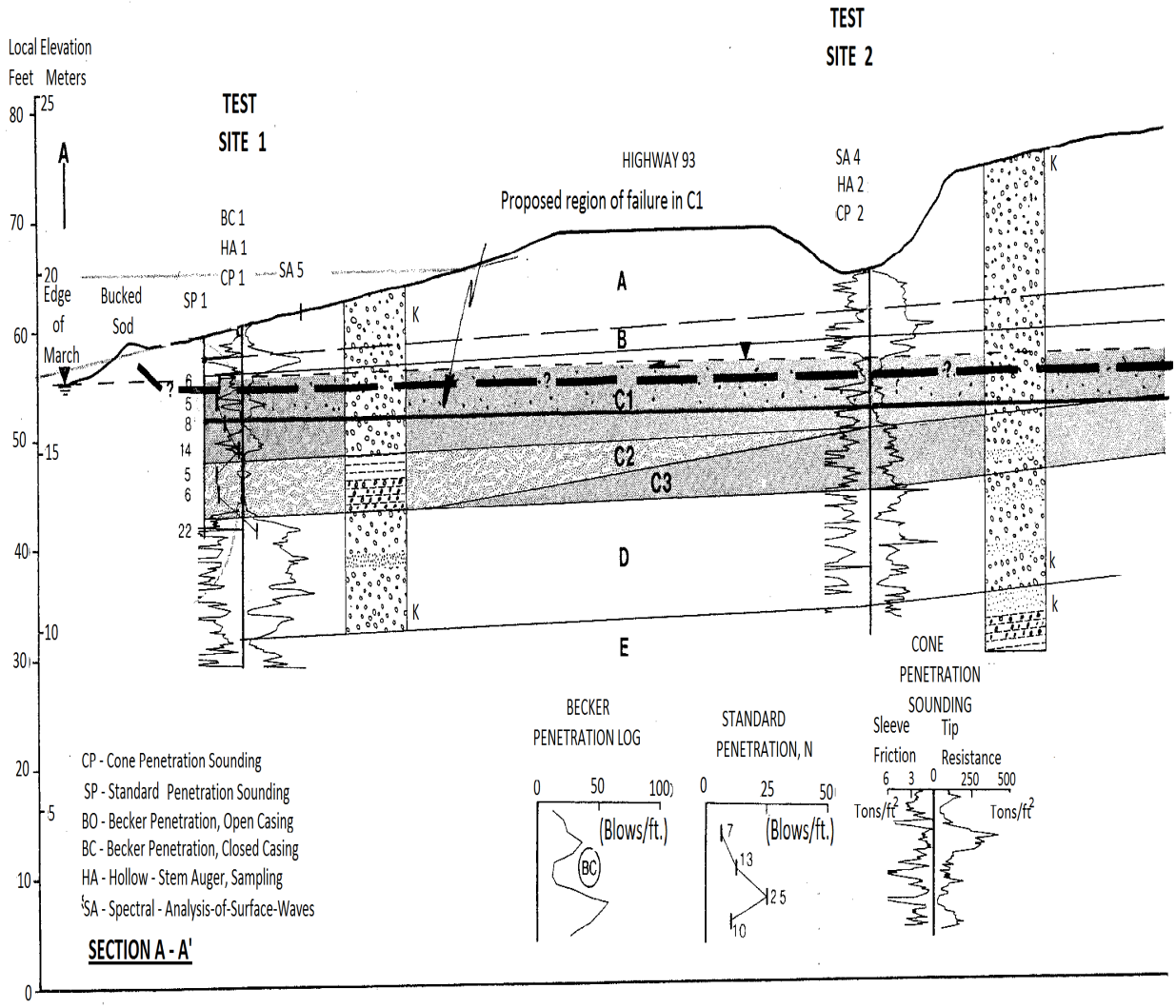


Figure 7.72. Soil profiles at the Whiskey Spring Site, Idaho (after Andrus et al., 1987)

A T_{15} thickness of 2.5 m for unit C1 soil was used in the FLAC models, according to which, the dominate soil period, after liquefaction, was calculated as 0.80 s. Using this as the critical period, seven synthetic motions were selected from the 30 motions generated at this site. The response spectra of the selected motions are shown in Figure 7.73 and the acceleration time histories are shown in Figures 7.74 to 7.80.

PROSHAKE is used to deconvolve the selected motions to the base of the FLAC model, as previously described. The motions developed for the FLAC input and the model results are given in Appendix M.

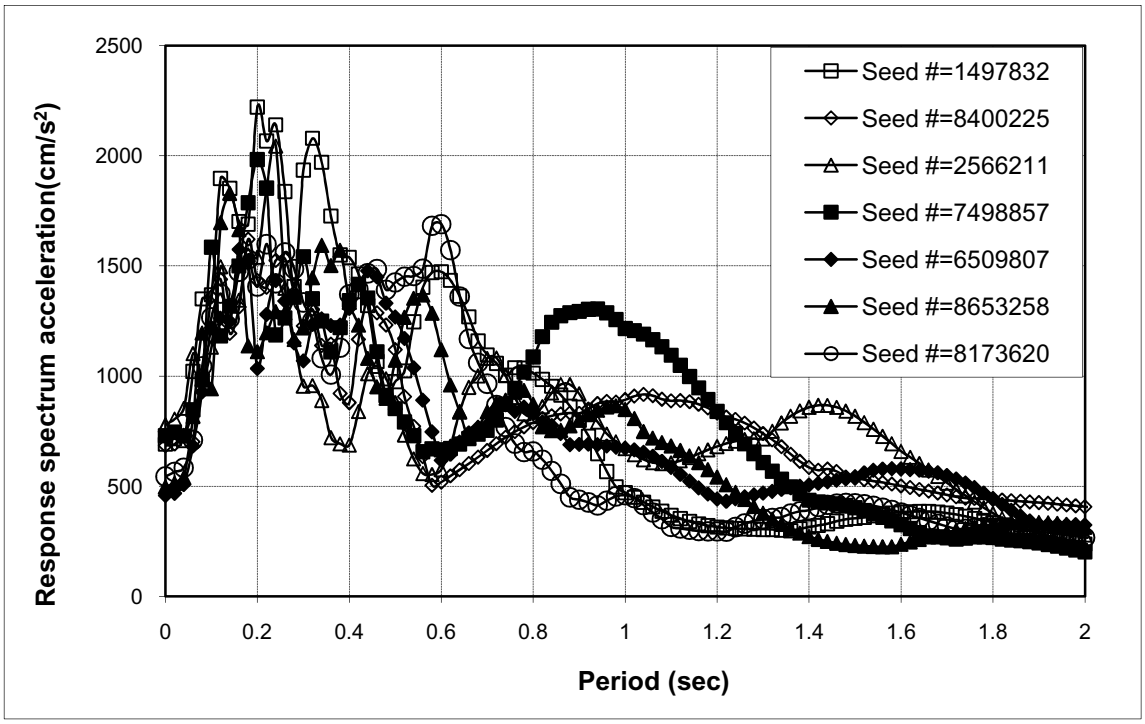


Figure 7.73. Response spectra of seven time histories generated from SMGS for Idaho Whiskey Springs site

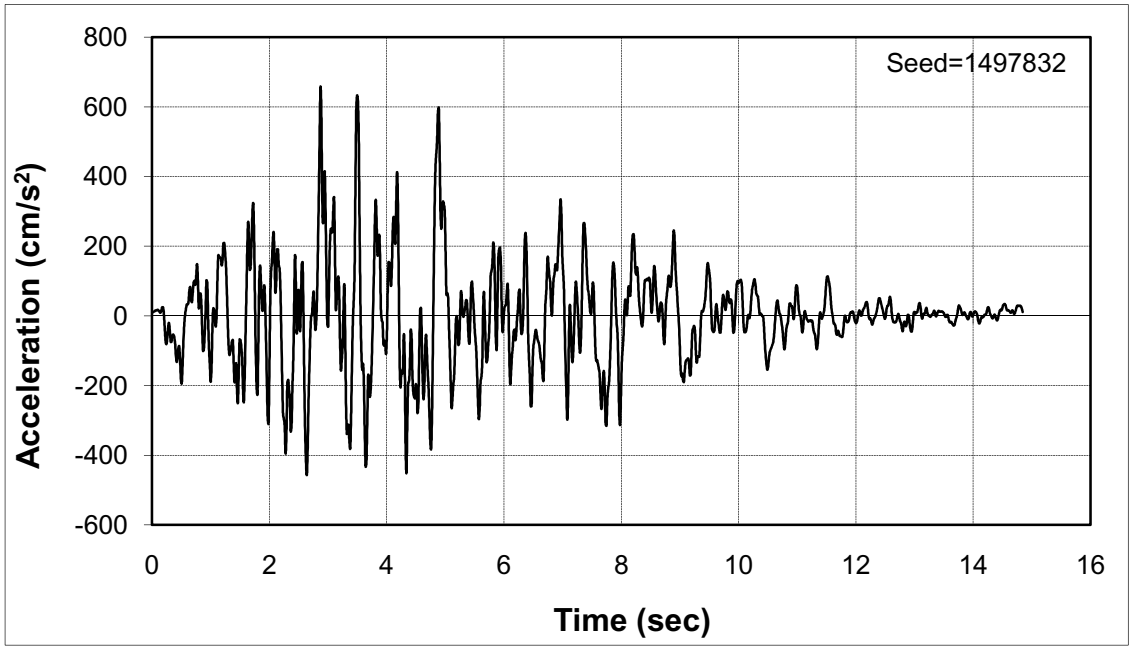


Figure 7.74. Idaho Whiskey Springs site model selected motion 1

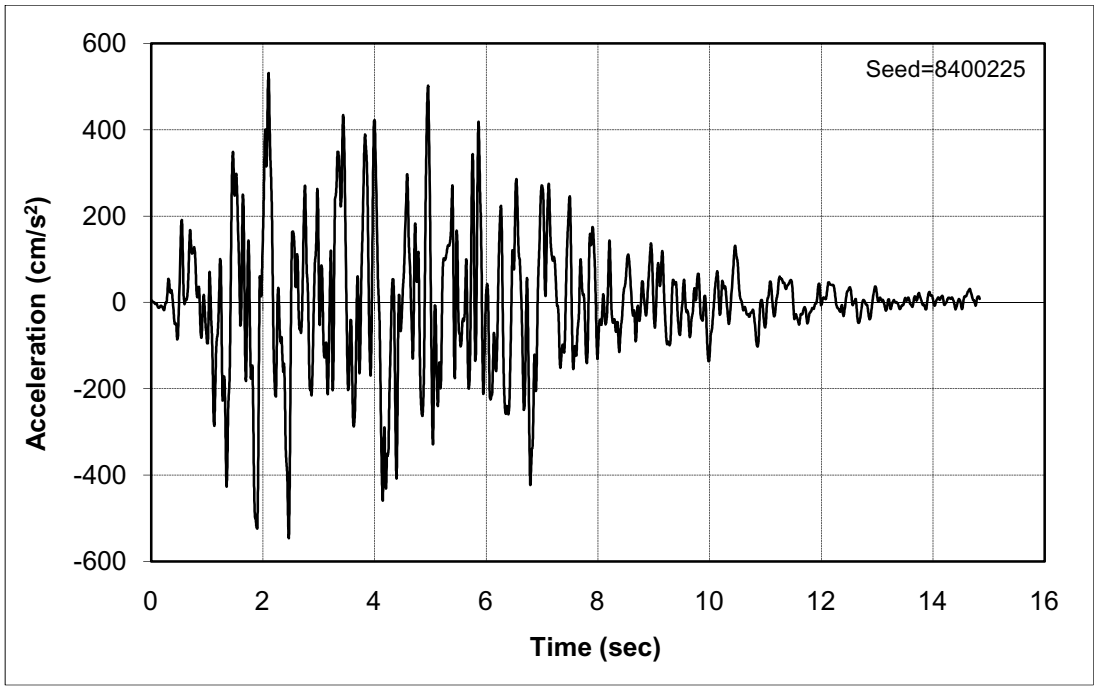


Figure 7.75. Idaho Whiskey Springs site model selected motion 2

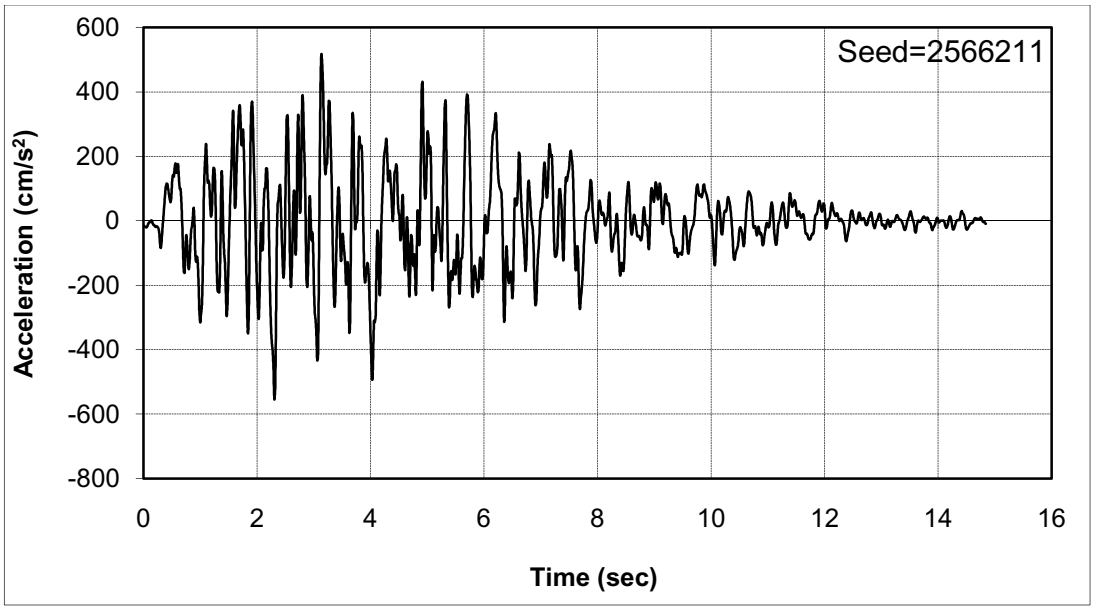


Figure 7.76. Idaho Whiskey Springs site model selected motion 3

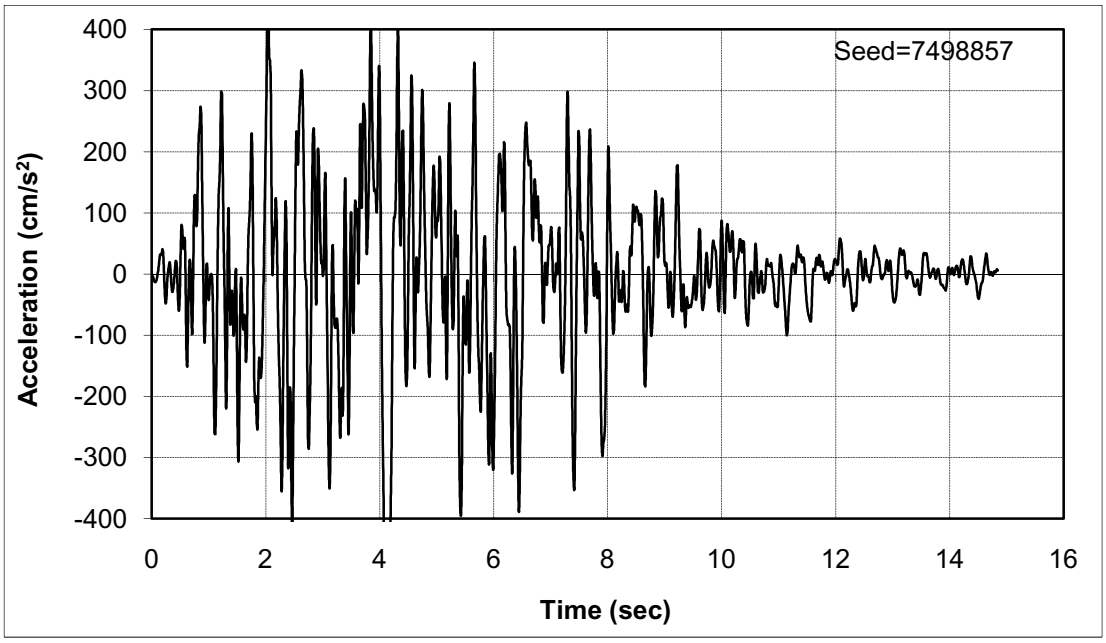


Figure 7.77. Idaho Whiskey Springs site model selected motion 4

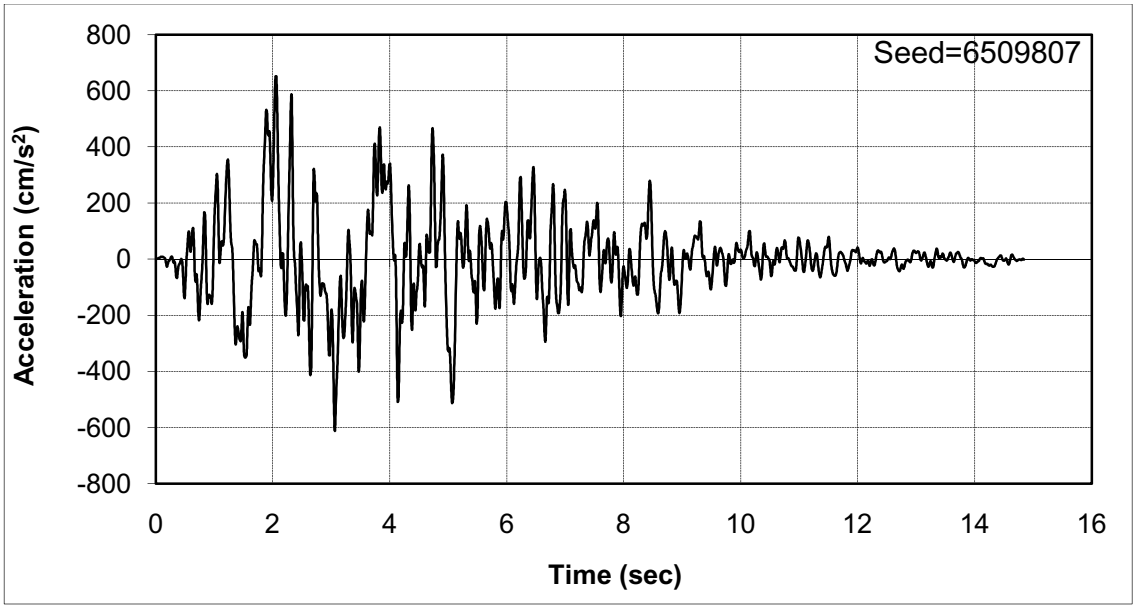


Figure 7.78. Idaho Whiskey Springs site model selected motion 5

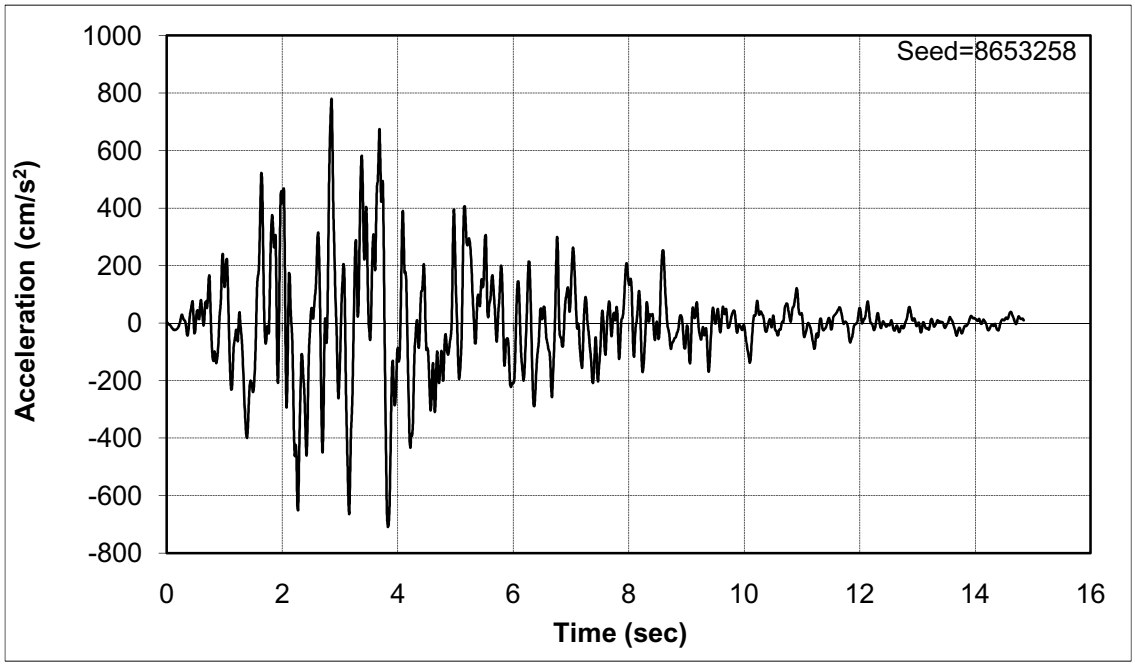


Figure 7.79. Idaho Whiskey Springs site model selected motion 6

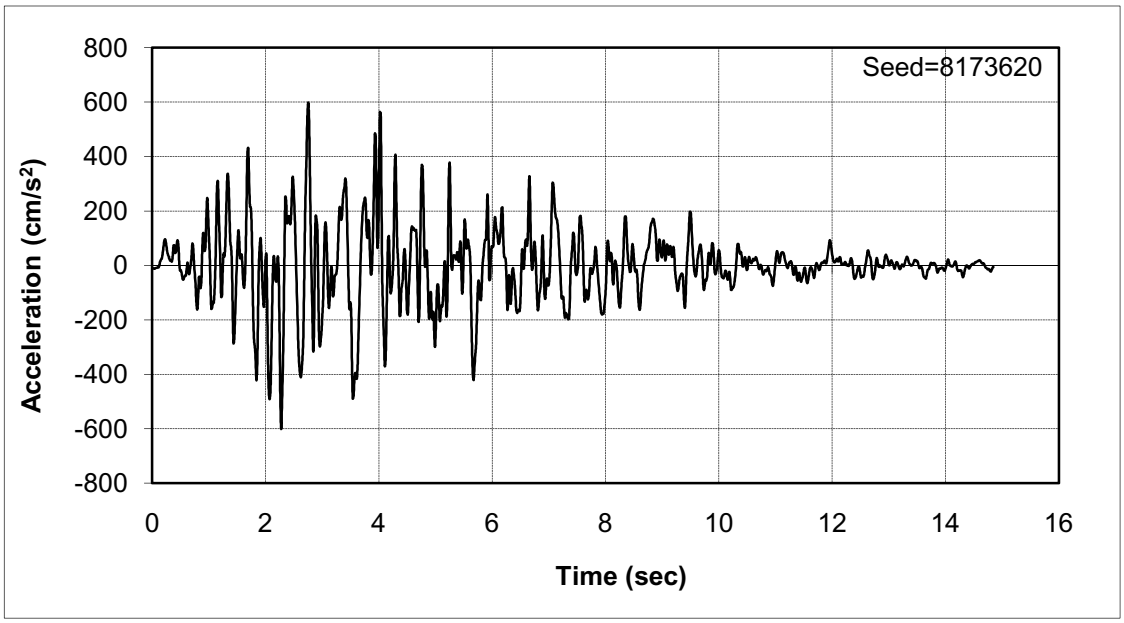


Figure 7.80. Idaho Whiskey Springs site model selected motion 7

The prediction from the FLAC model is compared with the actual lateral spread of 1.0 m. The FLAC model results for residual strength ratios of 0.16, 0.19, 0.20, 0.22 and the deviation from the actual displacement are shown in Table 7.45.

Because the residual strength ratio of 0.20 gave the best results, this value was used in the statistical analyses performed in Chapter 8.

7.14 **Northridge Balboa Site**

The M6.8 Northridge, California earthquake of January 17, 1994 was the largest earthquake to occur in the Los Angeles metropolitan area since the 1971 San Fernando Valley earthquake (Holzer et al., 1999). The location of the earthquake site is shown in Figure 7.81.

The Balboa Boulevard site is on the northern margin of the San Fernando Valley, where a 5 km long complex belt of ground cracks formed in Granada and Mission Hills. The cracks in most of the belt developed in Holocene alluvium on gentle south-sloping surfaces. Many cracks in the eastern third of the belt, however, formed on steep slopes in Miocene and Pliocene marine sediment and Pleistocene alluvium, which is exposed at the surface.

Table 7.45. Lateral spread calculation from FLAC model for residual strength ratio of 0.16, 0.19, 0.20, 0.22.

Residual Strength Ratio	Motion_1	Motion_2	Motion_3	Motion_4	Motion_5	Motion_6	Motion_7	Average	Derivation
0.16	0.82	1.47	1.46	1.48	1.38	1.40	1.49	1.36	1.19
0.19	0.66	1.17	1.2	0.98	1.08	1.10	1.15	1.05	0.22
0.20	0.61	1.13	1.12	0.94	1.00	1.05	1.09	0.99	0.20
0.22	0.58	1.05	1.04	0.85	0.93	0.96	0.99	0.91	0.33

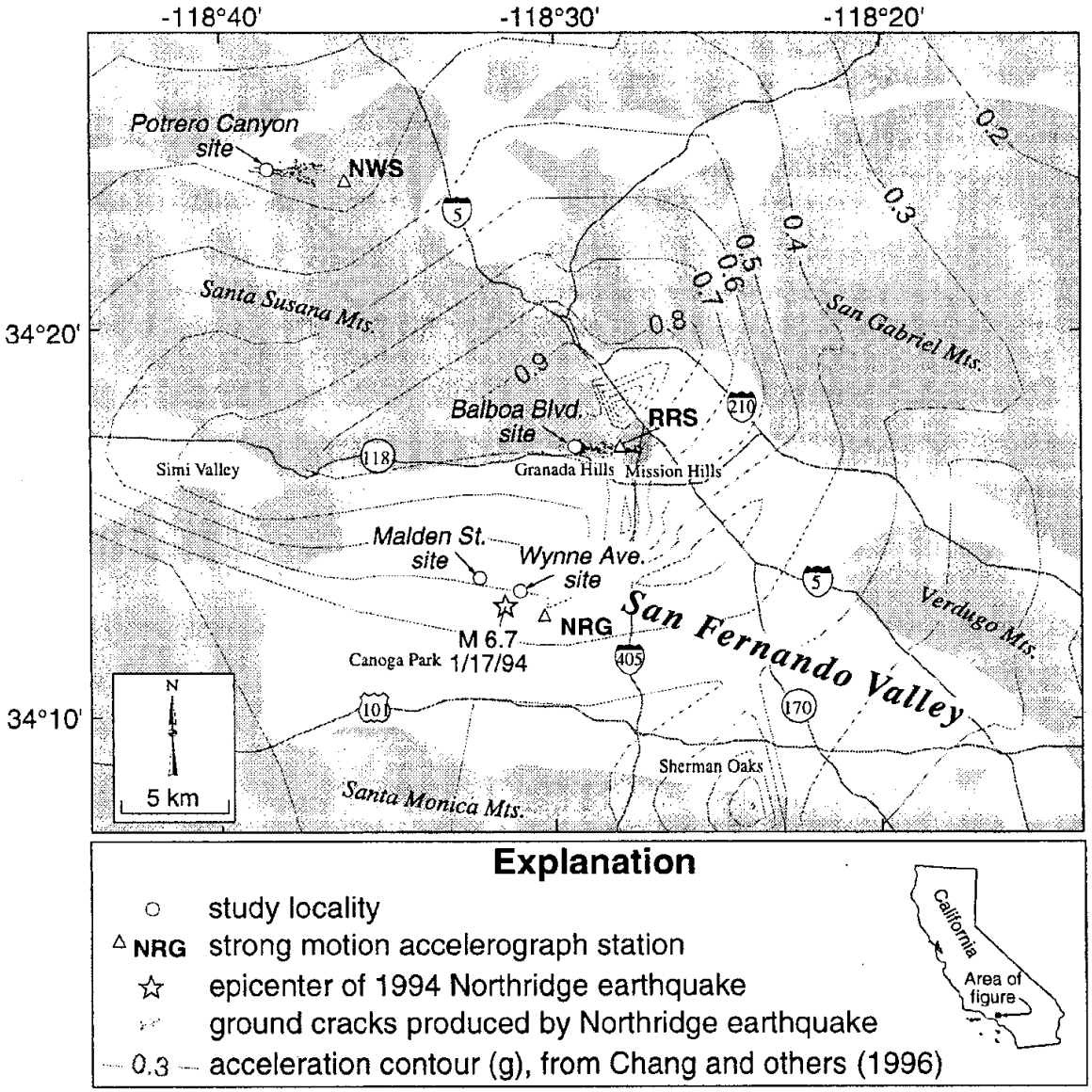


Figure 7.81. Map of sites location (from Chang et al., 1996)

Cracking in the western zone was generally perpendicular to the 1.6% southern regional topographical gradient. Aggregate displacements across the northern and southern margins of the failure zone were each about 0.5 m as computed from street centerline surveys. Horizontal displacements across individual cracks were small, less than a few centimeters (Holzer et al., 1999).

Subsurface exploration was conducted along a north-south 570-m long line in an unnamed alley, 40 m west of Balboa Boulevard, as shown in Figure 7.82. The site is underlain by Holocene silty sand to lean clay that ranges in thickness from approximately 8 to 10 m. The uppermost unit, A, is less than 1 m thick, and consists of fill and reworked sandy silt and lean clay with sand. The upper part of the primary Holocene section, unit B, consists of sheet flood and debris flow deposits; the lower part, unit C, consists of fluvial deposits.

All units are heterogeneous, ranging from clays to silty sands. Both Holocene units, B and C, have average fines (< 75 mm) of about 58%. The part of unit C that was below the water table has an average fines content of 52% and clay content of 18 percent, and does not differ materially from the dry part of C.

The part of unit C below the water table is considered in the model as the lateral spread layer, with a 3m T_{15} thickness, 6m water table, 6m depth to liquefaction layer, 52% fines content, 12 of N_{160} blow count , 0.11mm of D_{50} value and 0.5 m measured lateral spread.

The model will simulate the lateral spread in the north direction. The time history in 22° and 292° directions are downloaded from http://peer.berkeley.edu/ and rotated to the north direction.

Time histories in the 22° direction, 292° direction and calculated rotated motion to north direction are shown in Figure 7.83, Figure 7.84 and Figure 7.85.

PROSHAKE was used to deconvolve the above acceleration time history to the base of the FLAC model, as previously described. The FLAC model input motion and results are given in Appendix N.

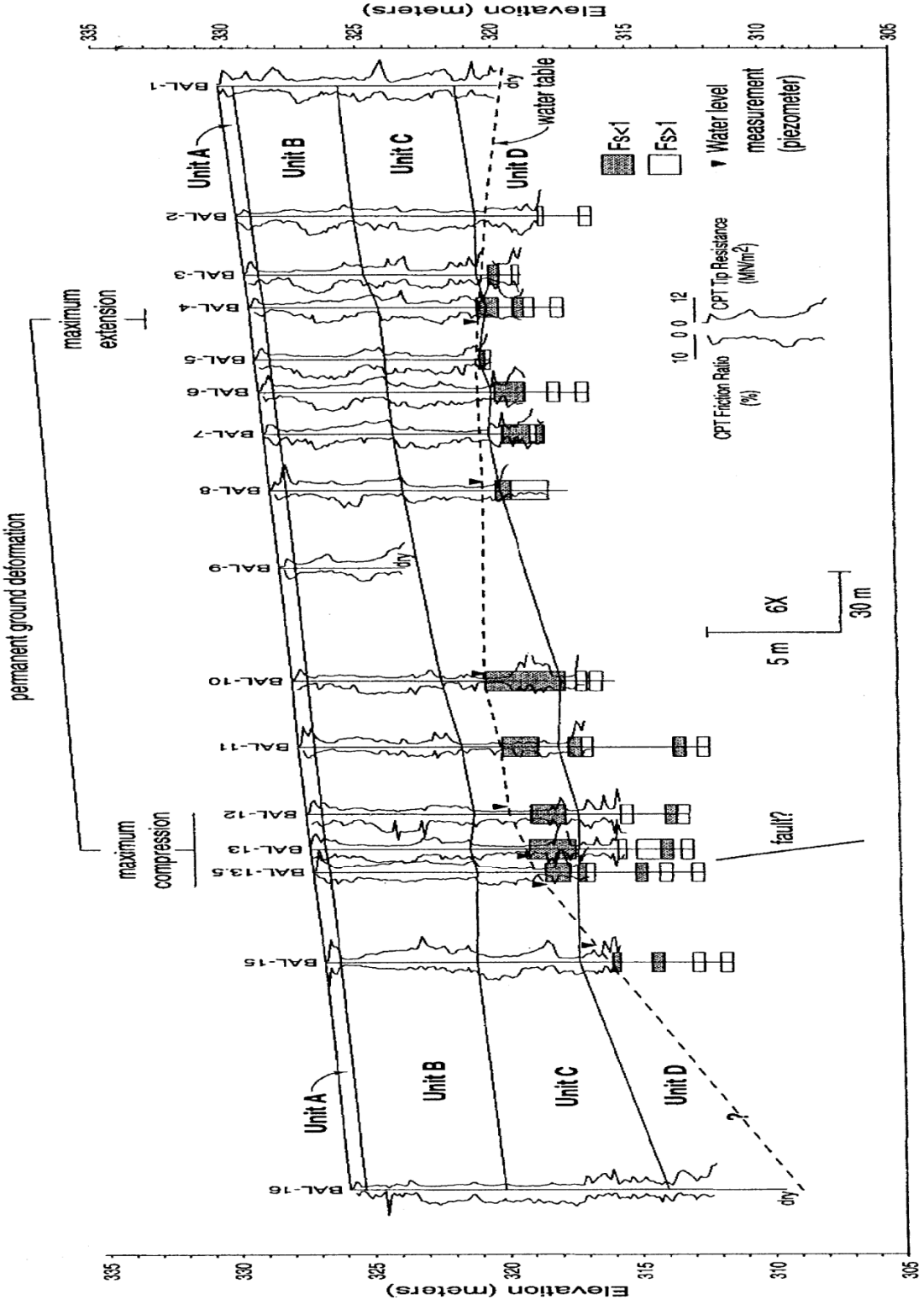


Figure 7.82. Subsurface Cross Section and Liquefaction-Susceptible Intervals of Soil Inferred from CPT and SPT at Northridge Balboa site (from Holzer et al., 1996)

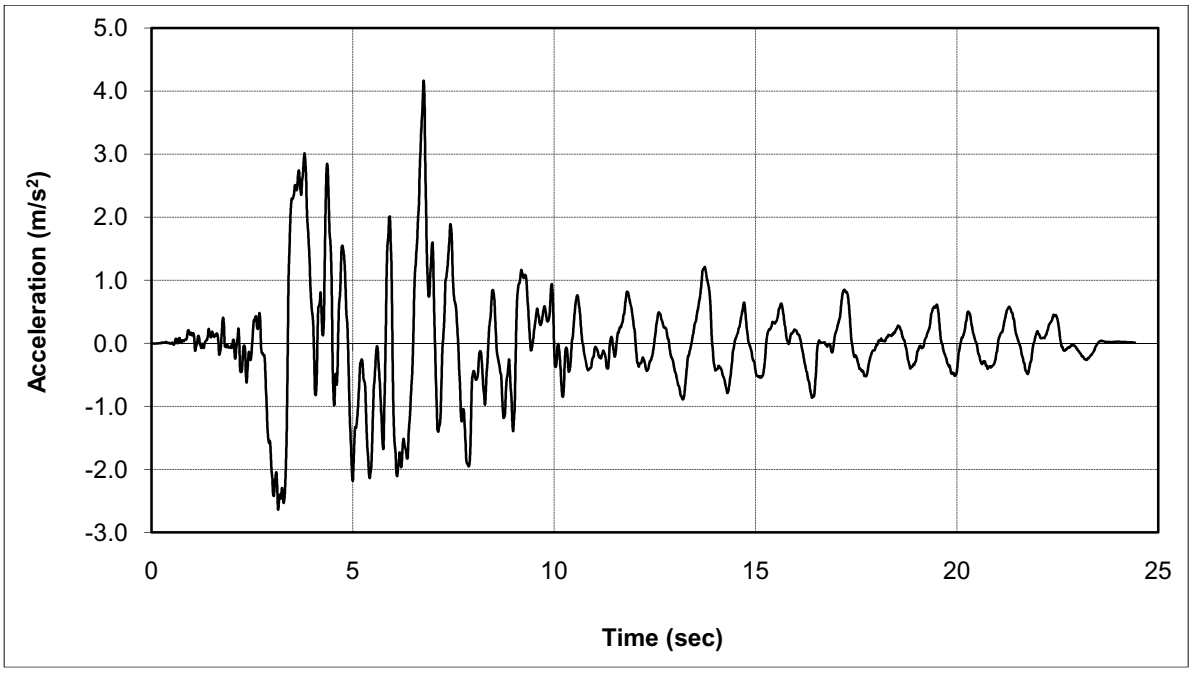


Figure 7.83. Earthquake motion in 22° direction at Northridge Balboa site

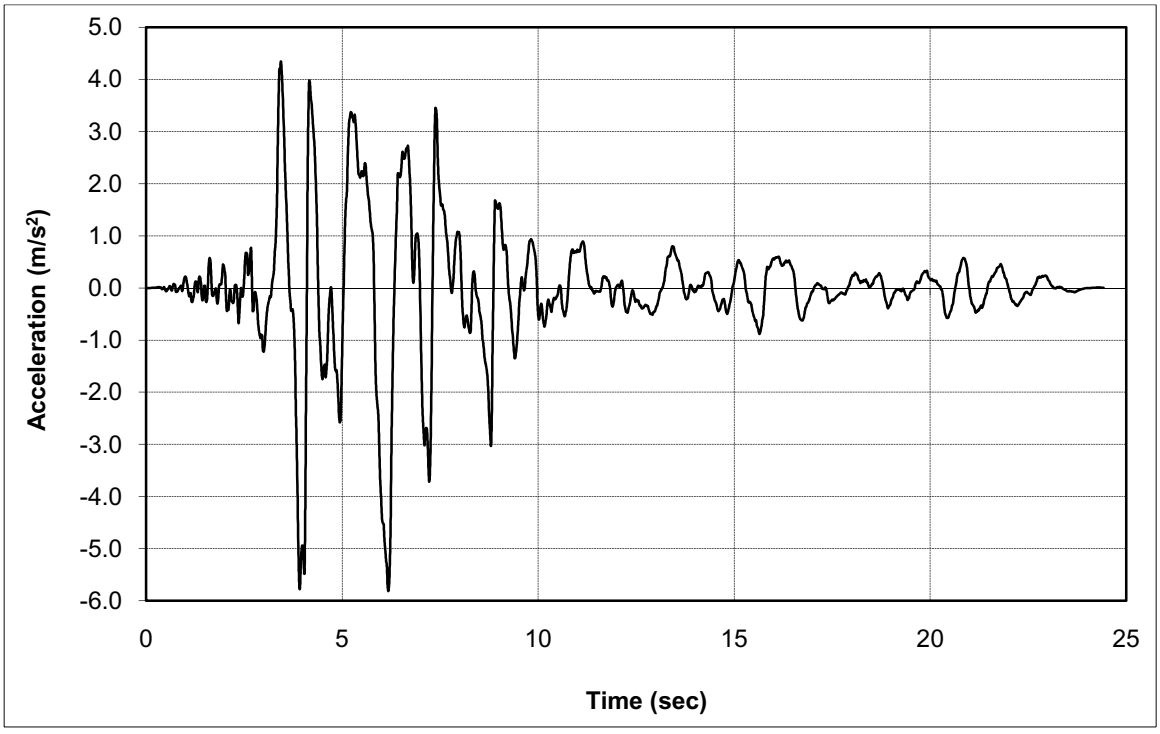


Figure 7.84. Earthquake motion in 292° direction at Northridge Balboa site

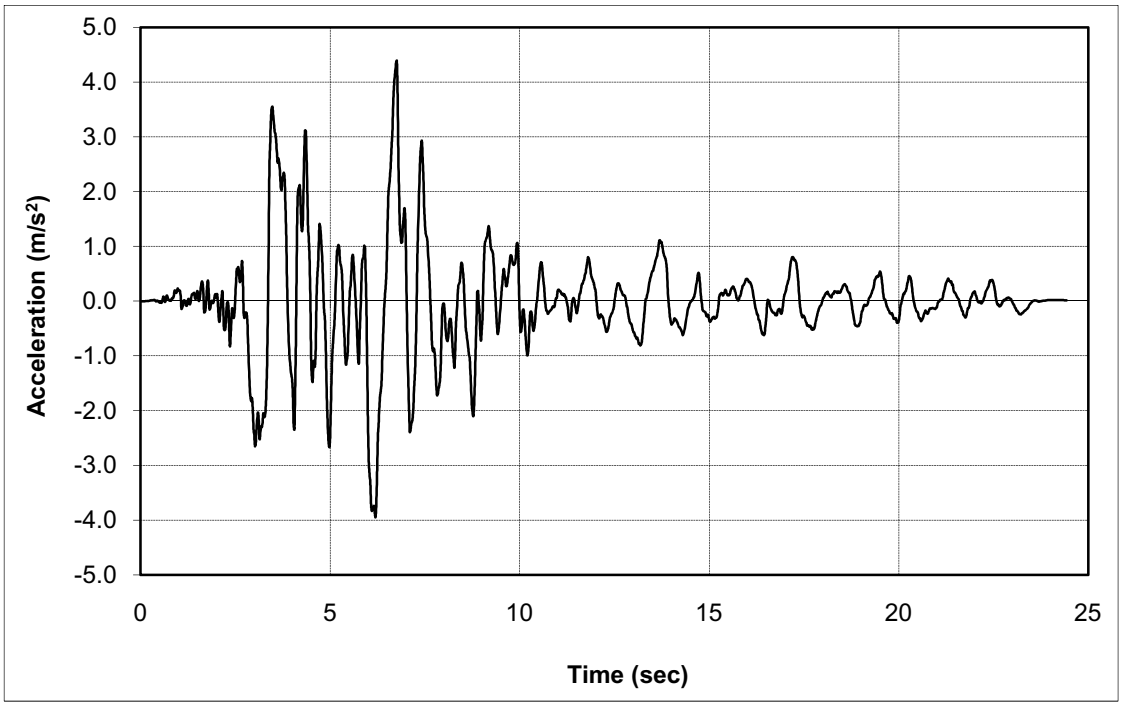


Figure 7.85. Rotated motion in the north direction at Northridge Balboa site

Using the actual soil profile and a trial and error method, the FLAC model was executed until the measured lateral spread of 0.5 m was matched. The simulation results from the FLAC model are shown in Appendix N. Table 7.46 lists the predicted lateral spread by the FLAC model with different residual strength ratios. Because the ratio of 0.16 gives the best results, this was used in the statistical analysis described in Chapter 8.

Table 7.46. Lateral spread prediction by FLAC model at Northridge Balboa site

Residual strength ratio	Predicted lateral spread (m)
0.15	0.42
0.16	0.58
0.17	0.75

7.15 Turkey Degirmenedere without T_{15}

For the Turkey Degirmenedere site, near the boring SPT-DN2 area as shown in Figure 7.62, the observed horizontal displacement from lateral spread was essentially zero (De Den, 1999; Cetin et al., 2004). This was because no T_{15} layer was present at this location. In order to take this into account, this area was modeled without a lateral spread layer. Subsequently, the FLAC model was designed to continually increase the residual strength ratio until the lateral spread was so small that it was insignificant. Surficial soils at this site consist of artificial fill comprised of brown gravelly sand to red silty clay ranging in thickness from 0.5 to 1 m. This fill layer is underlain by a thick silty sand layer with occasional gravelly sand and silty clay mixtures.

The sample from SPT-DN2 shows the SPT-N of 13 and the $(N_1)_{60}$ of 24. Considering the artificial fill on the top layer of the site, a SPT blow count of 18 was used in the modeling for the liquefaction layer to take into account the artificial fill soft layer on the surface. The fines content of the material is generally in the range of 11 to 14%, for which an average of 12% is used for the modeling.

Except for the revised soil properties mentioned above, the other unchanged soil properties and same earthquake motions are used for the Turkey Degirmenedere site case with lateral spread layer. Following the same procedure as in the Turkey Degirmenedere site with lateral spread layer, the residual strength ratio of 0.50 is obtained to achieve very small or no lateral displacement. The simulation results from the FLAC model are given in Appendix O.

Thus, the residual strength ratio of 0.5 was used for statistical analysis performed in Chapter 8.

7.16 Turkey, Sapanca Hotel Site

The 1999 M7.4 Kocaeli, Turkey Earthquake struck Lake Sapanca, which is located approximately 20 km east of the eastern end of Izmit Bay, and 10 km southwest of Adapazari, Turkey. This site was added to the analyses, because it is predominately a gravelly site that underwent lateral spread. This earthquake produced various ground effects along the shore, including offshore landslides, liquefaction, lateral spreads and subsidence. A prominent lateral spread happened at the Sapanca Hotel site which is located on the south shore of Sapanca Lake, 3.5 km south from the surface fault rupture which was submerged beneath the northern part of the lake. The Sapanca Hotel site extends 0.25 km along the southern shoreline. The hotel and swimming pool are located by the lakeshore, as shown in Figure 7.86 (De Den, 1999).

The displacement for Wall 1 was 121.2 cm, while the combined displacement of Wall 2, for the present and previous earthquake, is 227.8 cm. The total displacement using ground fissures is approximately 150 cm. A ground slope of 1.5 percent was calculated for most of the site with a 2.5% slope from SPT-SH4 to the shoreline (De Den, 1999**)**. An average of 2% slope was used for the FLAC modeling.

The soil profile shows that the layer with the thickness of 11 m below ground water is potentially liquefiable. Thus, in the FLAC model, the 11 m layer below the 1 m ground water depth was used as the lateral spread layer. The average blow count of 8 and average D_{50} of 4mm were applied for the FLAC model according to the soil properties. The nearest strong motion sensor to the site (Station SKR) was located approximately 10 km away in Adapazari as shown in Figure 7.86 (http://peer.berkeley.edu/publications/turkey/adapazari/phase4/sapanca/index.html).

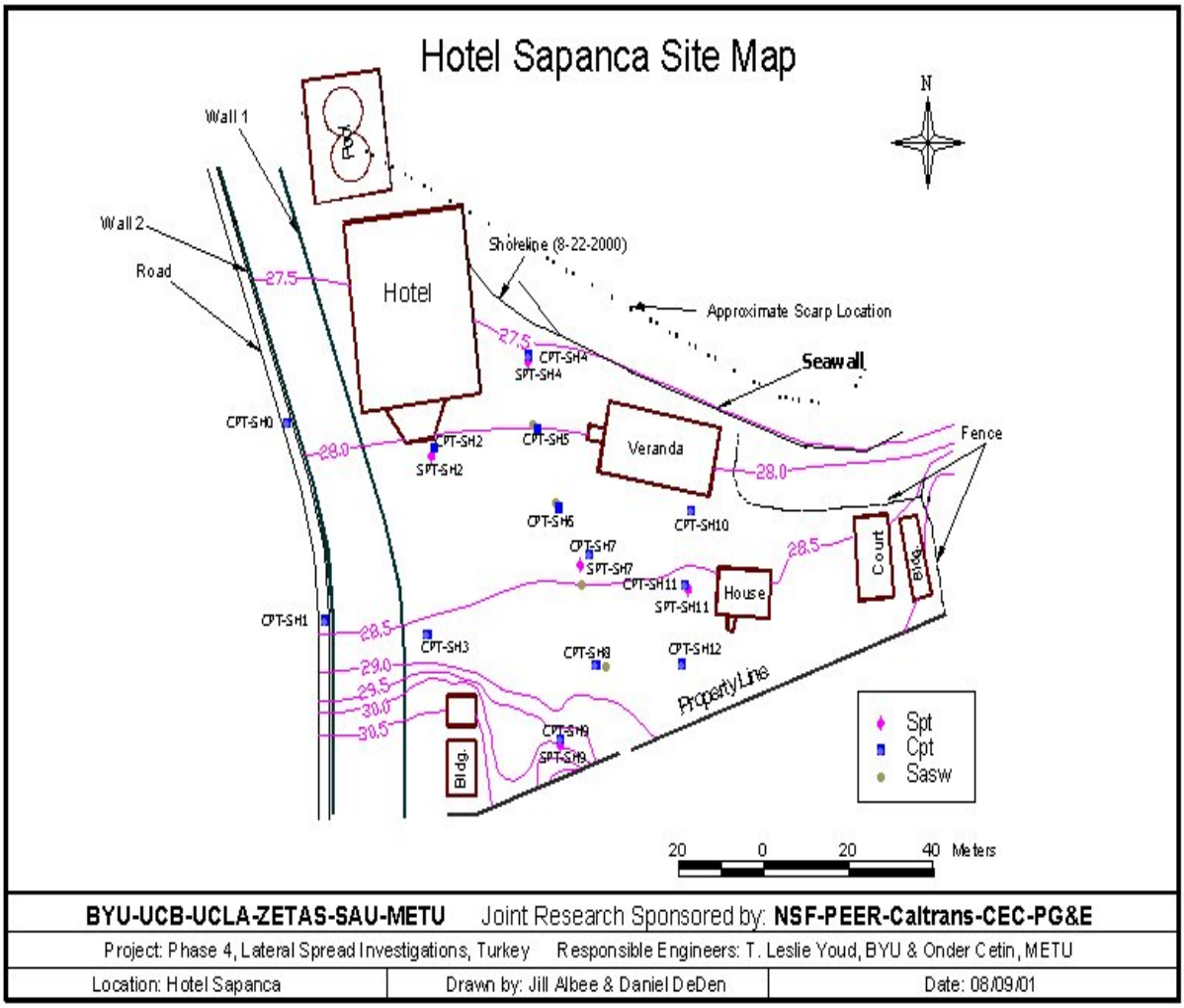


Figure 7.86. Map of Hotel Sapanca site with elevations and soil exploration locations

It measured a maximum acceleration of approximately 0.41g in the east-west direction. However, The SKR recording is about 3.7 km north of the fault trace. The Sapanca Hotel is about the same distance south of the fault trace in the middle of Lake Sapanca, as shown in Figure 7.87. The SKR recording and the Sapanca Hotel are about the same distance from the fault, but on opposite sides. Thus, it was assumed that the amplitude and duration of strong motion is about the same at both sites and no scaling was applied to the time history. The SKR motion is downloaded from http://peer.berkeley.edu/ as shown in Figure 7.88.

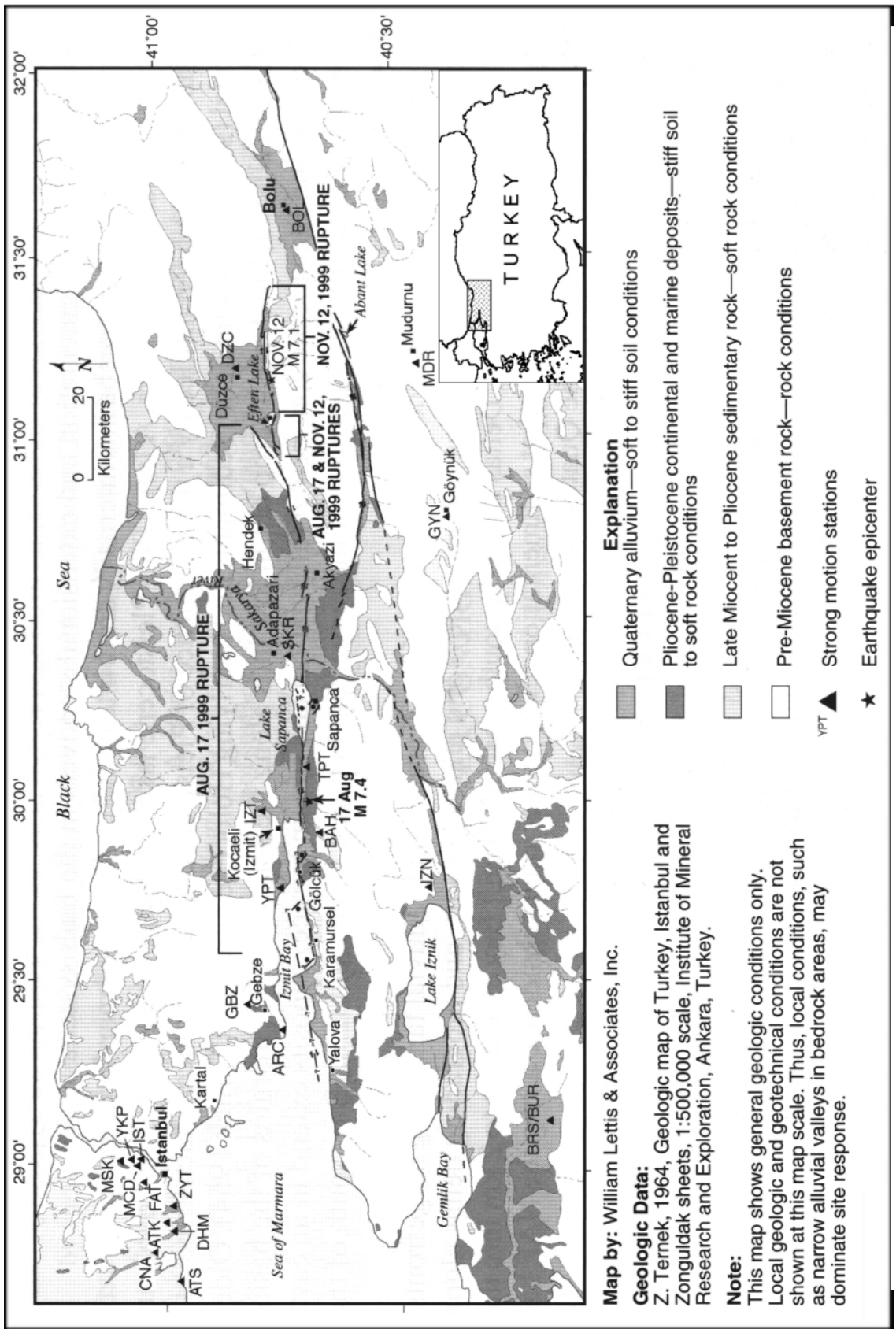


Figure 7.87. Map of Adapazari and Lake Sapanca region with locations of lateral spread, mapped fault rupture trace, and Strong Motion Station SKR (Lettis et al., 2000)

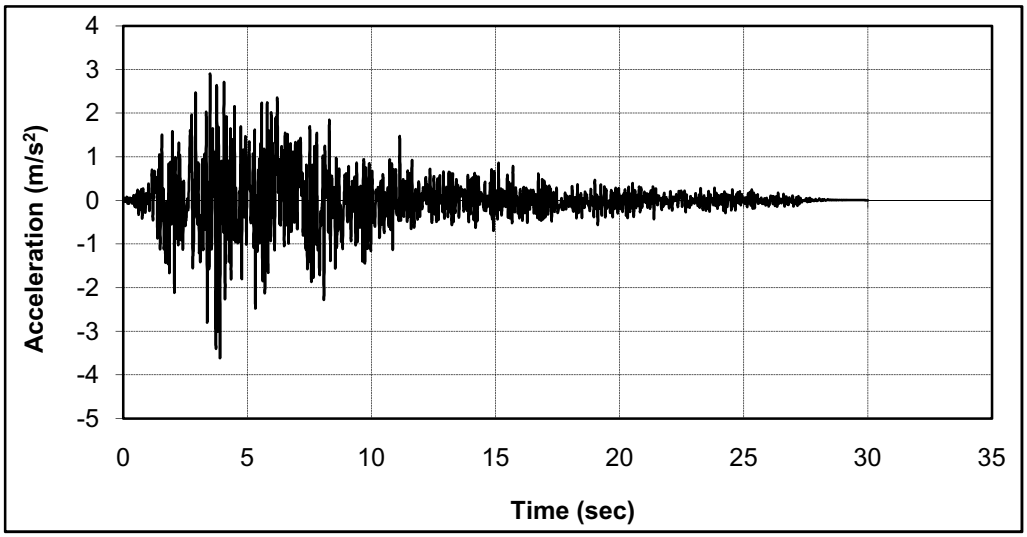


Figure 7.88. SKR motion downloaded for Sapanca Hotel site

PROSHAKE was used to deconvolve the motion to the base of the FLAC model, as previously discussed. The developed FLAC model input motions and results are given in Appendix P. The trial and error method is used to match the measure displacements. The FLAC model is design according to the actual soil profile.

The simulation results from the FLAC model with a residual strength ratio of 0.24, 0.25 and 0.26 are list in Table 7.47. The residual strength ratio of 0.25 produced the same lateral spread of 150 cm, as was recorded at this site. The simulation results from FLAC model are given in Appendix P. Thus, the residual strength ratio of 0.25 was used for the statistical analysis in Chapter 8.

Table 7.47. Lateral spread prediction by FLAC model at Turkey, Sapanca Hotel site

Residual strength radio	Predicted lateral spread (m)
0.24	0.16
0.25	0.15
0.26	0.13

CHAPTER 8

MODEL RESULTS AND ANALYSIS

8.1 Model Analysis Results

This section explores the possible correlation between the back-calculated values of S_r/σ_v' from Chapter 7 and the tabulated, site-specific soil properties, i.e., F_{15}, D_{5015}, average $(N_1)_{60}$, $(N_1)_{60CS}$ in the T_{15} layer from the respective cases histories shown in Table 8.1. The F_{15}, D_{5015}, and T_{15} layer properties were calculated using the methods described in Bartlett and Youd (1991; 1992). If correlation exists between these factors, regression equations will be developed to explain this correlation. Such equations will allow practicing engineers to estimate S_r/σ_v' ratios from standard geotechnical data for application to future lateral spread evaluations.

A total of sixteen case histories were back-analyzed using the developed FLAC modeling approach and the previously described procedures. The required input for the FLAC modeling for each case history consisted of: (1) ground water depth, (2) soil thickness above the T_{15} layer, (3) thickness of the T_{15} layer, ground slope, S, or free face ratio, W. The back-calculated soil parameters for each history study consist of the ratio of residual strength to residual shear modulus (S_r/G_r) and the ratio of residual strength to effective vertical stress (S_r/σ_v') for the T_{15} layer.

Table 8.1. Summary of model result, soil and earthquake parameters from case history data set.

Site & Model type	GW Depth (m)	TOP (m)	T_{15} (m)	D_{5015} (mm)	F_{15} (%)	Avg. $(N_1)_{60}$	Sr/Gr (kPa/kPa)	$(N_1)_{60CS}$	S_r/σ_v' (kPa/kPa)	M (M_w)	R (km)
Niigata Bandai, free face	0.9	0.9	6.0	0.27	9.3	8.5	0.045	9.2	0.065	7.5	21
Niigata Hotel, ground slope	1.2	2.2	12.0	0.27	7.0	8.6	0.045	8.8	0.085	7.5	21
Niigata Railway, ground slope	2.5	2.6	12.0	0.35	8.3	10.1	0.040	10.5	0.084	7.5	21
Niigata Showa, free face	0.9	1.0	4.0	0.12	31.0	6.5	0.032	12.3	0.090	7.5	21
Noshiro N-4 Section, ground slope	2.3	2.8	4.0	0.35	2.0	11.2	0.035	11.2	0.030	7.7	27
Noshiro S-7 Section, ground slope	1.7	1.8	4.7	0.35	3.8	7.6	0.055	7.6	0.030	7.7	27
San Fernando Juvenile Hall, ground	5.7	5.8	4.0	0.06	62.0	8.8	0.015	18.0	0.130	6.4	0.2
San Fernando, Jensen Filtration	5.0	5.2	5.1	0.08	47.0	9.2	0.015	17.0	0.060	6.4	0.5
Imperial Valley, Heber Road, free	1.6	1.6	8.0	0.12	20.0	5.3	0.045	9.0	0.080	6.6	1.6
Imperial Valley, River Park, ground	2.0	2.0	2.0	0.07	45.0	7.0	0.020	15.0	0.150	6.6	5
Turkey, Degirmenedere , ground	2.0	2.0	1.0	2.90	20.0	11.0	0.020	15.0	0.160	7.4	0.3
Wildlife, free face	3.0	3.0	3.0	0.08	32.5	8.0	0.025	14.0	0.210	6.6	28
Idaho, Whiskey Springs, ground	3.0	3.0	2.5	3.00	24.5	10.4	0.016	15.7	0.200	6.9	2
Northridge, Balboa , ground slope	6.0	6.0	3.0	0.11	35.0	11.5	0.005	21.0	0.160	6.7	7.5
Turkey, Degirmenedere without T_{15},	2.0	2.0	0.0	2.90	11.0	17.0	0.010	19.0	0.500	7.4	0.3
*Turkey, Sapanca Hotel, ground	1.0	1.0	10.0	4.00	4.0	8.0	0.050	8.0	0.250	7.4	3.7

*added later

However, as discussed in Chapter 3, a relationship was developed that allows S_r/G_r to be estimated from the $(N_1)_{60}$ value at a given case history site. Thus, only the S_r/σ_v' ratio required back-calculation.

The required earthquake parameters for the analyses consisted of earthquake magnitude (M), distance of site to earthquake source (R) and an acceleration time history for the candidate site for the FLAC analyses. As discussed in Chapter 7, actual acceleration time histories were used, when available at the case history site; otherwise, synthetic time histories were generated and selected according to the methods and criteria discussed in Chapter 3. Once S_r/σ_v' ratios had been back-calculated, these ratio were introduced as the dependent variable in regression analyses to see if they were correlated with soil properties and other factors as explained in the following paragraphs.

All the above-mentioned soil and earthquake properties are tabulated in Table 8.1 for the regression analysis.

8.2 Regression Analysis of Model Analysis Results

The back-calculated $S_r/\square_v$' values from the FLAC modeling for each case history were obtained in Chapter 7. Because the FLAC models developed in Chapter 7 already included ground surface topography, depth to the top of the T_{15} layer and the thickness of the T_{15} layer when developing the FLAC model at each case history site, the back-calculated S_r/σ_v' values already include the influence of these topographical and geometrical factors; hence, they are not considered in the following regression analysis. The influence of other soil factors, such as average fines content of the T_{15} layer, average of $(N_1)_{60}$ of the T_{15} layer and the average equivalent clean sand blow count for the T_{15} layer, are not directly present in the back-calculated values of S_r/σ_v'; thus, there should exist some correlation between these soil factors and S_r/σ_v', if such factors truly influence lateral spread displacement as suggested by Bartlett and Youd (1991, 1992).

To explore which factors have the most correlation and can be used to predict S_r/σ_v', exploratory regression analyses were performed as shown from Figures 8.1 to 8.9.

Of the soils factors shown in these plots, the average clean sand $(N_1)_{60CS}$, the average $(N_1)_{60}$ value and the average D_{50} value in the T_{15} layer are reasonably correlated with the back-calculated residual strength ratio. (The distance to the earthquake source, R, also shows some correlation with S_r/σ_v'; however, this effect has already been incorporated in developing the strong motion for the FLAC analyses and is not further considered.)

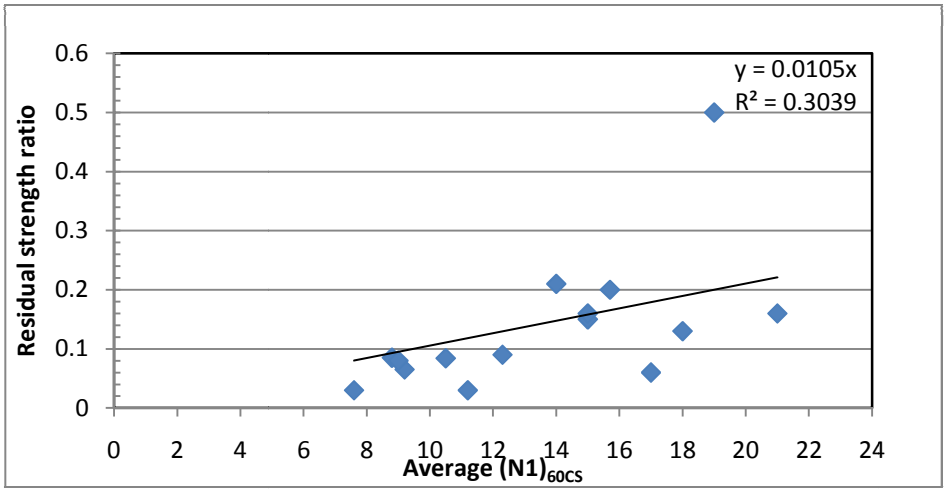


Figure 8.1. Relationship between residual strength ratio and average $(N_1)_{60CS}$ in the T_{15} layer

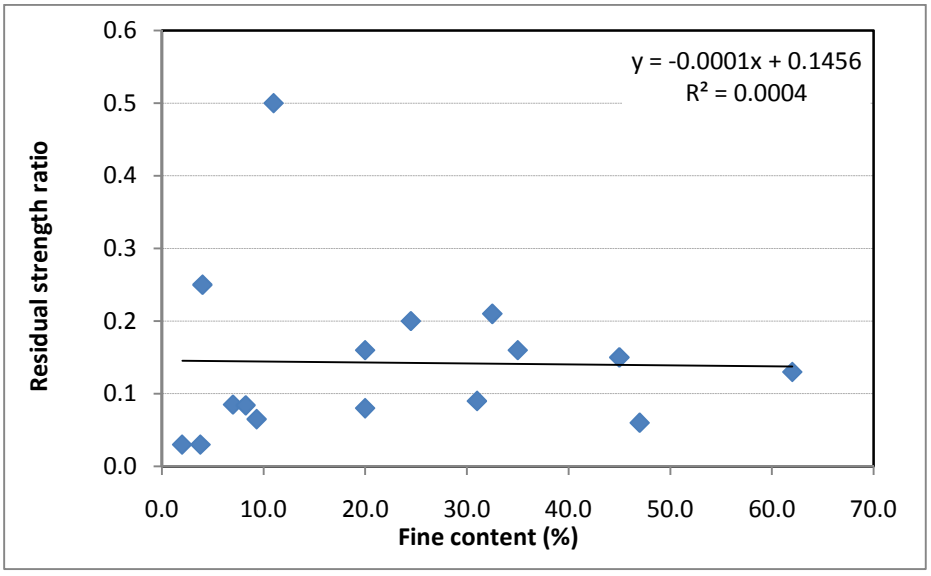


Figure 8.2. Relationship between residual strength ratio and average fines content in the T_{15} layer.

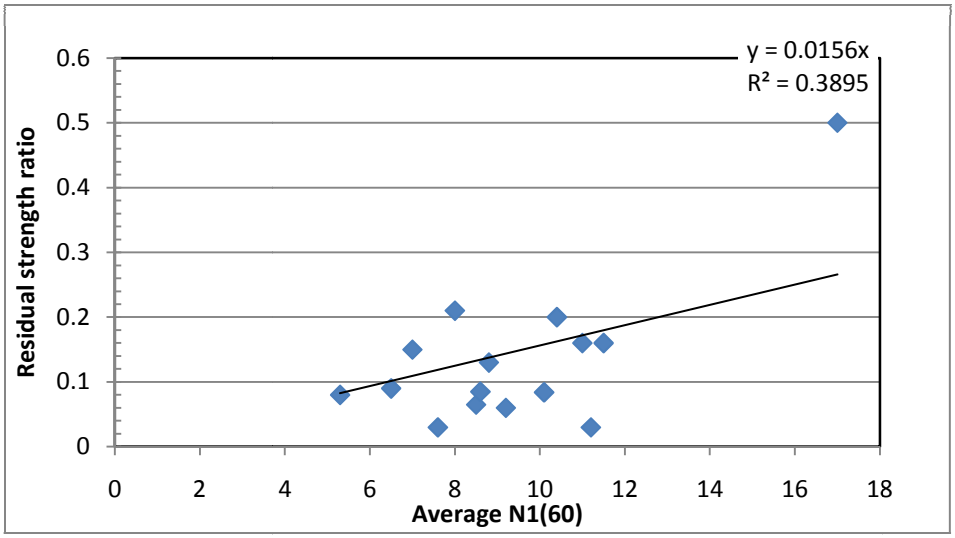


Figure 8.3. Relationship between residual strength ratio and the $(N_1)_{60}$ clean sand in the T_{15} layer.

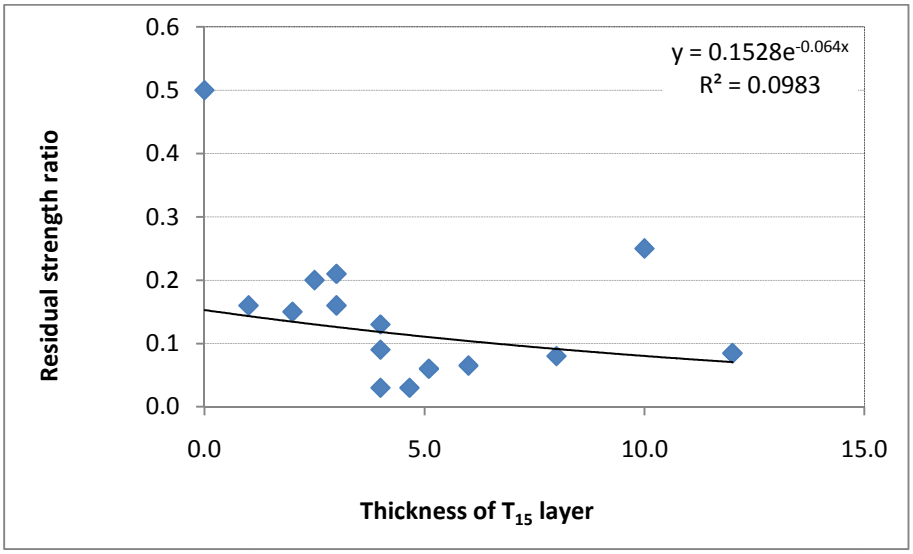


Figure 8.4. Relationship between residual strength ratio and T_{15} layer thickness

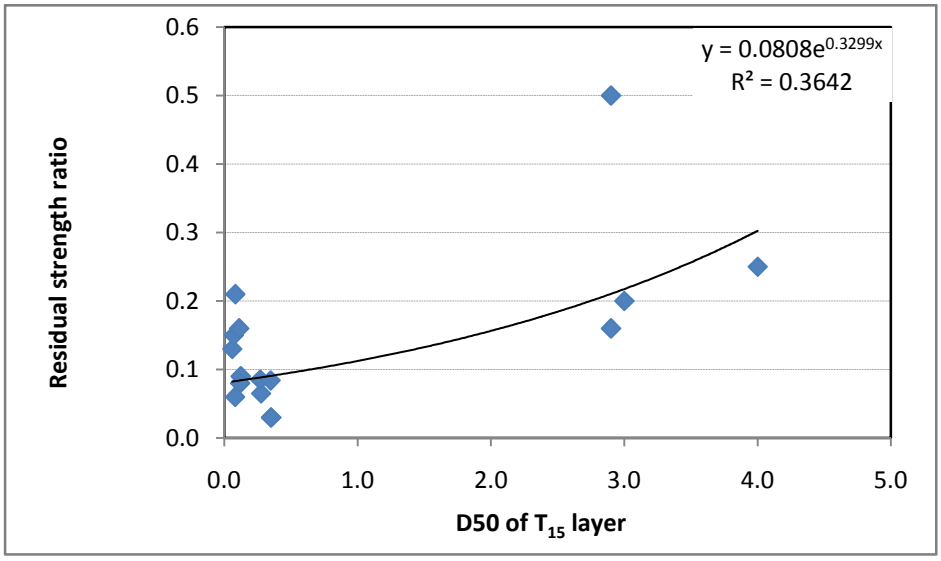


Figure 8.5. Relationship between residual strength ratio and the average D_{5015} in the T15 layer.

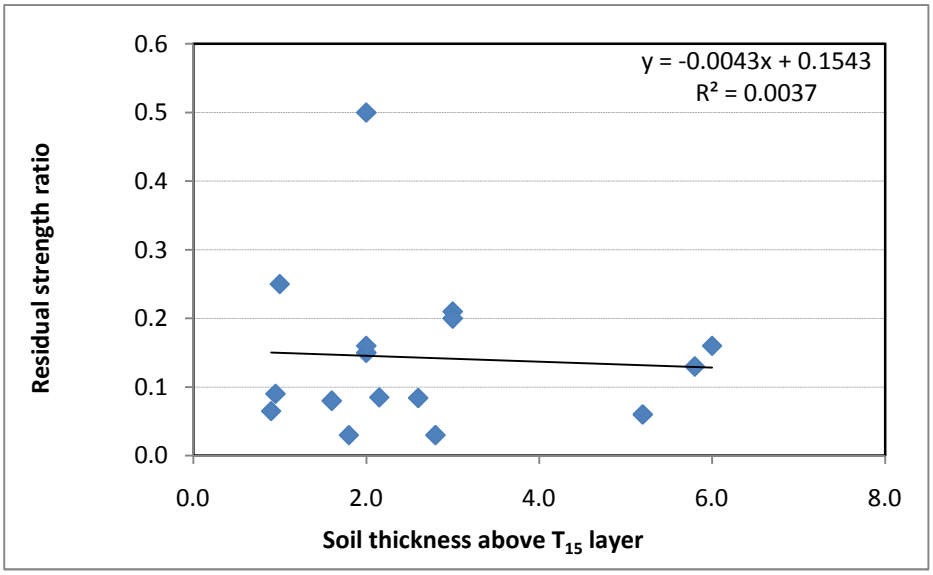


Figure 8.6. Relationship between residual strength ratio and soil thickness above the T_{15} layer

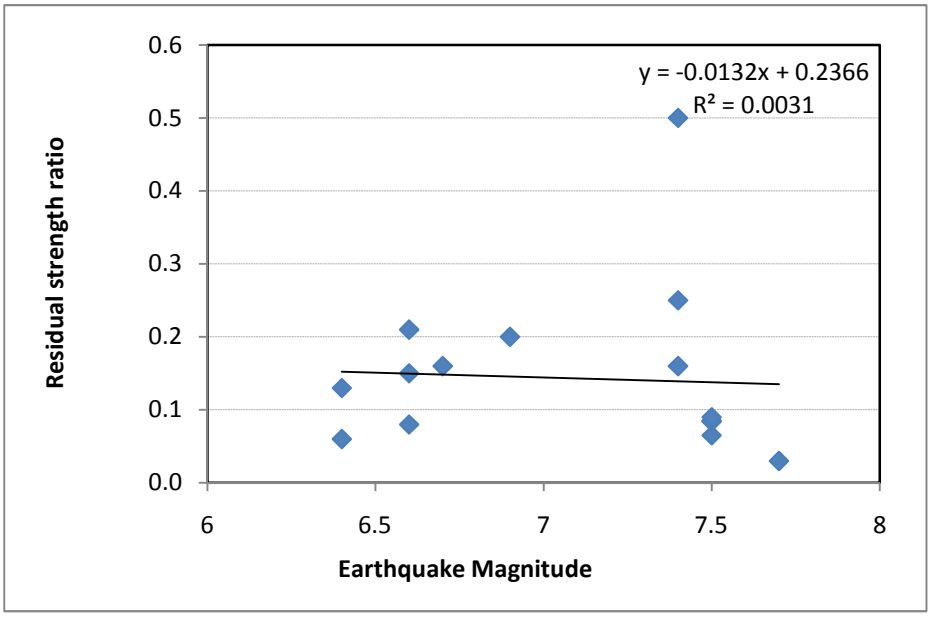


Figure 8.7. Relationship between residual strength ratio and earthquake magnitude

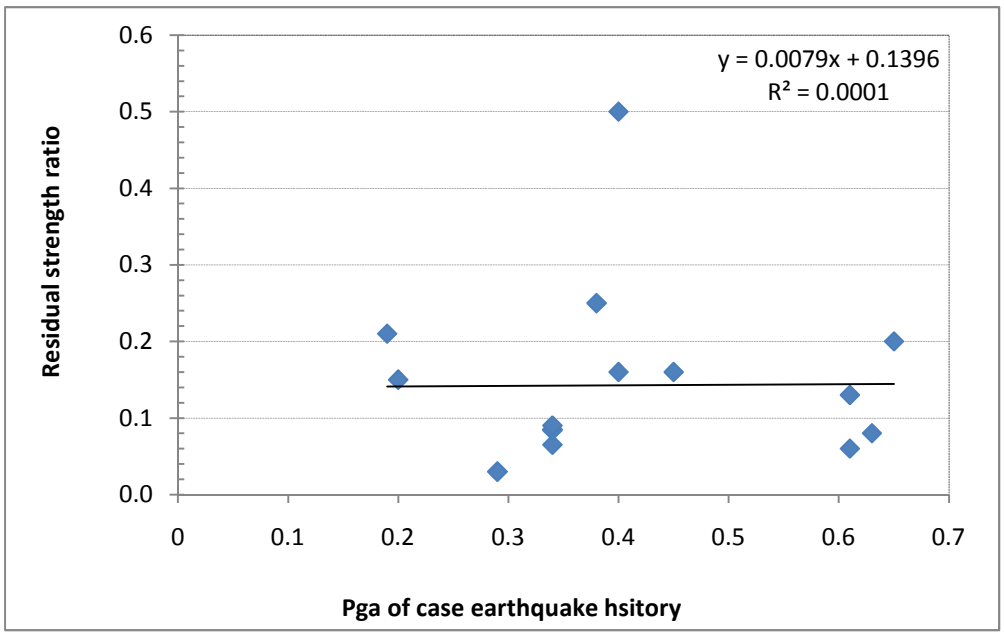


Figure 8.8. Relationship between residual strength ratio and earthquake peak ground acceleration

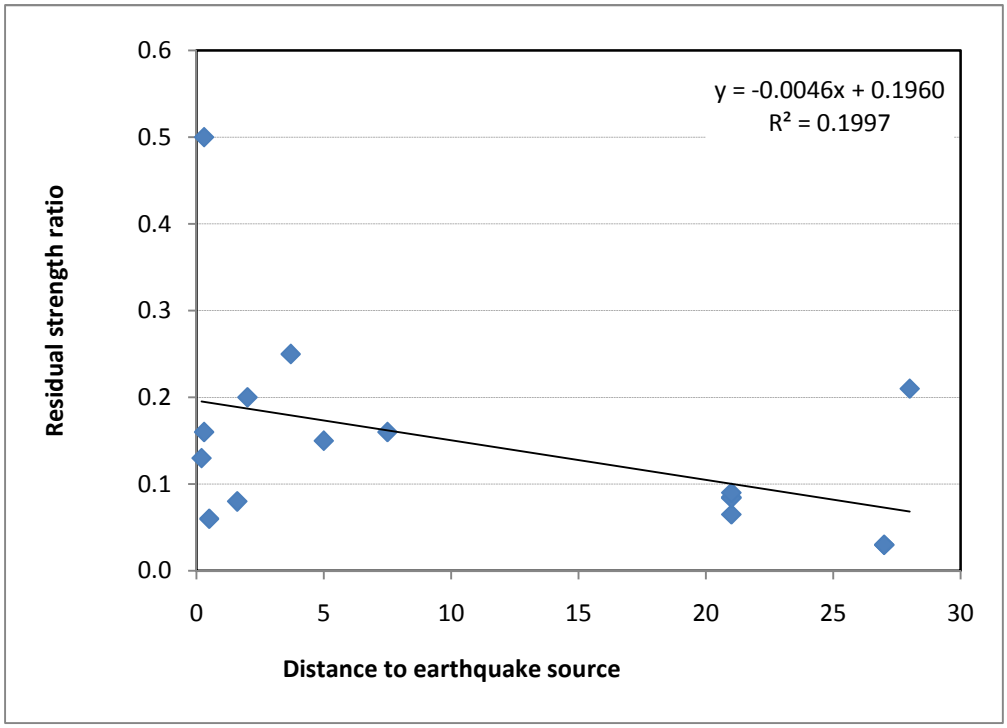


Figure 8.9. Relationship between residual strength ratio and distance to earthquake source

Many combinations of soil factors and different functional forms were explored to establish a regression relationship with S_r/σ_v'. The relationship with a relatively high coefficient of determination, R^2, was to express S_r/σ_v' as a function of $(N_1)_{60CS}$ and D_{5015}. This model is shown below and incorporates the influence: (1) increase density of the soil, (2) fines content of the soil by the clean sand adjustment and (3) mean grain size. The data used to develop this regression analysis are given in Table 8.2, which produced an R^2 value of 0.82 meaning that 82% of the variation in S_r/σ_v' is being explained by the independent variables.

The regression analysis results are shown in Table 8.3.

Table 8.2. Residual strength ratio and related soil parameters in regression analysis

Site & model type	S_r/σ_v'	$(N_1)_{60CS}$	D_{5015} (mm)
Niigata Bandai, free face	0.065	9.2	0.27
Niigata Hotel, ground slope	0.085	8.8	0.27
Niigata Railway, ground slope	0.084	10.5	0.35
Niigata Showa, free face	0.090	12.3	0.12
Noshiro N-4 Section, ground slope	0.030	11.2	0.35
Noshiro S-7 Section, ground slope	0.030	7.6	0.35
San Fernando Juvenile Hall, ground slope	0.130	18	0.06
San Fernando, Jensen Filtration Plant, free face	0.060	17	0.08
Imperial Valley, Heber Road, free face	0.080	9	0.12
Imperial Valley, River Park, ground slope	0.150	15	0.07
Turkey, Degirmenedere, ground slope	0.160	15	2.90
Wildlife, ground slope	0.210	15.7	0.08
Idaho, Whiskey Springs, ground slope	0.200	21	3.00
Northridge, Balboa , ground slope	0.160	19	0.11
Turkey, Degirmenedere without T15, ground slope	0.500	8	2.90

Table 8.3. Regression analysis result for residual strength ratio and soil parameters

	Coefficients	*Standard Error*	*t Stat*	*P-value*
Intercept	0	#N/A	#N/A	#N/A
$(N1)_{60CS}$	0.007518881	0.001836982	4.093062082	0.001269541
D5015	0.053130355	0.019568647	2.715075464	0.017678253

Regression Statistics	
Multiple R	0.905722993
R Square	0.820334141
Adjusted R Square	0.729590613
tandard Error	0.080002085
Observations	15

ANOVA

	df	*SS*	*MS*	*F*	*Significance F*
Regression	2	0.379901663	0.189950831	29.67827017	2.26196E-05
Residual	13	0.083204337	0.006400334		
Total	15	0.463106			

The regression equation is:

$$S_r/\square_v' = 0.00752 * (N1)_{60CS} + 0.0531* D_{5015}$$

where: $(N1)_{60CS}$ is the average $(N1)_{60}$ clean sands value in the T_{15} layer and D_{50} (mm) is the average D_{50} value in the T_{15} layer (Bartlett and Youd, 1991; 1992).

The P-values in Table 8.3 show that all regression coefficients are highly significant. These P-values represent probability values testing the null hypothesis that the partial slopes of the regression equation are zero. Because there is a low probability of this, then one can infer that all partial slopes are not zero and are significant in estimating the dependent variable.

Using the above equation, the predicted versus measured values of S_r/σ_v' are plotted in Figure 8.10.

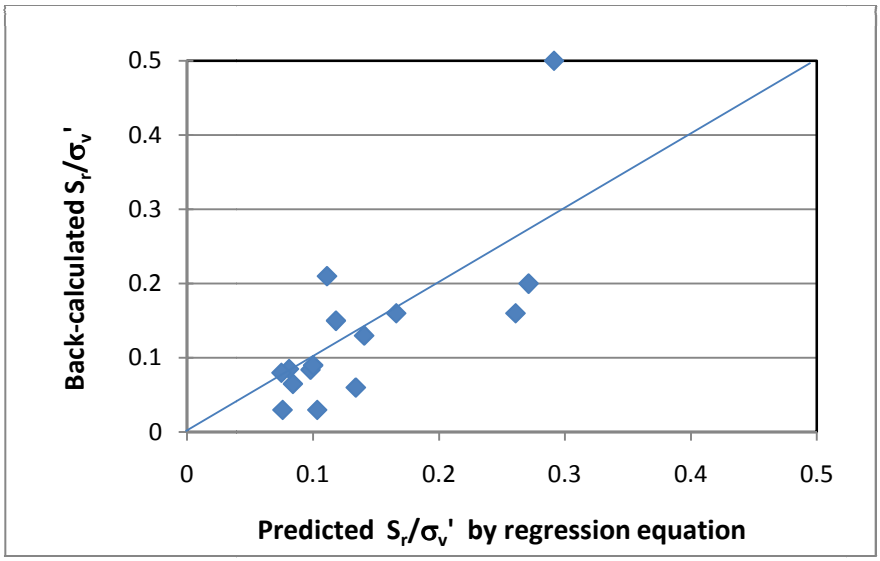


Figure 8.10. Predicted versus Back-calculated S_r/σ_v'

The relatively high R^2 squared value of 0.82 suggests that the residual strength ratio is reasonably estimated by $(N_1)_{60CS}$ and D_{5015}. However, there is a potential issue with the regression data set. The back-calculated S_r/σ_v' value of 0.5 is an extremely influential point in the regression, because it is far from the average of the remaining data. (This data point is from Degirmenedere, Turkey and is a gravelly site.) Because of its strong influence on the regression coefficients, it was decided to add another gravel site to the case history data set to improve the data support. The Sapanca Hotel in Turkey also underwent lateral spread and has gravel in the upper layers (see Chapter 7).

When the Sapanca Hotel case history was included in the regression analysis, the relationship with the highest R^2 value of 0.61 is a function of $(N_1)_{60CS}$ and D_{5015} as shown in Table 8.4.

The regression analysis result is shown in Table 8.5.

Table 8.4. Residual strength ratio and related soil parameters, including Turkey Sapanca Hotel case, in regression analysis

Site & model type	S_r/s_v'	$(N_1)_{60CS}$	D_{5015} (mm)
Niigata Bandai, free face	0.065	9.20	0.27
Niigata Hotel, ground slope	0.085	8.80	0.27
Niigata Railway, ground slope	0.084	10.50	0.35
Niigata Showa, free face	0.090	12.30	0.12
Noshiro N-4 Section, ground slope	0.030	11.20	0.35
Noshiro S-7 Section, ground slope	0.030	7.60	0.35
San Fernando Juvenile Hall, ground slope	0.130	18.00	0.06
San Fernando, Jensen Filtration Plant,free face	0.060	17.00	0.08
Imperial Valley, Heber Road, free face	0.080	9.00	0.12
Imperial Valley, River Park, ground slope	0.150	15.00	0.07
Turkey, Degirmenedere , ground slope	0.160	15.00	2.90
Wildlife, ground slope	0.210	14.00	0.08
Idaho, Whiskey Springs, ground slope	0.200	15.70	3.00
Northridge, Balboa , ground slope	0.160	21.00	0.11
Turkey, Degirmenedere, ground slope	0.500	19.00	2.90
Turkey, Sapanca Hotel, ground slope	0.250	8.00	4.00

Table 8.5. Regression analysis result for residual strength ratio and soil parameters including Turkey Sapanca Hotel case

	Coefficients	*Standard Error*	*t Stat*	*P-value*
Intercept	0	#N/A	#N/A	#N/A
(N1)60CS	0.007638909	0.001687595	4.526507462	0.000474516
D5015	0.050418497	0.014335736	3.516980123	0.003417916

Regression Statistics	
Multiple R	0.91714054
R Square	0.84114677
Adjusted R Square	0.758371539
Standard Error	0.077226111
Observations	16

ANOVA

	df	*SS*	*MS*	*F*	*Significance F*
Regression	2	0.442111789	0.221055895	37.06583357	4.26077E-06
Residual	14	0.083494211	0.005963872		
Total	16	0.525606			

Thus the equation to express the residual strength ratio can be written as:

$S_r/\square_v' = 0.007639 * (N1)60_{CS} + 0.050418* D_{5015}$

where: $(N1)60_{CS}$ is the average $(N1)_{60}$ clean sands value in the T_{15} layer and D_{50} (mm) is the average D50 value in the T_{15} layer (Bartlett and Youd, 1991; 1992). The R^2 value for this regression is 84% and all regression coefficients are highly significant (i.e., have a low probability of being zero). Accordingly, the predicted values of S_r/σ_v' from the

regression equation and the back-calculated values from the FLAC modeling are compared in Figure 8.11.

Thus, with a reasonably high R^2 value of 84 percent, it is concluded that the values of S_r/σ_v' are reasonably predicted from $(N_1)_{60CS}$ and D_{5015} for this dataset that includes the addition of the Sapanca Hotel, Turkey case history. However, the two gravel sites from Turkey (Degirmenedere and Sapanca Hotel) are potential outliers, as seen in Table 8.6, because their standard residual values are greater than two standard deviations.

Another regression analysis was performed to evaluate if an intercept was justified in the regression model. The regression results produced a P-value of 0.35 for the intercept coefficient, which indicates that there is a 35% probability that this coefficient is zero. This probability is sufficiently high so as to preclude the use of an intercept in the final regression model; hence, it was omitted.

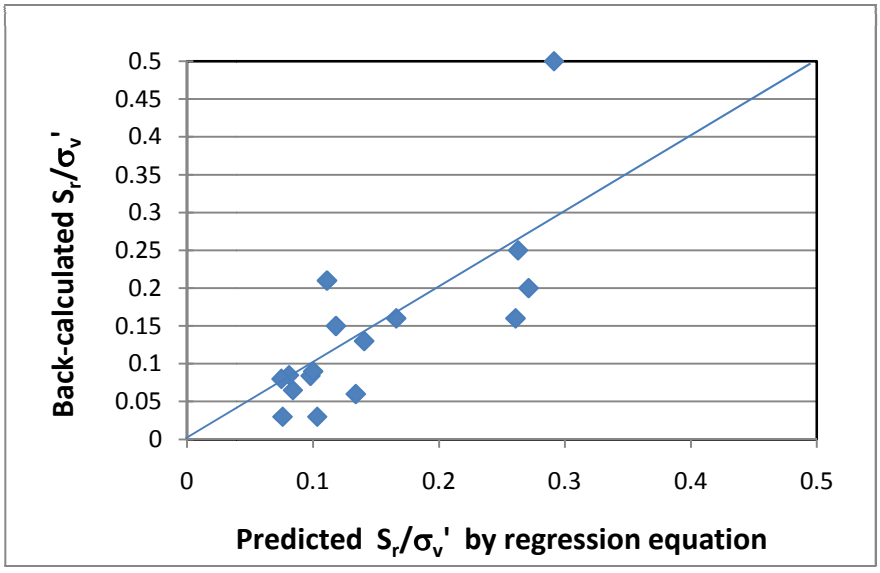


Figure 8.11. Predicted versus back-calculated values of S_r/σ_v'

Table 8.6. Regression analysis results showing standardized residual values.

Observation	*Predicted Sr/sv'*	*Residuals*	*Standard Residuals*
1	0.088212531	-0.023212531	-0.275844921
2	0.084978647	2.13534E-05	0.000253752
3	0.102821379	-0.018821379	-0.223662894
4	0.105590023	-0.015590023	-0.185263243
5	0.108480676	-0.078480676	-0.9326211
6	0.079375719	-0.049375719	-0.586753835
7	0.148598828	-0.018598828	-0.221018218
8	0.141538799	-0.081538799	-0.968962144
9	0.078910479	0.001089521	0.012947262
10	0.124857038	0.025142962	0.298785107
11	0.269849432	-0.109849432	-1.305390108
12	0.117284668	0.092715332	1.101777905
13	0.280632135	-0.080632135	-0.958187857
14	0.175414661	-0.015414661	-0.183179341
15	0.078510878	0.171489122	2.037882205
16	0.302188273	0.197811727	2.35068554

Lastly, Figure 8.12 compares the average $(N1)_{60}$ value in the T_{15} versus values of S_r/σ_v' (this study) with the relation proposed by other researchers (Olson and Stark, 2002) for flow failure conditions. This comparison plot shows that the back-calculated S_r/σ_v' values from this study, which focused on lateral spread failures, are similar to those values of previous researchers, but are more variable. This is most likely due to the wider range of soil types, site and failure conditions consider by this modeling study. This plot also suggests that some of the variability in predicting S_r/σ_v' can be reduced by including other soil factors such as the clean sands correction and the mean grain size in the regression relation, as has been done in this study. These soil factors (fines content and mean grain size) also contribute to predicting S_r/σ_v' as demonstrated by this modeling study and should be included in the regression model.

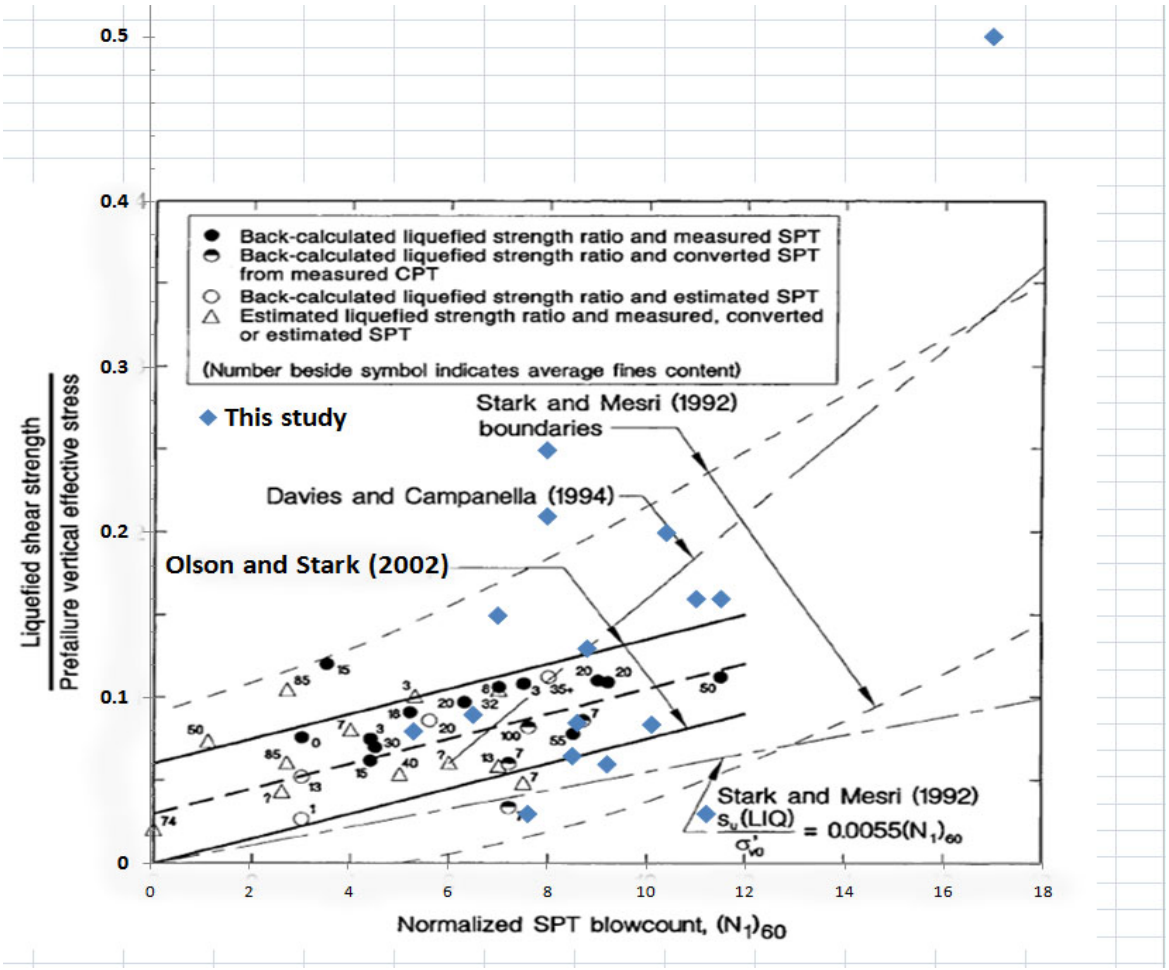


Figure 8.12. Comparison between the average $(N1)_{60}$ value versus values of S_r/σ_v' (this study) with the relation proposed by other researchers Olson and Stark (2002) for flow failure conditions

8.3 Conclusion

The residual strength ratio values, S_r/σ_v', obtained from the FLAC model back-analysis can be reasonably estimated from the average equivalent blow count for clean sand in the T_{15} layer and the average D_{50} value in that same layer. A relatively high percentage of the variability shown in the dependent variable is captured by the independent variables, as indicated by an R^2 value of 84%.

The recommended regression equation is:

$$S_r/\sigma_v' = 0.007639 * (N1)_{60CS} + 0.050418* D_{5015}$$

where: $(N1)_{60CS}$ is the average $(N1)_{60}$ clean sands value in the T_{15} layer and D_{50} (mm) and is the average D50 value in the T_{15} layer (Bartlett and Youd, 1991; 1992).

Thus, regarding soil factors, it is concluded that the residual strength ratio that develops during liquefaction-induced lateral spread is correlated with the SPT blow count, fines content and the mean grain size of the T_{15} layer. (Fines content is mentioned here because it is accounted for in the proposed model by the clean sands correction of the SPT blow count).

Finally, it is concluded that the above regression equation can be used in conjunction with the developed FLAC modeling procedures to estimate the amount of lateral spread displacement at potentially lateral spread sites. Because of the limited data available for gravelly sites, it is difficult to judge the robustness of the above equation for these soils.

CHAPTER 9

CONCLUSIONS AND RECOMMENDATIONS

9.1 Conclusions

The purpose of this research is to develop a practical numerical modeling approach for estimating lateral spread displacement and to calibrate it with lateral spread case histories. The numerical model developed herein was developed using FLAC (Fast Lagrangian Analysis of Continua; Itasca 2005) and was applied to case histories of liquefaction-induced lateral spread (Bartlett and Youd, 1991; 1992; 1995; Youd et al. 2001) to back-calculate important model inputs and to correlate them with subsurface geotechnical data so that the model can be used for forecasting. The modeling approach was developed so that the residual strength ratio (i.e., residual strength divided by the in situ vertical effective stress) was back-calculated by matching the observed horizontal displacement at the respective case history sites. For some sites, the Youd et al. (2002) regression model was used to interpolate the measured displacements in order to obtain a better spatial distribution for FLAC modeling and calibration. In addition, some case history sites lacked strong motion records and the calibration was done using synthetic records generated by a stochastical simulation program SGMS V. 5 (Halldorsson B. et al).

Ultimately the back-calculated residual strength ratio values were correlated with SPT blow count, fines content and mean grain-size from the case history sites so the model could be used for forecasting. The development of these soil factors is based upon regression analyses done by Bartlett and Youd (1991; 1992; 1995) and Youd et al. (2001). Equations for estimating the residual strength ratio from site-specific soil factors were developed using multiple linear regression (MLR) analysis.

The recommended regression equation is:

$$S_r/\sigma_v' = 0.007639 * (N1)_{60CS} + 0.050418* D_{5015}$$

where: $(N1)_{60CS}$ is the average $(N1)_{60}$ clean sands value in the T_{15} layer and D_{50} (mm) and is the average D50 value in the T_{15} layer (Bartlett and Youd, 1991; 1992).

The following procedures were performed by this research to develop the modeling approach and the above equations.

(1) A noncoupled total stress FLAC model was developed that used external functions to estimate pore water pressure generation. An algorithm was developed in FLAC that calculates the excess pore pressure as a function of the number and magnitude of the shear stress cycles for an input acceleration time history. Additional functions were developed that degrade the soil's shear modulus and shear strength as a function of excess pore water generation. For postliquefaction behavior, a constant residual strength and residual shear modulus were used. The residual shear modulus was linked to the residual shear strength via the average clean sands SPT blow count for the critical layer. In addition, postliquefaction loading and unloading stiffness are considered differently, so that the unloading modulus is ten times stiffer than the loading modulus. Damping in the

FLAC model was automatically accounted for by the shape and area of the hysteresis loop for the layer undergoing significant pore pressure generation and lateral spread. For nonliquefied layers, FLAC's hysteresis damping option was used.

(2) The developed FLAC model and modeling procedures were tested using strong motion data from the Wildlife, California and Kobe, Japan instrumentation arrays. In terms of ground response below and above the liquefied layer, the FLAC model produced reasonably good agreement with the recorded strong motion response and the estimated stress-strain behavior. However, for the case of Wildlife, the modeling approach did not match the measured pore pressure response. It was concluded that this mismatch is most likely due to pore pressure migration that the FLAC model does not model. Nonetheless, it was concluded that the modeling procedures capture the fundamental mechanisms and behavior of liquefaction and its affect on the ground response and lateral spread displacement.

(3) The FLAC model was used to model 16 case histories of liquefaction-induced ground failure worldwide and the back-calculated residual strength ratio for each case was obtained. The input acceleration time histories for the back analyses were either obtained from strong motion recorded at or nearby the site, or they were synthetically generated. The synthetically generated time histories were appropriate for each site's earthquake magnitude and seismic source distance. The surface time histories were deconvolved to the depth corresponding to the base of the FLAC model developed for each case history site. They were input as stress time histories with a quiet boundary and convolved upward through the FLAC model. The residual strength ratio for these

analyses was determined by changing the input value until a reasonable match of the recorded displacements was obtained.

(4) Subsequently, multiple linear regression (MLR) analyses were performed on the back-calculated residual strength ratios to correlate these values with soil factors. It was concluded that the residual strength ratio is mainly correlated with the SPT blow count (i.e., $(N_1)_{60}$) and the fines content and mean grain size of the lateral spread zone.

9.2 Recommendations

Several recommendations for further research are as follows:

1) Additional lateral spread cases should be modeled using the designed FLAC procedures to strengthen the regression database as new data become available.
2) This approach does not account for postliquefaction dilation of the soil directly, but its effect is manifest by an increase in the residual strength ratio. The FLAC model could be modified to take into account the dilation, but insufficient information is available to calibrate such a model.
3) Laboratory testing could be executed to check the unloading stiffness and evaluate the ten times stronger unloading stiffness used in this approach.
4) More research could be focused on the influence that the equivalent clean sand blow count (i.e., soil density) has on the degraded shear modulus prior to liquefaction. This approach used an approximation, which was suggested in the literature and somewhat verified by the modeling for the Wildlife and Kobe arrays, but further work is required.

5) A fully-coupled FLAC effective stress model may be also useful, if calibrated, and if its input parameters are few and can be easily derived. However, the pore pressure dissipation and redistribution during the liquefaction process is difficult to model. Also, such a model will be more difficult to calibrate and implement. It is difficult to back-estimate the required parameters for such a model from standard geotechnical data. Thus, this uncoupled, total stress model can still be useful because of its efficiency, calibration and ability to be forecasted.

APPENDIX A

NIIGATA BANDAI DATA

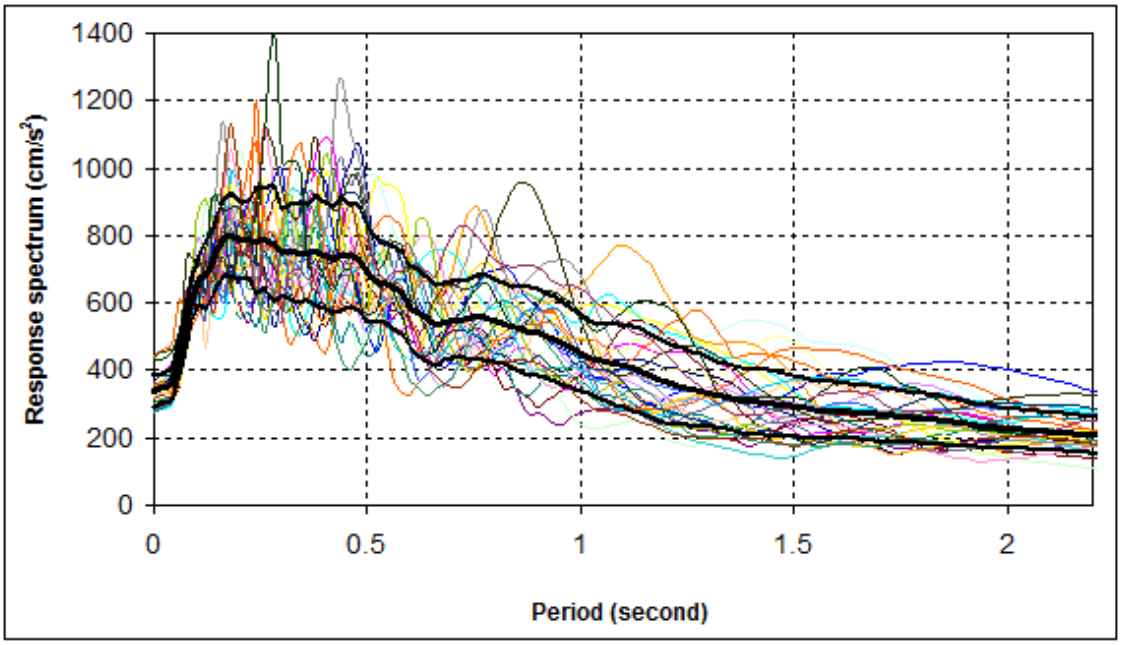


Figure A.1. Response spectra of generated thirty motions

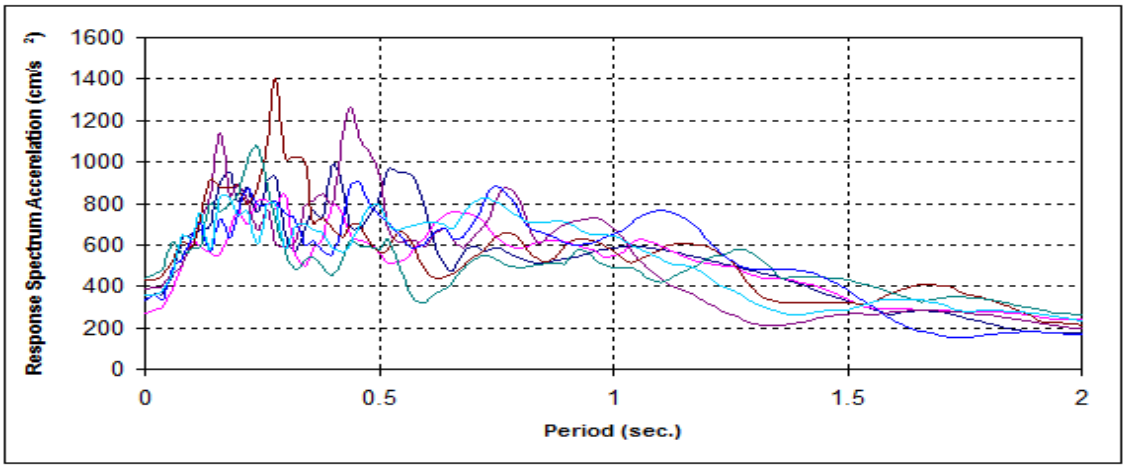


Figure A.2. Response spectra of selected seven motions

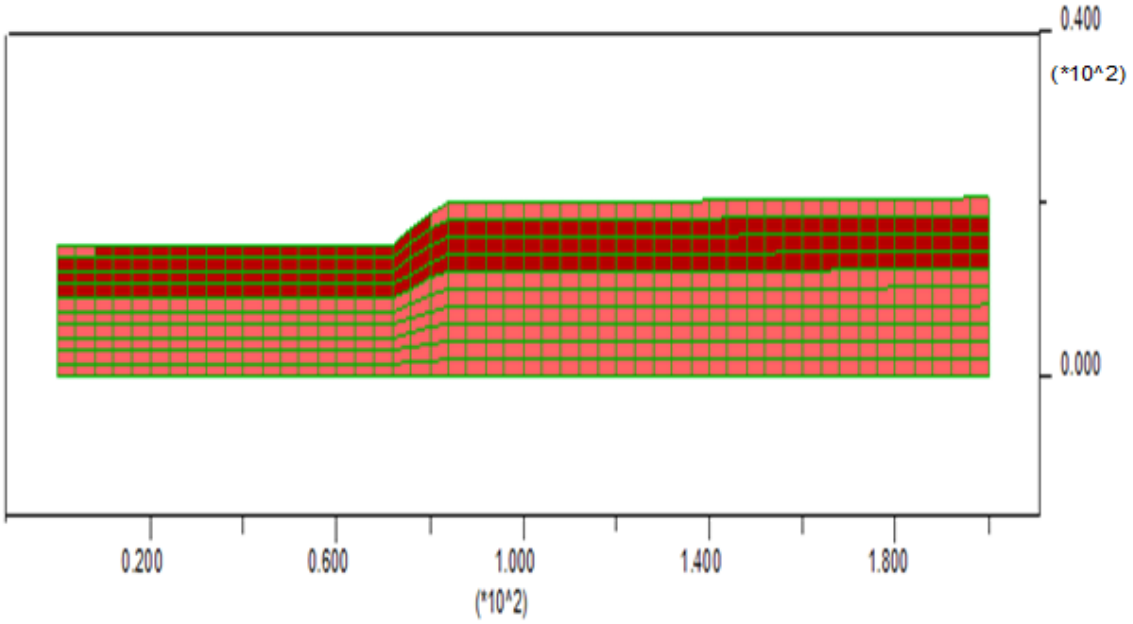


Figure A.3. Niigata Bandai section FLAC model scheme

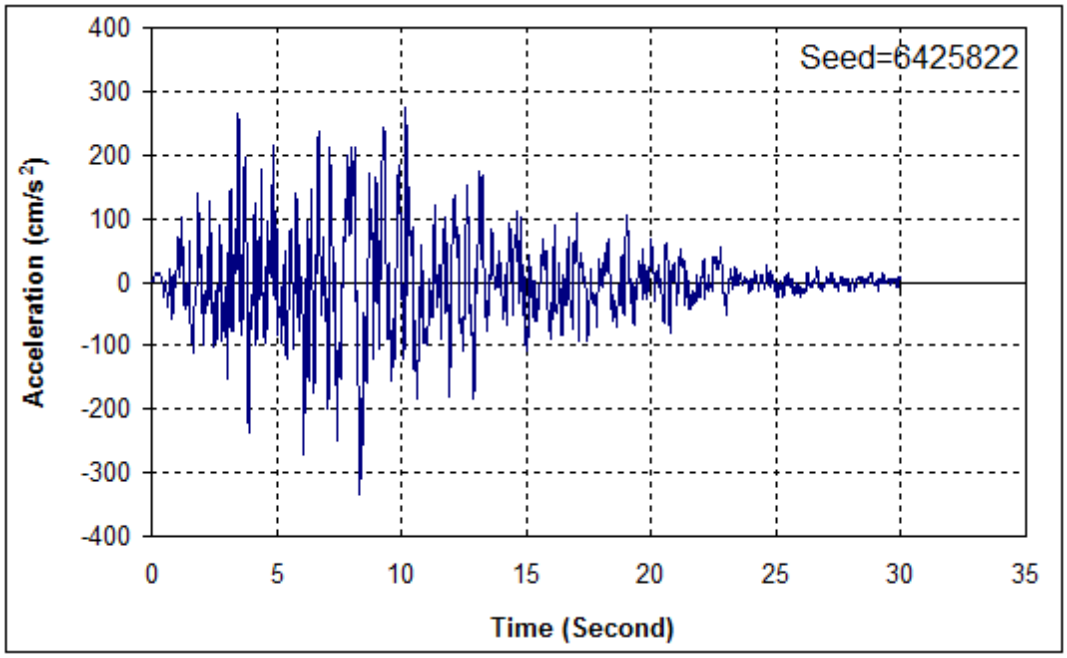


Figure A.4. Niigata Bandai section model selected motion 1

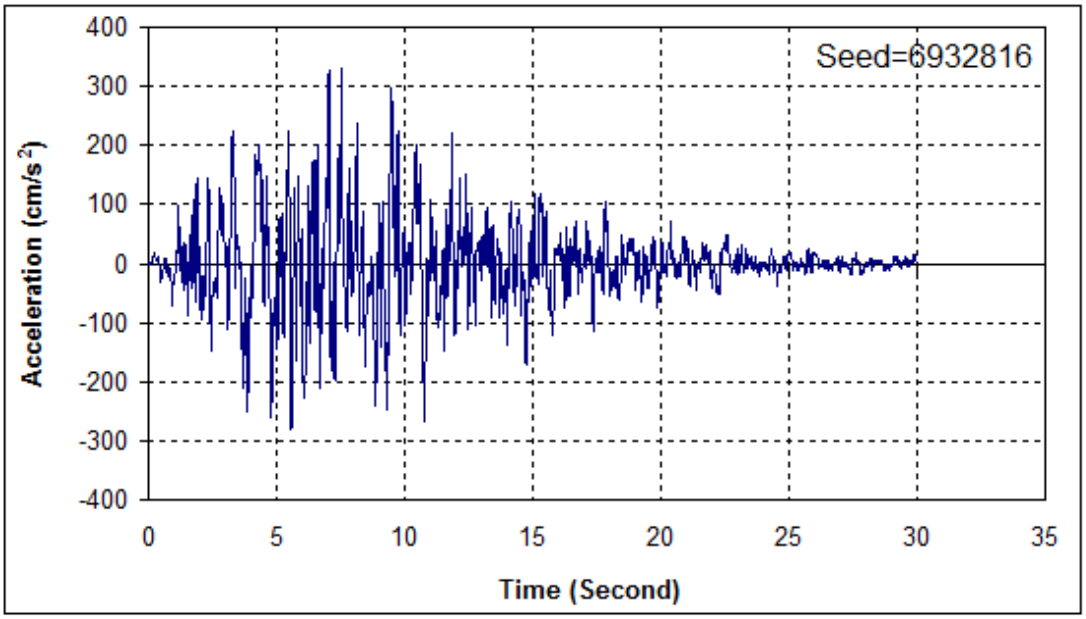


Figure A.5. Niigata Bandai section model selected motion 2

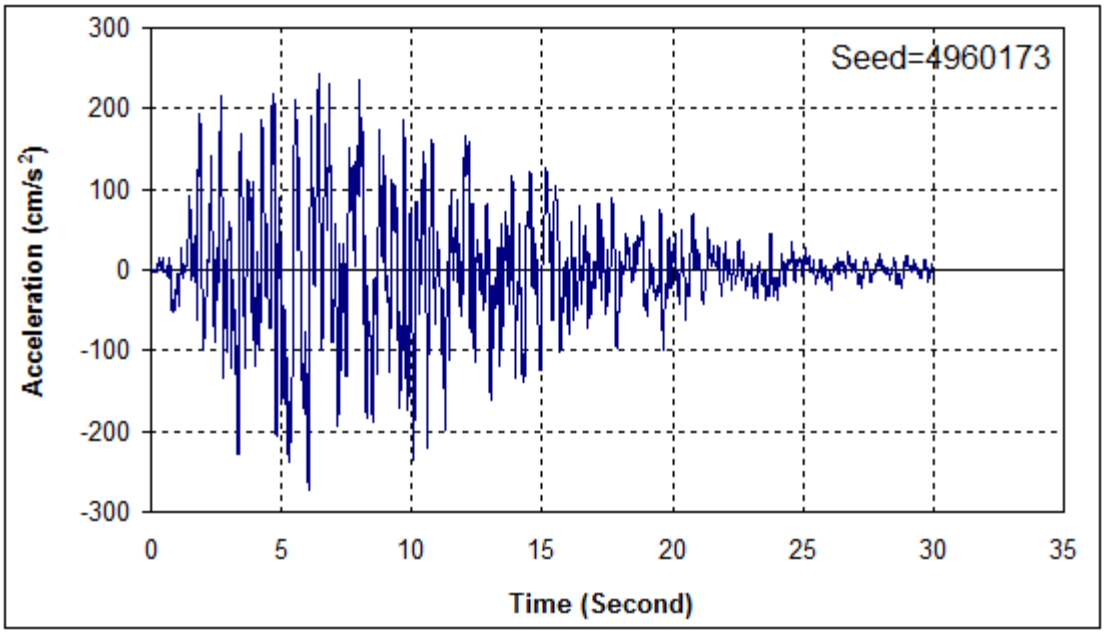


Figure A.6. Niigata Bandai section model selected motion 3

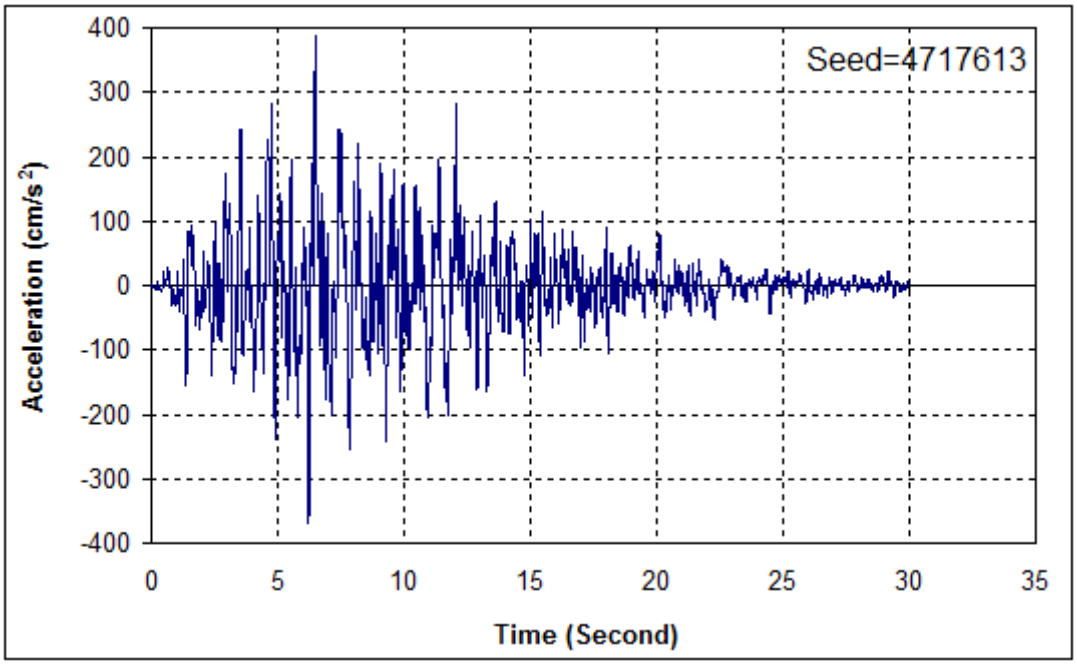


Figure A.7. Niigata Bandai section model selected motion 4

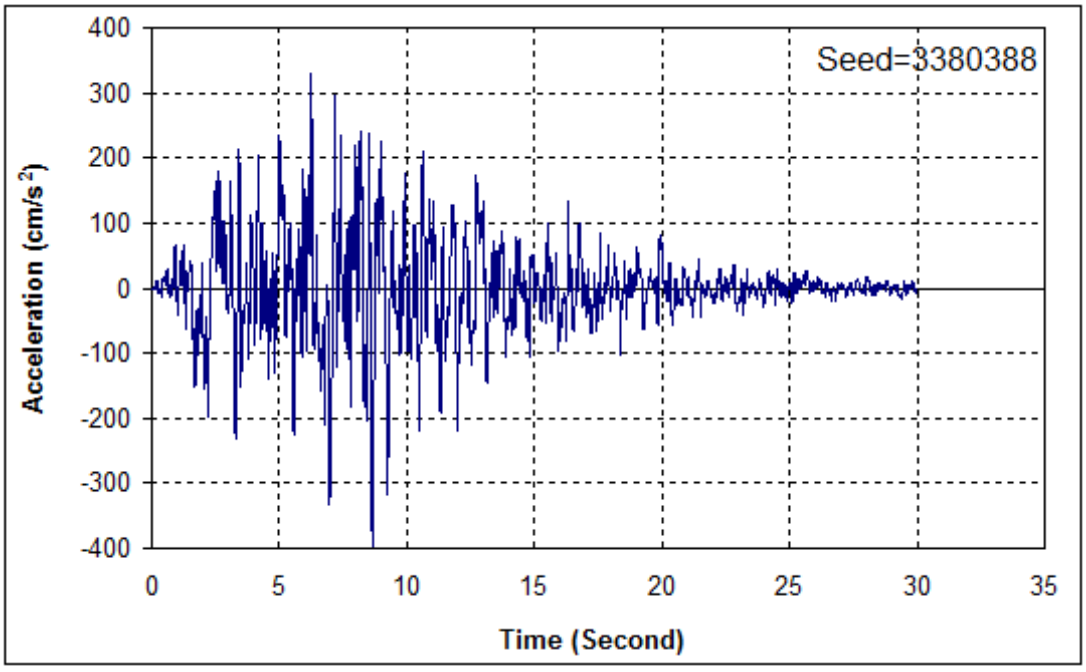


Figure A.8. Niigata Bandai section model selected motion 5

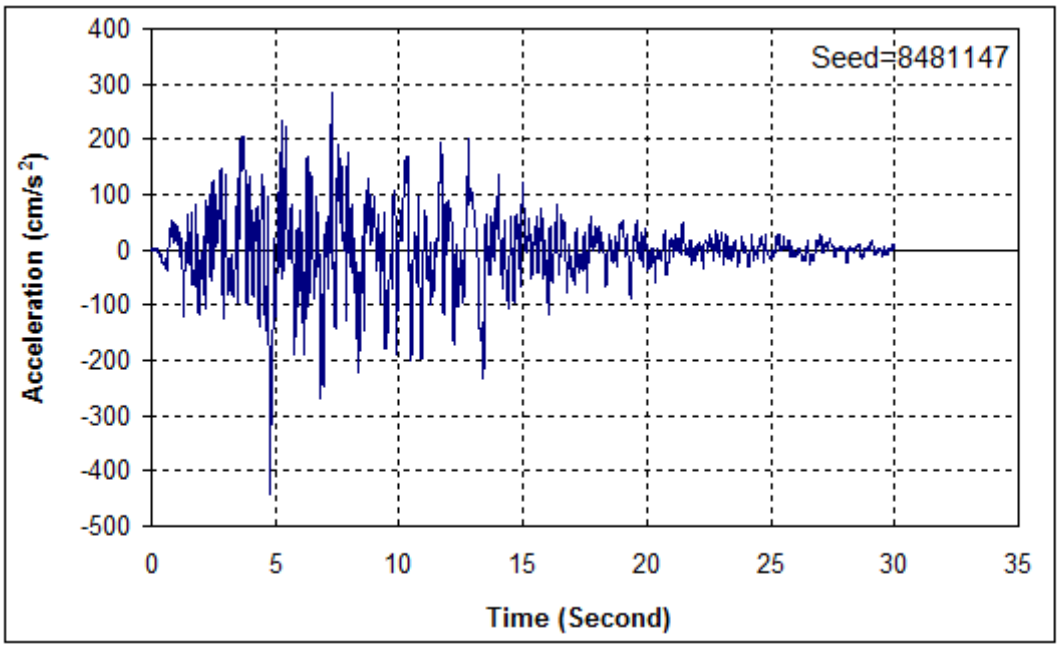


Figure A.9. Niigata Bandai section model selected motion 6

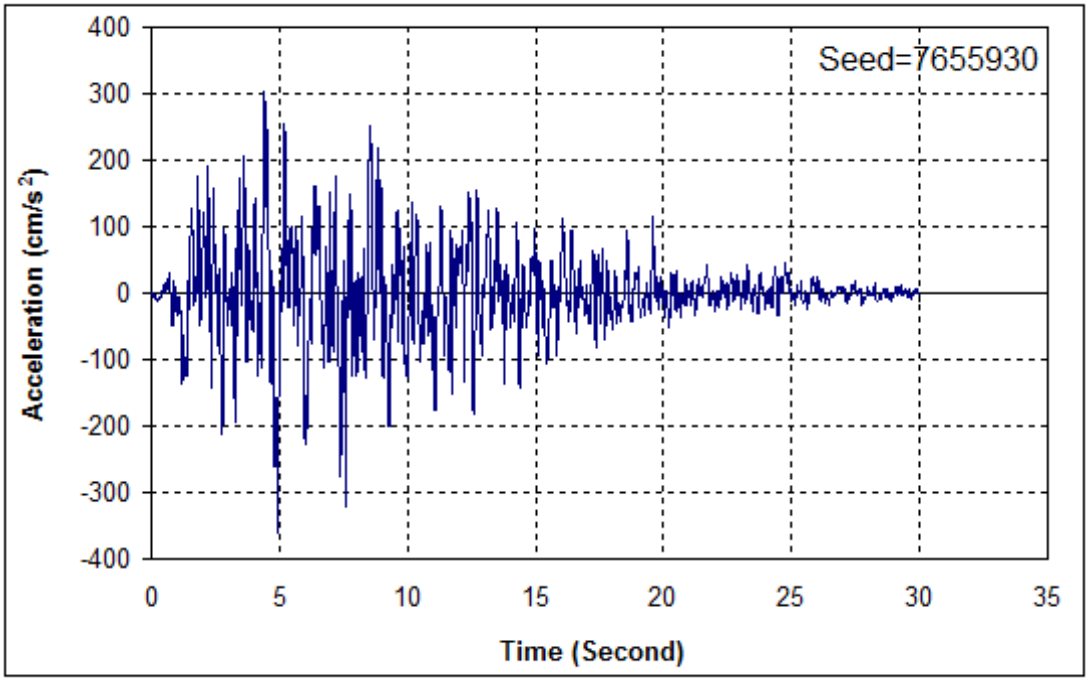


Figure A.10. Niigata Bandai section model selected motion 7

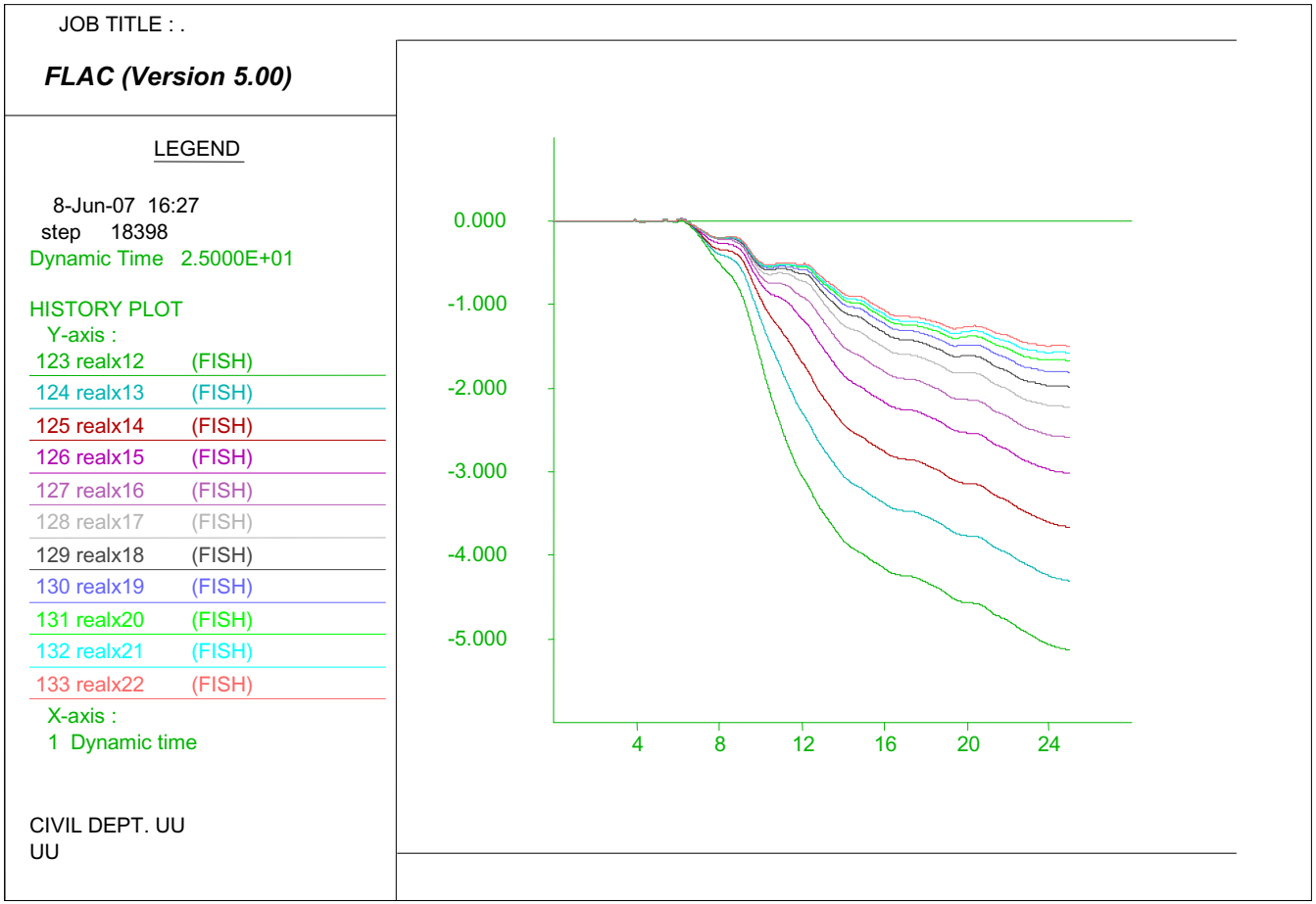


Figure A.11. Niigata Bandai section model later spreading prediction loaded by motion 1 with residual strength ratio of 0.065

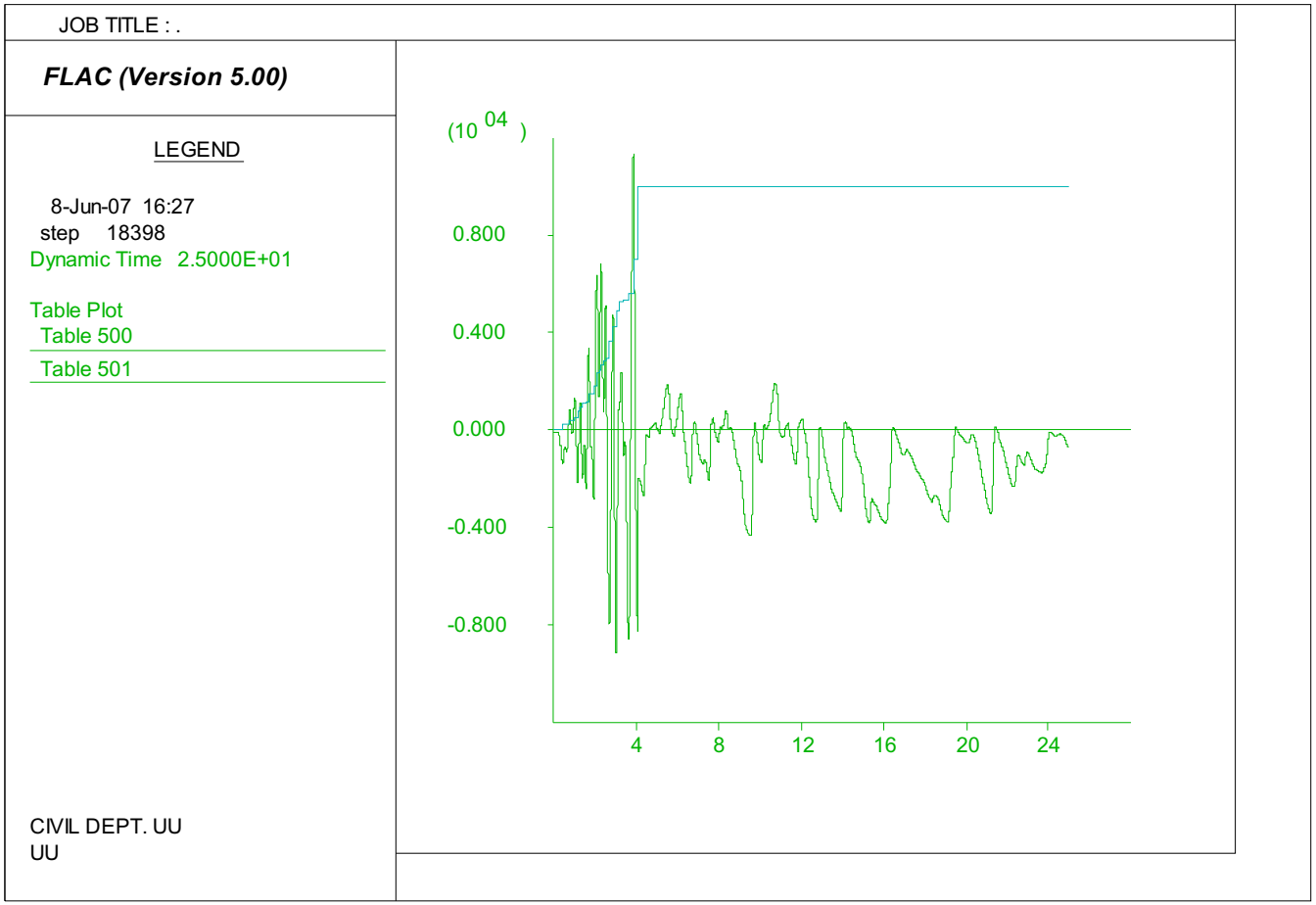


Figure A.12. Niigata Bandai section model pore water generation history loaded by motion 1 with residual strength ratio of 0.065

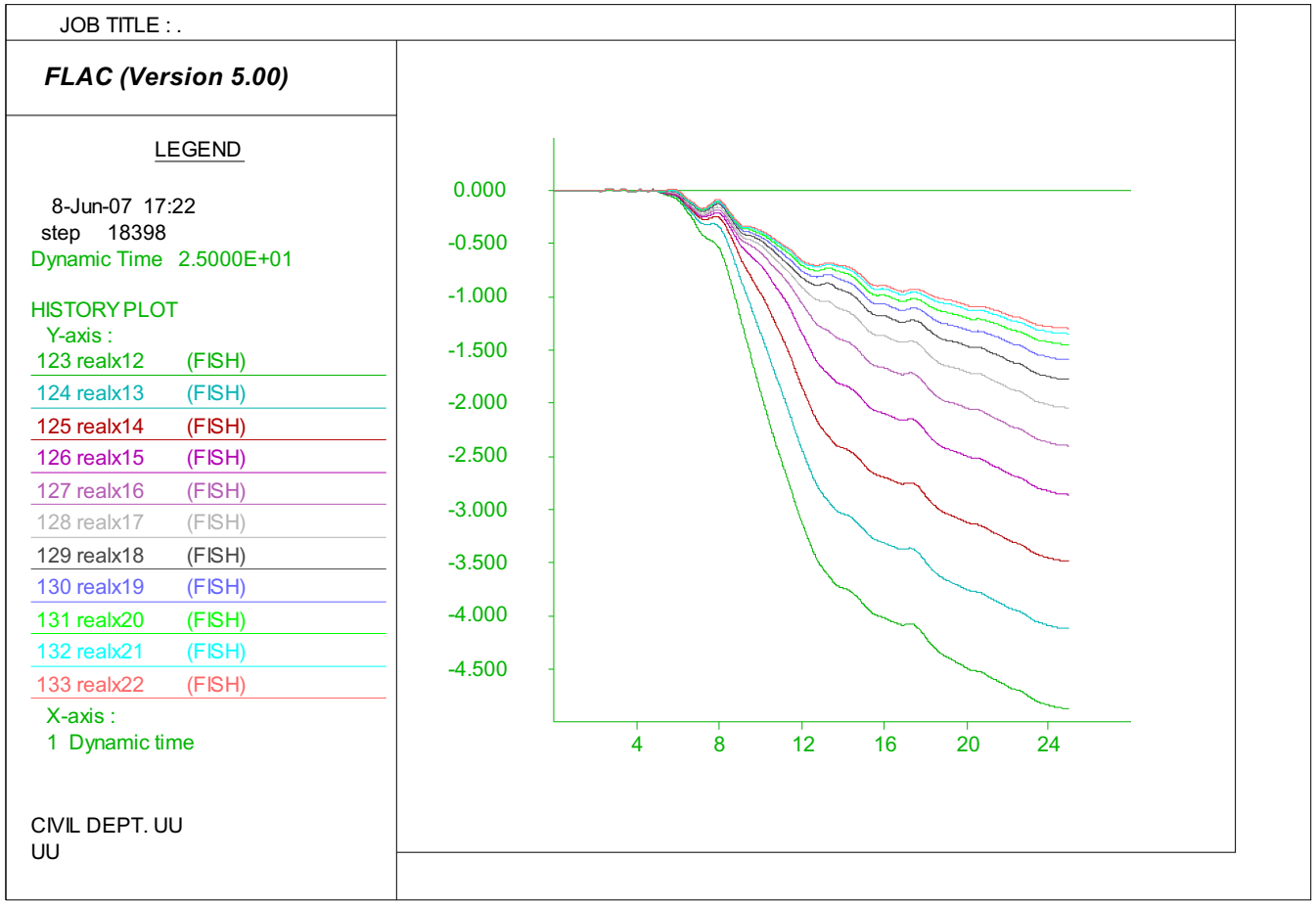


Figure A.13. Niigata Bandai section model later spreading prediction loaded by motion 2 with residual strength ratio of 0.065

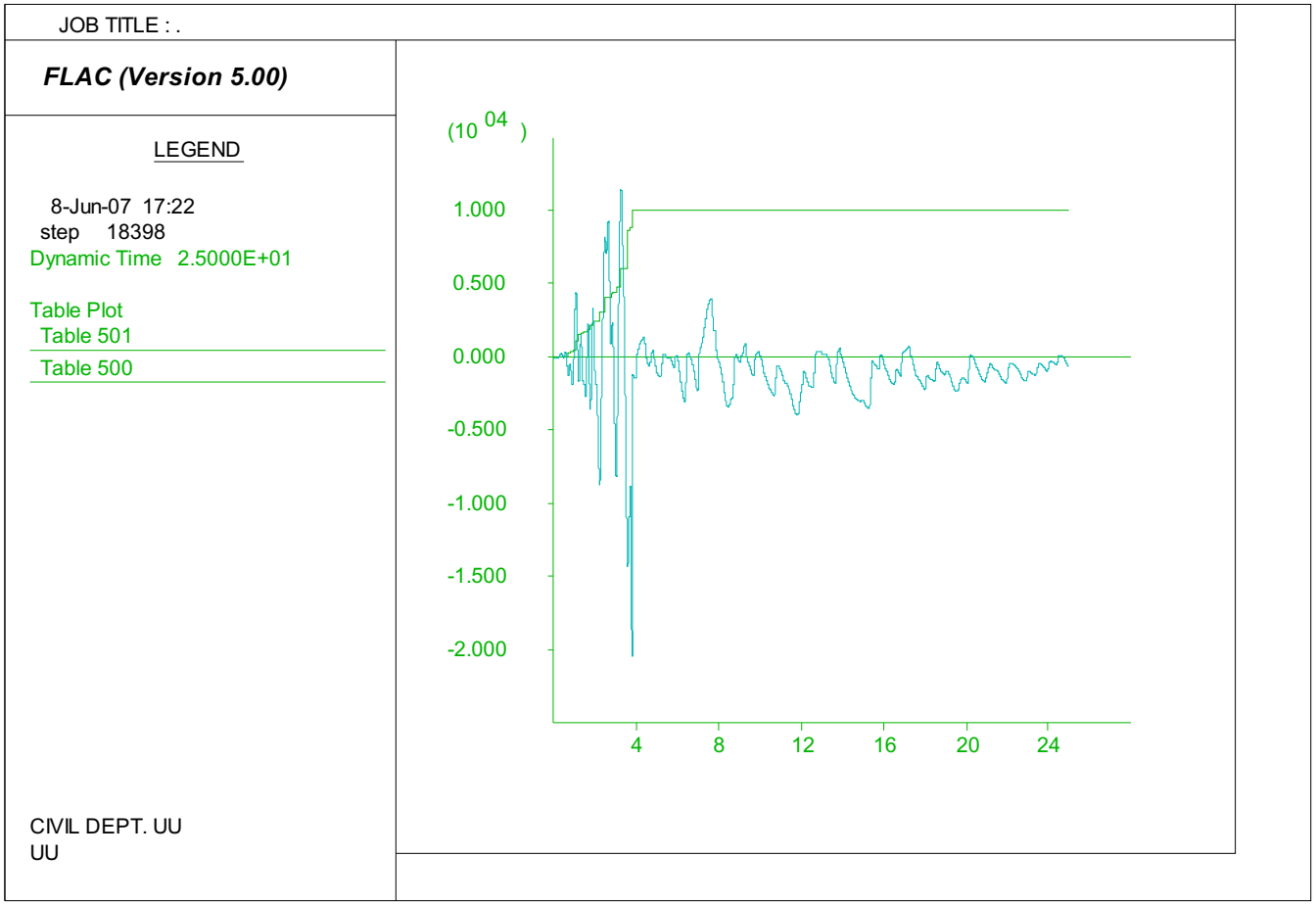


Figure A.14. Niigata Bandai section model pore water generation history loaded by motion 2 with residual strength ratio of 0.065

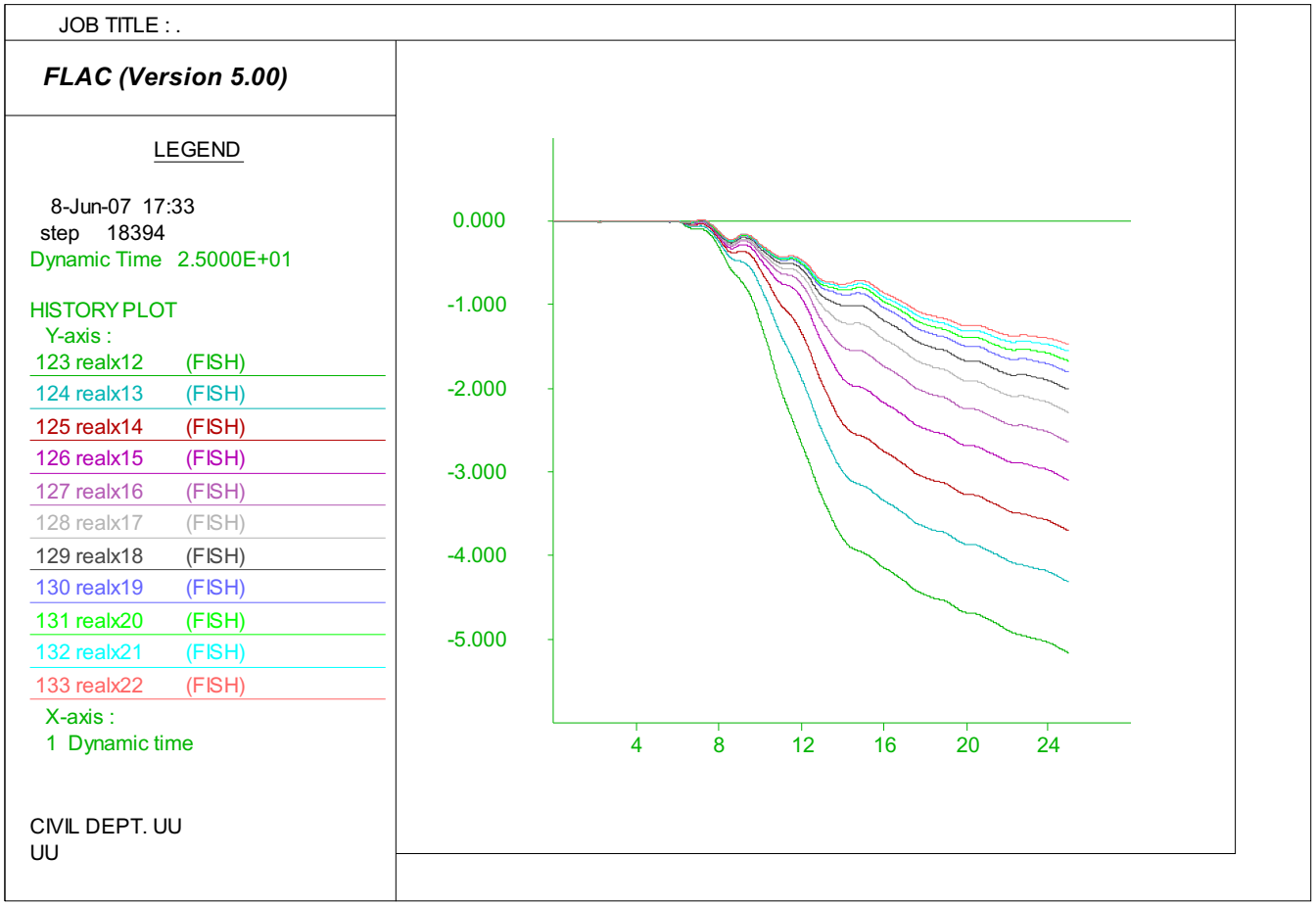


Figure A.15. Niigata Bandai section model later spreading prediction loaded by motion 3 with residual strength ratio of 0.065

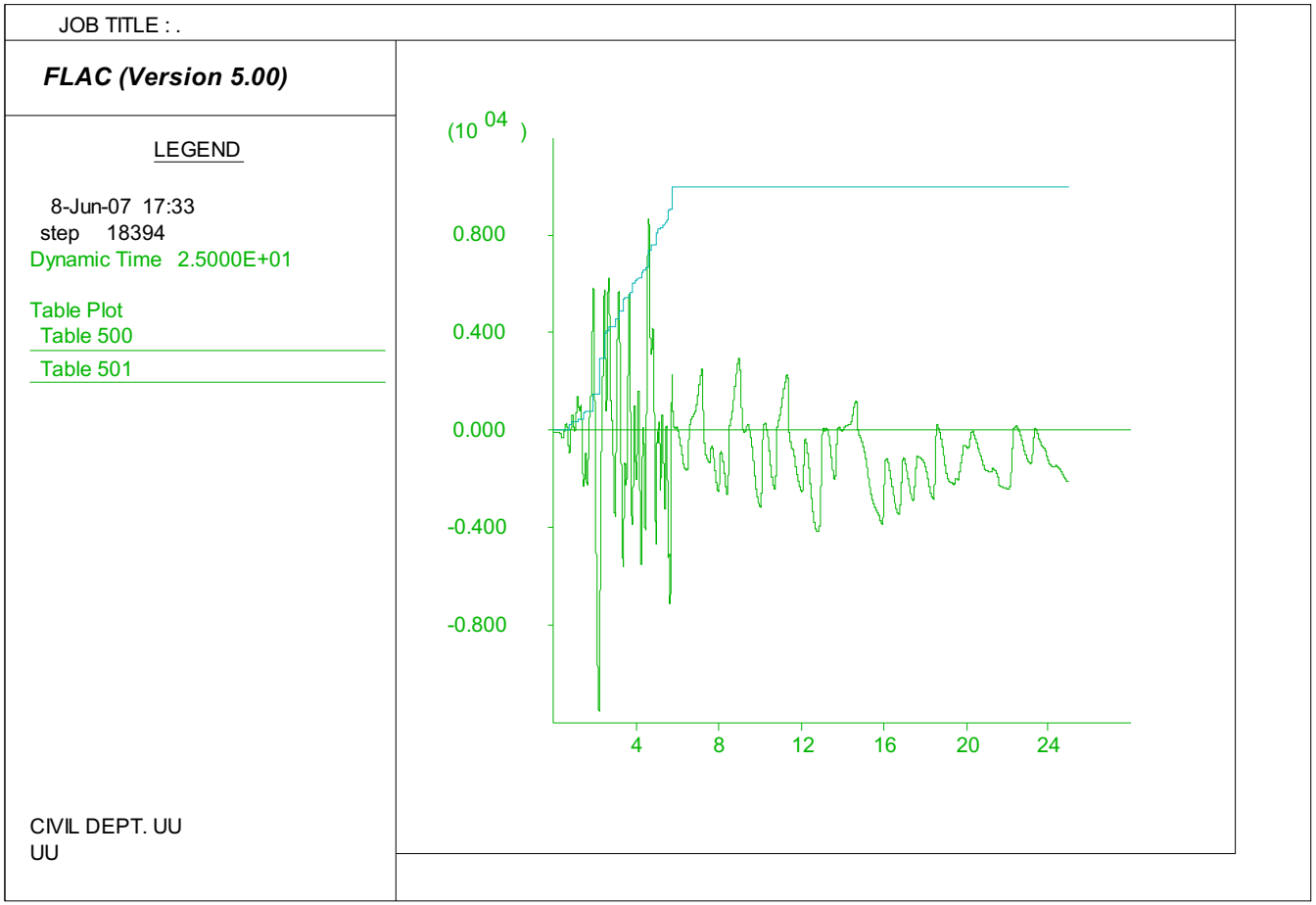


Figure A.16. Niigata Bandai section model pore water generation history loaded by motion 3 with residual strength ratio of 0.065

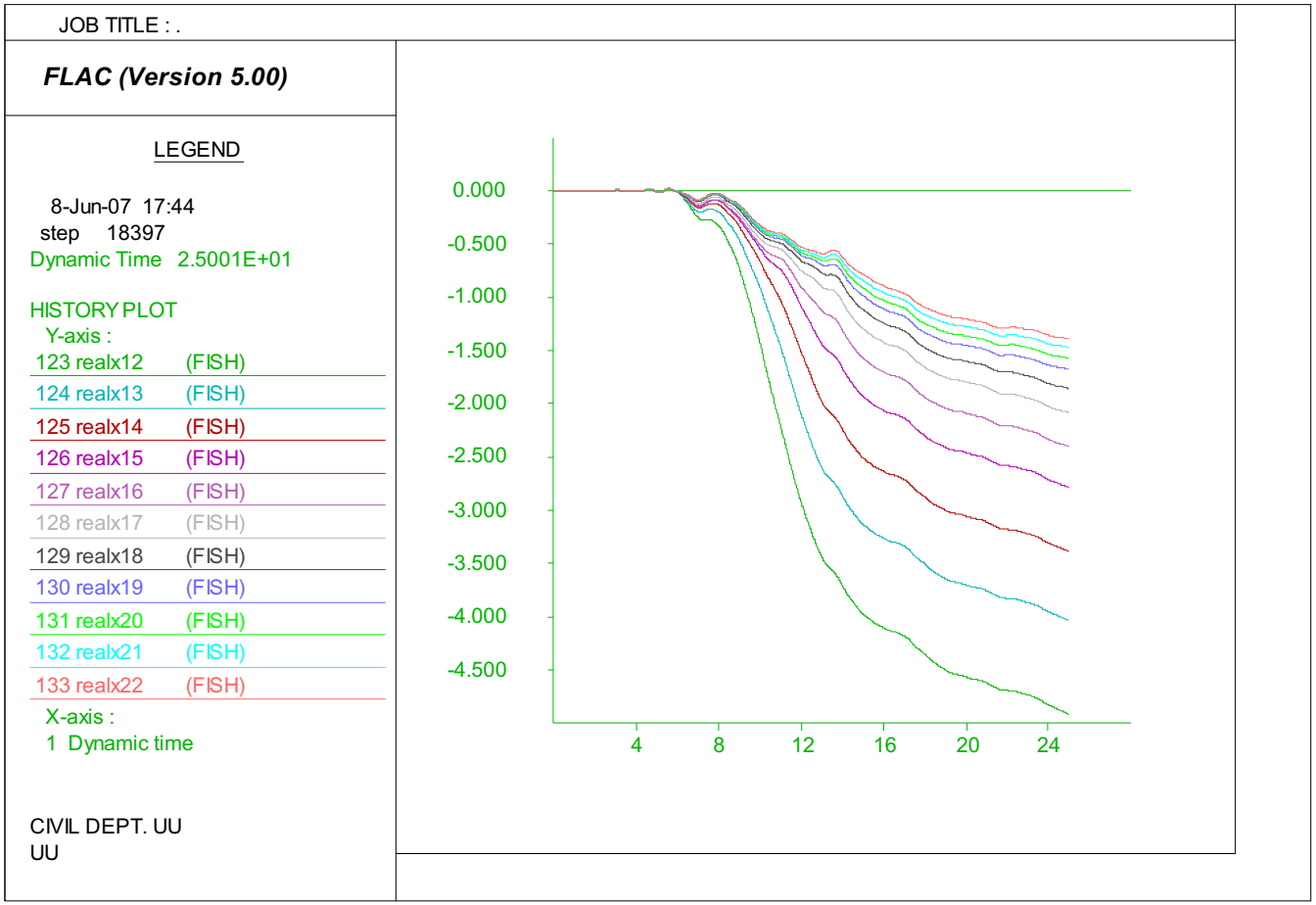


Figure A.17. Niigata Bandai section model later spreading prediction loaded by motion 4 with residual strength ratio of 0.065

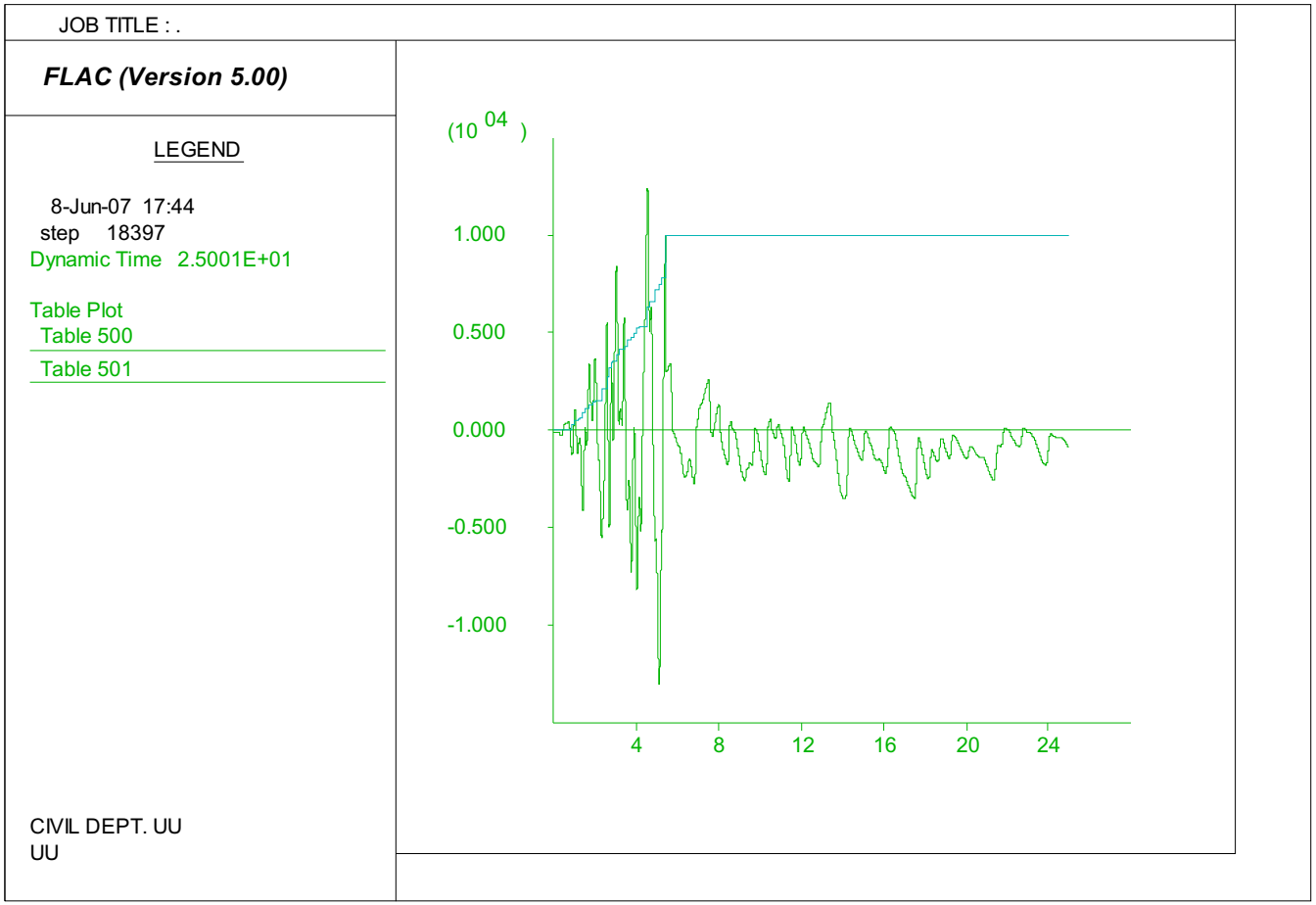


Figure A.18. Niigata Bandai section model pore water generation history loaded by motion 4 with residual strength ratio of 0.065

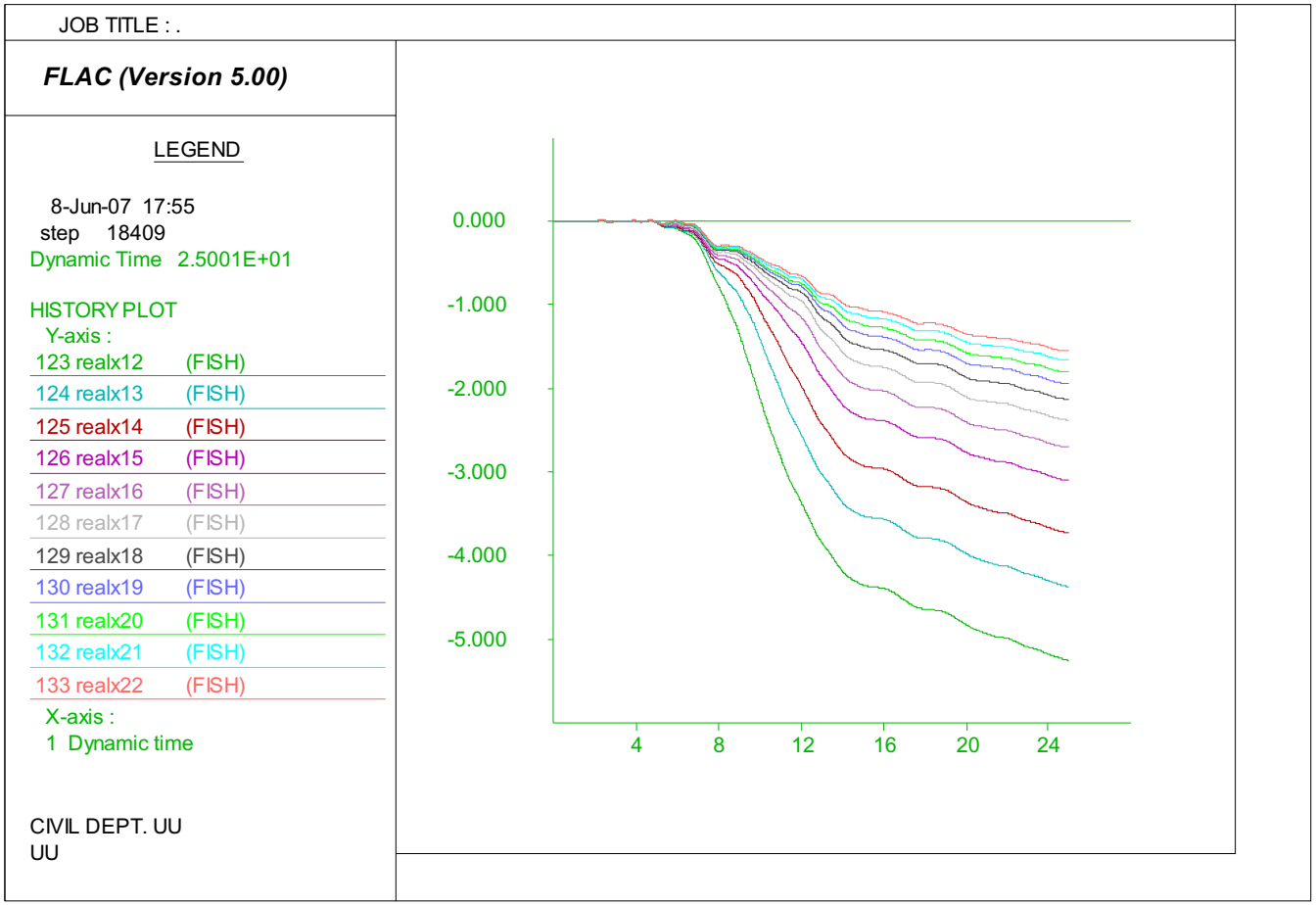


Figure A.19. Niigata Bandai section model later spreading prediction loaded by motion 5 with residual strength ratio of 0.065

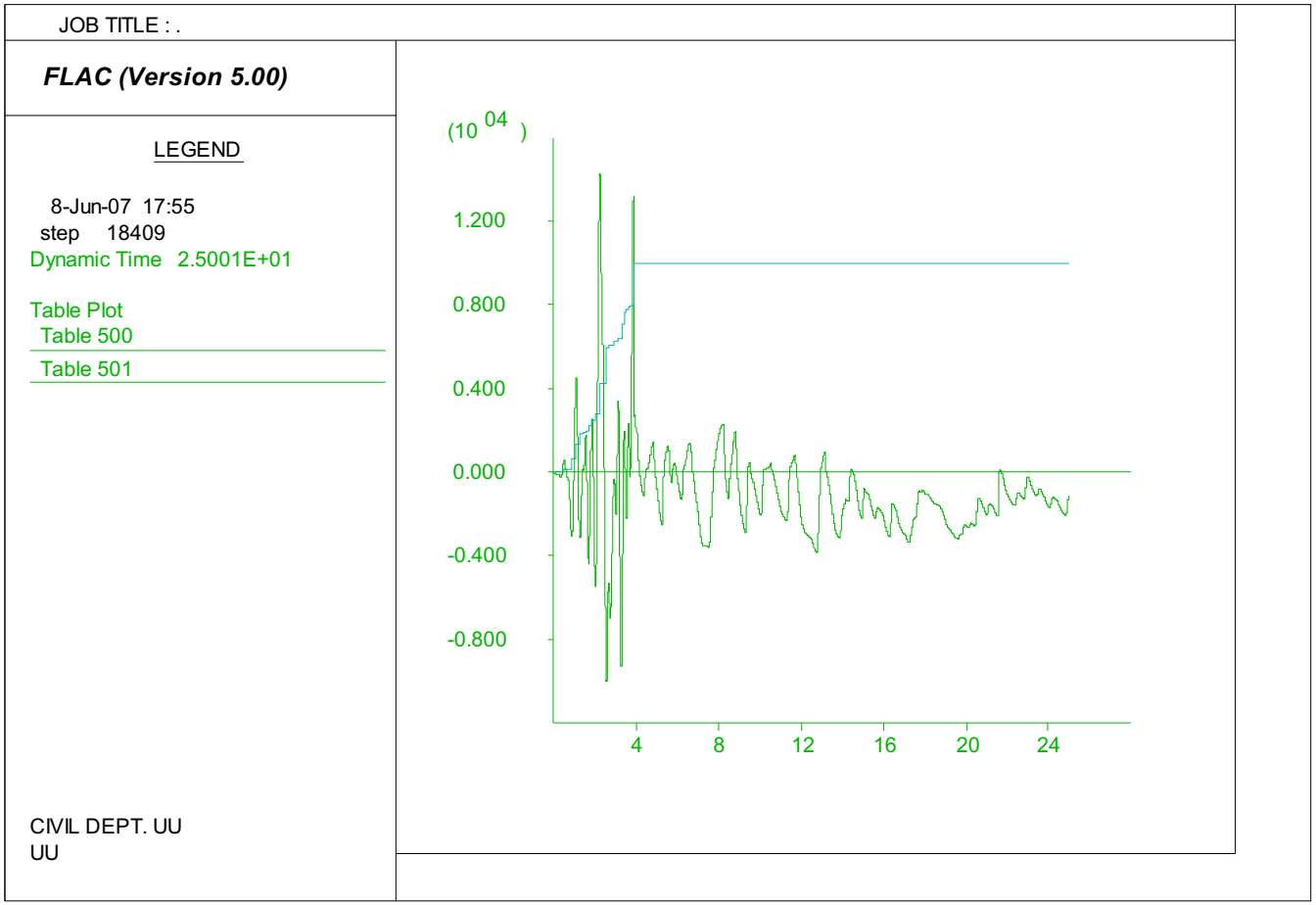


Figure A.20. Niigata Bandai section model pore water generation history loaded by motion 5 with residual strength ratio of 0.065

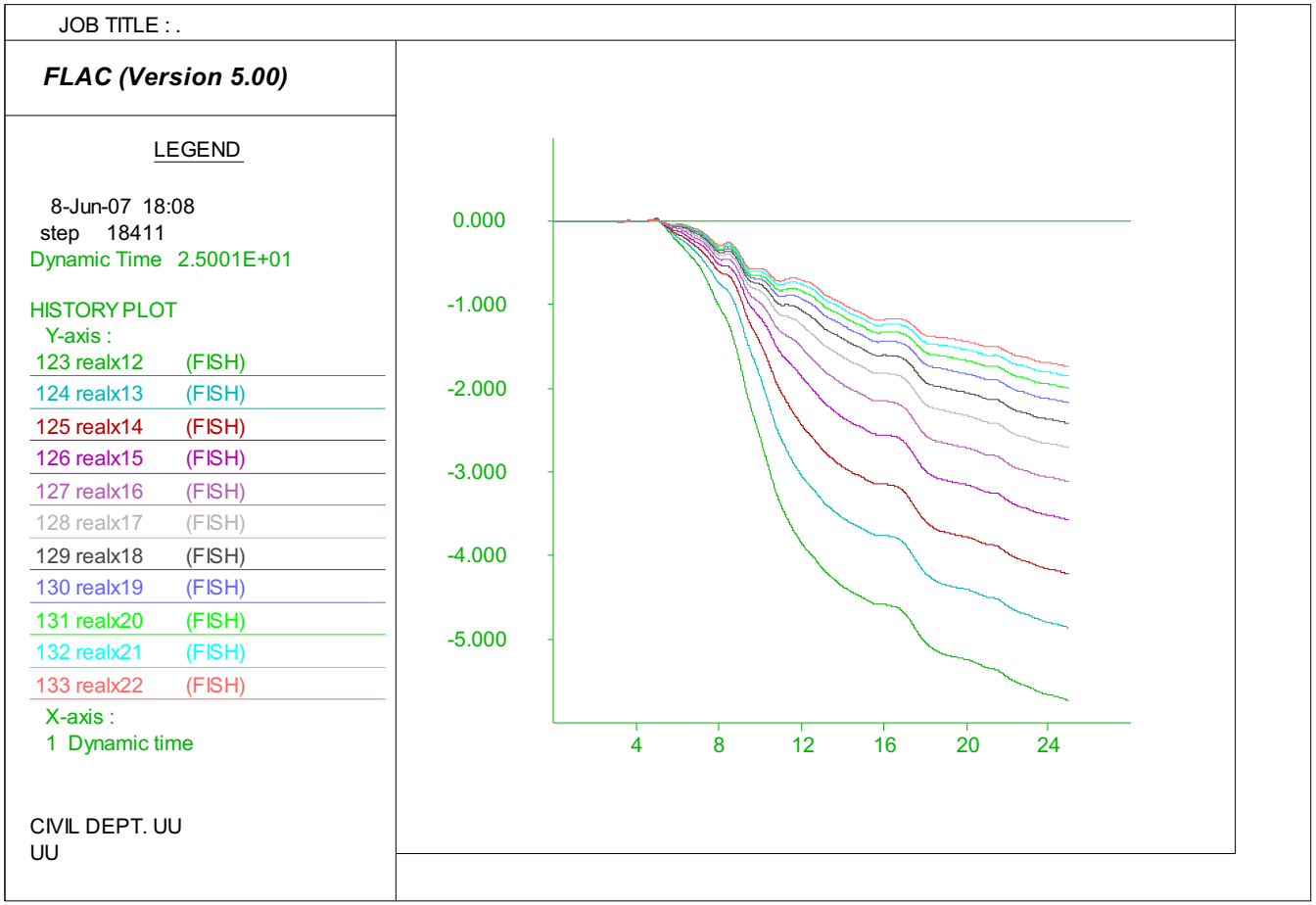


Figure A.21. Niigata Bandai section model later spreading prediction loaded by motion 6 with residual strength ratio of 0.065

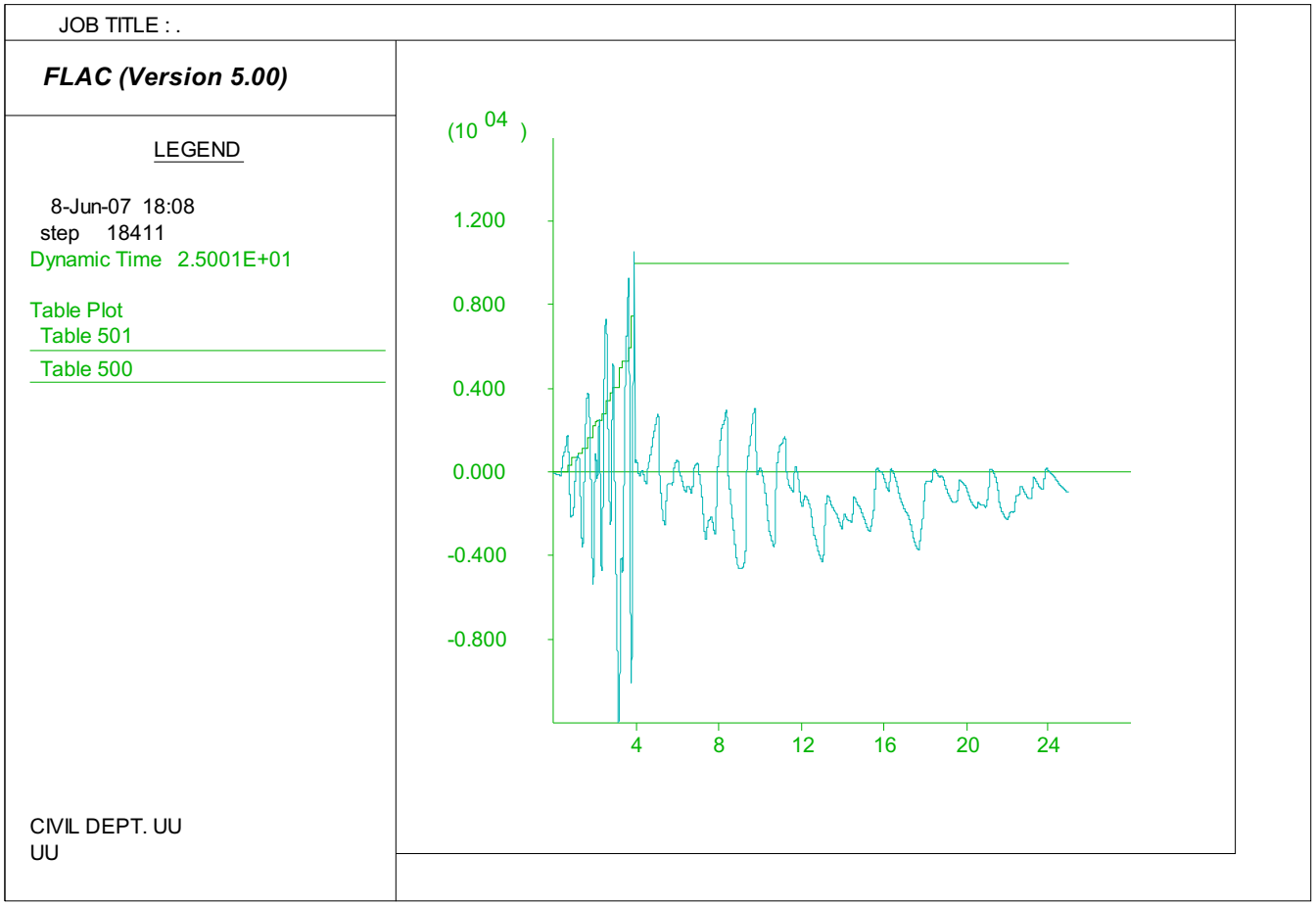


Figure A.22. Niigata Bandai section model pore water generation history loaded by motion 6 with residual strength ratio of 0.065

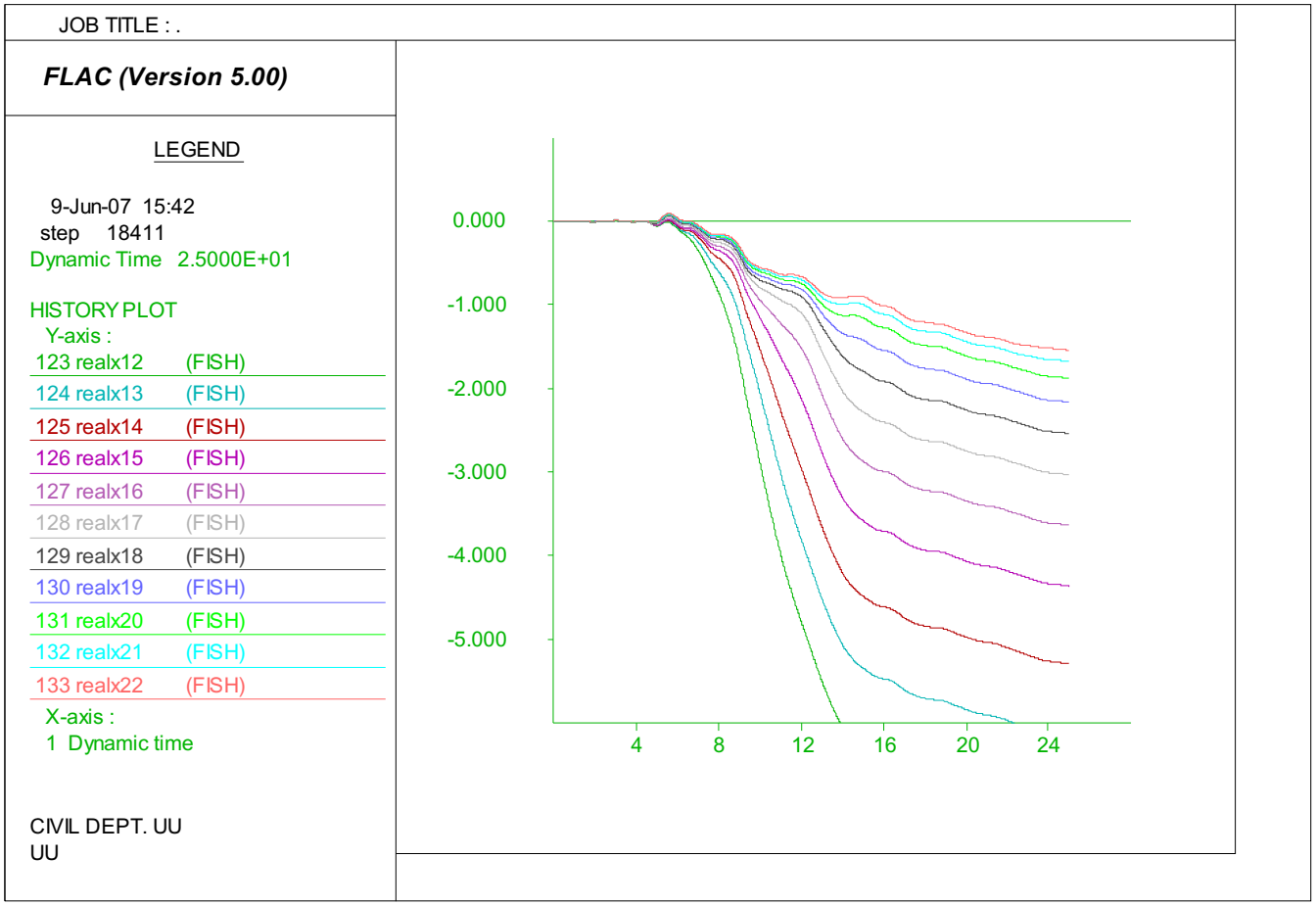


Figure A.23. Niigata Bandai section model later spreading prediction loaded by motion 7 with residual strength ratio of 0.065

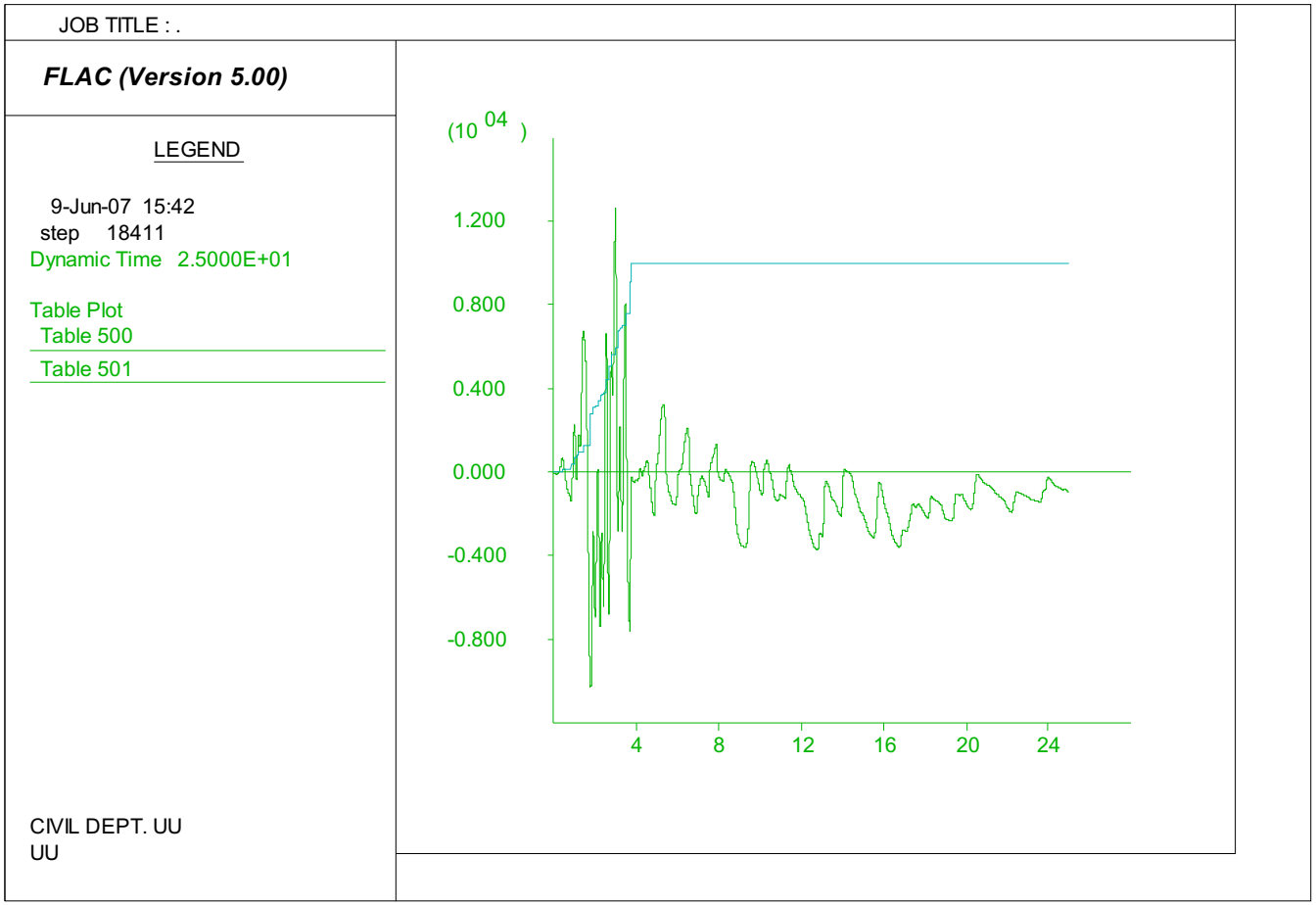


Figure A.24. Niigata Bandai section model pore water generation history loaded by motion 7 with residual strength ratio of 0.065

APPENDIX B

NIIGATA HOTEL DATA

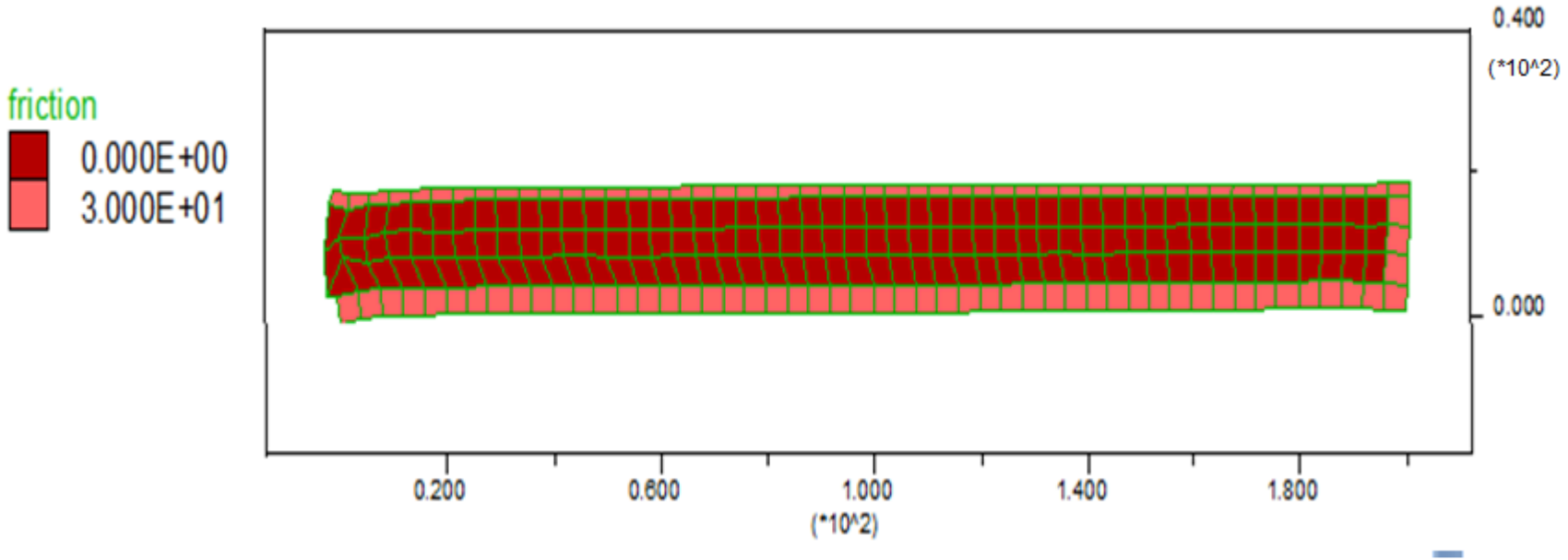


Figure B.1. Niigata Hotel section model soil properties change after liquefaction loaded by motion 1 with residual strength ratio of 0.085.

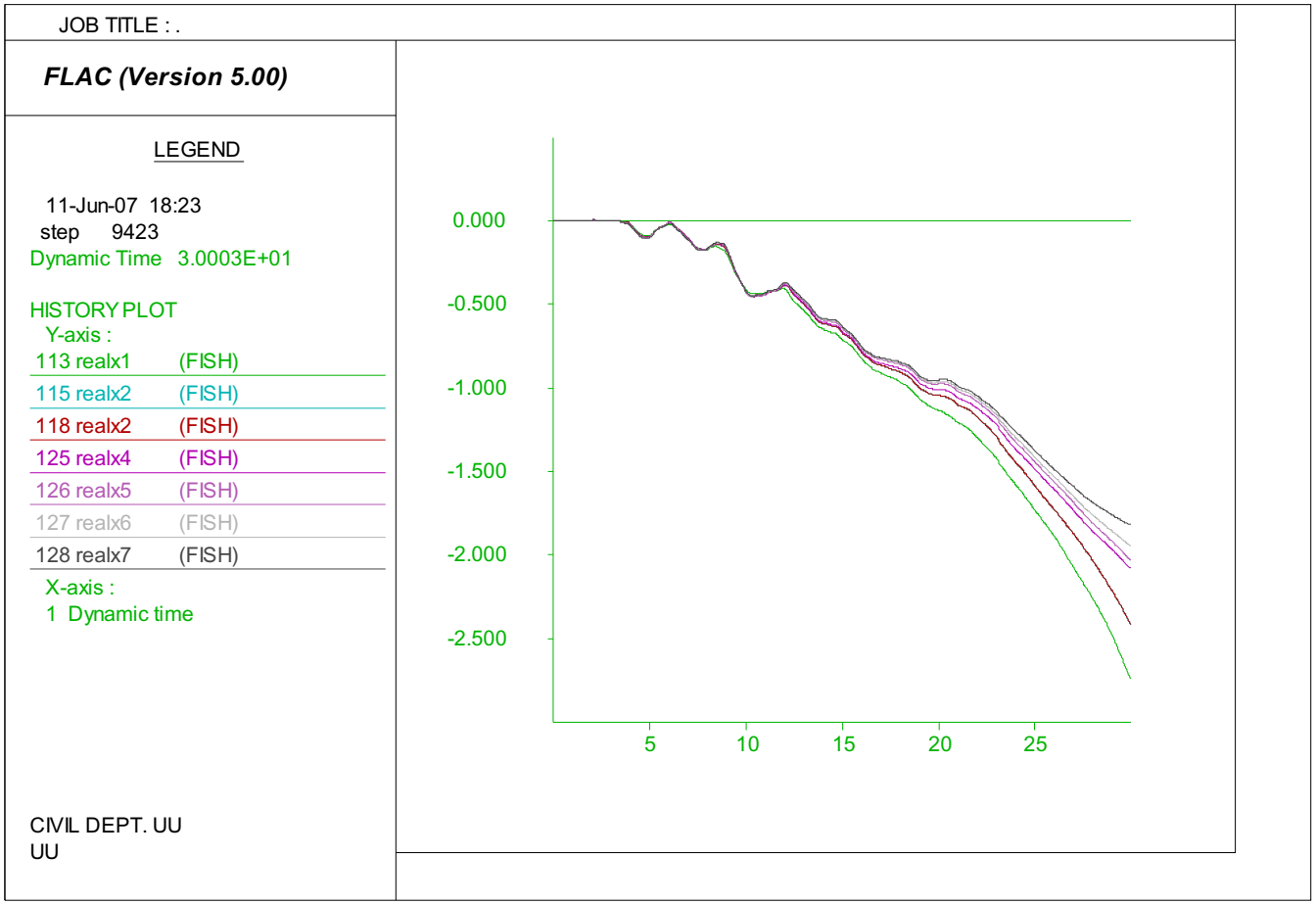


Figure B.2. Niigata Hotel section model later spreading prediction loaded by motion 1 with residual strength ratio of 0.085.

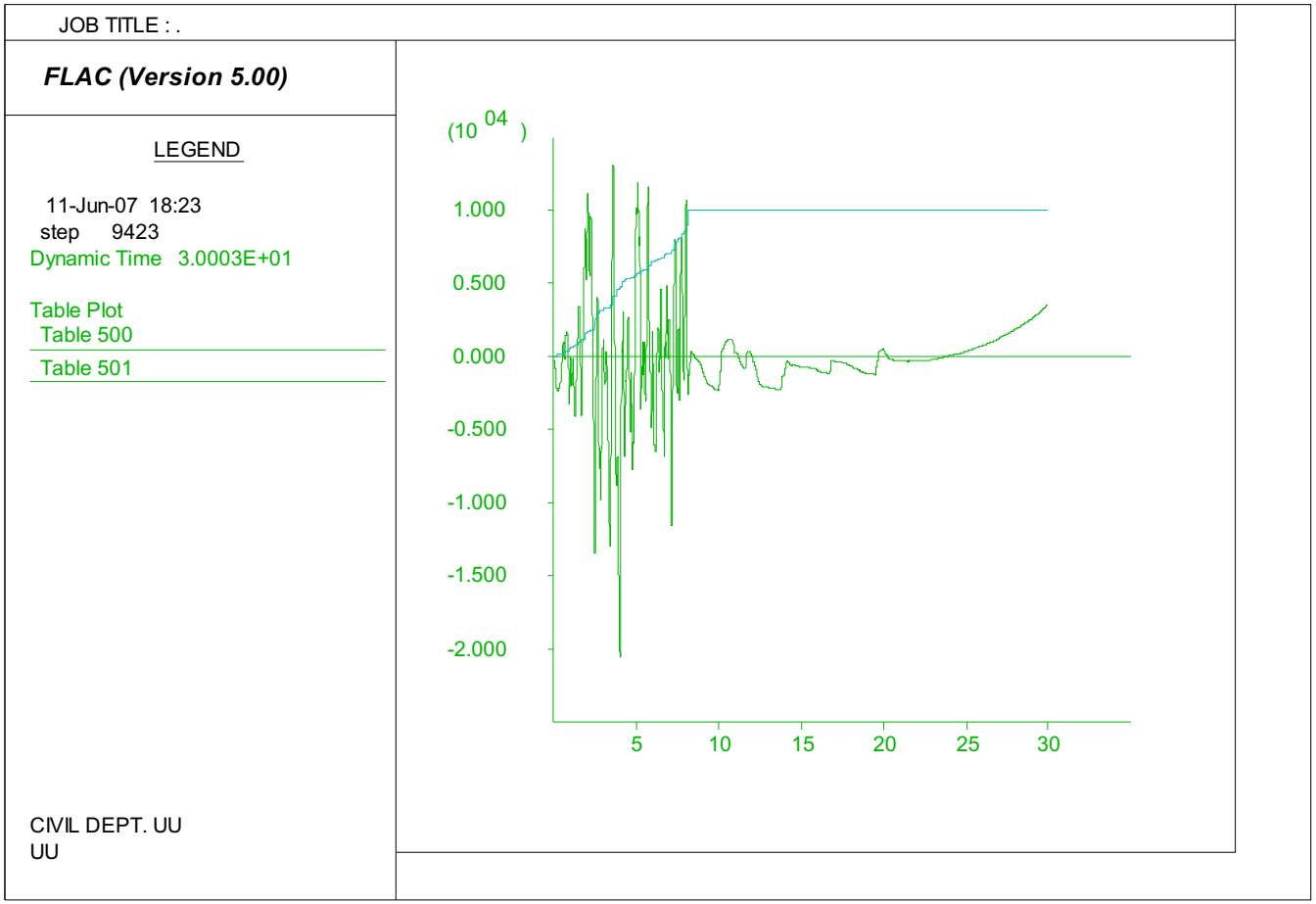


Figure B.3. Niigata Hotel section model pore water generation history loaded by motion 1 with residual strength ratio of 0.085.

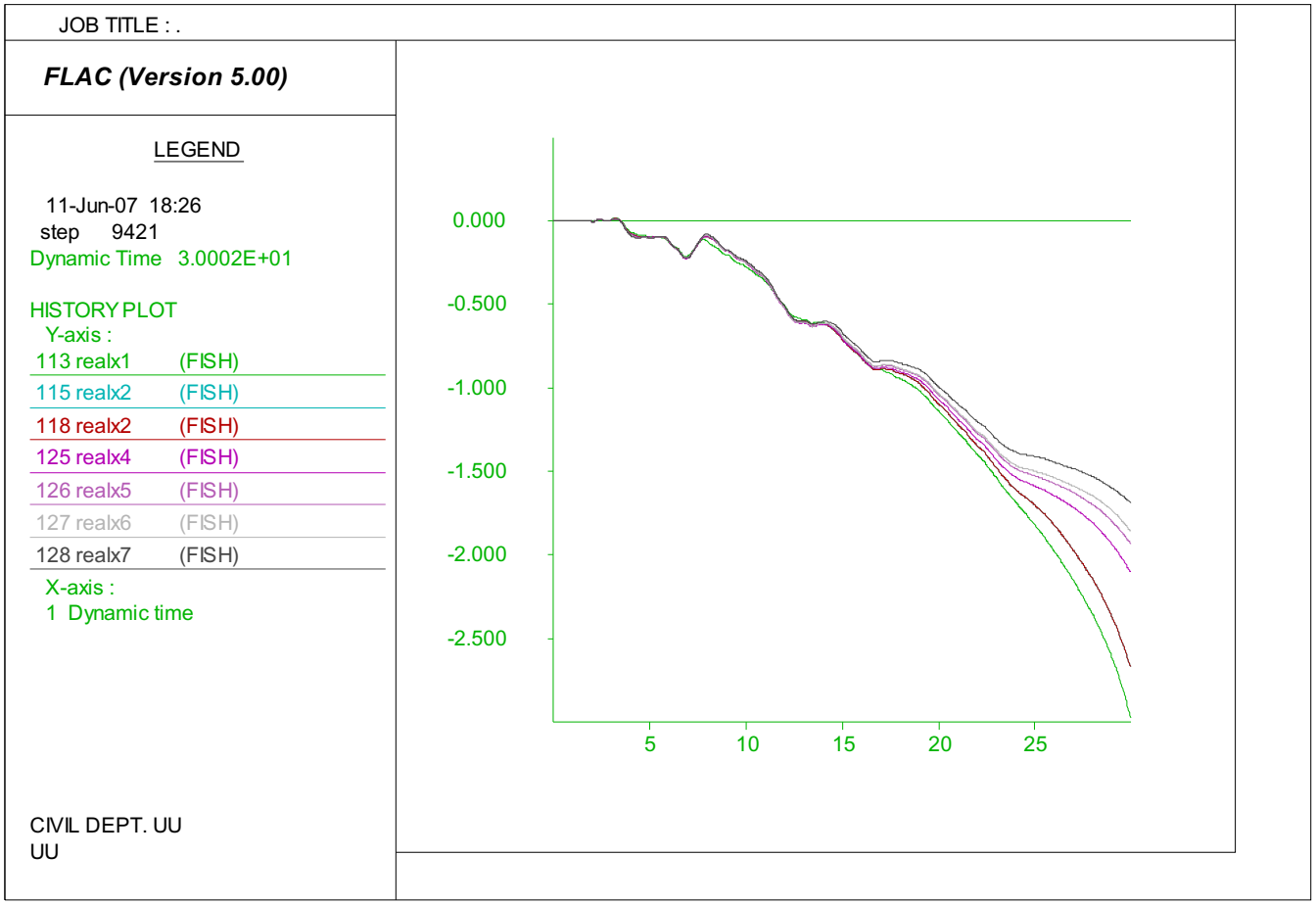


Figure B.4. Niigata Hotel section model later spreading prediction loaded by motion 2 with residual strength ratio of 0.085.

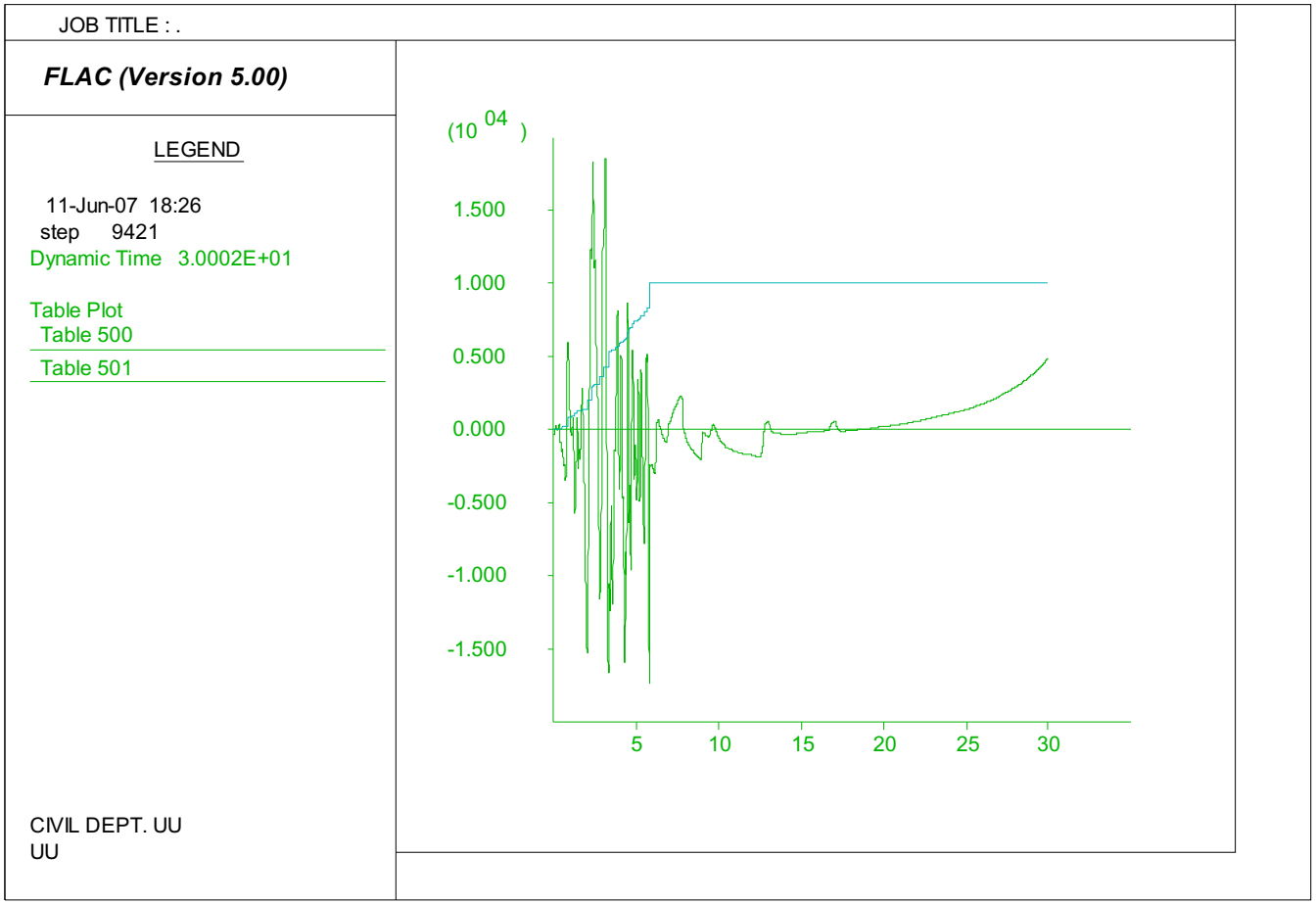


Figure B.5. Niigata Hotel section model pore water generation history loaded by motion 2 with residual strength ratio of 0.085.

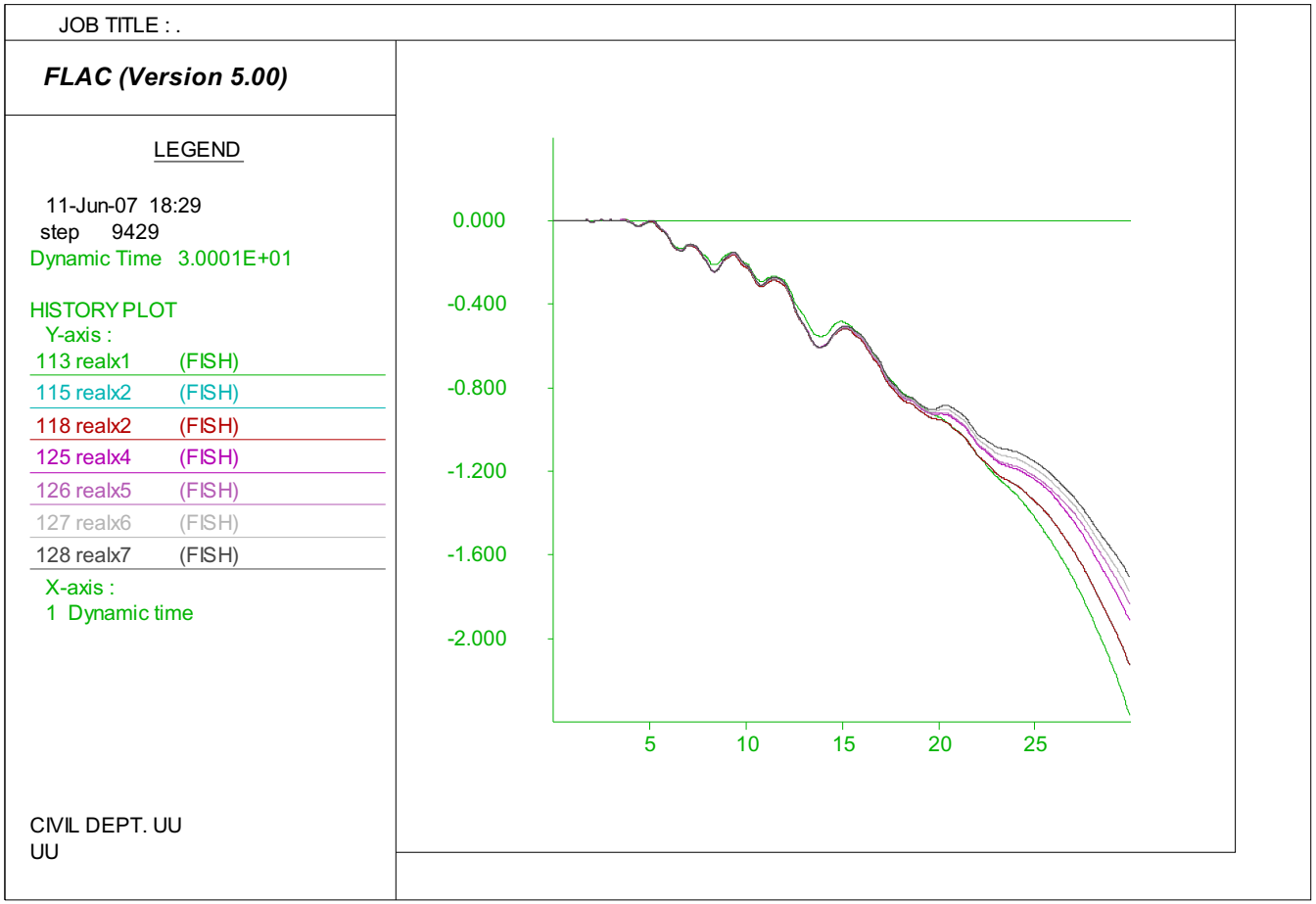


Figure B.6. Niigata Hotel section model later spreading prediction loaded by motion 3 with residual strength ratio of 0.085.

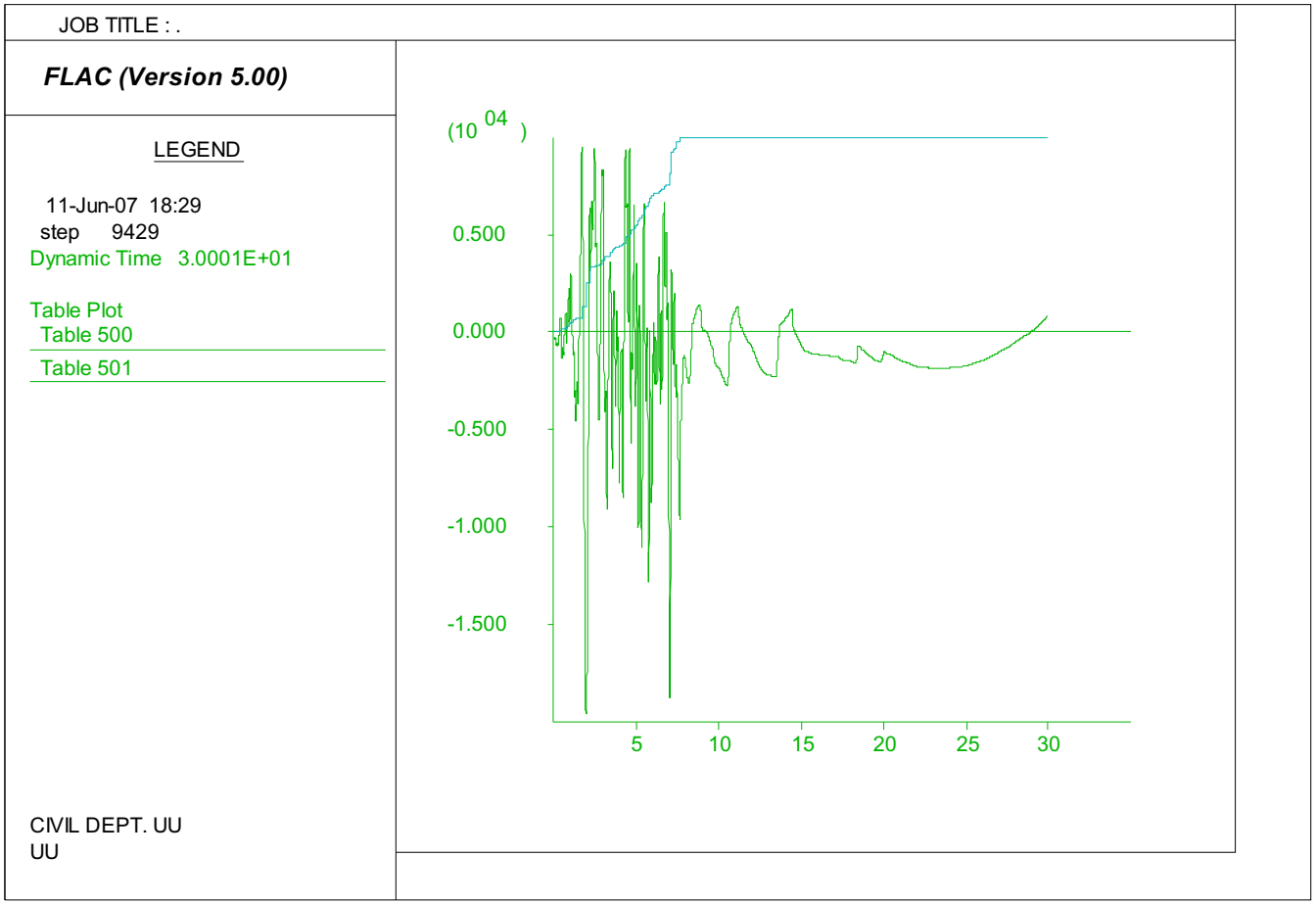


Figure B.7. Niigata Hotel section model pore water generation history loaded by motion 3 with residual strength ratio of 0.085.

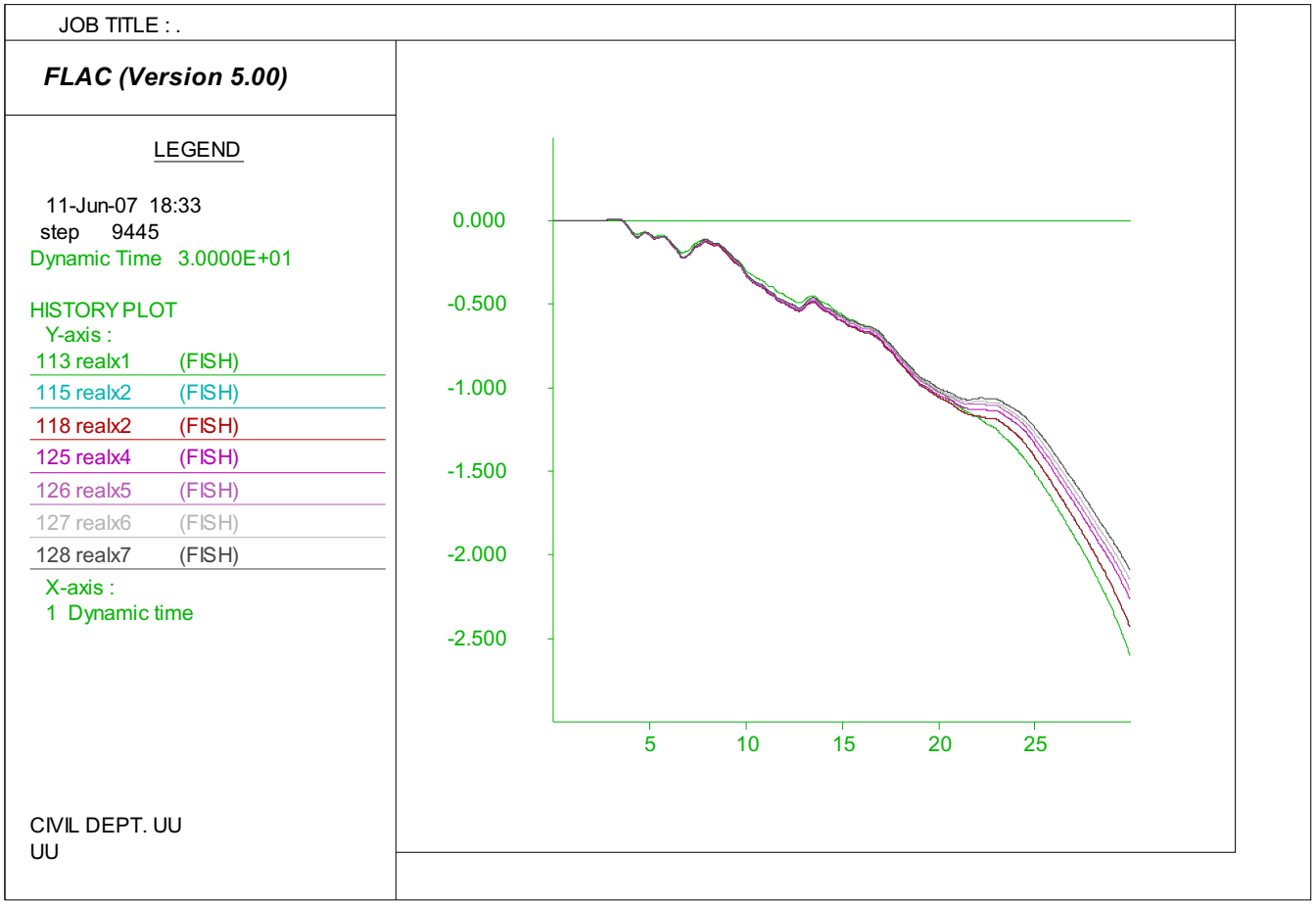


Figure B.8. Niigata Hotel section model later spreading prediction loaded by motion 4 with residual strength ratio of 0.085.

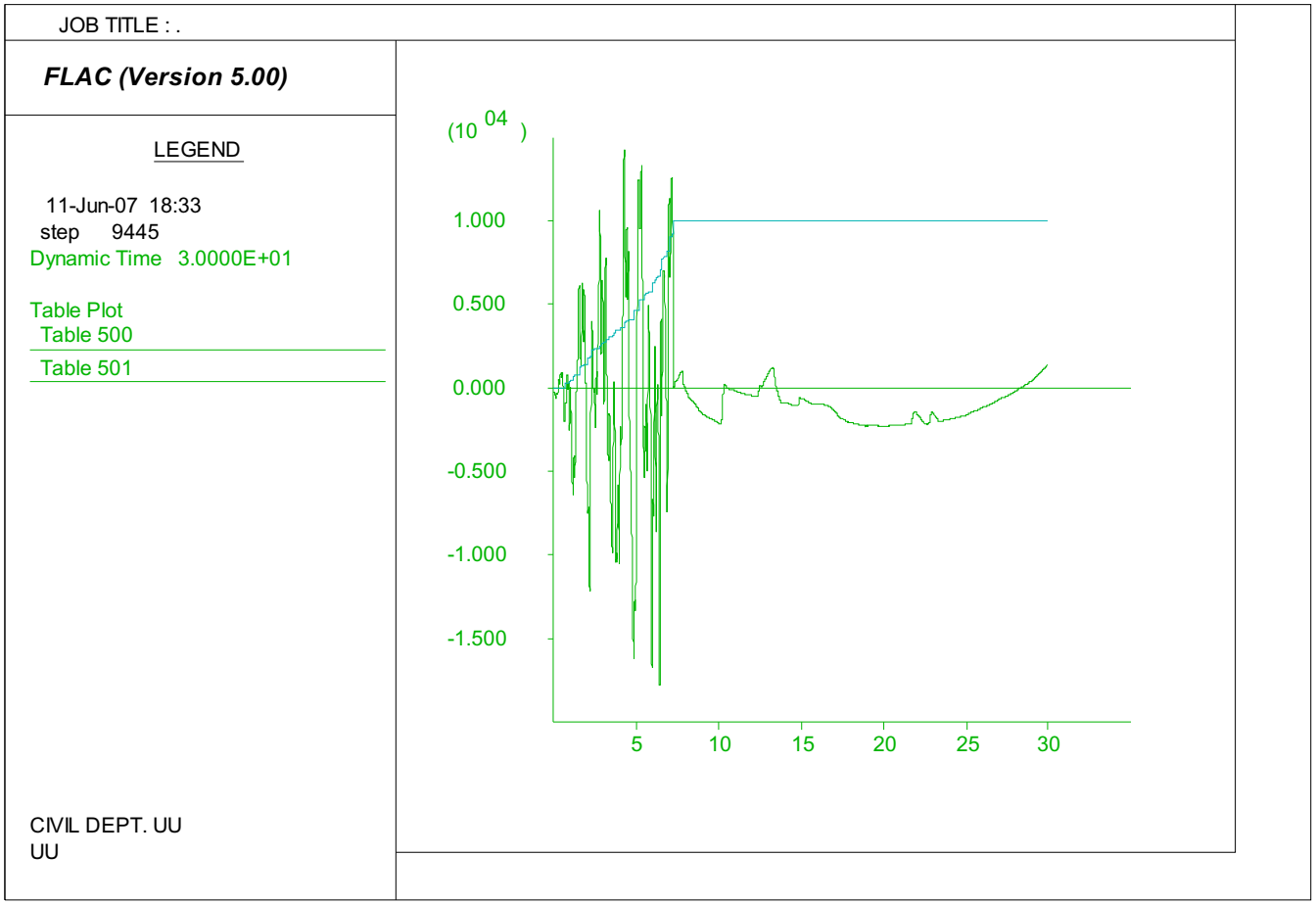


Figure B.9. Niigata Hotel section model pore water generation history loaded by motion 4 with residual strength ratio of 0.085.

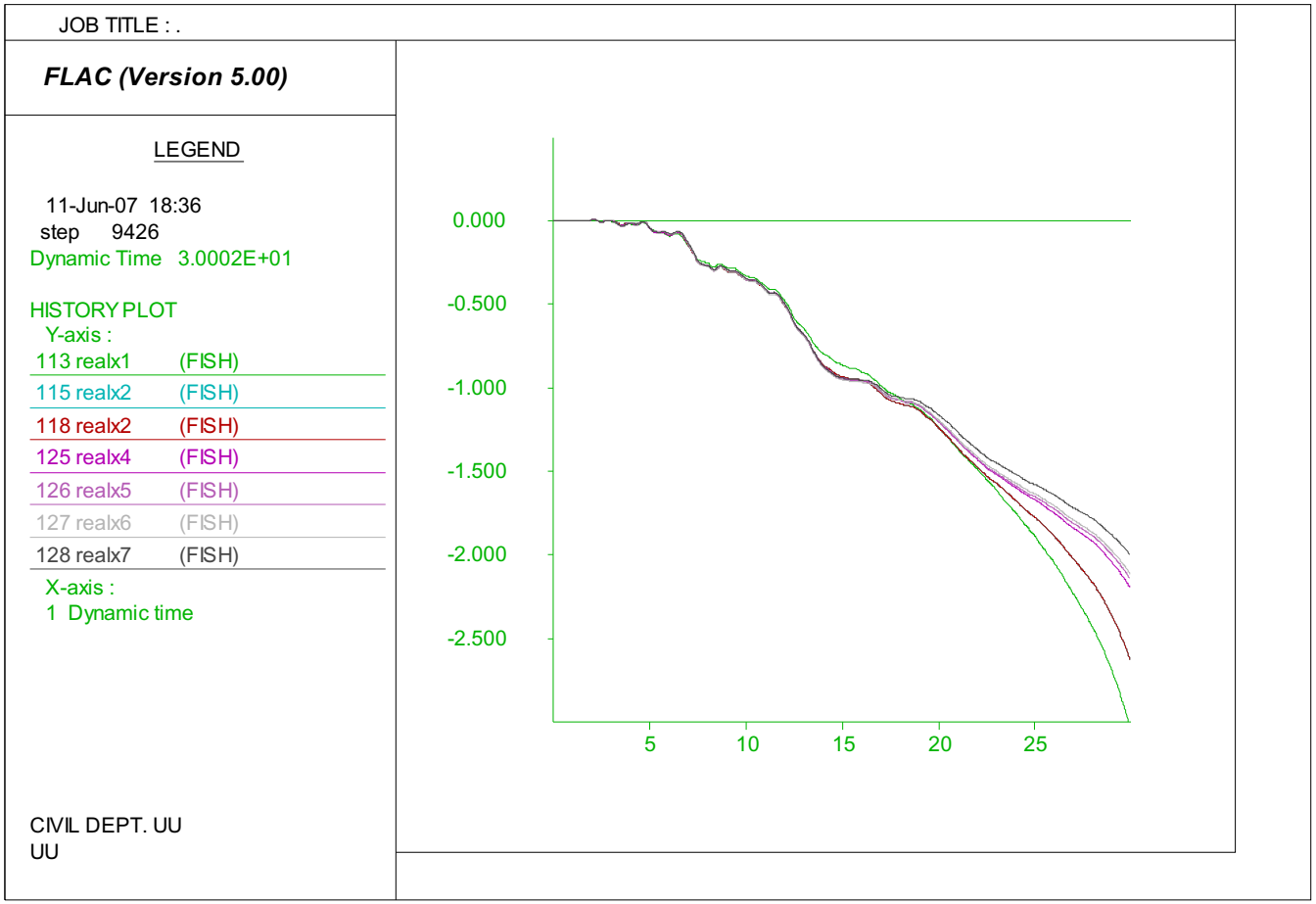


Figure B.10. Niigata Hotel section model later spreading prediction loaded by motion 5 with residual strength ratio of 0.085.

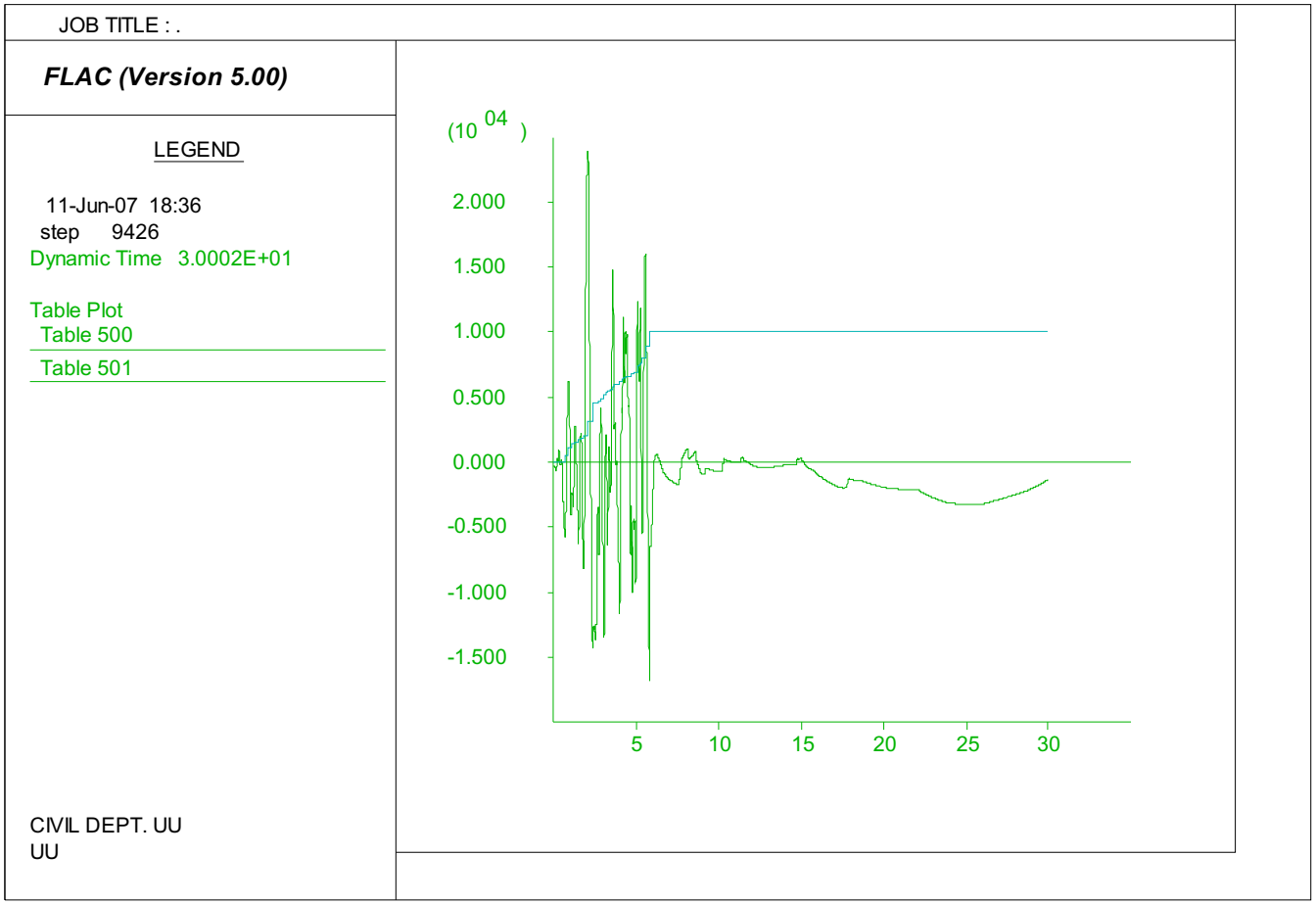


Figure B.11. Niigata Hotel section model pore water generation history loaded by motion 5 with residual strength ratio of 0.085.

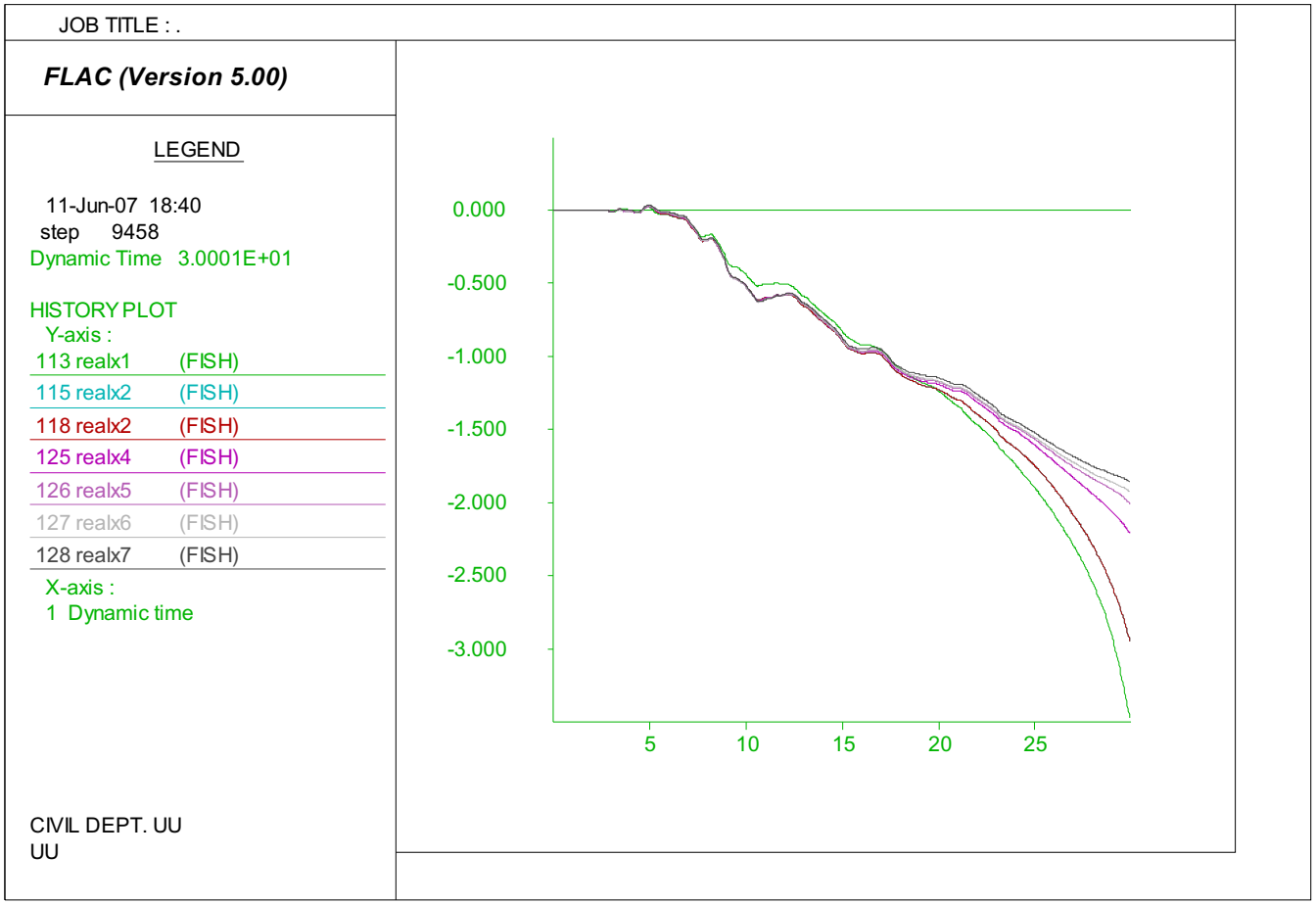


Figure B.12. Niigata Hotel section model later spreading prediction loaded by motion 6 with residual strength ratio of 0.085.

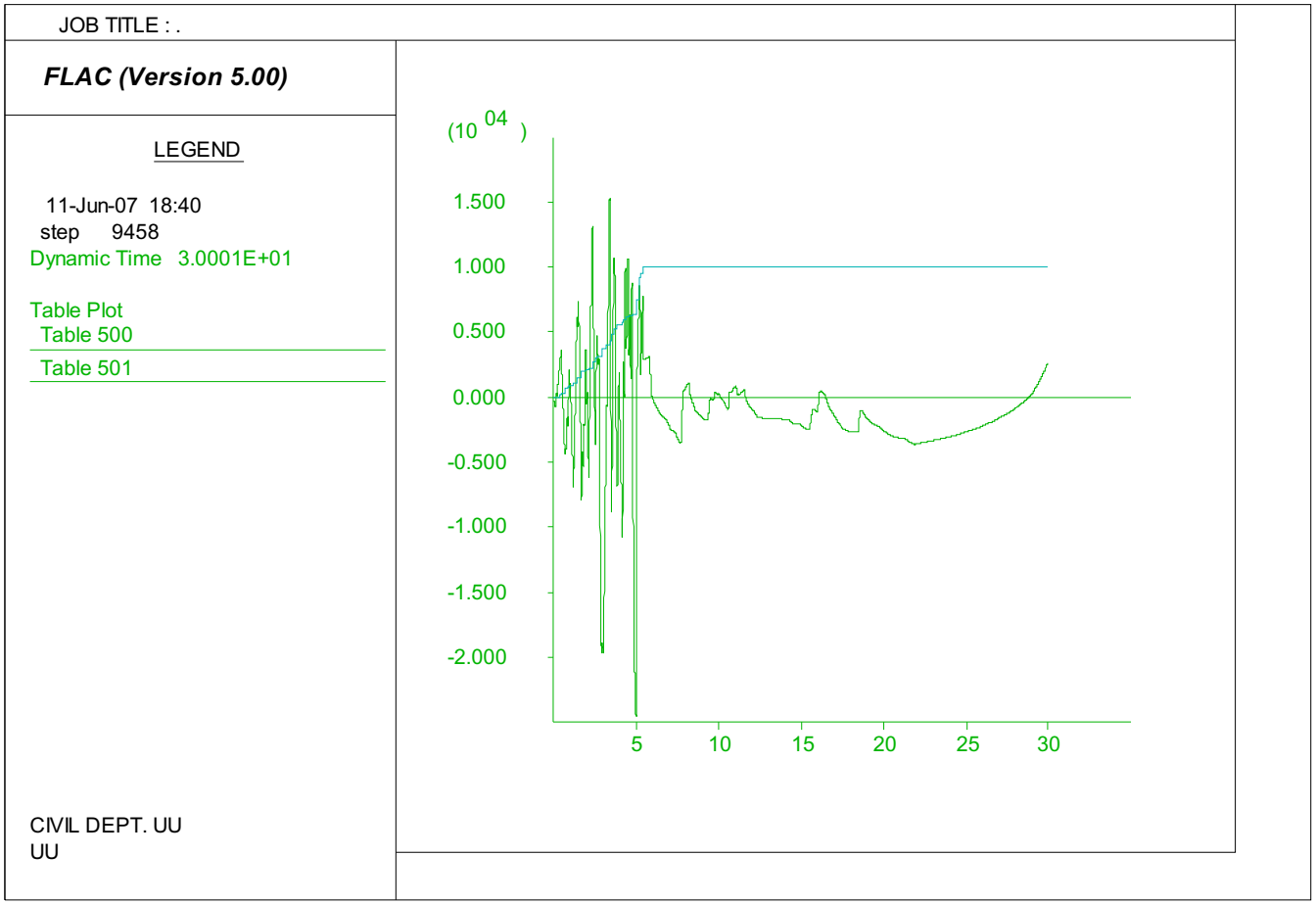


Figure B.13. Niigata Hotel section model pore water generation history loaded by motion 6 with residual strength ratio of 0.085.

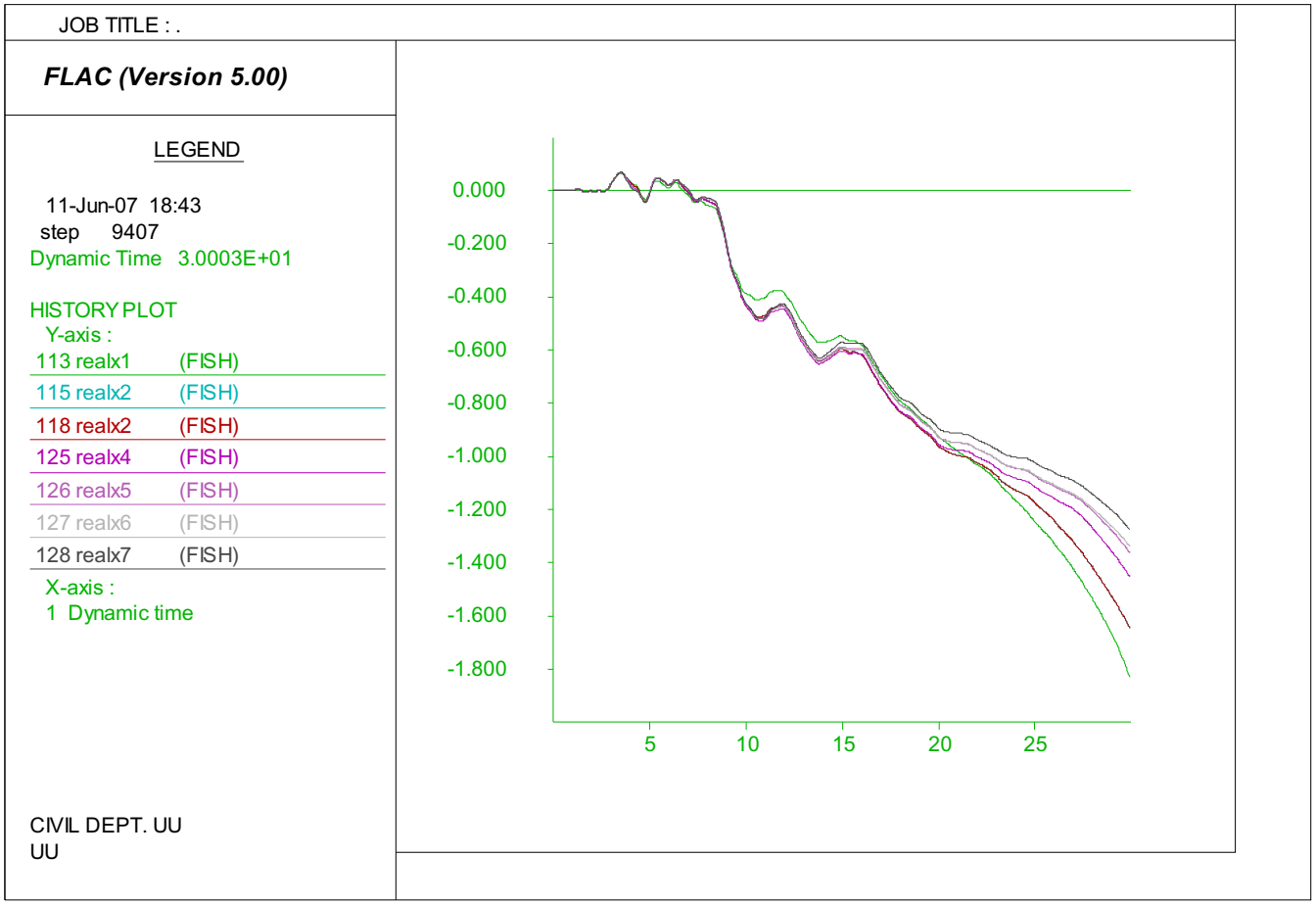


Figure B.14. Niigata Hotel section model later spreading prediction loaded by motion 7 with residual strength ratio of 0.085.

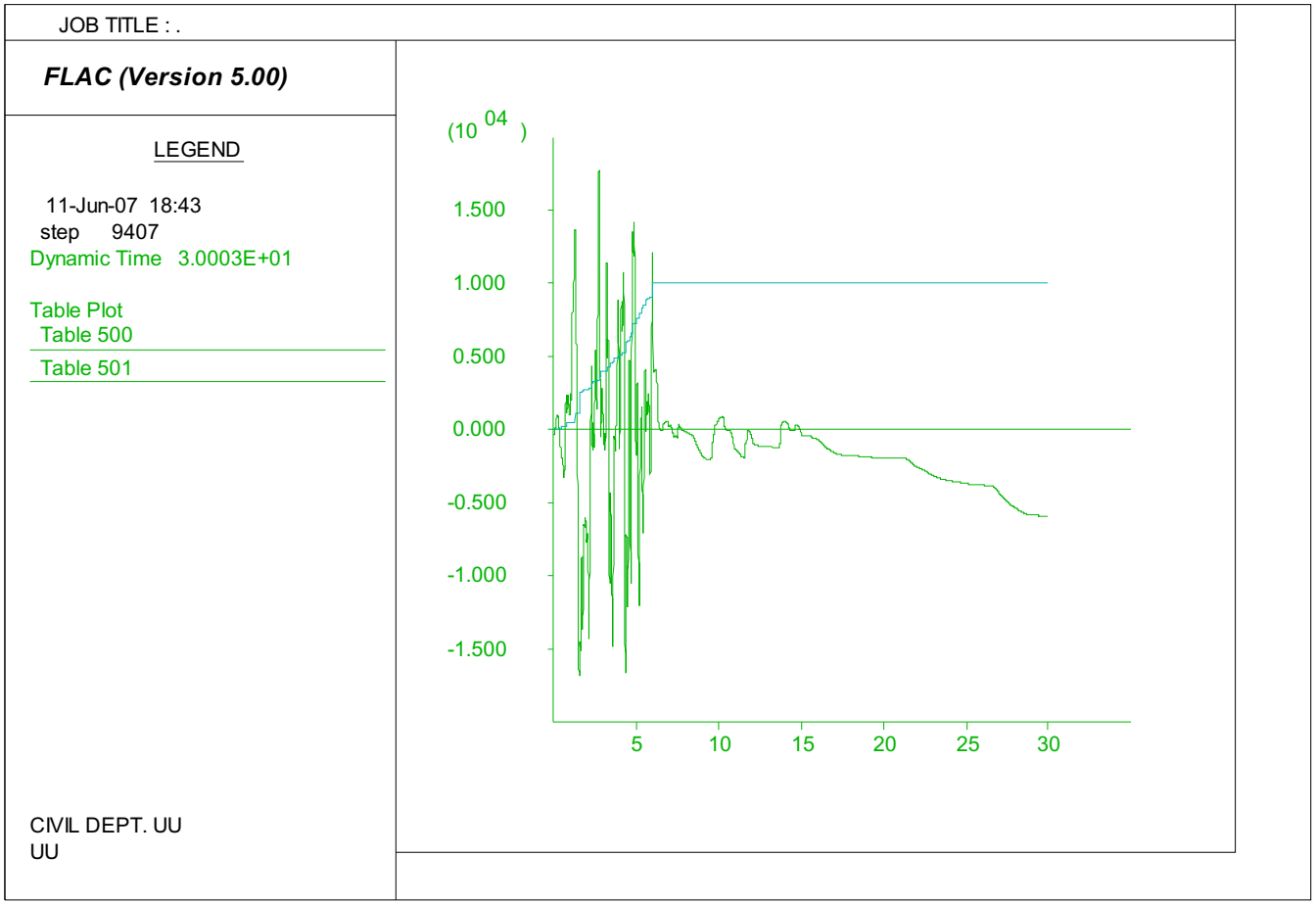


Figure B.15. Niigata Hotel section model pore water generation history loaded by motion 7 with residual strength ratio of 0.085.

APPENDIX C

NIIGATA SITE RAILWAY SECTION DATA

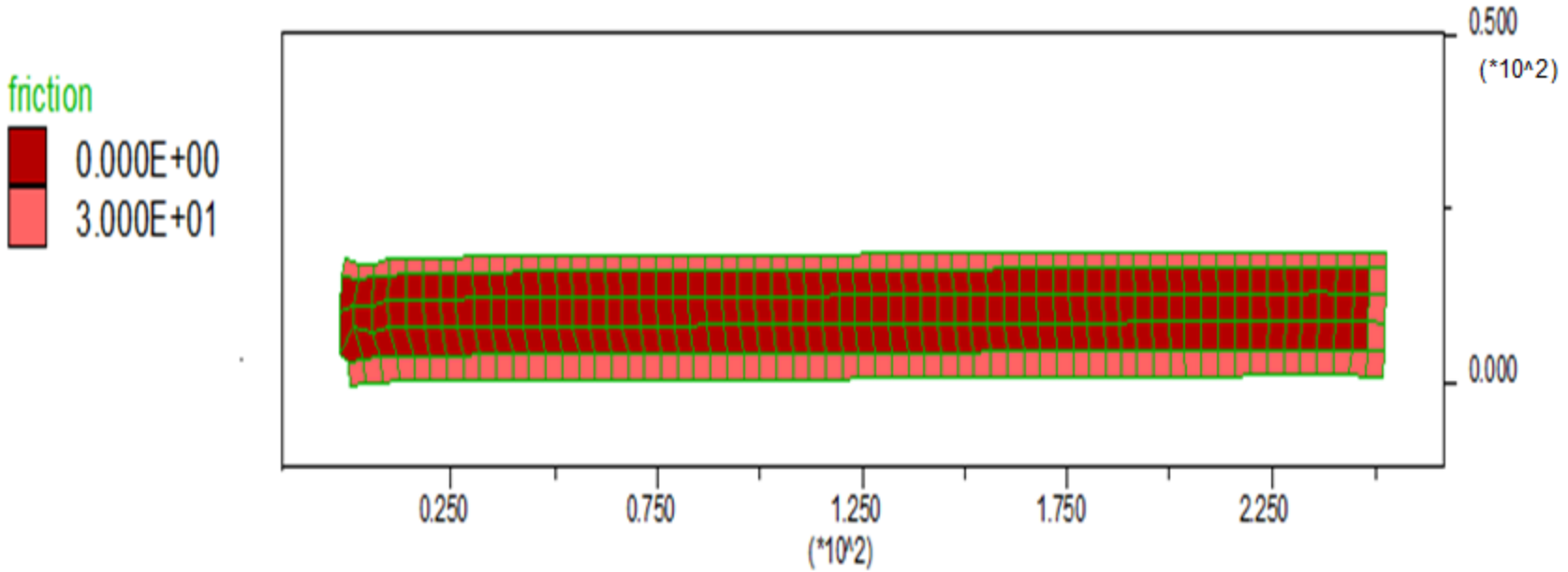


Figure C.1. Niigata railway section model soil properties change after liquefaction loaded by motion 1 with residual strength ratio of 0.085.

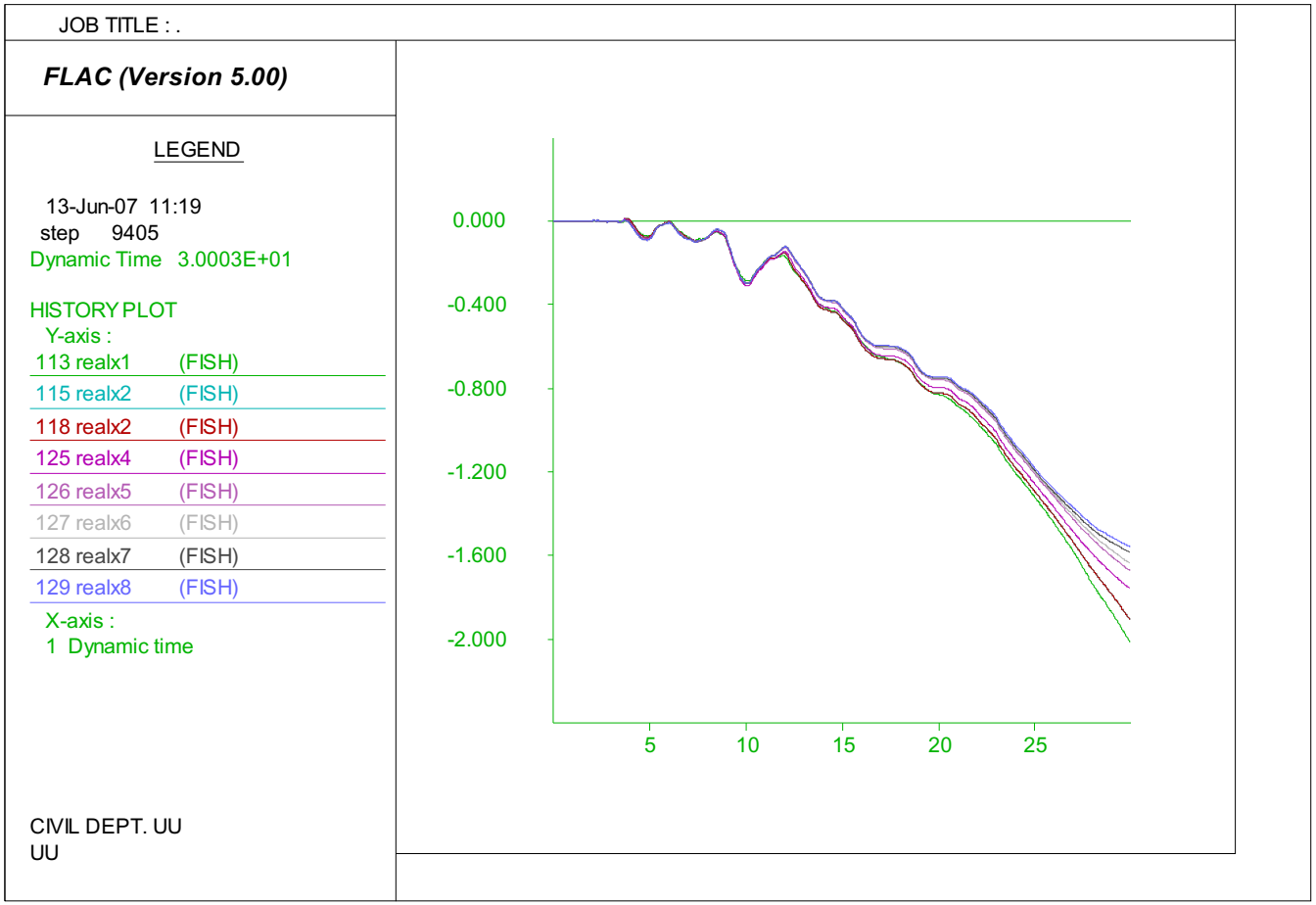


Figure C.2. Niigata railway section model later spreading prediction loaded by motion 1 with residual strength ratio of 0.085.

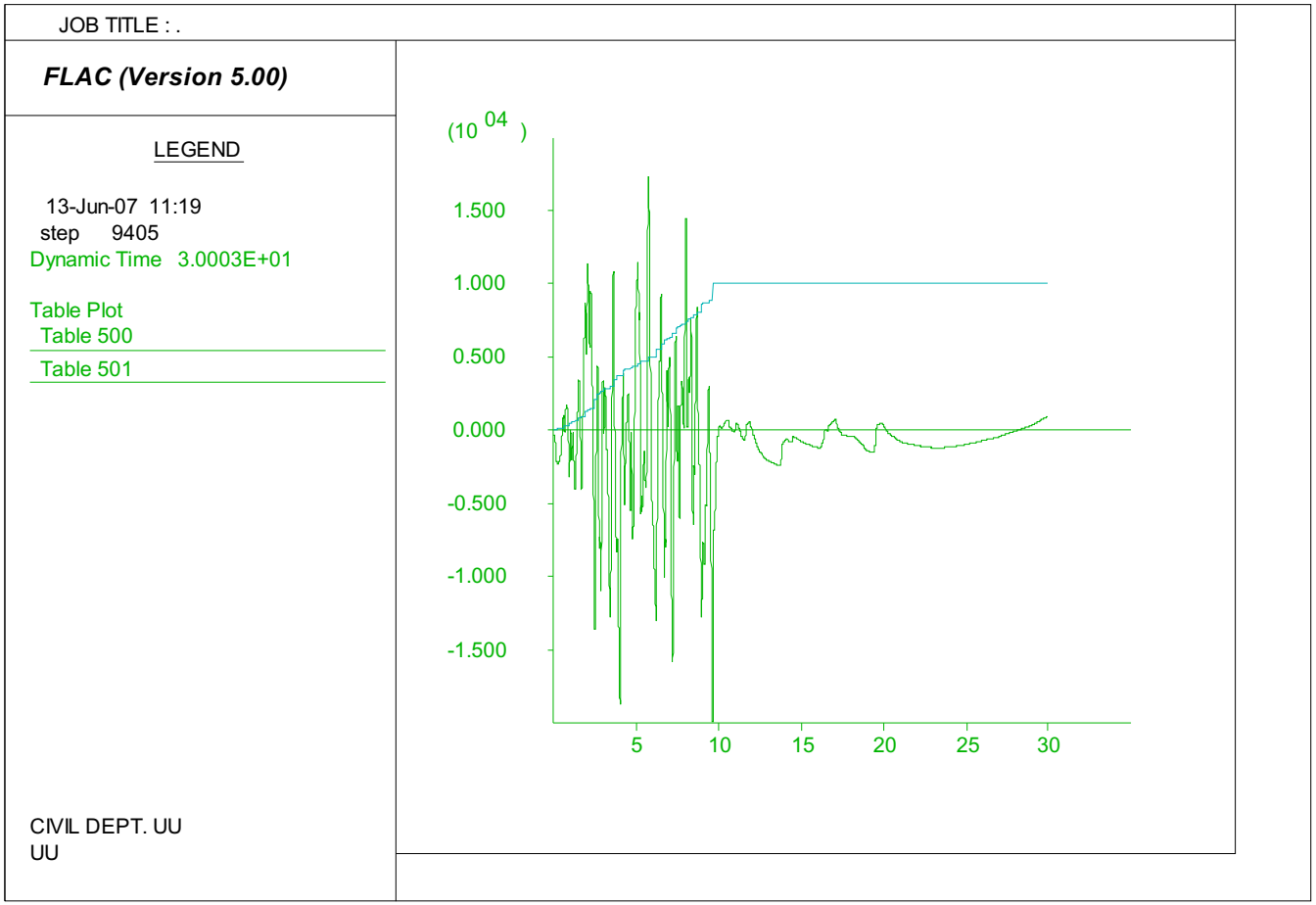


Figure C.3. Niigata railway section model pore water generation history loaded by motion 1 with residual strength ratio of 0.085.

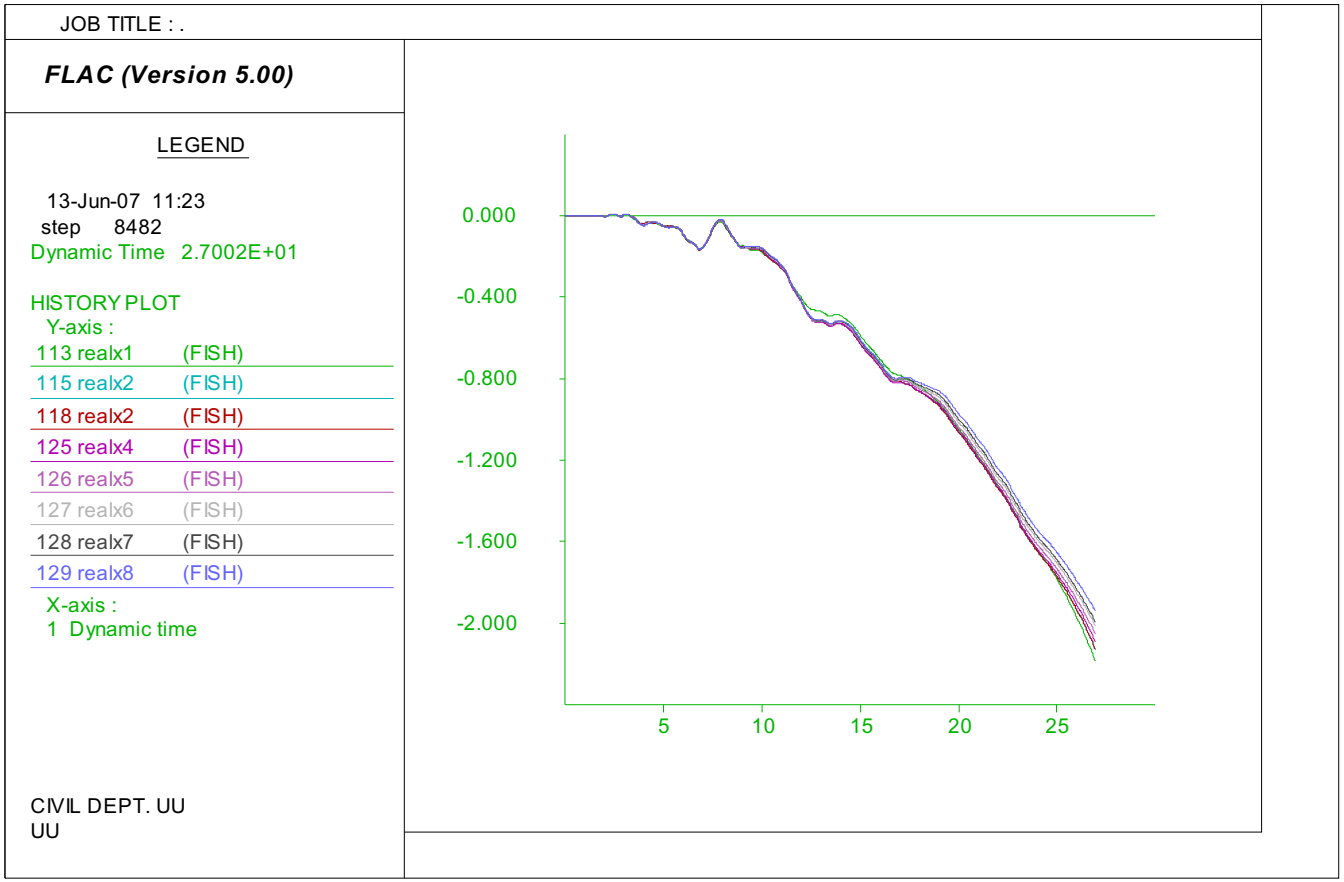


Figure C.4. Niigata railway section model later spreading prediction loaded by motion 2 with residual strength ratio of 0.085.

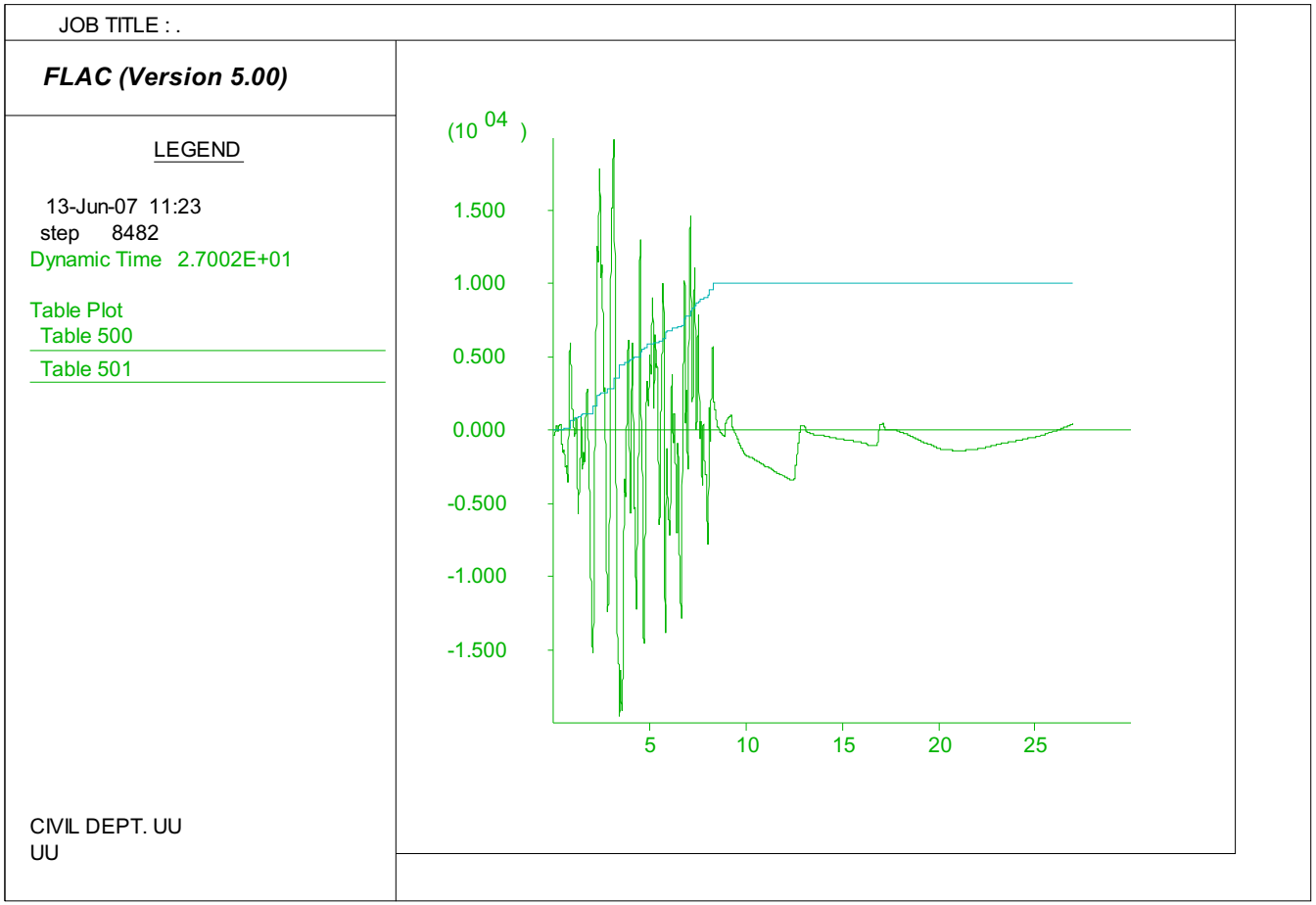


Figure C.5. Niigata railway section model pore water generation history loaded by motion 2 with residual strength ratio of 0.085.

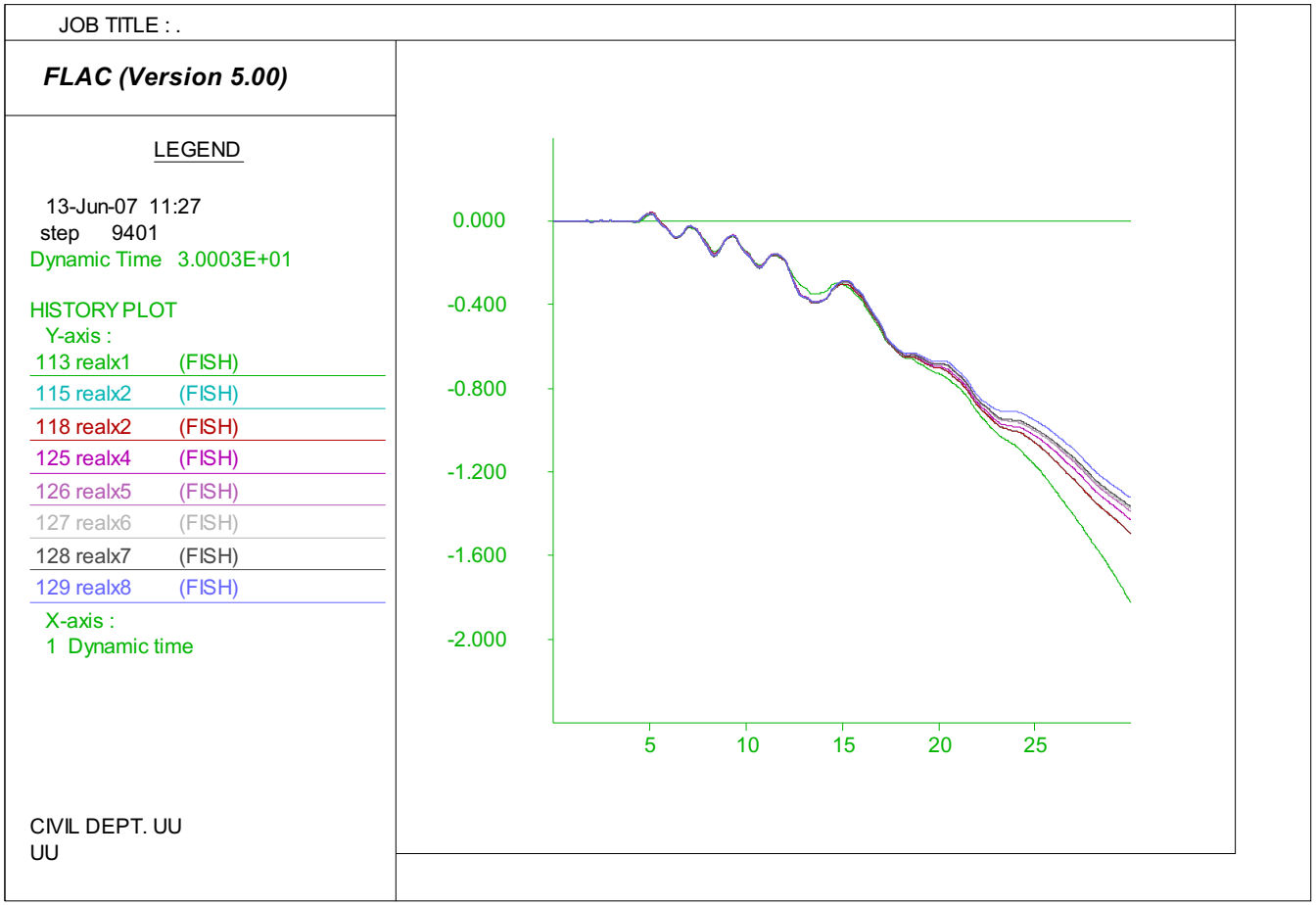


Figure C.6. Niigata railway section model later spreading prediction loaded by motion 3 with residual strength ratio of 0.085.

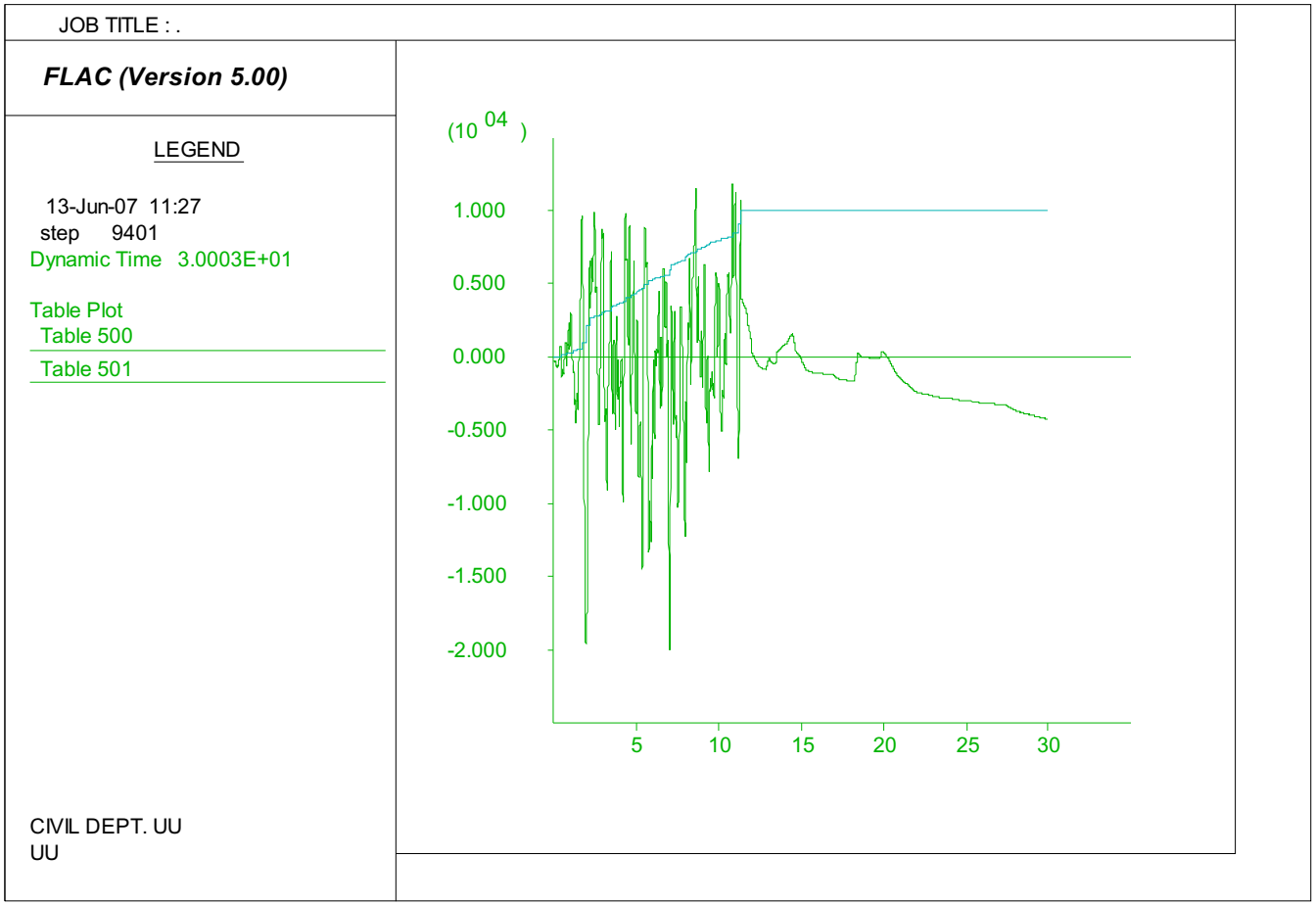


Figure C.7. Niigata railway section model pore water generation history loaded by motion 3 with residual strength ratio of 0.085.

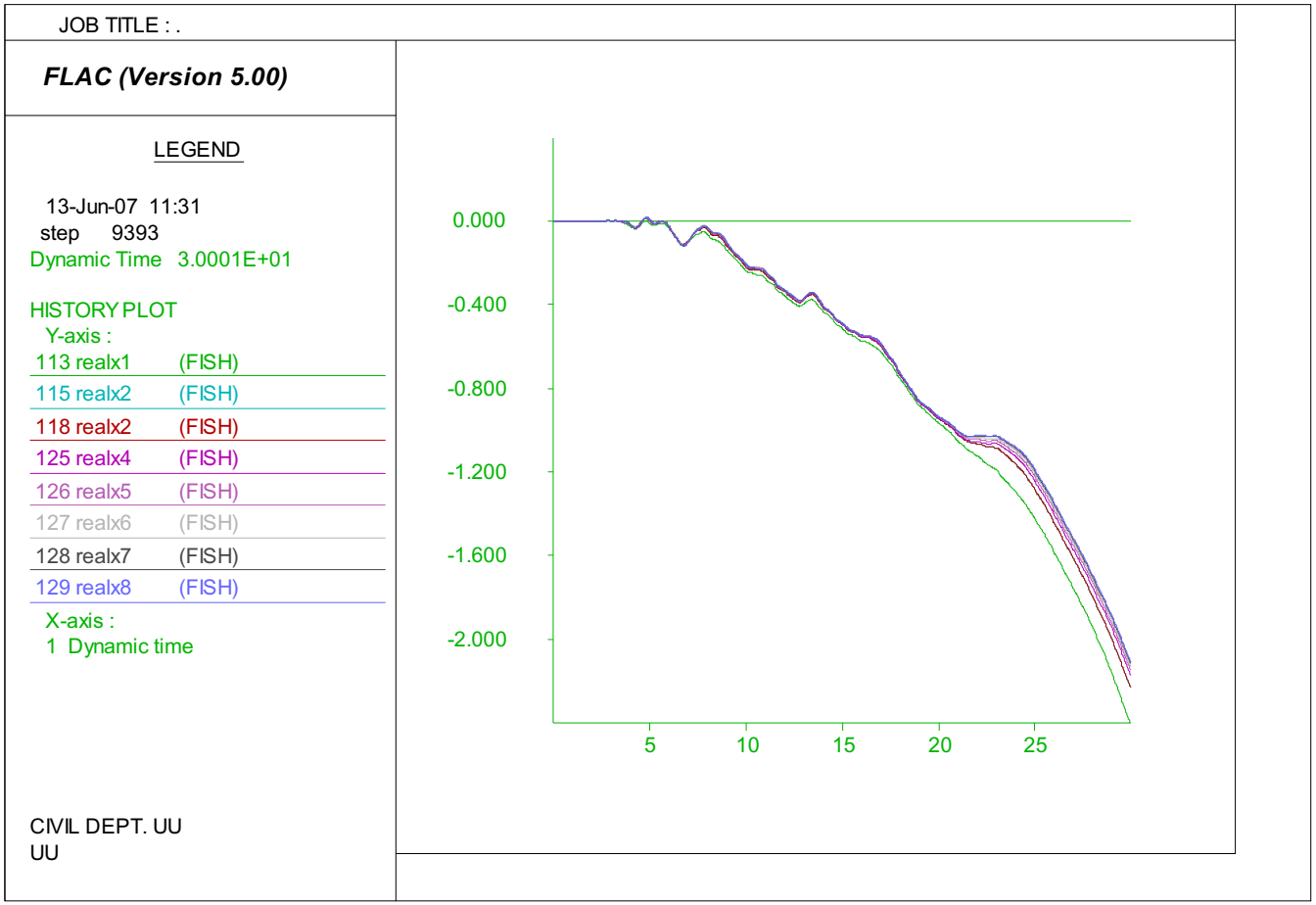


Figure C.8. Niigata railway section model later spreading prediction loaded by motion 4 with residual strength ratio of 0.085.

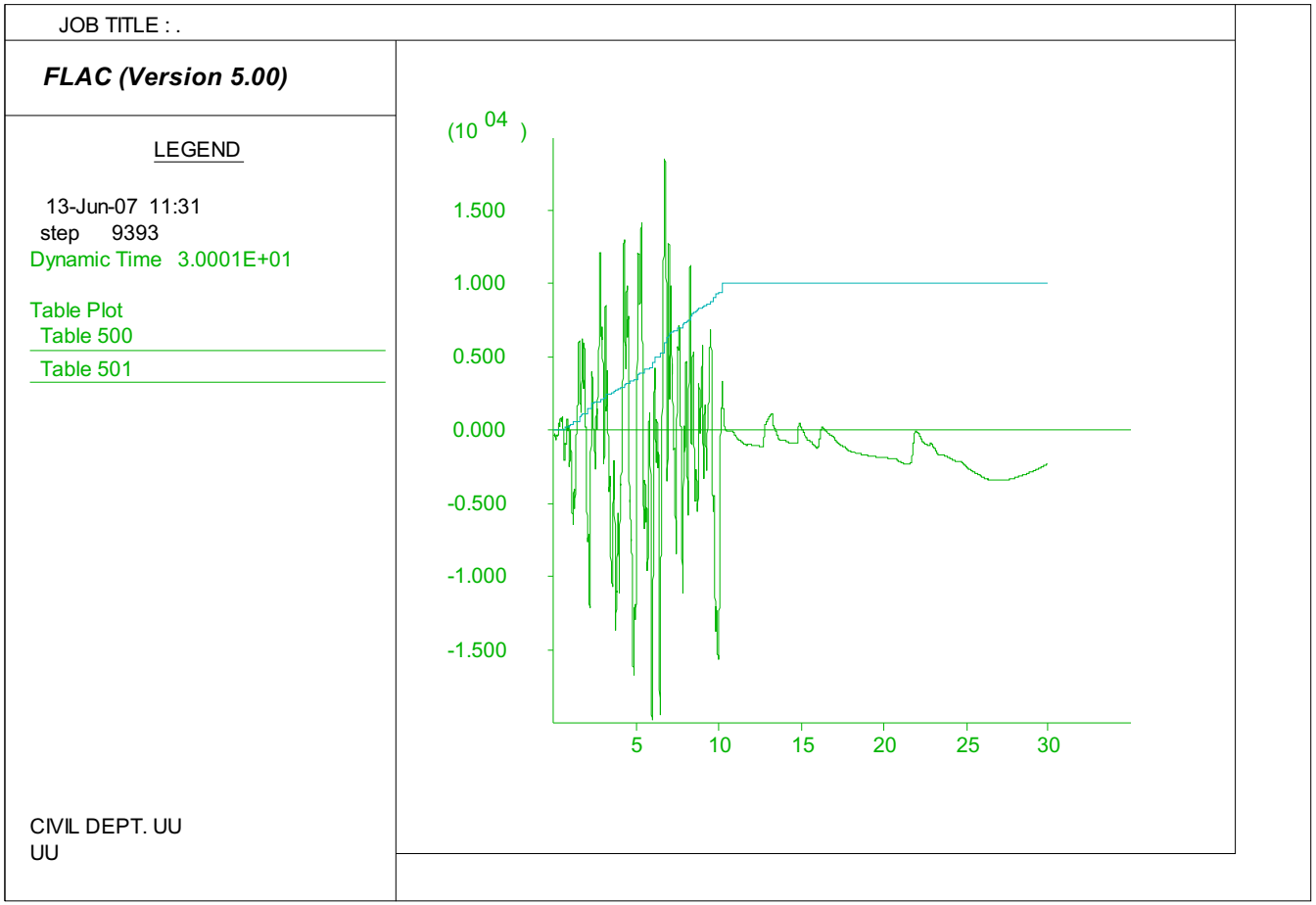


Figure C.9. Niigata railway section model pore water generation history loaded by motion 4 with residual strength ratio of 0.085.

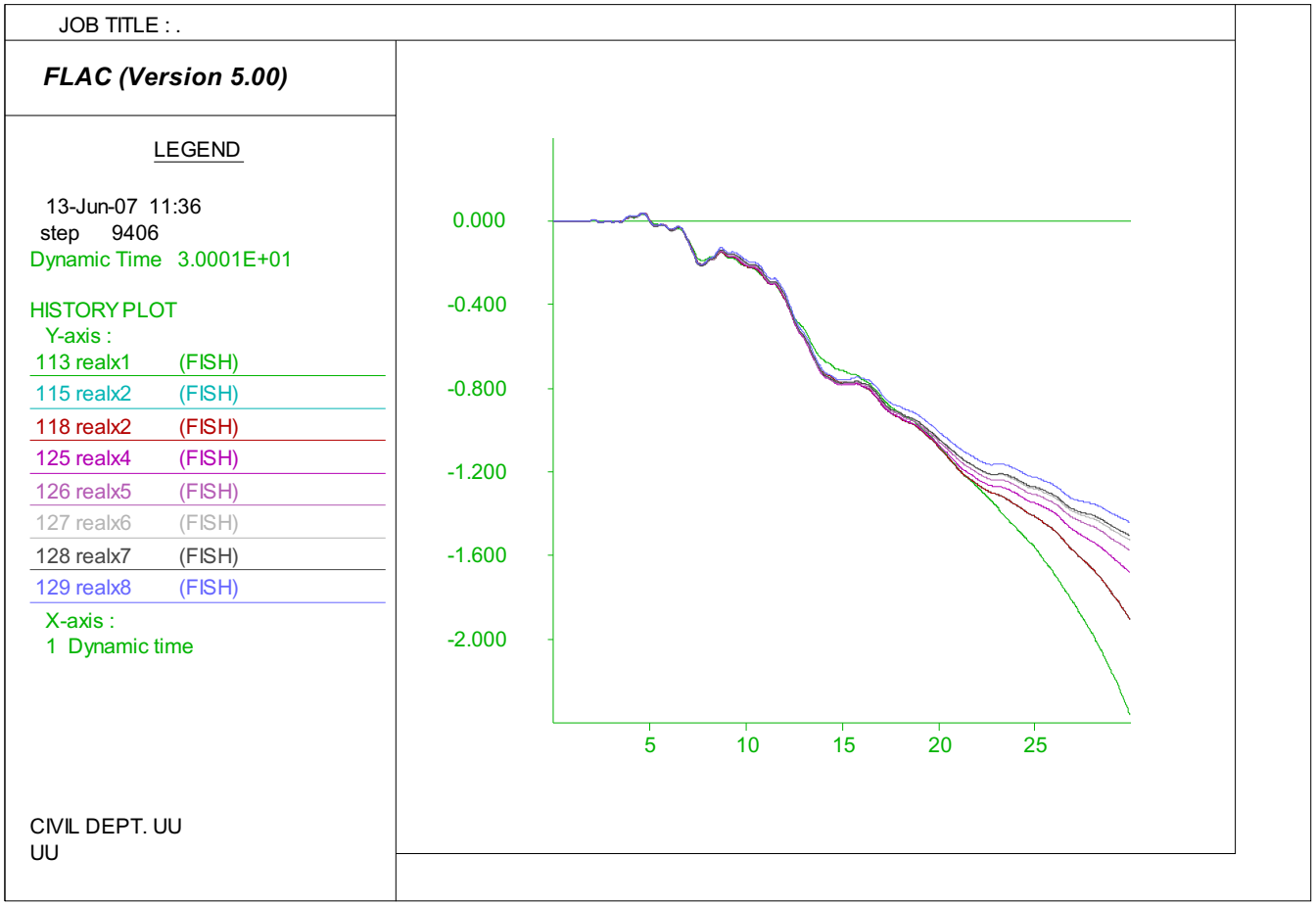


Figure C.10. Niigata railway section model later spreading prediction loaded by motion 5 with residual strength ratio of 0.085.

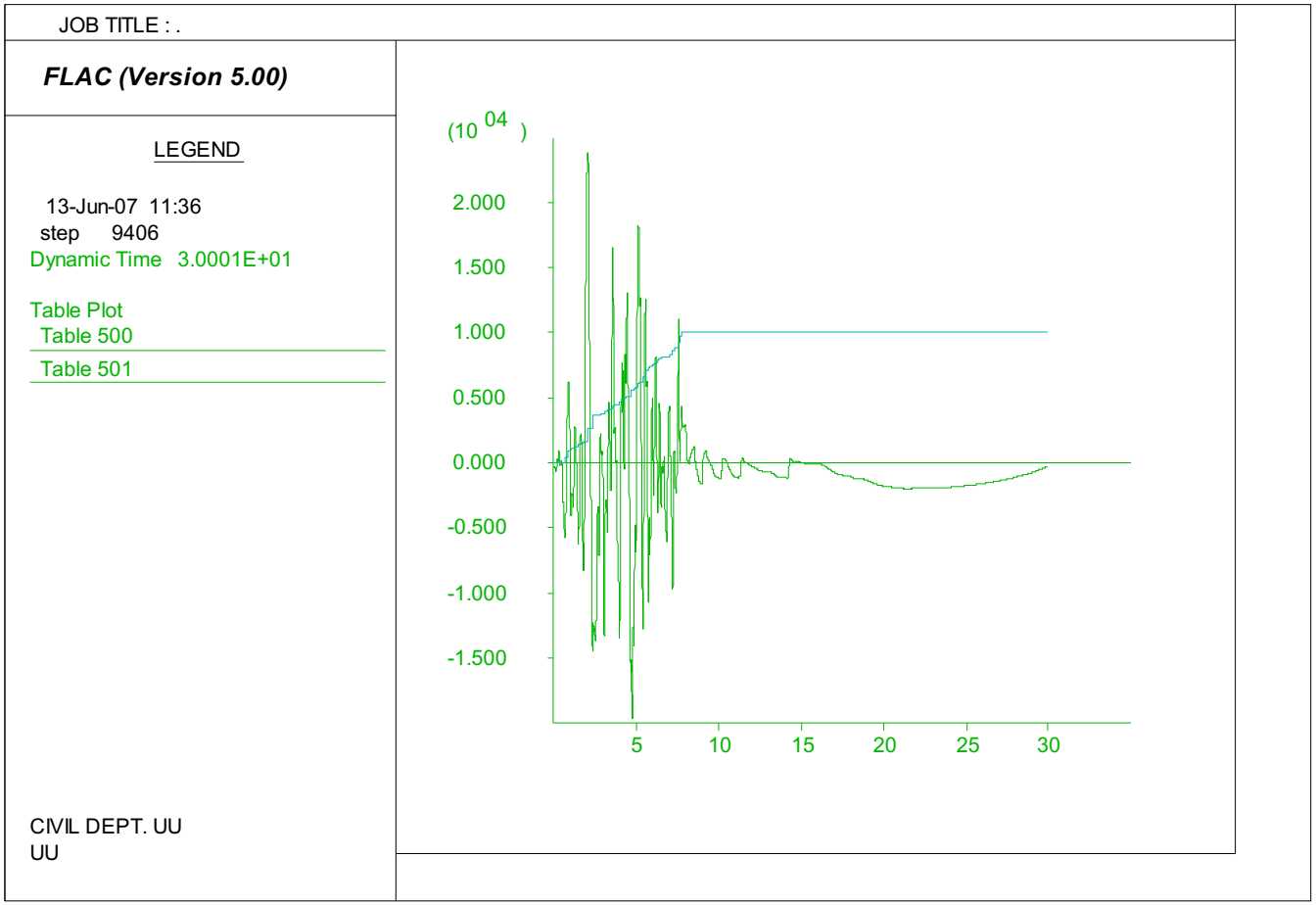


Figure C.11. Niigata railway section model pore water generation history loaded by motion 5 with residual strength ratio of 0.085.

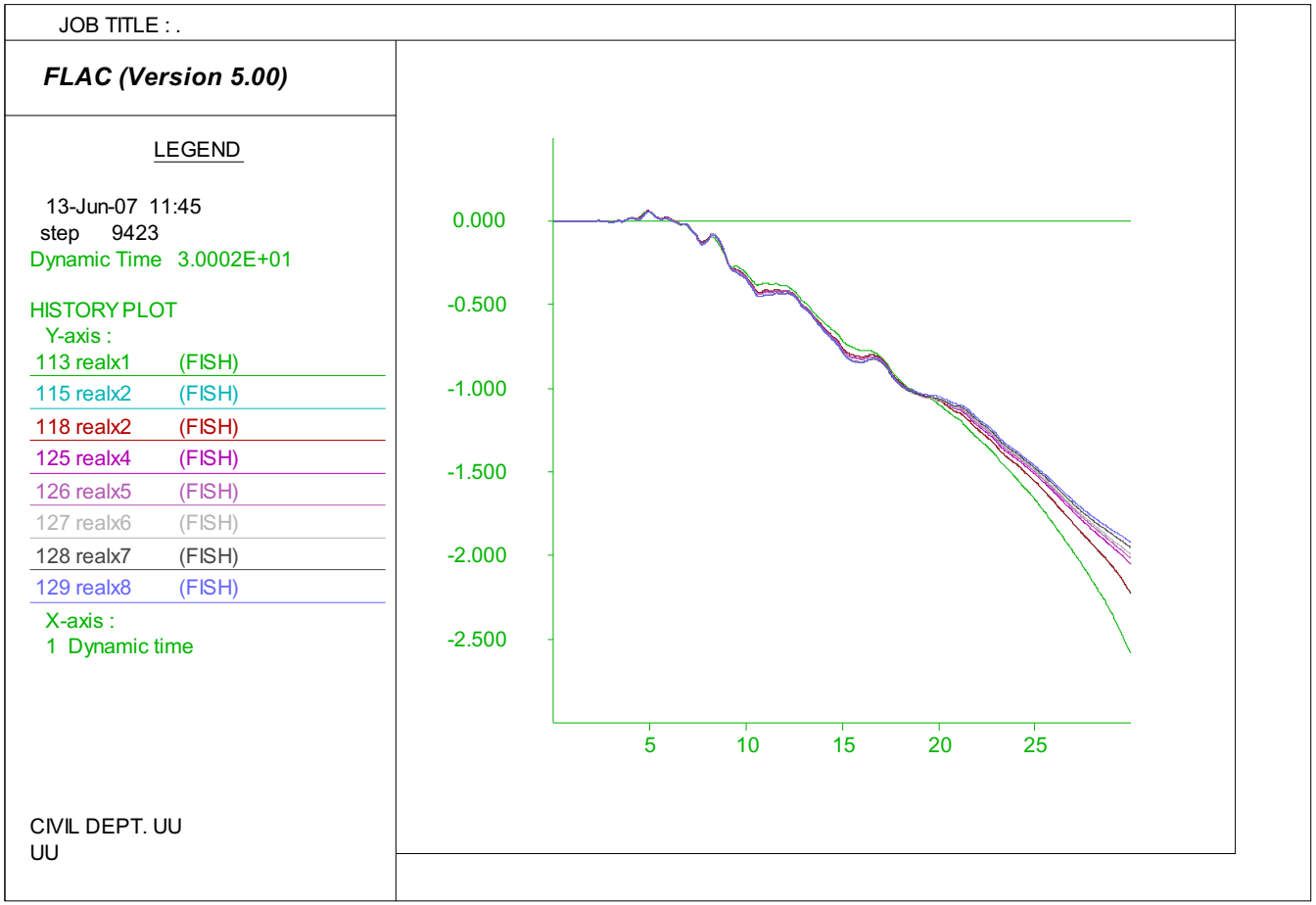


Figure C.12. Niigata railway section model later spreading prediction loaded by motion 6 with residual strength ratio of 0.085.

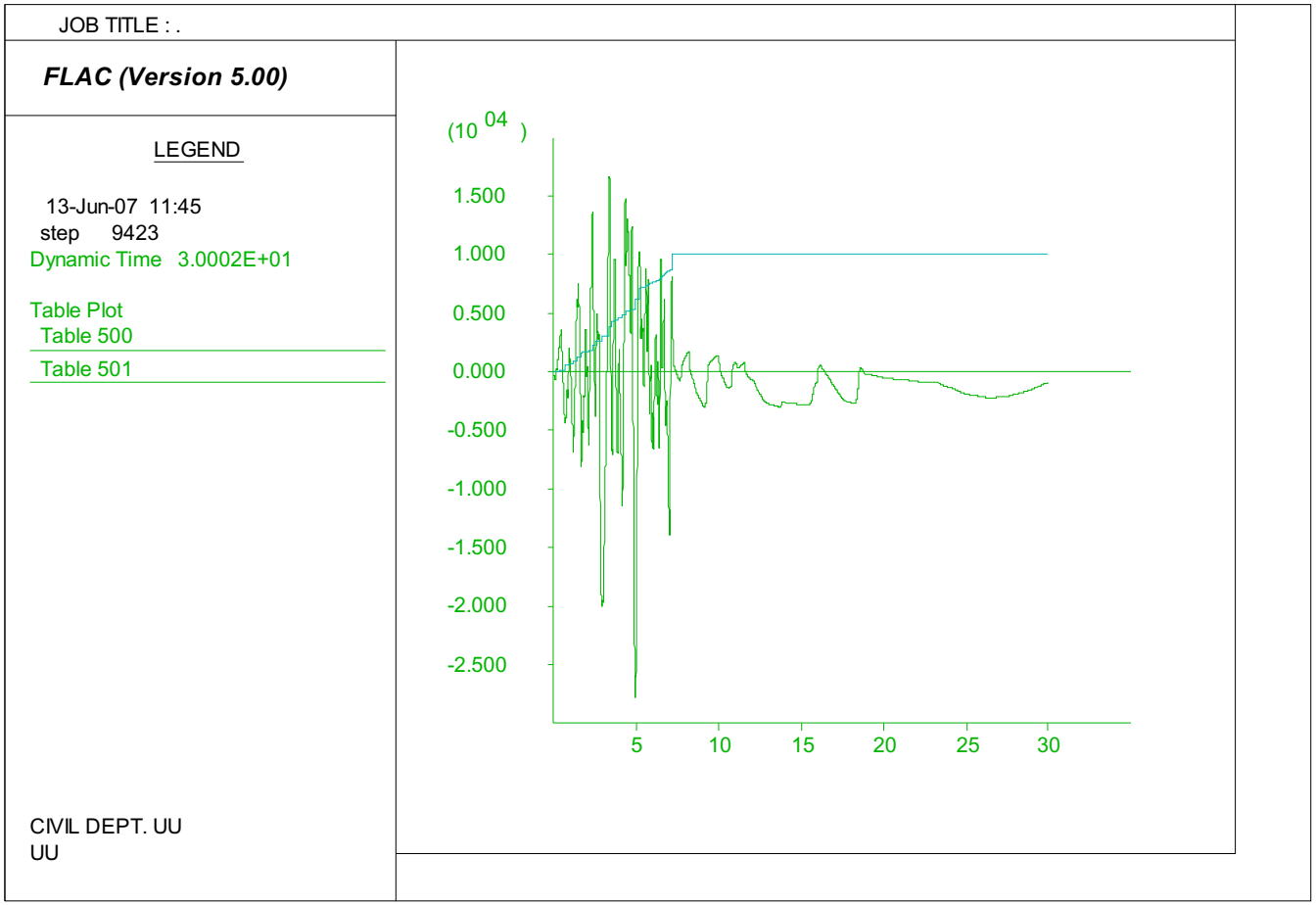


Figure C.13. Niigata railway section model pore water generation history loaded by motion 6 with residual strength ratio of 0.085.

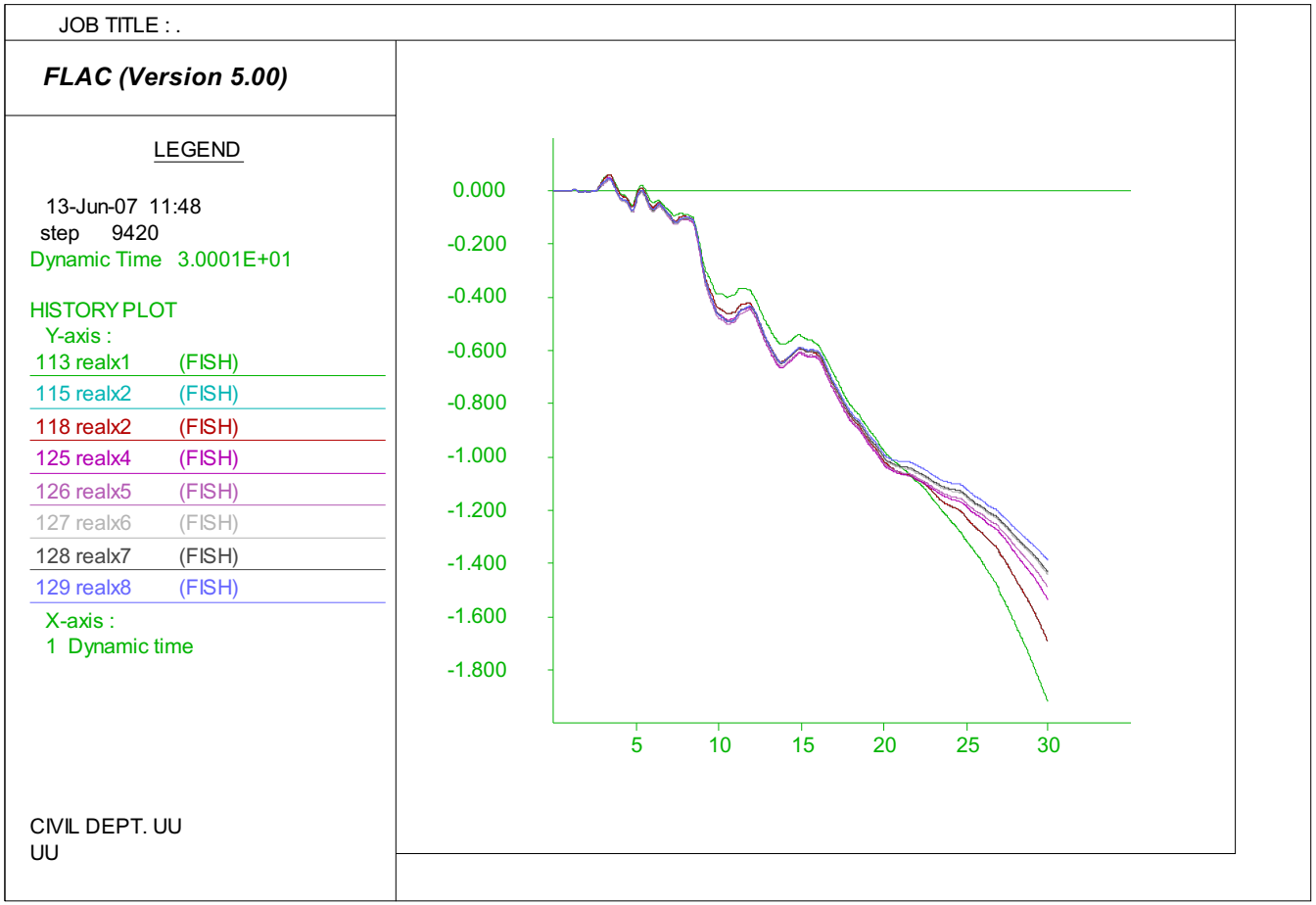


Figure C.14. Niigata railway section model later spreading prediction loaded by motion 7 with residual strength ratio of 0.085.

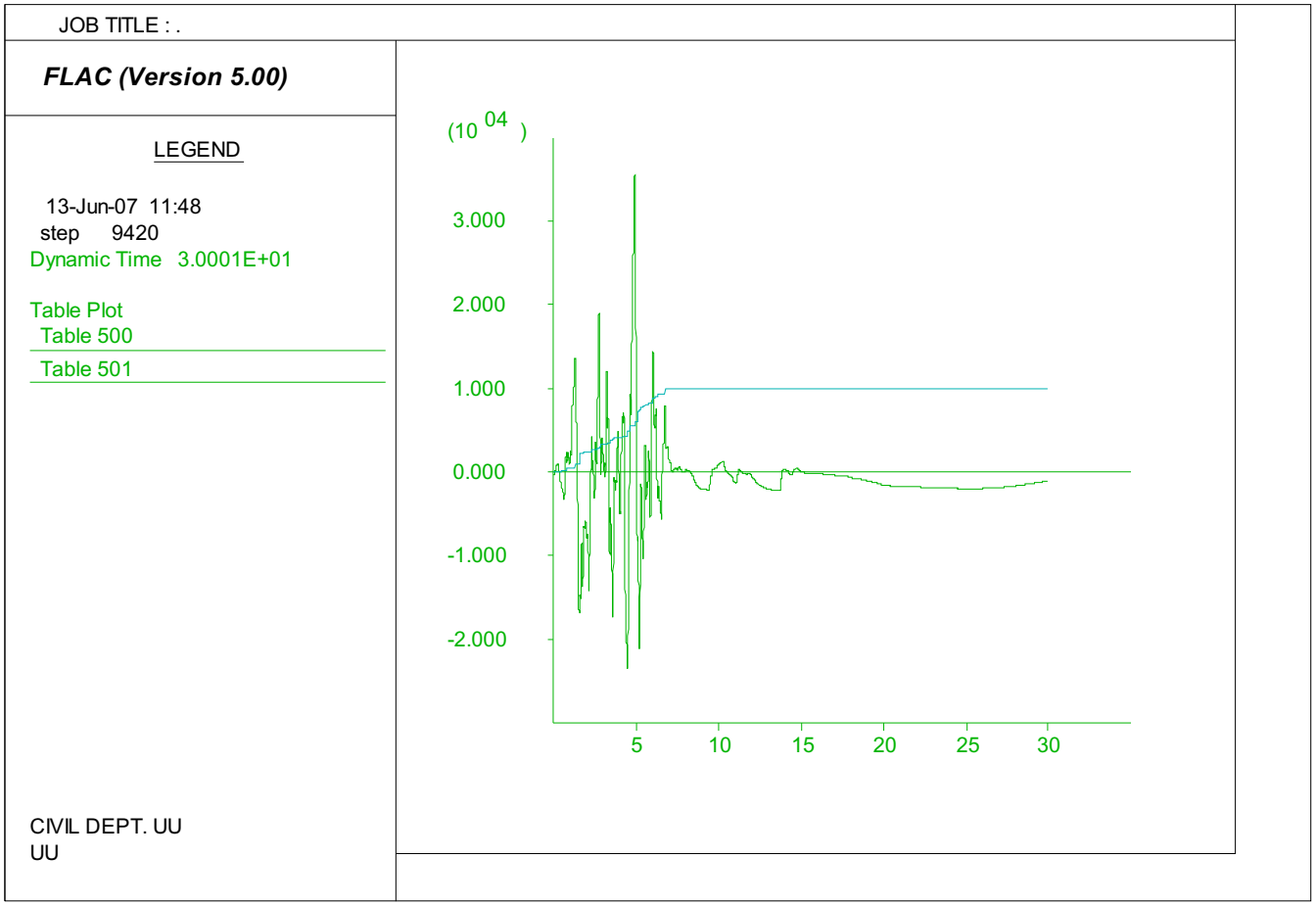


Figure C.15. Niigata railway section model pore water generation history loaded by motion 7 with residual strength ratio of 0.085.

APPENDIX D

NIIGATA SHOWA SECTION DATA

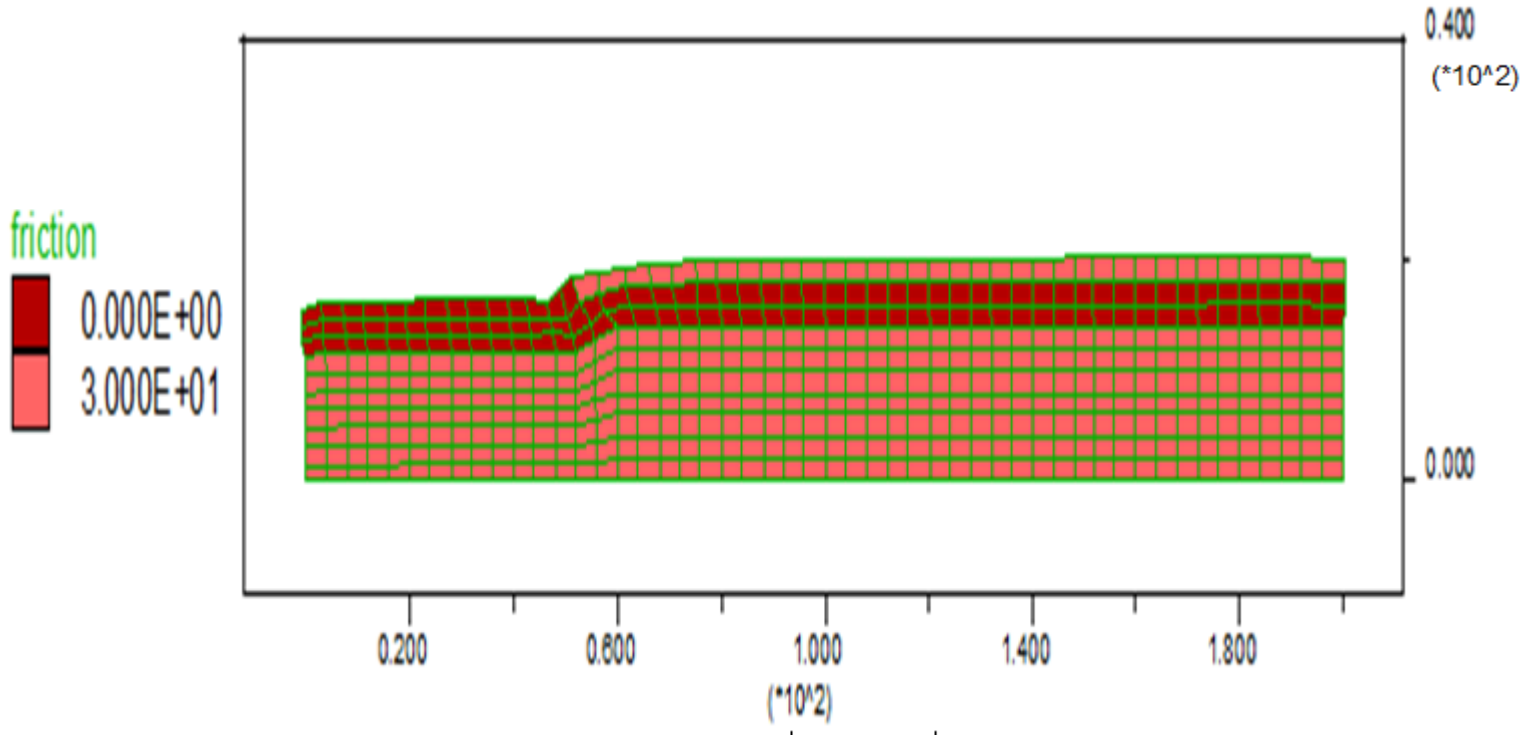


Figure D.1. Niigata Showa section model soil properties change after liquefaction loaded by motion 1 with residual strength ratio of 0.09.

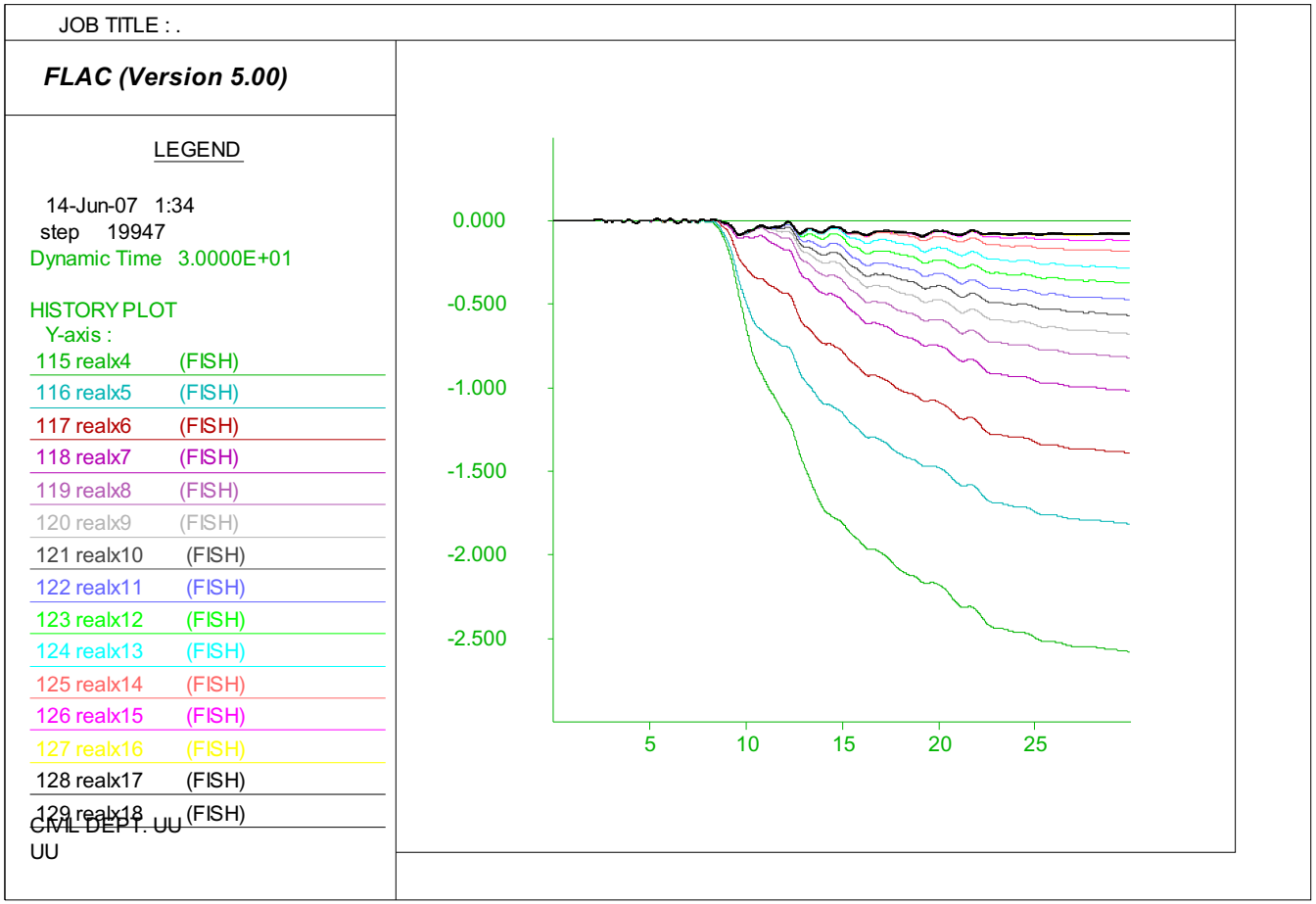


Figure D.2. Niigata Showa section model later spreading prediction loaded by motion 1 with residual strength ratio of 0.09.

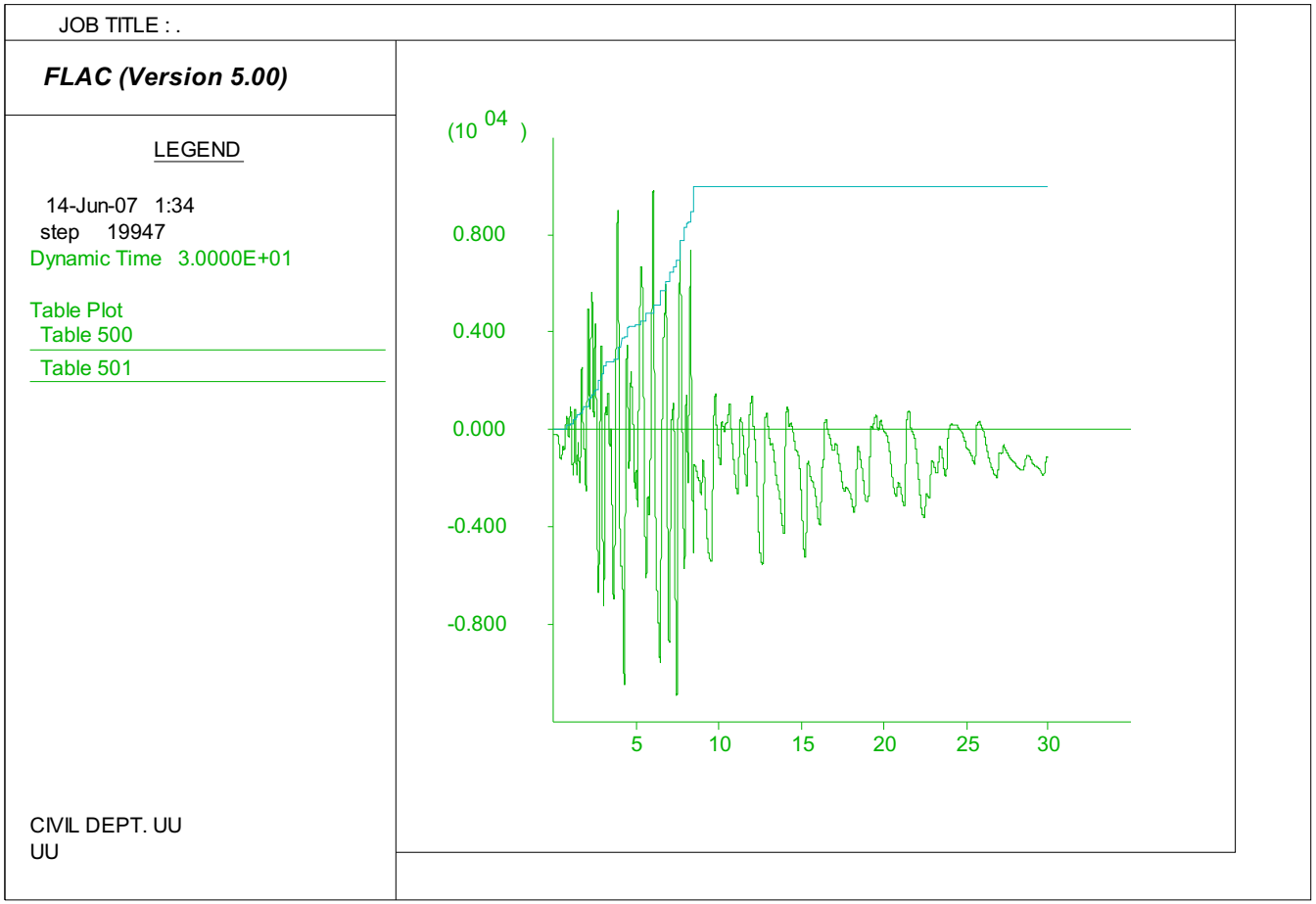


Figure D.3. Niigata Showa section model pore water generation history loaded by motion 1 with residual strength ratio of 0.09.

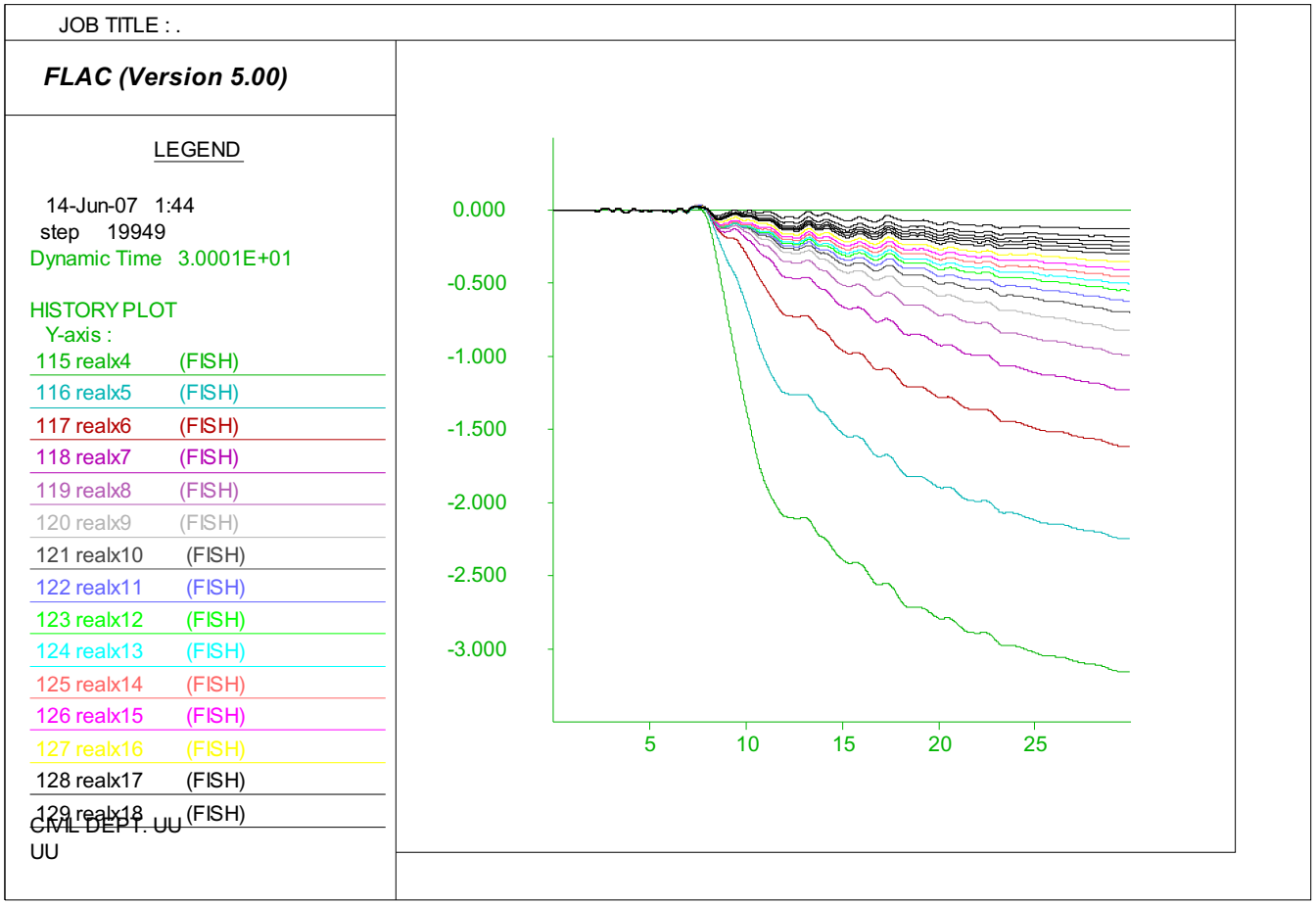


Figure D.4. Niigata Showa section model later spreading prediction loaded by motion 2 with residual strength ratio of 0.09.

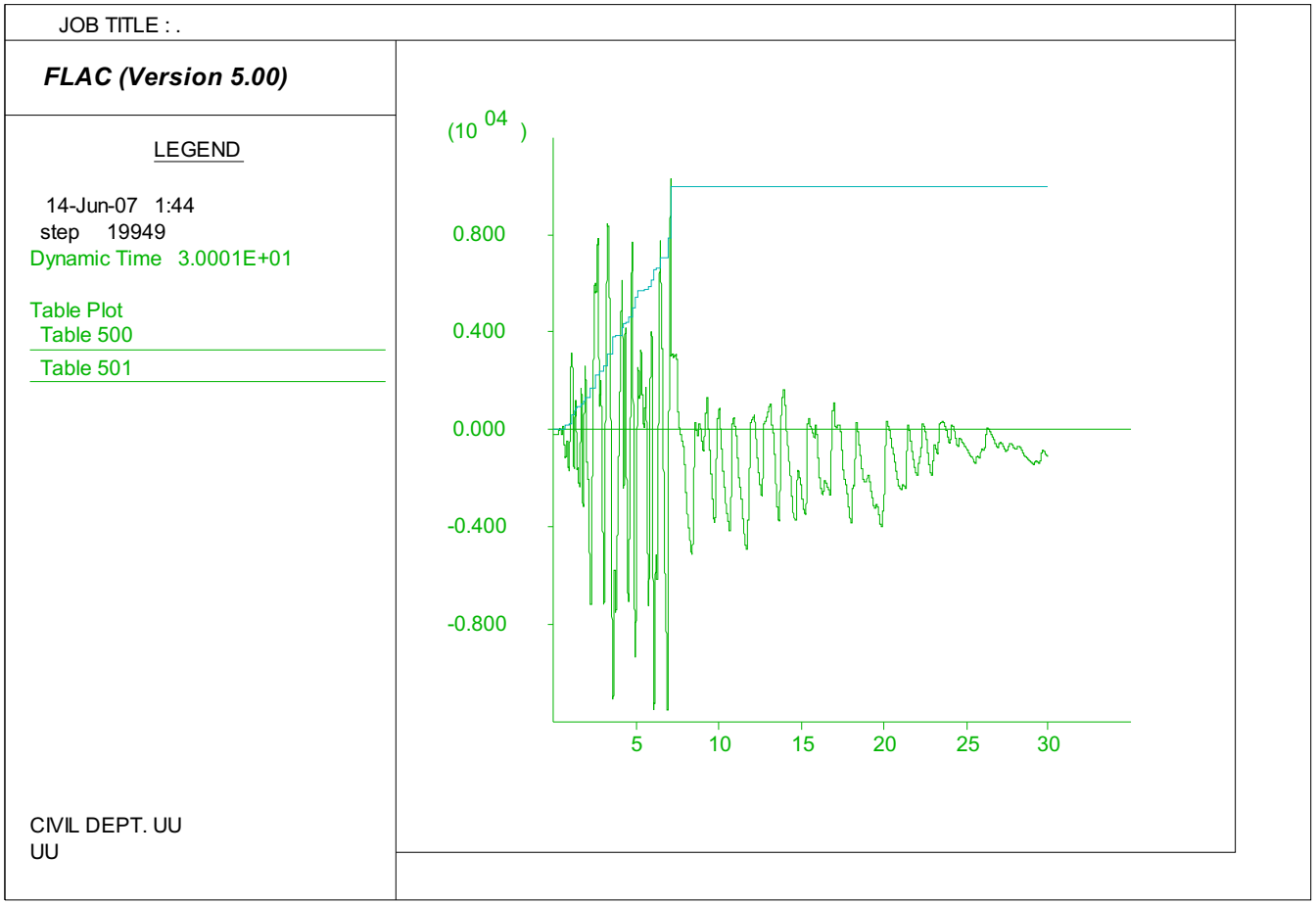


Figure D.5. Niigata Showa section model pore water generation history loaded by motion 2 with residual strength ratio of 0.09.

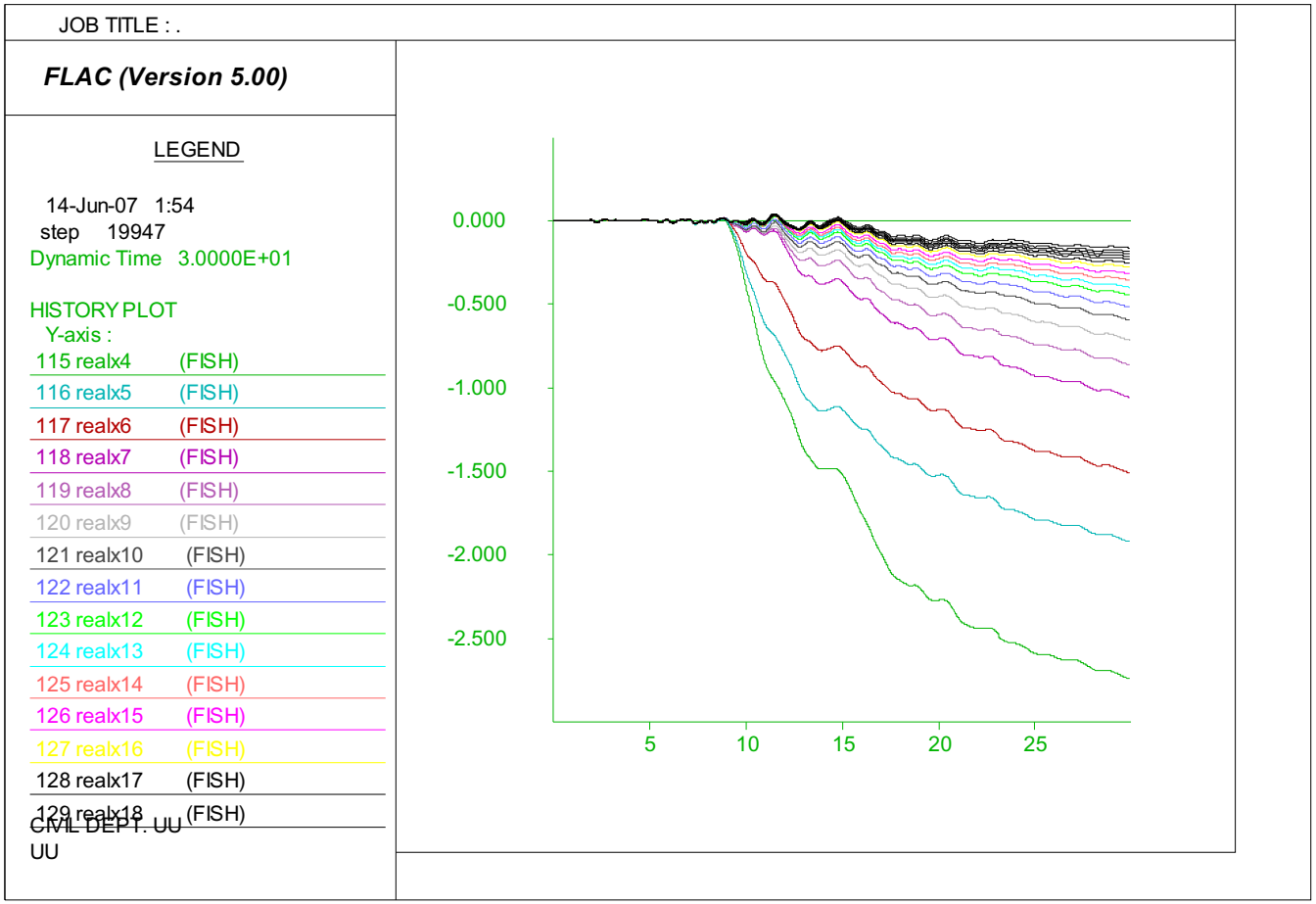


Figure D.6. Niigata Showa section model later spreading prediction loaded by motion 3 with residual strength ratio of 0.09.

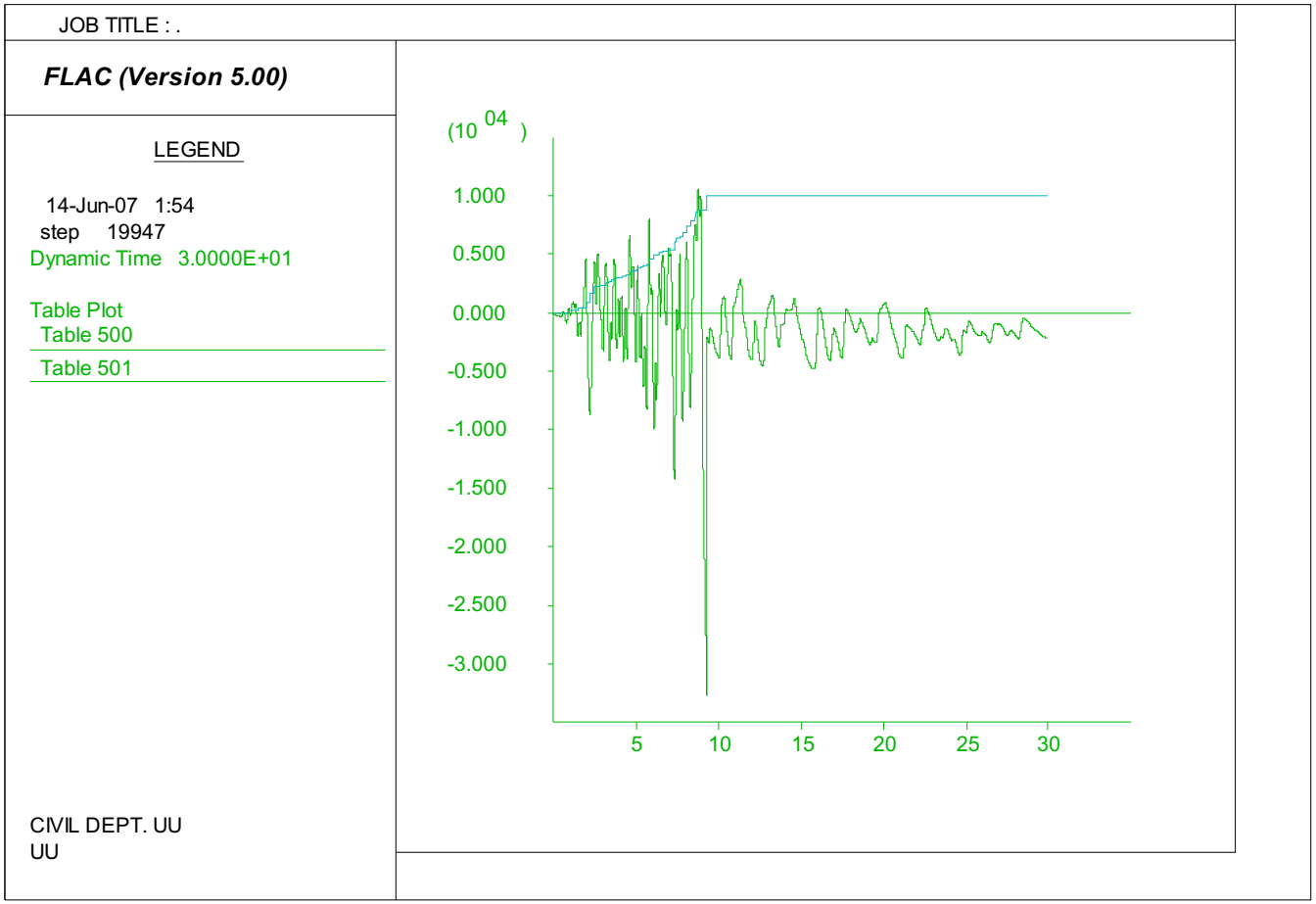


Figure D.7. Niigata Showa section model pore water generation history loaded by motion 3 with residual strength ratio of 0.09.

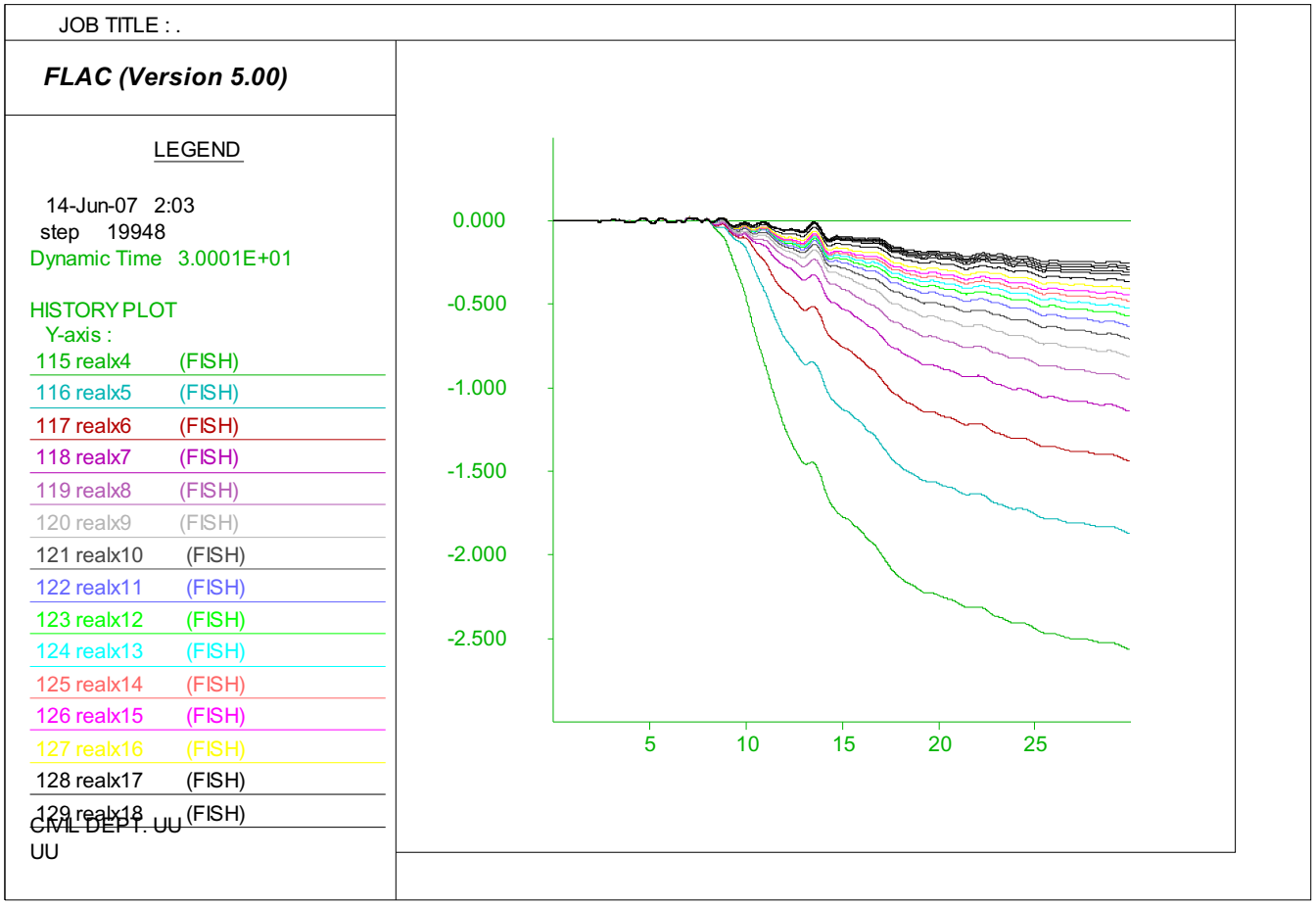


Figure D.8. Niigata Showa section model later spreading prediction loaded by motion 4 with residual strength ratio of 0.09.

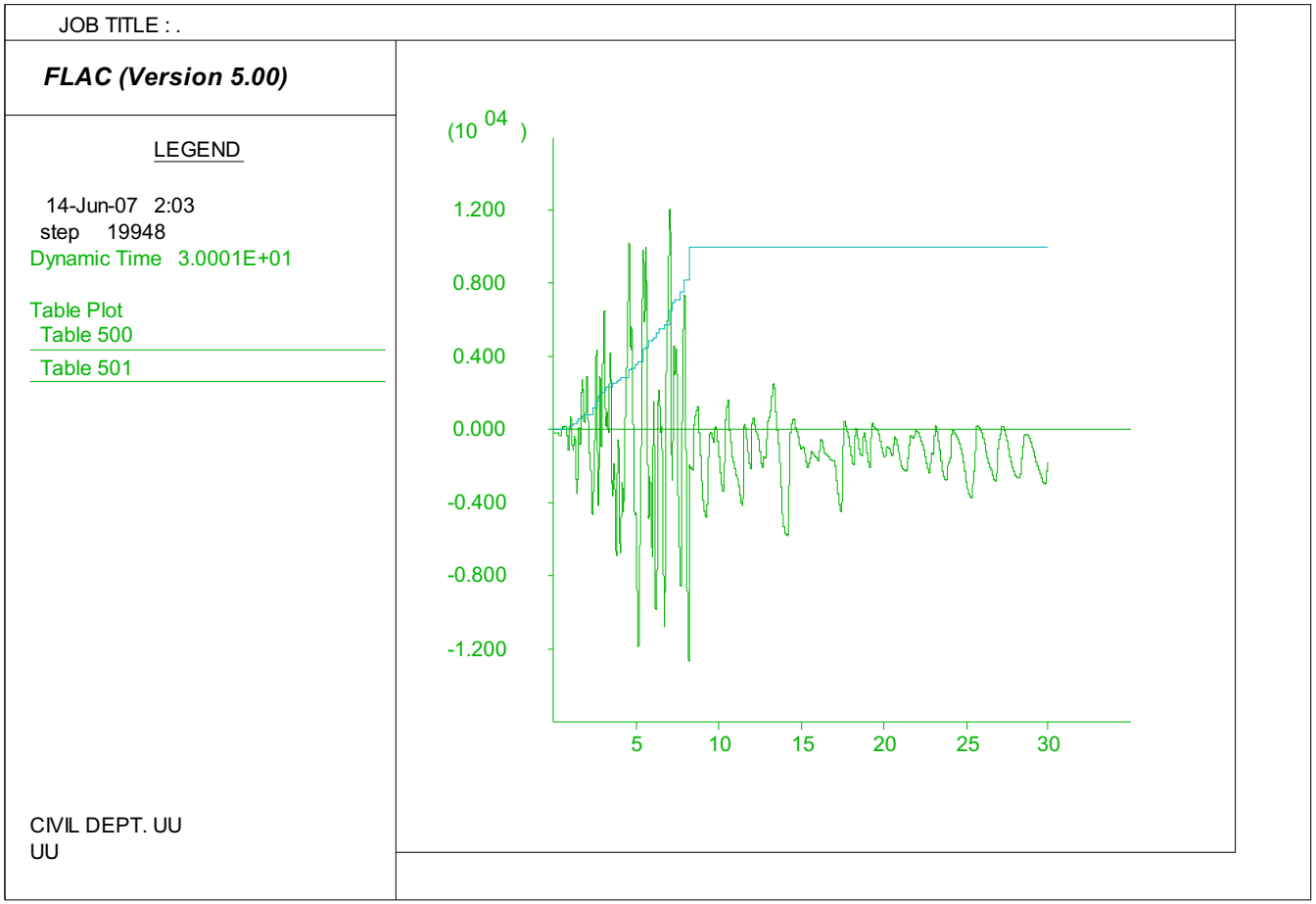


Figure D.9. Niigata Showa section model pore water generation history loaded by motion 4 with residual strength ratio of 0.09.

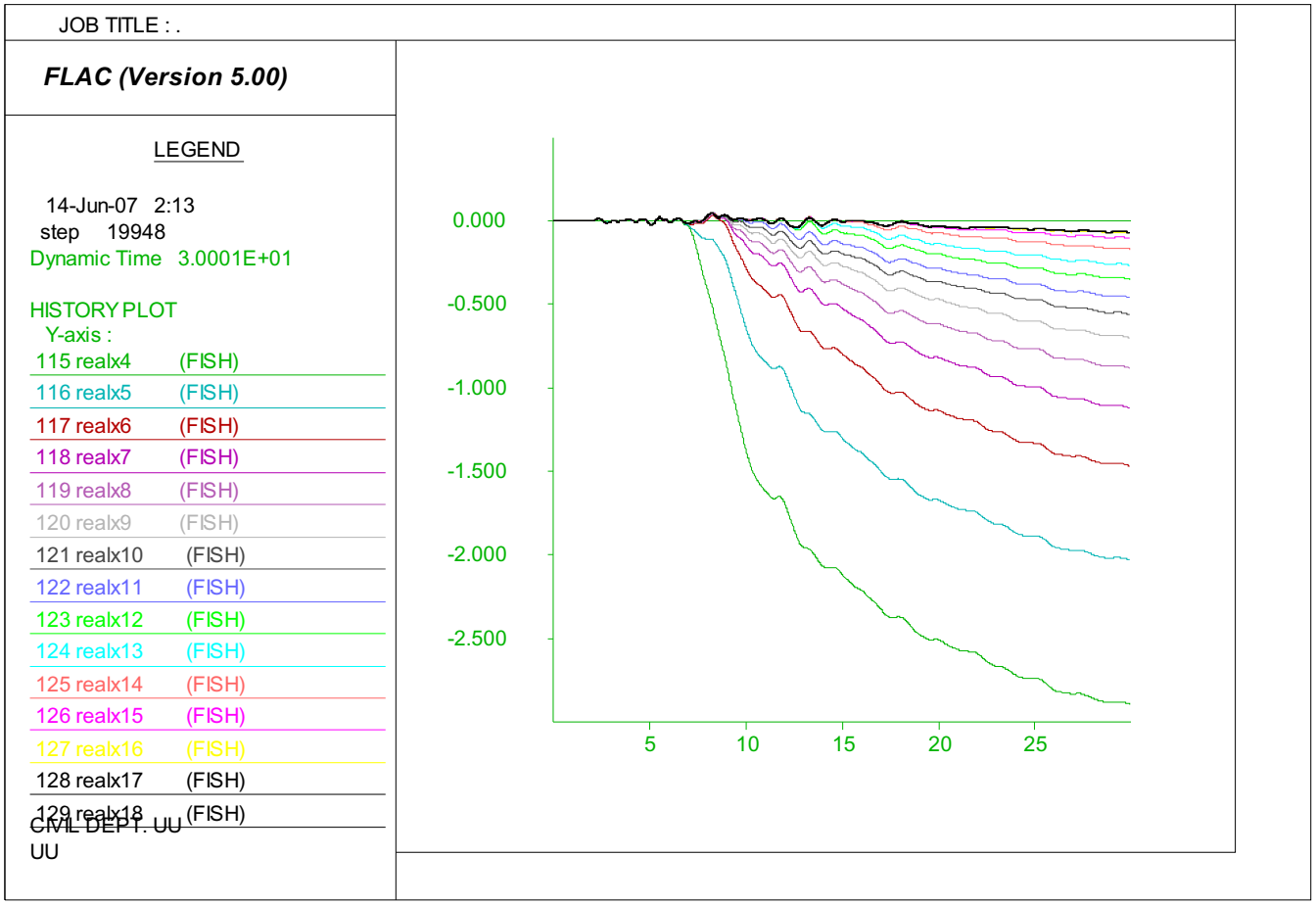


Figure D.10. Niigata Showa section model later spreading prediction loaded by motion 5 with residual strength ratio of 0.09.

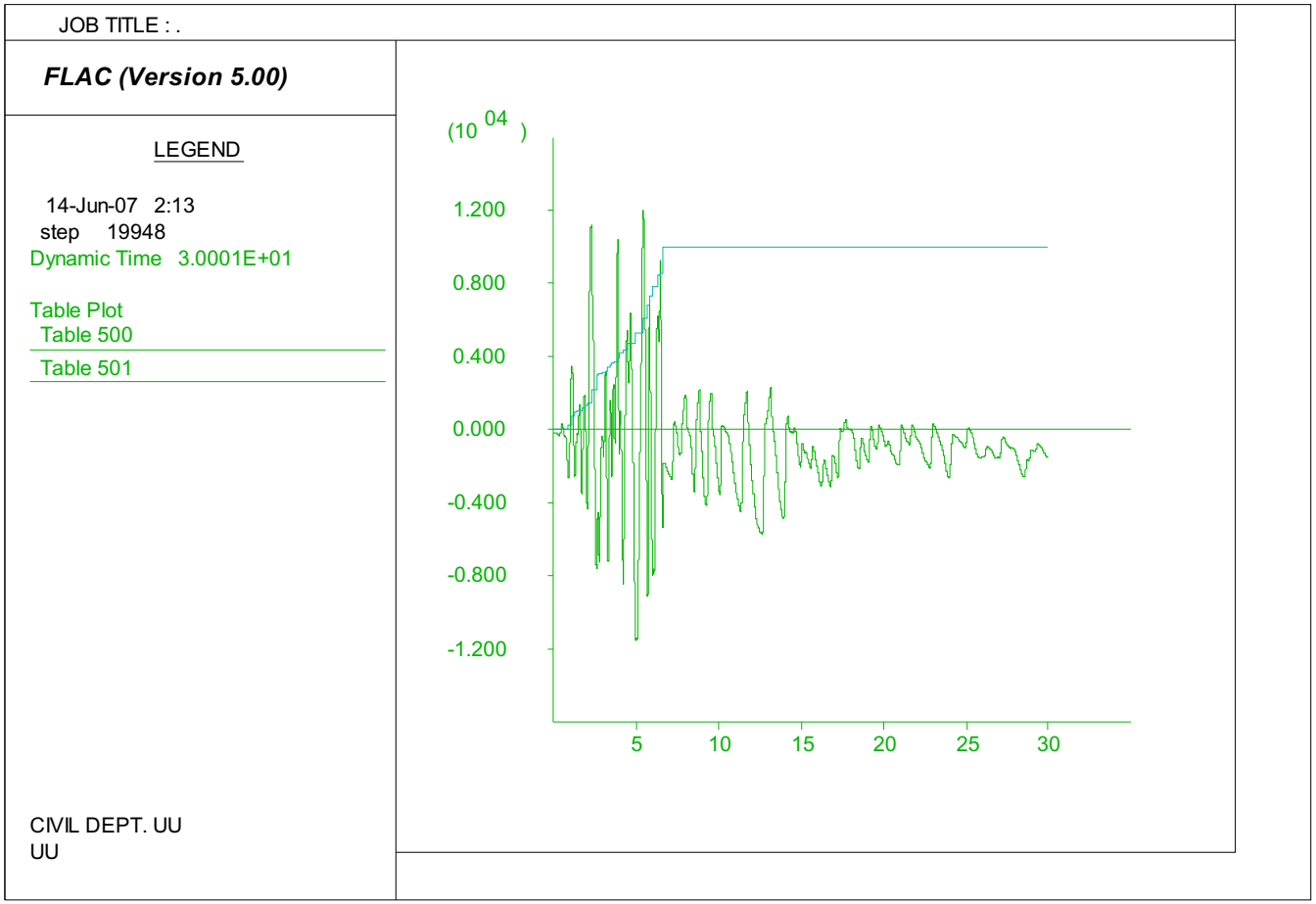


Figure D.11. Niigata Showa section model pore water generation history loaded by motion 5 with residual strength ratio of 0.09.

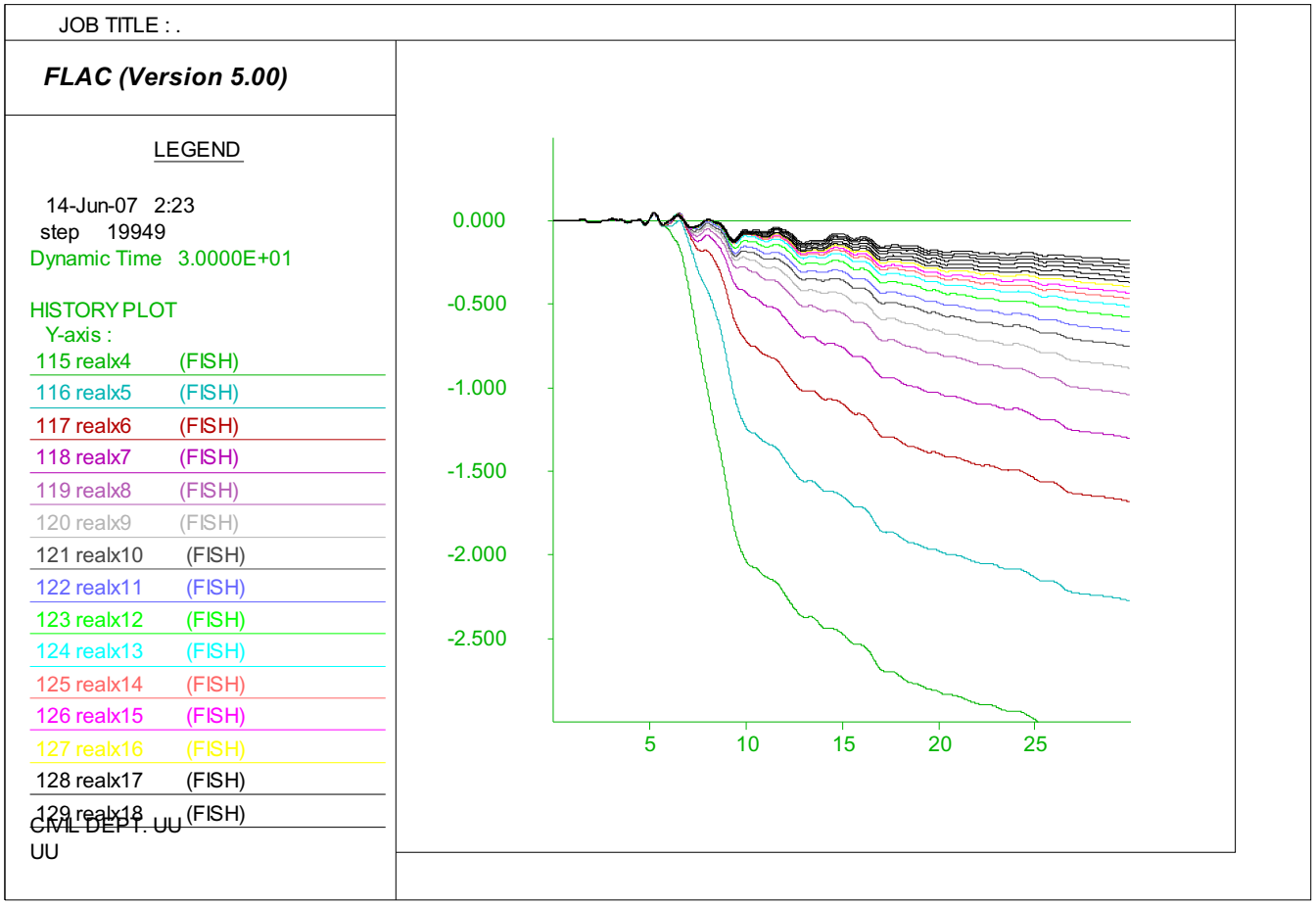


Figure D.12. Niigata Showa section model later spreading prediction loaded by motion 6 with residual strength ratio of 0.09.

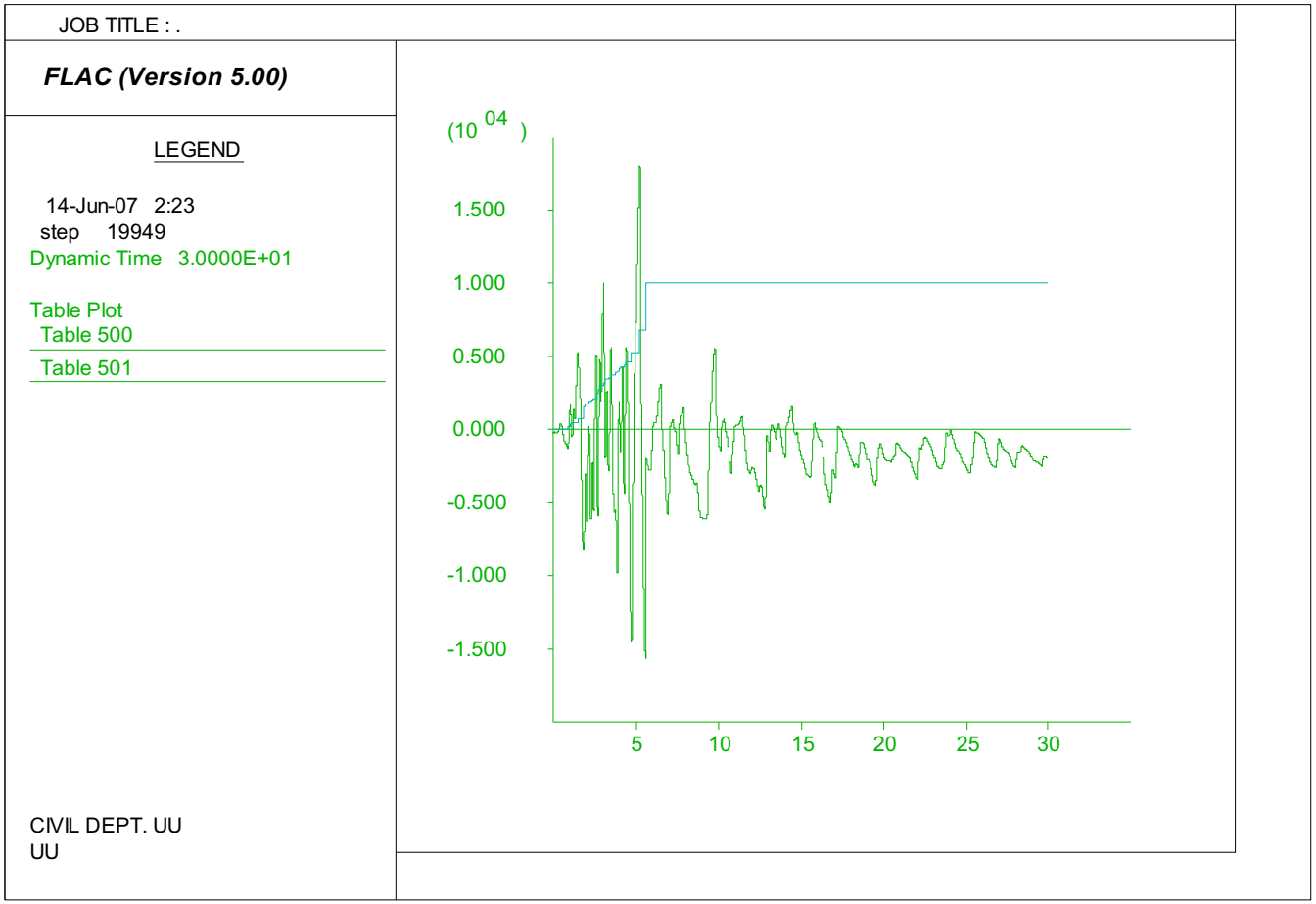


Figure D.13. Niigata Showa section model pore water generation history loaded by motion 6 with residual strength ratio of 0.09.

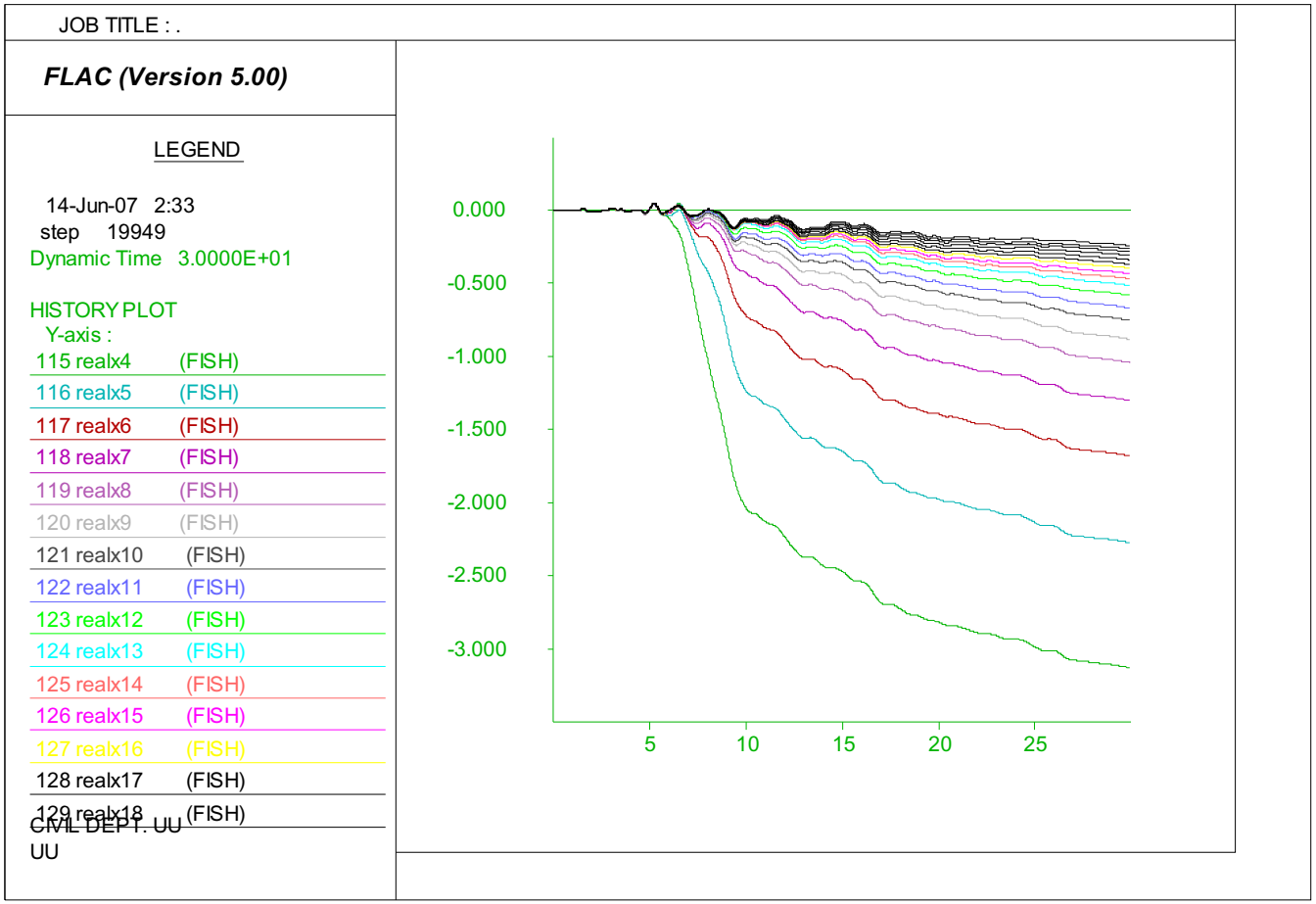


Figure D.14. Niigata Showa section model later spreading prediction loaded by motion 7 with residual strength ratio of 0.09.

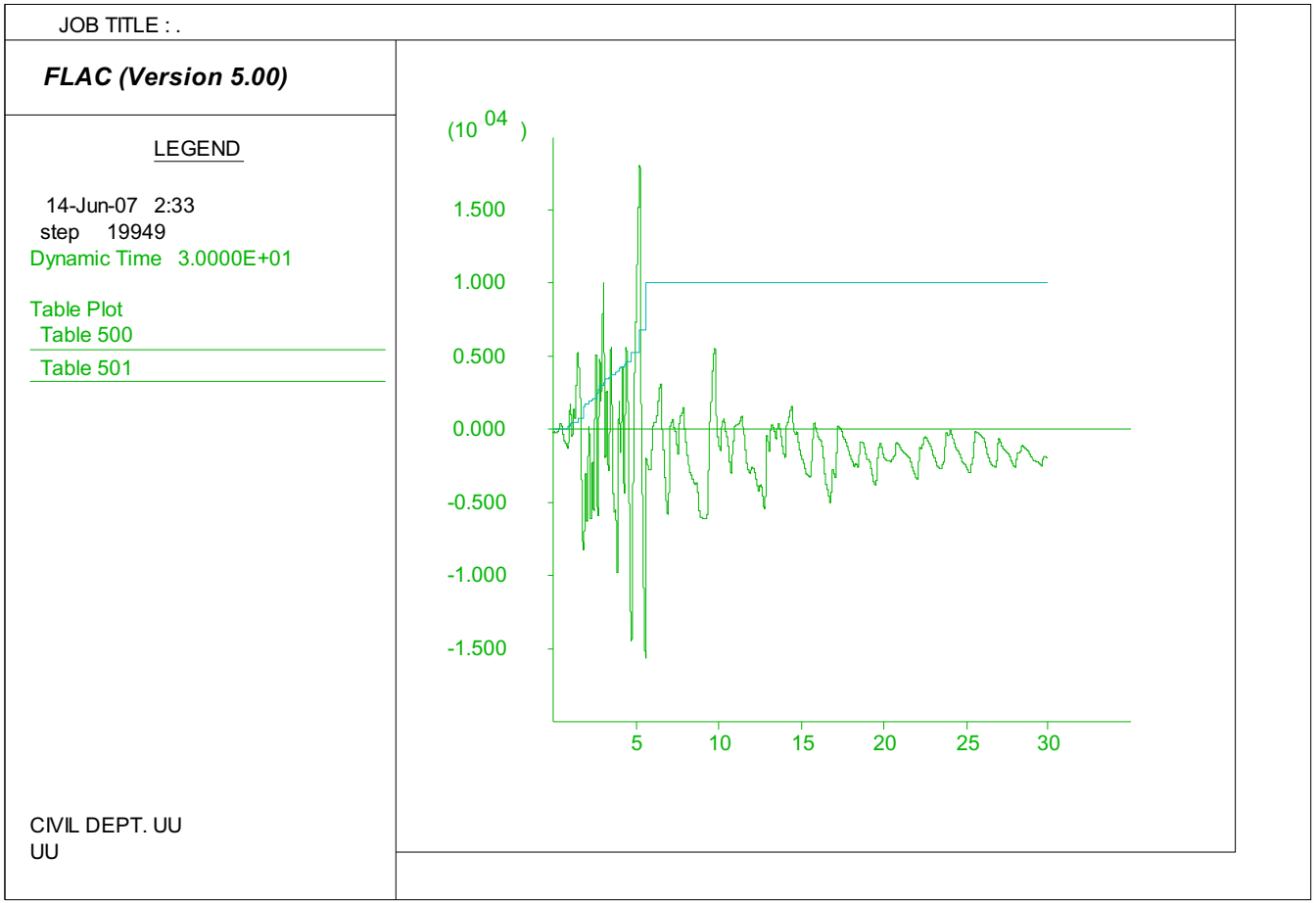


Figure D.15. Niigata Showa section model pore water generation history loaded by motion 7 with residual strength ratio of 0.09.

APPENDIX E

NOSHIRO SITE N-4 SECTION DATA

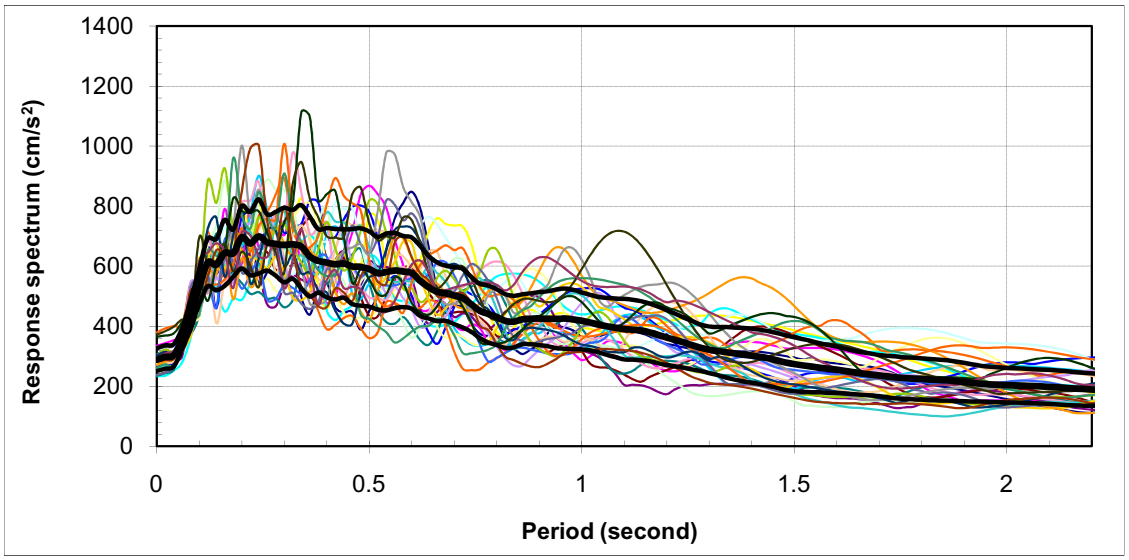


Figure E.1. Response spectra of generated thirty motions

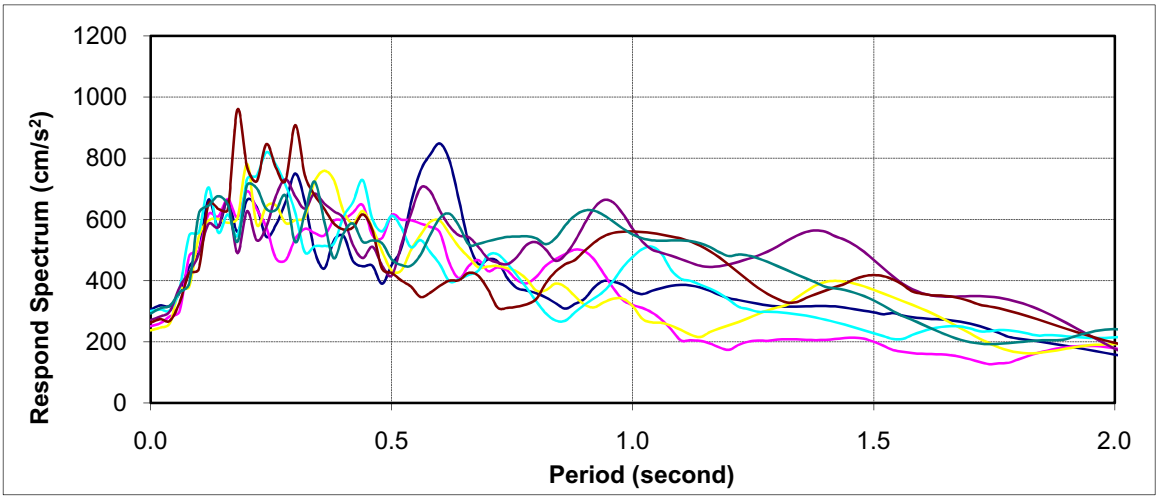


Figure E.2. Response spectra of selected seven motions

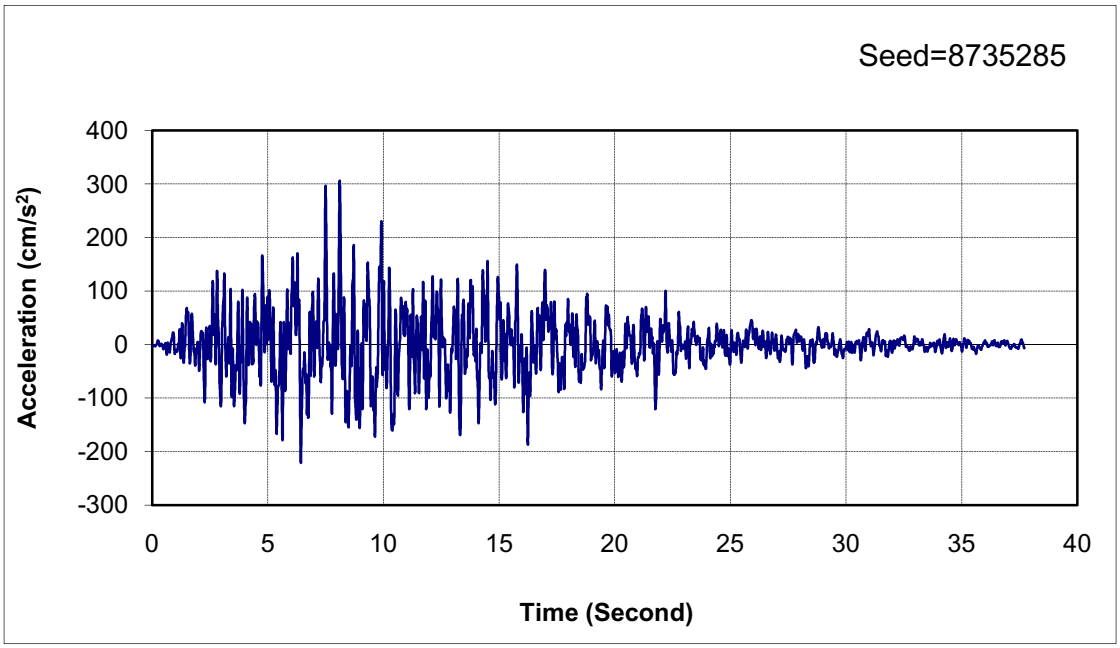


Figure E.3. NOSHIRO N-4 Section selected motion 1

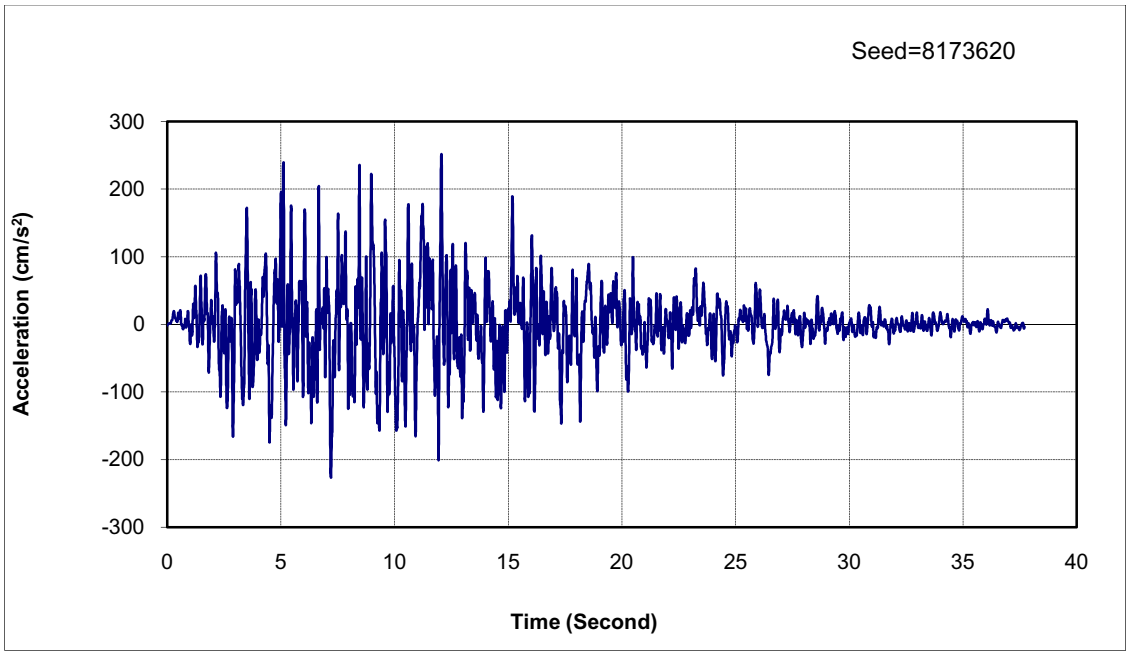


Figure E.4. NOSHIRO N-4 Section selected motion 2

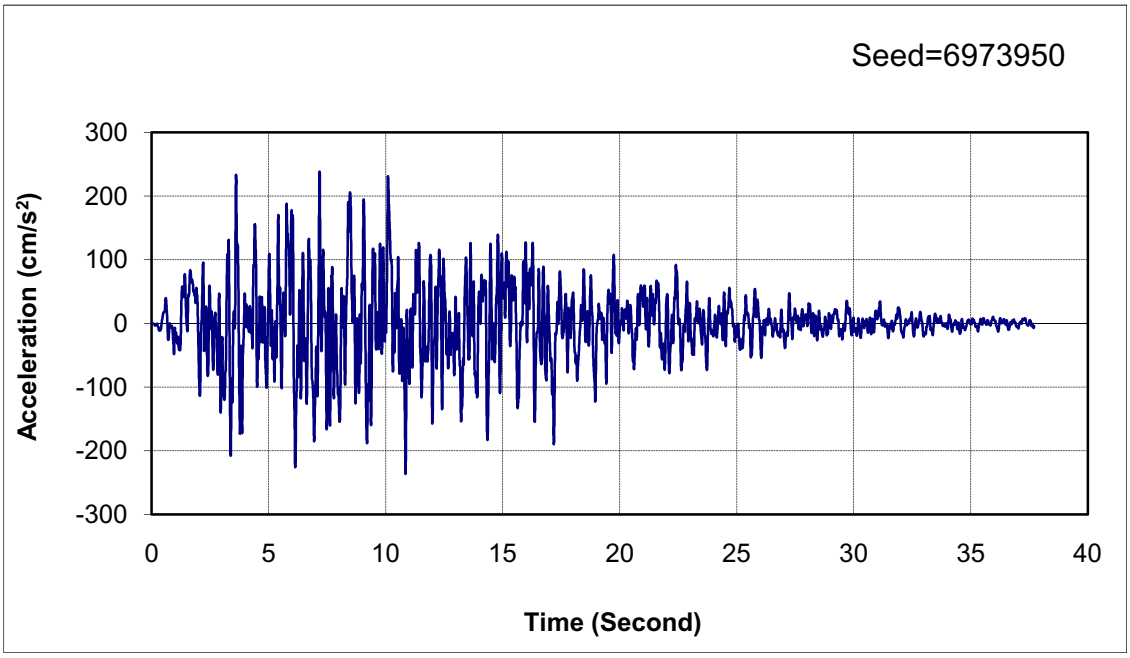


Figure E.5. NOSHIRO N-4 Section selected motion 3

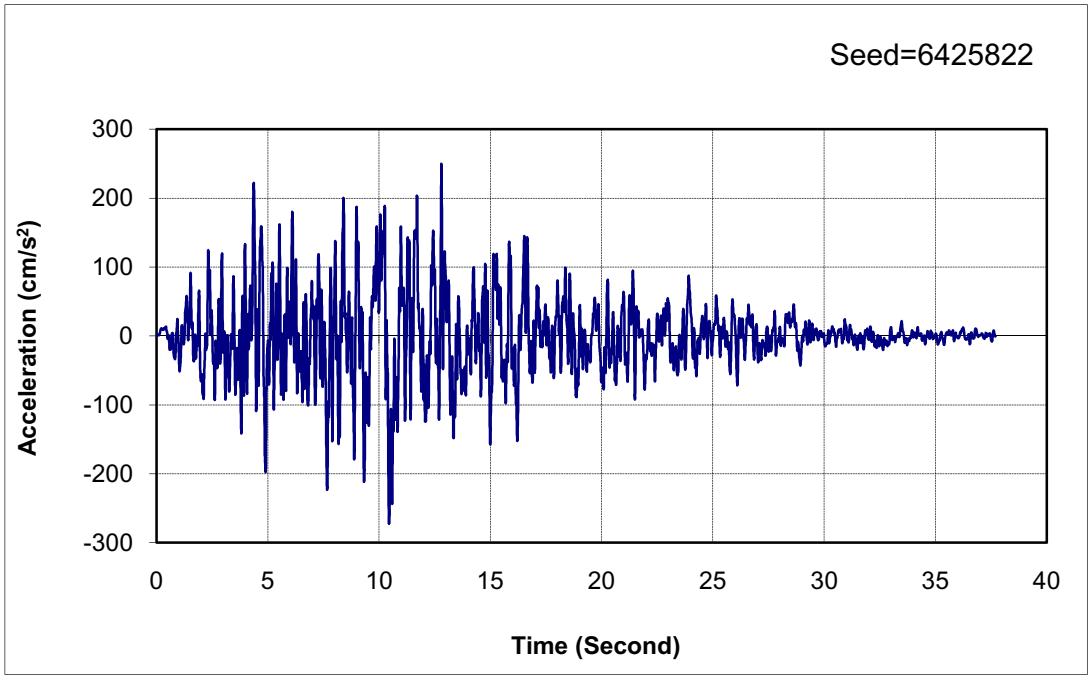


Figure E.6. NOSHIRO N-4 Section selected motion 4

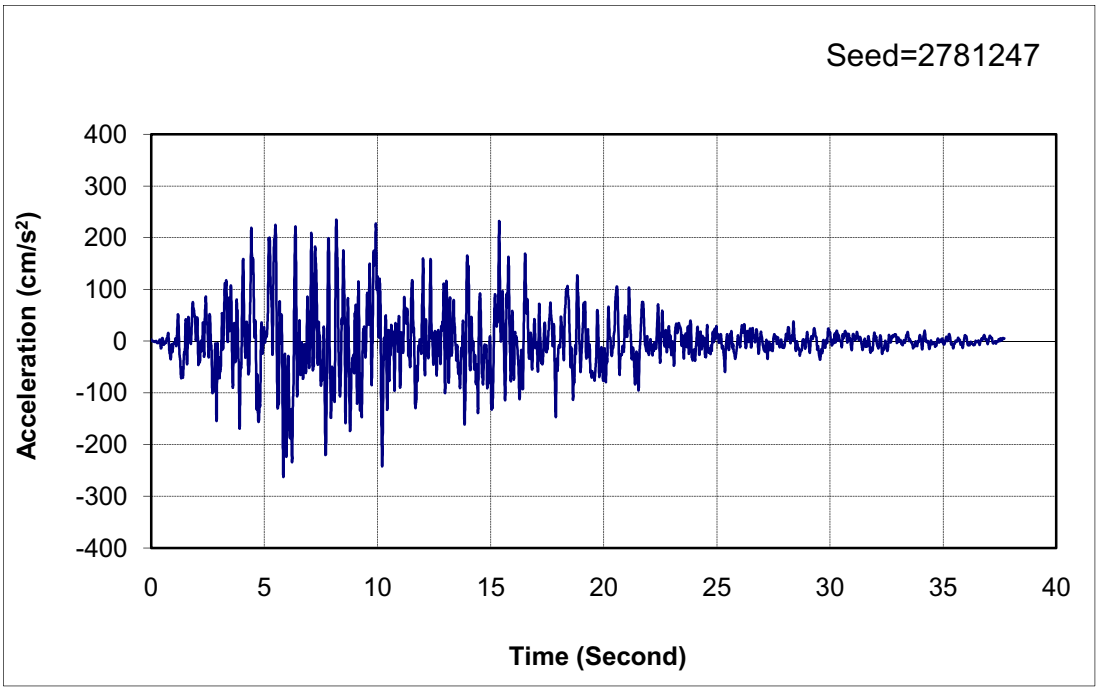


Figure E.7. NOSHIRO N-4 Section selected motion 5

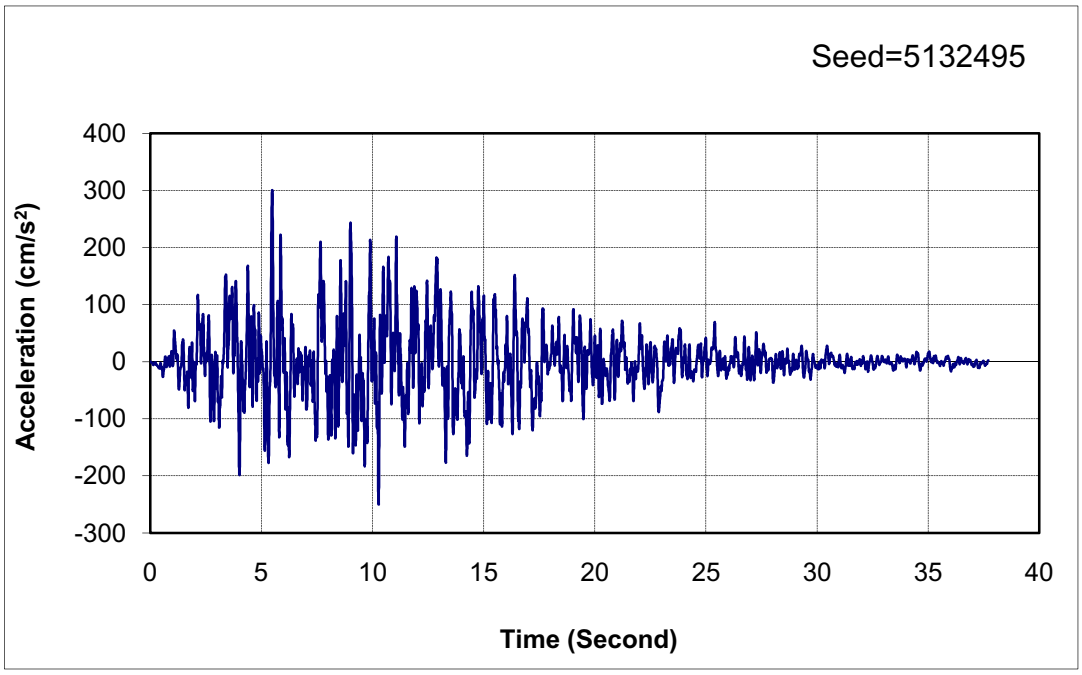


Figure E.8. NOSHIRO N-4 Section selected motion 6

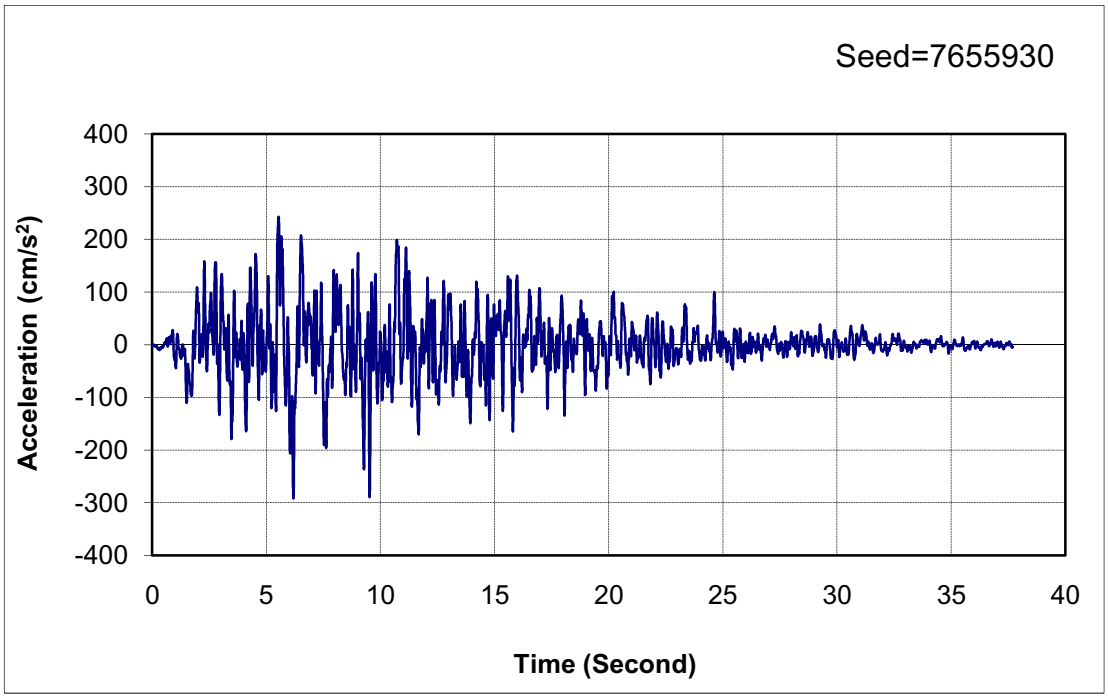


Figure E.9. NOSHIRO N-4 Section selected motion 7

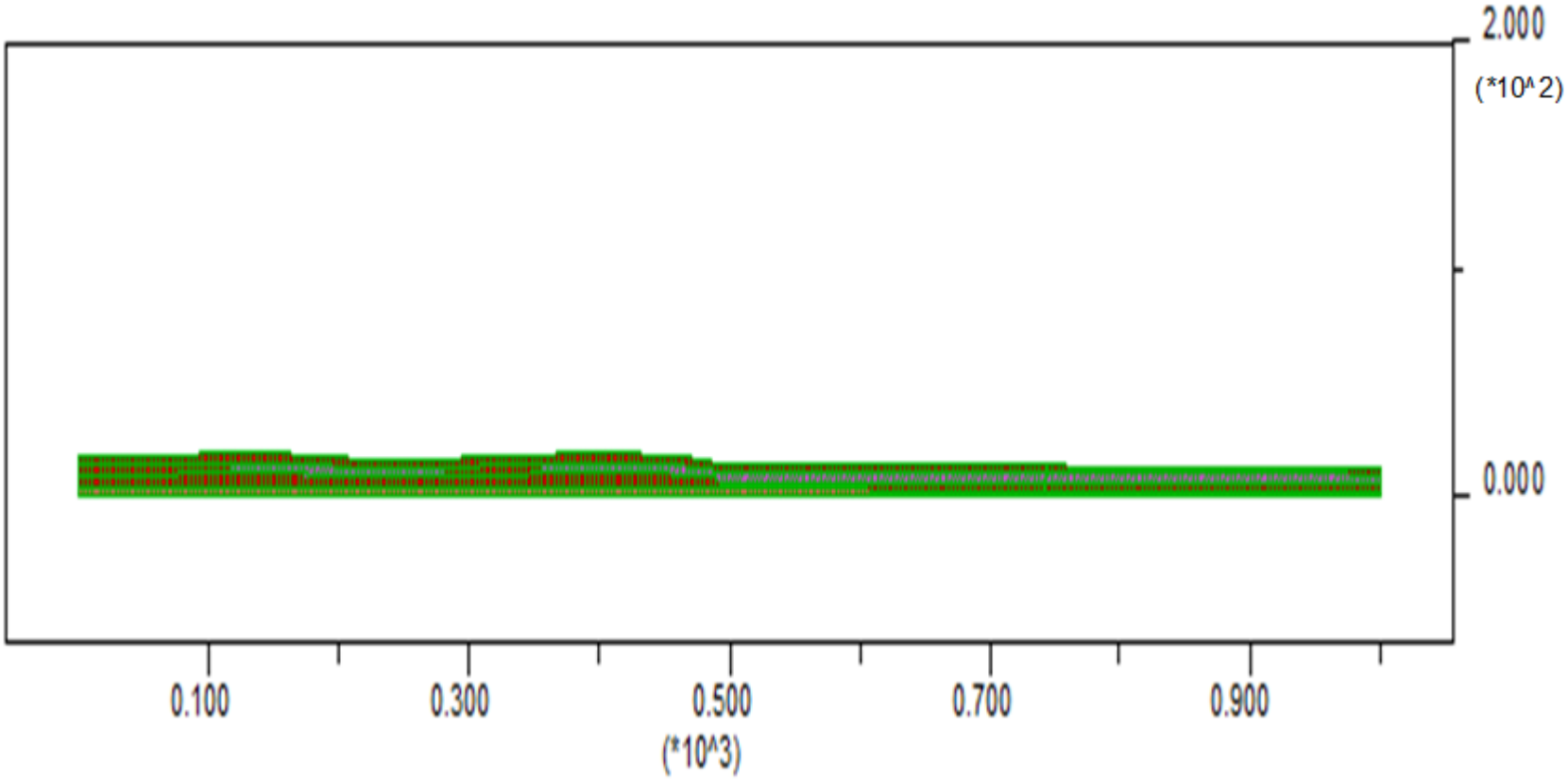


Figure E.10. Model design mesh (both Y axis & X axis in meters)

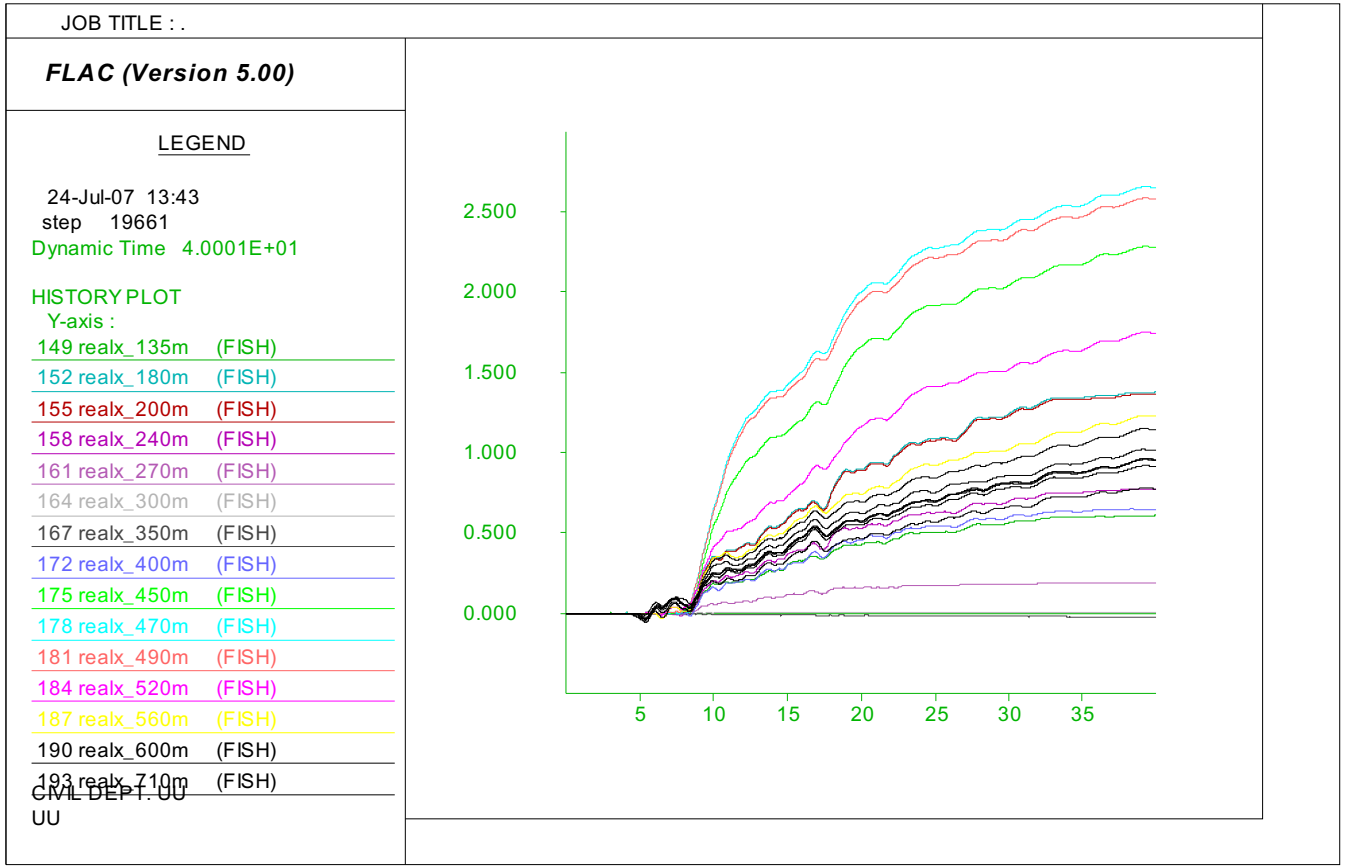


Figure E.11. Model later spreading prediction loaded by motion 1 with residual strength ratio of 0.03 (Y axis in meter and X axis in second)

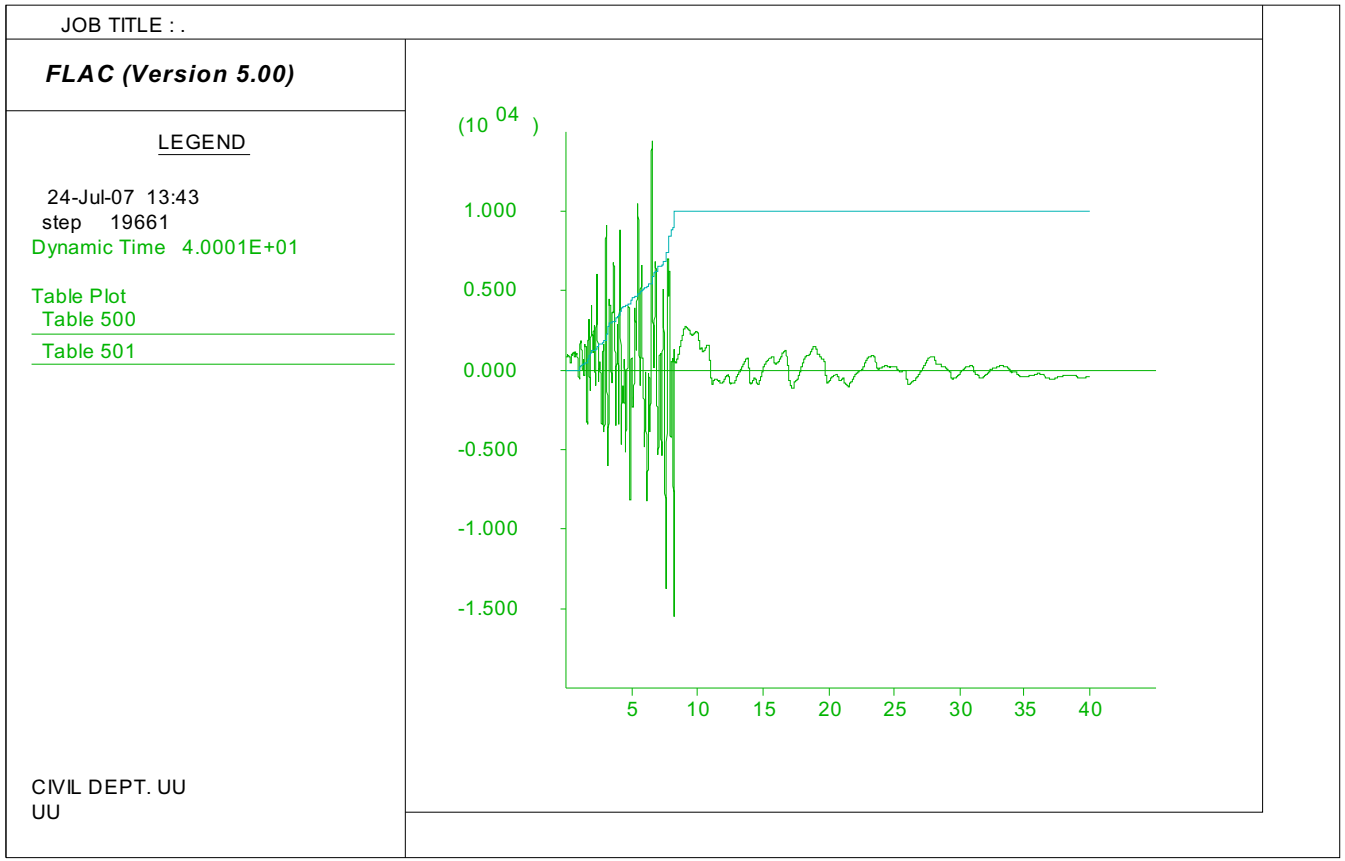


Figure E.12. Model pore water generation history loaded by motion 1 with residual strength ratio of 0.03: Shear stress (Y axis in Pa) and r_u (Y axis multiplied by 1000) vs. time (X axis in seconds).

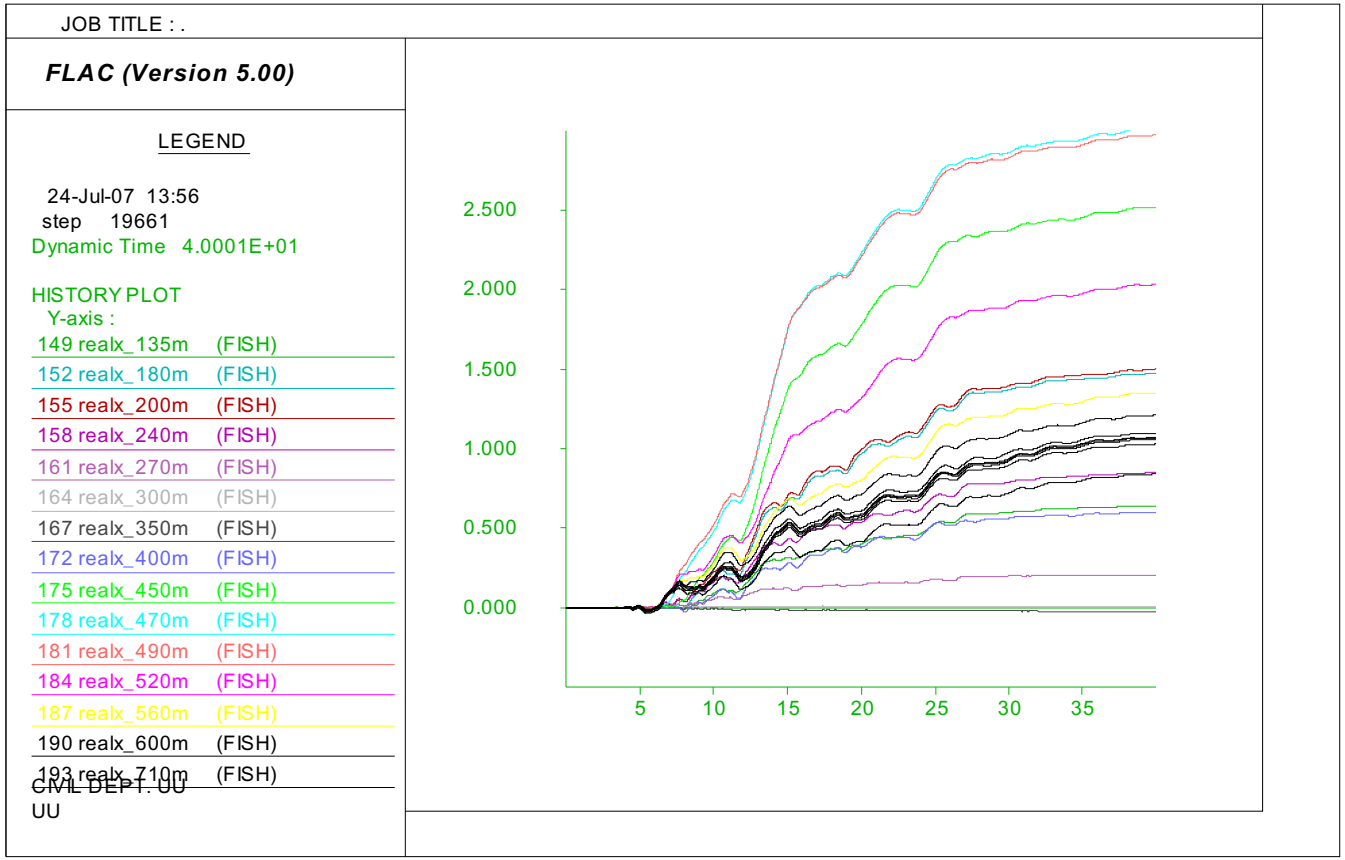


Figure E.13. Section model later spreading prediction loaded by motion 2 with residual strength ratio of 0.03 (Y axis in meter and X axis in second)

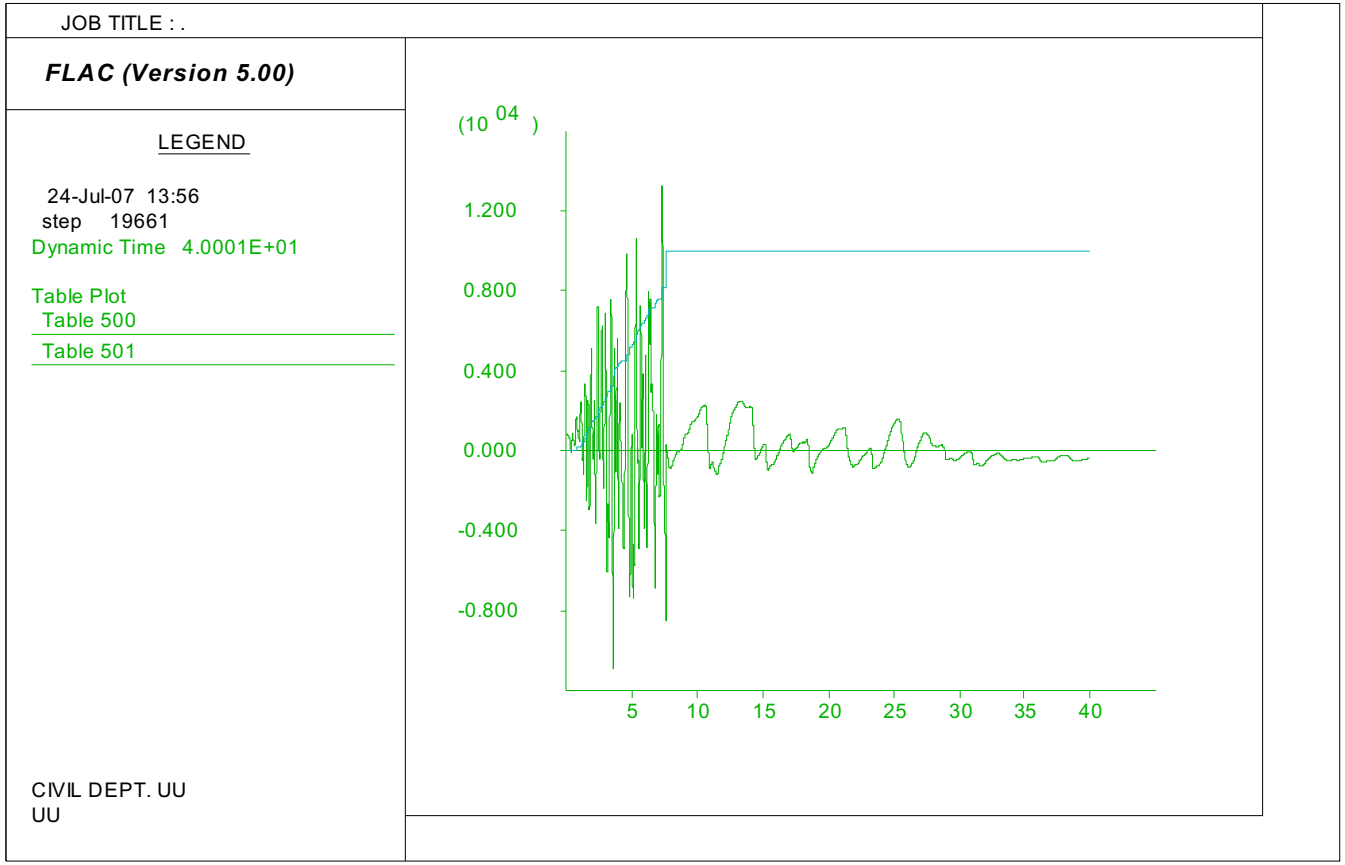


Figure E.14. Model pore water generation history loaded by motion 2 with residual strength ratio of 0.03: Shear stress (Y axis in Pa) and r_u (Y axis multiplied by 1000) vs. time (X axis in seconds).

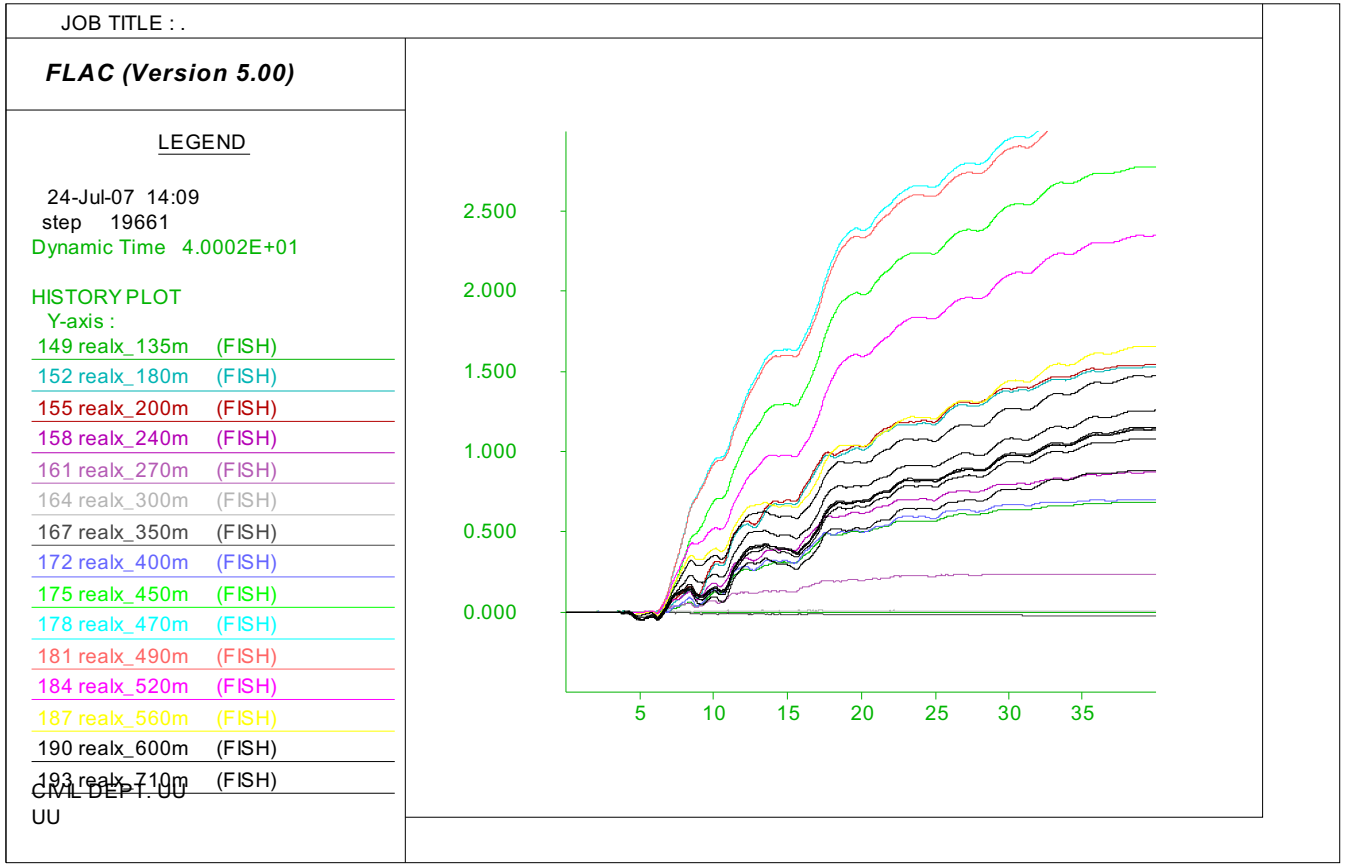


Figure E.15. Model later spreading prediction loaded by motion 3 with residual strength ratio of 0.03 (Y axis in meter and X axis in second)

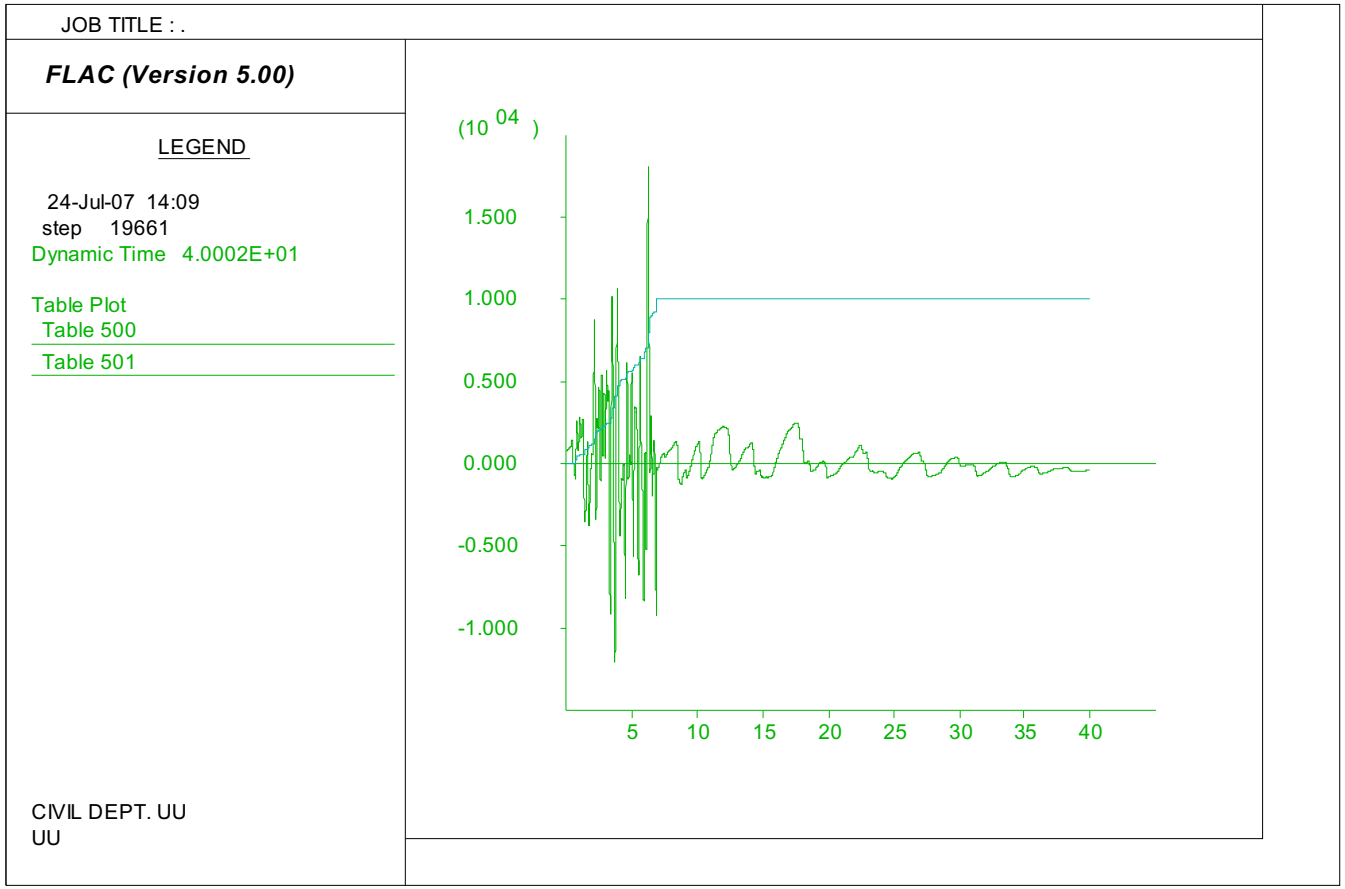


Figure E.16. Model pore water generation history loaded by motion 3 with residual strength ratio of 0.03: Shear stress (Y axis in Pa) and r_u (Y axis multiplied by 1000) vs. time (X axis in seconds).

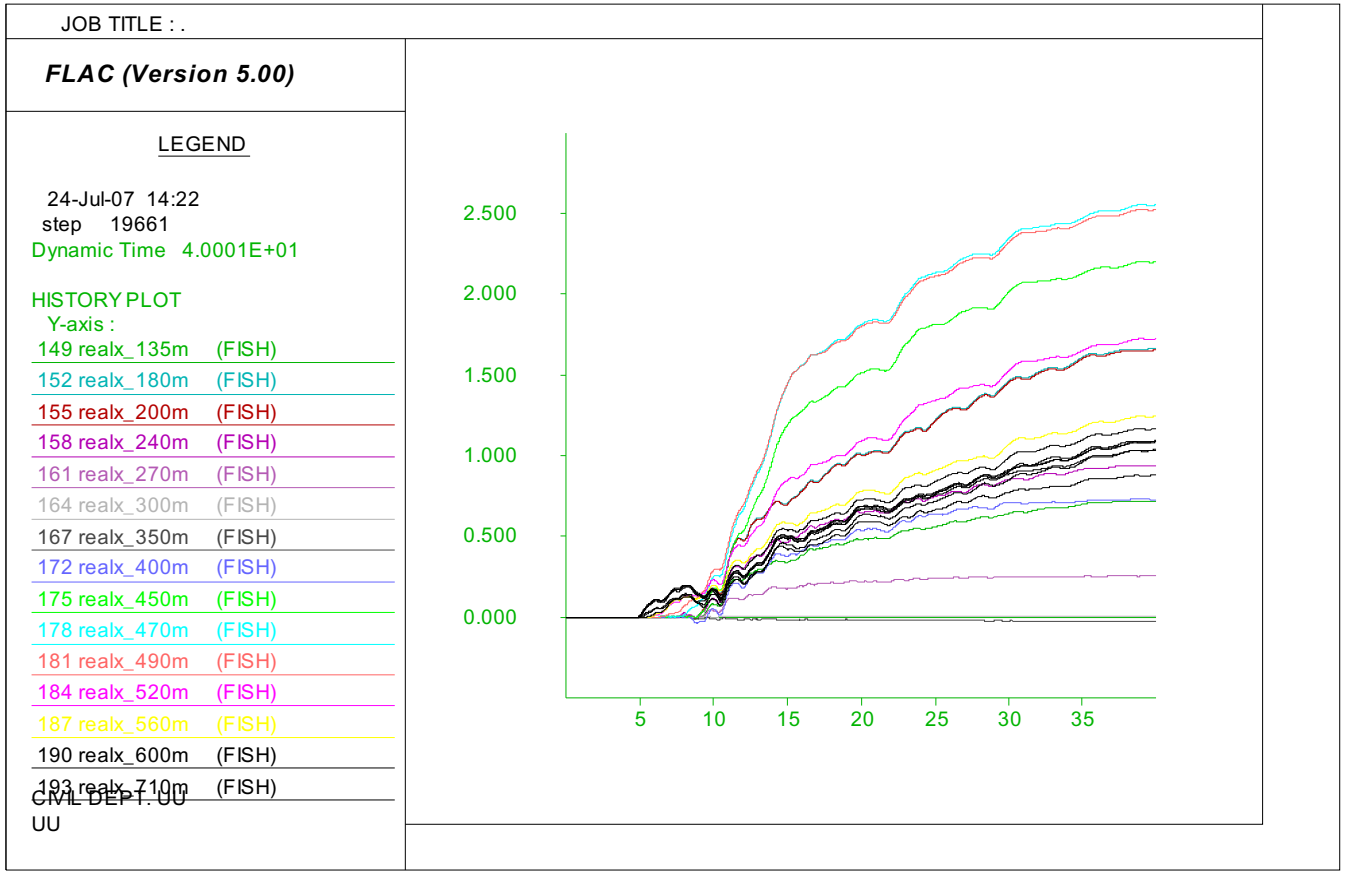


Figure E.17. Model later spreading prediction loaded by motion 4 with residual strength ratio of 0.03 (Y axis in meter and X axis in second)

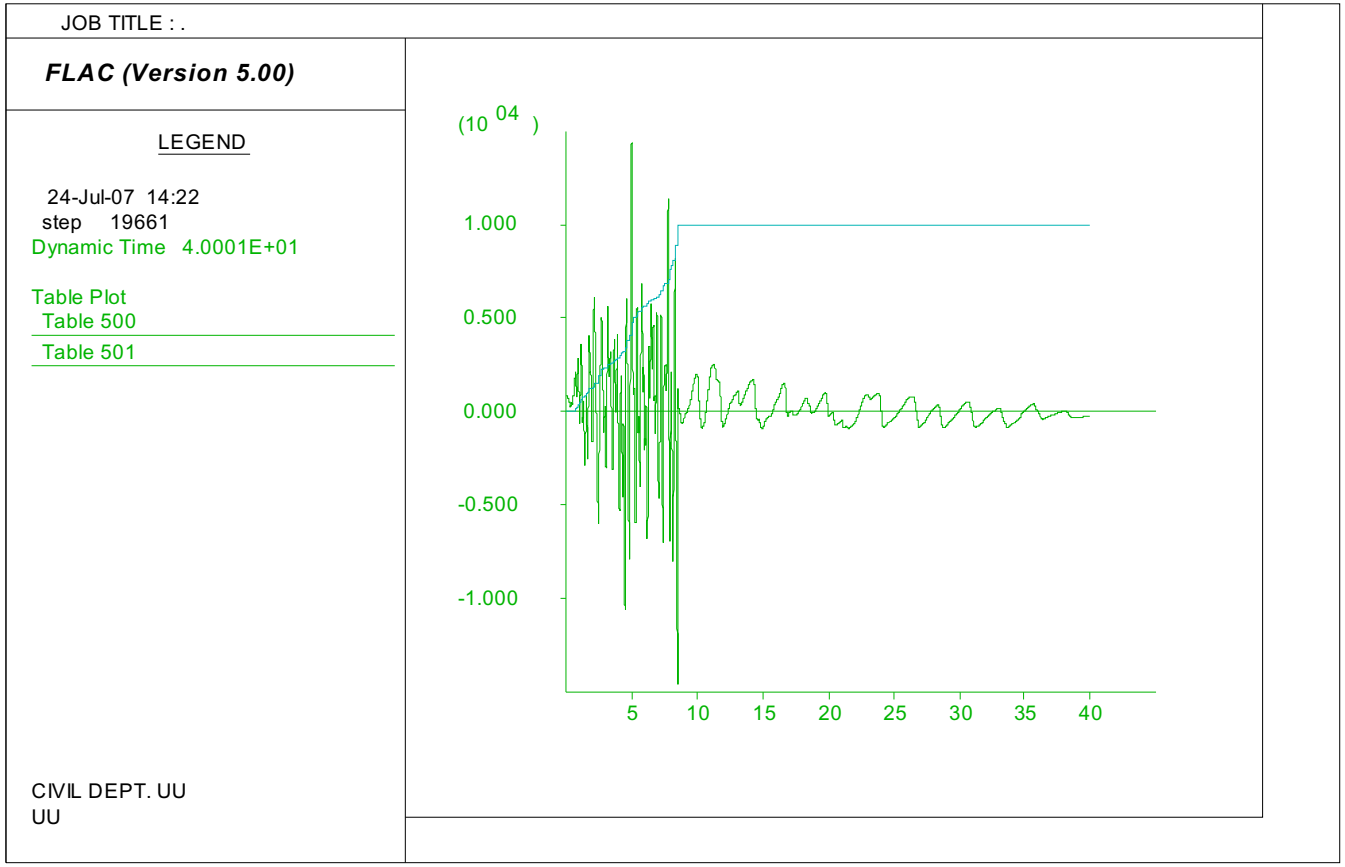


Figure E.18. Model pore water generation history loaded by motion 4 with residual strength ratio of 0.03: Shear stress (Y axis in Pa) and r_u (Y axis multiplied by 1000) vs. time (X axis in seconds).

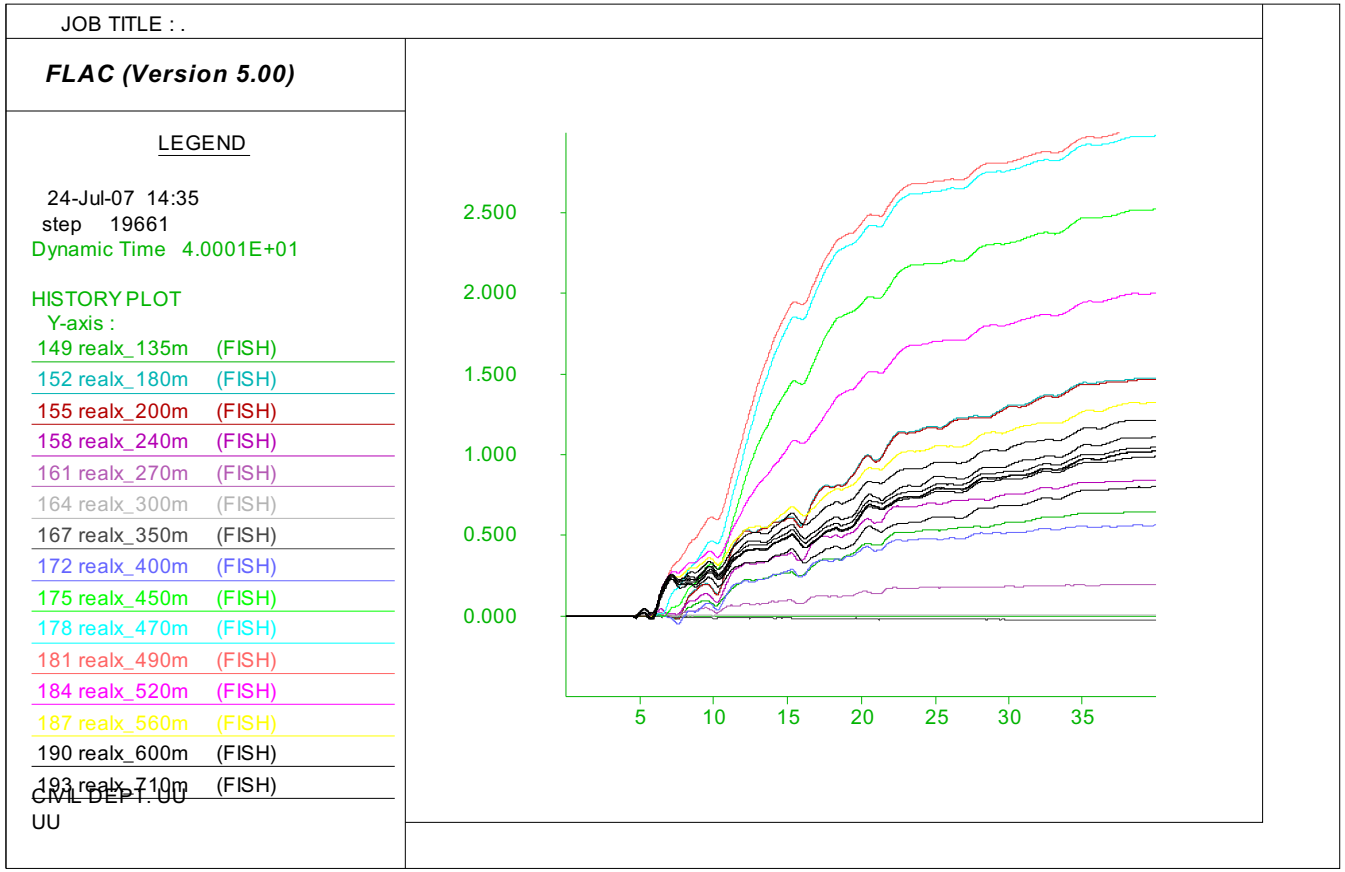


Figure E.19. Model later spreading prediction loaded by motion 5 with residual strength ratio of 0.03 (Y axis in meter and X axis in second)

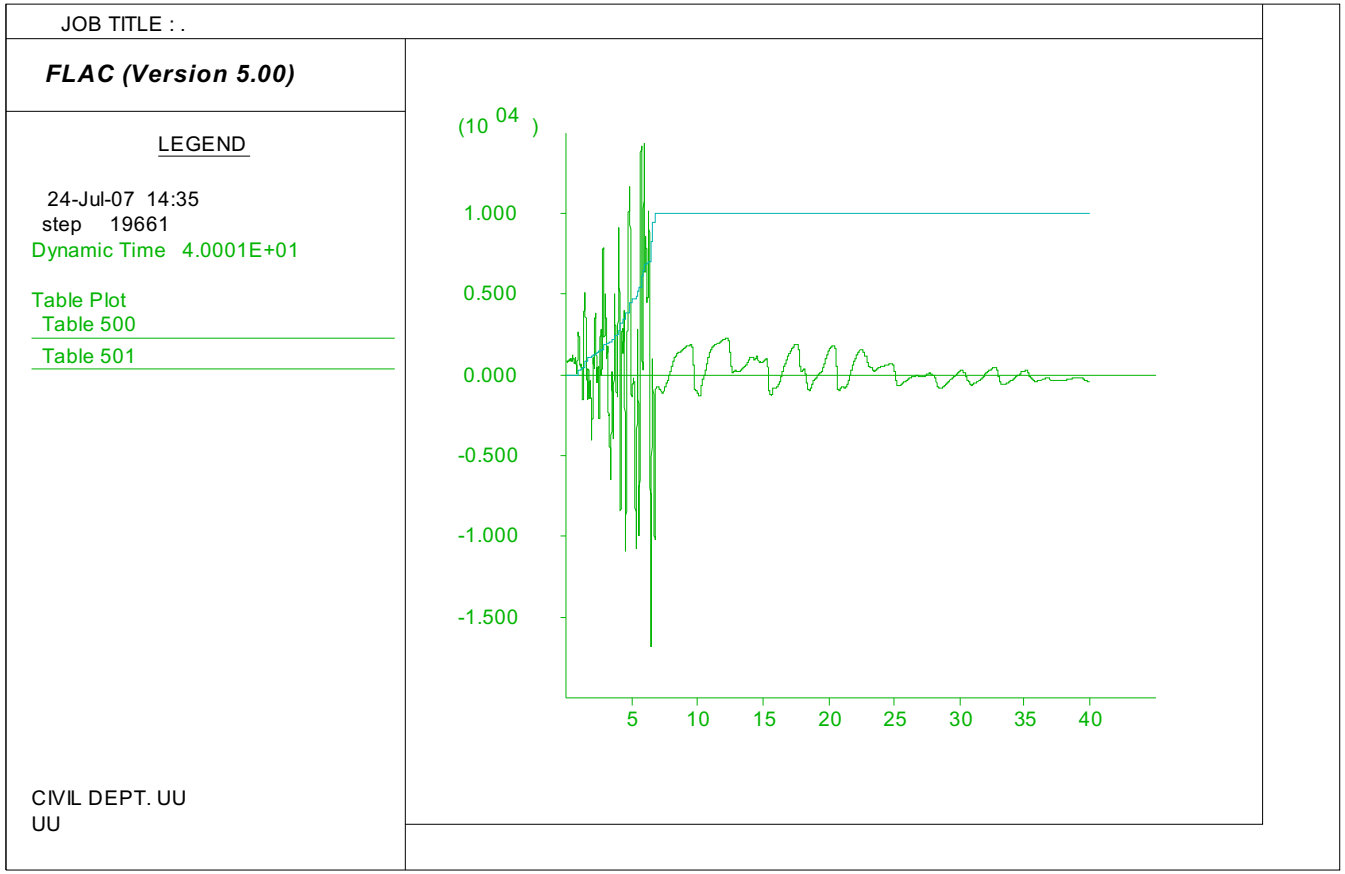


Figure E.20. Model pore water generation history loaded by motion 5 with residual strength ratio of 0.03: Shear stress (Y axis in Pa) and r_u (Y axis multiplied by 1000) vs. time (X axis in seconds).

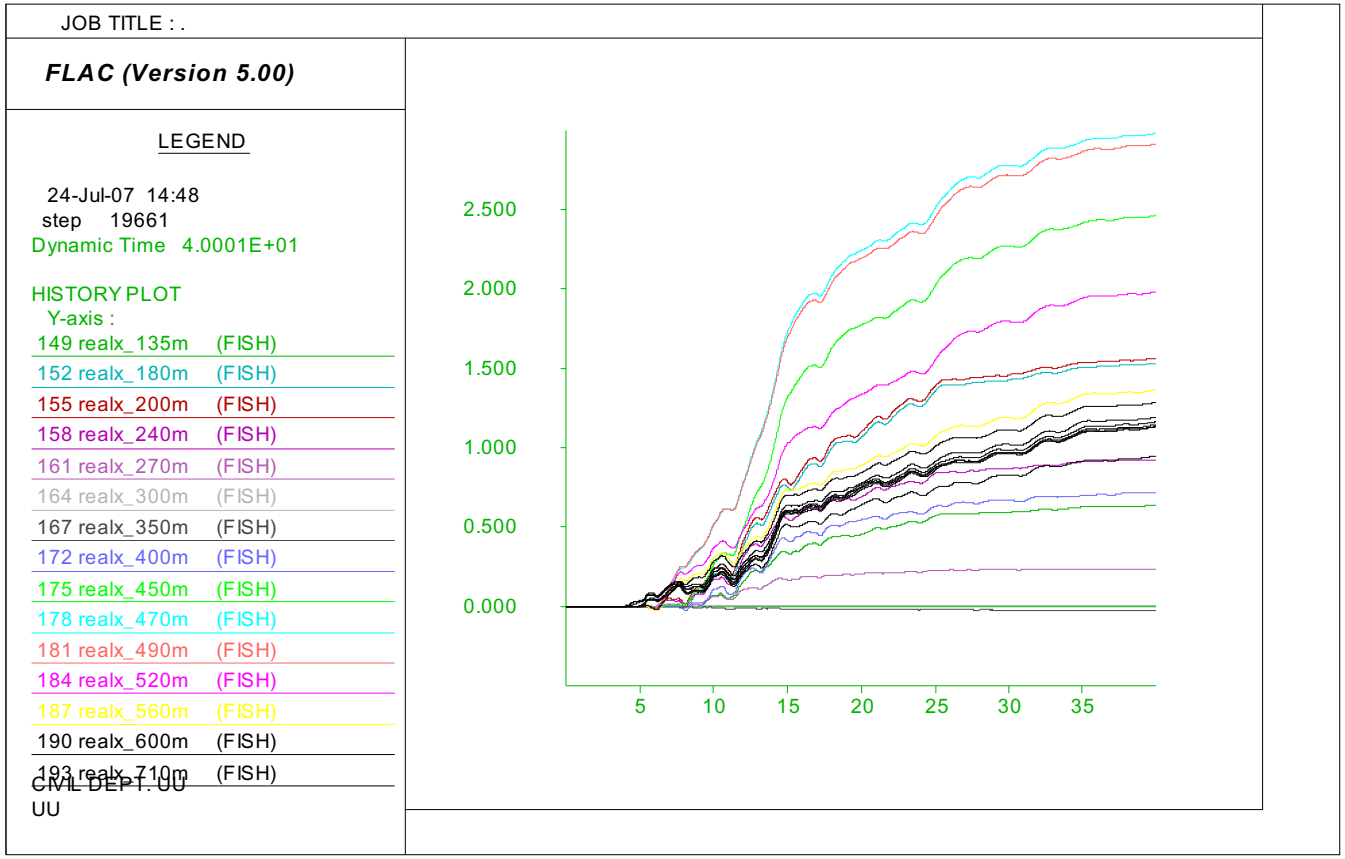


Figure E. 21. Model later spreading prediction loaded by motion 6 with residual strength ratio of 0.03 (Y axis in meter and X axis in second)

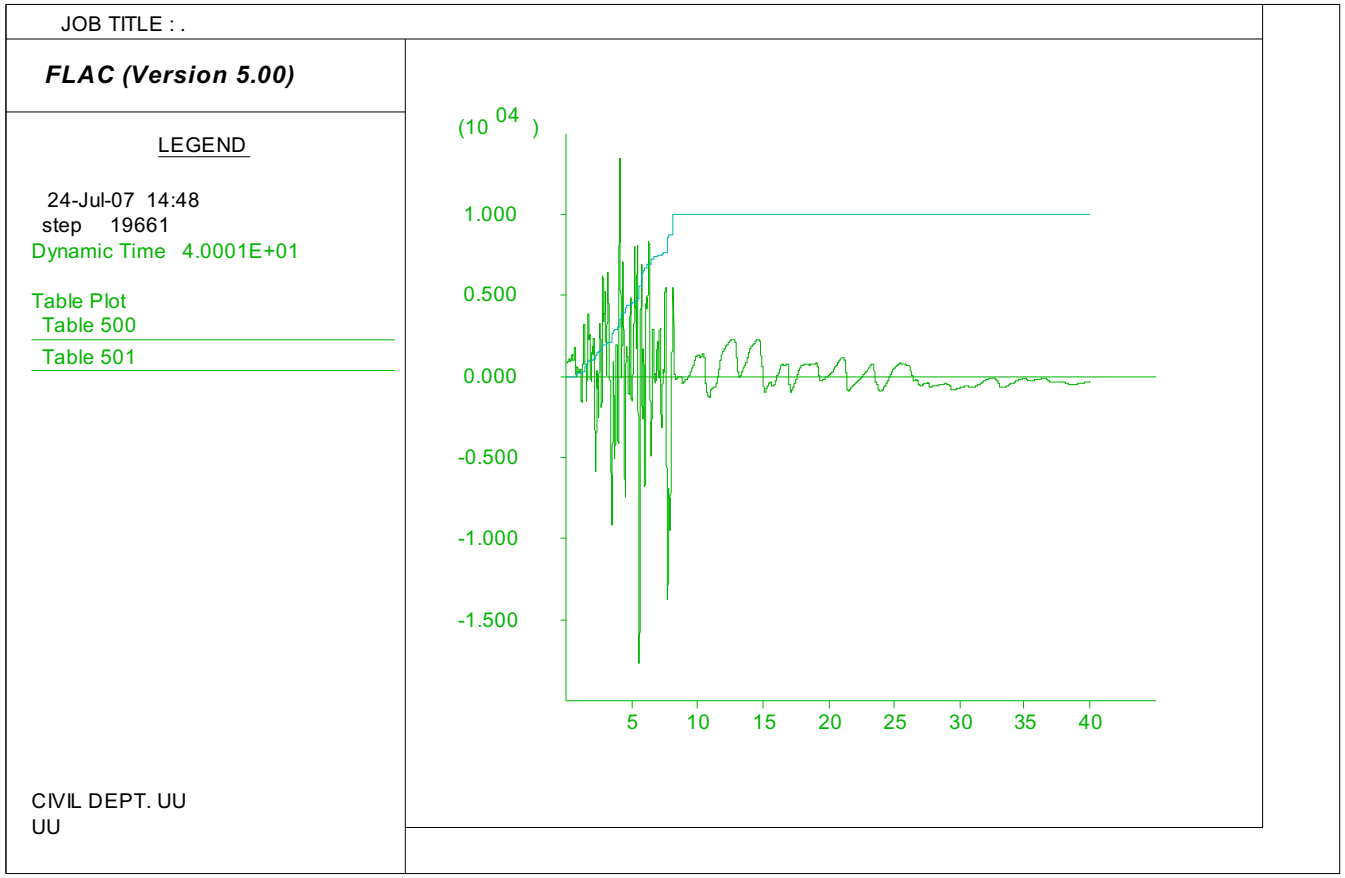


Figure E.22. Model pore water generation history loaded by motion 6 with residual strength ratio of 0.03: Shear stress (Y axis in Pa) and r_u (Y axis multiplied by 1000) vs. time (X axis in seconds).

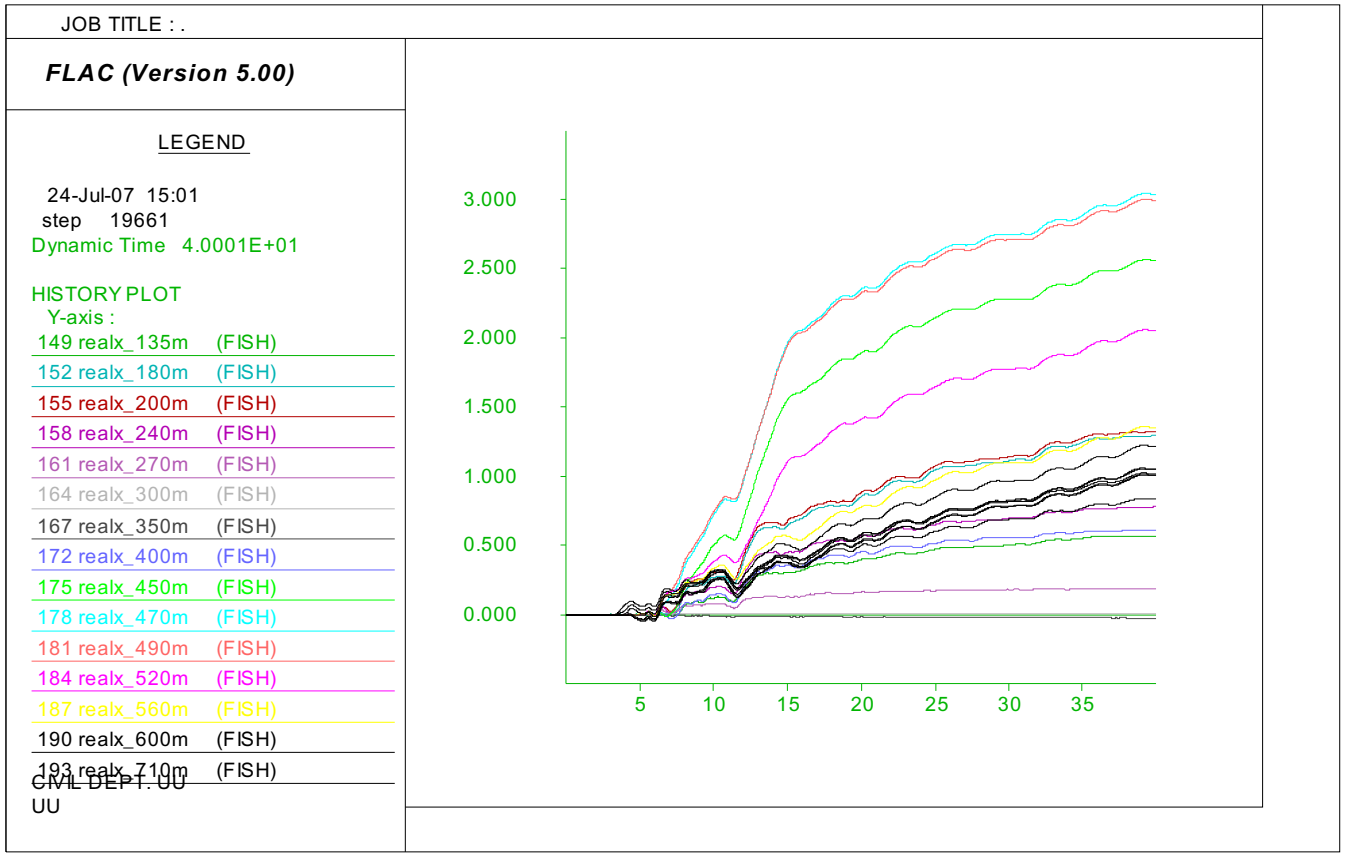


Figure E.23. Model later spreading prediction loaded by motion 7 with residual strength ratio of 0.03 (Y axis in meter and X axis in second)

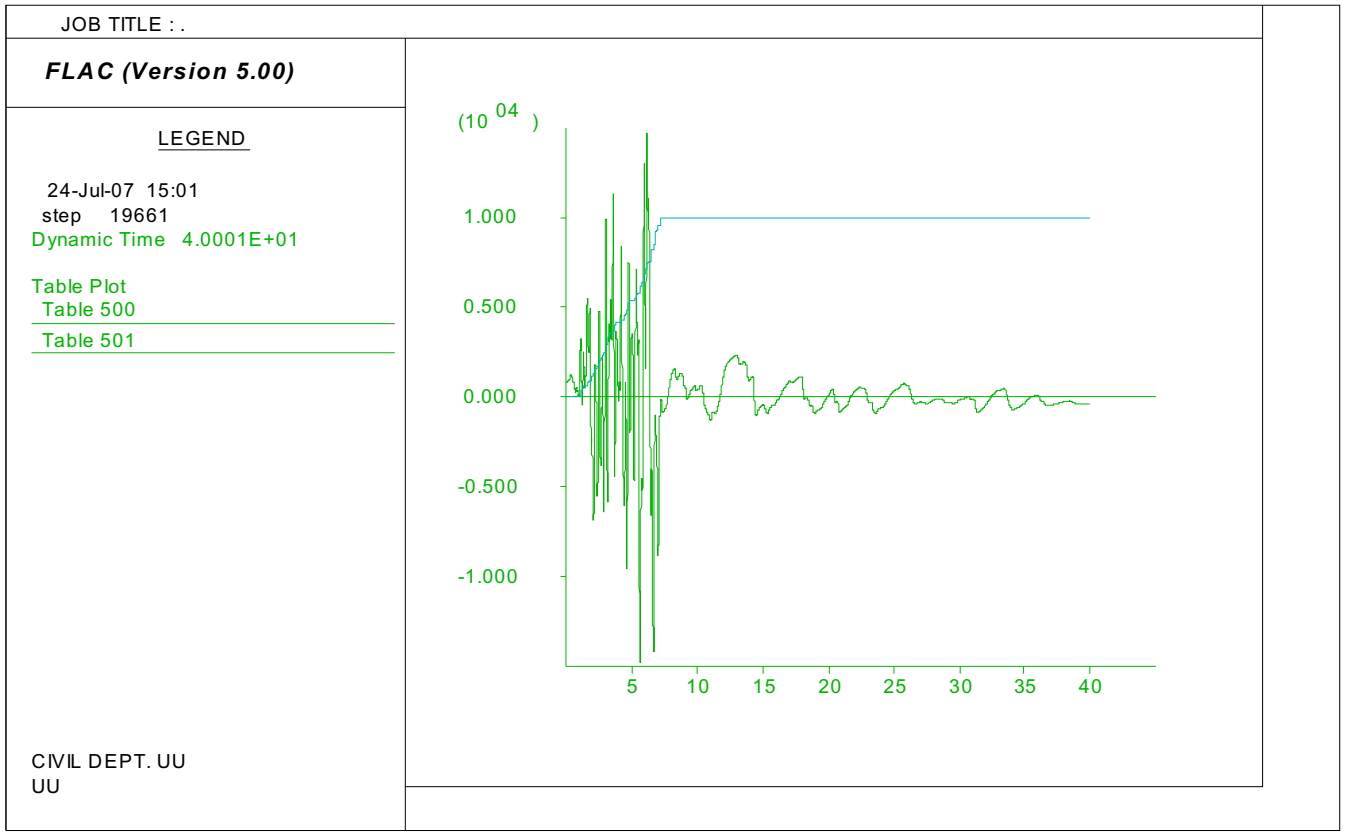


Figure E.24. Model pore water generation history loaded by motion 7 with residual strength ratio of 0.03: Shear stress (Y axis in Pa) and r_u (Y axis multiplied by 1000) vs. time (X axis in seconds).

APPENDIX F

NOSHIRO SITE S-7 SECTION DATA

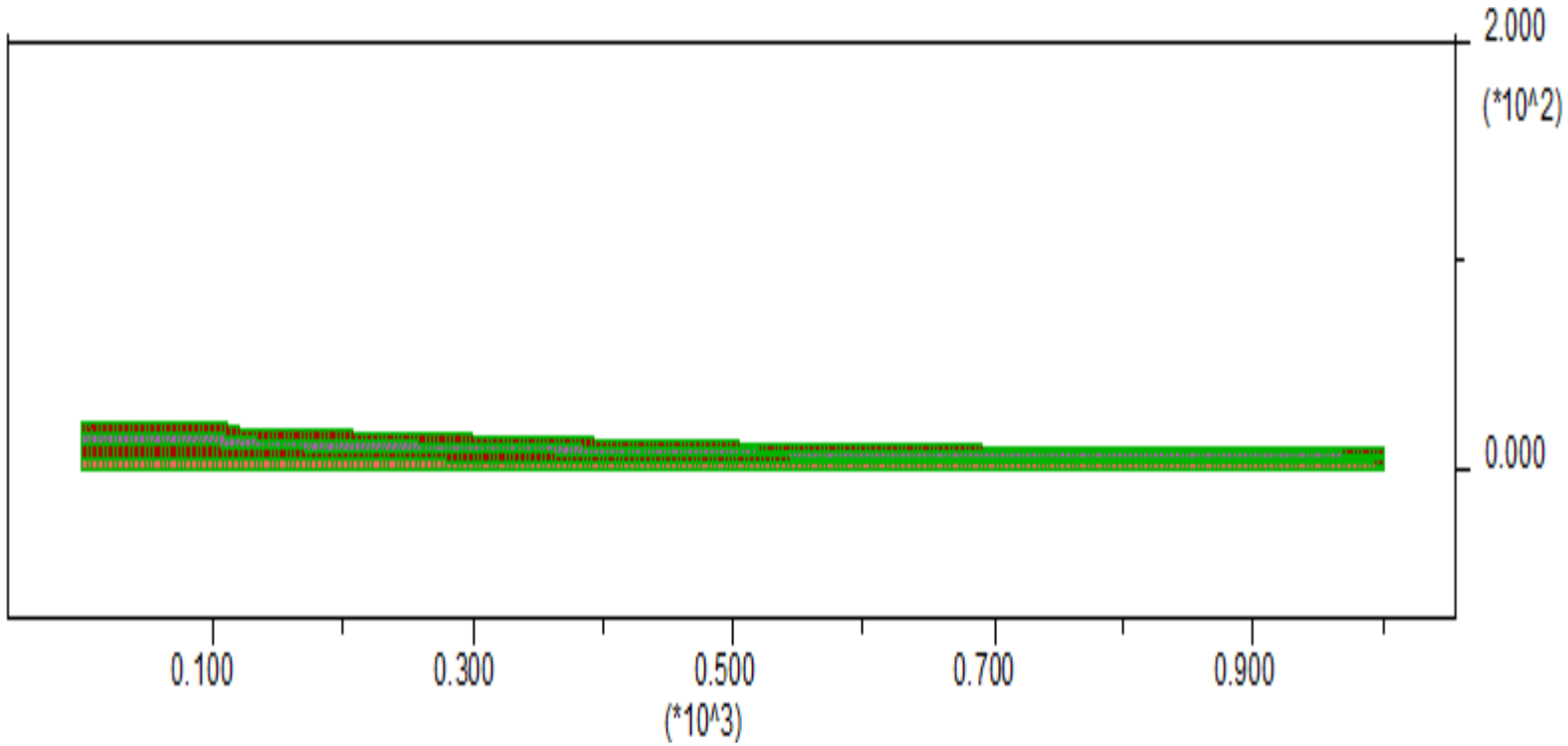


Figure F.1. Model design mesh

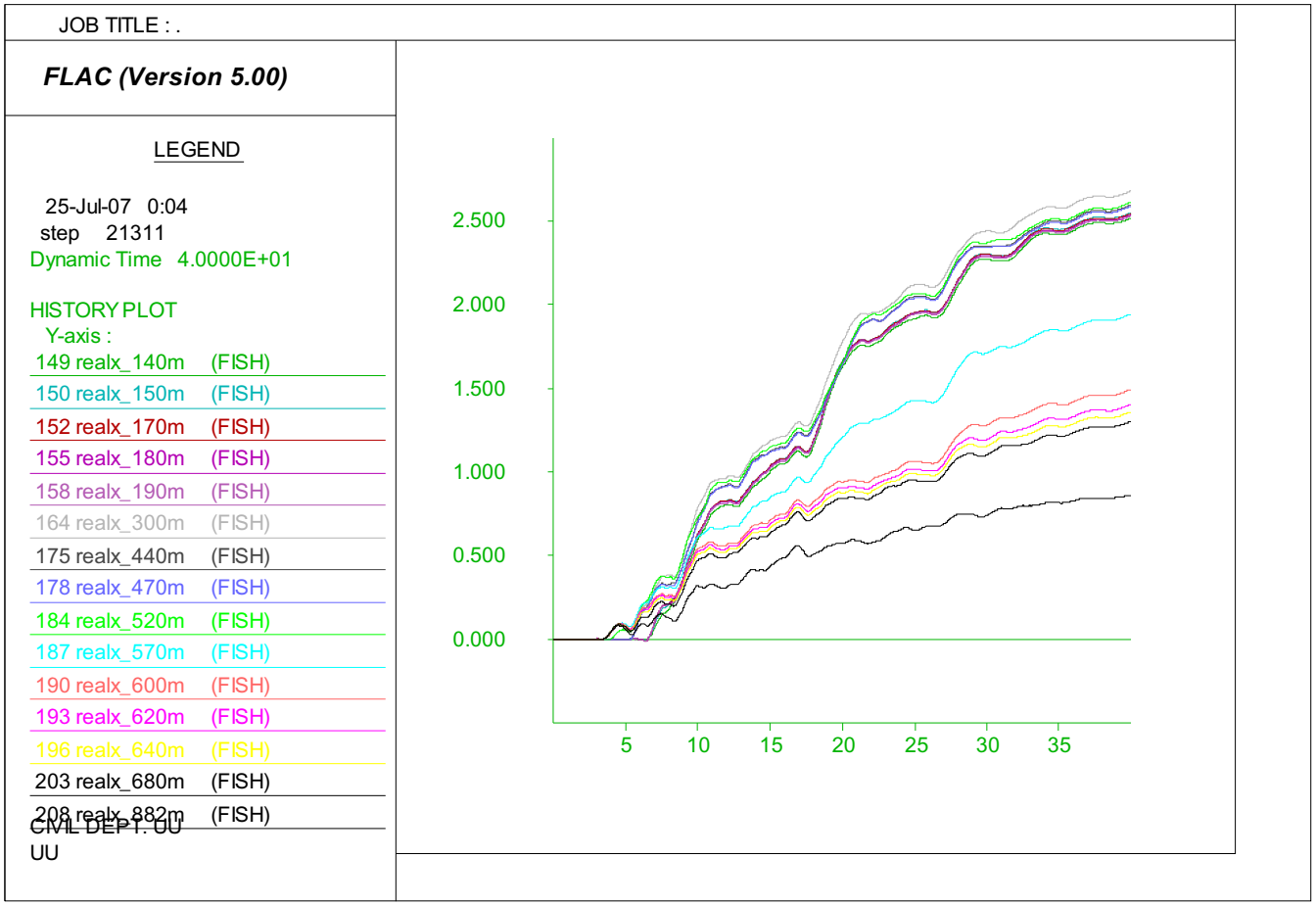


Figure F.2. Model later spreading prediction loaded by motion 1 with residual strength ratio of 0.03 (Y axis in meter and X axis in seconds).

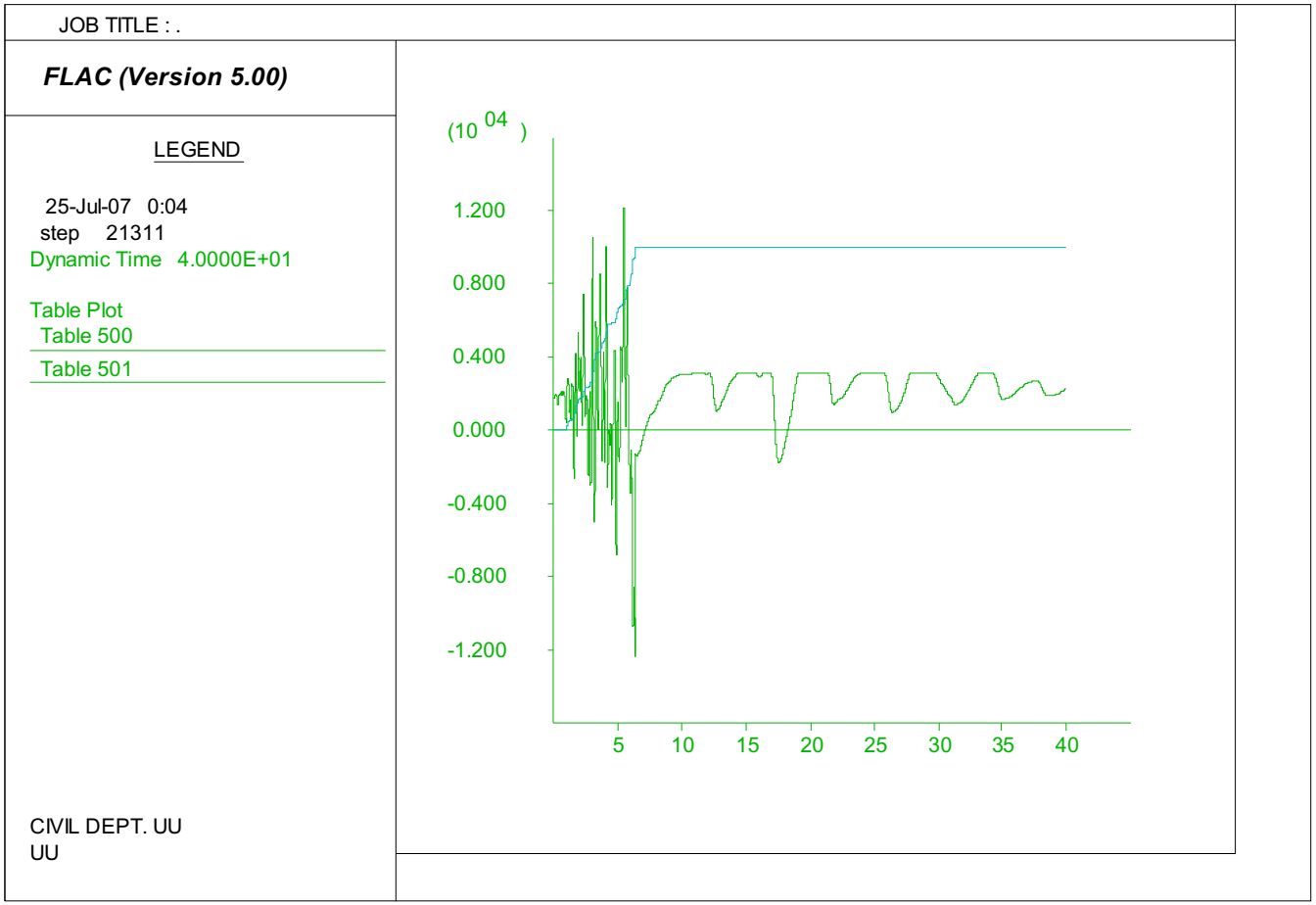


Figure F.3. Model pore water generation history loaded by motion 1 with residual strength ratio of 0.03: Shear stress (Y axis in Pa) and r_u (Y axis multiplied by 1000) vs. time (X axis in seconds).

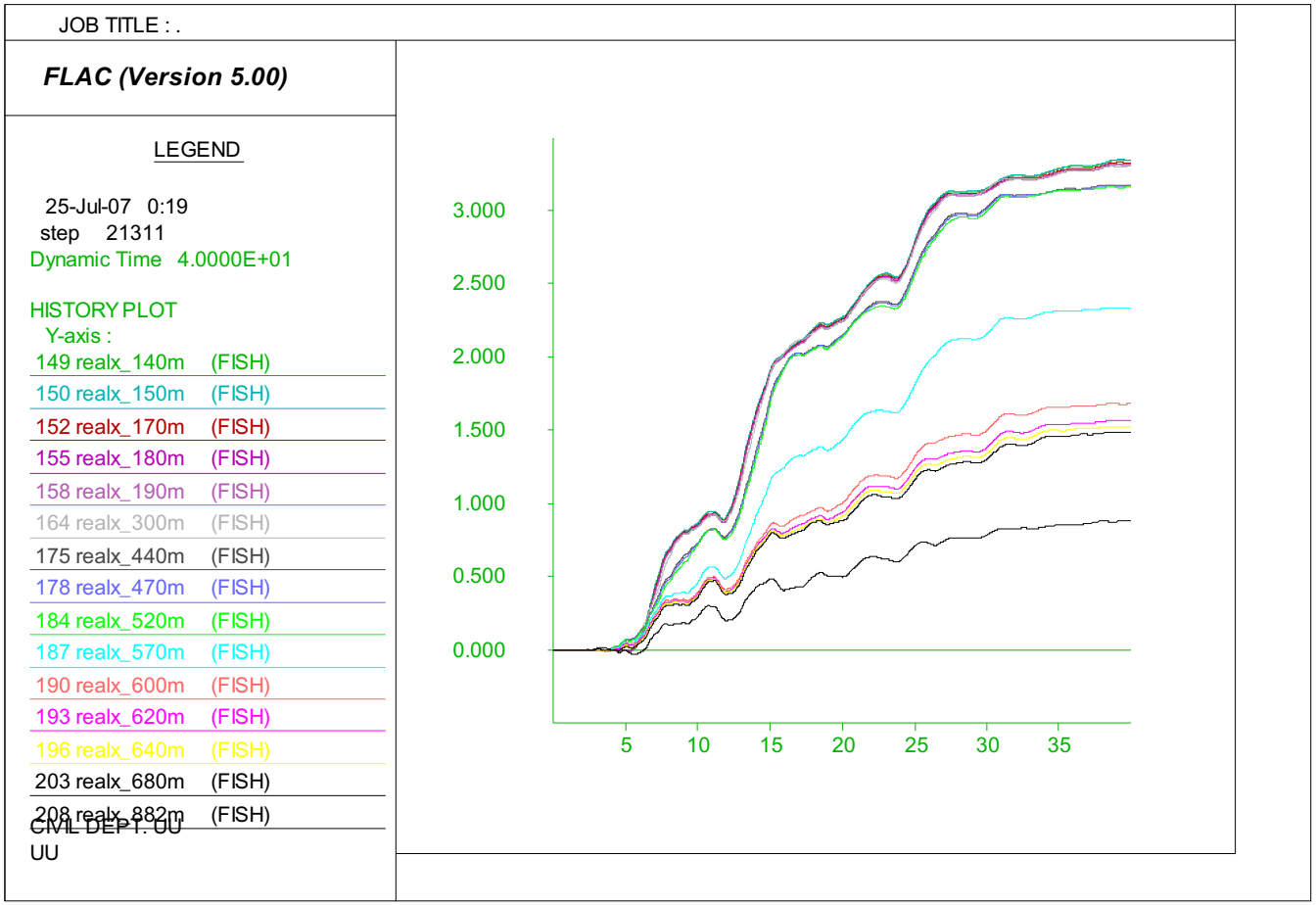


Figure F.4. Model later spreading prediction loaded by motion 2 with residual strength ratio of 0.03 (Y axis in meter and X axis in seconds).

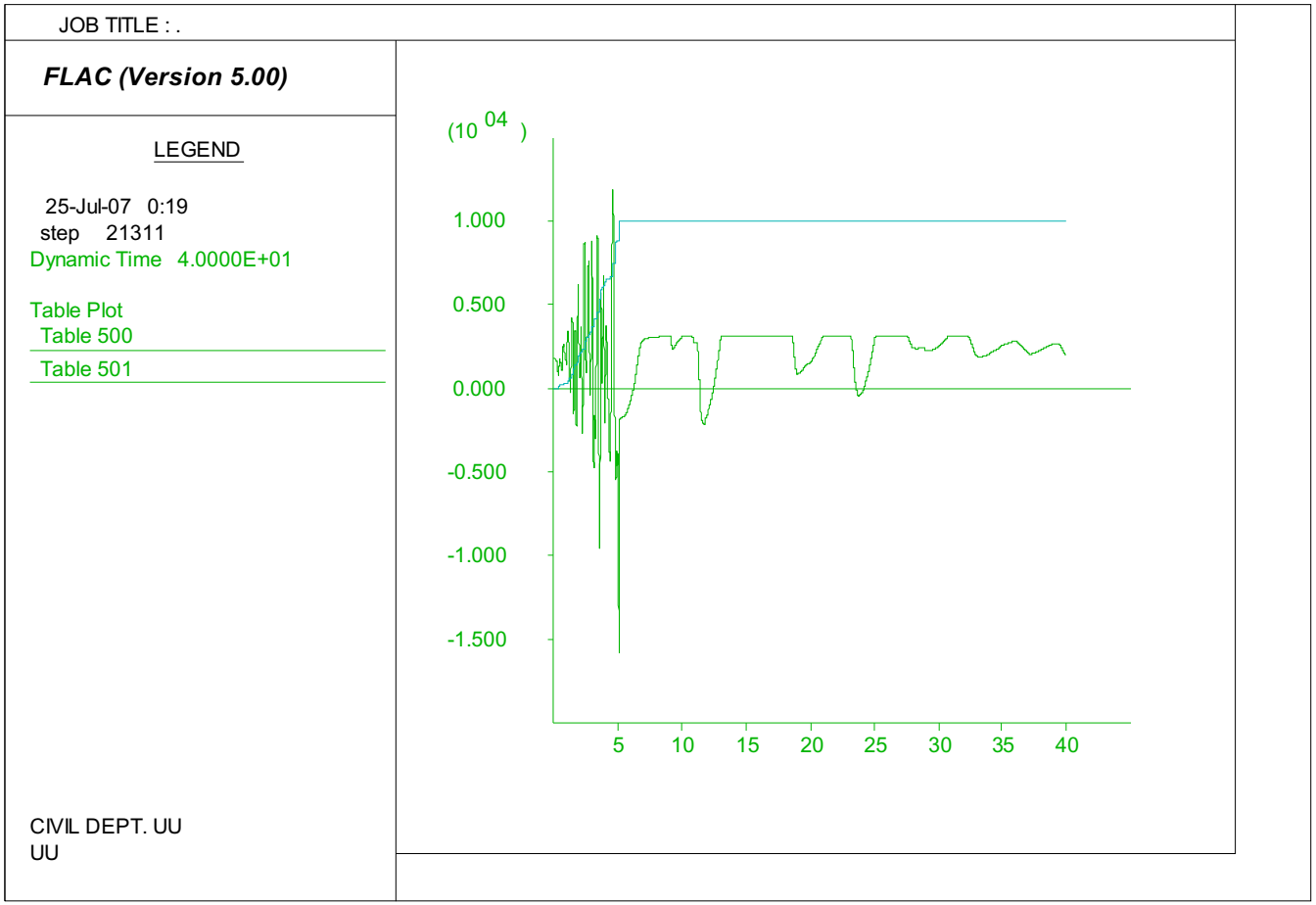


Figure F.5. Model pore water generation history loaded by motion 2 with residual strength ratio of 0.03: Shear stress (Y axis in Pa) and r_u (Y axis multiplied by 1000) vs. time (X axis in seconds).

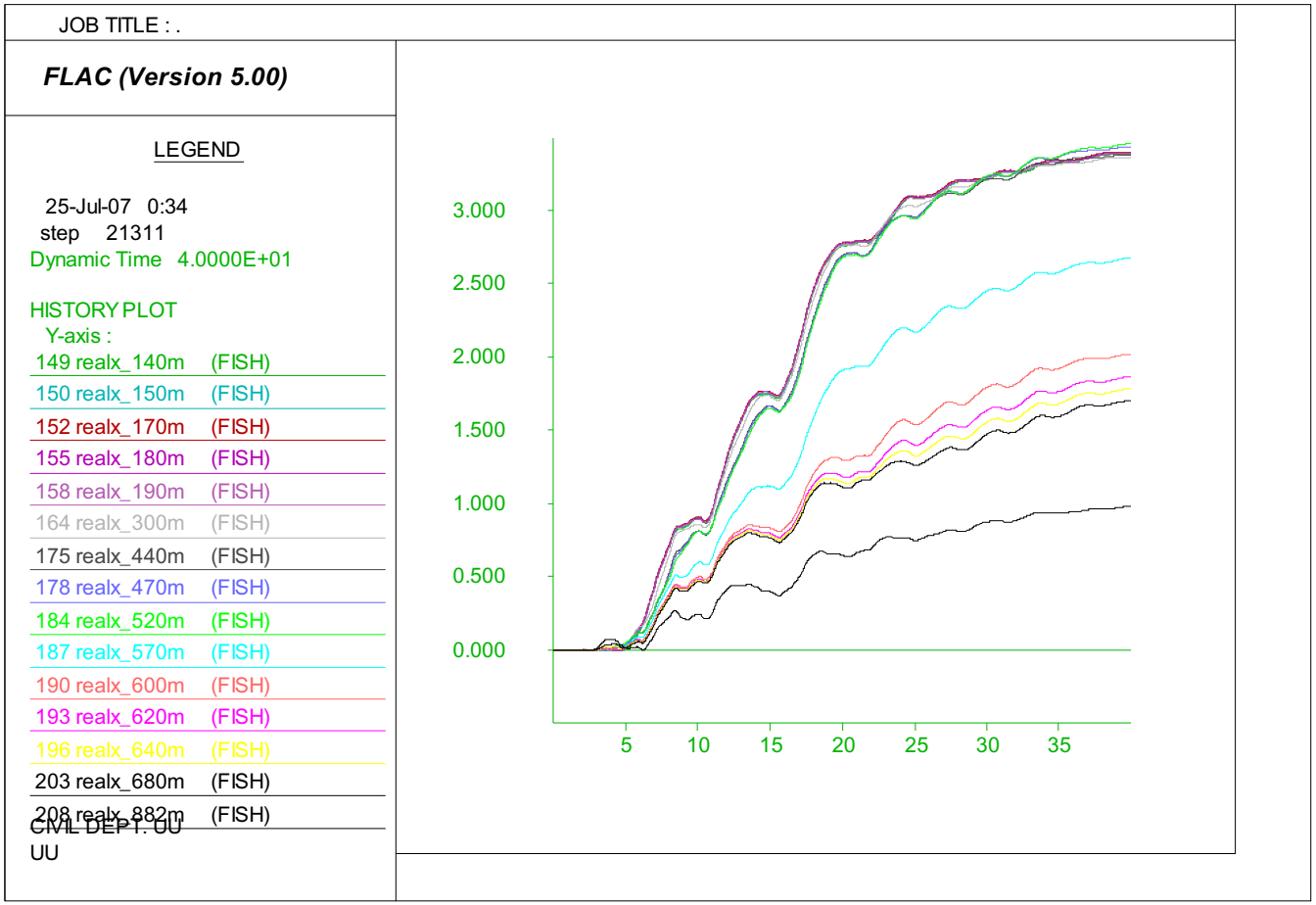


Figure F.6. Model later spreading prediction loaded by motion 3 with residual strength ratio of 0.03 (Y axis in meter and X axis in seconds).

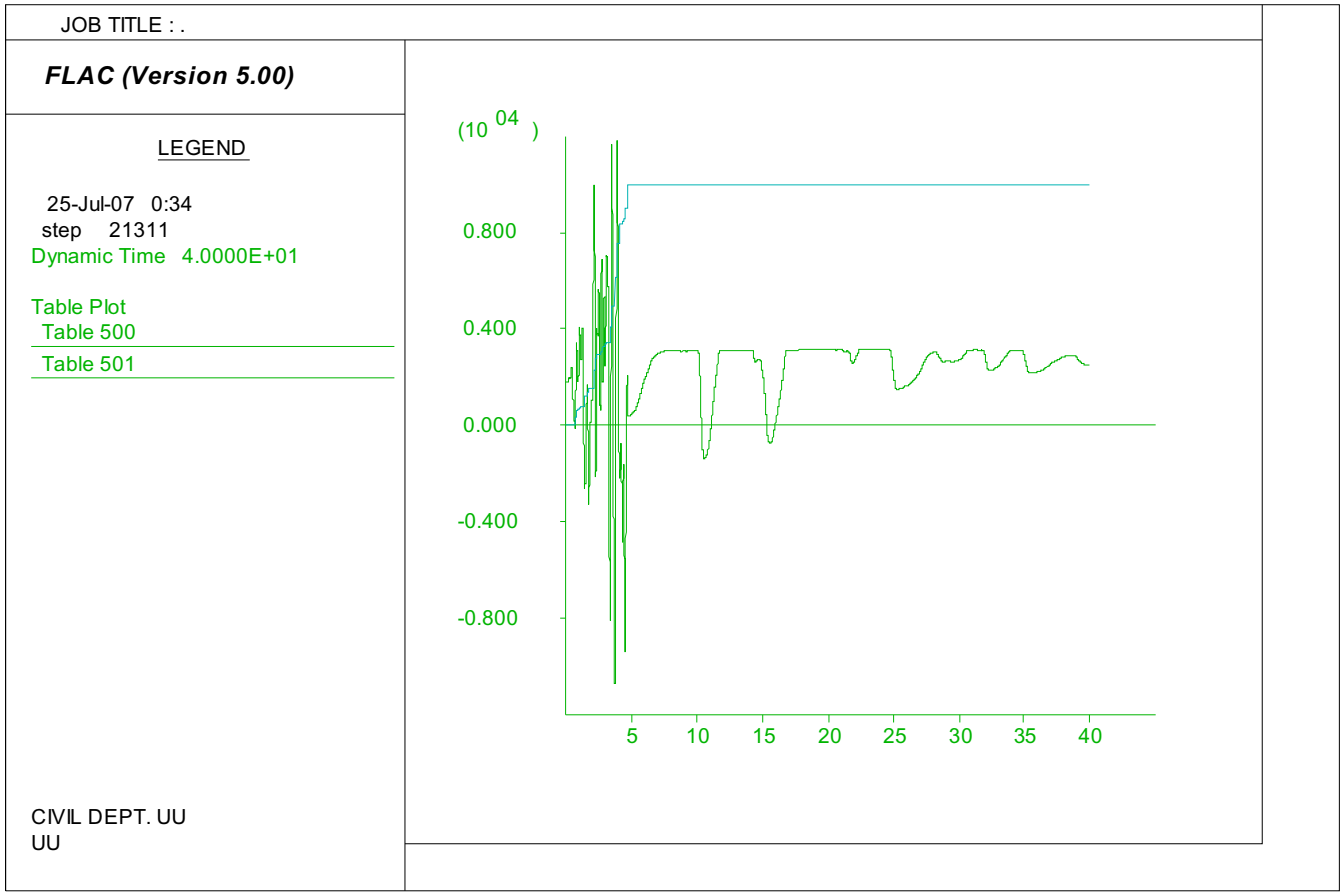


Figure F.7. Model pore water generation history loaded by motion 3 with residual strength ratio of 0.03: Shear stress (Y axis in Pa) and r_u (Y axis multiplied by 1000) vs. time (X axis in seconds).

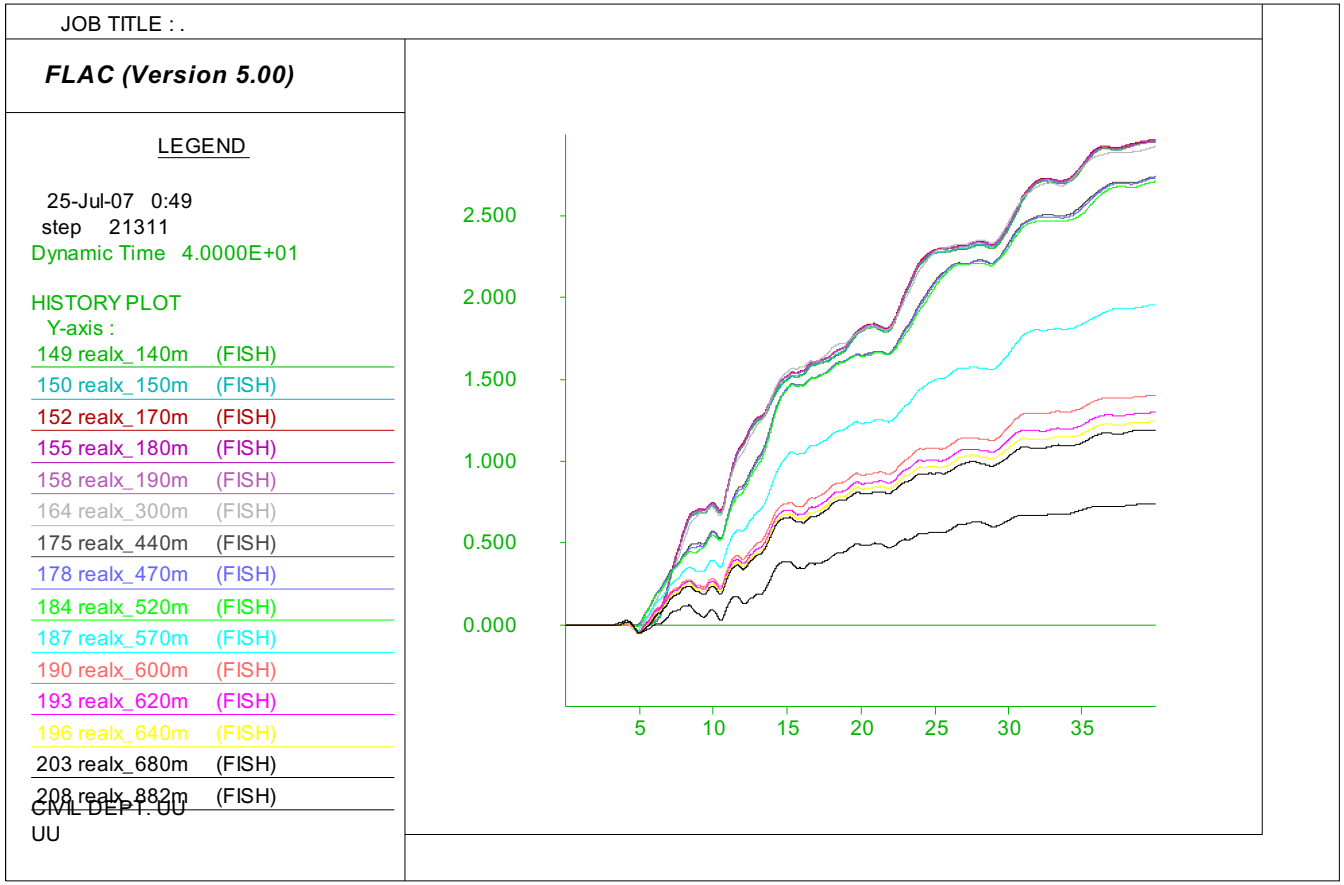


Figure F.8. Section Figure VI-. Model later spreading prediction loaded by motion 4 with residual strength ratio of 0.03 (Y axis in meter and X axis in seconds).

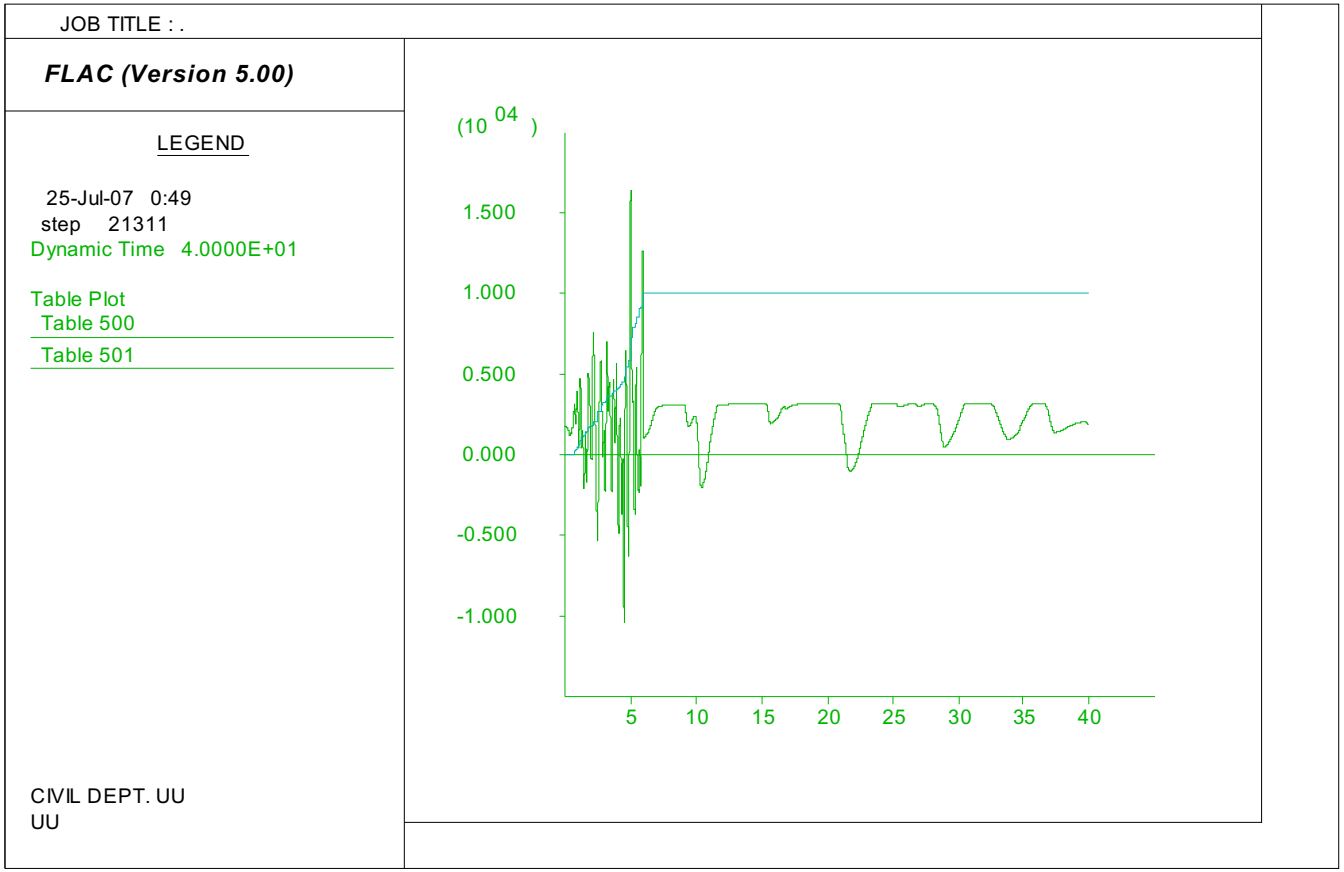


Figure F.9. Model pore water generation history loaded by motion 4 with residual strength ratio of 0.03: Shear stress (Y axis in Pa) and r_u (Y axis multiplied by 1000) vs. time (X axis in seconds).

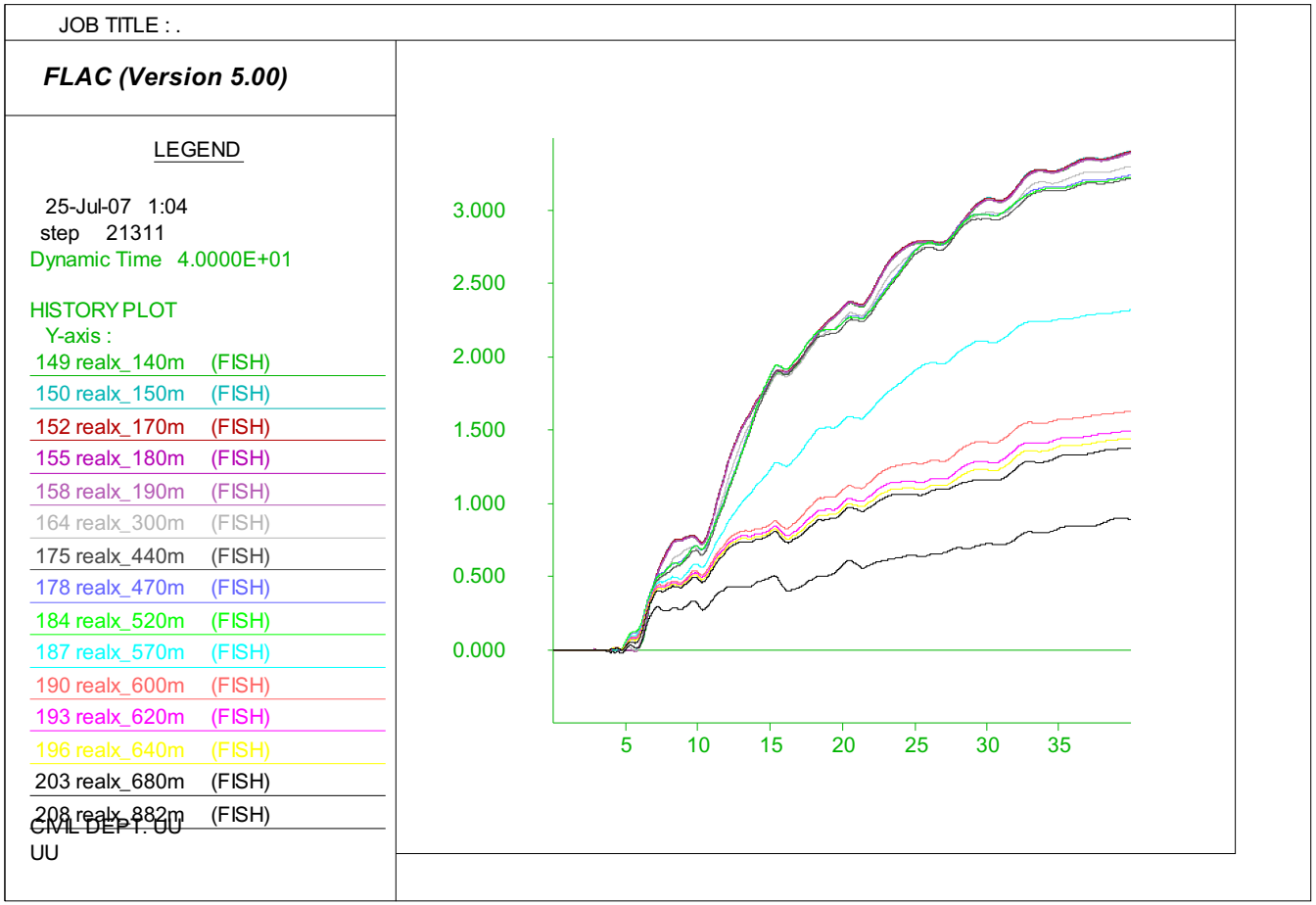


Figure F.10. Model later spreading prediction loaded by motion 5 with residual strength ratio of 0.03 (Y axis in meter and X axis in seconds).

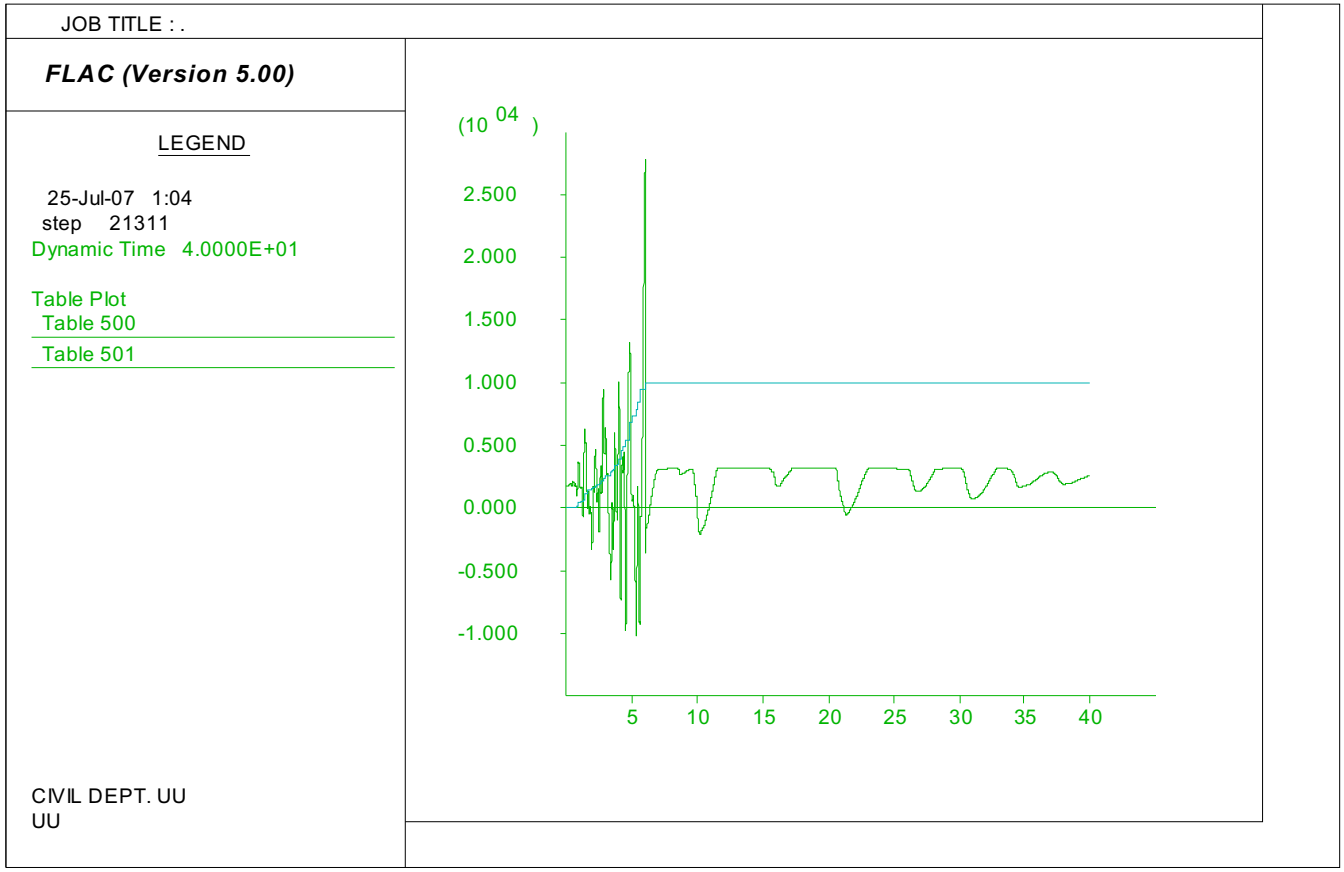


Figure F.11. Model pore water generation history loaded by motion 5 with residual strength ratio of 0.03: Shear stress (Y axis in Pa) and r_u (Y axis multiplied by 1000) vs. time (X axis in seconds).

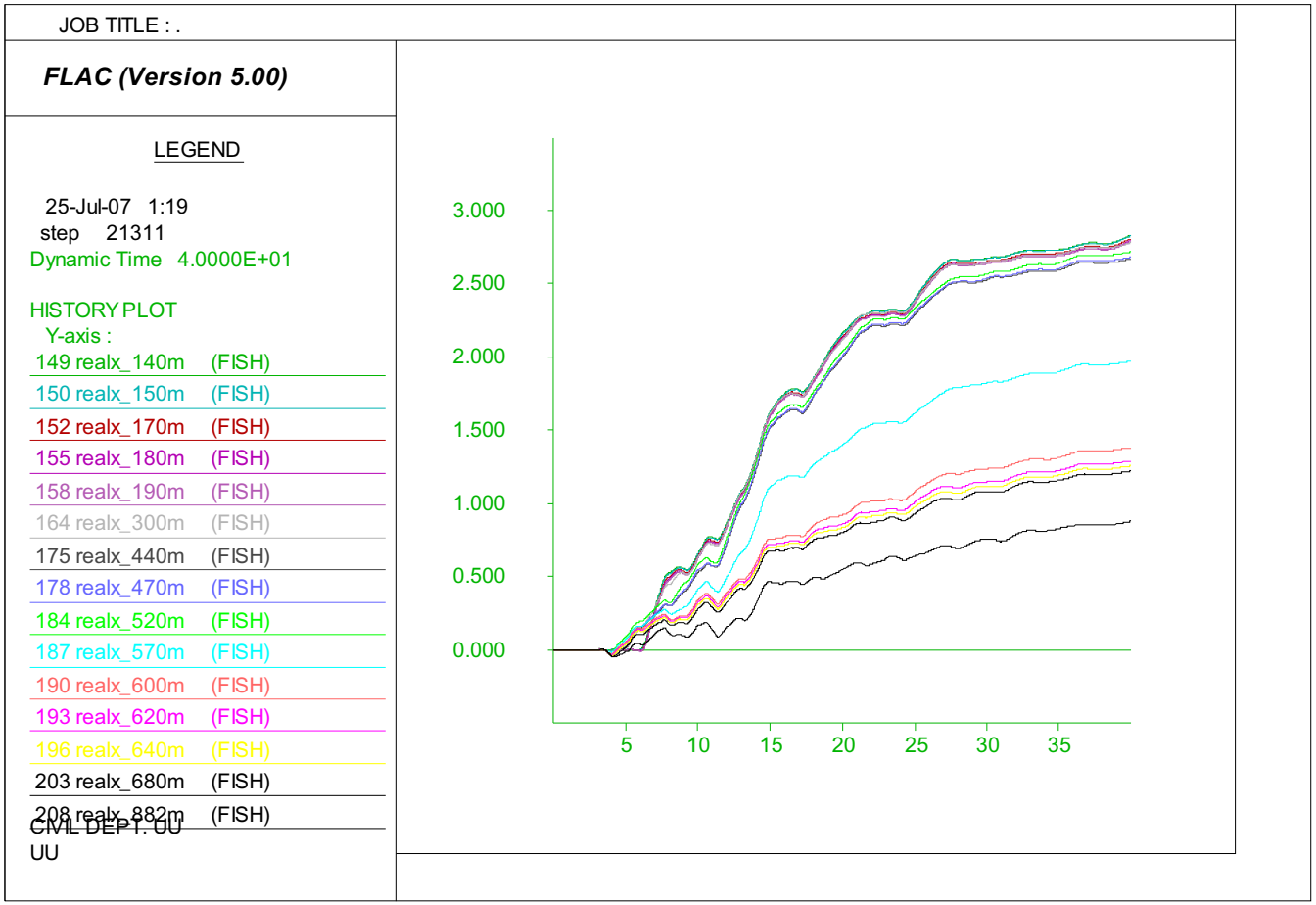


Figure F.12. Model later spreading prediction loaded by motion 6 with residual strength ratio of 0.03 (Y axis in meter and X axis in seconds).

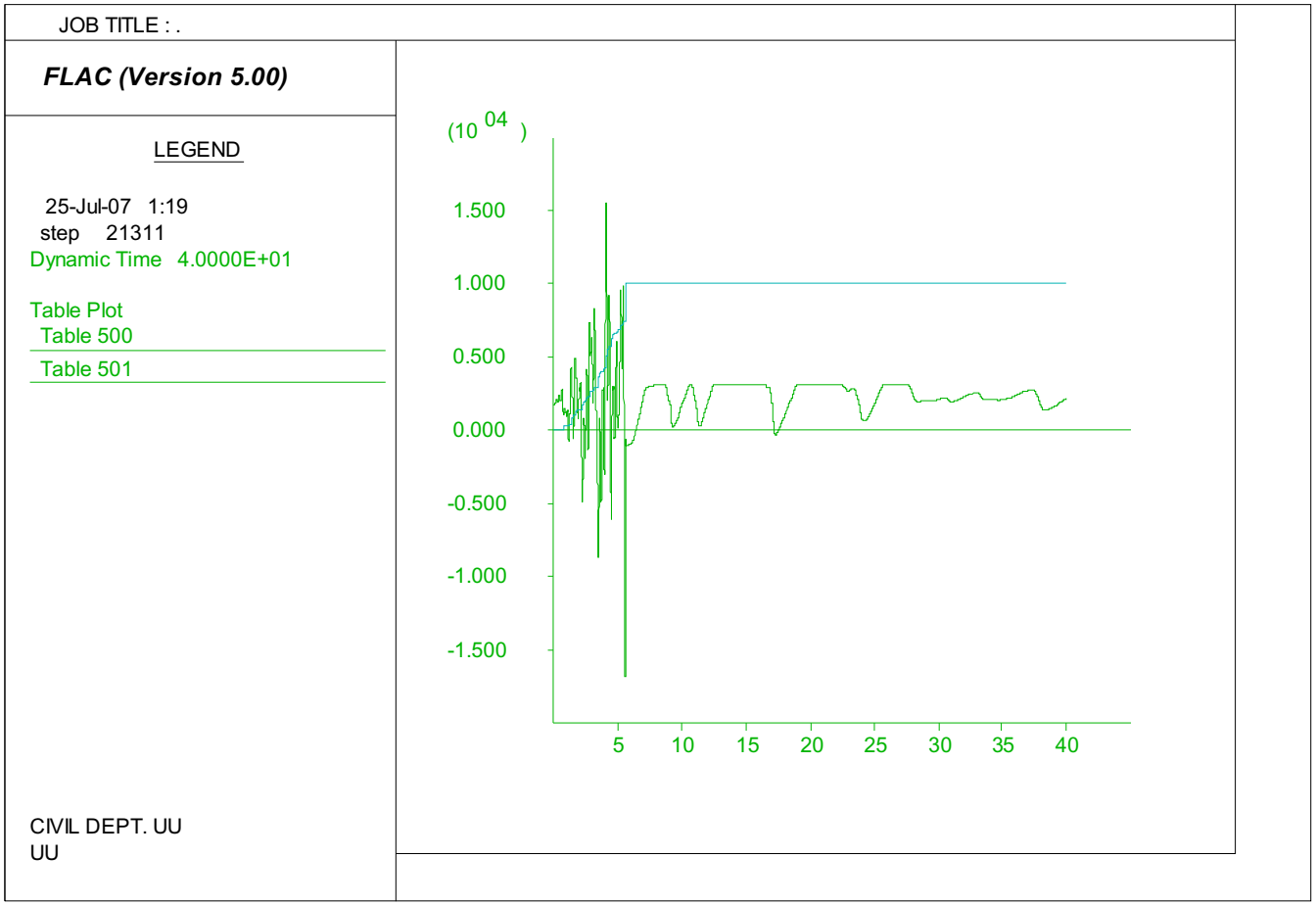


Figure F.13. Model pore water generation history loaded by motion 6 with residual strength ratio of 0.03: Shear stress (Y axis in Pa) and r_u (Y axis multiplied by 1000) vs. time (X axis in seconds).

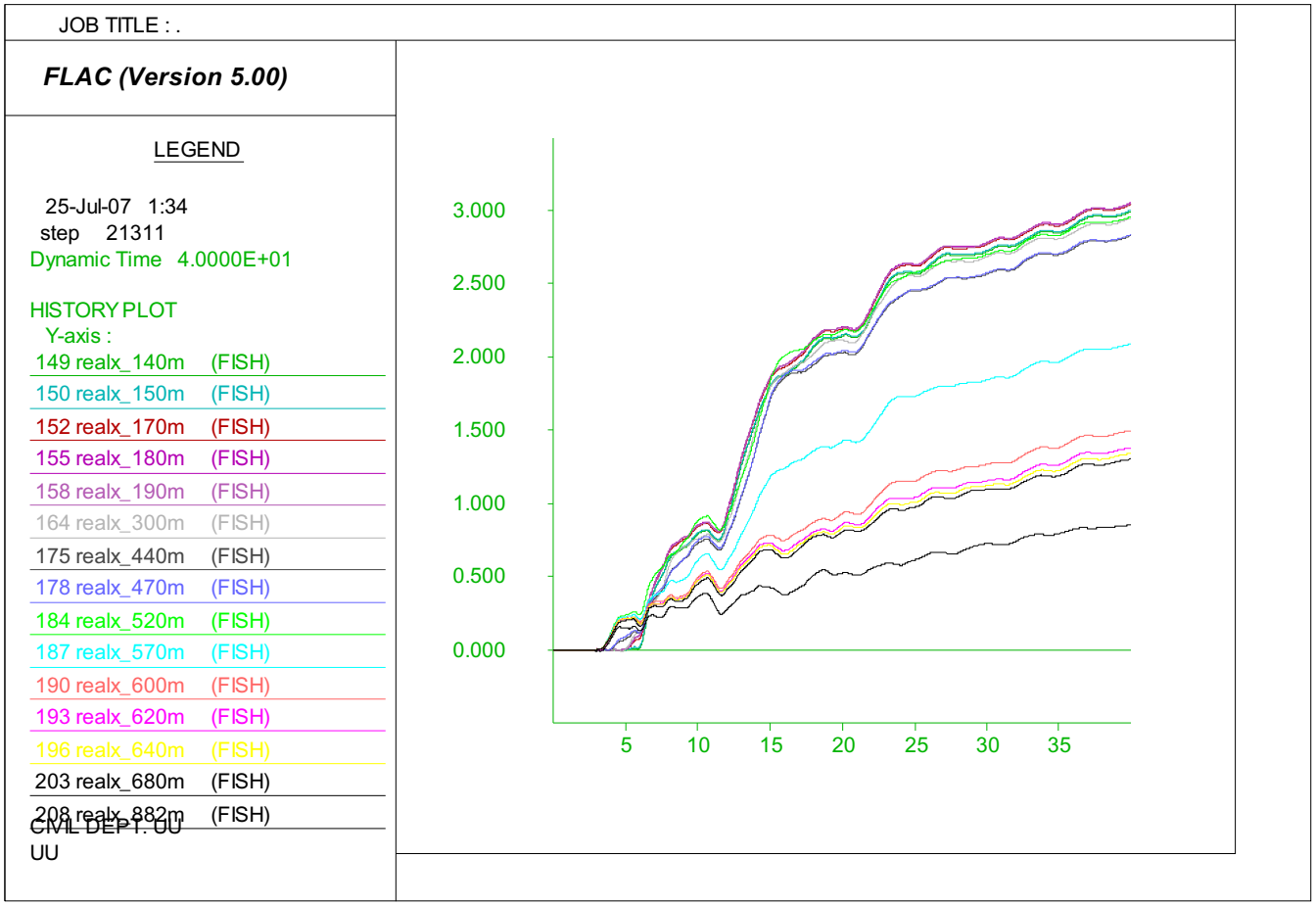


Figure F.14. Model later spreading prediction loaded by motion 7 with residual strength ratio of 0.03 (Y axis in meter and X axis in seconds).

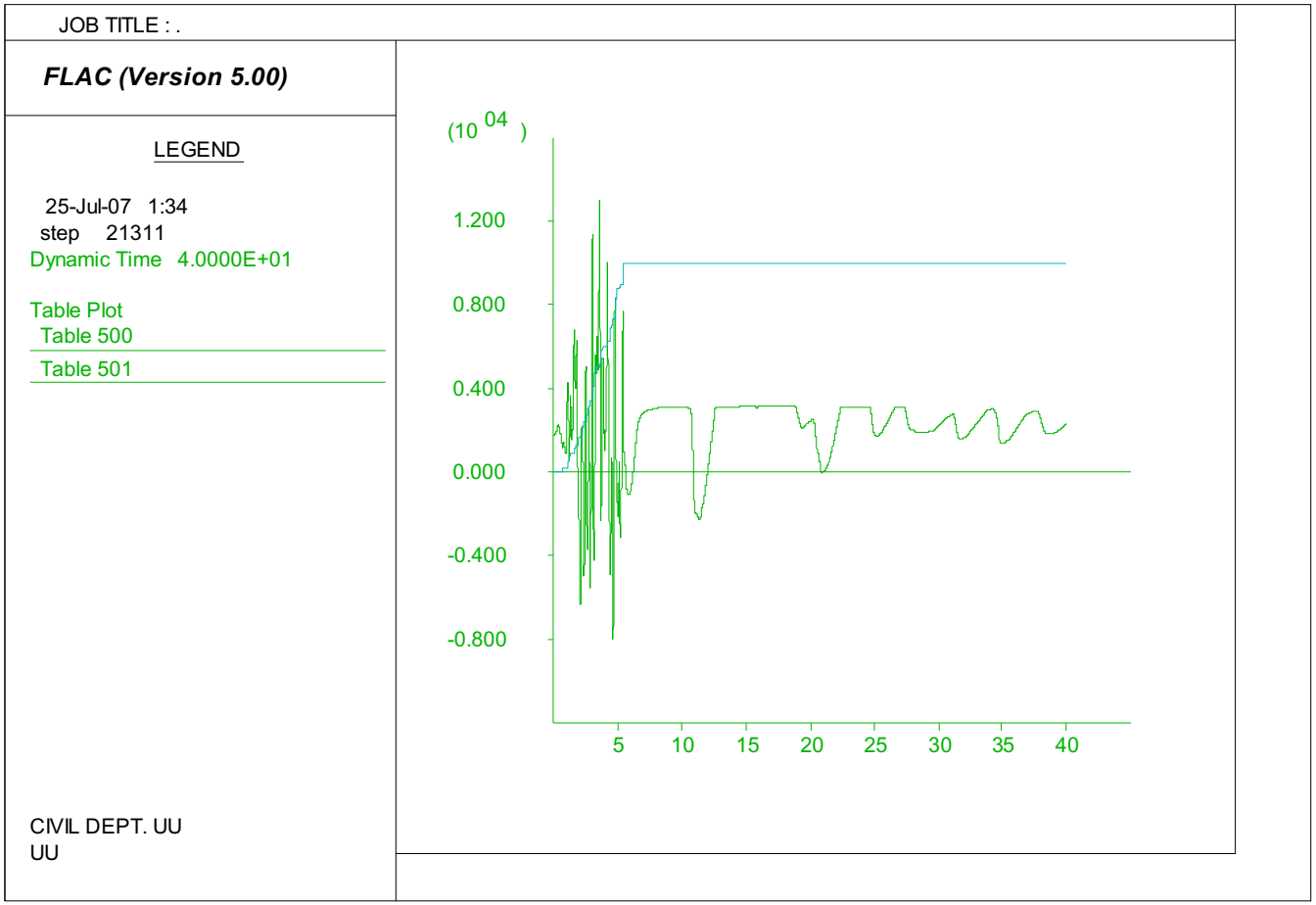


Figure F.15. Model pore water generation history loaded by motion 7 with residual strength ratio of 0.03: Shear stress (Y axis in Pa) and r_u (Y axis multiplied by 1000) vs. time (X axis in seconds).

APPENDIX G

SAN FERNANDO SITE JUVENILE HALL SECTION DATA

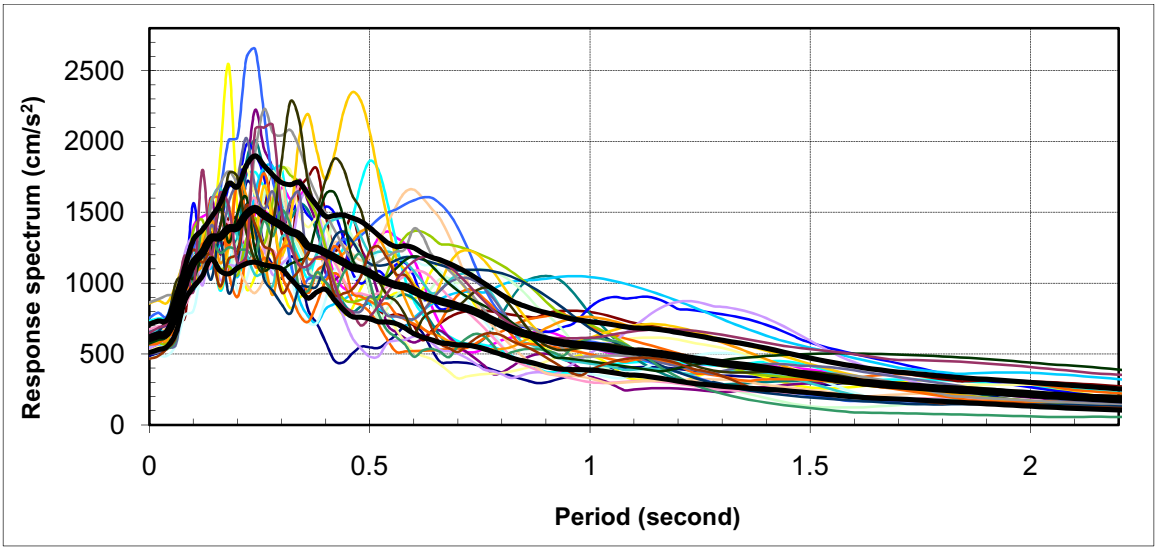


Figure G.1. Response spectra of generated thirty motions.

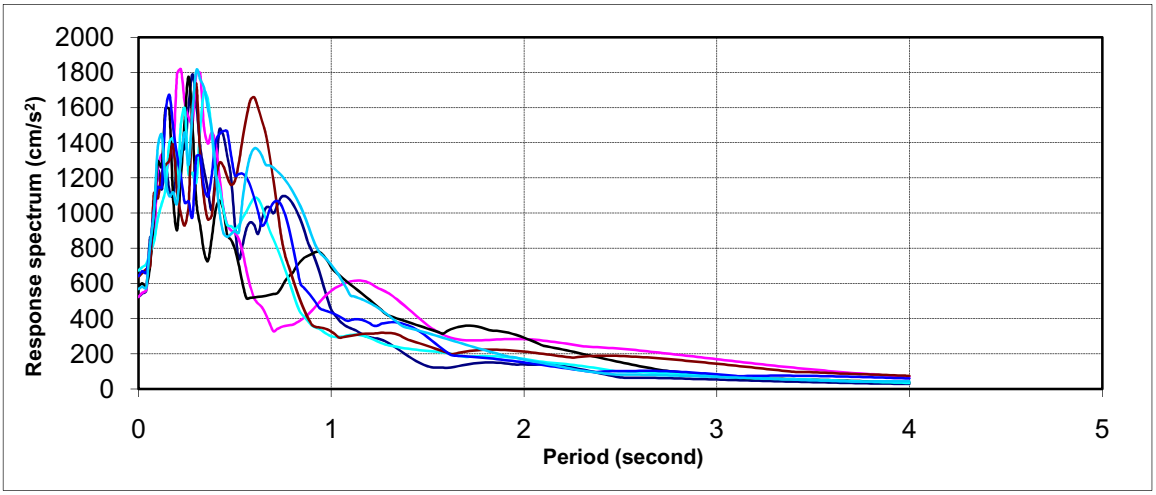


Figure G.2. Response spectra of selected seven motions.

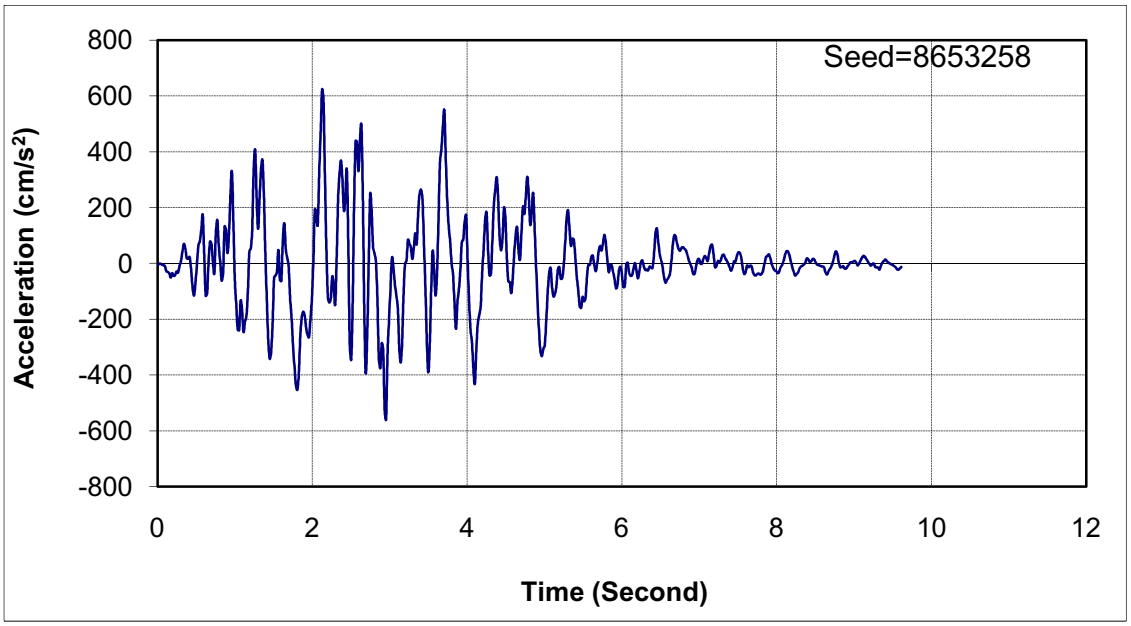


Figure G.3. Selected motion 1.

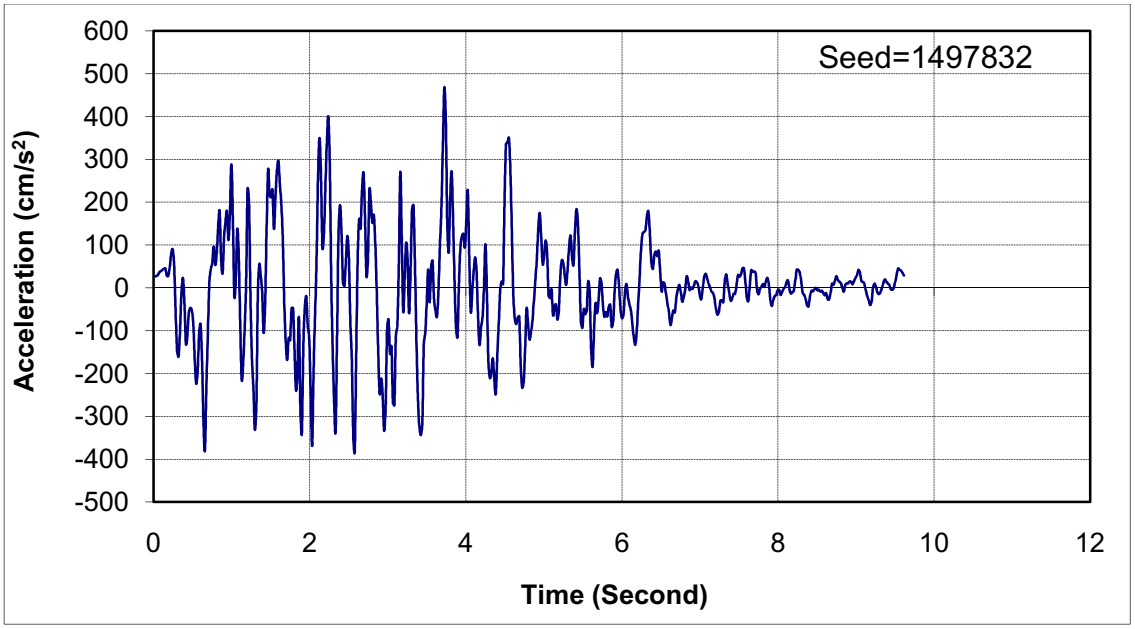


Figure G.4. Selected motion 2.

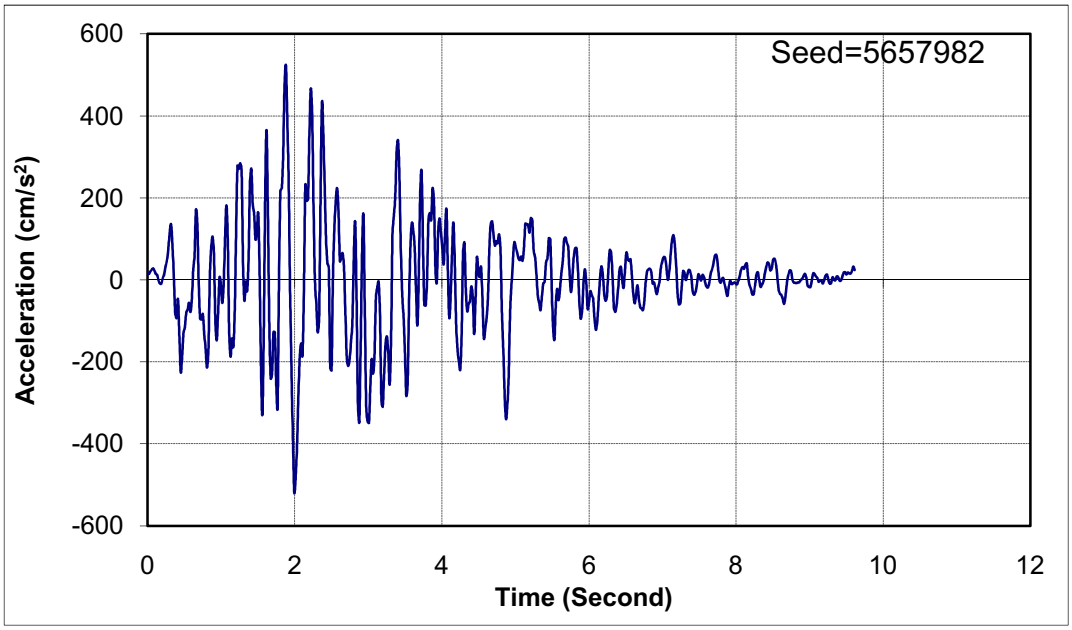


Figure G.5. Selected motion 3.

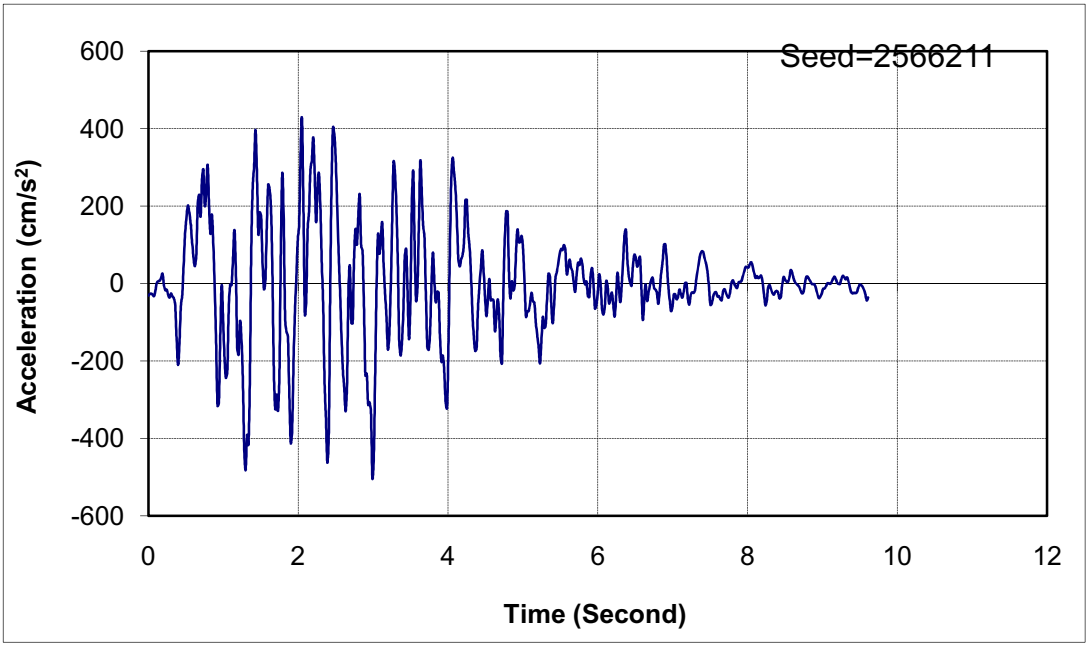


Figure G.6. Selected motion 4.

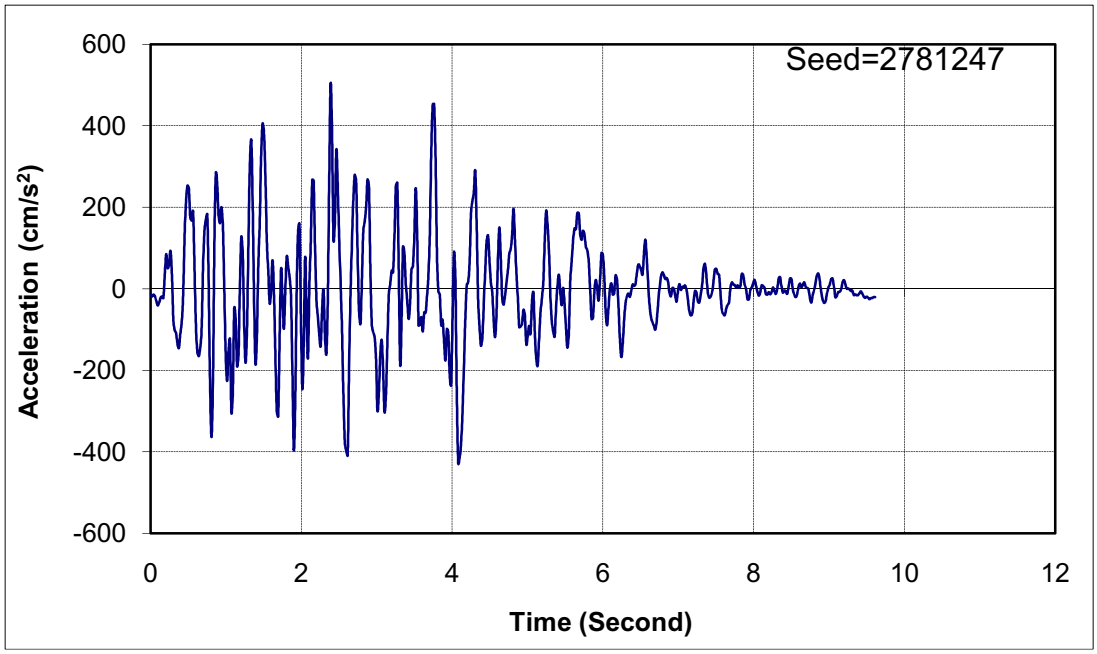


Figure G.7. Selected motion 5.

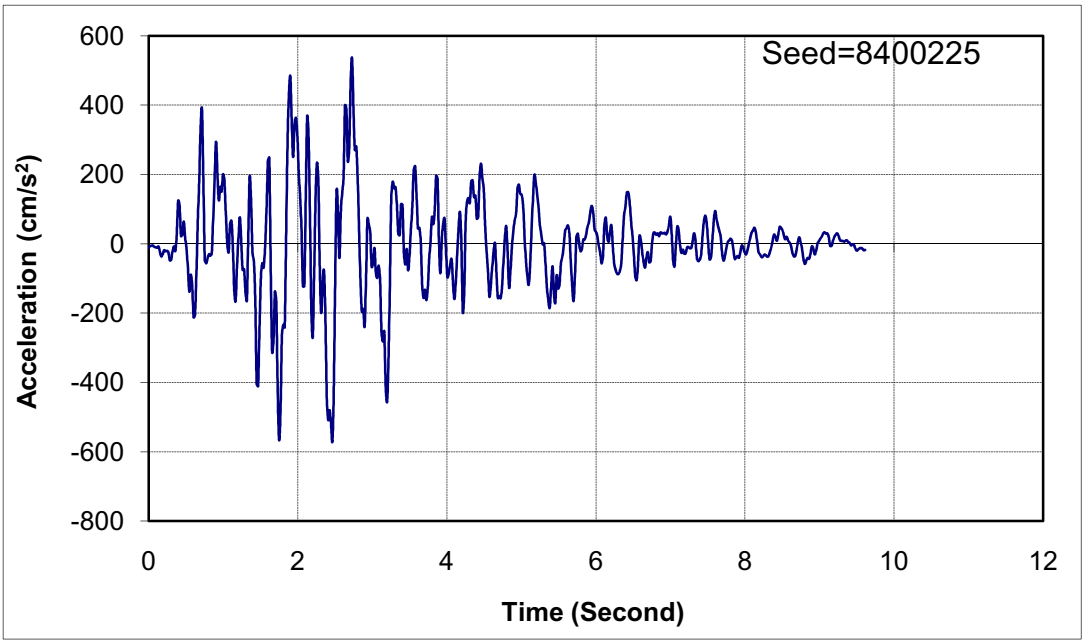


Figure G.8. Selected motion 6.

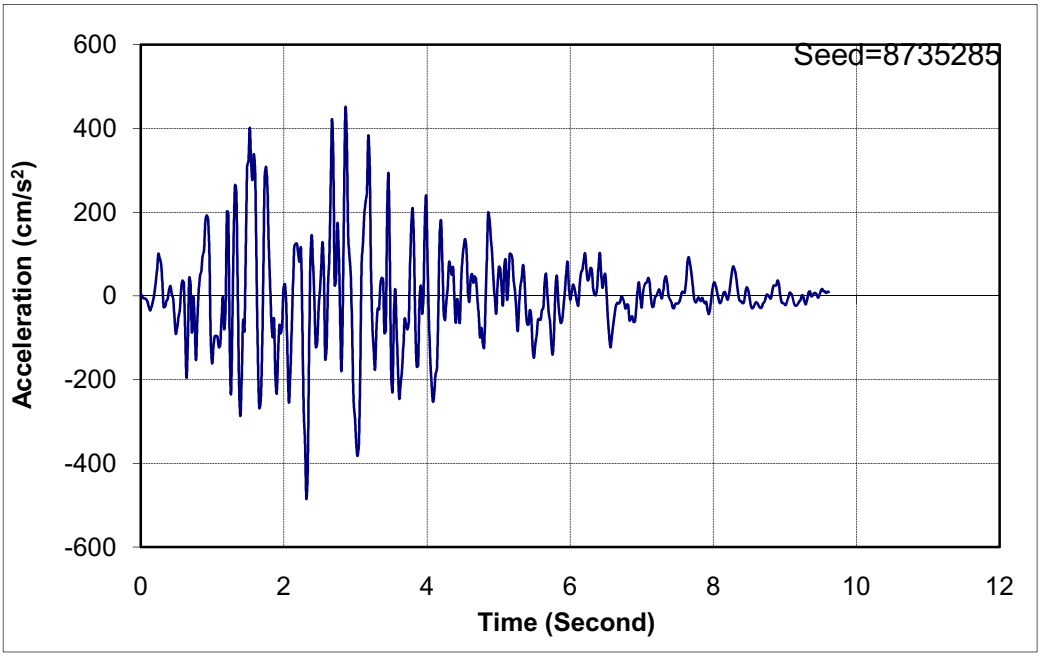


Figure G.9. Selected motion 7.

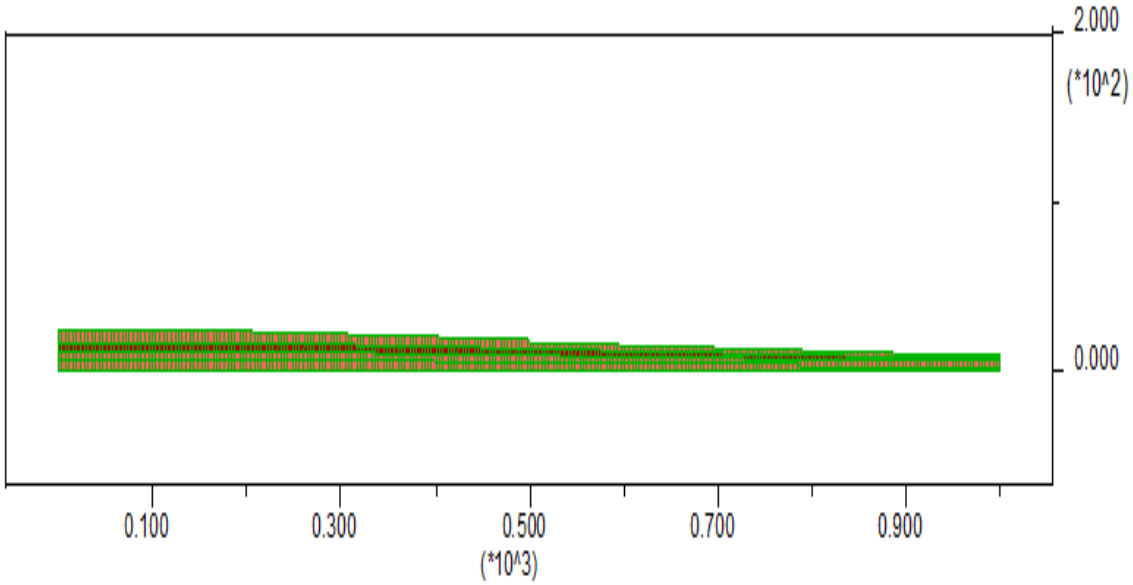


Figure G.10. Model design mesh (both Y axis & X axis in meters).

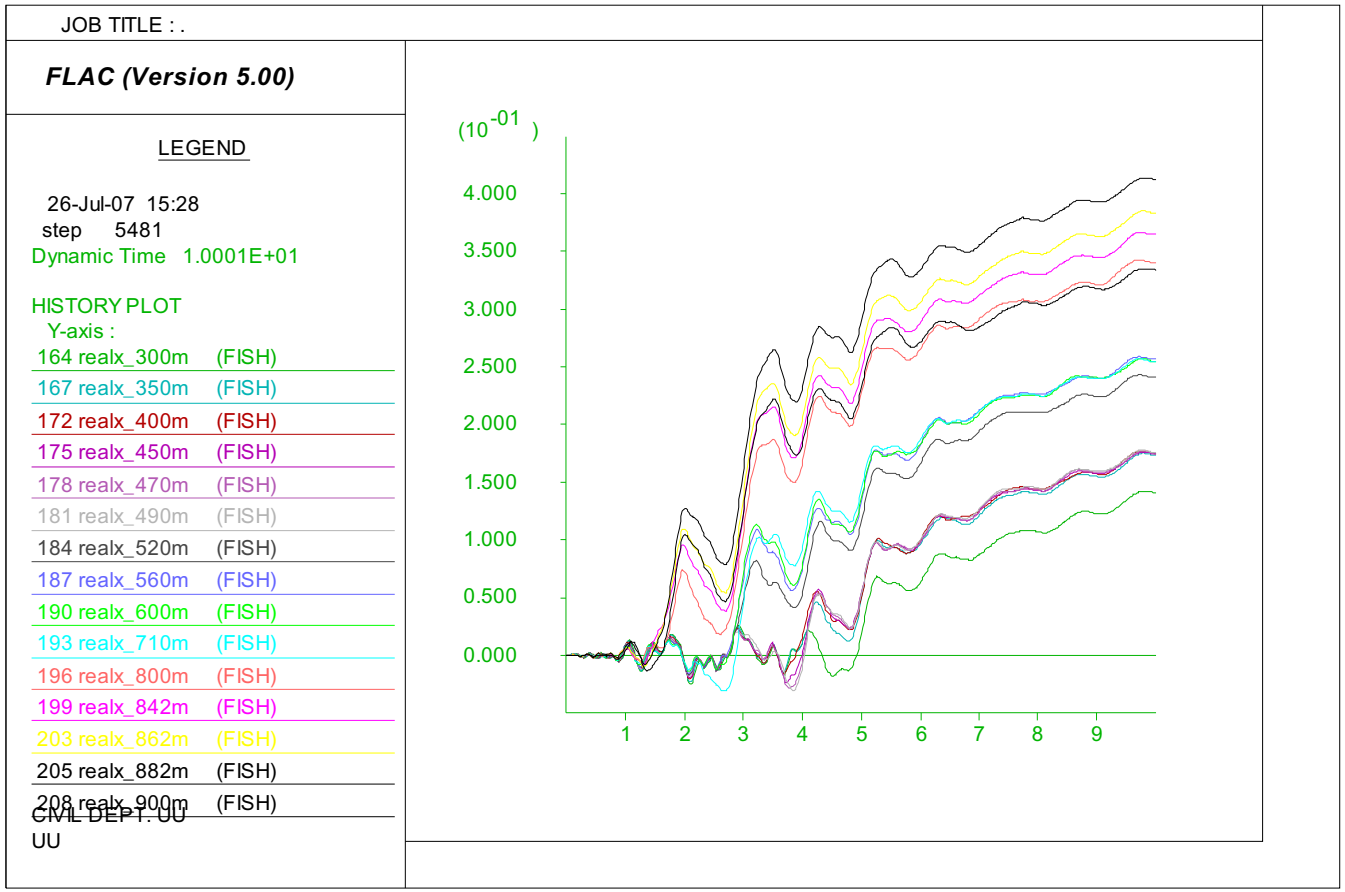


Figure G.11. Model later spreading prediction loaded by motion 1 with residual strength ratio of 0.14 (Y axis in meter and X axis in seconds).

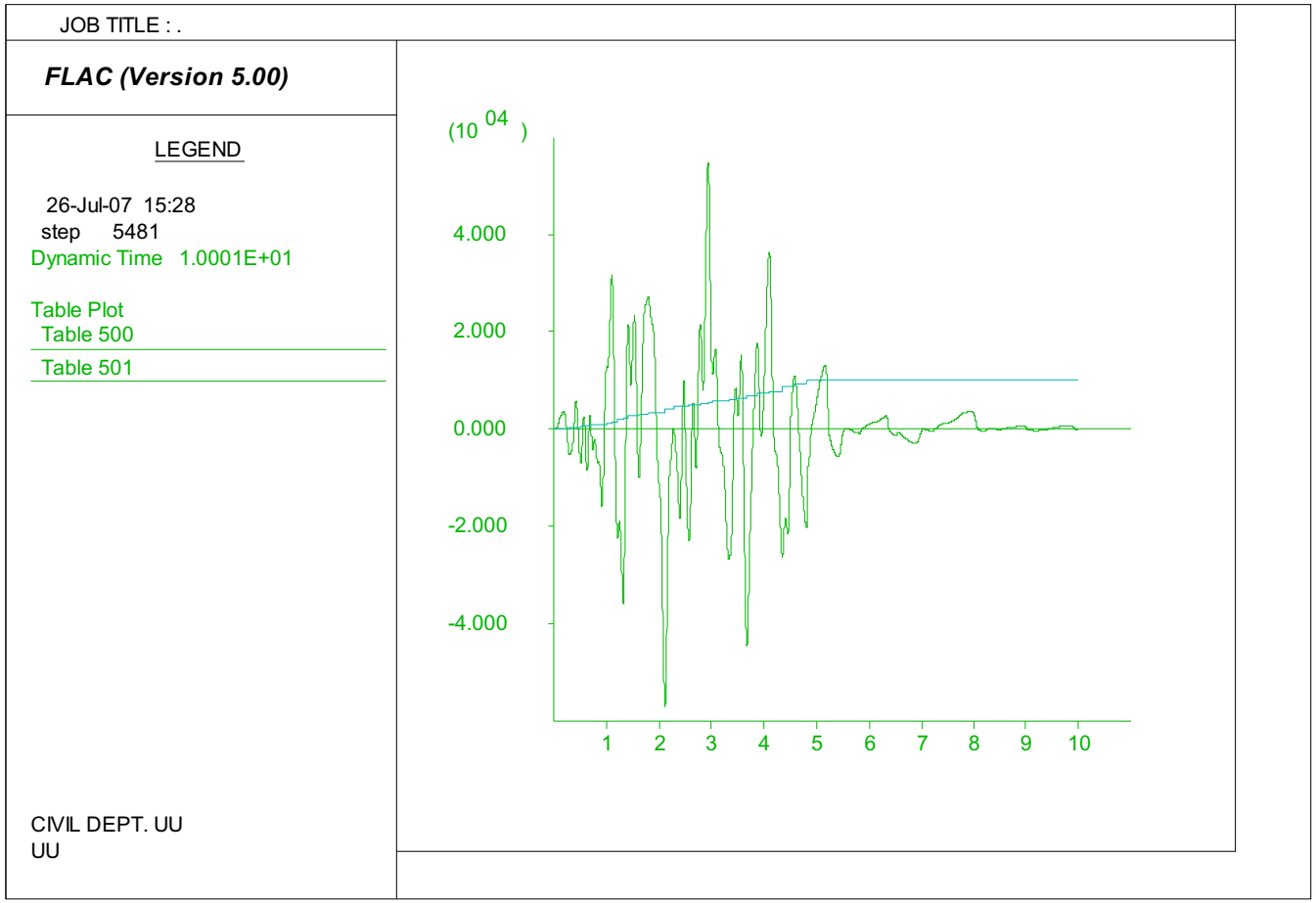


Figure G.12. Model pore water generation history loaded by motion 1 with residual strength ratio of 0.014: Shear stress (Y axis in Pa) and r_u (Y axis multiplied by 1000) vs. time (X axis in seconds).

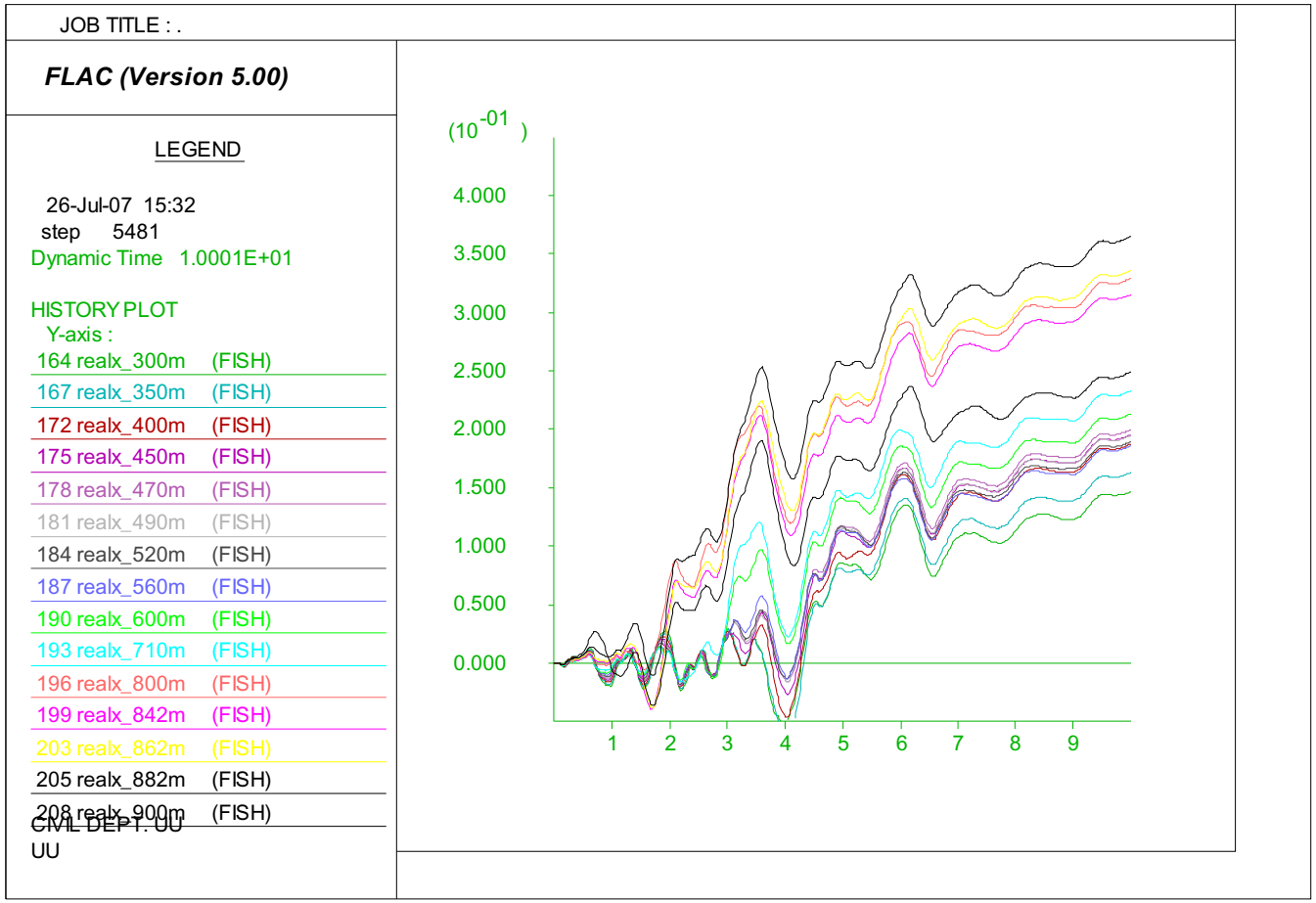


Figure G.13. Model later spreading prediction loaded by motion 2 with residual strength ratio of 0.14 (Y axis in meter and X axis in seconds).

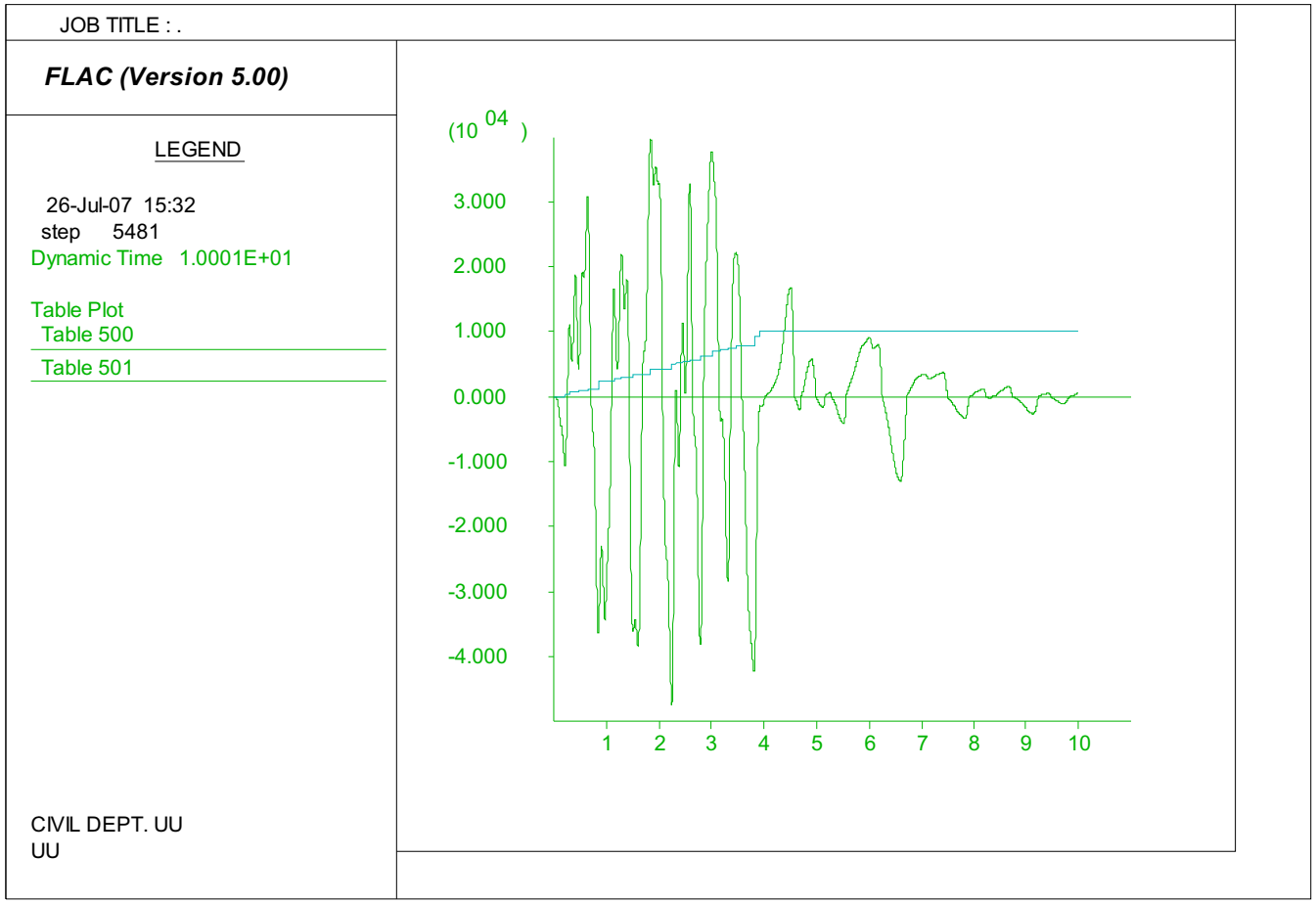


Figure G.14. Model pore water generation history loaded by motion 2 with residual strength ratio of 0.14: Shear stress (Y axis in Pa) and r_u (Y axis multiplied by 1000) vs. time (X axis in seconds).

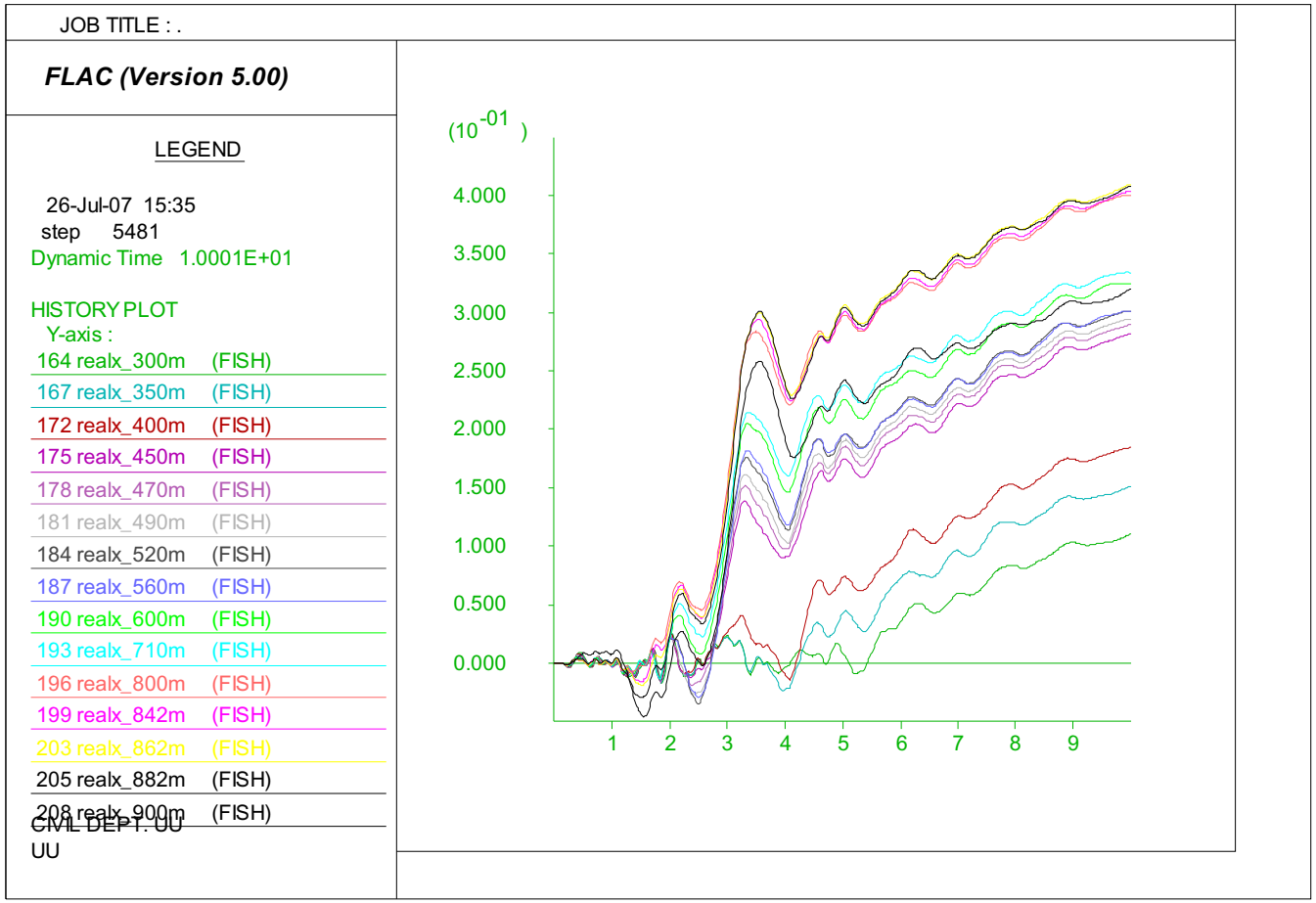


Figure G.15. Model later spreading prediction loaded by motion 3 with residual strength ratio of 0.14 (Y axis in meter and X axis in seconds).

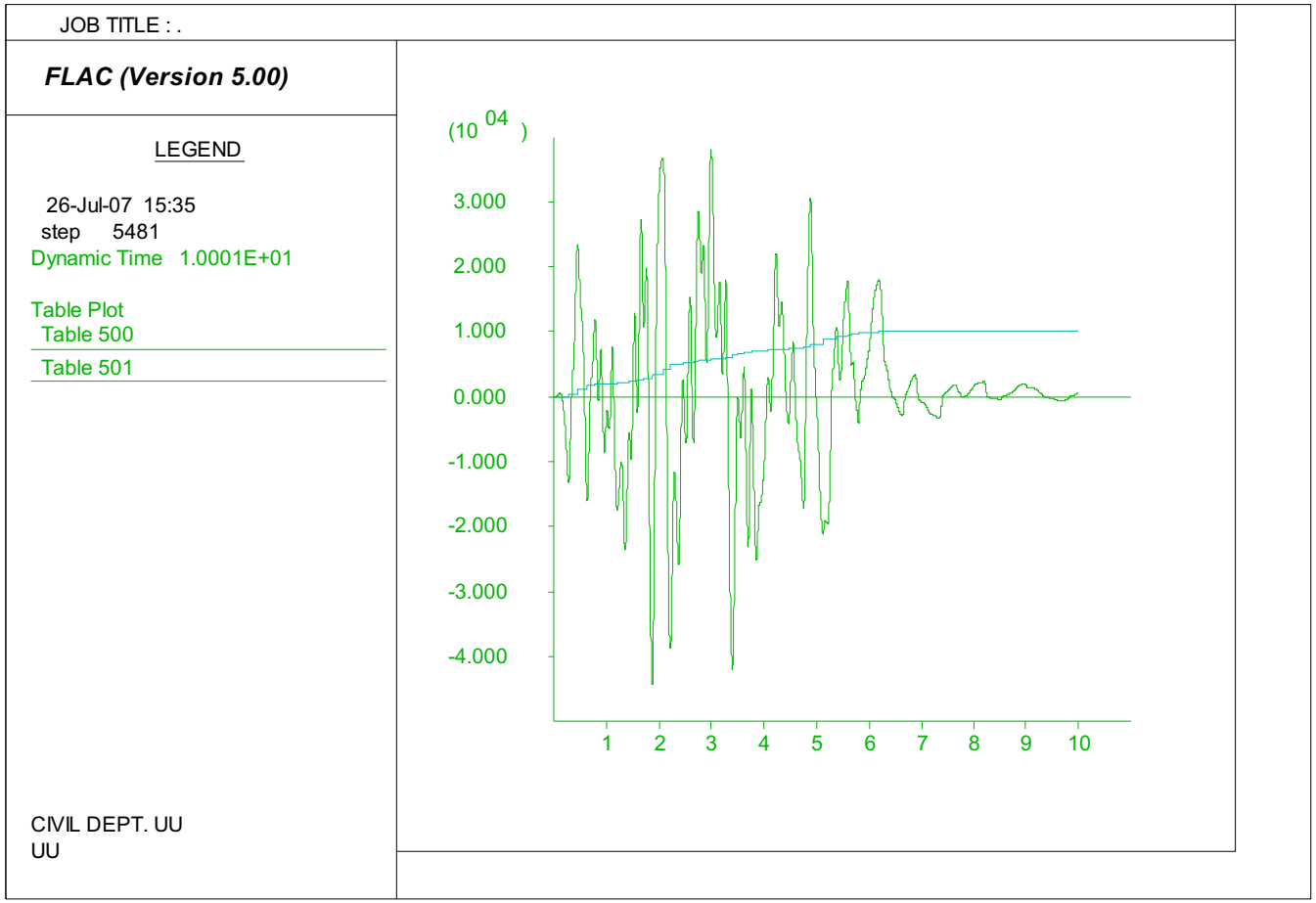


Figure G.16. Model pore water generation history loaded by motion 3 with residual strength ratio of 0.14: Shear stress (Y axis in Pa) and r_u (Y axis multiplied by 1000) vs. time (X axis in seconds).

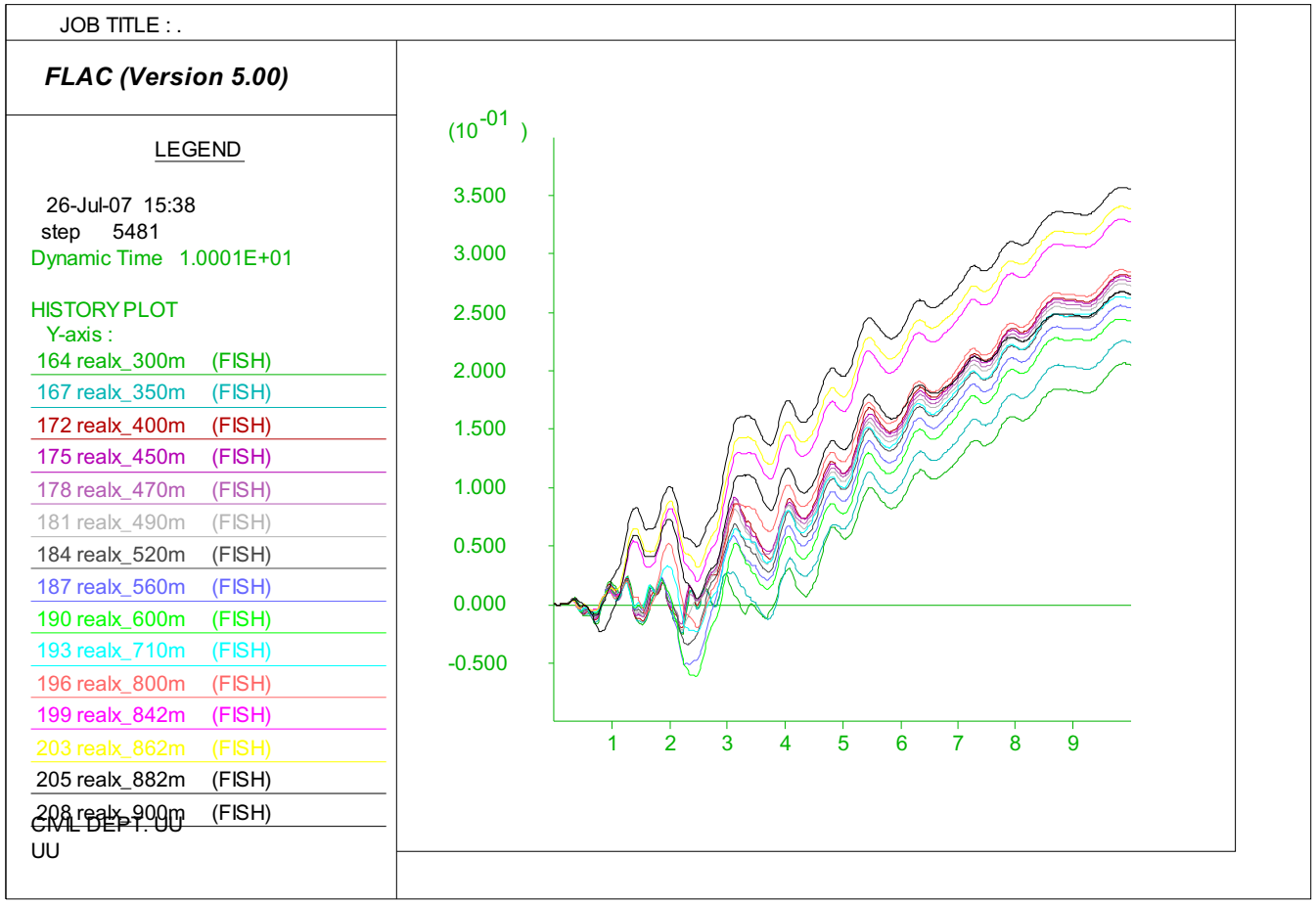


Figure G.17. Model later spreading prediction loaded by motion 4 with residual strength ratio of 0.14 (Y axis in meter and X axis in seconds).

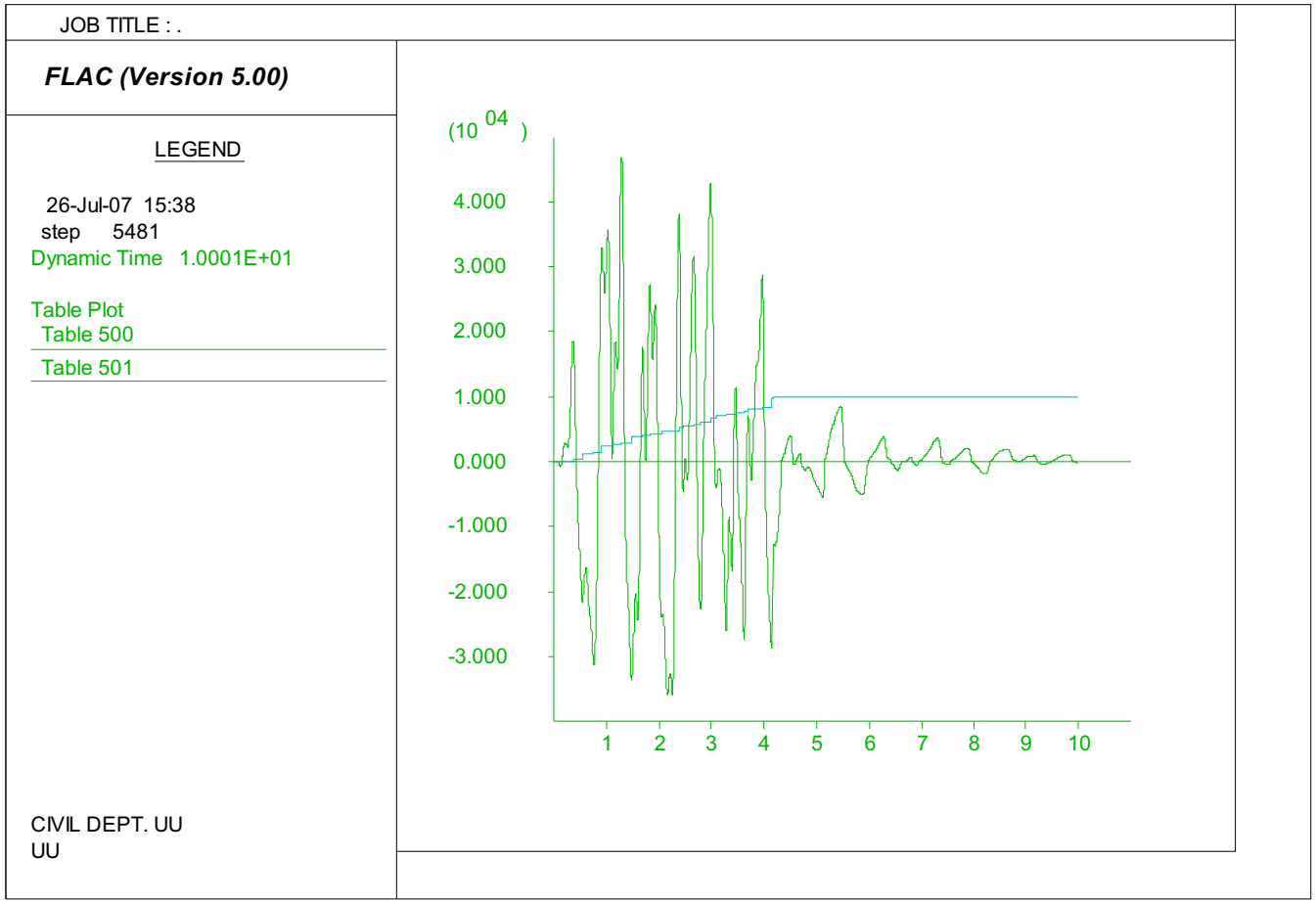


Figure G.18. Model pore water generation history loaded by motion 4 with residual strength ratio of 0.14: Shear stress (Y axis in Pa) and r_u (Y axis multiplied by 1000) vs. time (X axis in seconds).

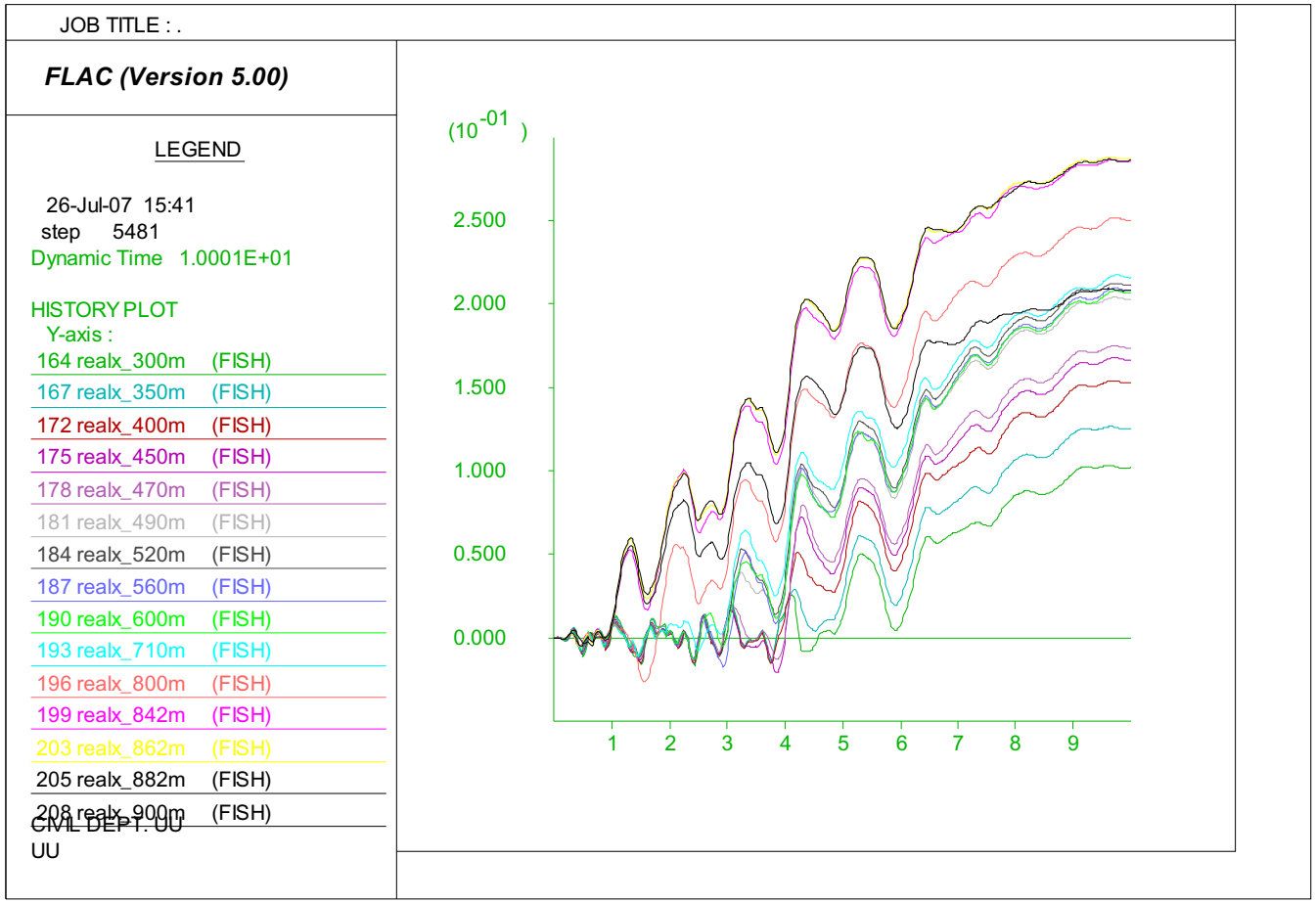


Figure G.19. Model later spreading prediction loaded by motion 5 with residual strength ratio of 0.14 (Y axis in meter and X axis in seconds).

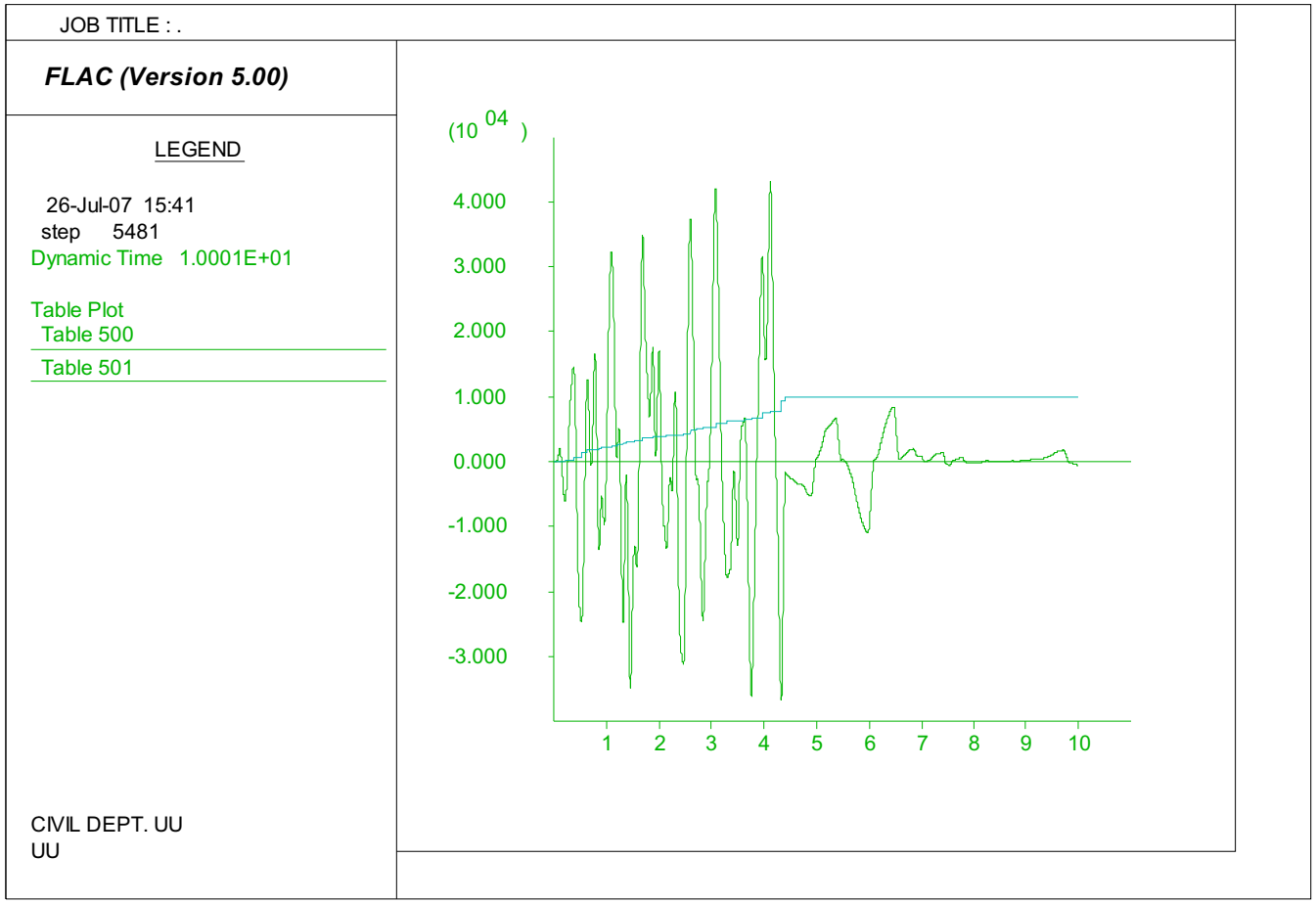


Figure G.20. Model pore water generation history loaded by motion 5 with residual strength ratio of 0.14: Shear stress (Y axis in Pa) and r_u (Y axis multiplied by 1000) vs. time (X axis in seconds).

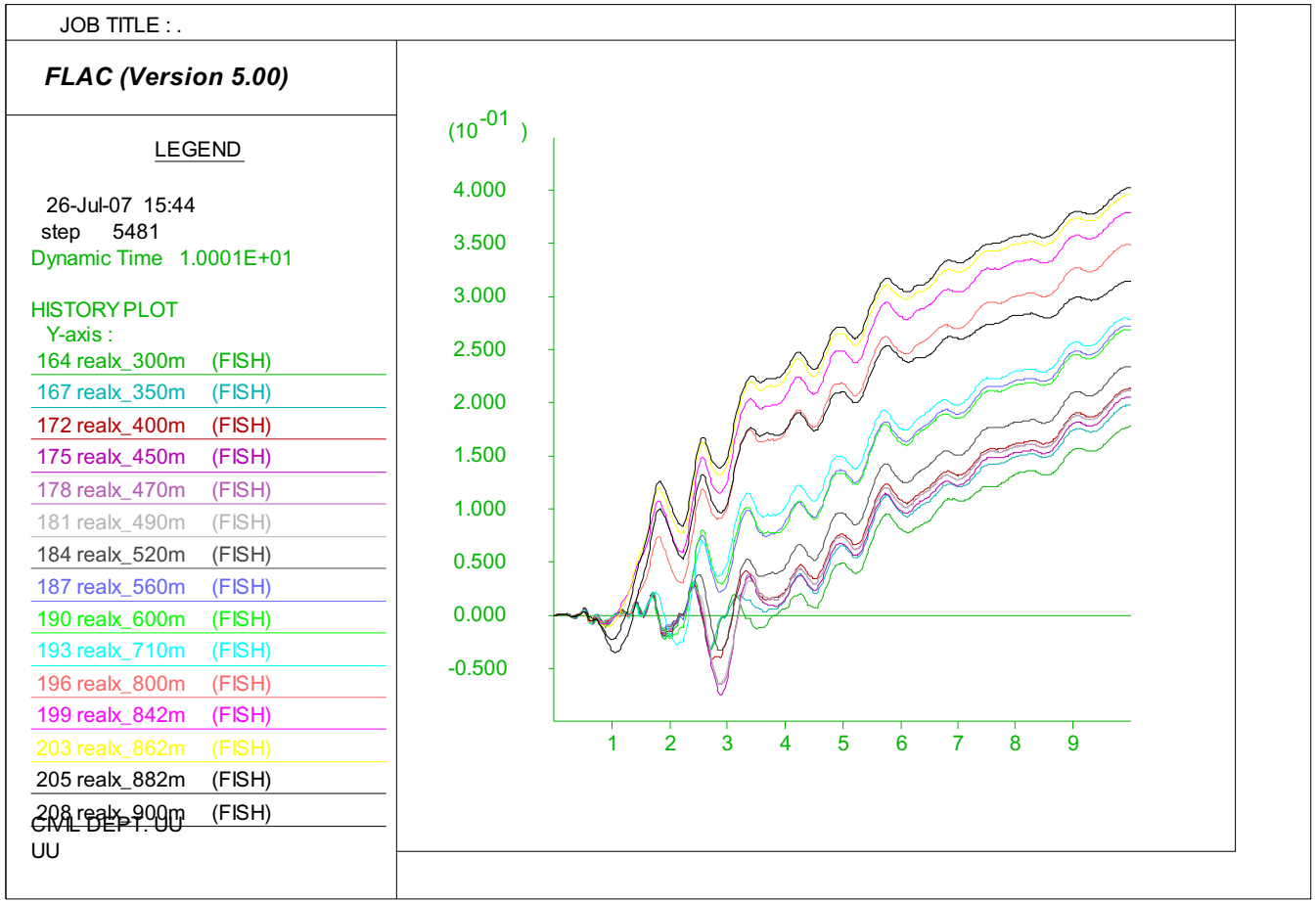


Figure G.21. Model later spreading prediction loaded by motion 6 with residual strength ratio of 0.14 (Y axis in meter and X axis in seconds).

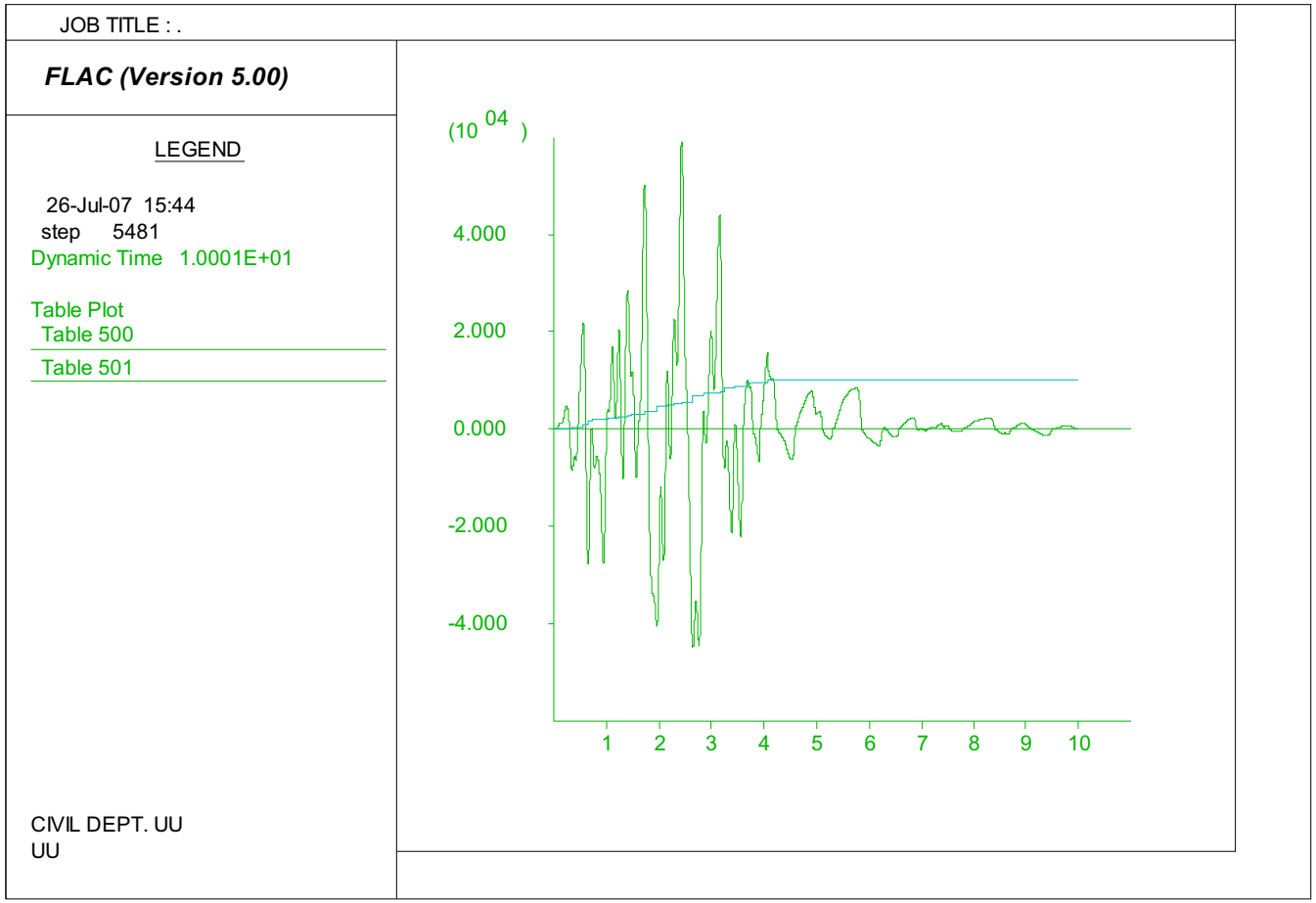


Figure G.22. Model pore water generation history loaded by motion 6 with residual strength ratio of 0.15: Shear stress (Y axis in Pa) and r_u (Y axis multiplied by 1000) vs. time (X axis in seconds).

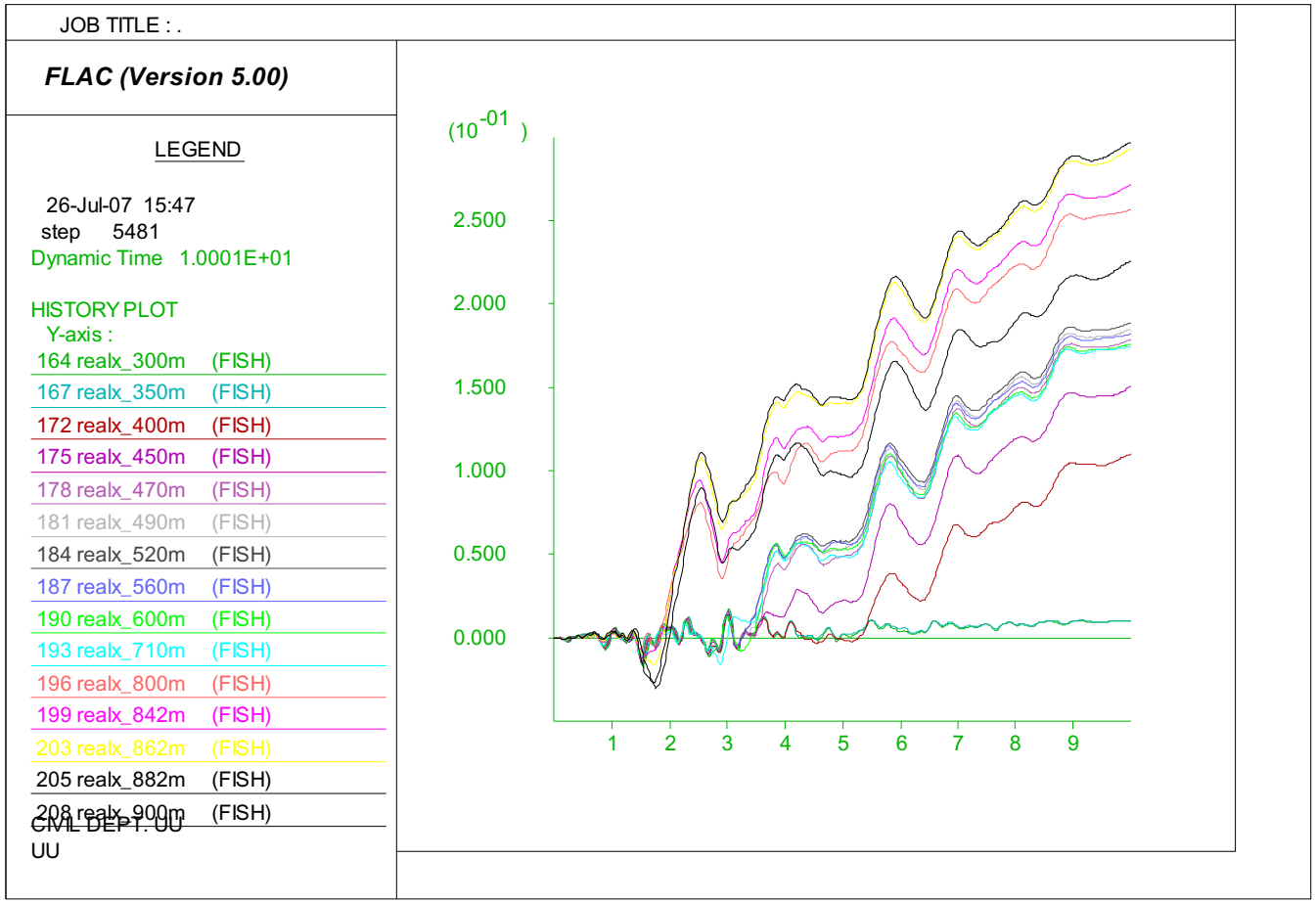


Figure G.23. Model later spreading prediction loaded by motion 7 with residual strength ratio of 0.14 (Y axis in meter and X axis in seconds).

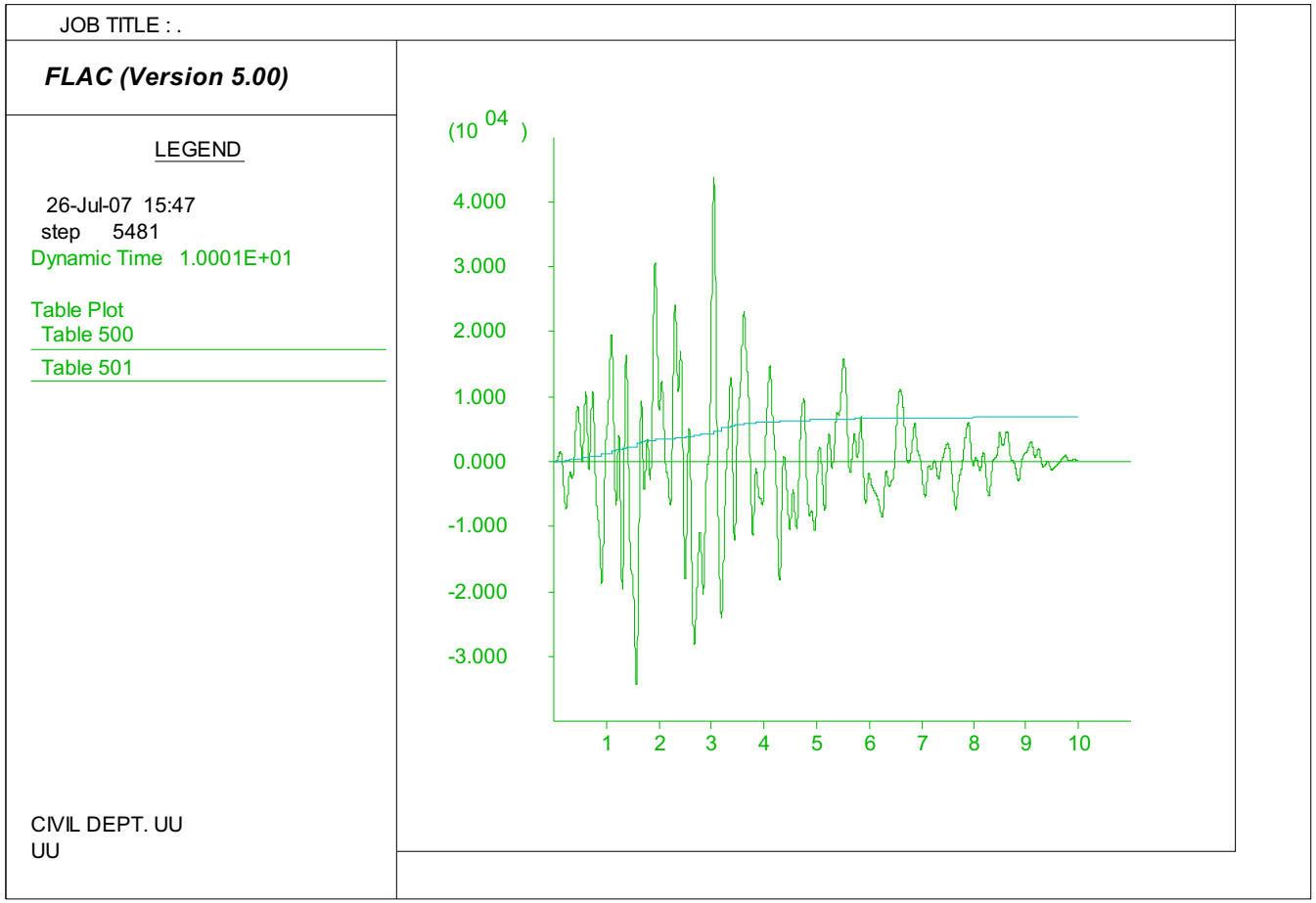


Figure G.24. Model pore water generation history loaded by motion 7 with residual strength ratio of 0.14: Shear stress (Y axis in Pa) and r_u (Y axis multiplied by 1000) vs. time (X axis in seconds).

APPENDIX H

SAN FERNANDO SITE JENSEN FILTRATION PLANT

SECTION DATA

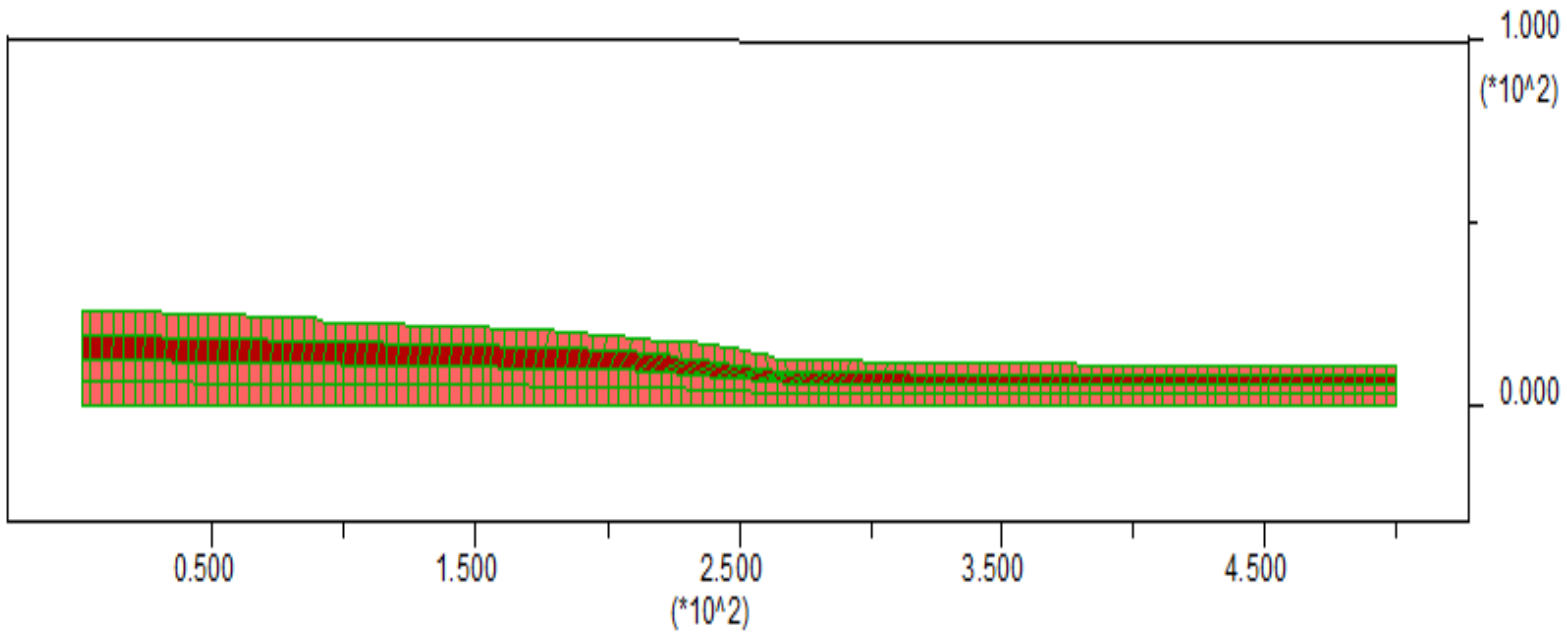


Figure H.1. Model soil properties change after liquefaction loaded by motion 1 with residual strength ratio of 0.06 (both Y axis & X axis in meters).

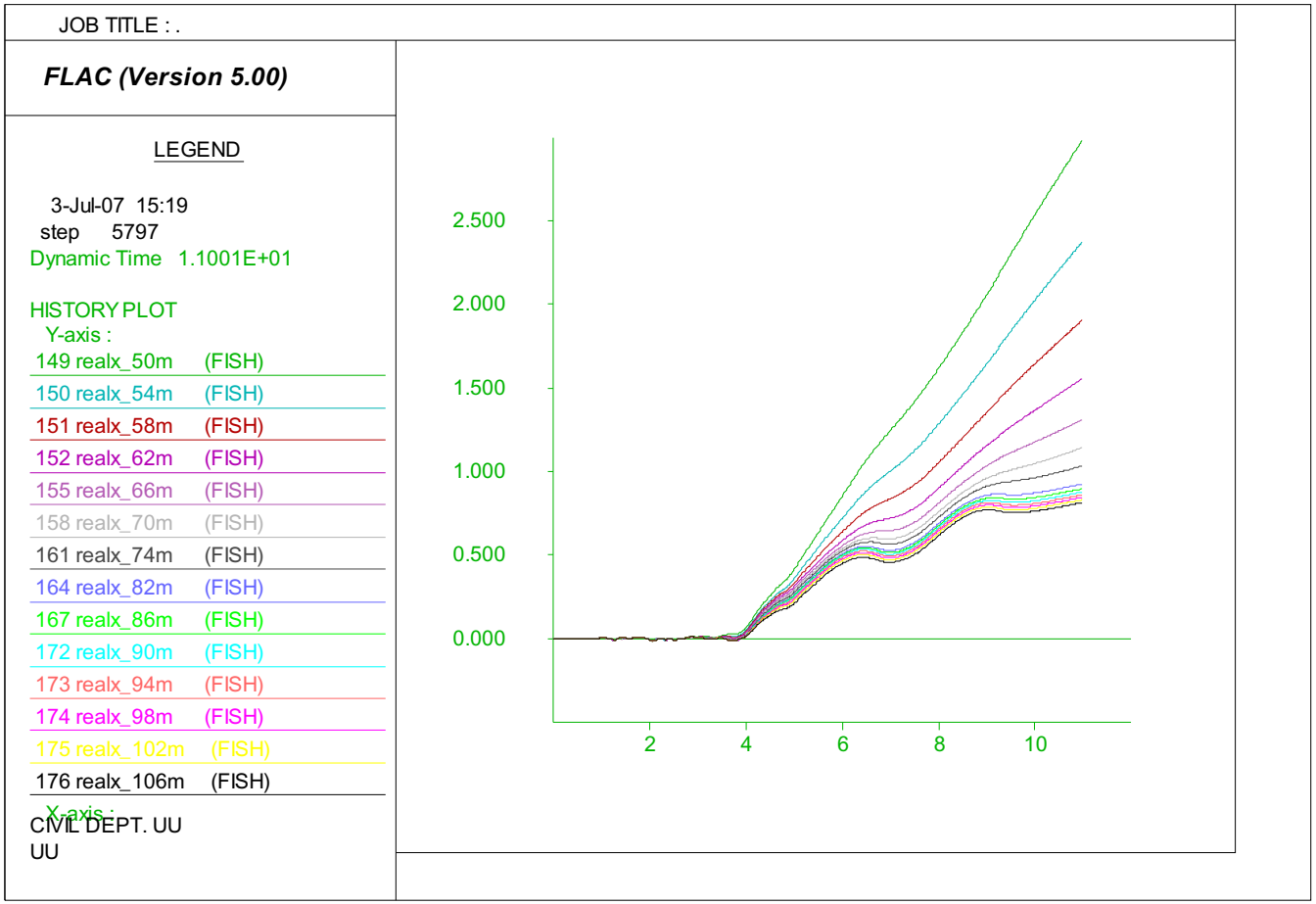


Figure H.2. Model later spreading prediction loaded by motion 1 with residual strength ratio of 0.06 (Y axis in meter and X axis in seconds).

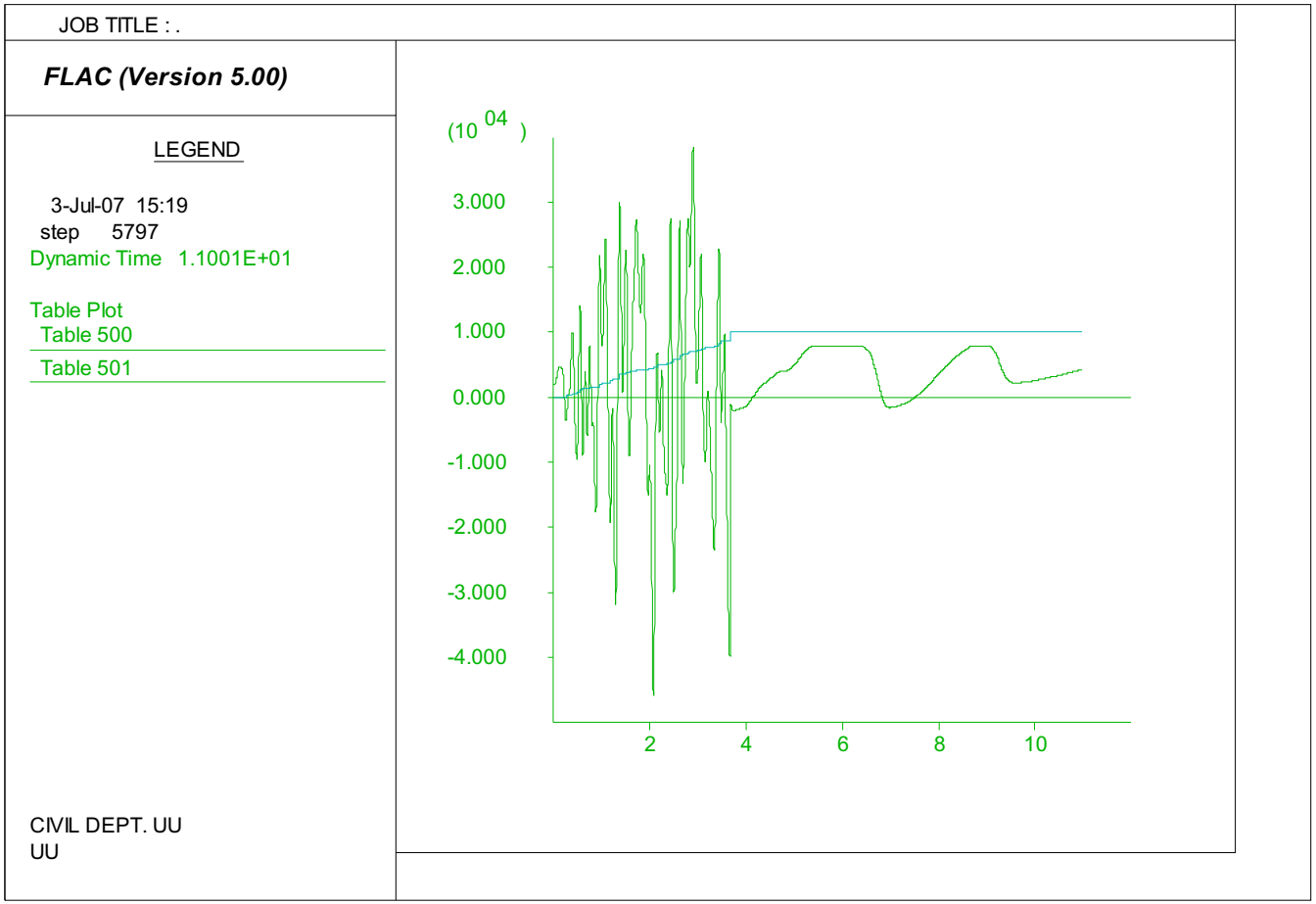


Figure H.3. Model pore water generation history loaded by motion 1 with residual strength ratio of 0.06: Shear stress (Y axis in Pa) and r_u (Y axis multiplied by 1000) vs. time (X axis in seconds).

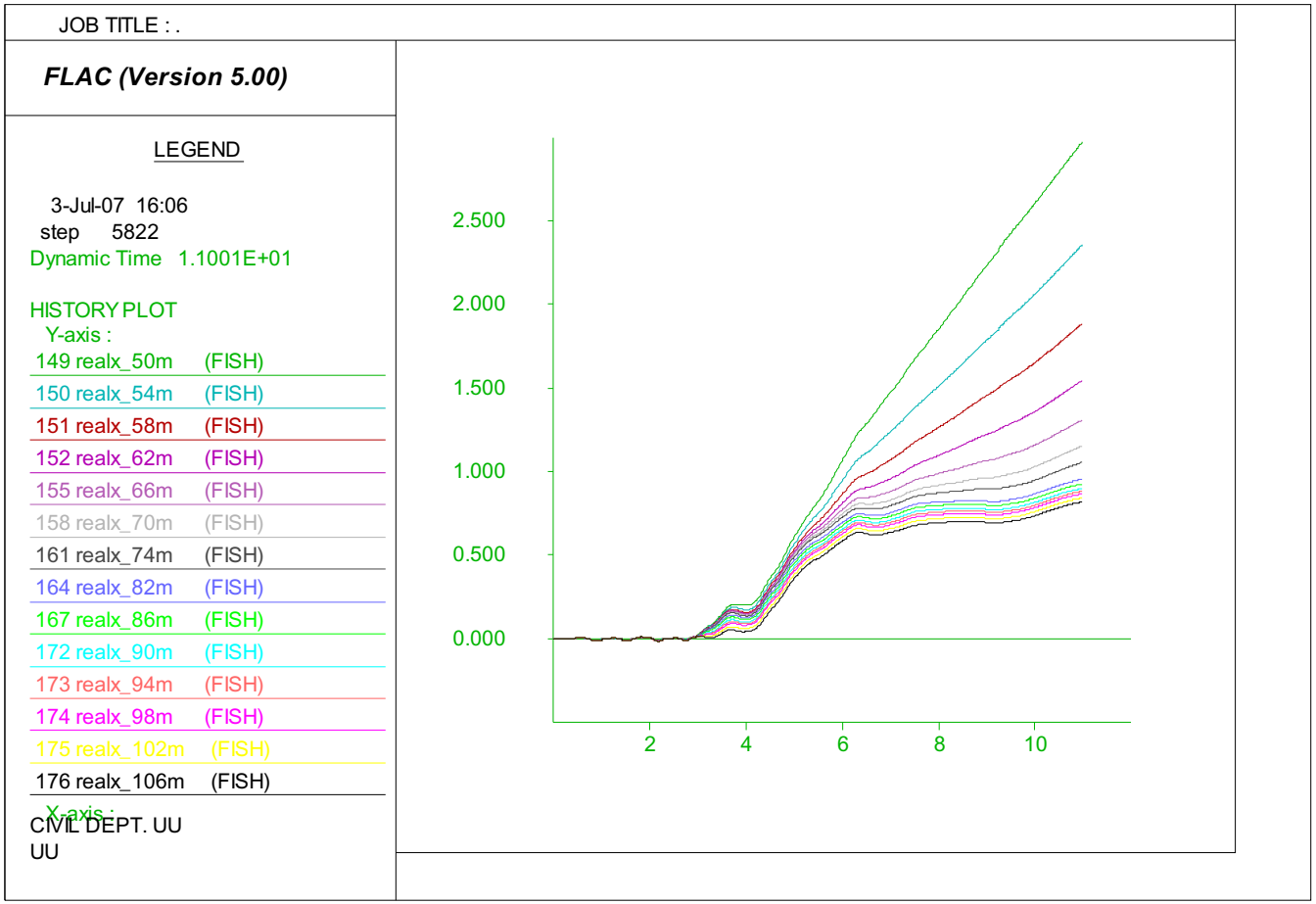


Figure H.4. Model later spreading prediction loaded by motion 2 with residual strength ratio of 0.06 (Y axis in meter and X axis in seconds).

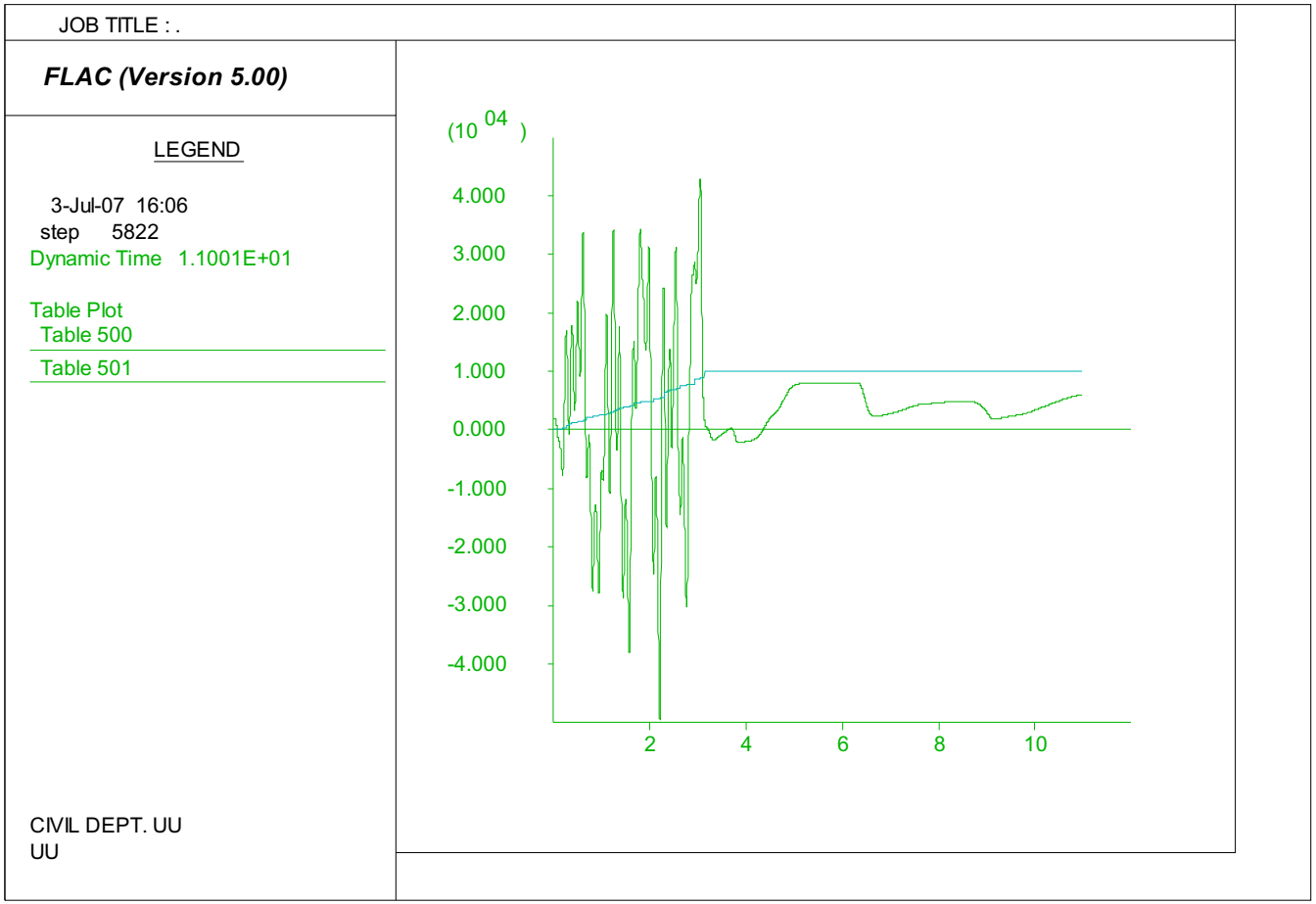


Figure H.5. Model pore water generation history loaded by motion 2 with residual strength ratio of 0.06: Shear stress (Y axis in Pa) and r_u (Y axis multiplied by 1000) vs. time (X axis in seconds).

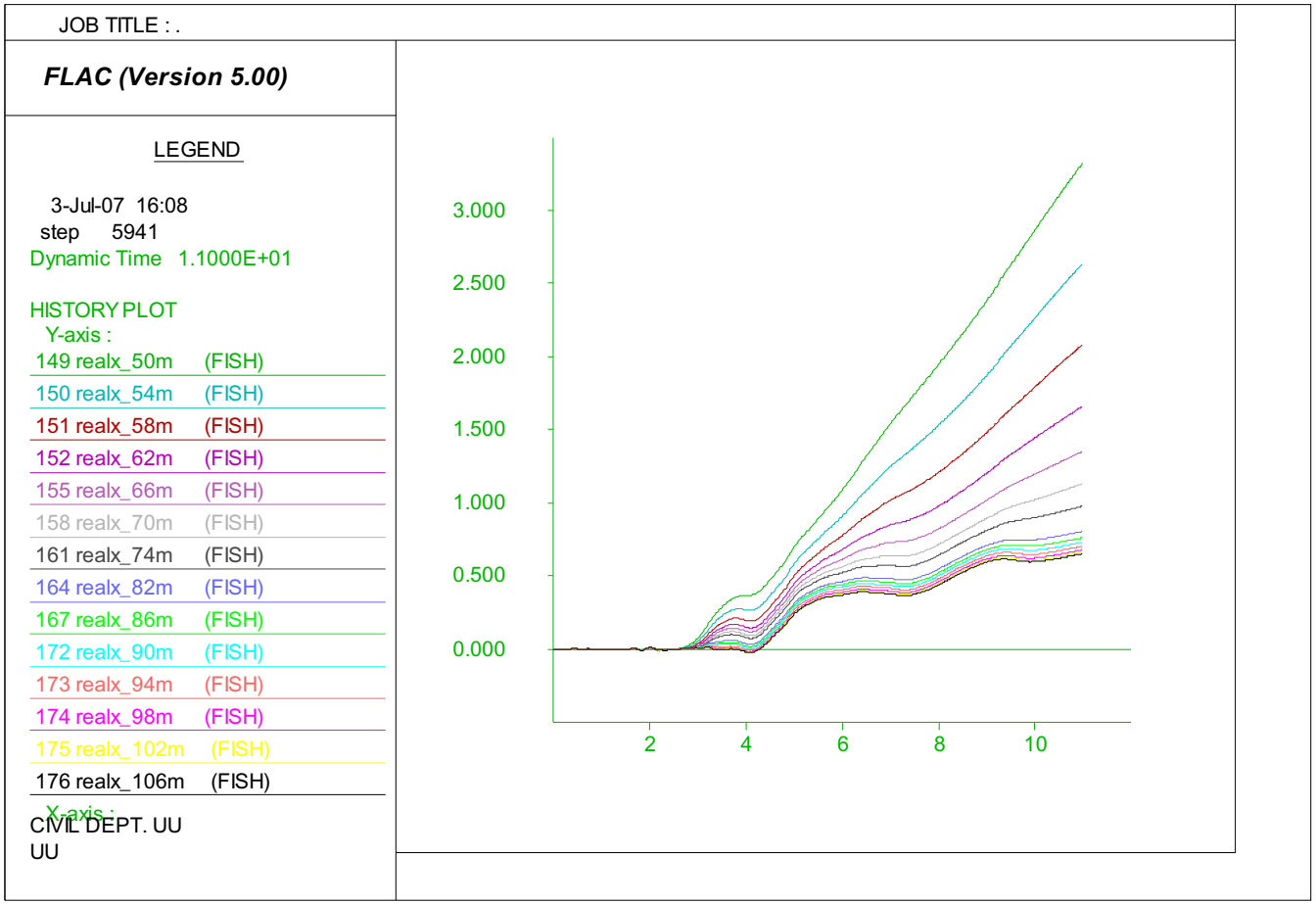


Figure H.6. Model later spreading prediction loaded by motion 3 with residual strength ratio of 0.06 (Y axis in meter and X axis in seconds).

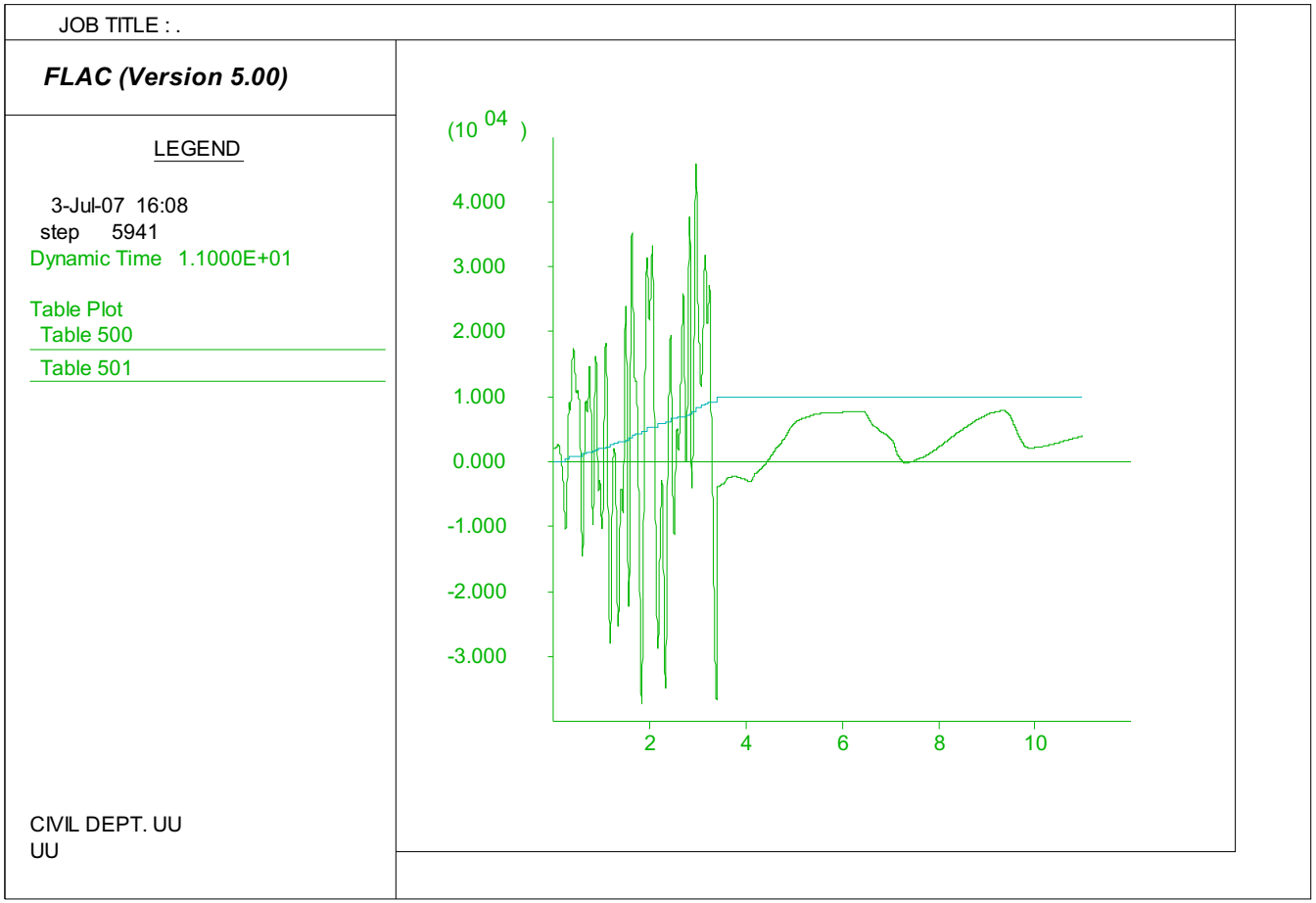


Figure H.7. Model pore water generation history loaded by motion 3 with residual strength ratio of 0.06: Shear stress (Y axis in Pa) and r_u (Y axis multiplied by 1000)

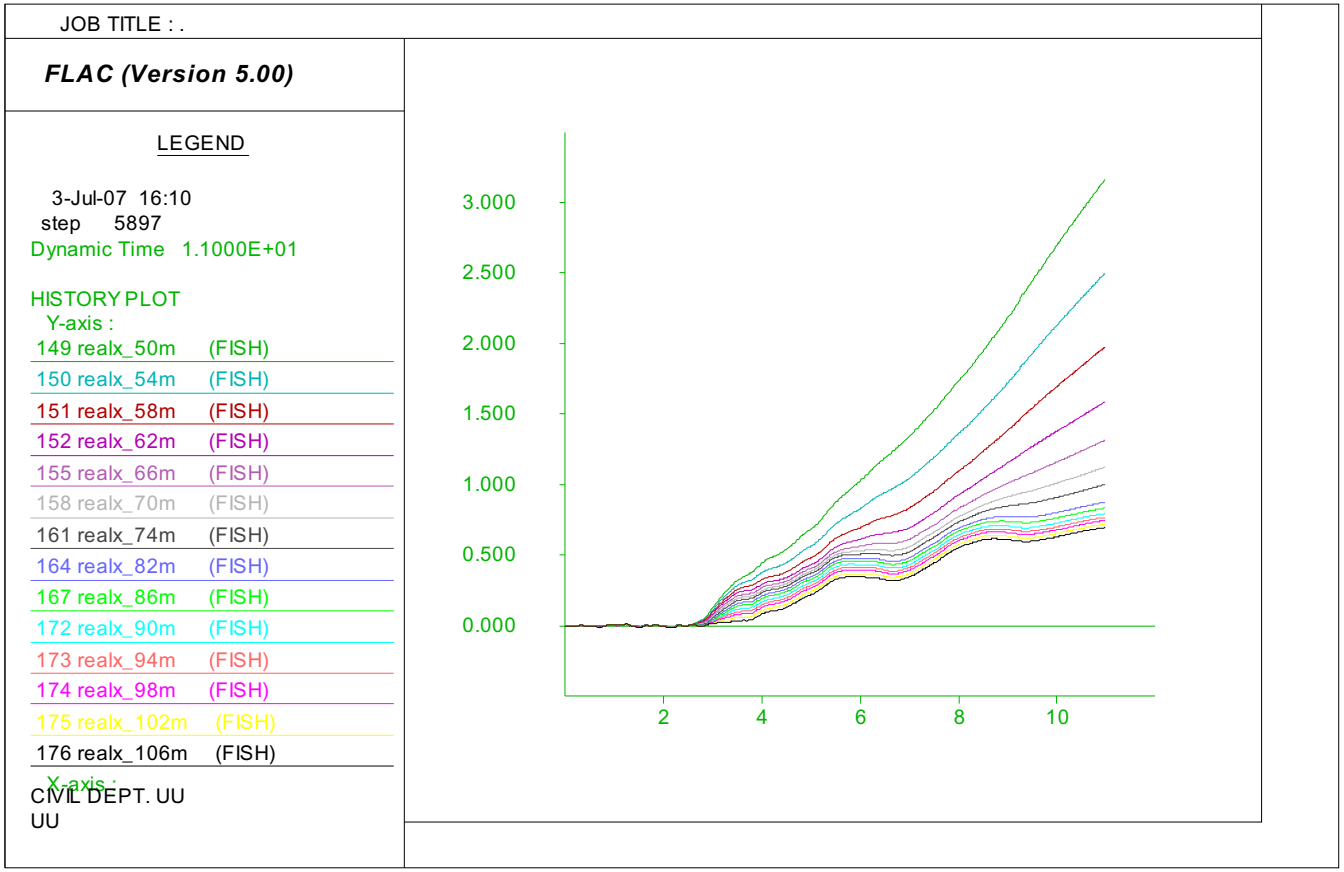


Figure H.8. Model later spreading prediction loaded by motion 4 with residual strength ratio of 0.06 (Y axis in meter and X axis in seconds).

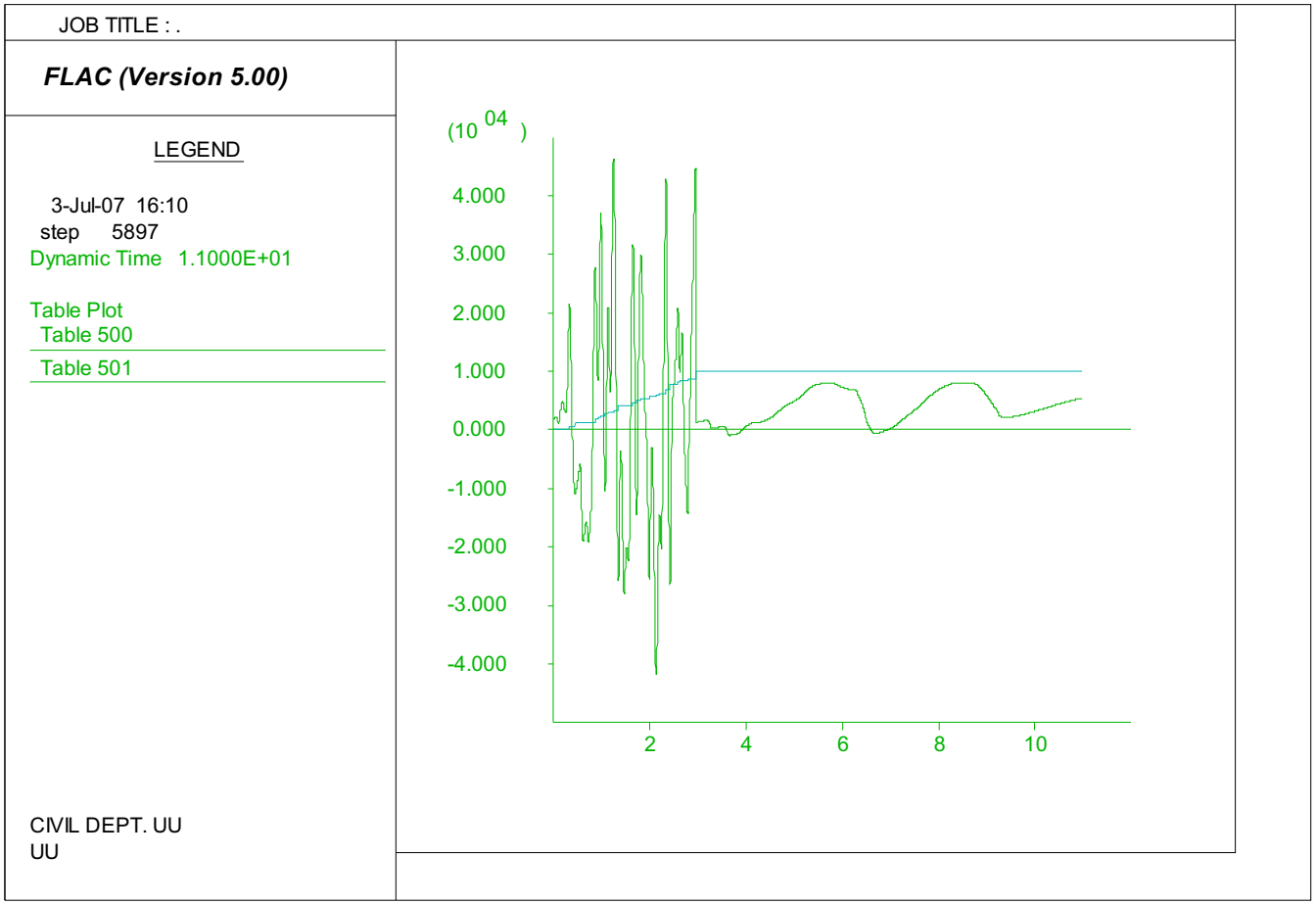


Figure H.9. Pore water generation history loaded by motion 4 with residual strength ratio of 0.06: Shear stress (Y axis in Pa) and r_u (Y axis multiplied by 1000) vs. time (X axis in seconds).

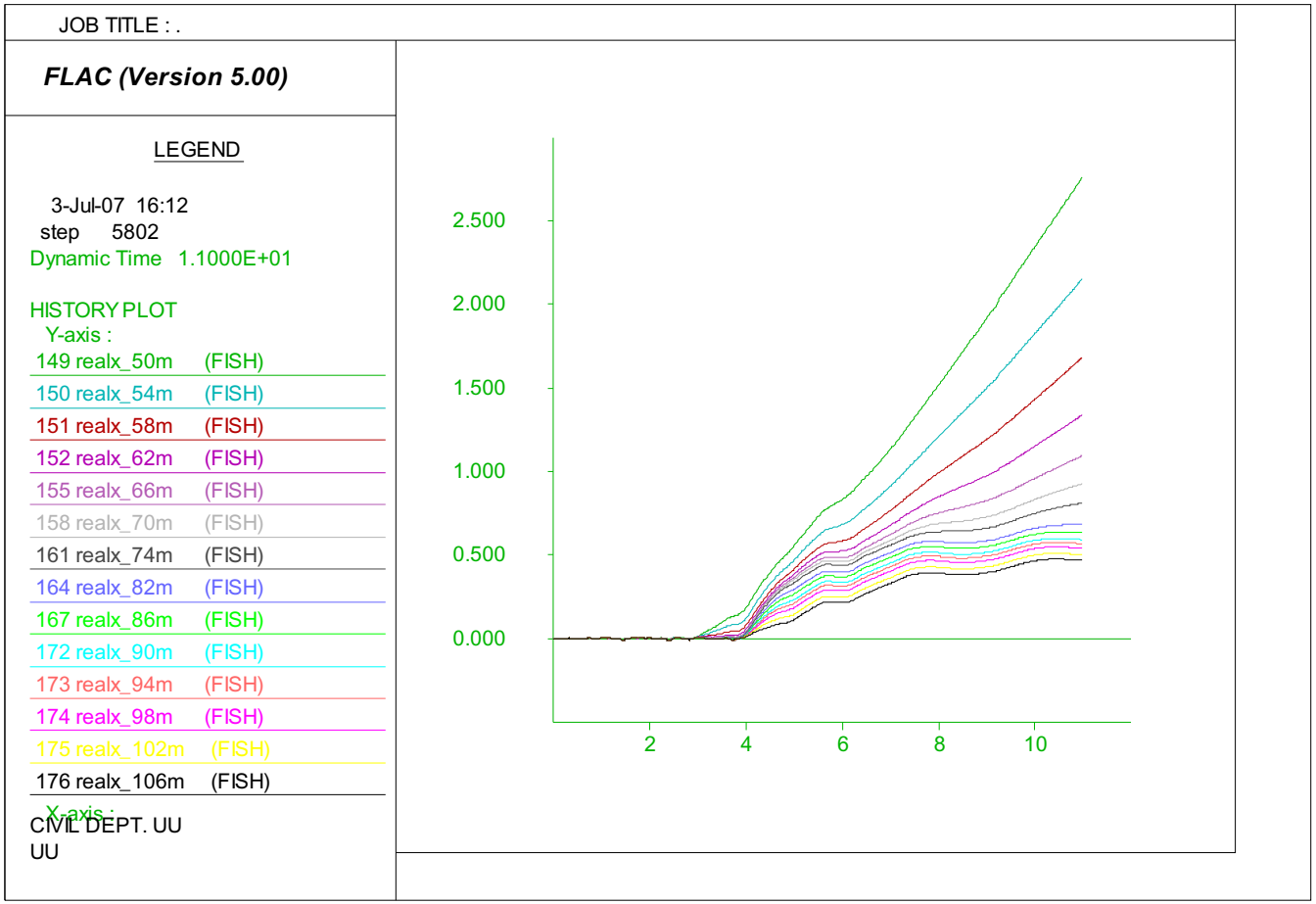


Figure H.10. Model later spreading prediction loaded by motion 5 with residual strength ratio of 0.06 (Y axis in meter and X axis in seconds).

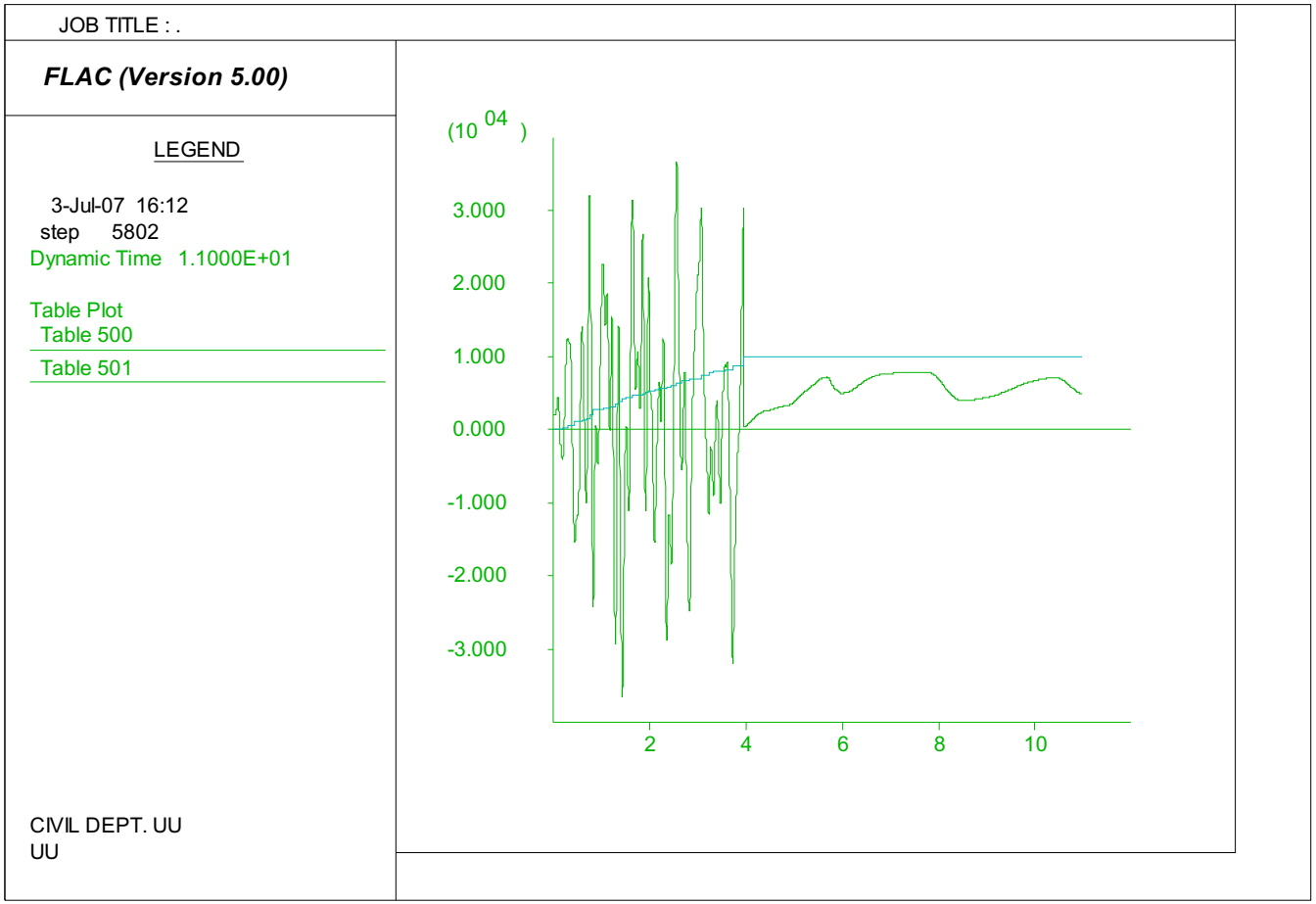


Figure H.11. Model pore water generation history loaded by motion 5 with residual strength ratio of 0.06: Shear stress (Y axis in Pa) and r_u (Y axis multiplied by 1000) vs. time (X axis in seconds).

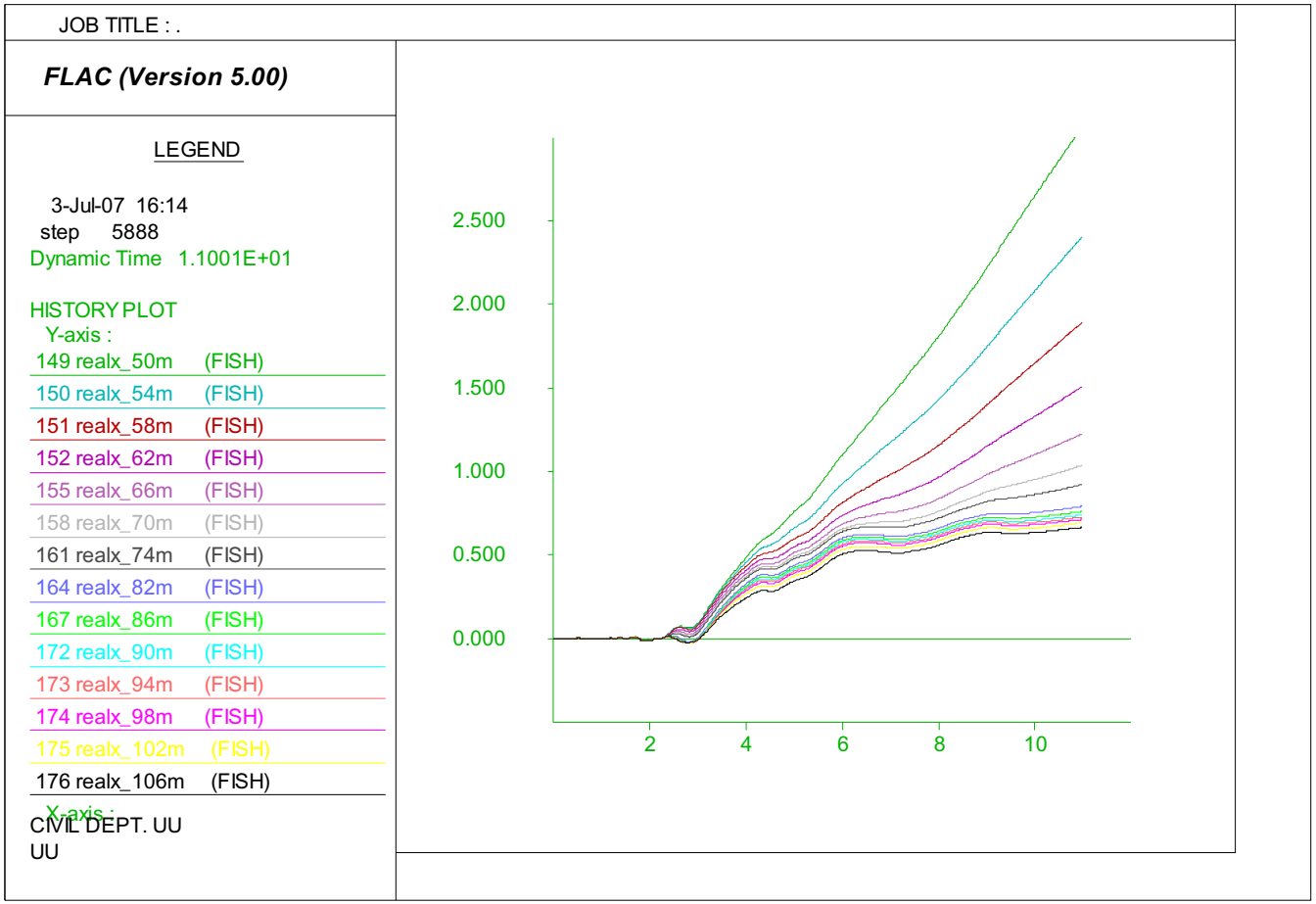


Figure H.12. Model later spreading prediction loaded by motion 6 with residual strength ratio of 0.06 (Y axis in meter and X axis in seconds).

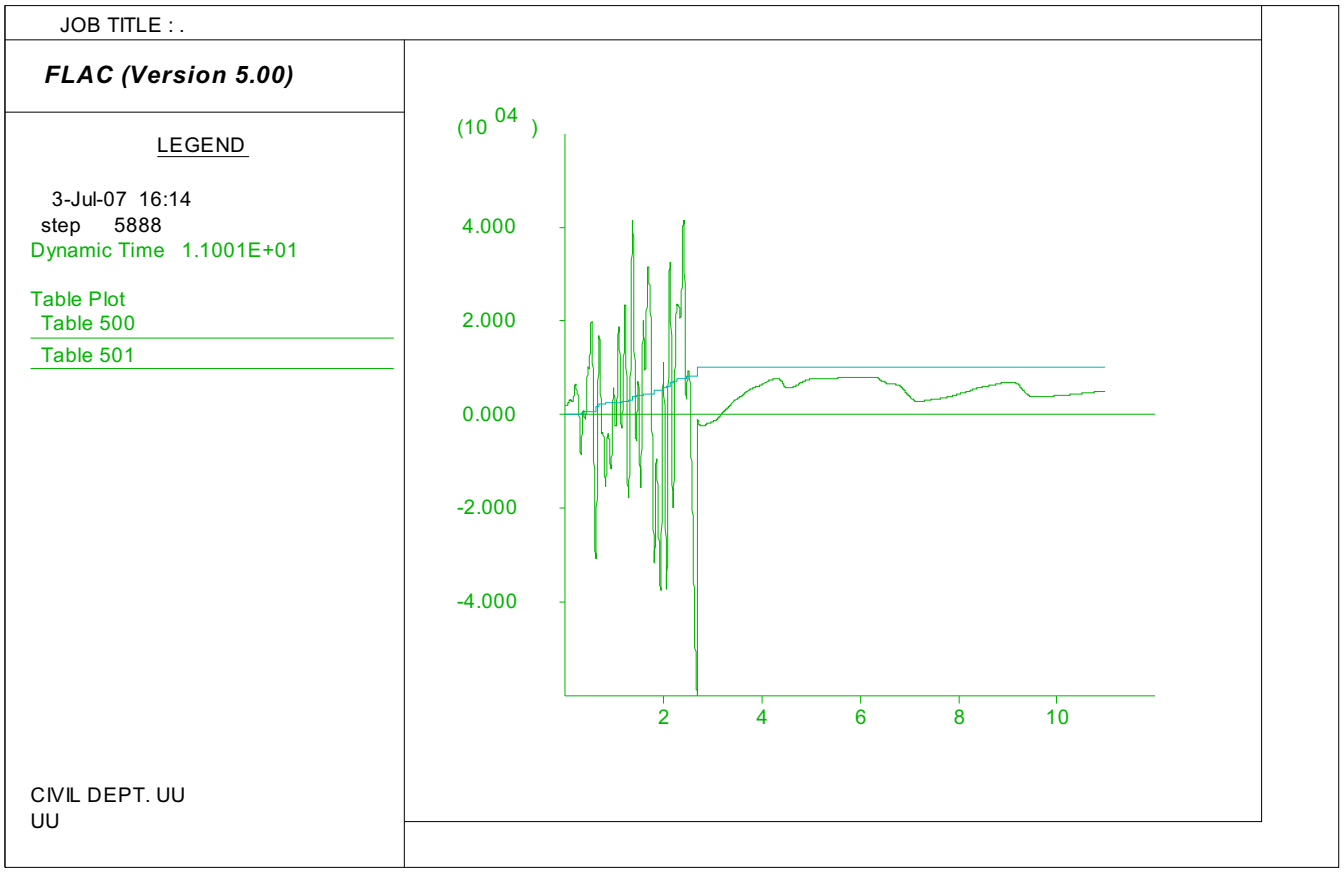


Figure H.13. Model pore water generation history loaded by motion 6 with residual strength ratio of 0.06: Shear stress (Y axis in Pa) and r_u (Y axis multiplied by 1000) vs. time (X axis in seconds).

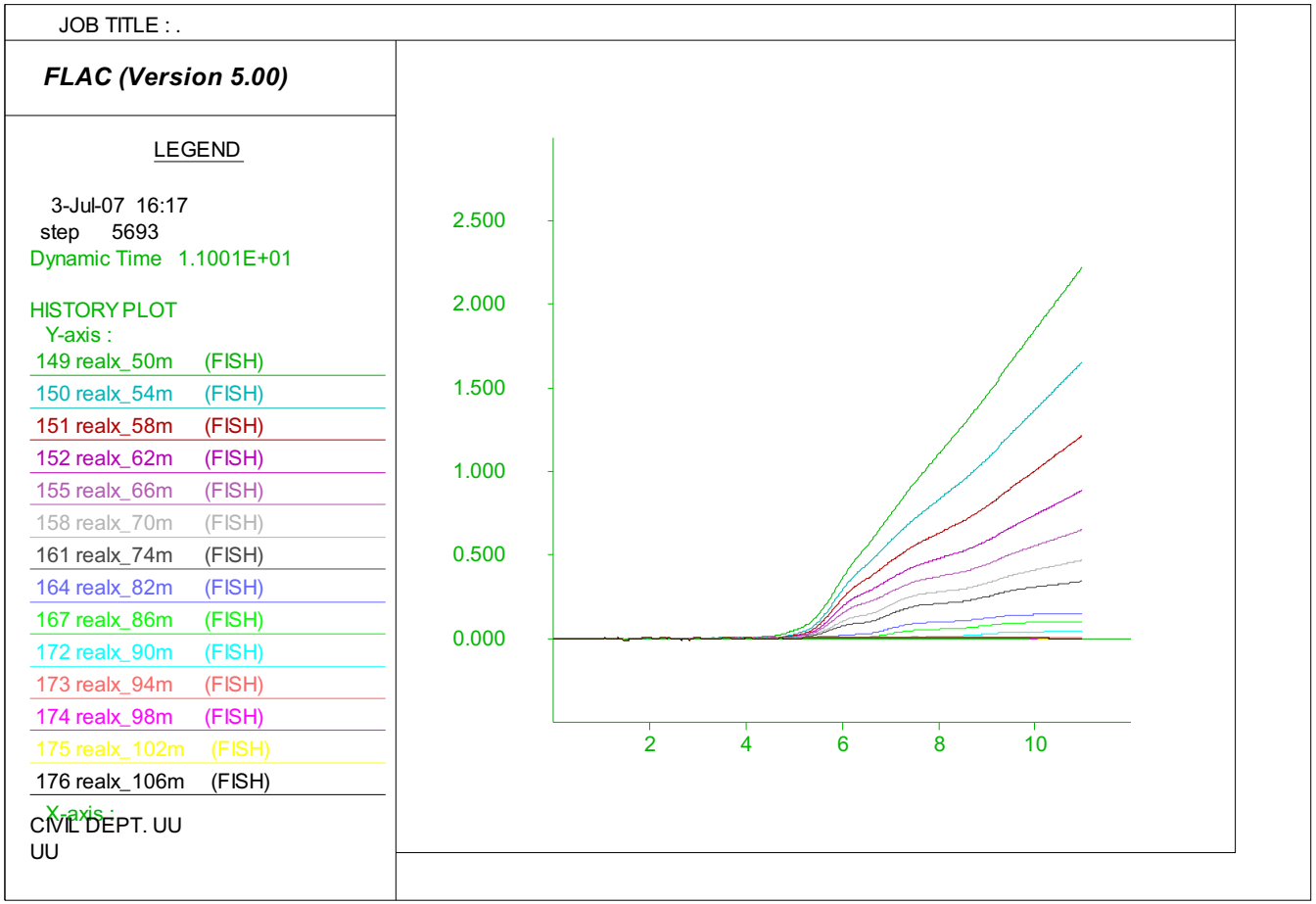


Figure H.14. Model later spreading prediction loaded by motion 7 with residual strength ratio of 0.065 (Y axis in meter and X axis in seconds).

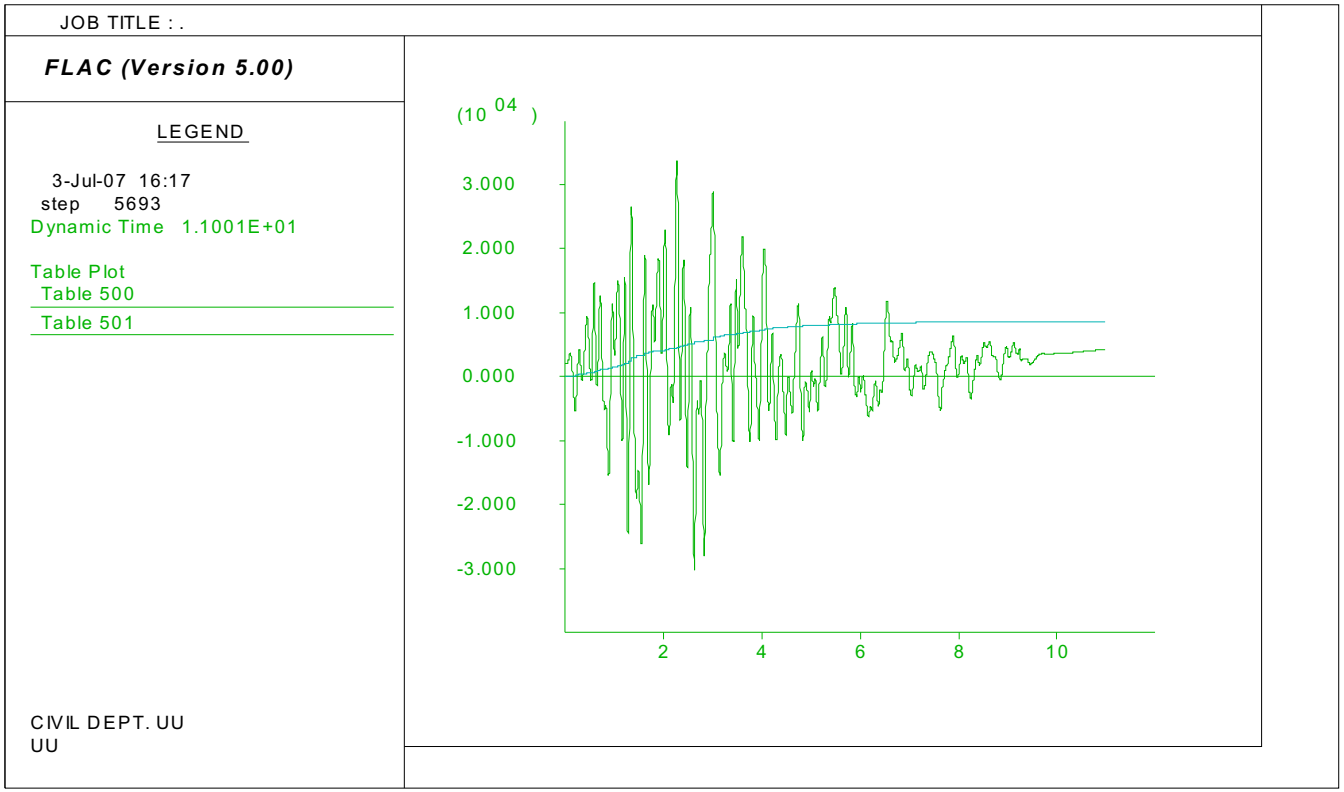


Figure H.15. Pore water generation history loaded by motion 7 with residual strength ratio of 0.06: Shear stress (Y axis in Pa) and r_u (Y axis multiplied by 1000) vs. time (X axis in seconds).

APPENDIX I

IMPERIAL VALLEY SITE HEBER ROAD SECTION DATA

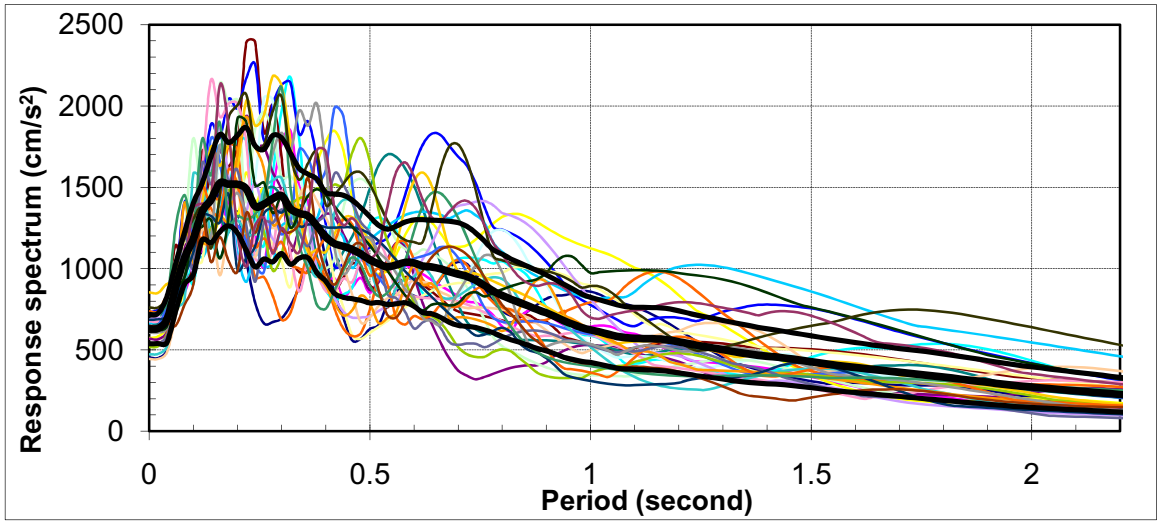


Figure I.1. Imperial Valley Heber Road Response spectra of generated thirty motions

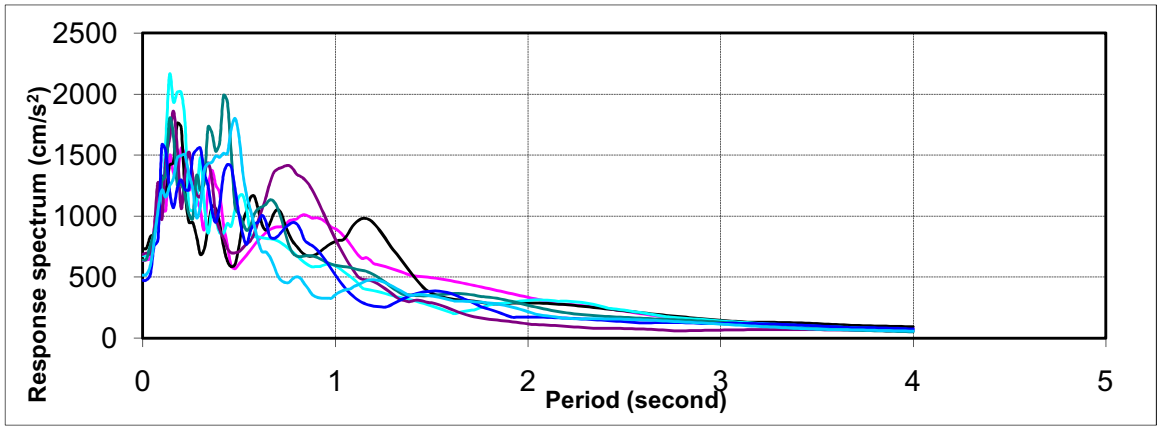


Figure I.2. Imperial Valley Heber Road Response spectra of selected seven motions

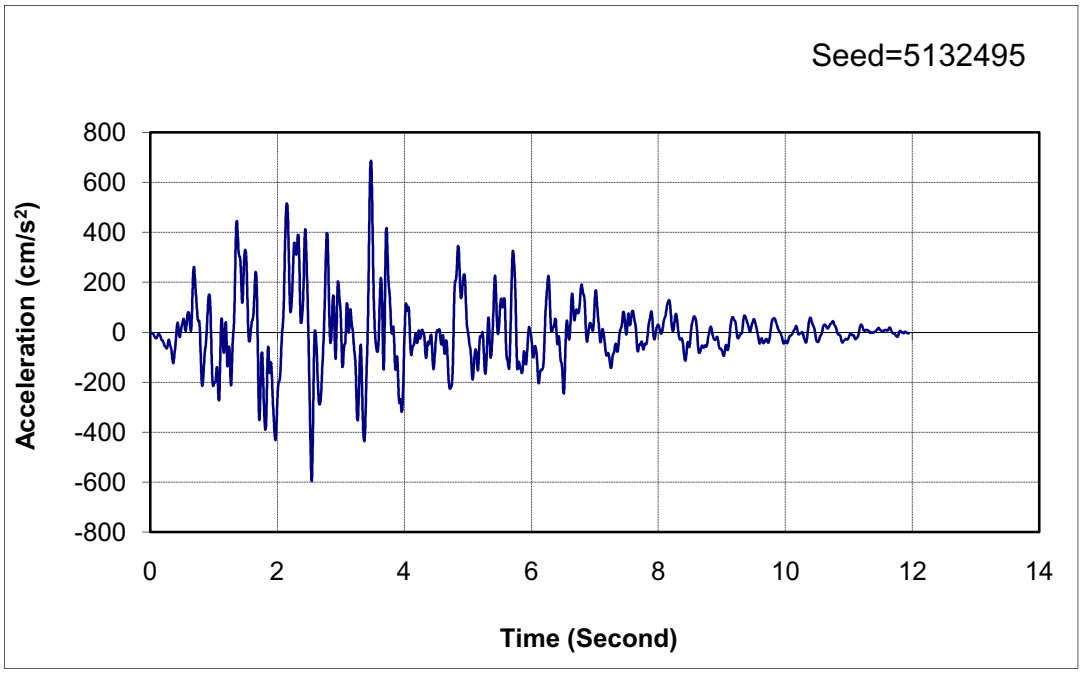


Figure I.3. Imperial Valley Heber Road selected motion 1

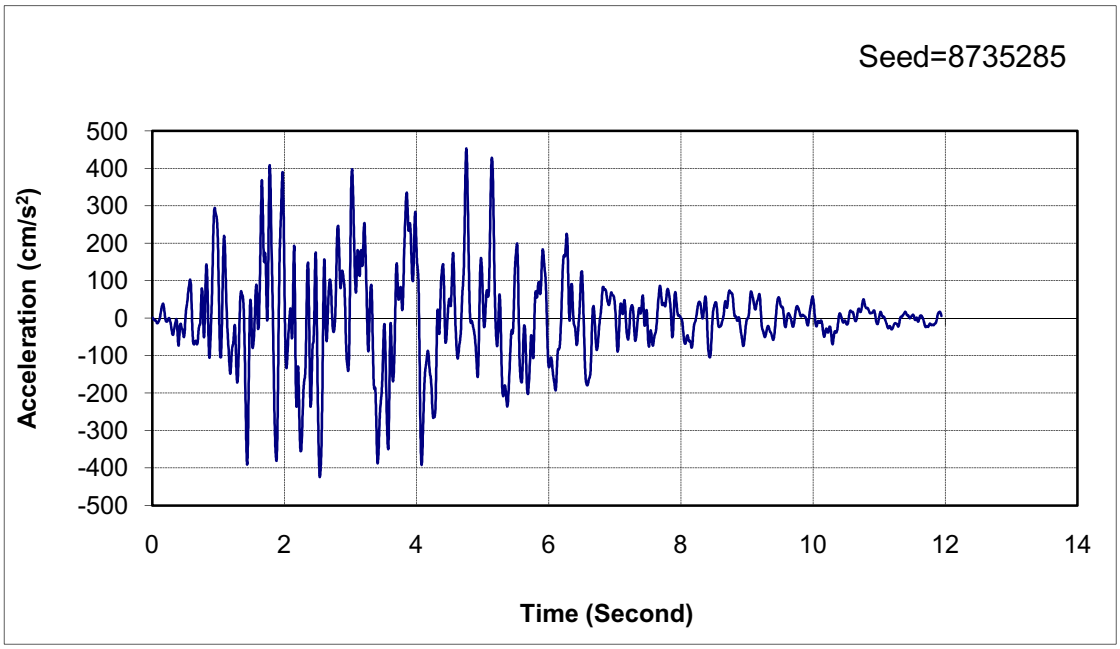


Figure I.4. Imperial Valley Heber Road selected motion 2

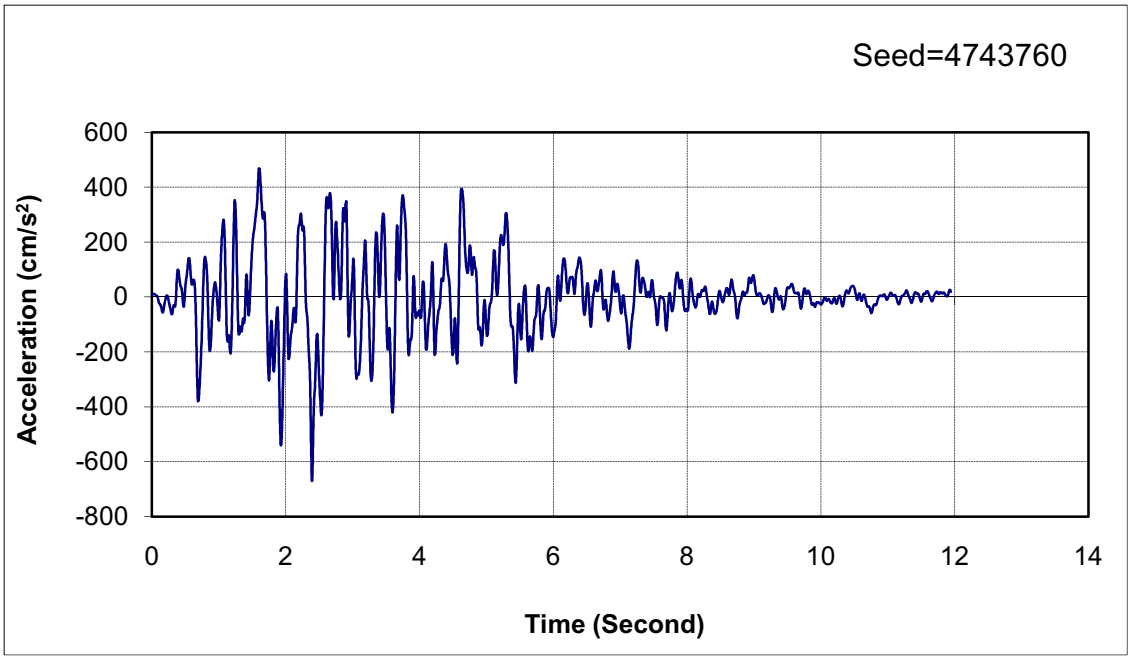


Figure I.5. Imperial Valley Heber Road selected motion 3

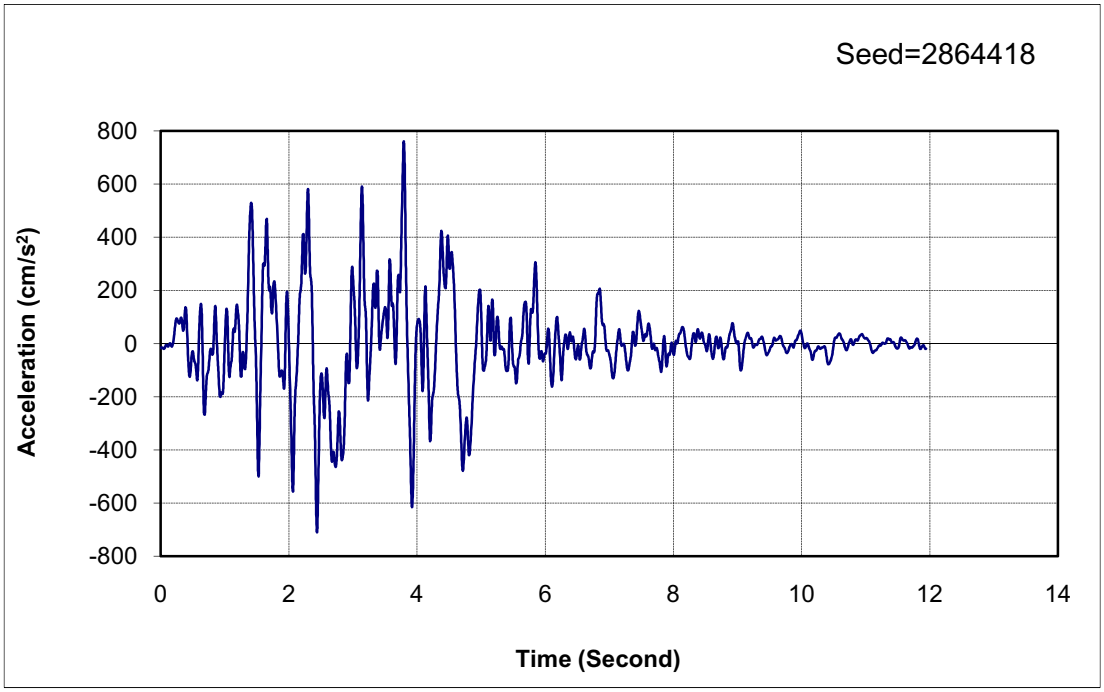


Figure I.6. Imperial Valley Heber Road selected motion 4

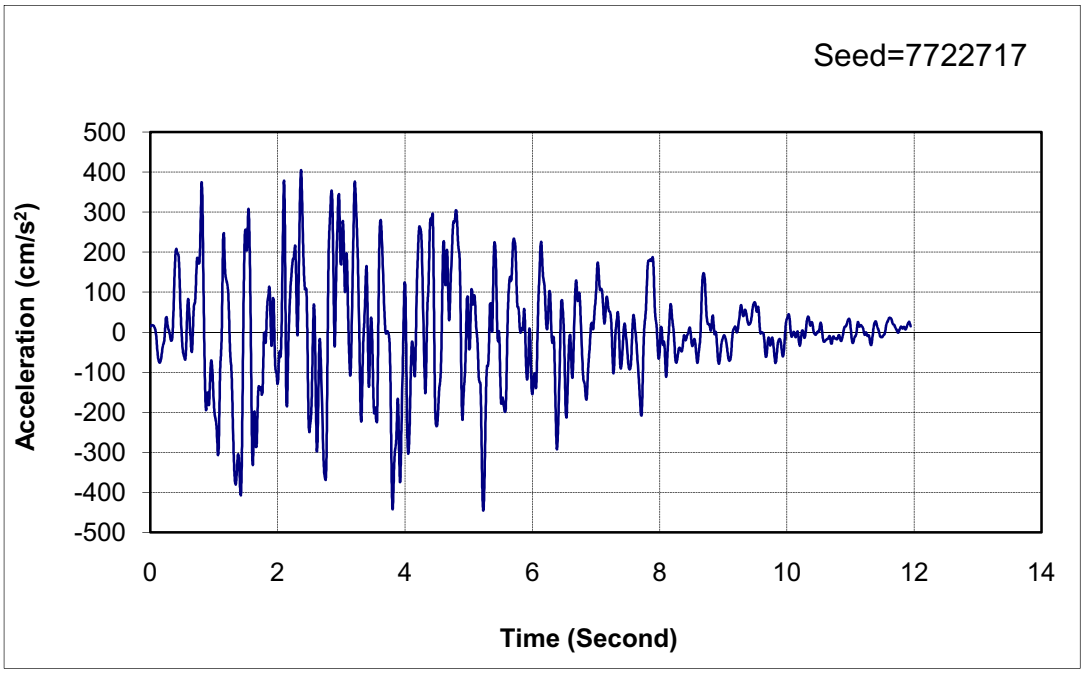


Figure I.7. Imperial Valley Heber Road selected motion 5

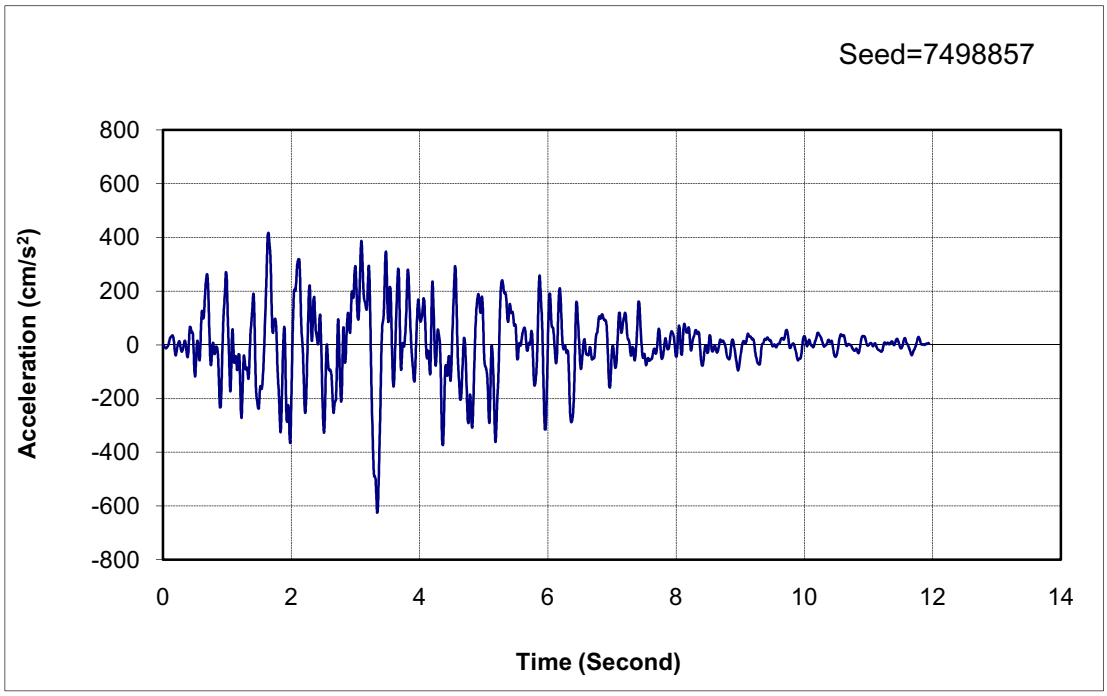


Figure I.8. Imperial Valley Heber Road selected motion 6

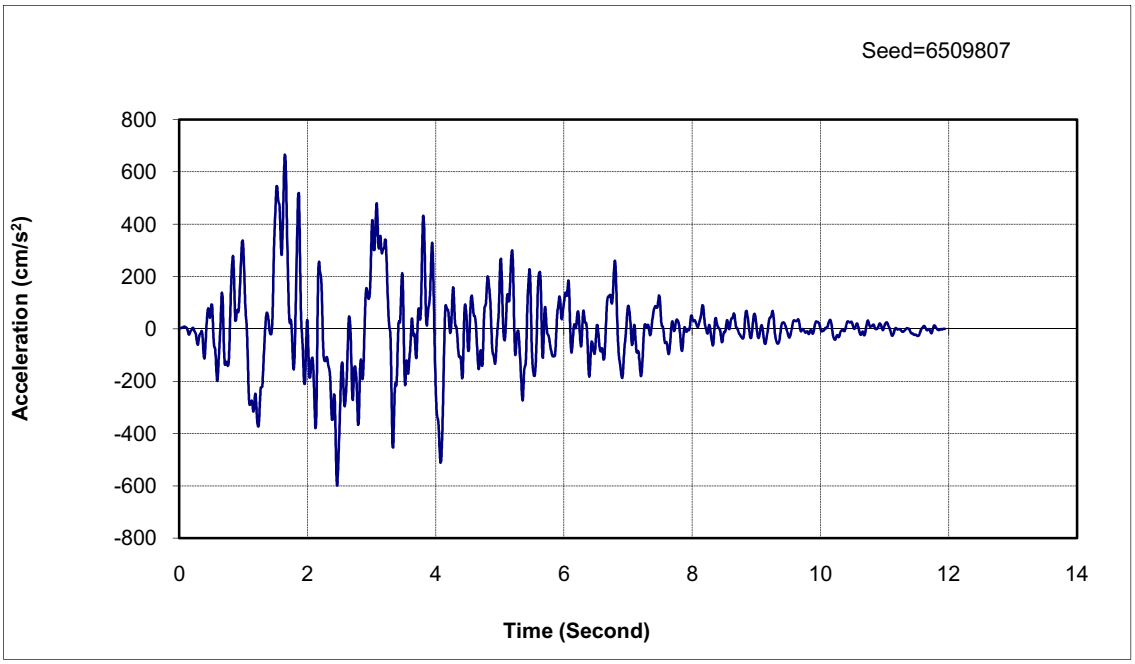


Figure I.9. Imperial Valley Heber Road selected motion 7 let all the main

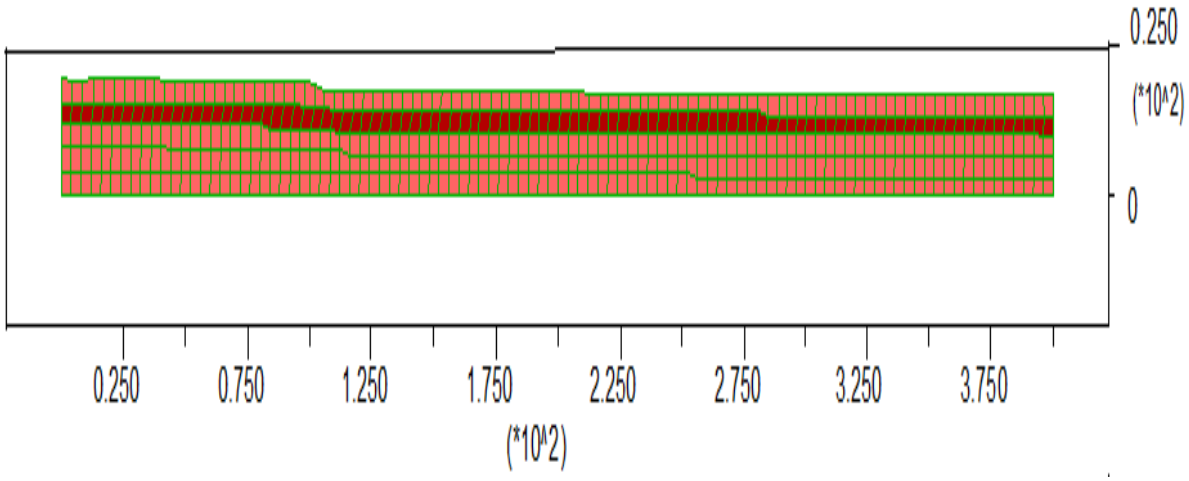


Figure I.10. Imperial Valley Heber Road FLAC model scheme (both Y axis & X axis in meters)

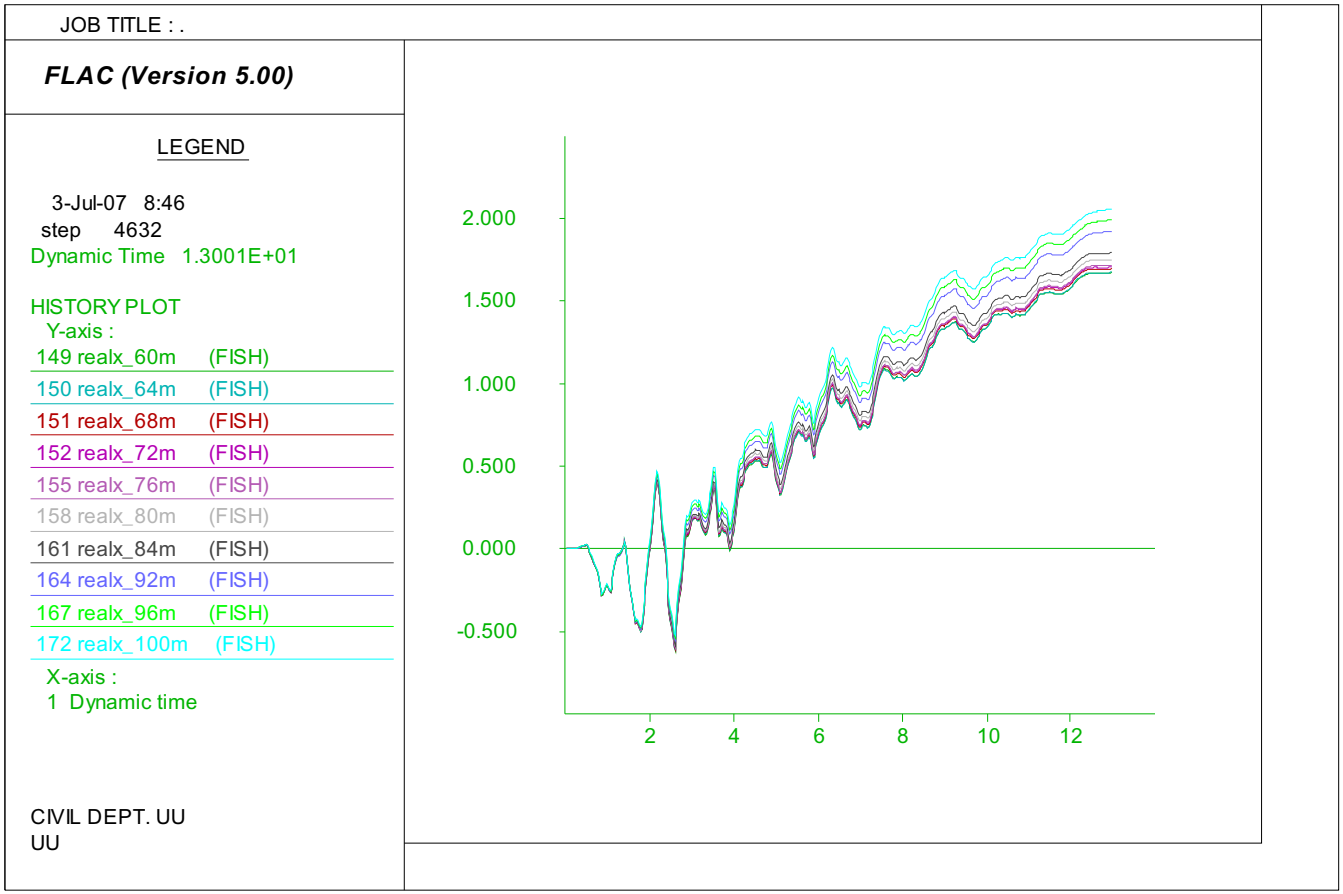


Figure I.11. Imperial Valley Heber Road model lateral spreading loaded by motion 1 with residual strength ratio of 0.08 (Y axis in meter and X axis in second)

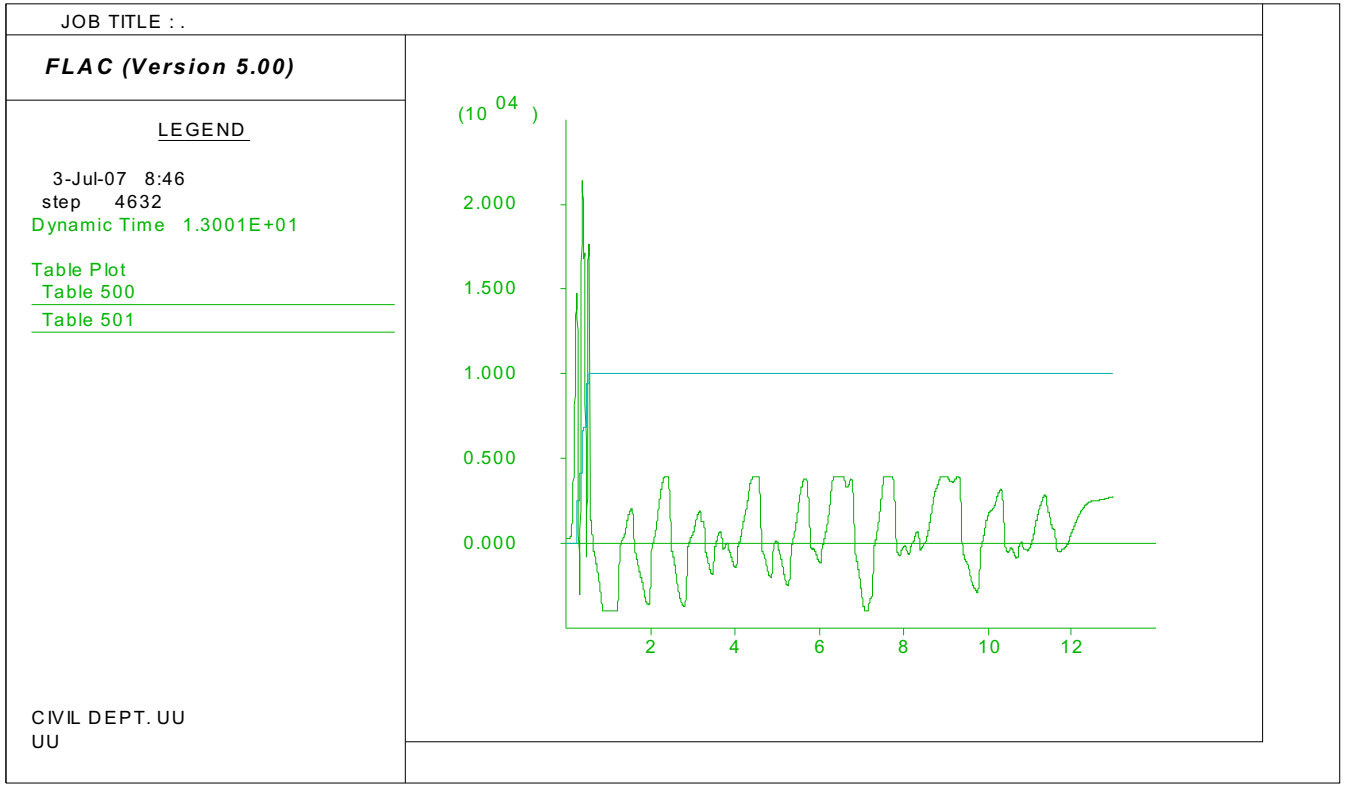


Figure I.12. Imperial Valley Heber Road pore water generation history loaded by motion 1 with residual strength ratio of 0.08: Shear stress (Y axis in Pa) and r_u (Y axis multiplied by 1000) vs. time (X axis in seconds).

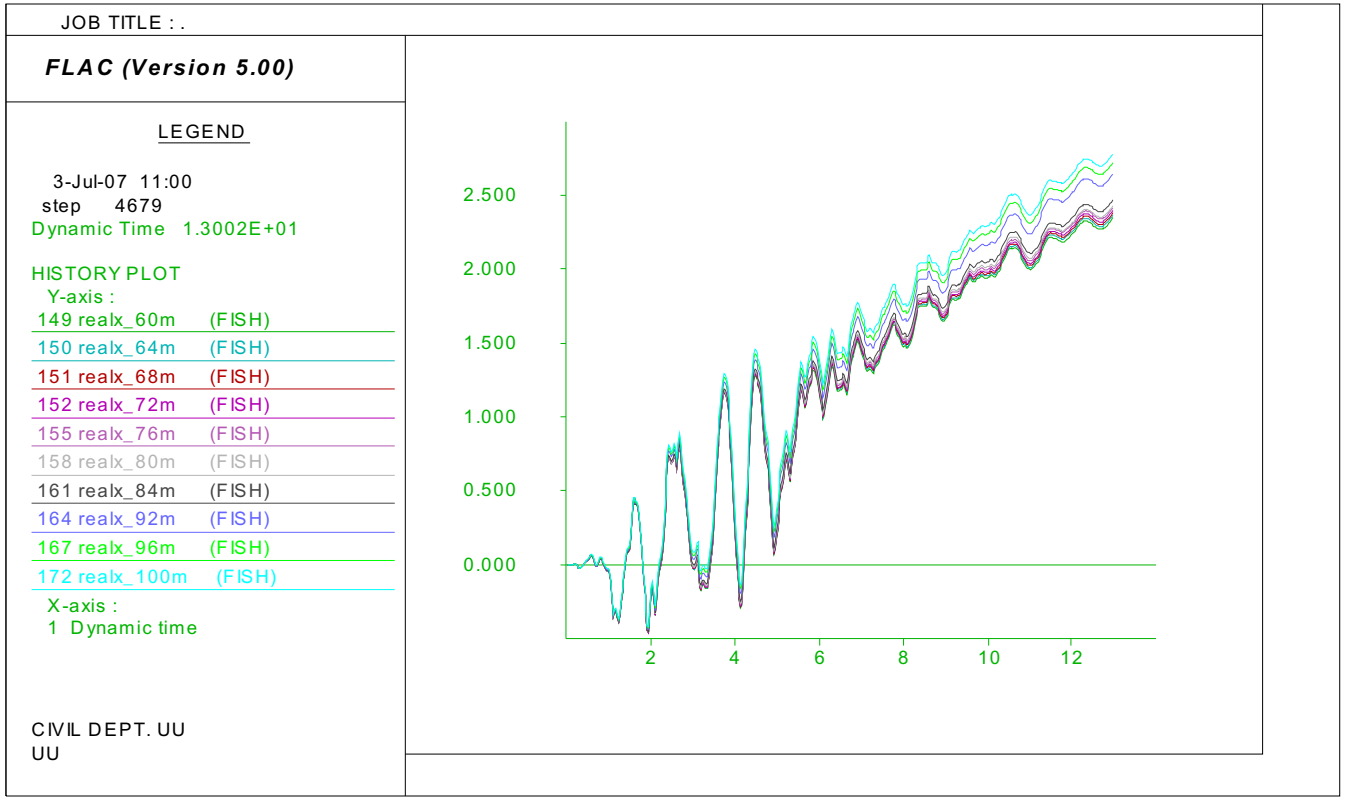


Figure I.13. Imperial Valley Heber Road model later spreading prediction loaded by motion 2 with residual strength ratio of 0.08 (Y axis in meter and X axis in second)

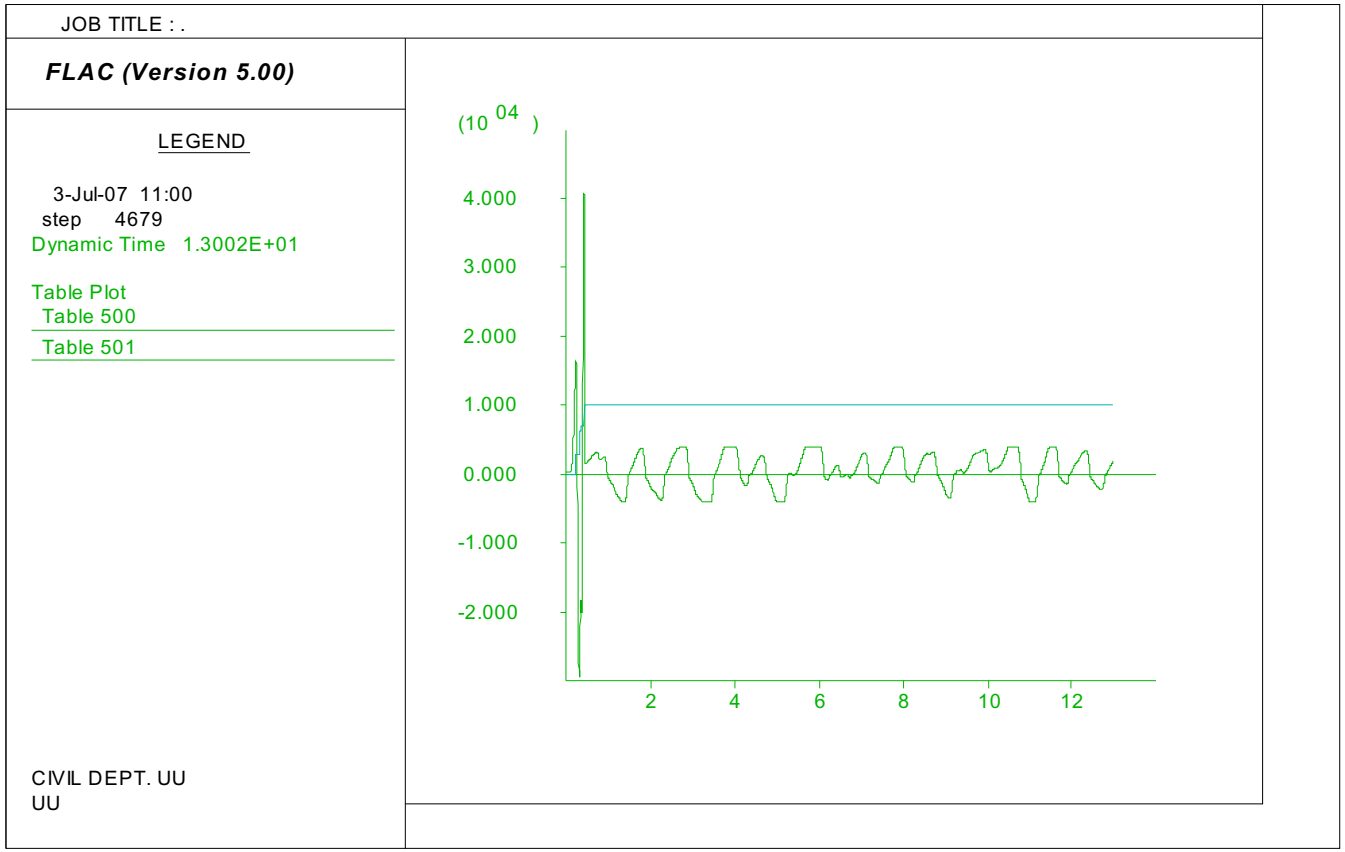


Figure I.14. Imperial Valley Heber Road model pore water generation history loaded by motion 2 with residual strength ratio of 0.08: Shear stress (Y axis in Pa) and r_u (Y axis multiplied by 1000) vs. time (X axis in seconds).

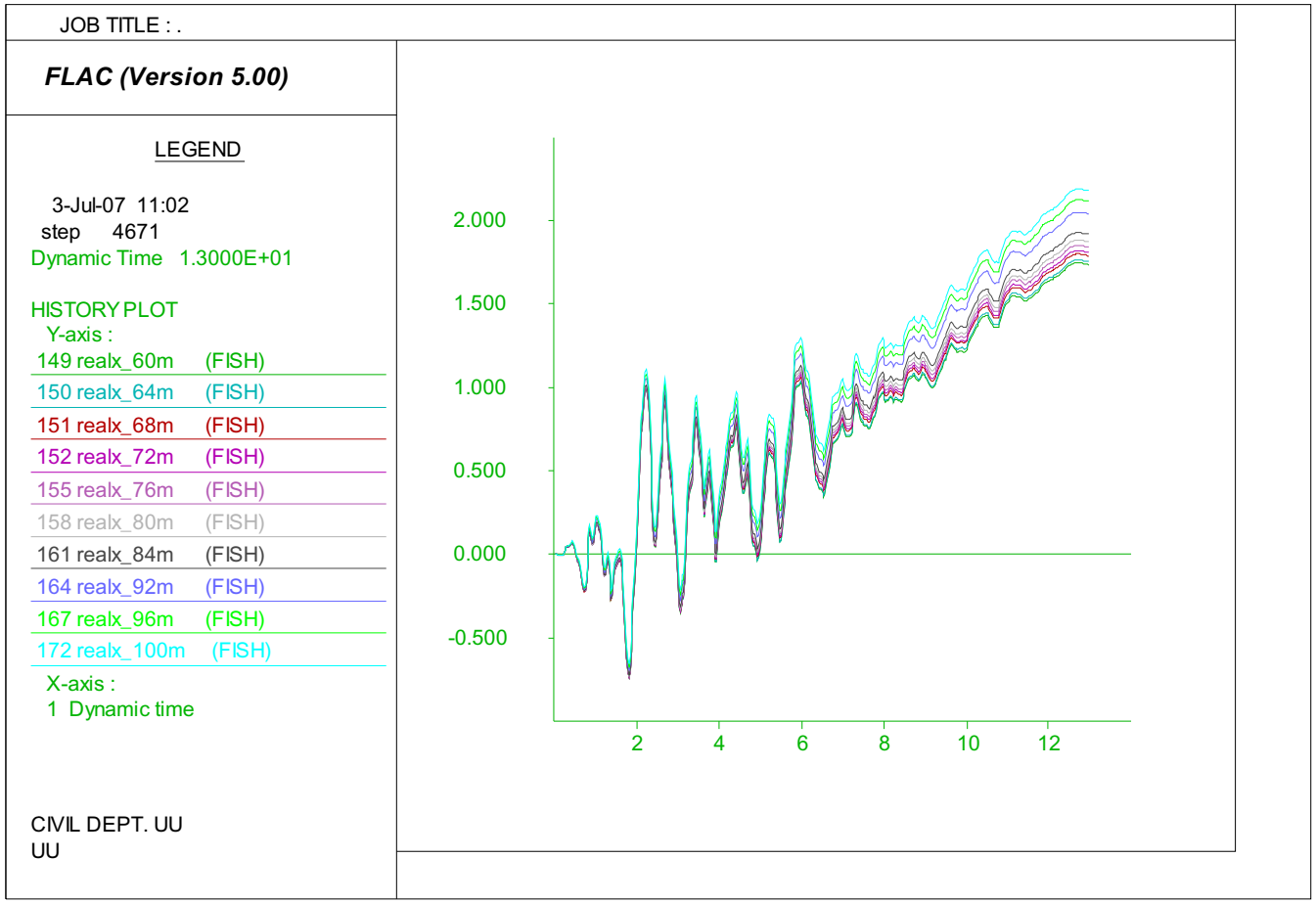


Figure I.15. Imperial Valley Heber Road model later spreading prediction loaded by motion 3 with residual strength ratio of 0.08 (Y axis in meter and X axis in second)

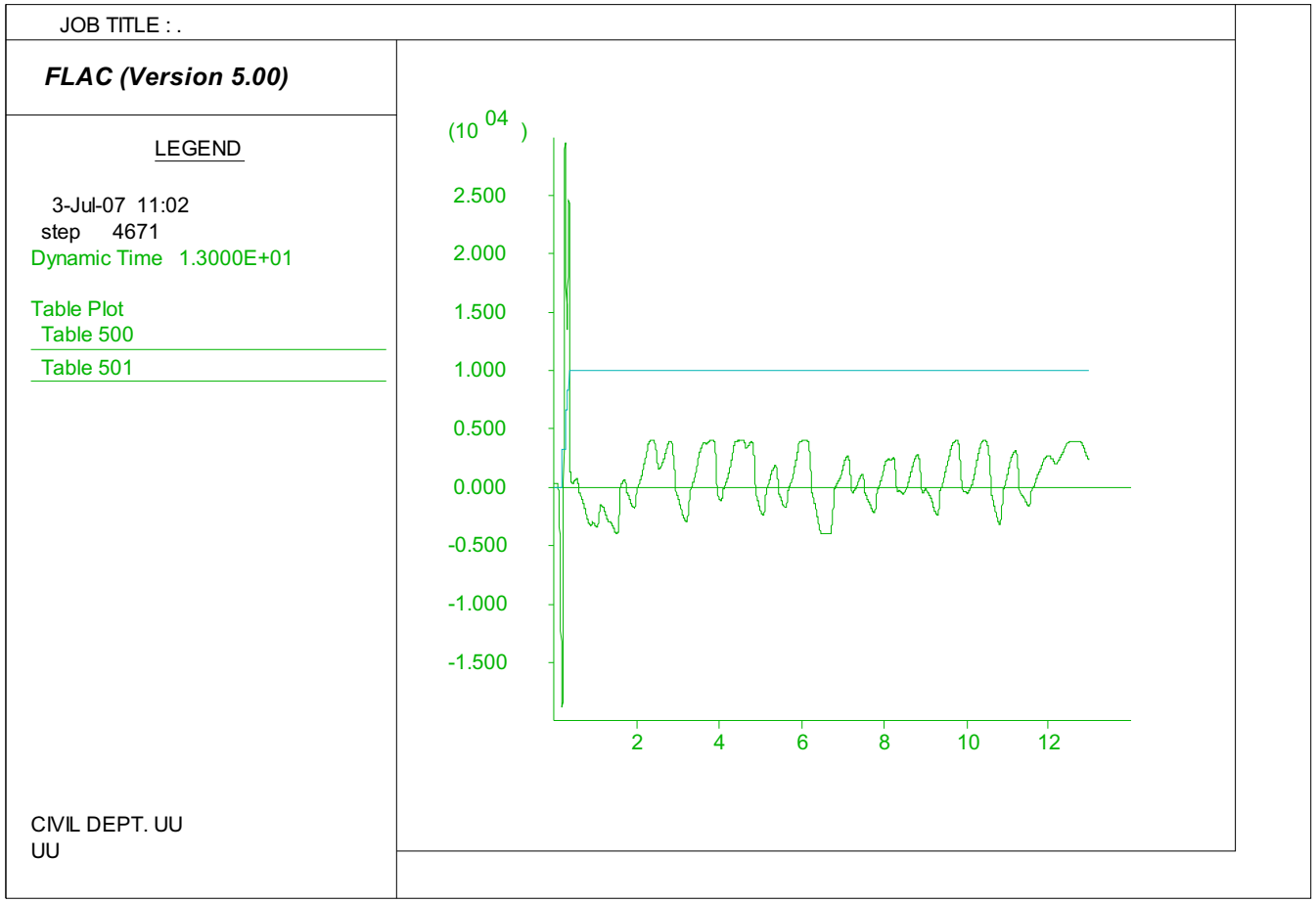


Figure I.16. Imperial Valley Heber Road model pore water generation history loaded by motion 3 with residual strength ratio of 0.08: Shear stress (Y axis in Pa) and r_u (Y axis multiplied by 1000) vs. time (X axis in seconds).

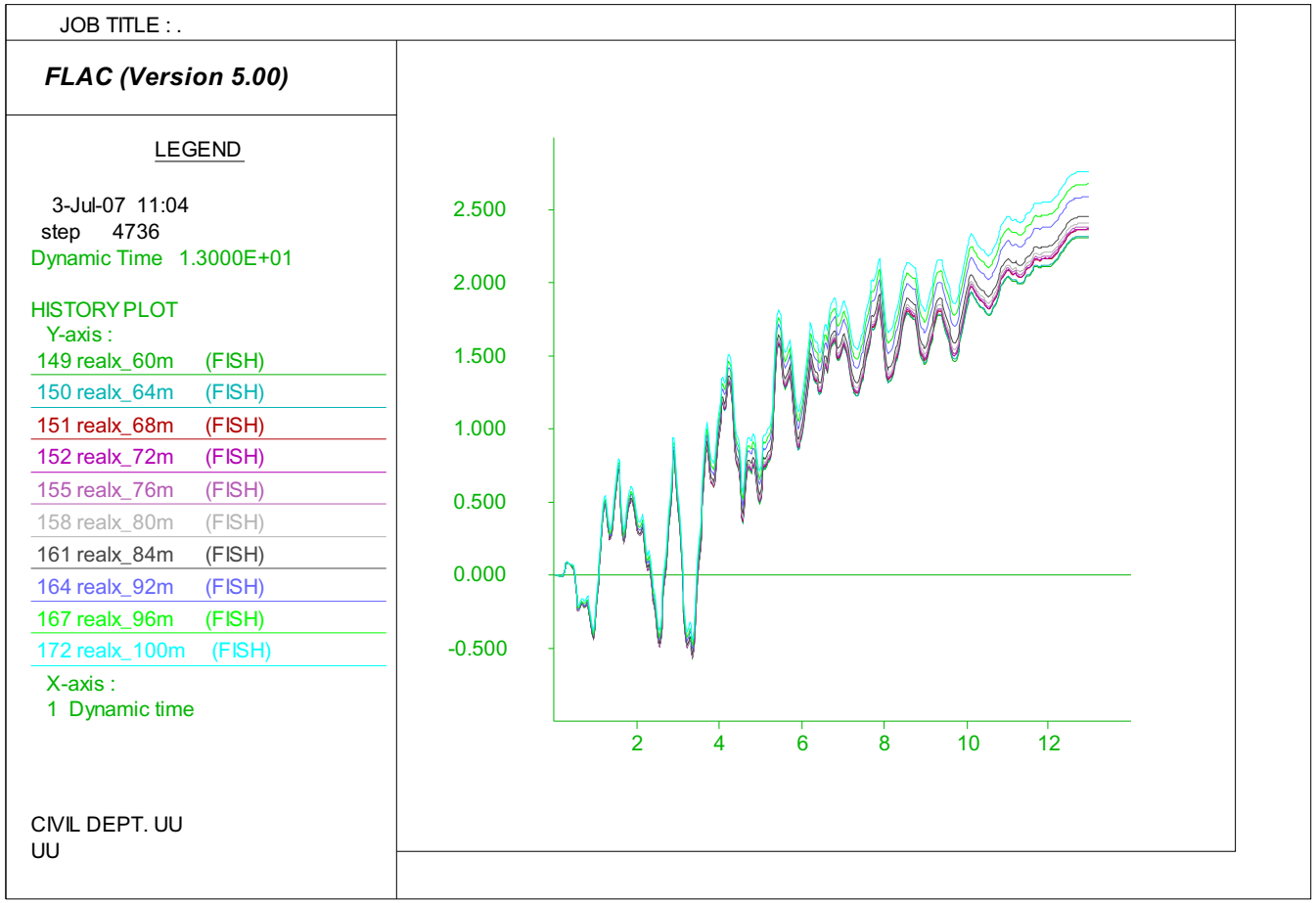


Figure I.17. Imperial Valley Heber Road model later spreading prediction loaded by motion 4 with residual strength ratio of 0.08 (Y axis in meter and X axis in second)

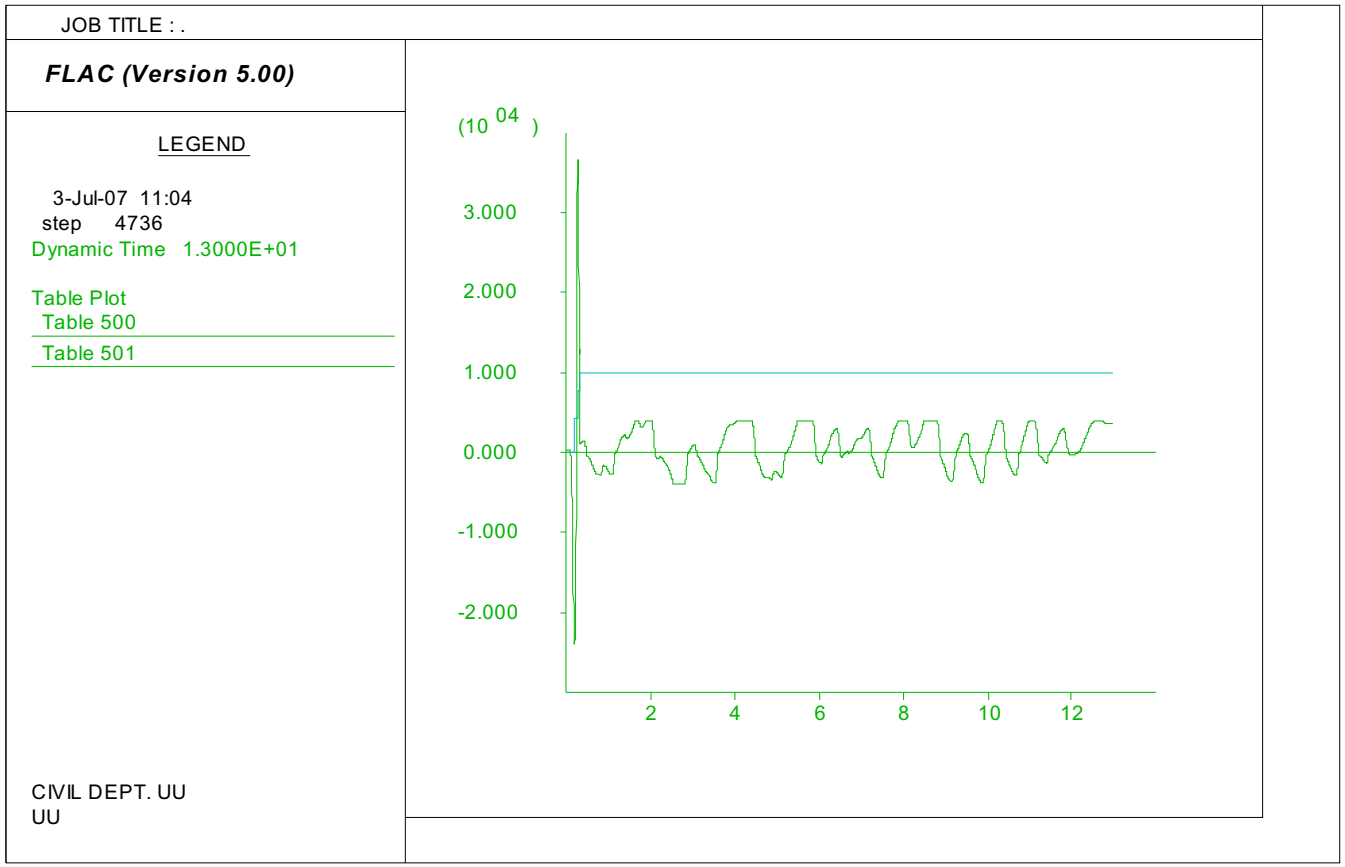


Figure I.18. Imperial Valley Heber Road model pore water generation history loaded by motion 4 with residual strength ratio of 0.08: Shear stress (Y axis in Pa) and r_u (Y axis multiplied by 1000) vs. time (X axis in seconds).

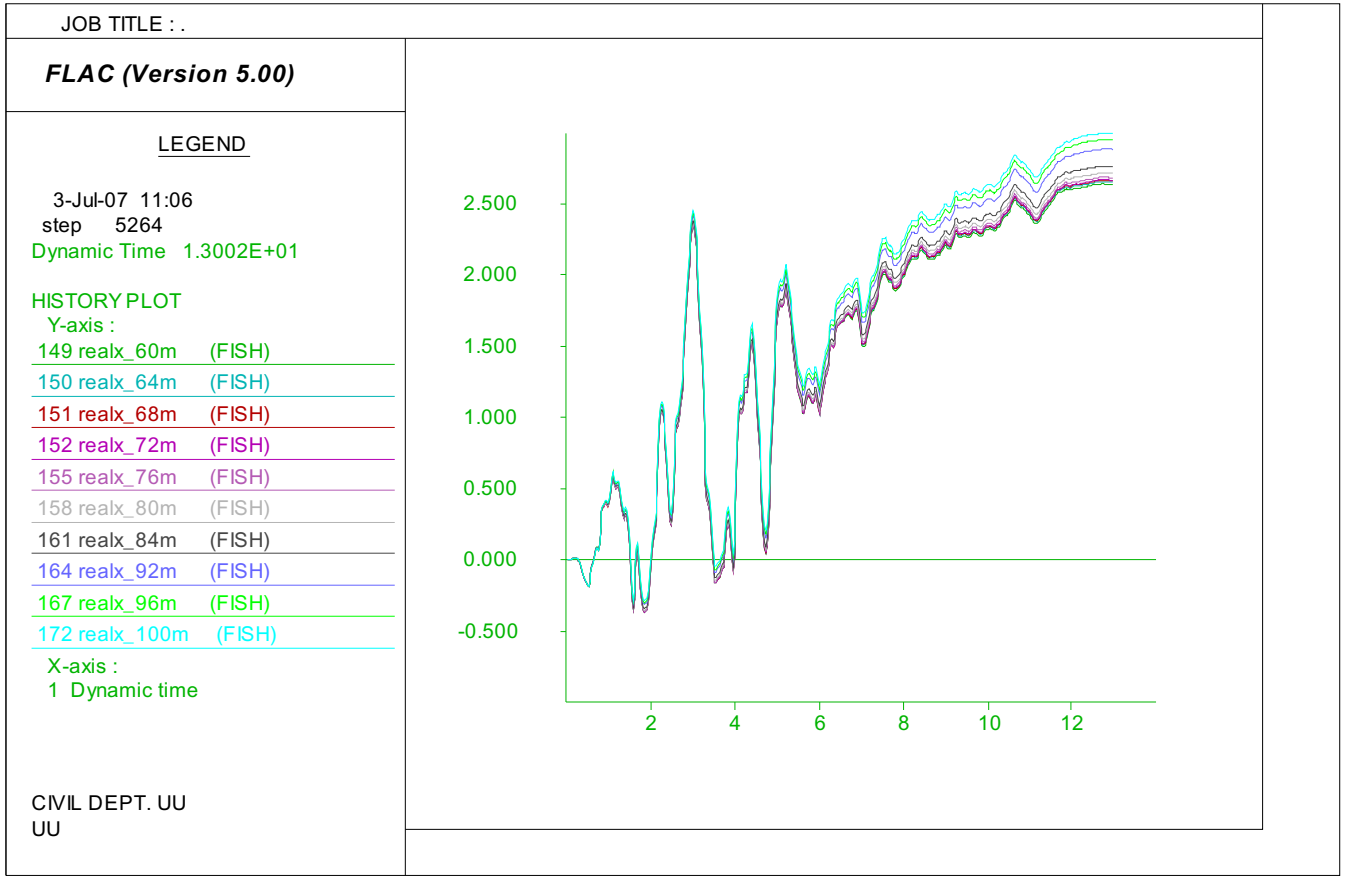


Figure I.19. Imperial Valley Heber Road model later spreading prediction loaded by motion 5 with residual strength ratio of 0.08 (Y axis in meter and X axis in second)

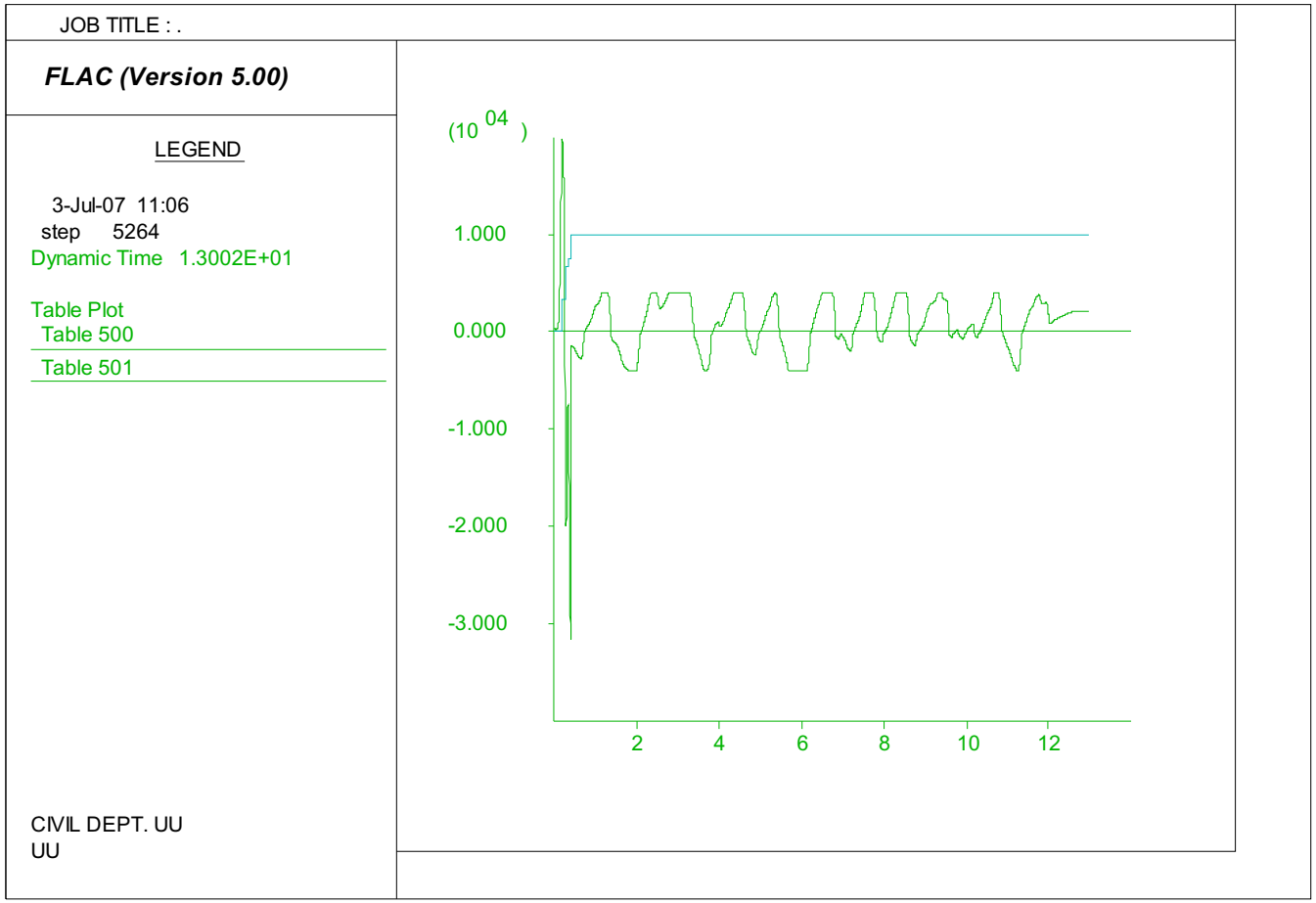


Figure I.20. Imperial Valley Heber Road model pore water generation history loaded by motion 5 with residual strength ratio of 0.08: Shear stress (Y axis in Pa) and r_u (Y axis multiplied by 1000) vs. time (X axis in seconds).

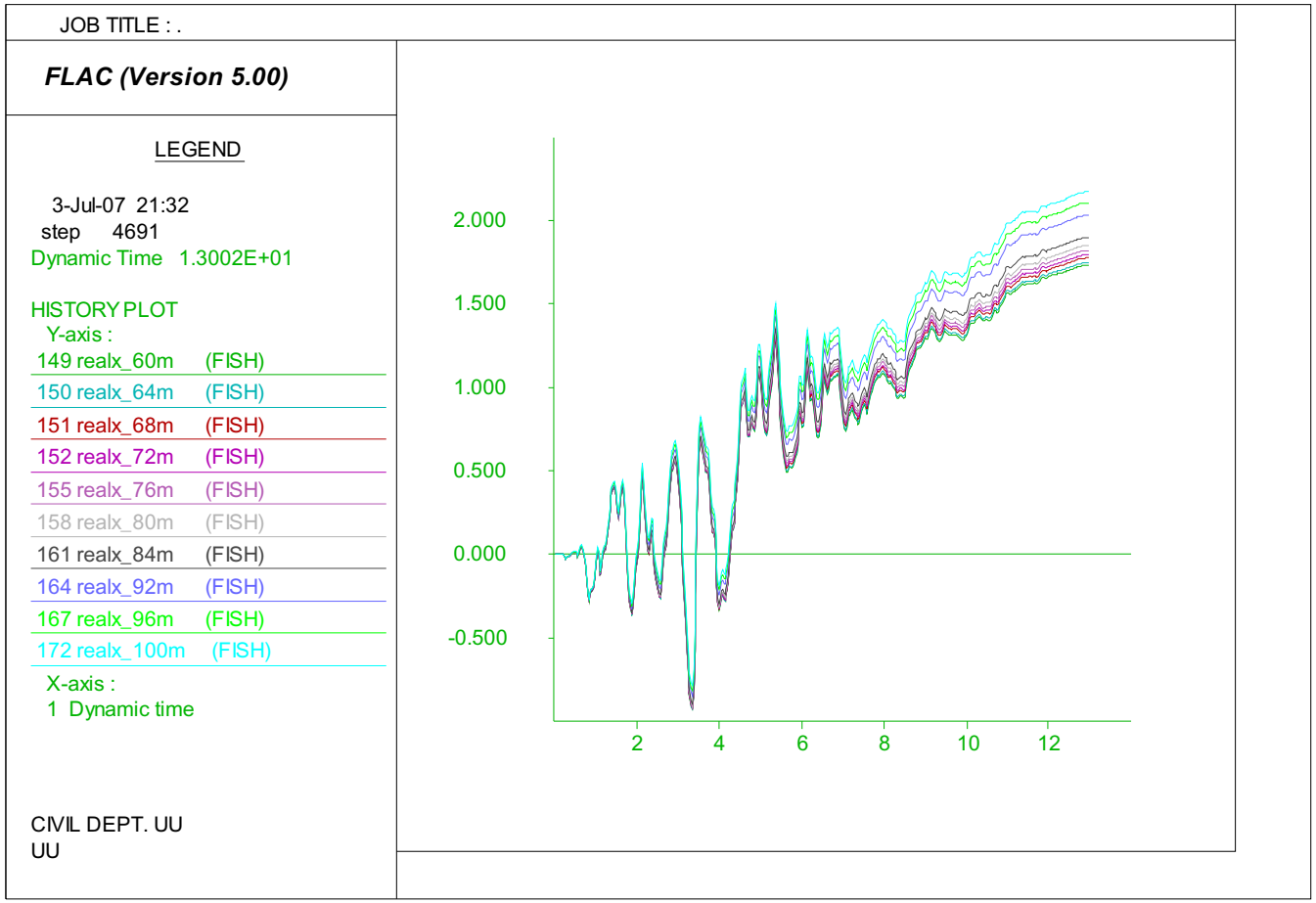


Figure I.21. Imperial Valley Heber Road model later spreading prediction loaded by motion 6 with residual strength ratio of 0.08 (Y axis in meter and X axis in second)

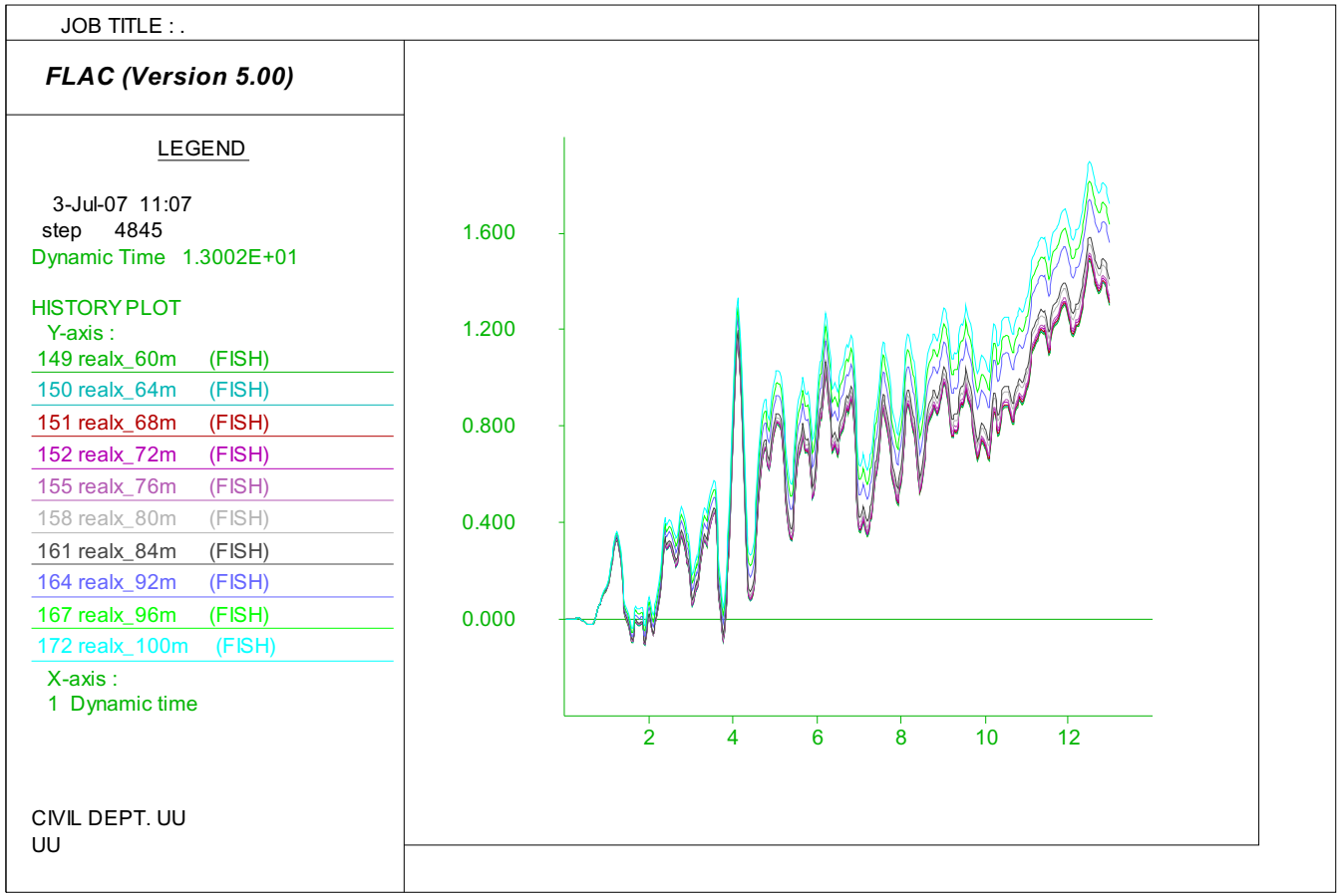


Figure I.22. Imperial Valley Heber Road model later spreading prediction loaded by motion 7 with residual strength ratio of 0.08 (Y axis in meter and X axis in second)

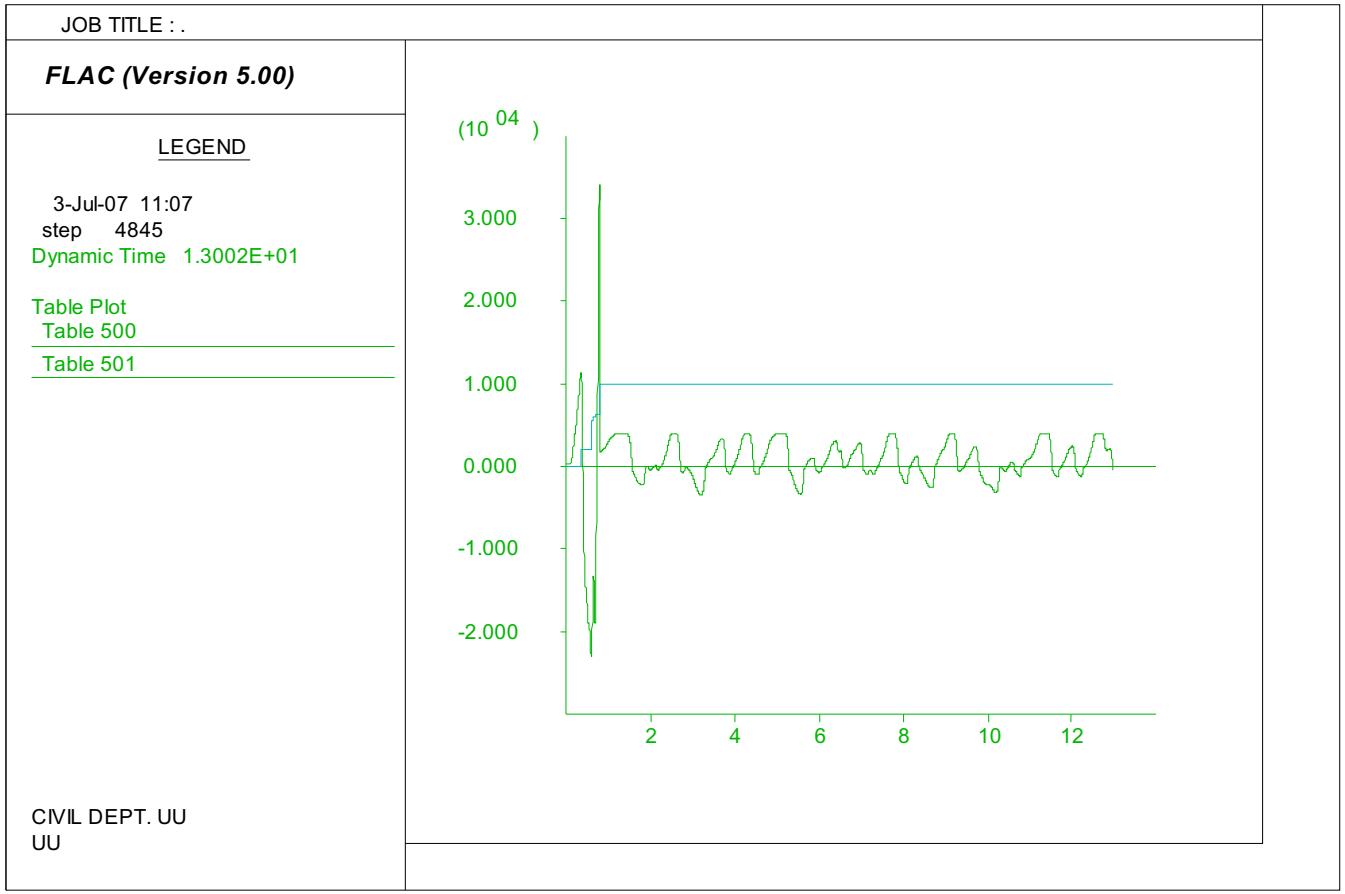


Figure I.23. Imperial Valley Heber Road model pore water generation history loaded by motion 7 with residual strength ratio of 0.08: Shear stress (Y axis in Pa) and r_u (Y axis multiplied by 1000) vs. time (X axis in seconds).

APPENDIX J

IMPERIAL VALLEY SITE RIVER PARK SECTION DATA

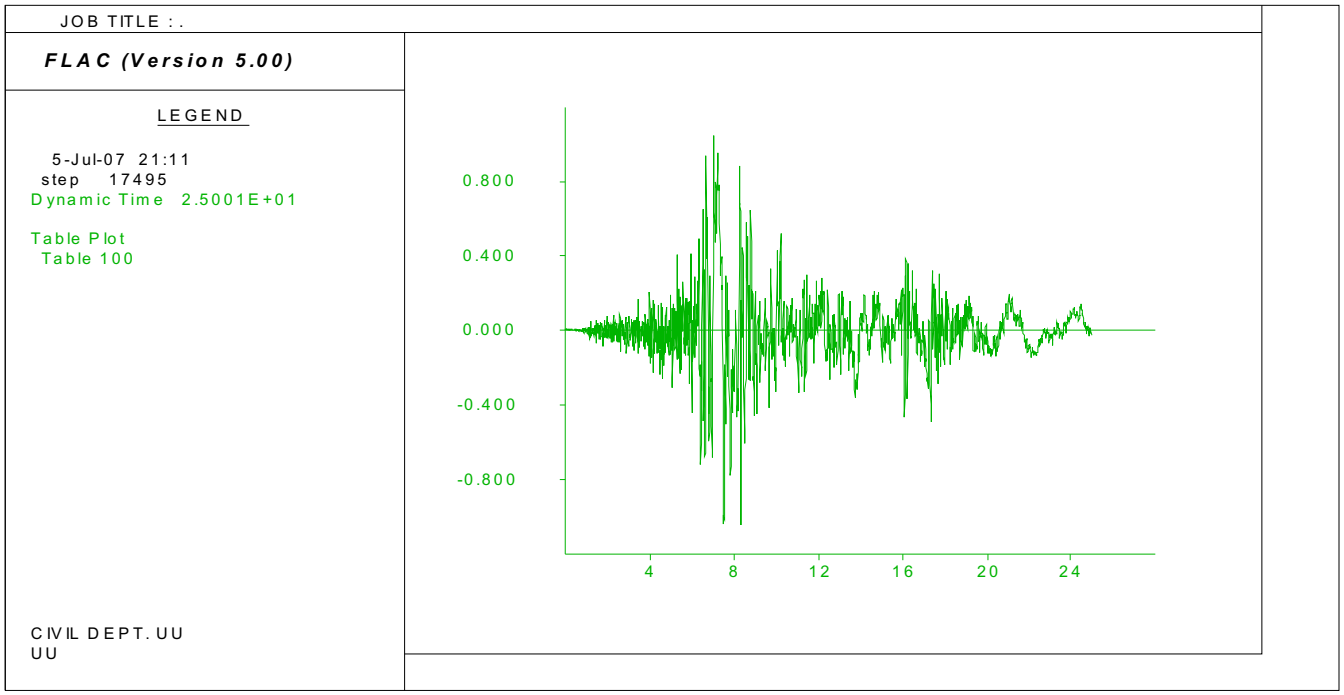


Figure J.1. Model input motion in 315° direction (Y axis in m/s^2 and X axis in second)

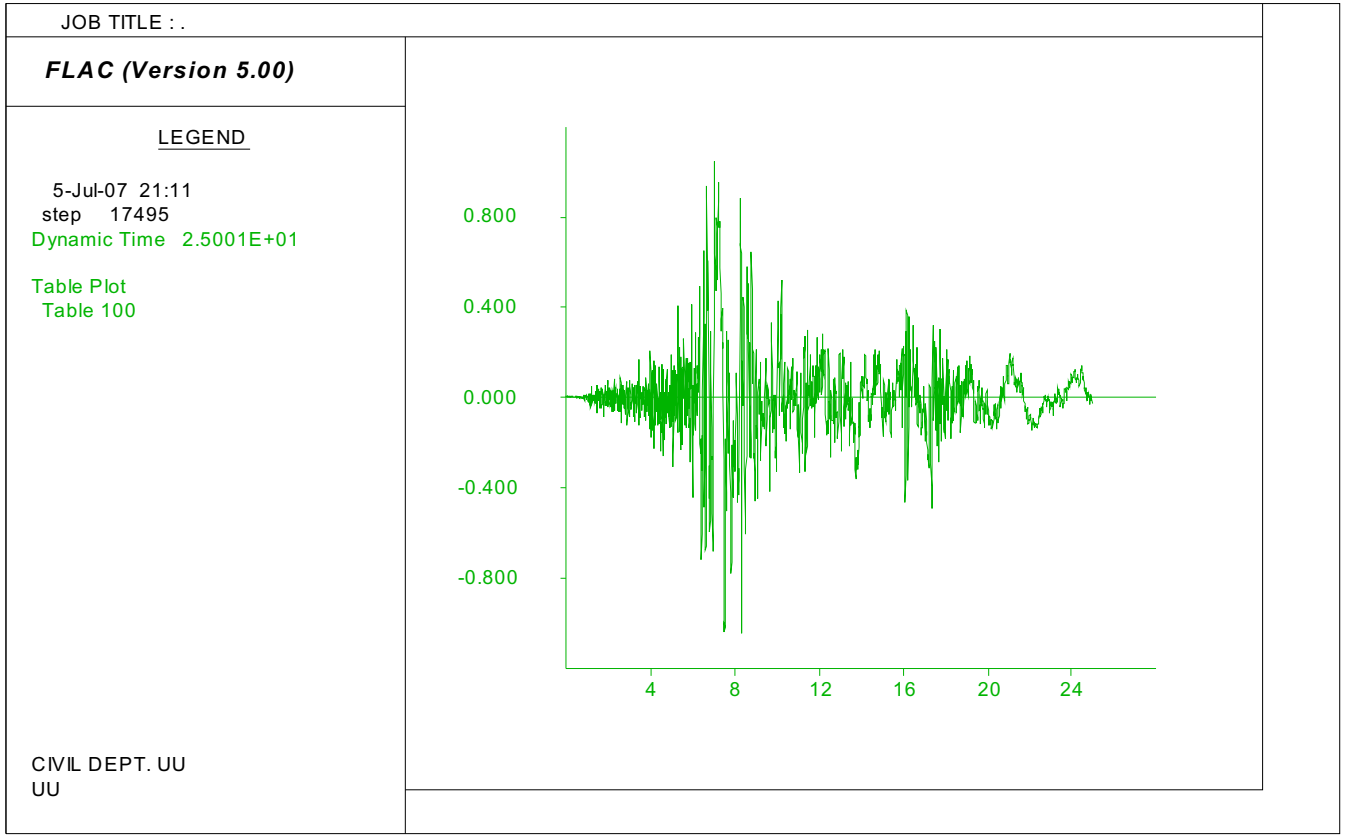


Figure J.2. Model input motion in 225° direction (Y axis in m/s^2 and X axis in second)

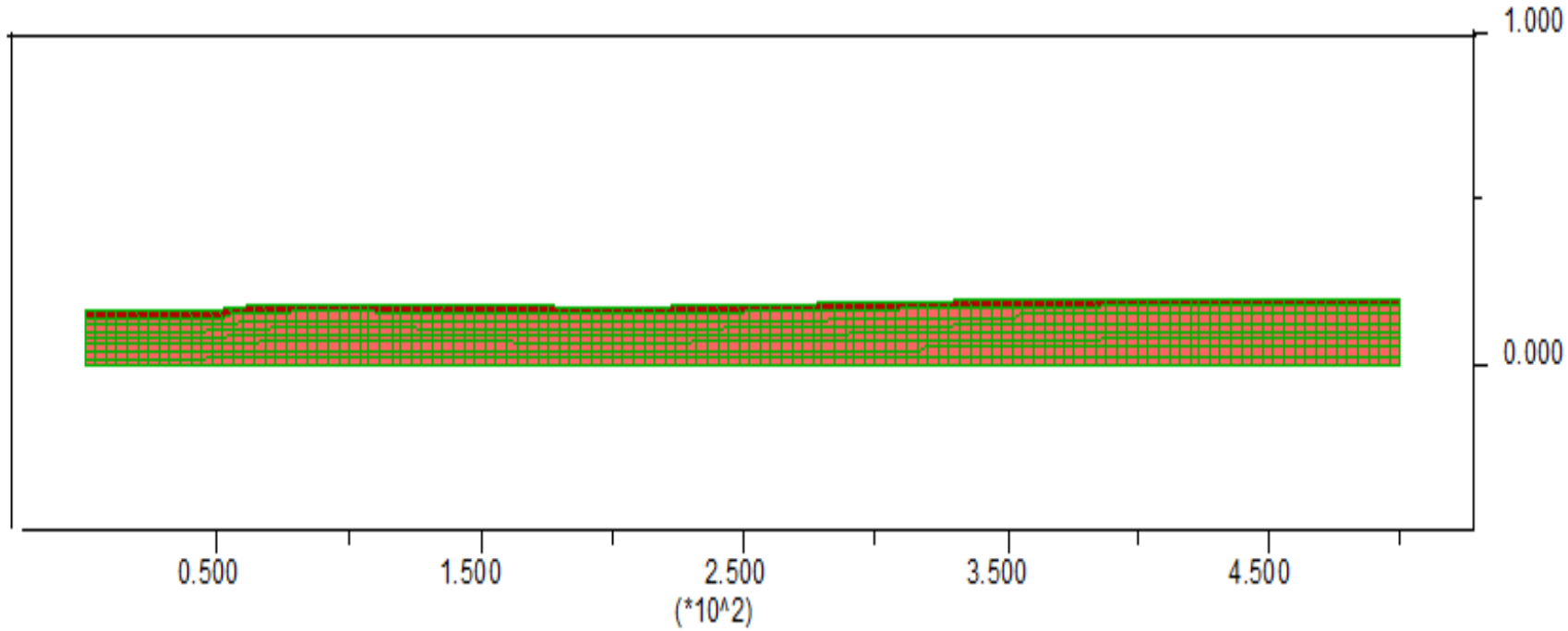


Figure J.3. Model design mesh (both Y axis & X axis in meters)

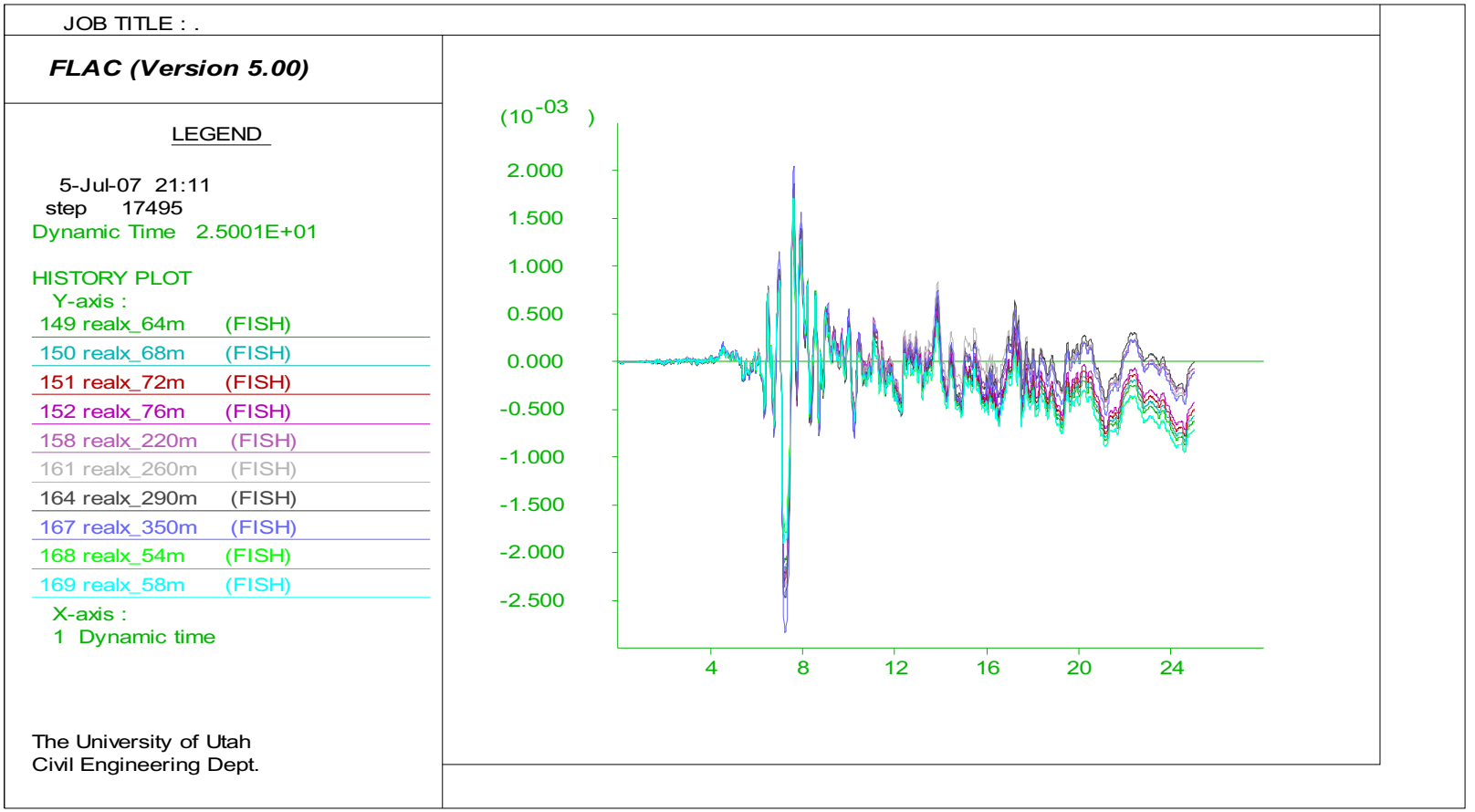


Figure J.4. Model later spreading prediction in 315° direction (Y axis in meter and X axis in second)

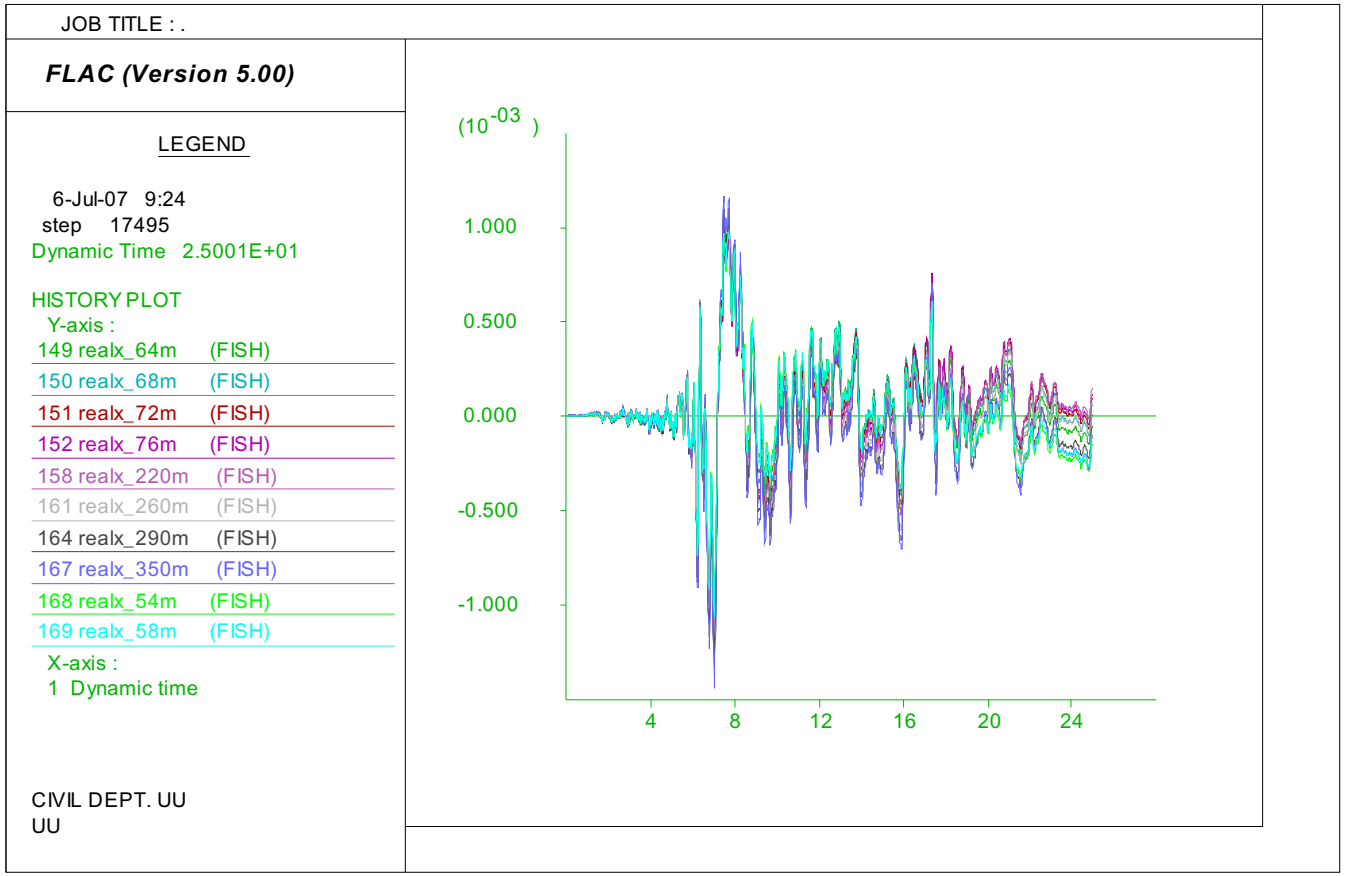


Figure J.5. Model later spreading prediction in 225° direction (Y axis in meter and X axis in second)

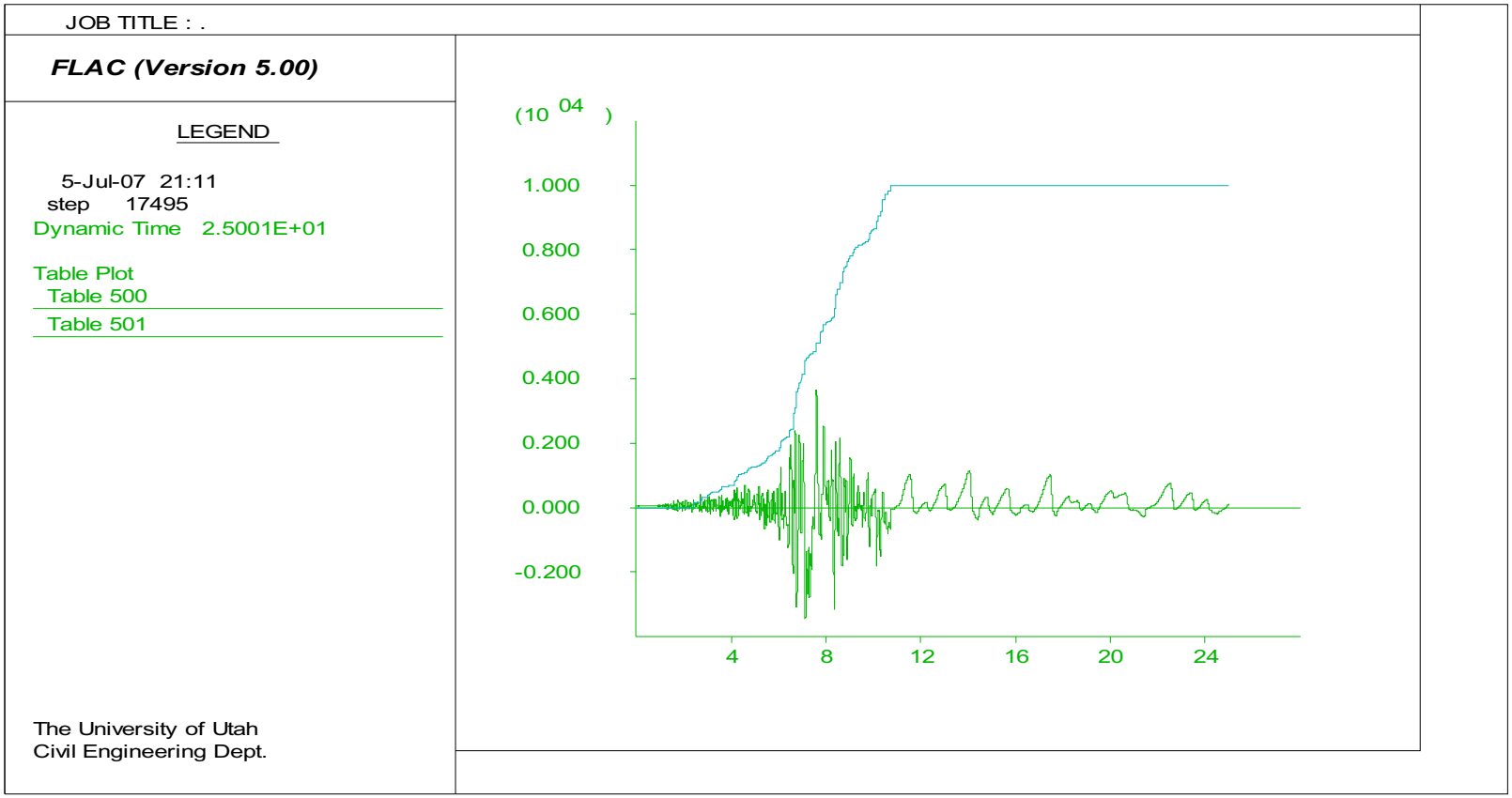


Figure J.6. Model pore water generation history in 315° direction: Shear stress (Y axis in Pa) and r_u (Y axis multiplied by 1000) vs. time (X axis in seconds).

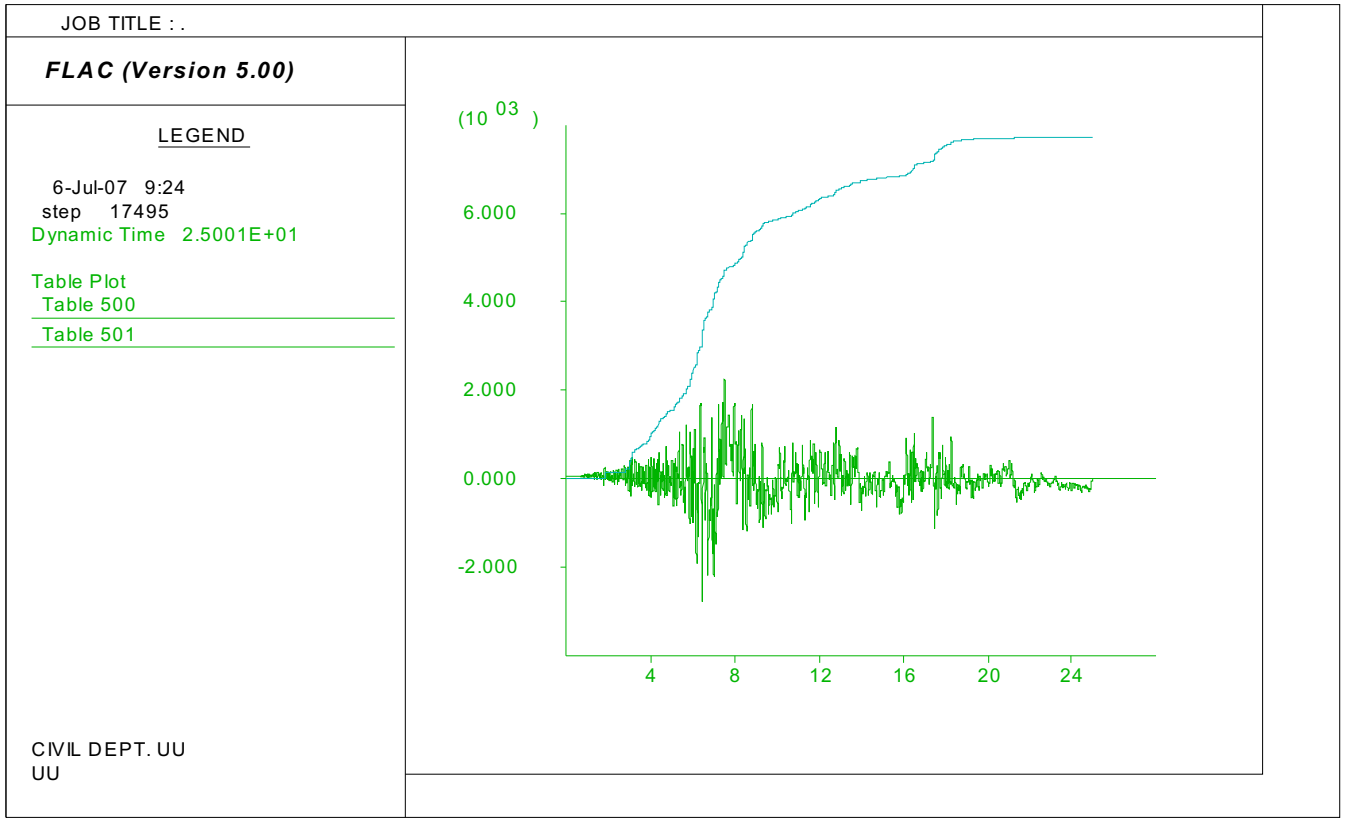


Figure J.7. Model pore water generation history in 225° direction: Shear stress (Y axis in Pa) and r_u (Y axis multiplied by 1000) vs. time (X axis in seconds).

APPENDIX K

TURKEY DEGIRMENEDERE SITE DATA

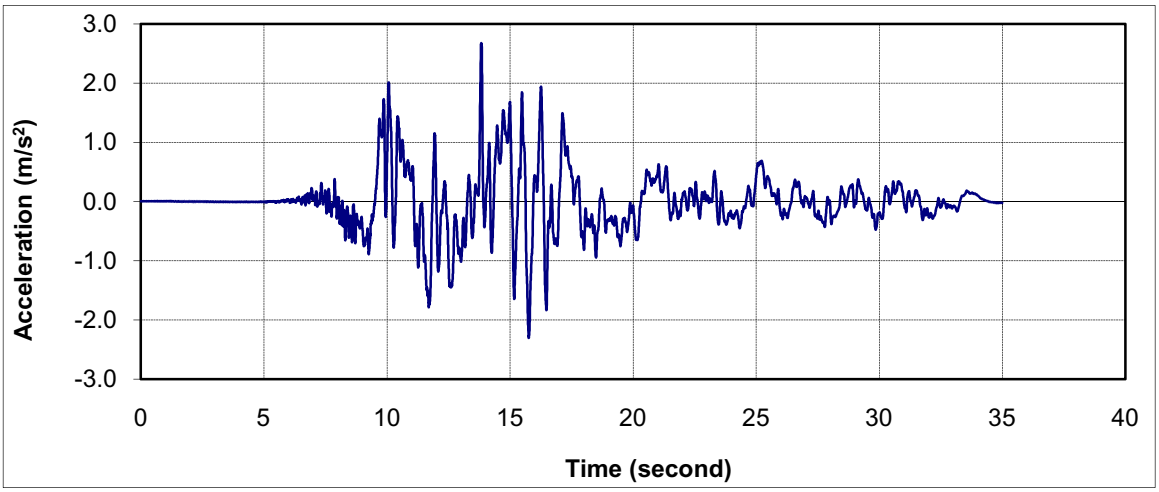


Figure K.1. Time history at YPT in 60° directions.

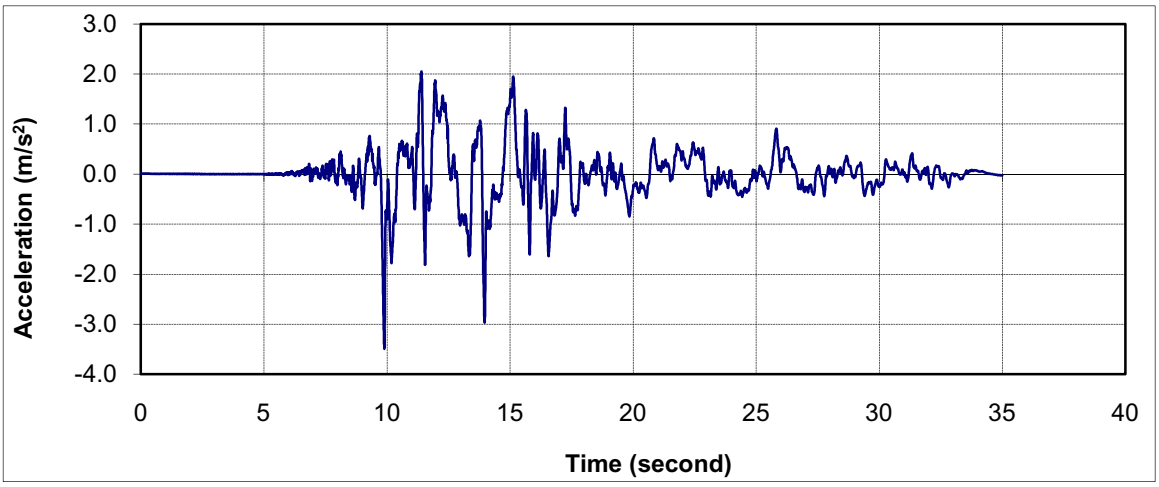


Figure K.2. Time history at YPT in 330° directions.

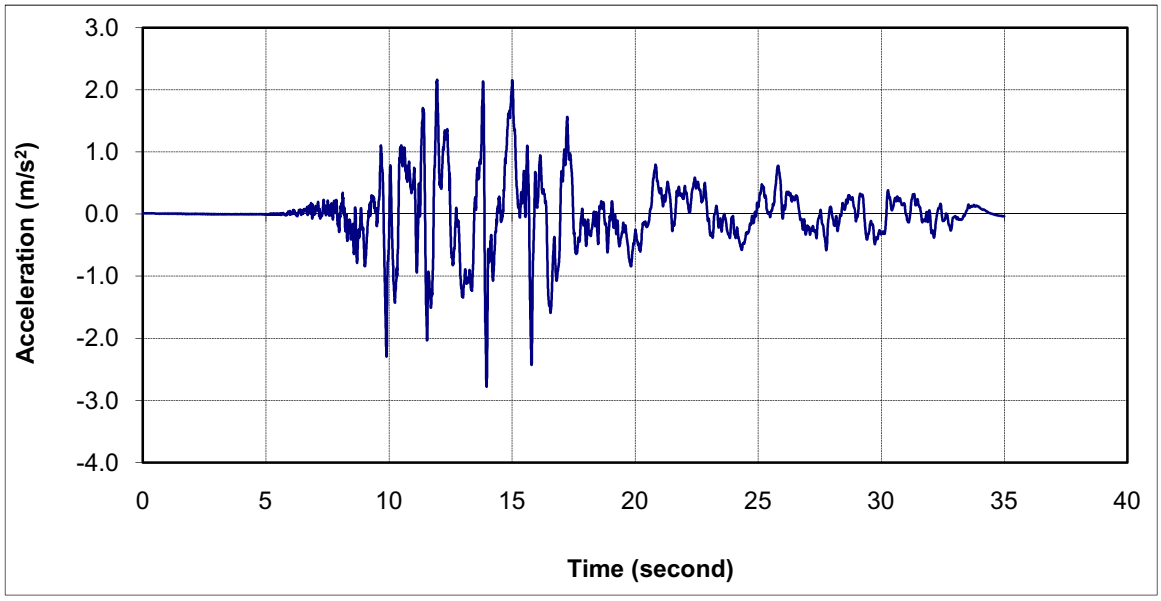


Figure K.3. Time history at YPT in 0° directions.

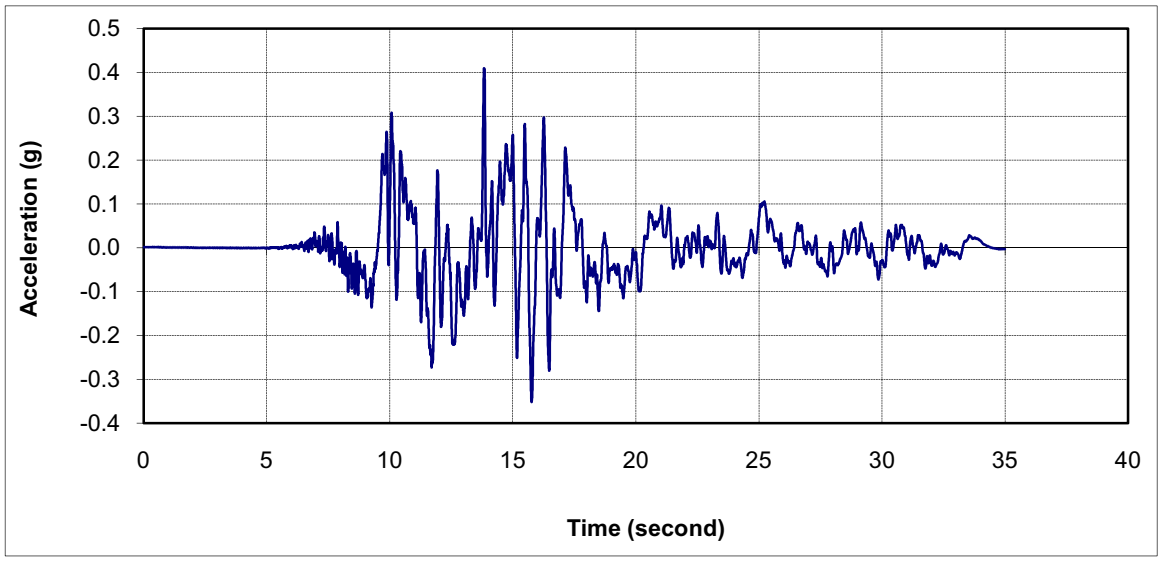


Figure K.4. Time history adjusted to 0.4g.

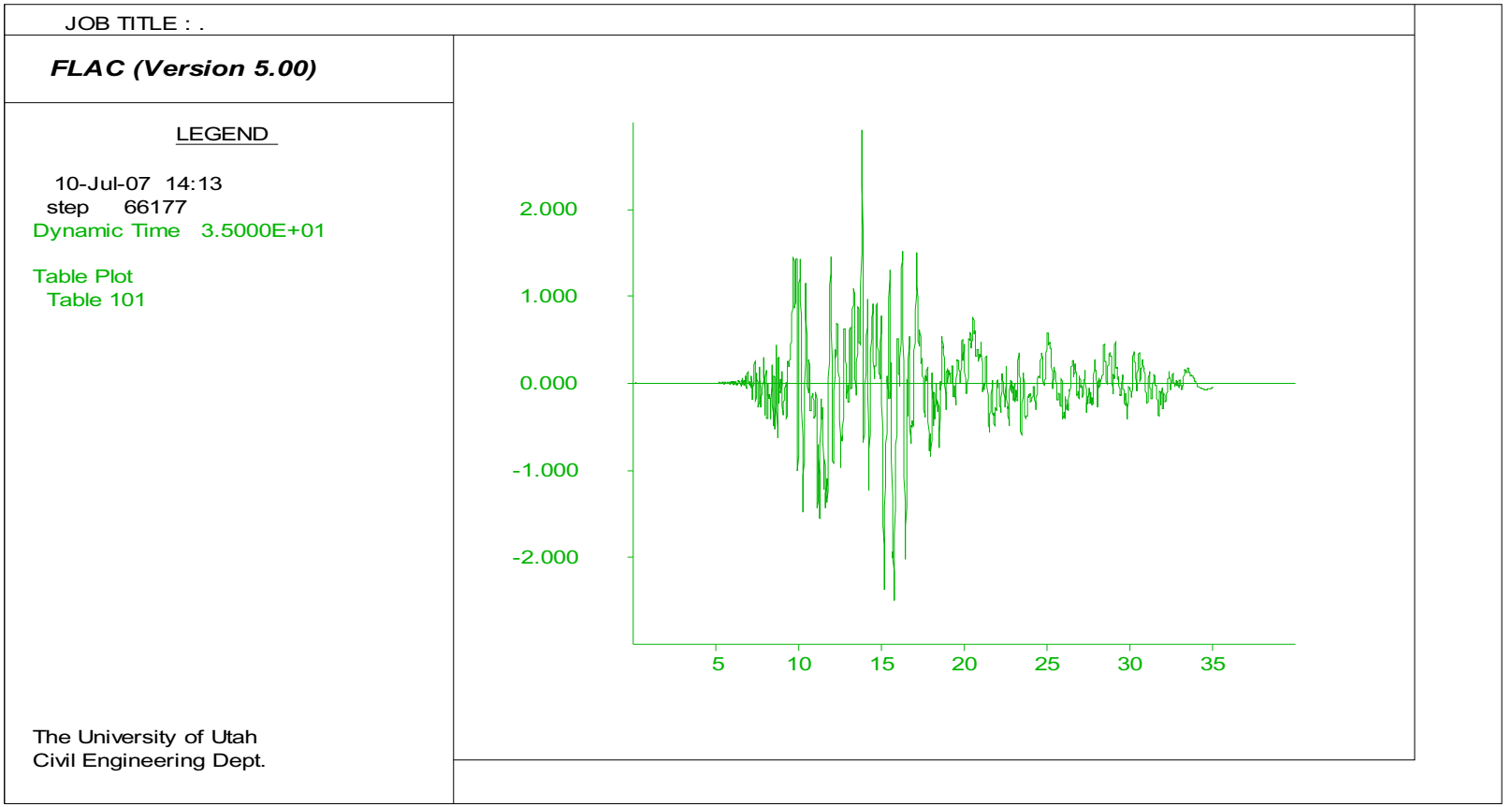


Figure K.5. Time history input for FLAC model (Y axis in m/s^2 and X axis in seconds).

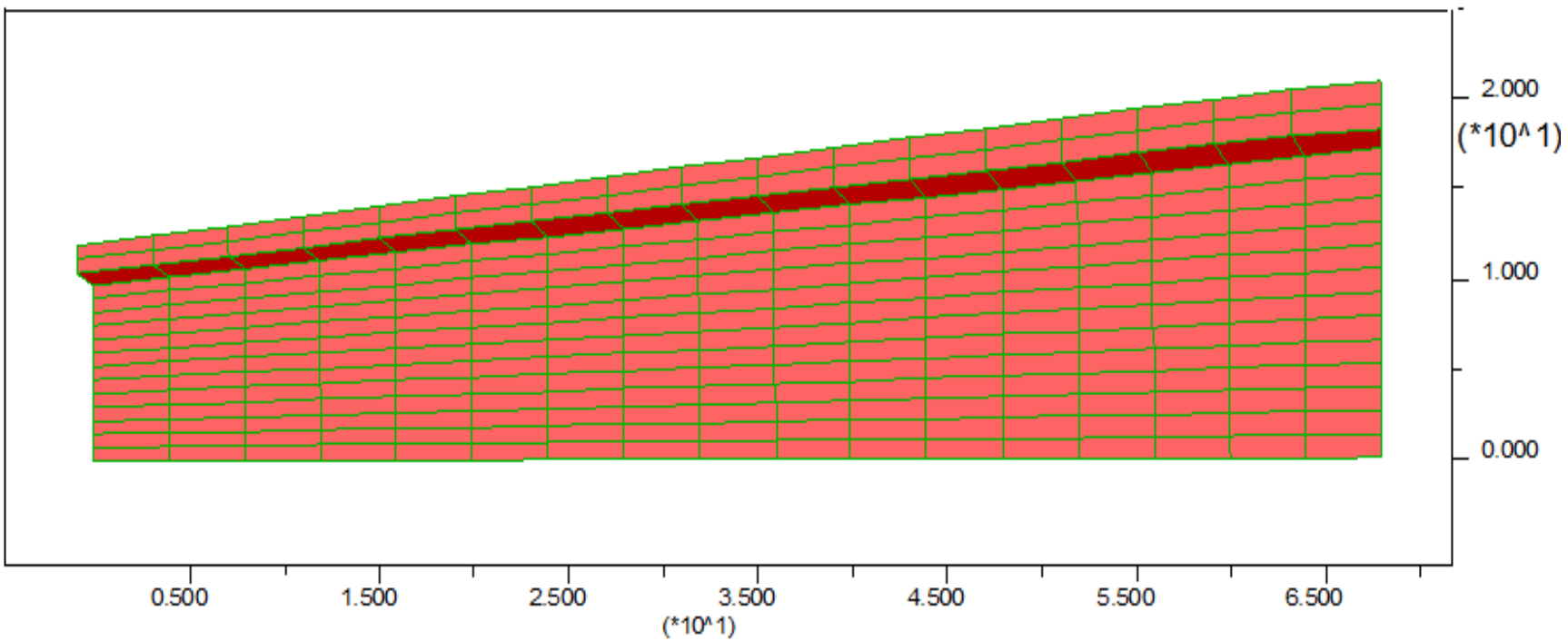


Figure K.6. Model design mesh (Y axis in m/s^2 and X axis in seconds).

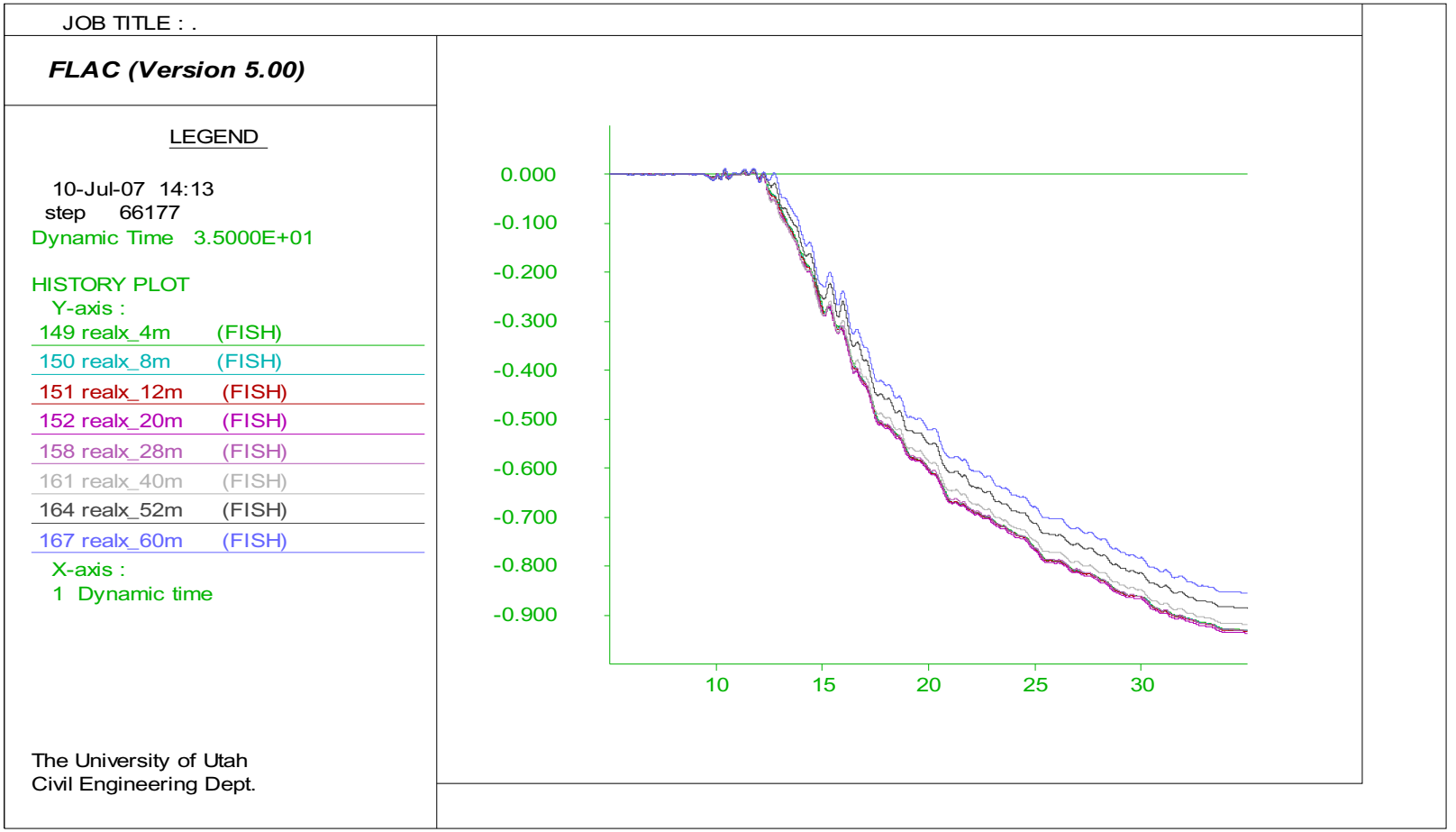


Figure K.7. Model later spreading prediction (Y axis in meter and X axis in seconds).

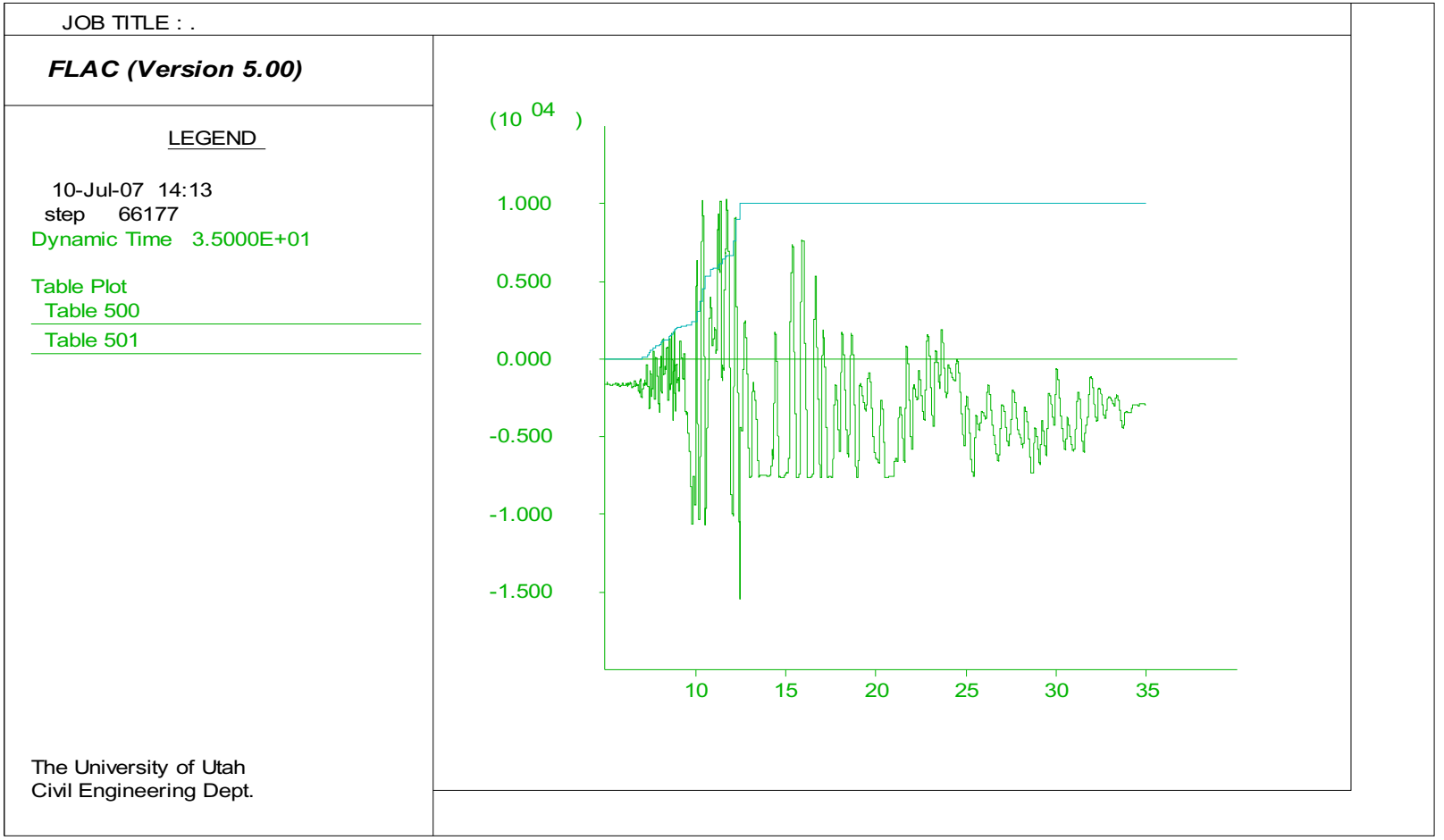


Figure K.8. Model pore water generation: Shear stress (Y axis in Pa) and r_u (Y axis multiplied by 1000) vs. time (X axis in seconds).

APPENDIX L

WILDLIFE SITE DATA

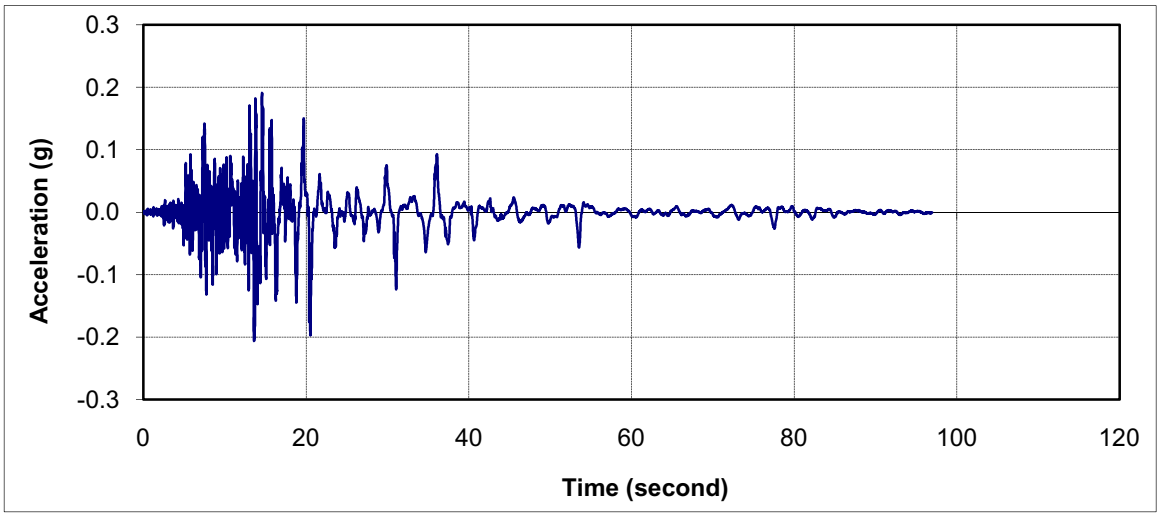


Figure L.1. Time history in 0° direction, Wildlife

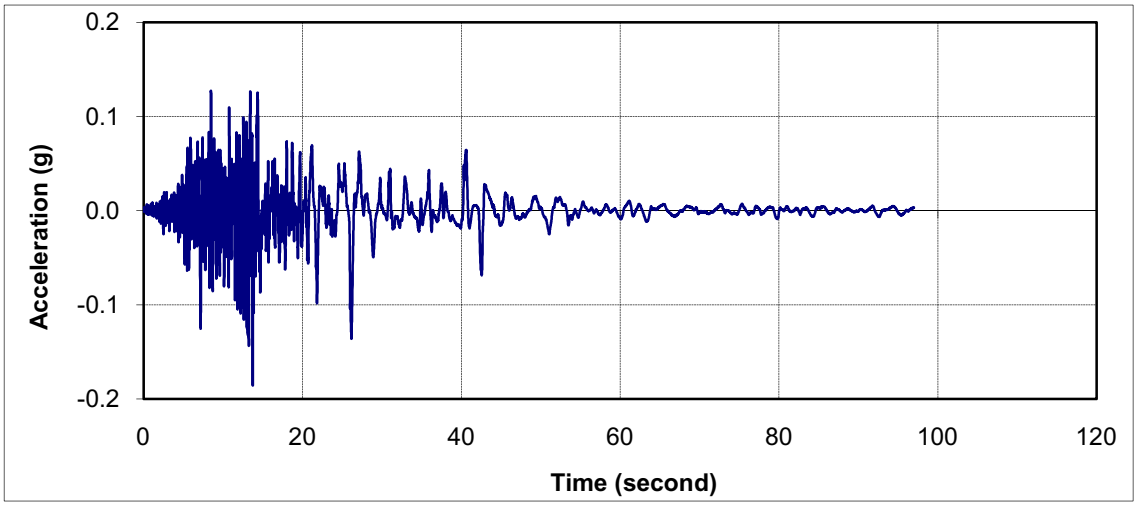


Figure L.2. Time history in 90° direction to North, Wildlife

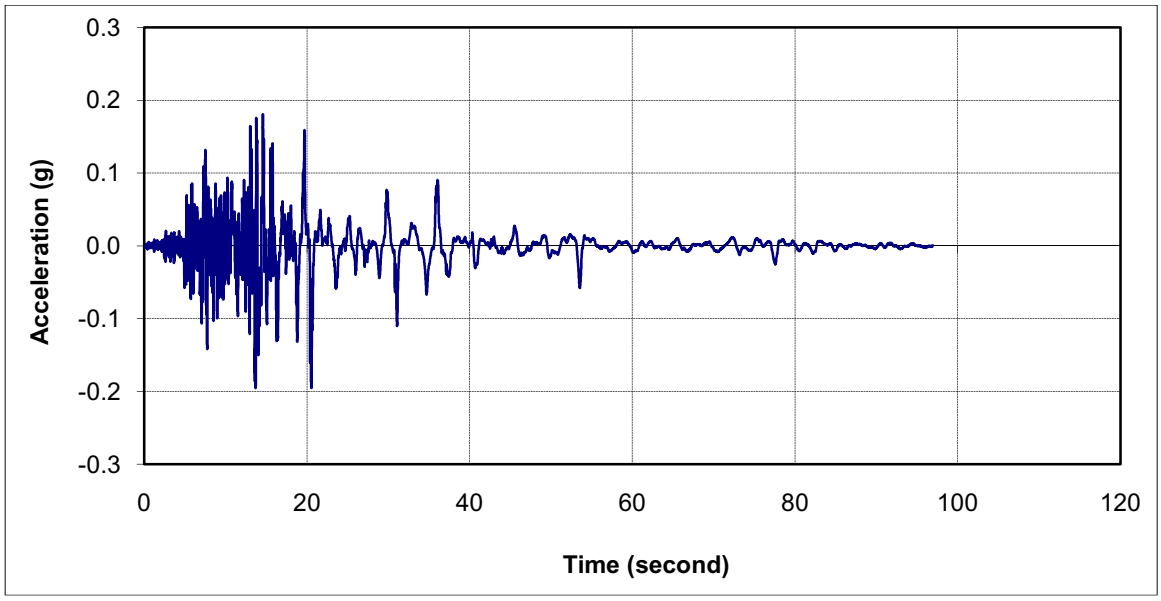


Figure L.3. Time history in 15° direction to North, Wildlife

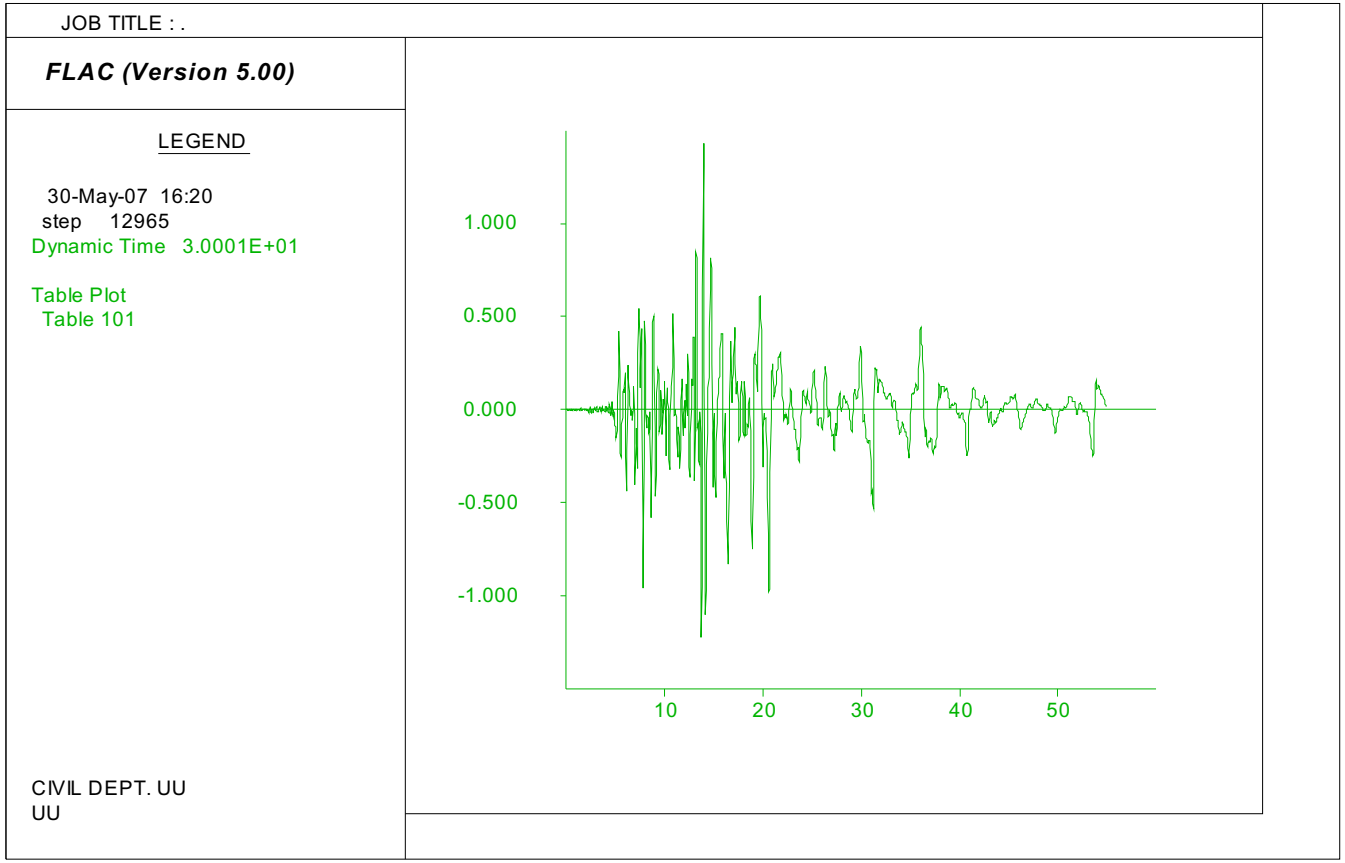


Figure L.4. Time history developed for FLAC Model, Wildlife (Y axis in m/s^2 and X axis in second)

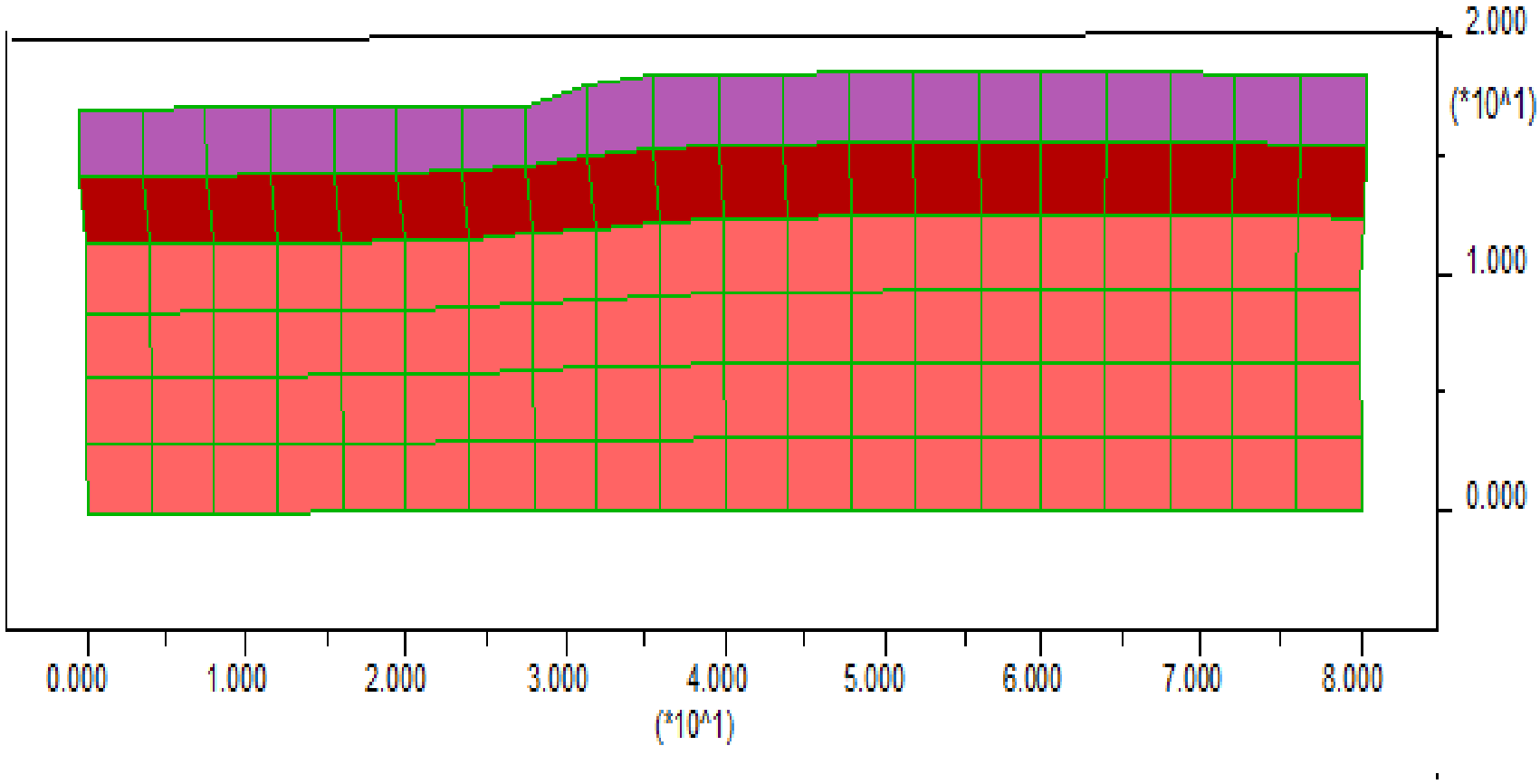


Figure L.5. Model soil properties change after liquefaction loaded (Y axis in m/s^2 and X axis in second)

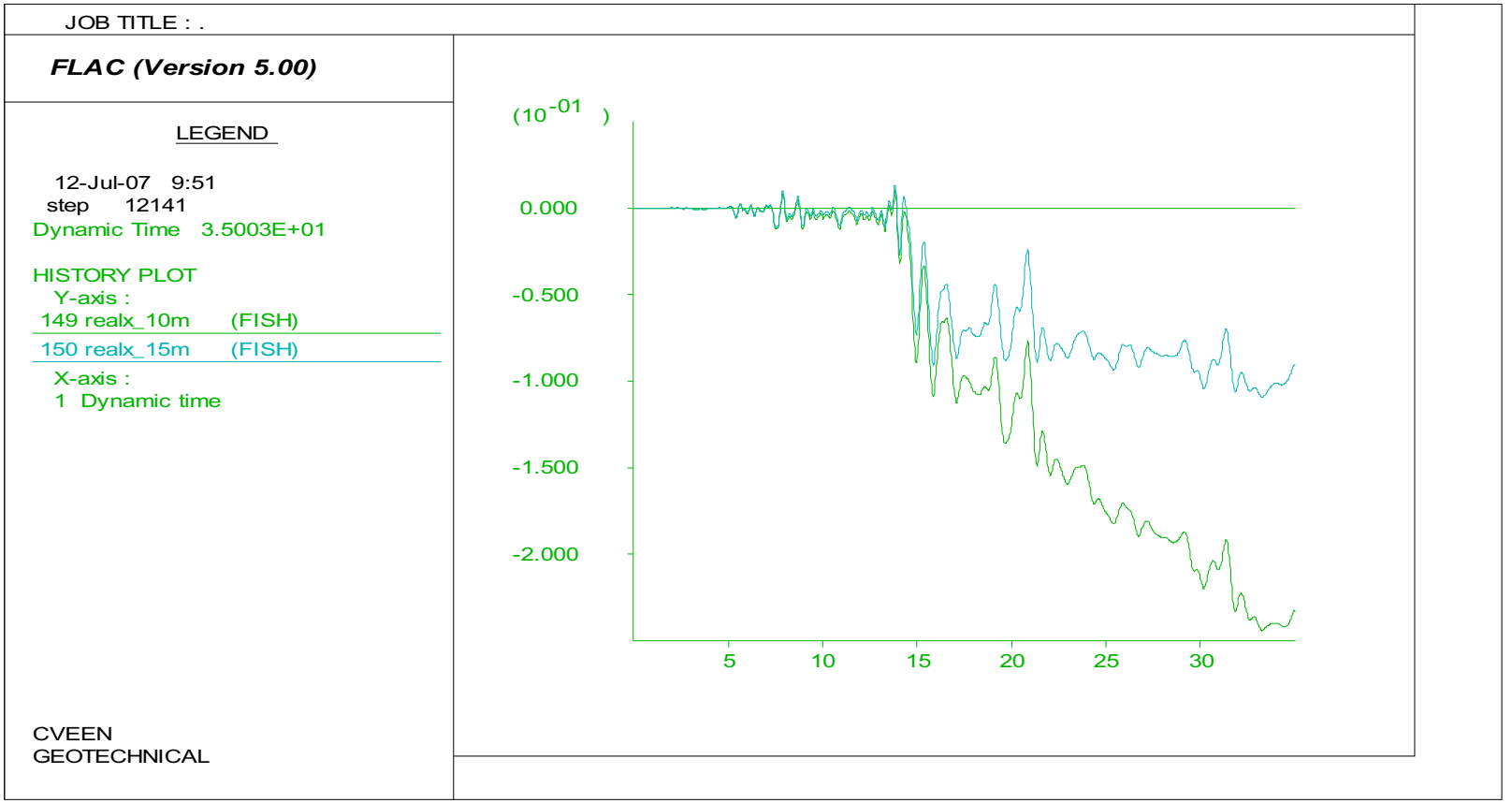


Figure L.6. Model prediction of lateral spread, Wildlife (Y axis in meter and X axis in second)

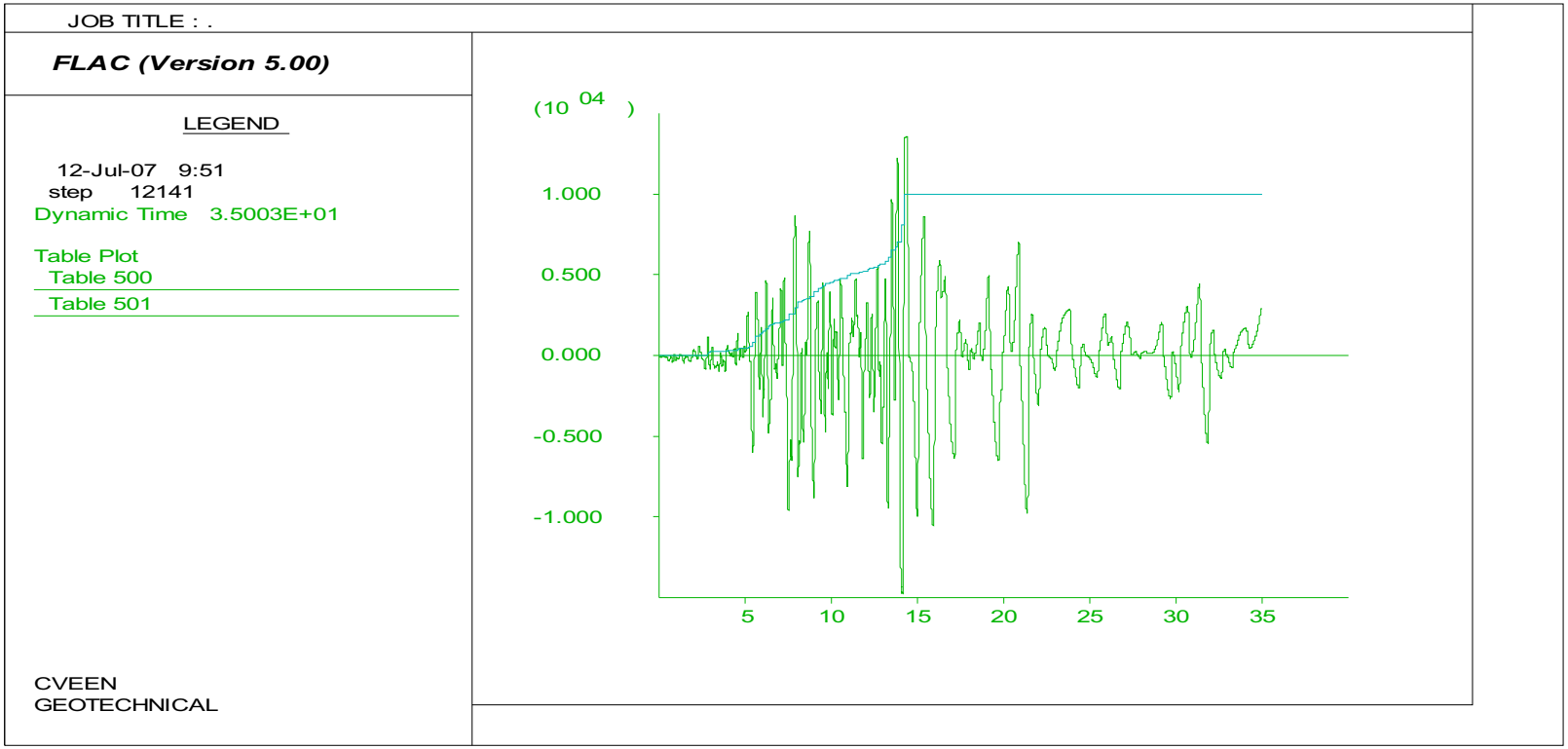


Figure L.7. Predicted liquefaction time history, Wildlife: Shear stress (Y axis in Pa) and r_u (Y axis multiplied by 1000) vs. time (X axis in seconds).

APPENDIX M

IDAHO WHISKEY SPRINGS SITE DATA

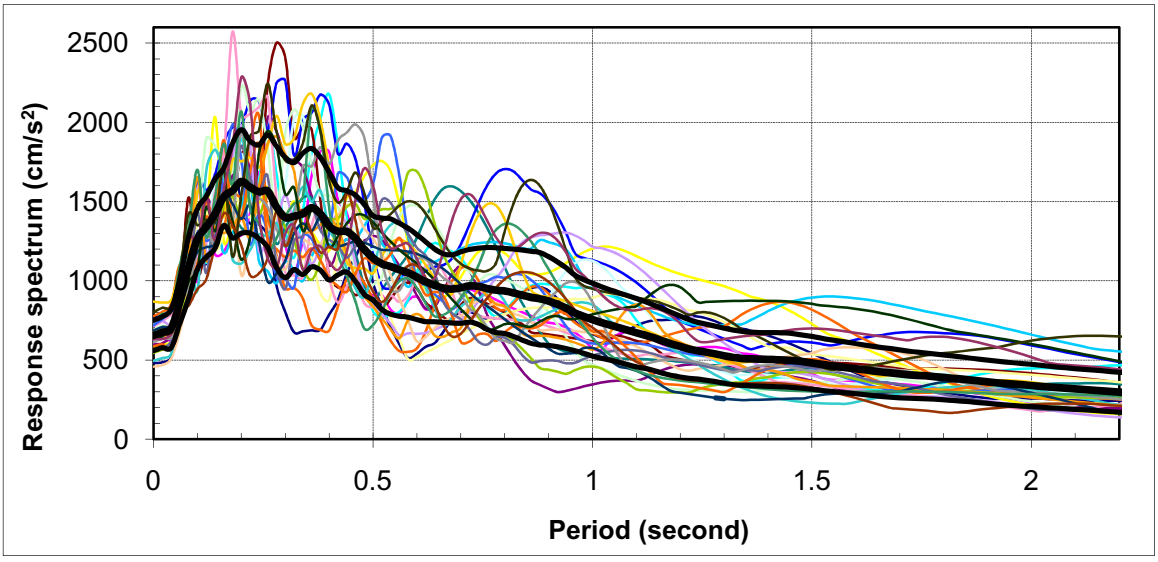


Figure M.1. Response spectra of generated thirty motions

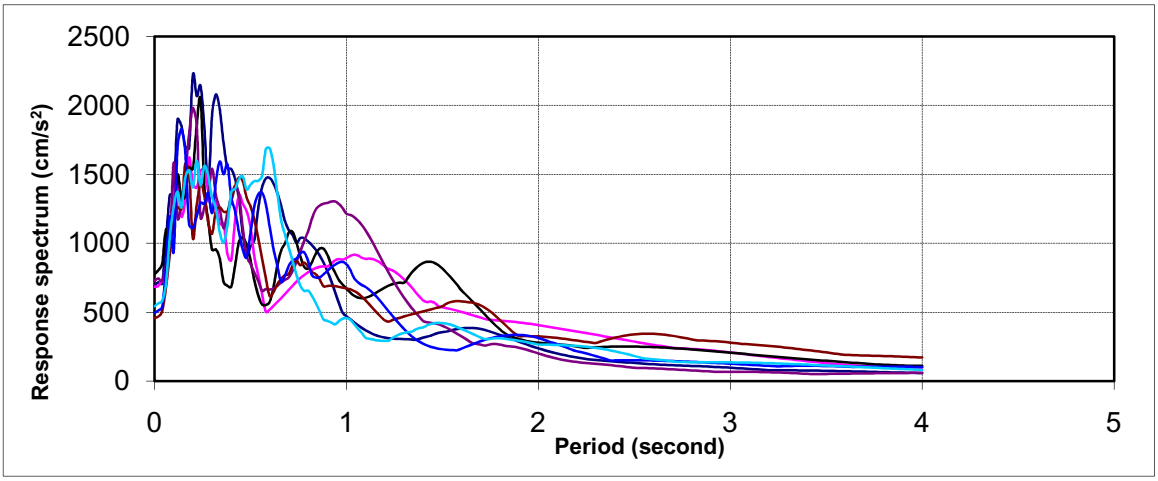


Figure M.2. Response spectra of selected seven motions

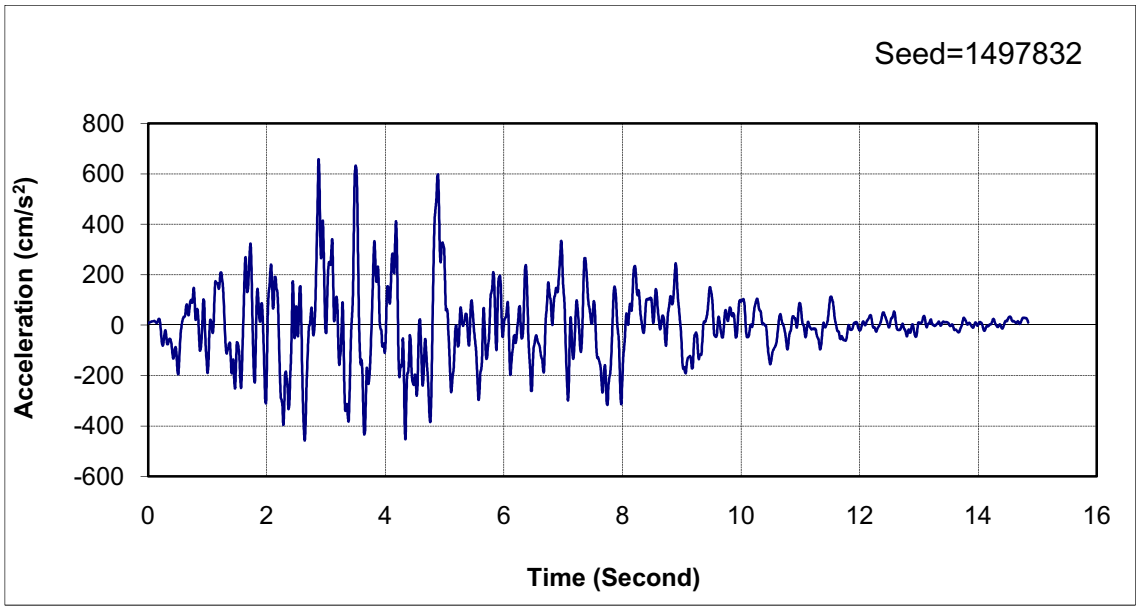


Figure M.3. IDAHO WHISKEY SPRINGS section model selected motion 1

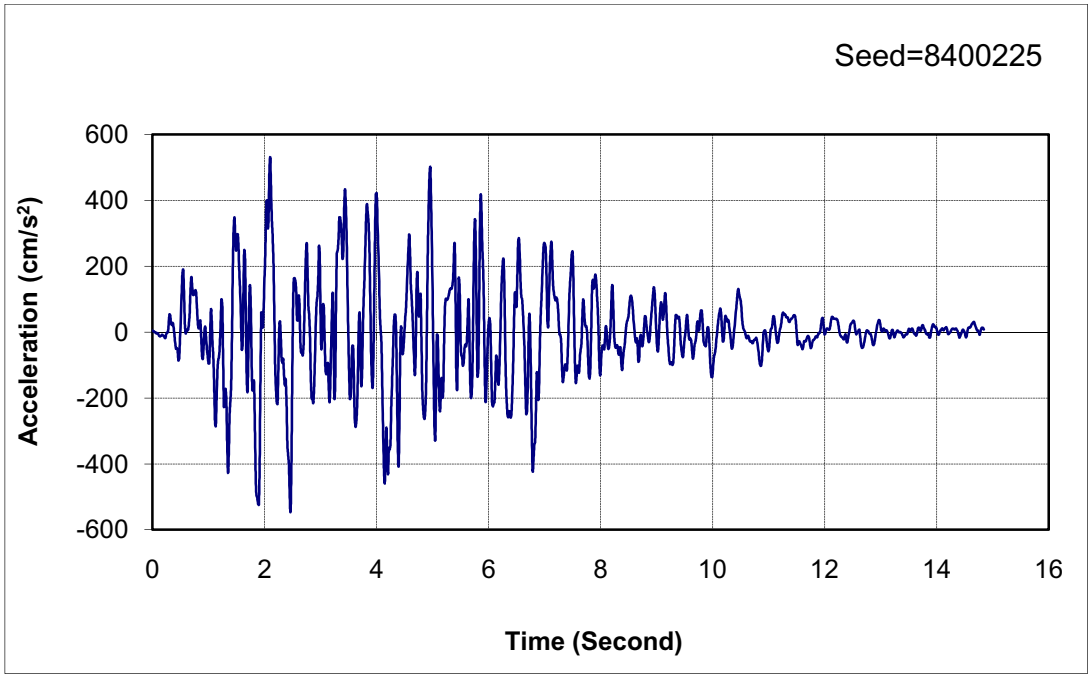


Figure M.4. IDAHO WHISKEY SPRINGS section model selected motion 2

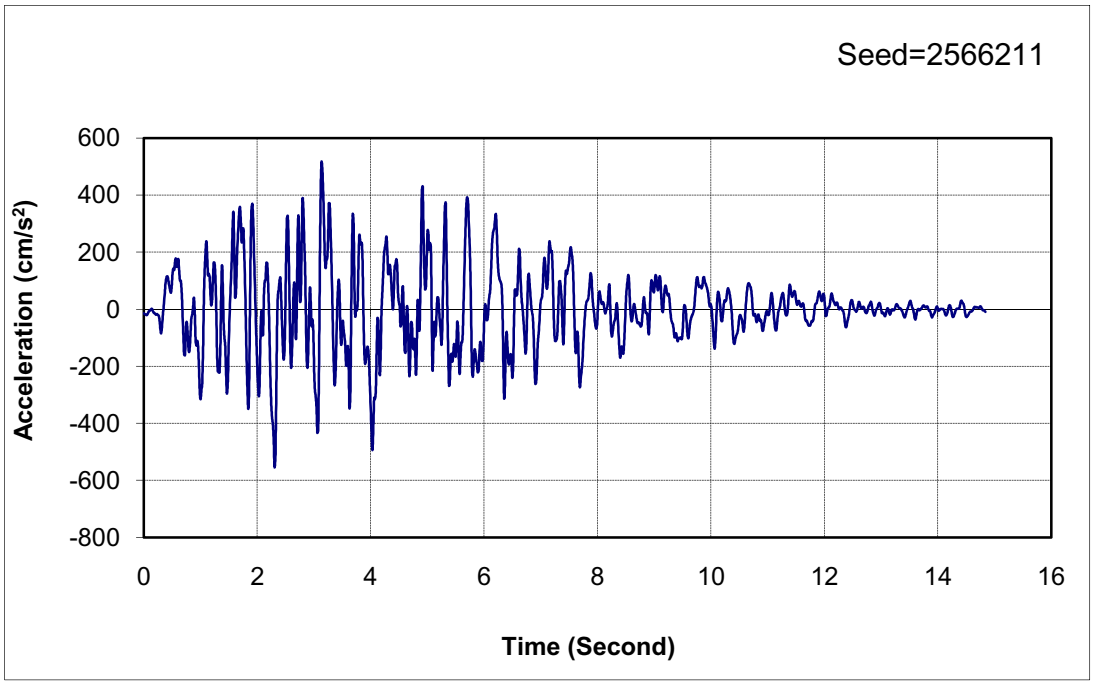


Figure M.5. IDAHO WHISKEY SPRINGS section model selected motion 3

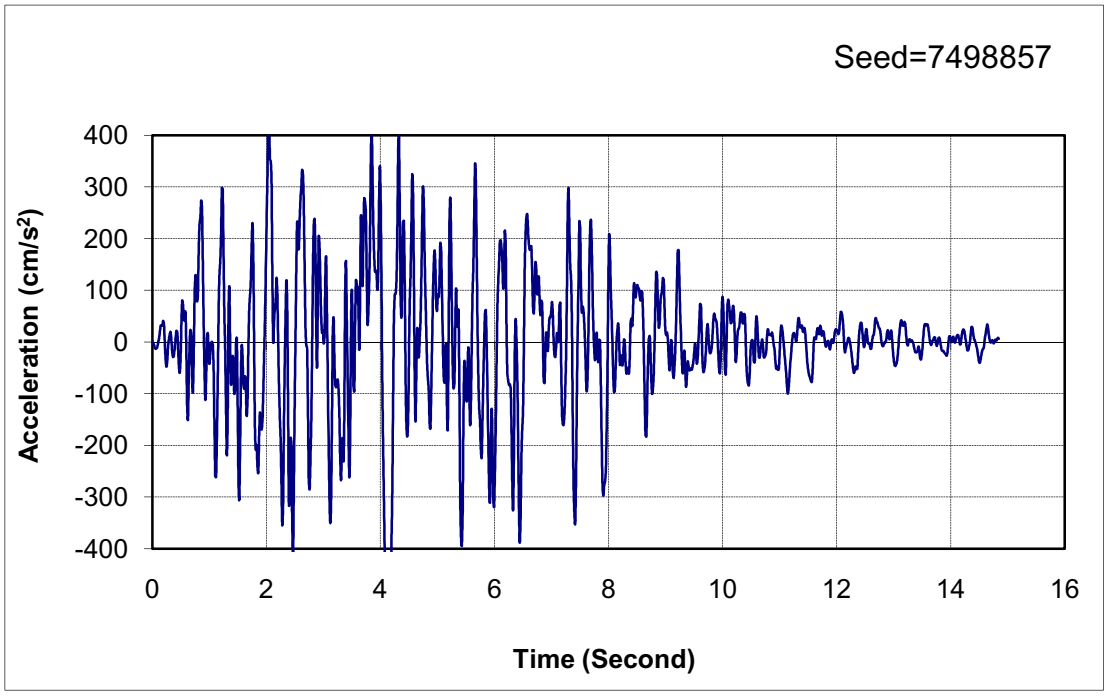


Figure M.6. IDAHO WHISKEY SPRINGS section model selected motion 4

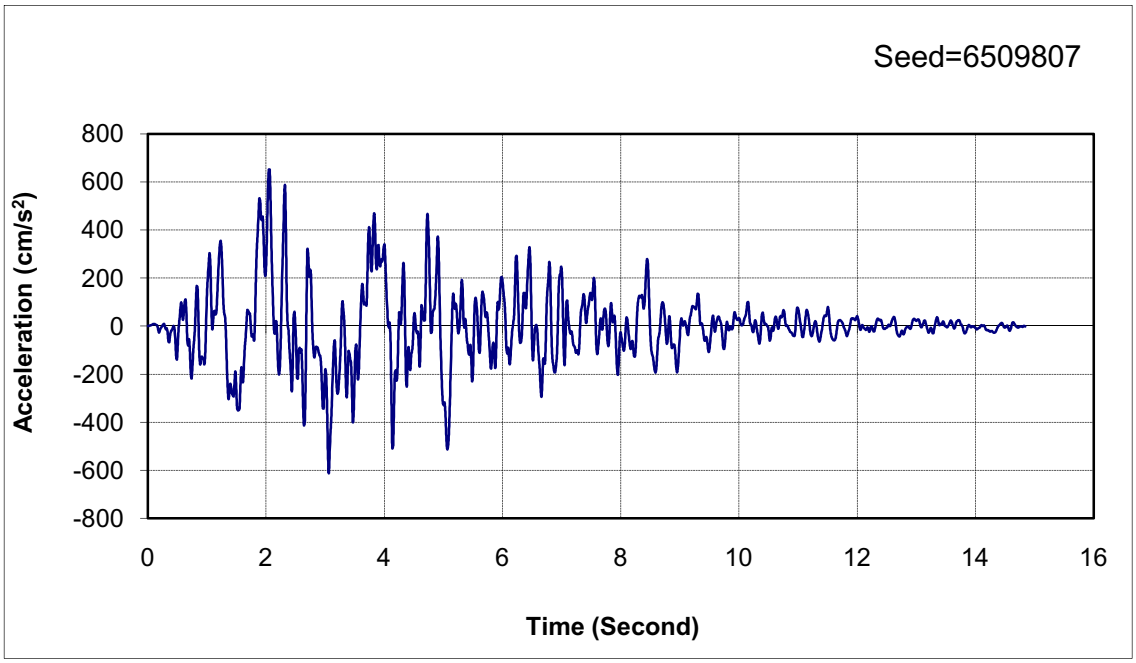


Figure M.7. IDAHO WHISKEY SPRINGS section model selected motion 5

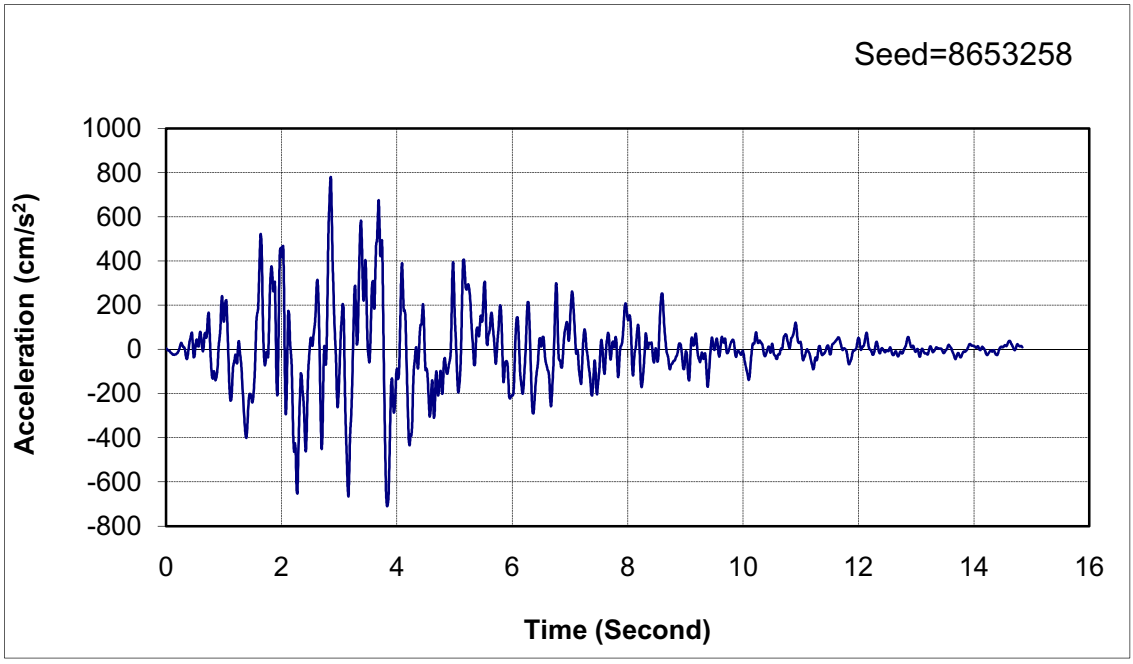


Figure M.8. IDAHO WHISKEY SPRINGS section model selected motion 6

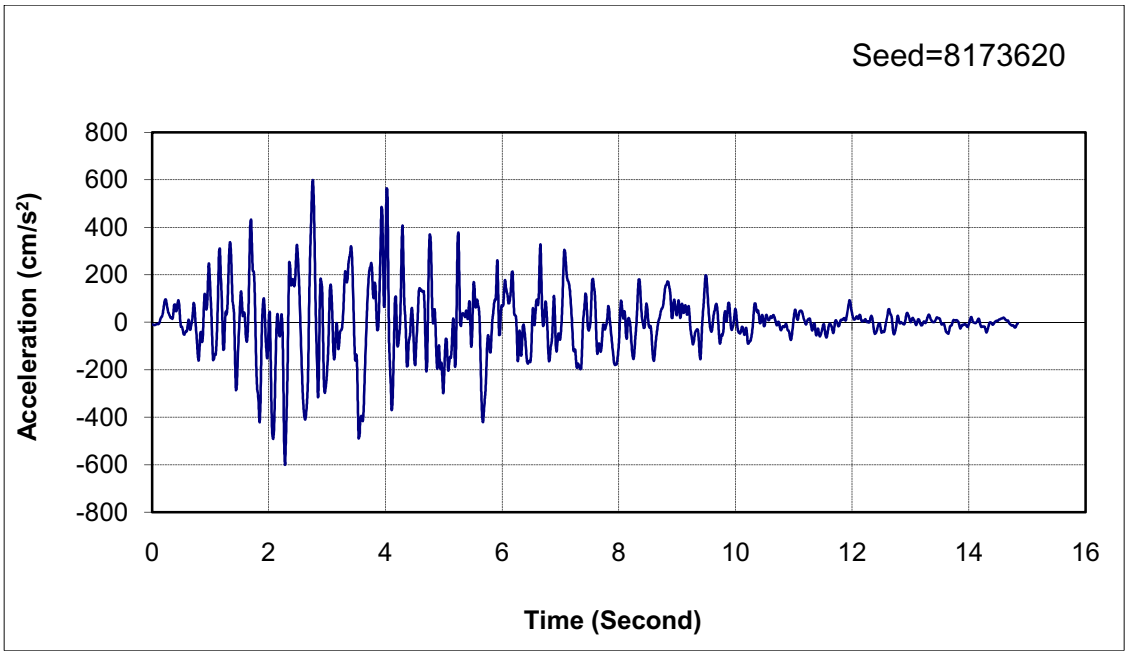


Figure M.9. IDAHO WHISKEY SPRINGS section model selected motion 7

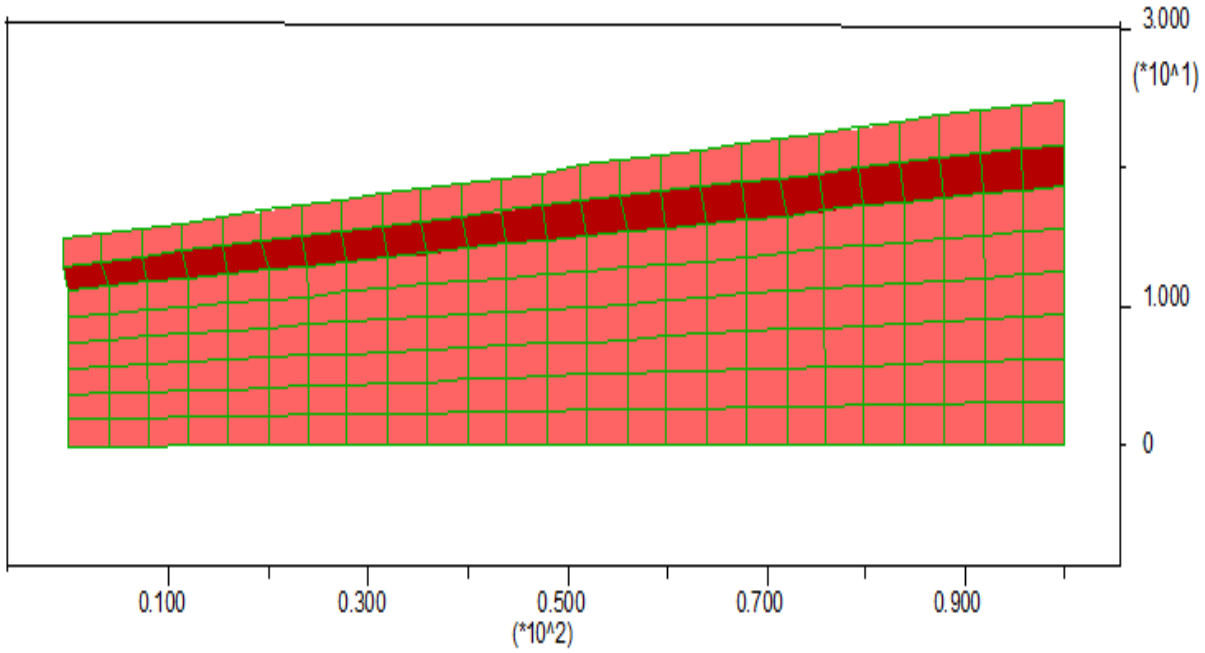


Figure M.10. Model design mesh (Y axis in m/s^2 and X axis in second)

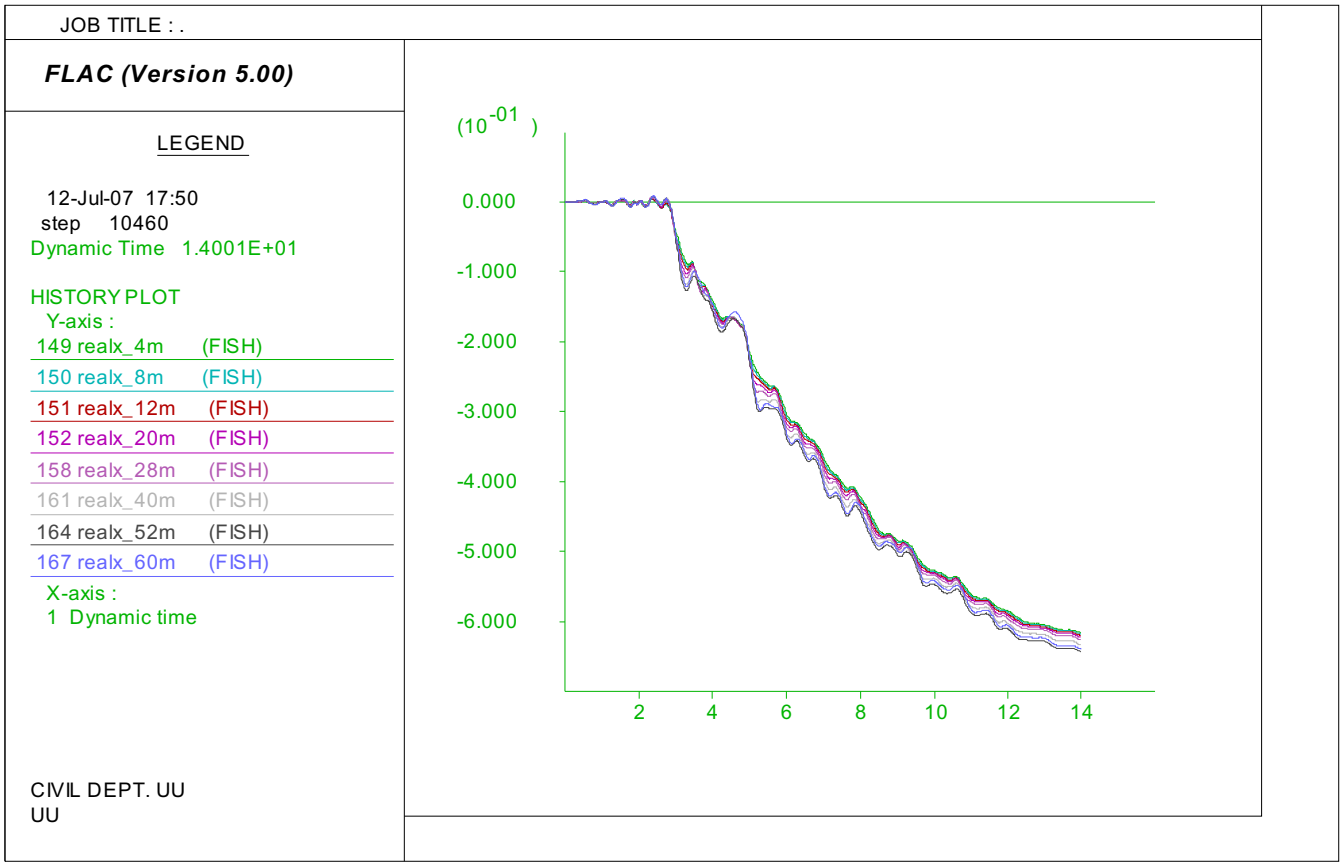


Figure M.11. Model later spreading prediction loaded by motion 1 with residual strength ratio of 0.2 (Y axis in meter and X axis in second)

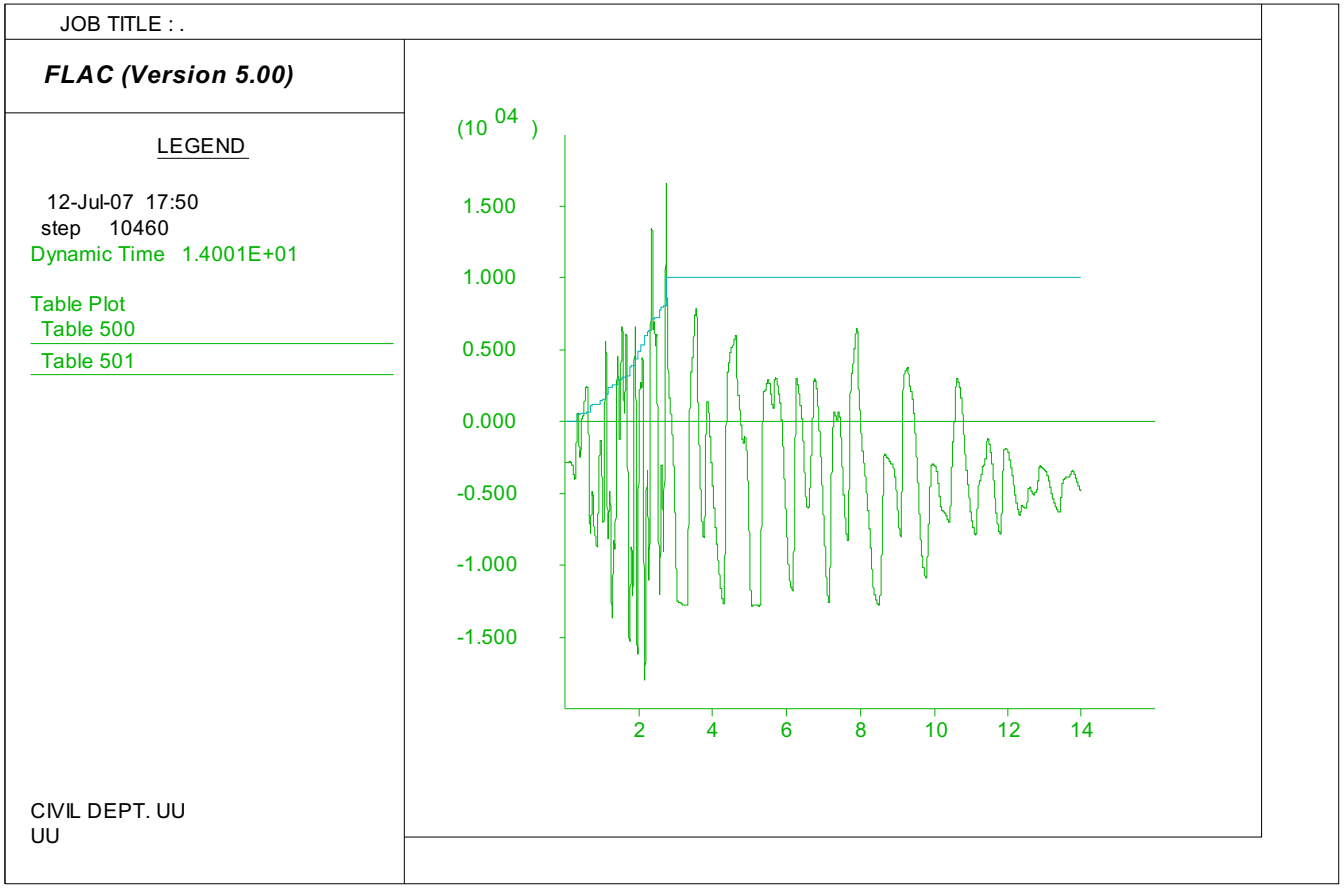


Figure M.12. Model pore water generation history loaded by motion 1 with residual strength ratio of 0.2: Shear stress (Y axis in Pa) and r_u (Y axis multiplied by 1000) vs. time (X axis in seconds).

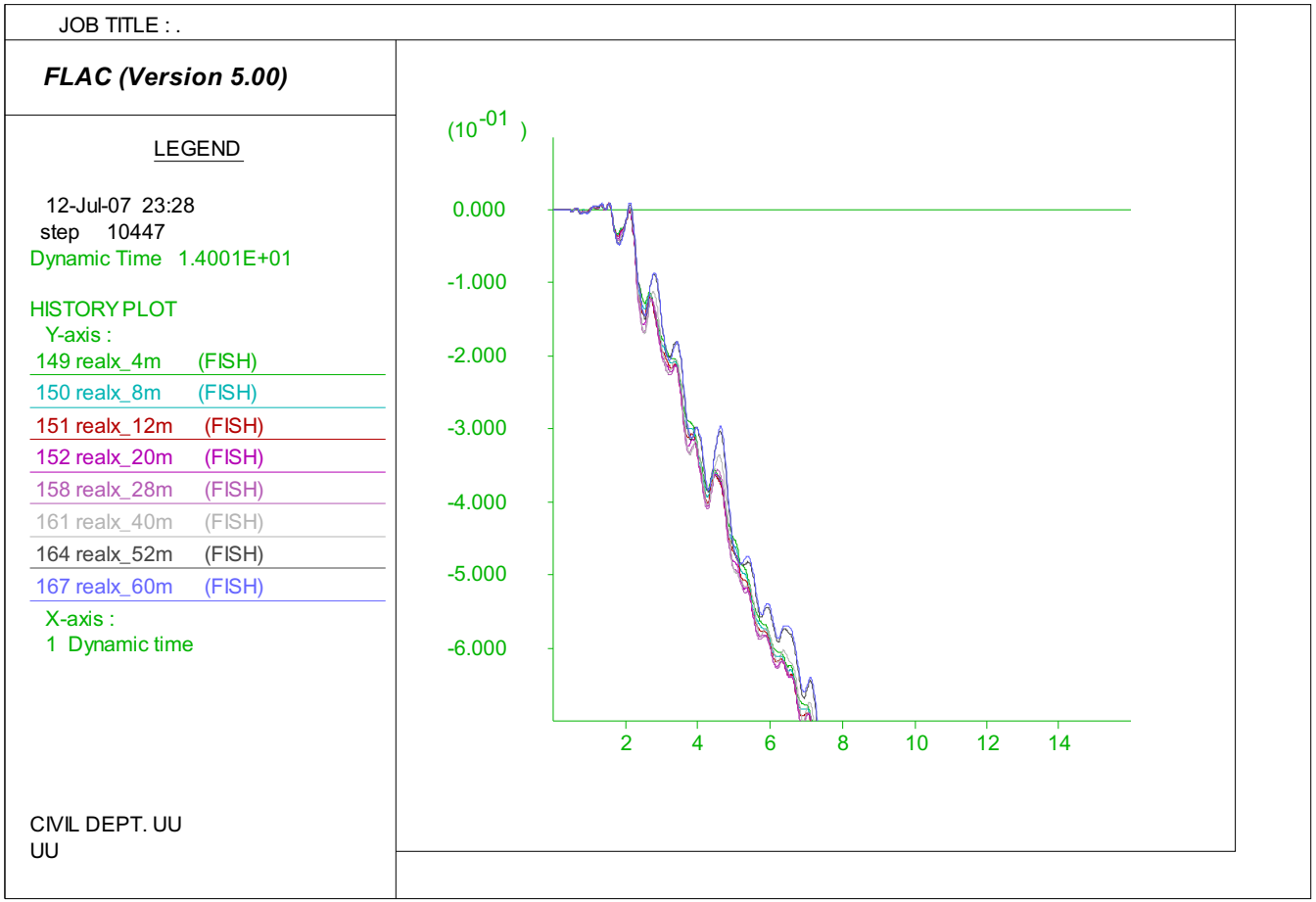


Figure M.13. Model later spreading prediction loaded by motion 2 with residual strength ratio of 0.2 (Y axis in meter and X axis in second)

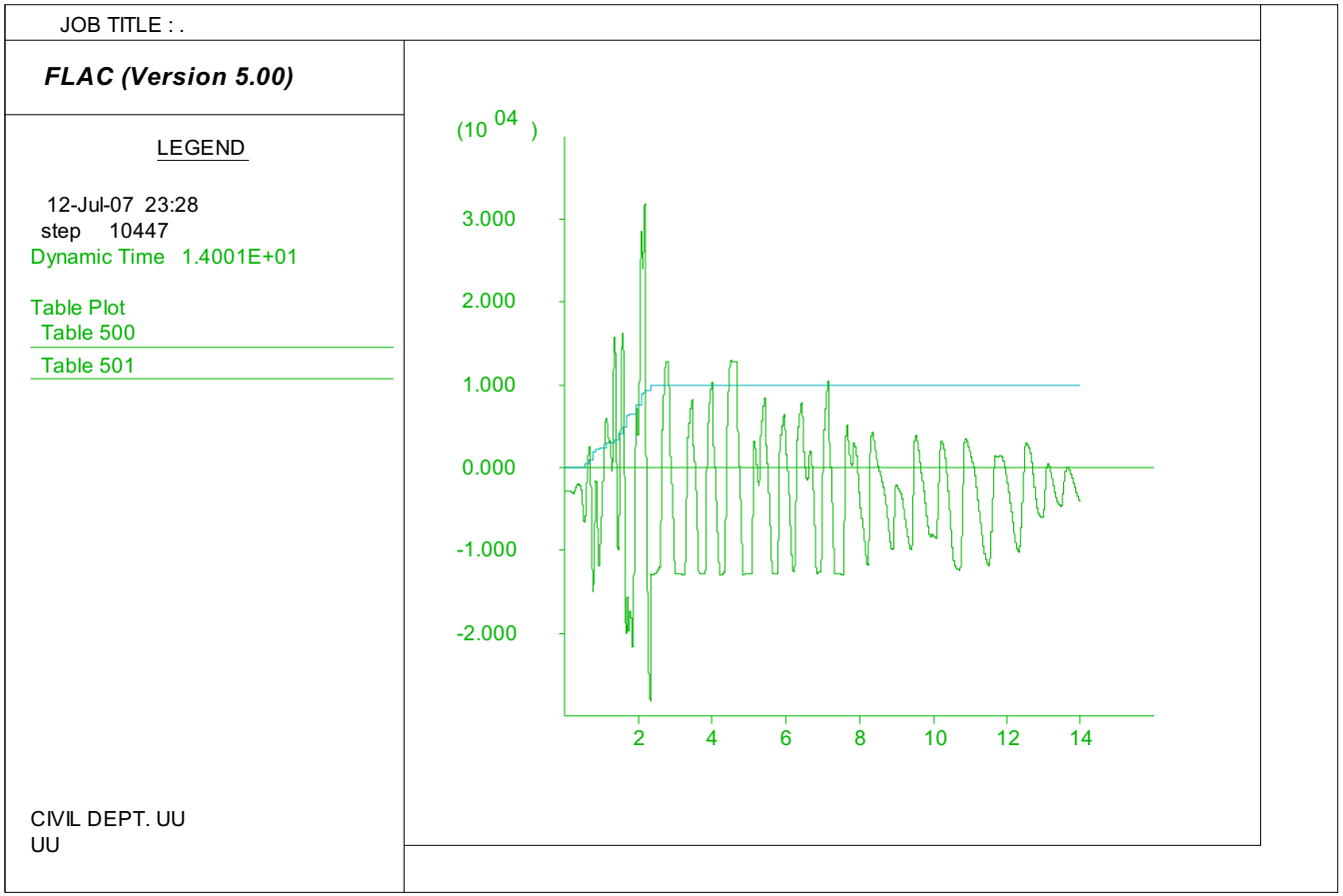


Figure M.14. Model pore water generation history loaded by motion 2 with residual strength ratio of 0.2: Shear stress (Y axis in Pa) and r_u (Y axis multiplied by 1000) vs. time (X axis in seconds).

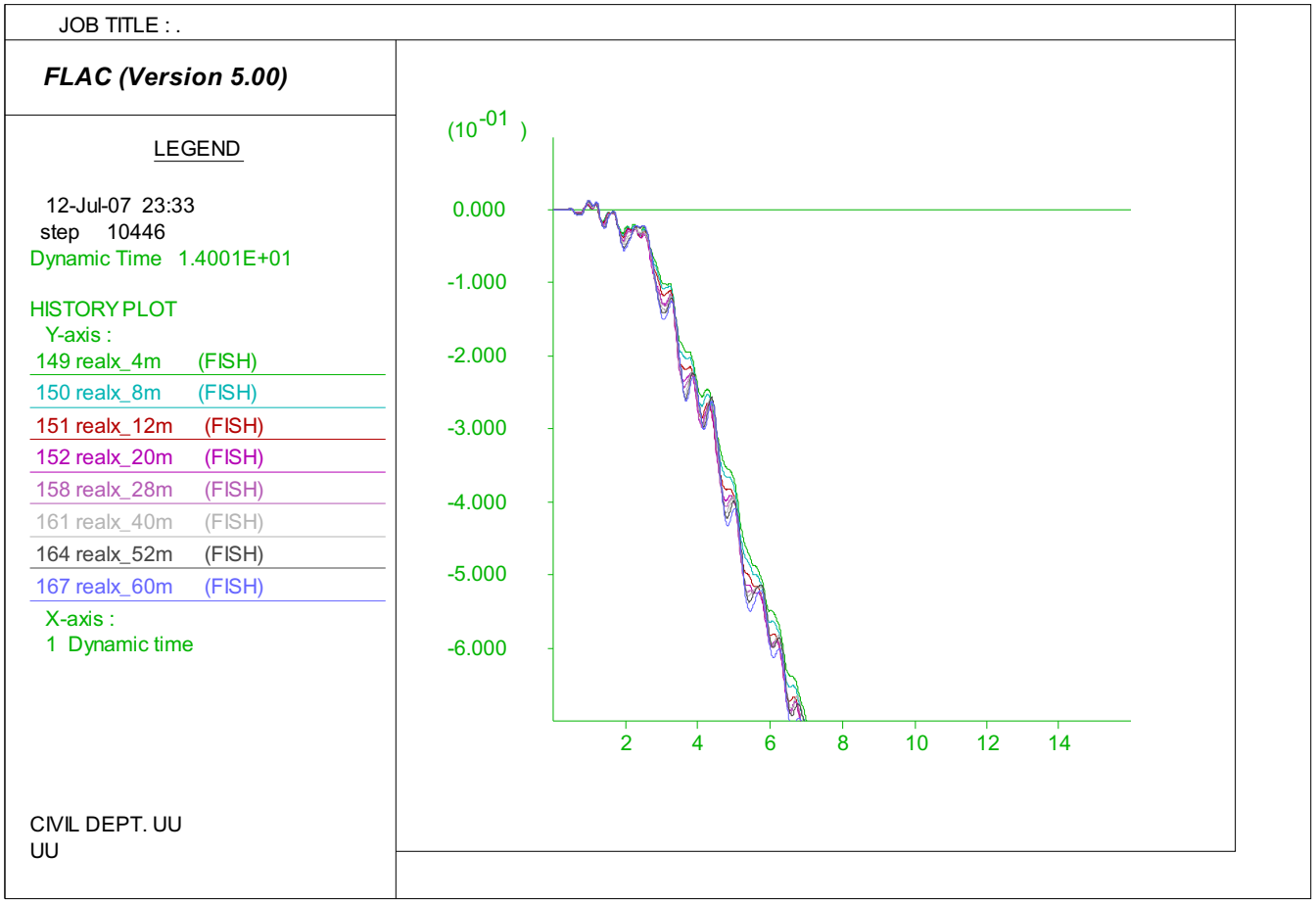


Figure M.15. Model later spreading prediction loaded by motion 3 with residual strength ratio of 0.2 (Y axis in meter and X axis in second)

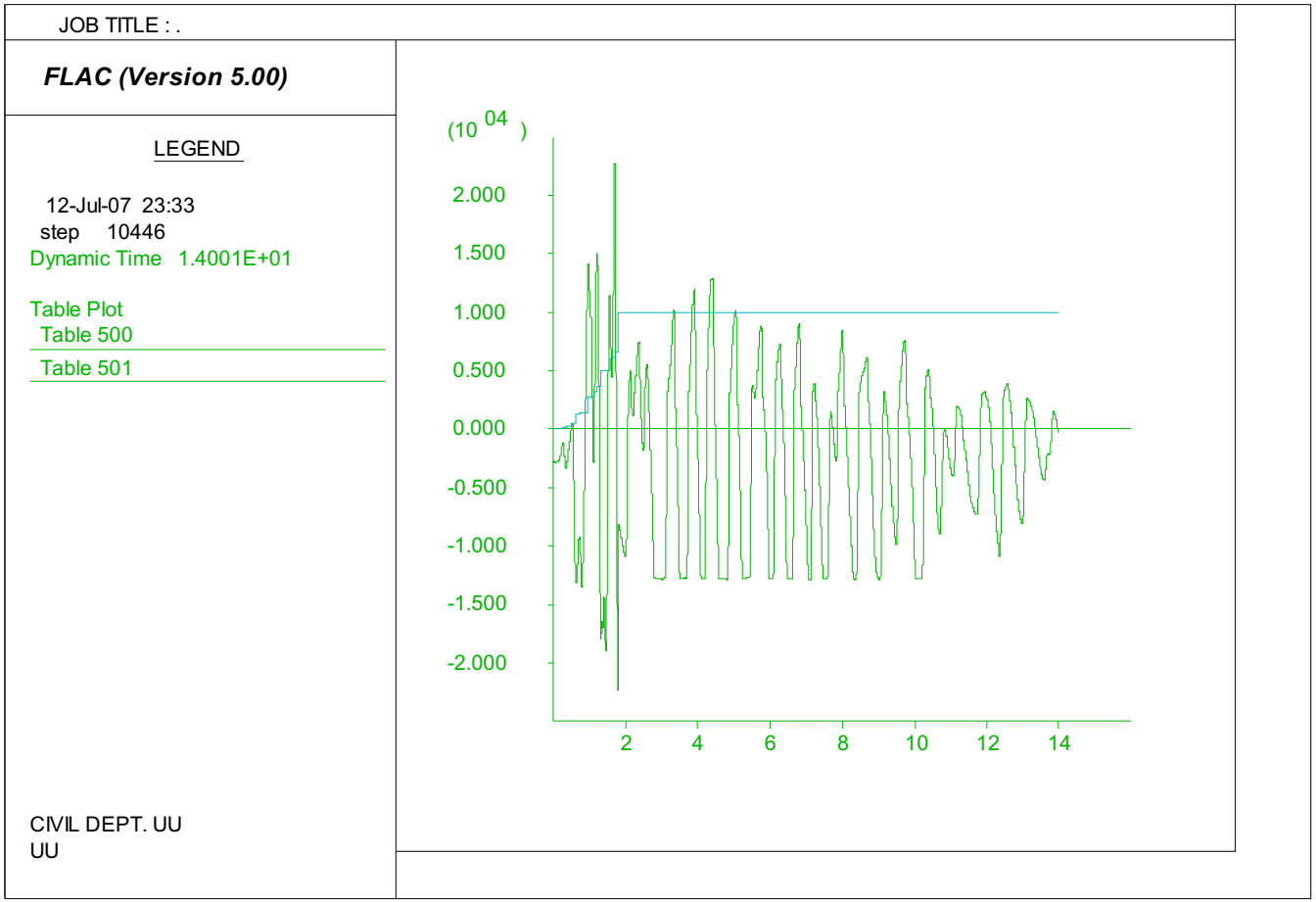


Figure M.16. Model pore water generation history loaded by motion 3 with residual strength ratio of 0.2: Shear stress (Y axis in Pa) and r_u (Y axis multiplied by 1000) vs. time (X axis in seconds).

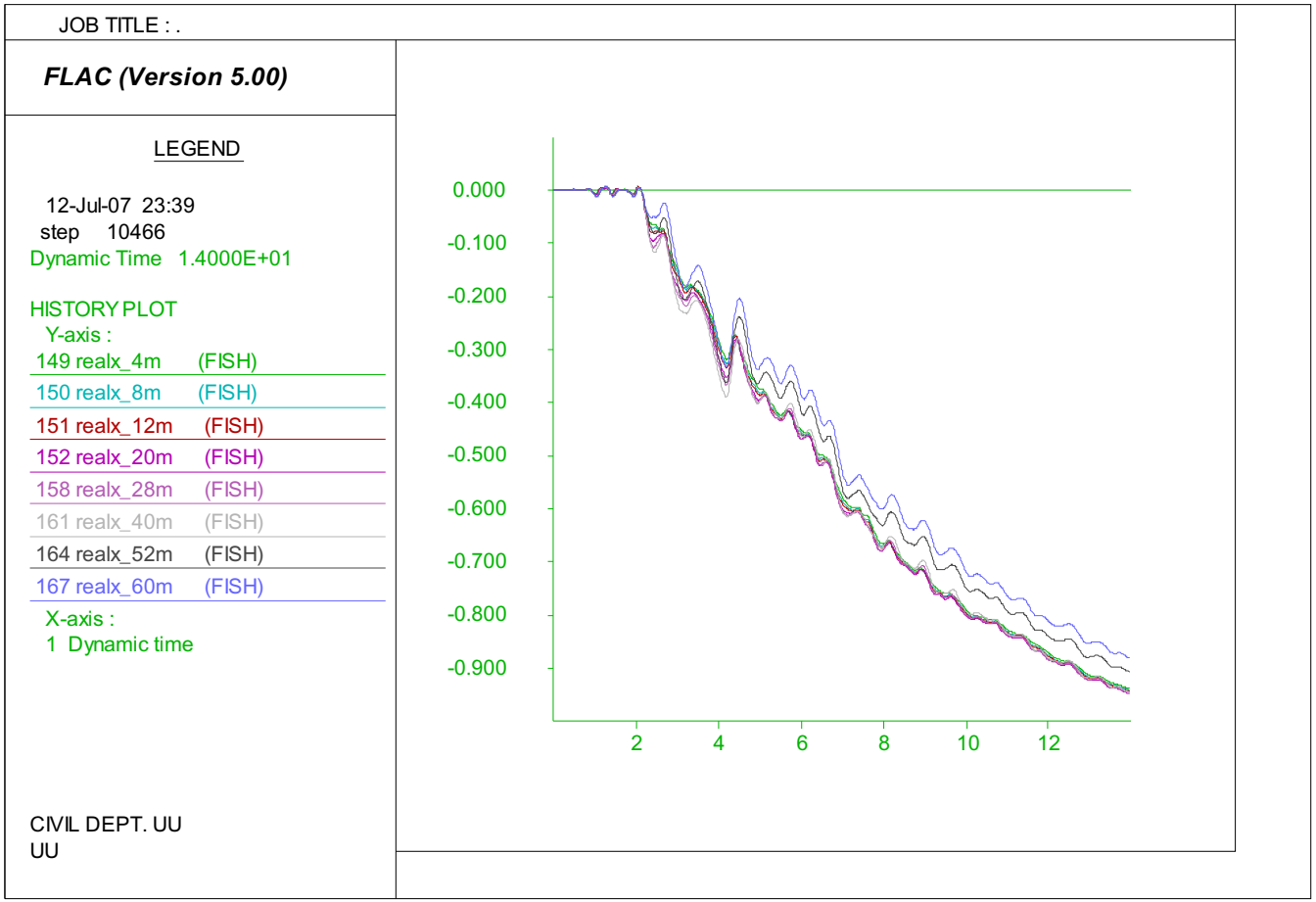


Figure M.17. Model later spreading prediction loaded by motion 4 with residual strength ratio of 0.2 (Y axis in meter and X axis in second)

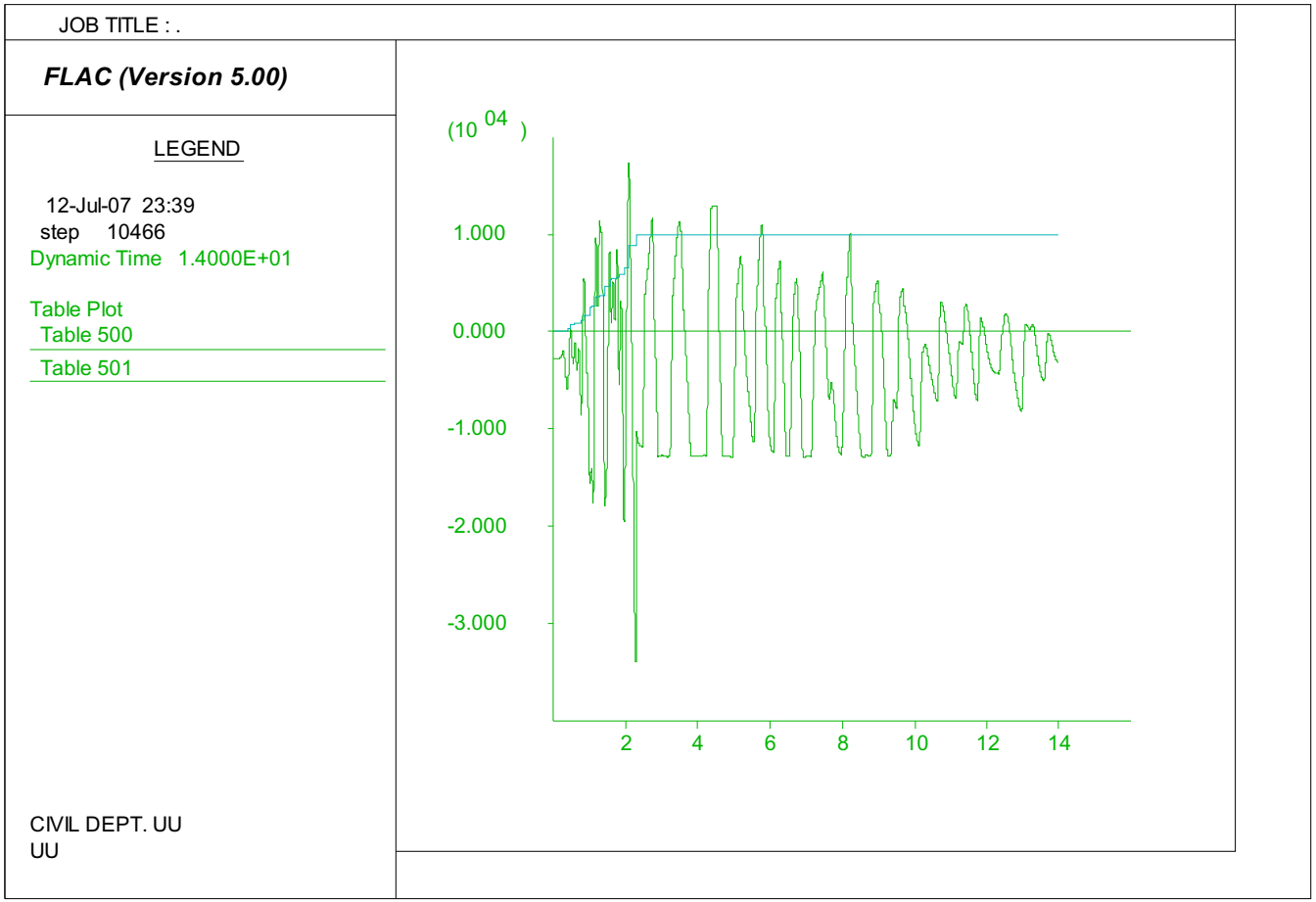


Figure M.18. Model pore water generation history loaded by motion 4 with residual strength ratio of 0.2: Shear stress (Y axis in Pa) and r_u (Y axis multiplied by 1000) vs. time (X axis in seconds).

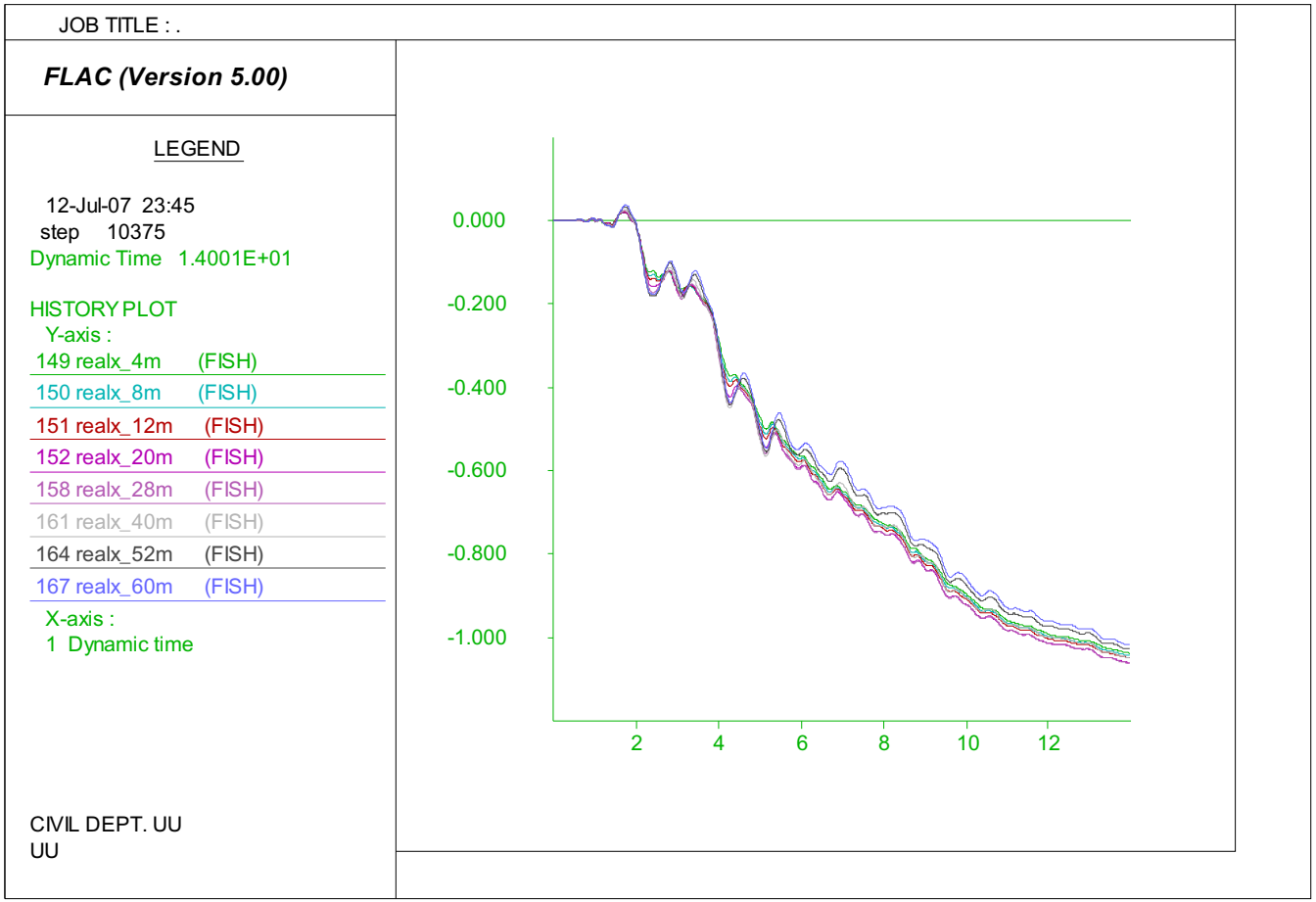


Figure M.19. Model later spreading prediction loaded by motion 5 with residual strength ratio of 0.2 (Y axis in meter and X axis in second)

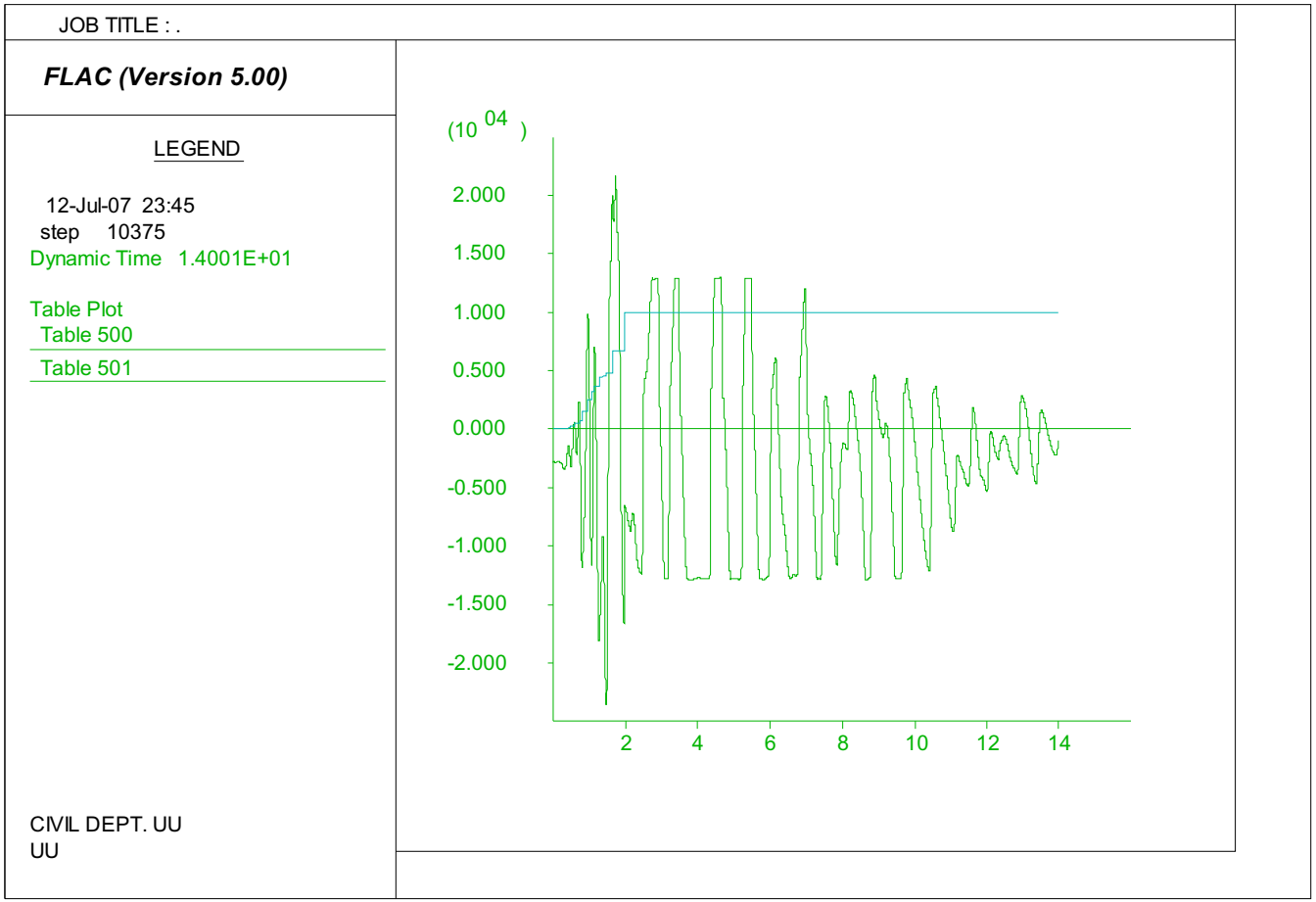


Figure M.20. Model pore water generation history loaded by motion 5 with residual strength ratio of 0.2: Shear stress (Y axis in Pa) and r_u (Y axis multiplied by 1000) vs. time (X axis in seconds).

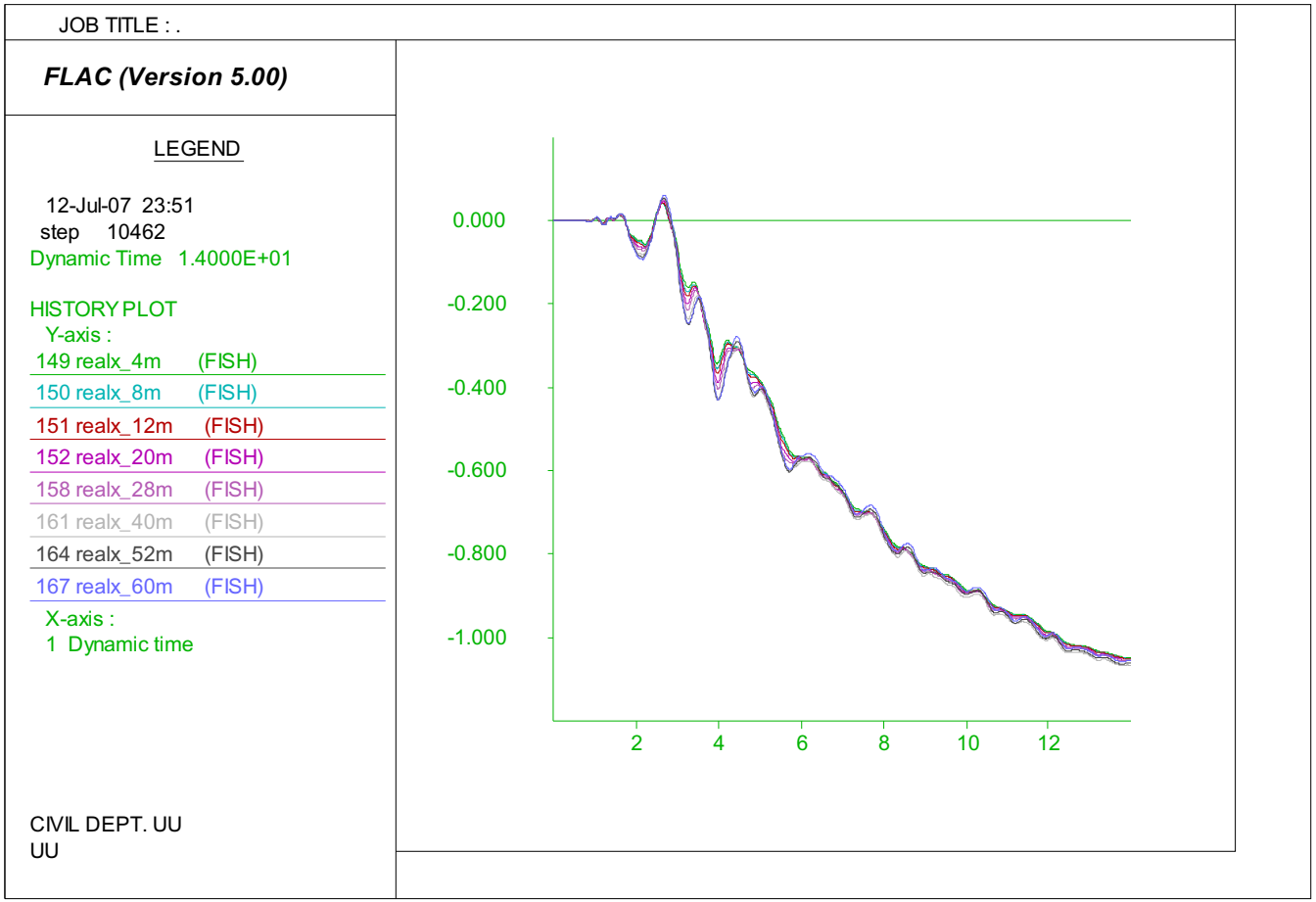


Figure M.21. Model later spreading prediction loaded by motion 6 with residual strength ratio of 0.2 (Y axis in meter and X axis in second)

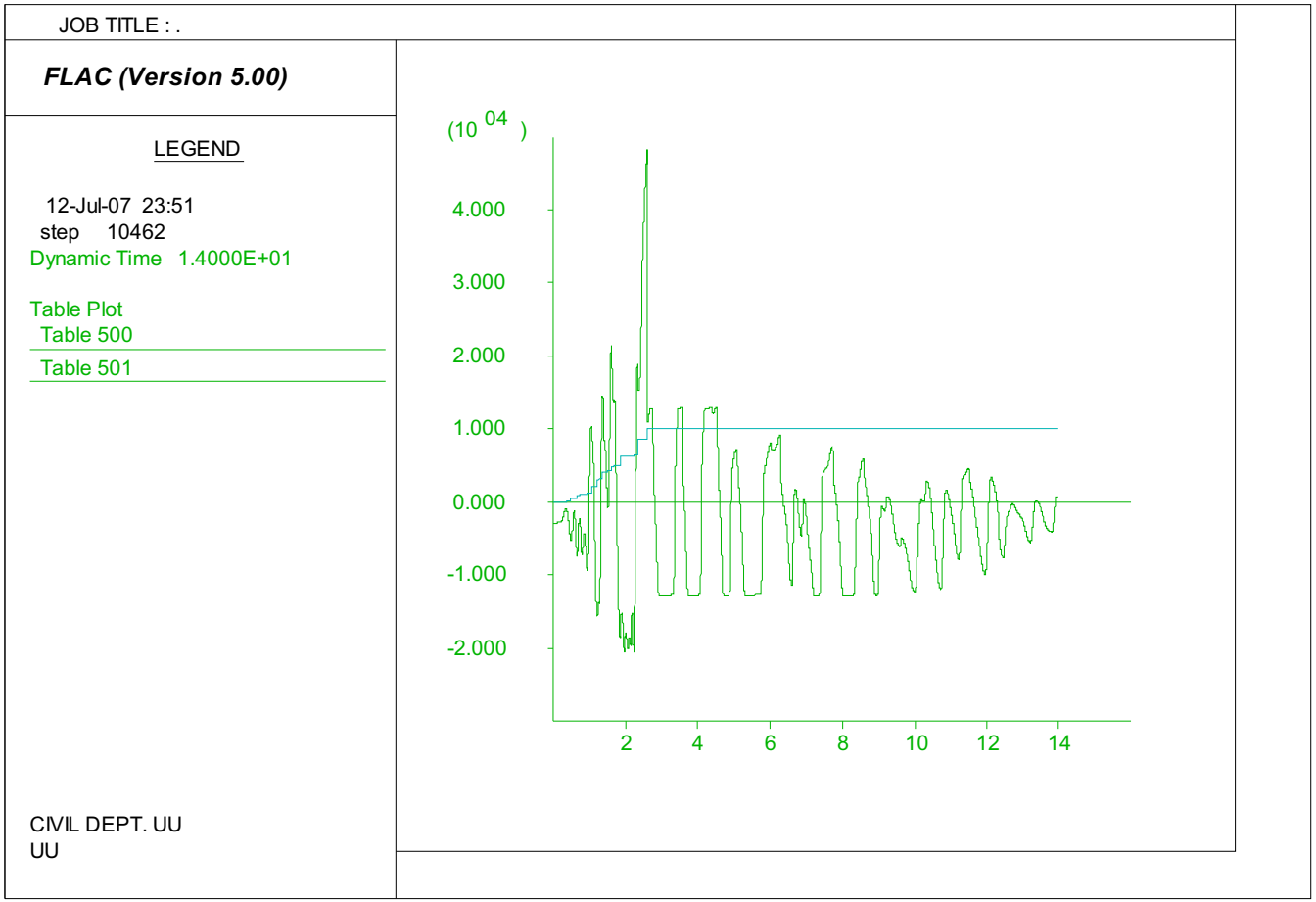


Figure M.22. Model pore water generation history loaded by motion 6 with residual strength ratio of 0.02: Shear stress (Y axis in Pa) and r_u (Y axis multiplied by 1000) vs. time (X axis in seconds).

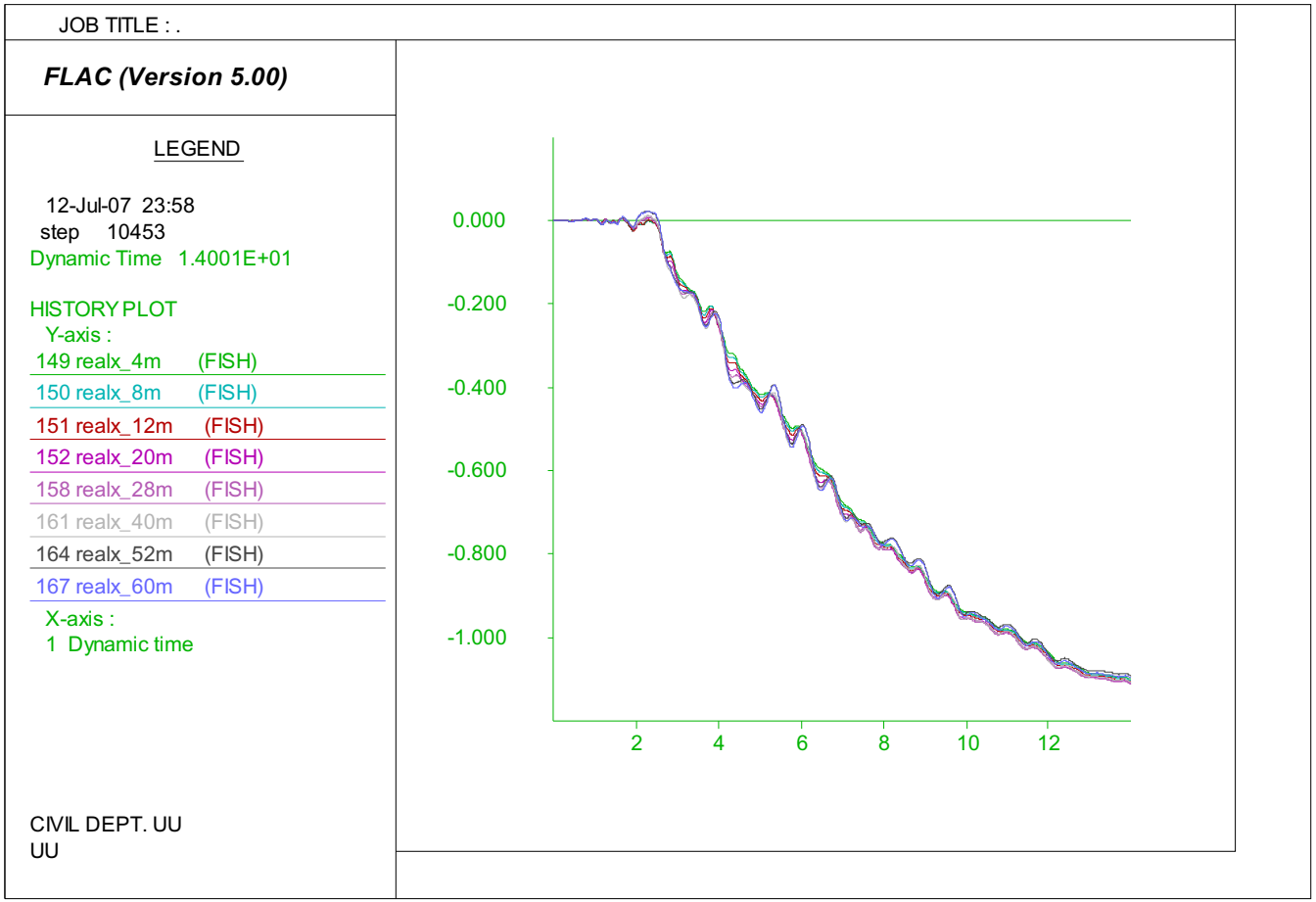


Figure M.23. Model later spreading prediction loaded by motion 7 with residual strength ratio of 0.2 (Y axis in meter and X axis in second)

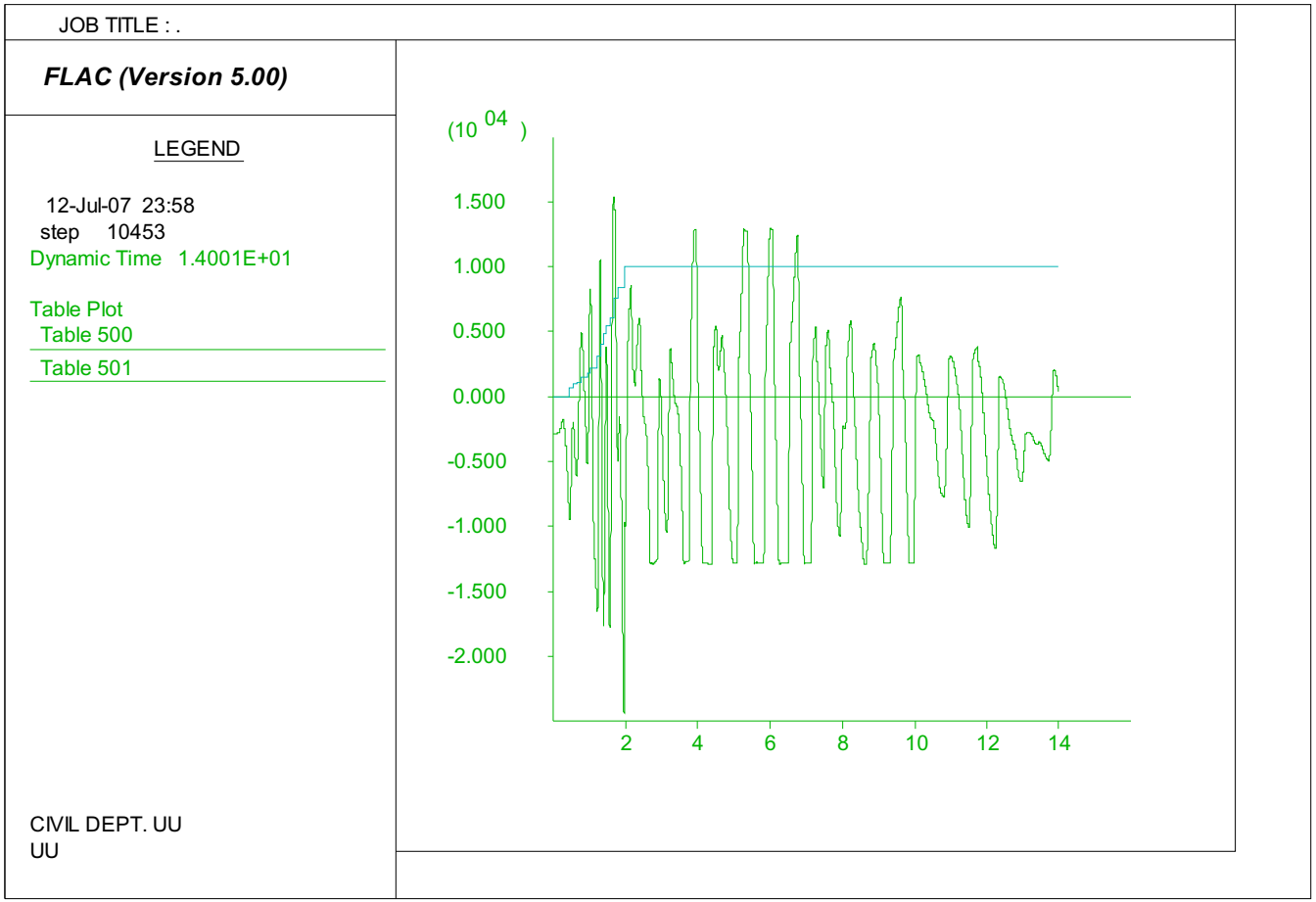


Figure M.24. Model pore water generation history loaded by motion 7 with residual strength ratio of 0.2: Shear stress (Y axis in Pa) and r_u (Y axis multiplied by 1000) vs. time (X axis in seconds).

APPENDIX N

NORTHRIDGE BALBOA SITE DATA

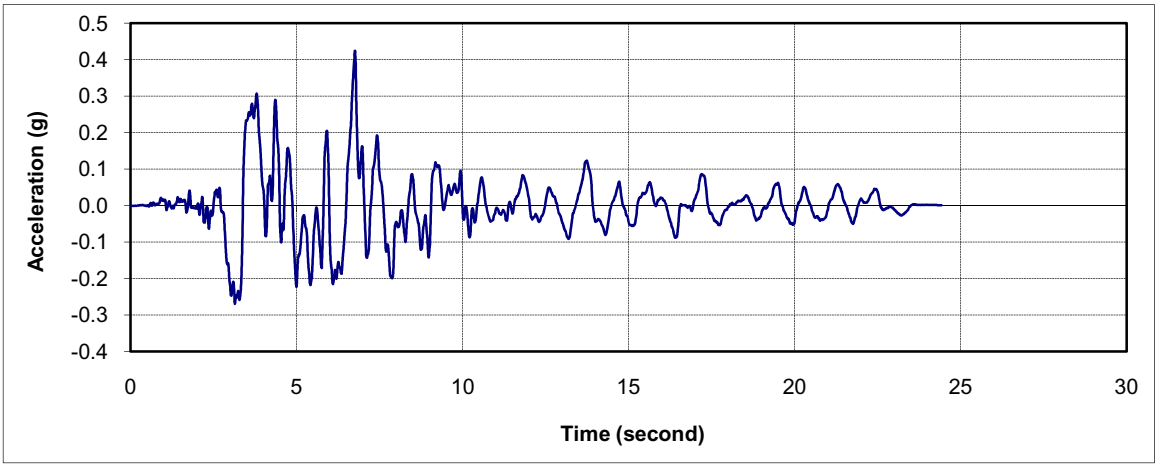


Figure N.1. Download earthquake motion in 22° from North direction.

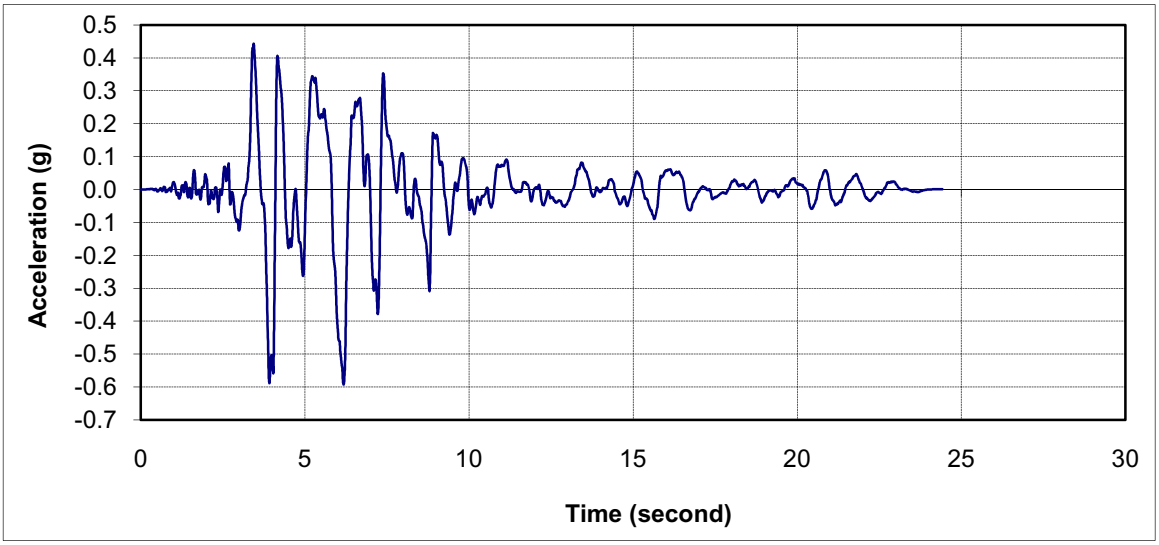


Figure N.2. Download earthquake motion in 292° from North direction.

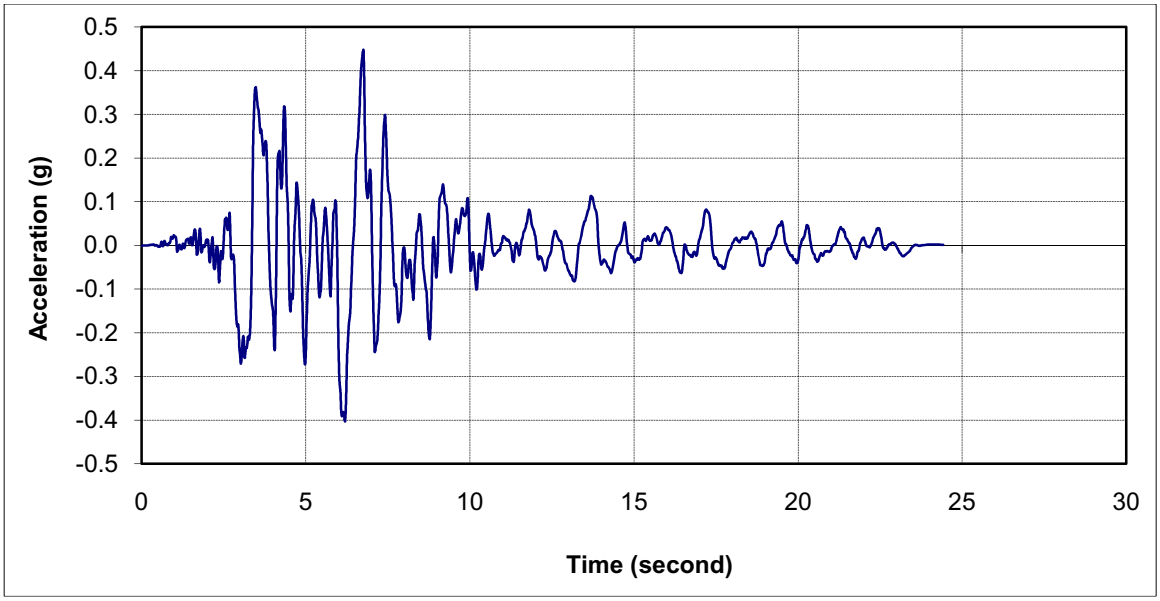


Figure N.3. Calculated rotated motion in North direction.

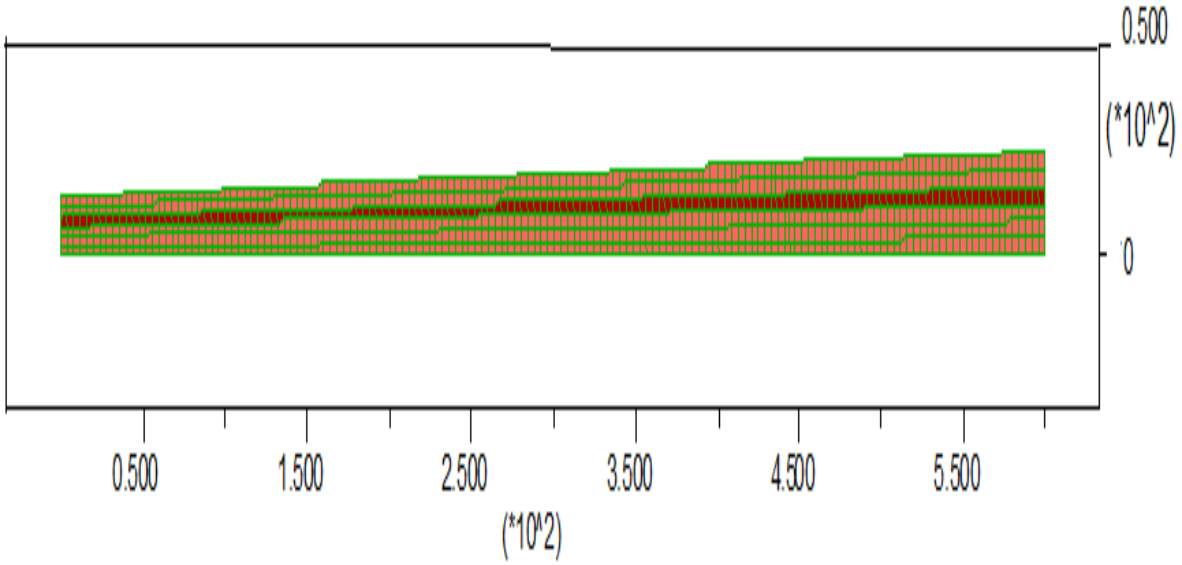


Figure N.4. Model design mesh (both Y axis & X axis in meters).

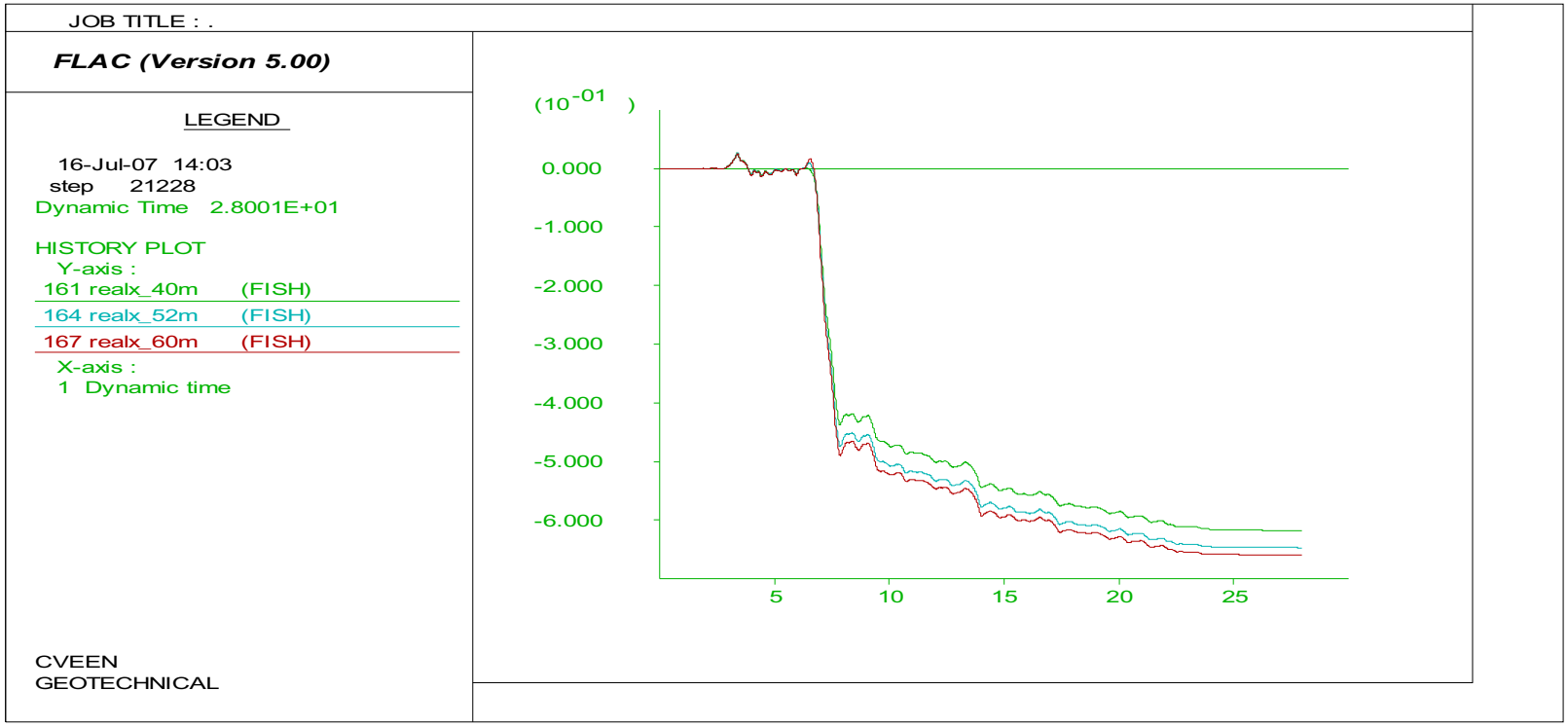


Figure N.5. Prediction of lateral spread from FLAC Figure XIV-. Model (Y axis in meter and X axis in seconds).

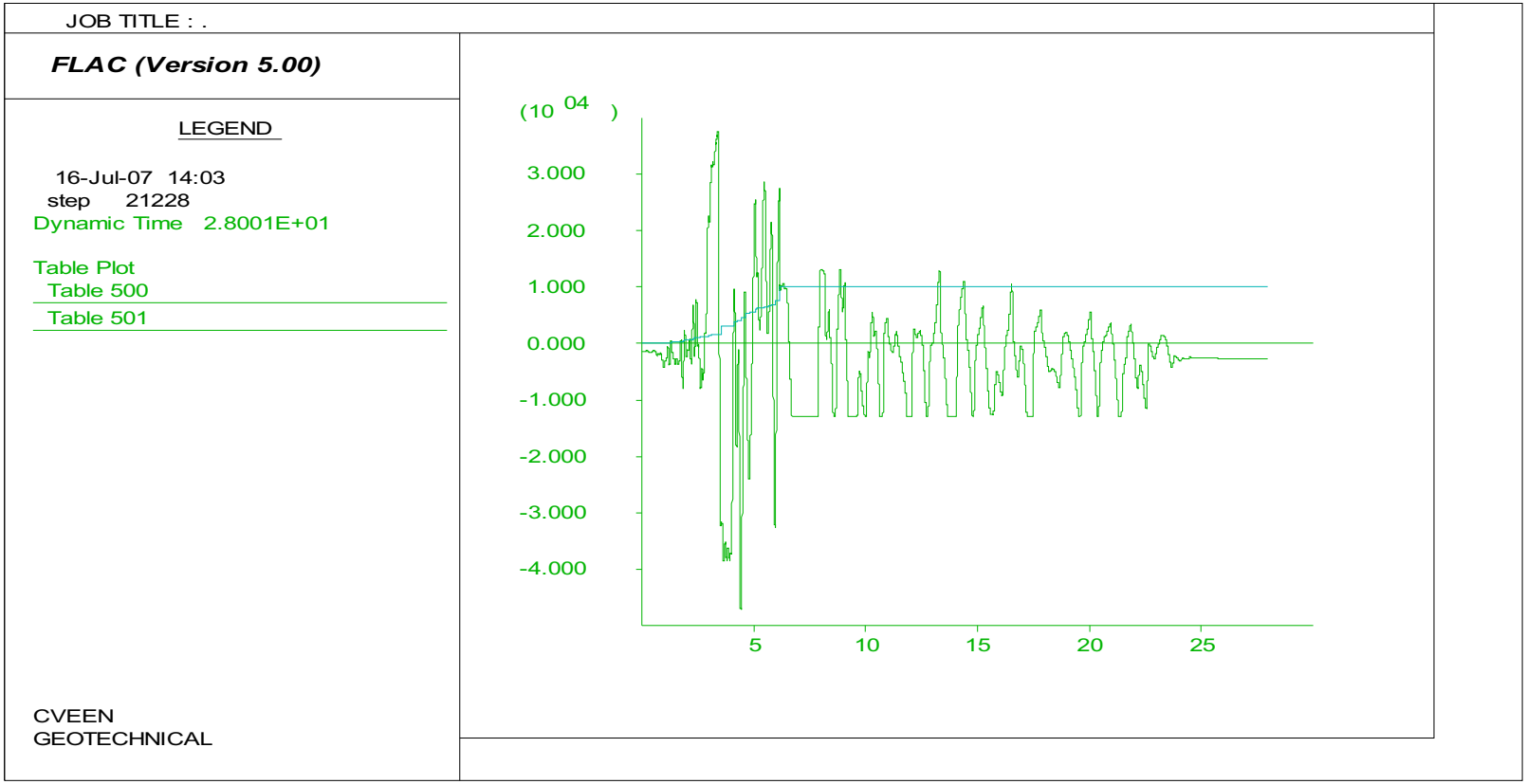


Figure N.6. Predicted liquefaction time history from FLAC Figure XIV-. Model: Shear stress (Y axis in Pa) and r_u (Y axis multiplied by 1000) vs. time (X axis in seconds).

APPENDIX O

TURKEY, DEGIRMENEDERE WITHOUT T_{15} DATA

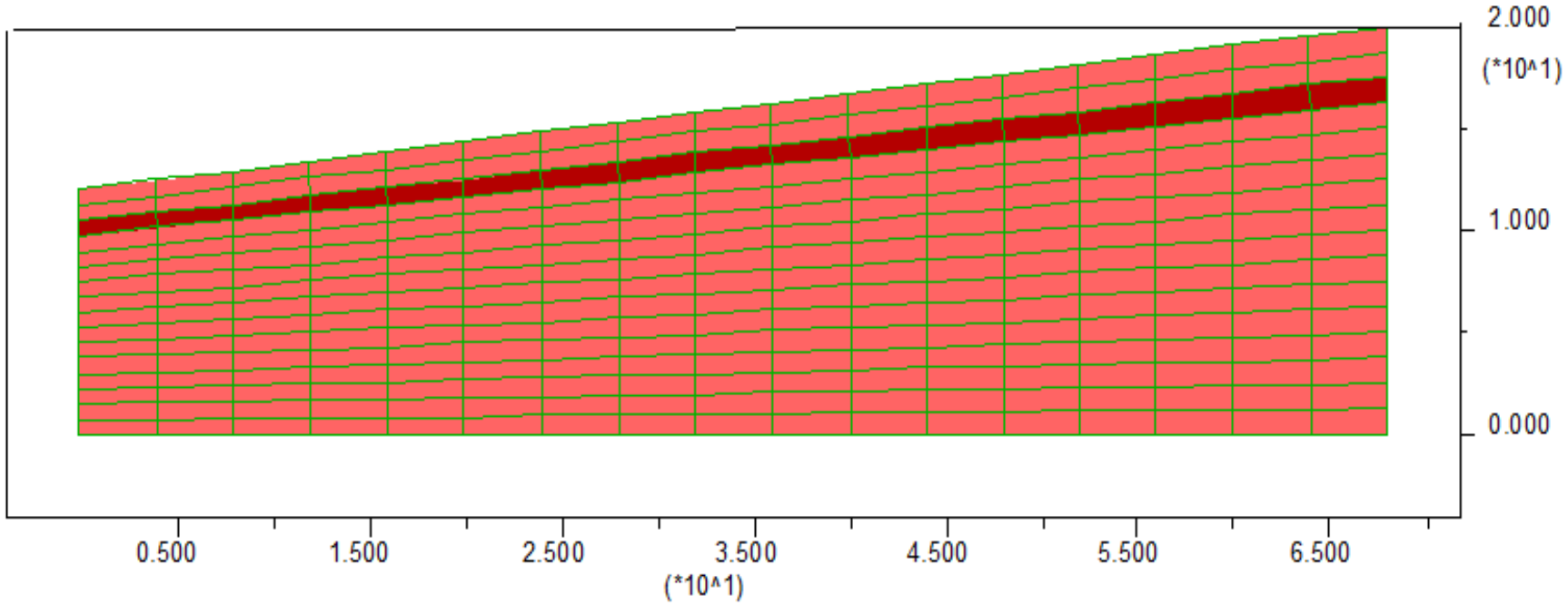


Figure O.1. Model soil properties change after liquefaction (both Y axis & X axis in meters).

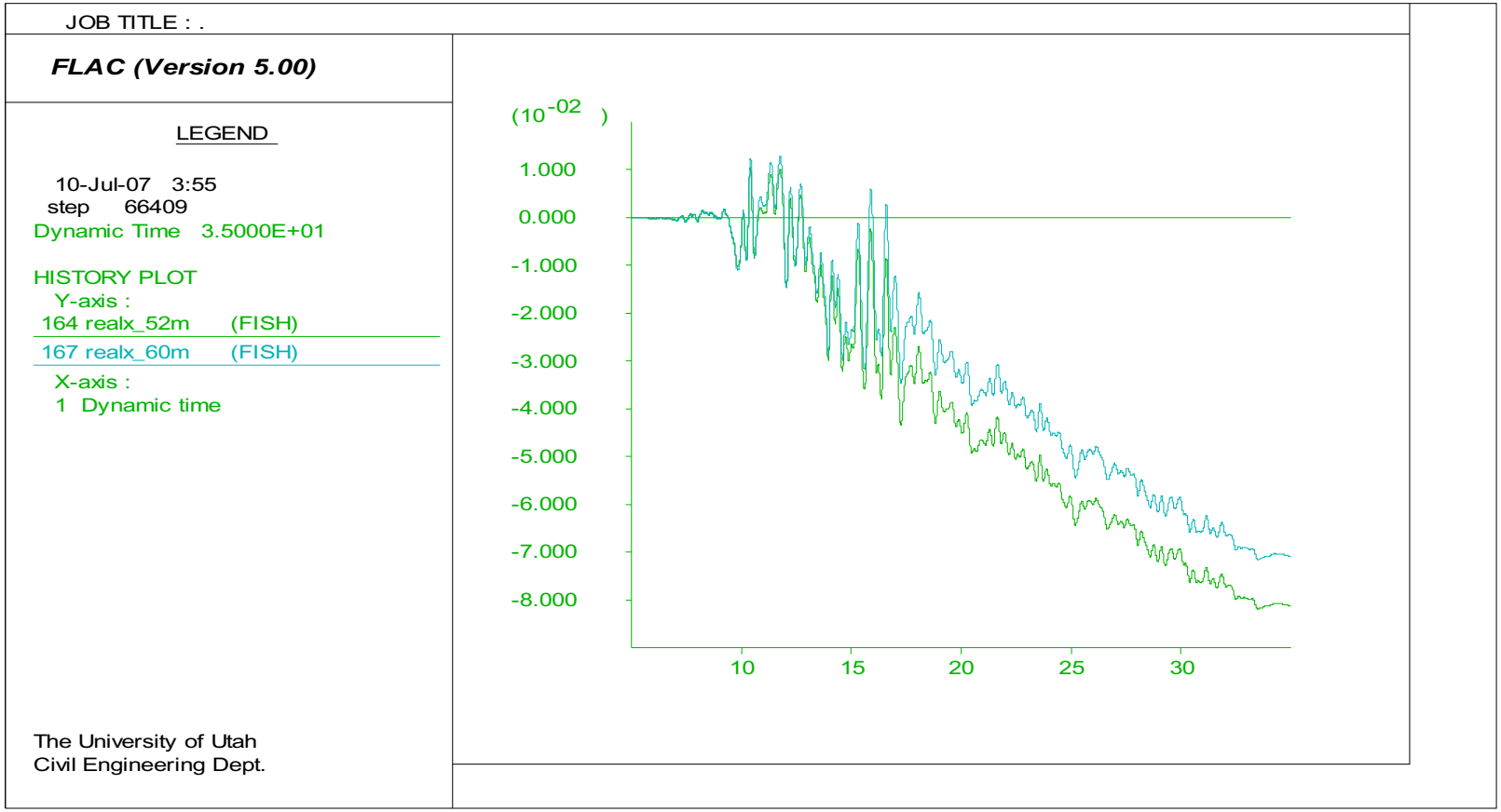


Figure O.2. Model later spreading prediction (Y axis in meter and X axis in second).

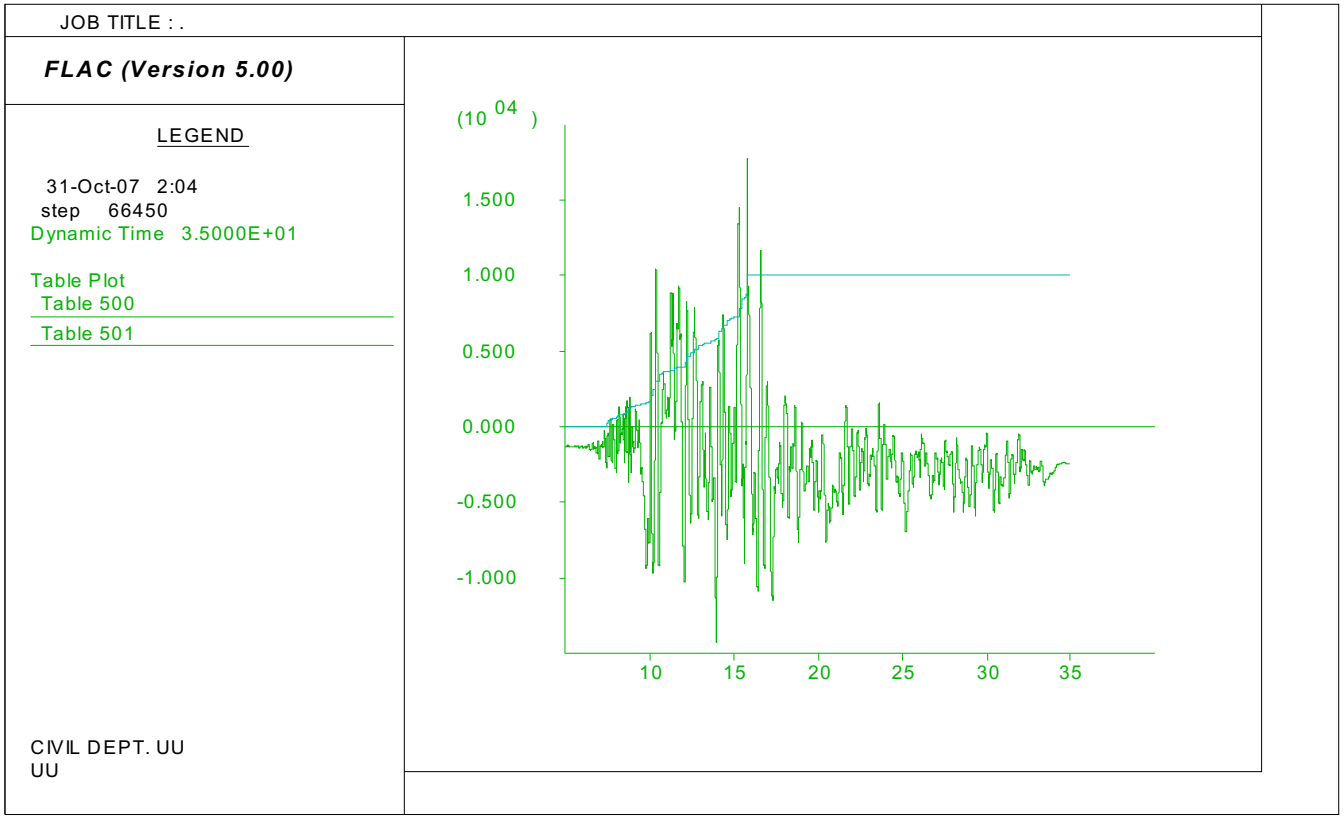


Figure O.3. Model pore water generation history: Shear stress (Y axis in Pa) and r_u (Y axis multiplied by 1000) vs. time (X axis in seconds).

APPENDIX P

TURKEY, SAPANCA HOTEL DATA

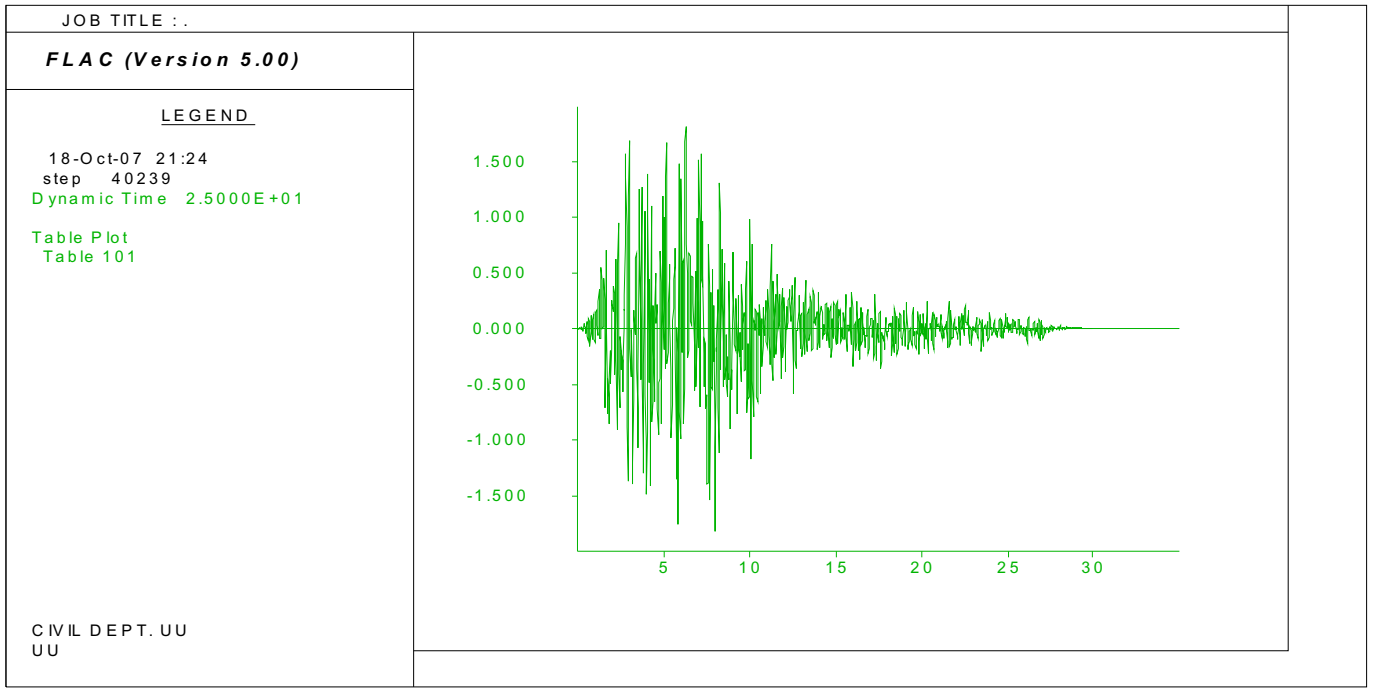


Figure P.1. FLAC model input motion (Y axis in m/s^2 and X axis in seconds).

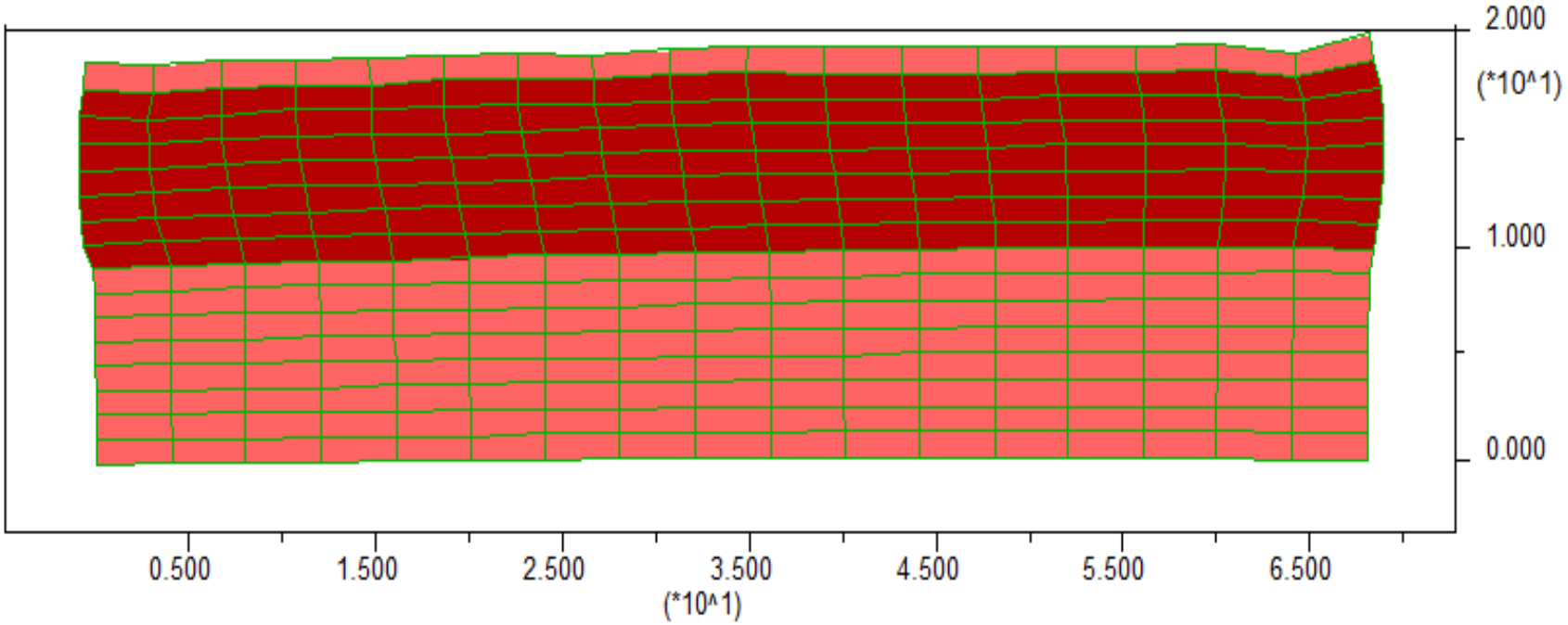


Figure P.2. Soil properties change after liquefaction (both Y axis & X axis in meters).

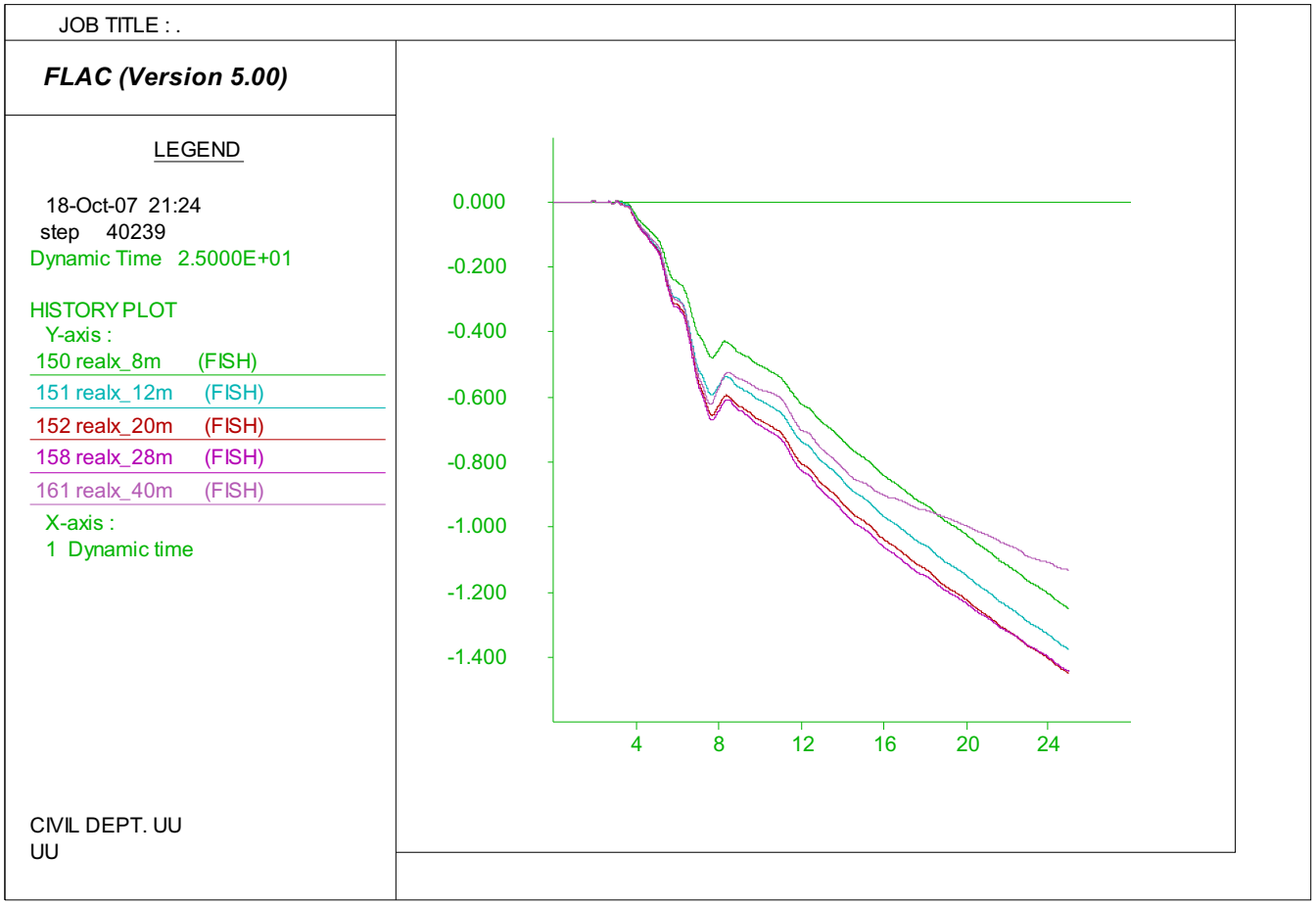


Figure P.3. Model later spreading prediction with residual strength ratio of 0.25(Y axis in meter and X axis in seconds).

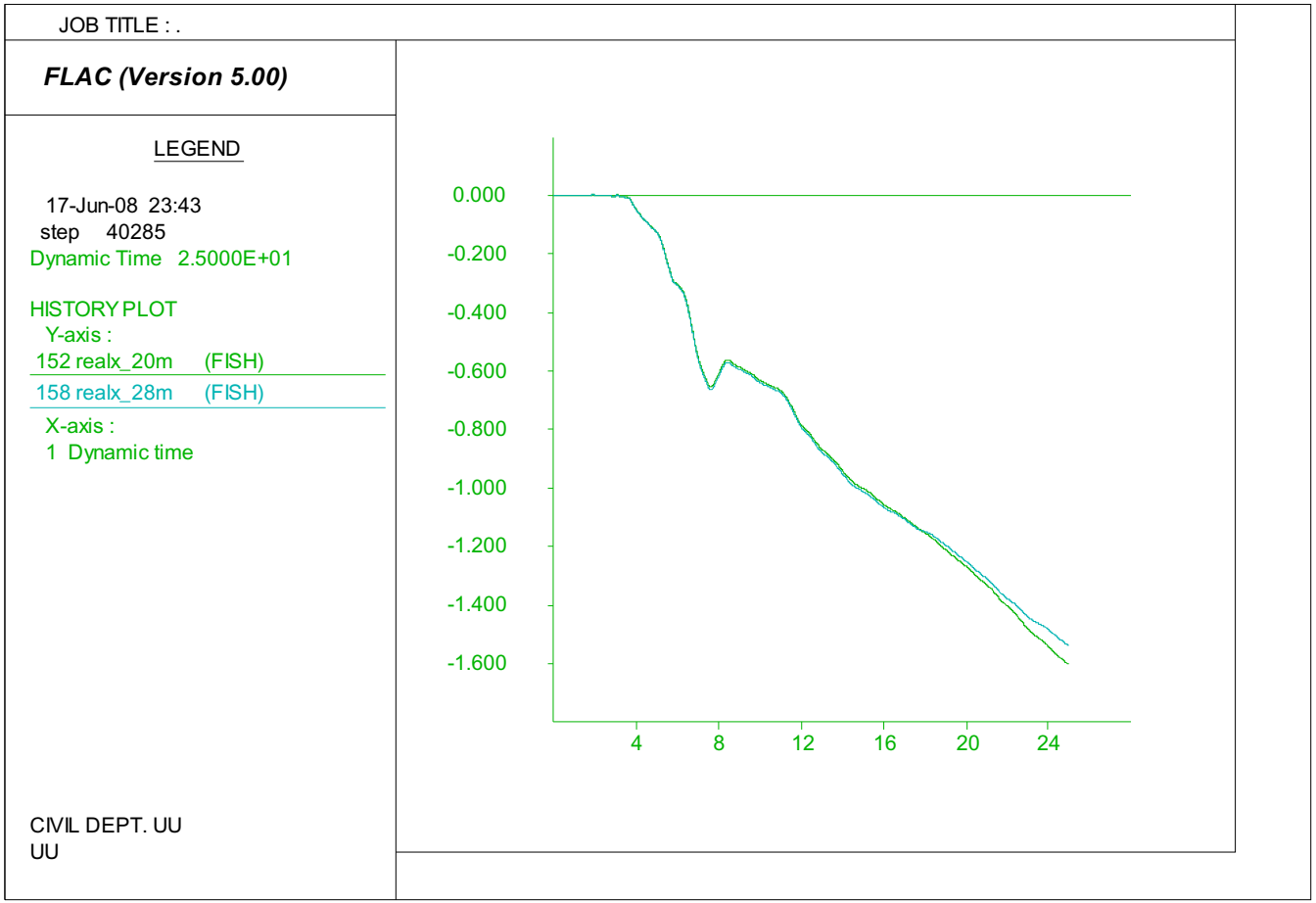


Figure P.4. Model later spreading prediction with residual strength ratio of 0.24(Y axis in meter and X axis in seconds).

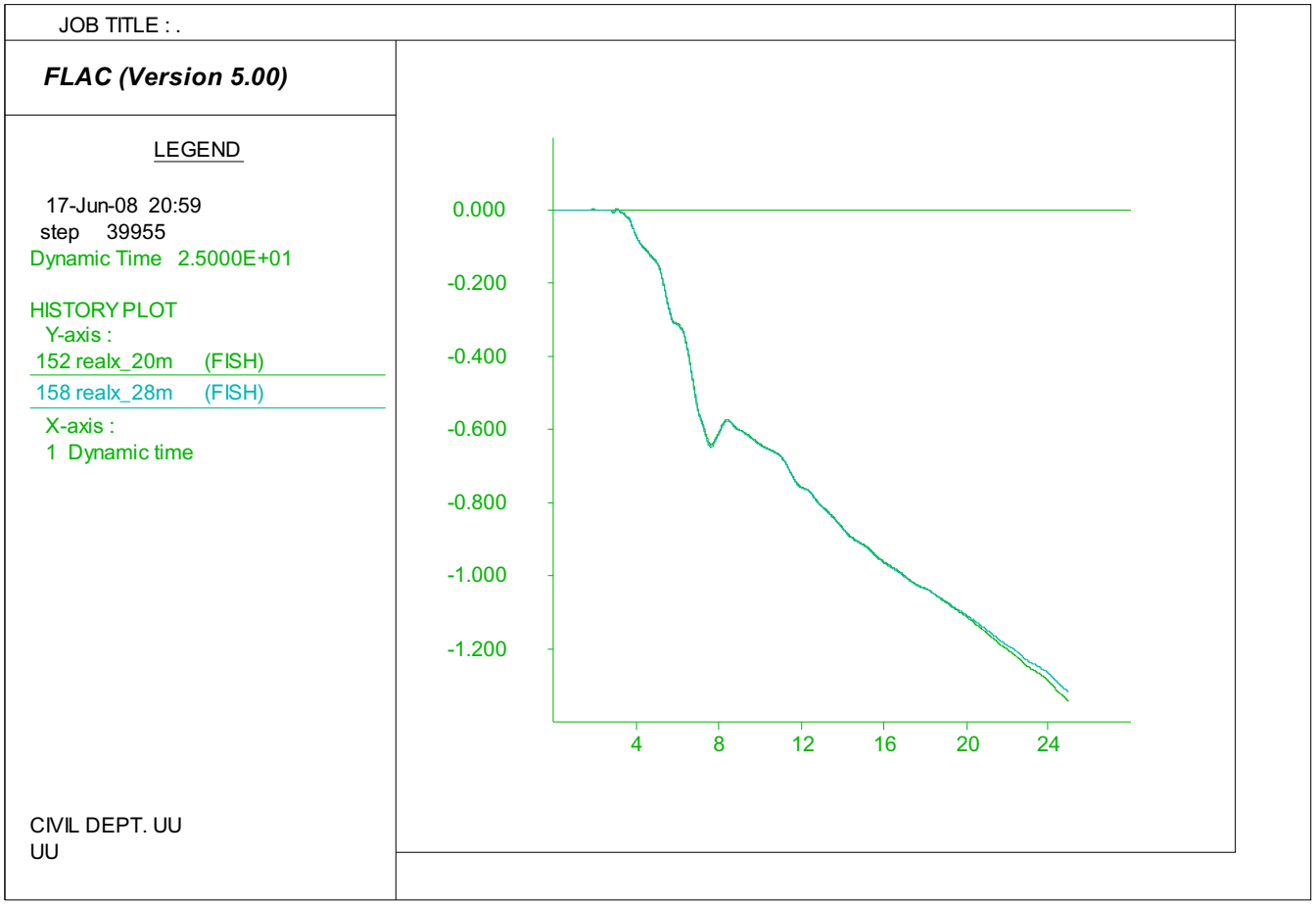


Figure P.5. Model later spreading prediction with residual strength ratio of 0.26(Y axis in meter and X axis in seconds).

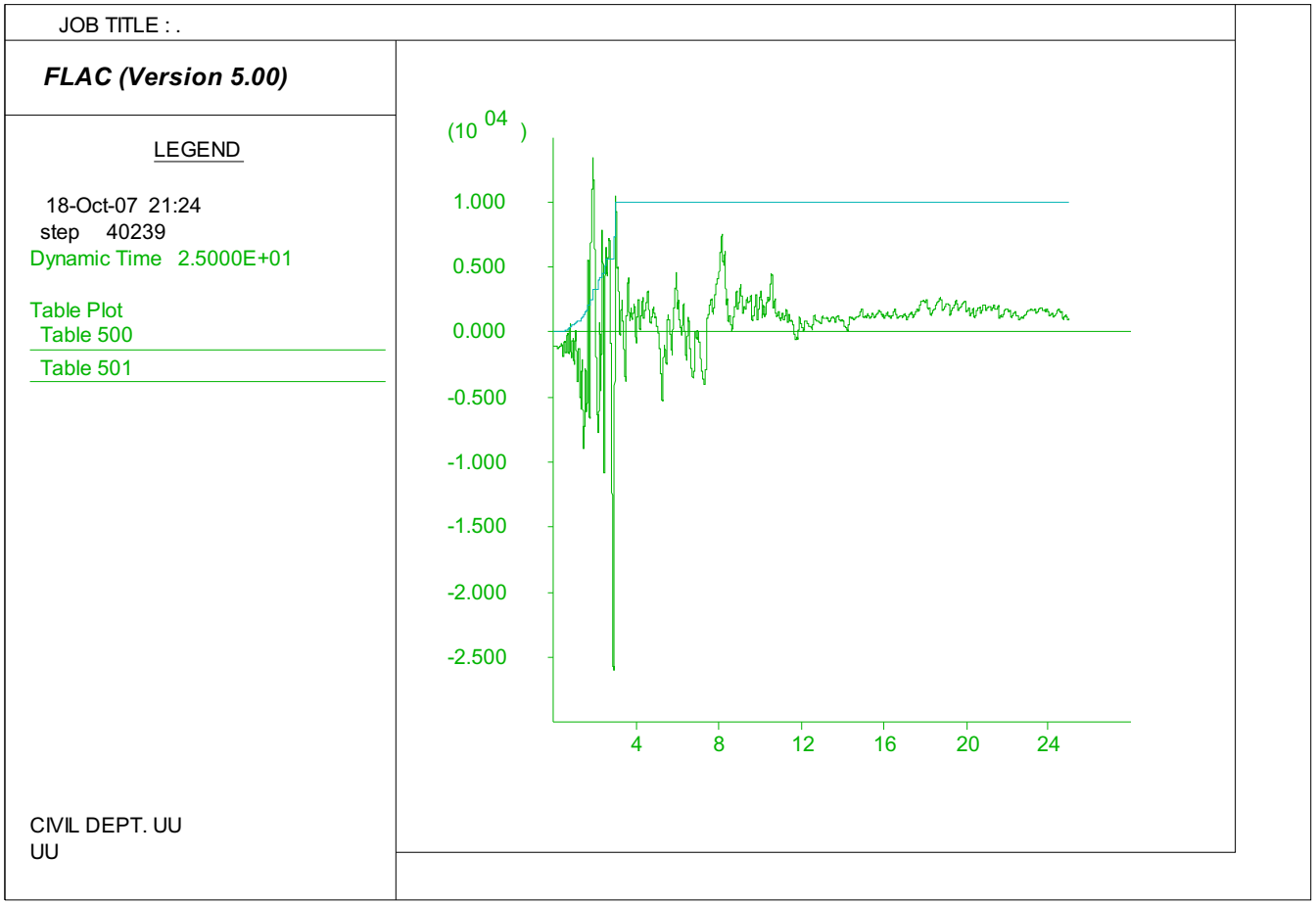


Figure P.6. Model pore water generation history: Shear stress (Y axis in Pa) and r_u (Y axis multiplied by 1000) vs. time (X axis in seconds)

REFERENCE

Andrus, R. D., Stoke, K. H., and Roesset, J. M. (1991). "Liquefaction of Gravelly Soil at Pence Rance During the 1983 Borah Peak, Idaho Earthquake," Processing of the Fifth International Conference on Soil Dynamics and Earthquake Engineering, Karlsruhe, Germany, Sept. 1991.

Andrus, R. D. and Youd T. L. (1987). "Subsurface Investigation of a Liquefaction-Induced Lateral Spread Thousand Springs Valley, Idaho," US Army Corps of Engineers, Miscellaneous Paper GL-87-8.

Arulanandan, K. (1996). "Application of Numerical Procedures in Geotechnical Earthquake Engineering," Proc., Application of Numerical Procedures in Geotechnical Earthquake Engineering, National Science Foundation Workshop/Conference, October pp. 28-30.

Arulanandan, K., Muraleetharan, K., and Yogachandran, C. (1997). "Seismic Response of Soil Deposits in San Francisco Marina District," J. Geotech. and *Geoenvir*. Engrg., ASCE, 123(10), 965-974.

Atigh, E., and Byrne, P. M. (2004). "Liquefaction flow of submarine slopes under partially undrained conditions: an effective stress approach," Can. Geotech. Journal, 41(1), 154-165.

Bartlett, S. F. and Youd T. L. (1995). "Empirical Prediction of Liquefaction- induced Lateral Spreads," ," J. Geotech. and *Geoenvir*. Engrg., ASCE, 121 (4), 316 –329.

Bartlett, S. F. and Youd, T. L. (1990). "Evaluation of Ground Failure Displacement Associated wit hSoil Liquefaction: Compilation of Case Histories," Miscellaneous Paper S-73-1, Department of the Army, U.S. Army Corps of Engineering, Washington, D.C., 84 p.

Bartlett, S. F. and Youd, T. L. (1991). "Case Histories of Lateral Spreads Caused by the 1964 Alaska Earthquake." Case History Volume, US-Japan Workshop on Liquefaction, Large Ground Deformation, and Their Effects on Lifelines, National Center for Earthquake Engineering Research, State University of New York at Buffalo, Red Jacket Quadrangle, Buffalo, NY, 127 p.

Bartlett, S. F. and Youd, T. L. (1992). "Empirical analysis of horizontal ground displacement generated by liquefaction-induced lateral spreads," Technical report NCEER-92-0021, National Center for Earthquake Engineering Research, State University of New York, Buffalo, pp. 5-14-15.

Bartlett, S. F. (1991) "Empirical Analysis of Horizontal Ground Displacement Generated by Liquefaction-Induced Lateral Spreads", Ph.D Dissertation, Brigham Young University.

Beaty, M. and Byrne, P. M. (1998). "An effective stress model for predicting liquefaction behavior of sand, " Geotechnical Earthquake Engineering and Soil Dynamics III. Edited by P. Dakoulas, M. Yegian, and R Holtz (eds.), ASCE, Geotechnical Special Publication 75 (1): 766-777.

Beaty, M. and Byrne, P. M. (1999). "A synthesized approach for modeling liquefaction and displacements," FLAC and Numerical Modeling in Geomechanics, Edited by Christine Detournay & Roger Hart, Itasca Consulting Group Inc., A.A. Balkema, 1999.

Beaty, M. and Byrne, P. M. (2008). "Liquefaction and Deforation Analysis Using a Total Stress Approach," *J. Geotech. and Geoenvir. Engrg.*, ASCE 134(8), 1059-1071.

Bennett, M. J., McLaughlin, P. V., Sarmiento, J., and Youd, T. L. (1984). "Geotechnical investigation of liquefaction sites, Imperial Valley, Calif." *U.S. Geological Survey Open File Report*, *84-252*.

Boore, D. M. (2003). "Simulation of ground motion using the stochastic method." Pure Appl. Geophys. 160(3-4), 635-676.

Byrne, P. M. (1991). "A Cyclic Shear-Volume Coupling and Pore Pressure Model for Sand," Proceedings of the Second International Conference on Recent Advances in Geotechnical Earthquake Engineering and Soil Dynamics, Vol. 1, Prakash, S., editor, University of Missouri, Rolla, Missouri, pp.47 – 55.

Byrne, P. M., and Puebla, H. (2000). "CANLEX full-scale experiment and modeling" Can. Geotech. Journal, 37(3), 543-562.

Byrne, P. M., Jinto, H., and Salgado, F. (1992). "Earthquake Induced Displacements of Soil- Structure Systems," Proceedings of 10th World Conference in Earthquake Engineering, Madrid, Spain, 1407-1412.

Byrne, P. M., Park, S., Beaty, M., Sharp, M., Gonzalez, L., and Abdoun, T. (2004). "Numerical modeling of liquefaction and comparison with centrifuge tests," Can. Geotech. Journal, 41(5), 193–211.

Byrne, P. M., Roy, D., Campanella, R. G. & Hughes, J. (1995). "Predicting liquefaction response of granular soils from pressuremeter tests," ASCE National Convention, SanDiego, Oct. 23-27, ASCE, Geotechnical Special Publication 6: 122-135.

Castro, G. (1969). "Liquefaction of Sands", Harvard Soil Mechanics Series 87, Harvard University, Cambridge, Massachusetts.

Cetin, O. K., Youd, T. L., and Seed, R. B. (2004). "Liquefaction-Induced Lateral Spreading at Izmit Bay During the Kocaeli (Izmit)-Turkey Earthquake" *J. Geotech. and Geoenvir. Engrg.*, ASCE, 130(12),1300-1313.

Cetin, O. K., Youd, T. L., Seed, R. B., Bray J. D., Stewart, J. P. Durgunoglu, H. T., Lettis, W., and Yilmaz, M. T. (2004). "Liquefaction-Induced Lateral Spreading at Izmit Bay During the Kocaeli (Izmit)-Turkey Earthquake," *J. Geotech. and Geoenvir. Engrg.*, ASCE, 130(12), 1300-1313.

Chang, S. W., Bray, J. D., and Seed, R. B. (1996). "Engineering implications of ground motions from Northridge earthquake," Seismological Soc. Of American Bull., 86(1B), 270-288.

Chang, S. W., Bray, J. D., and Seed, R. B. (1996). "Engineering implications of ground motions from Northridge earthquake," Seismological Soc. Of American Bull., 86(1B), 270-288.

Cooke, H. G. (2000). "Ground Improvement for Liquefaction Mitigation at Existing Bridges," Dissertation for Doctor in Philosophy in Civil Engineering, Virginia Polytechnic Institute and State University, Blacksburg, Virginia.

Dawson, E. M., Roth, W. H., Nesarajah, S., Bureau, G. and Davis, **C. A.** (2001). "A practice oriented pore-pressure generation model", Proceedings of the Second International FLAC Symposium, Lyon France, Oct. 29-31, 2001, published by A.A. Balkema Publishers.

De Alba, P., Chan, C. K., and Seed, H. B. (1975) "Determination of soil liquefaction characteristics by large-scale laboratory tests," Report EERC 75-14, Earthquake Engineering Research Center, University of California, Berkeley.

De Den, D. W. (1999) "Analysis of Lateral Spreads Generated by the 1999 Kocaeli, Turkey Earthquake," Master Thesis, Brigham Young University

Dealba, P., Chan, C. K., and Seed, H. B. (1975). "Determination of soil liquefaction characteristics by large-scale laboratory tests," Report EERC 75-14, Earthquake Engineering Research Center, University of California, Berkeley.

Dobry, R., Elgamal, A. W., Baziar, M., and Vucetic, M. (1989). "Pore pressure and acceleration response of wildlife site during the 1987 earthquake." Proc., 2nd U.S.–Japan Workshop on Liquefaction, Large Ground deformation and Their Effects on Lifelines, National Center for Earthquake Engineering Research, Buffalo, N.Y., 145–160.

Dobry, R. and Abdoun, T. (1998). "Post-Triggering Response of Liquefaction Sand in the Free Field and Near Foundations," Geotechnical Earthquake Engineering and Soil Dynamics III, ASCE Geotechnical Special Publication No. 75, Volume 1, pp. 270 – 300.

Dobry, R., Ladd, R. S., Yokel, F. Y., Chung, R. M., and Powell, D. (1982). "Prediction of Pore Water Pressure Buildup and Liquefaction of Sands During Earthquakes by the Cyclic Strain Method," *National Bureau of Standards Building Science Series 138*, 150 pp.

EduPro Civil Systems, Inc. (1998). "User's Manual", Version 1.1, Redmond Washington.

Elgamal, A.W., Zeghal, M., and Parra, E. (1996). "Liquefaction of reclaimed island in Kobe, Japan," *J. Geotech. and Geoenvir. Engrg.*, ASCE, 122(1), 39-49.

Finn, W. D. L. and Ledbetter, R. H. (1991). "Evaluation of Liquefaction Effects and Remediation Strategies by Deformation Analysis," Proceedings of the International Conference on Geotechnical Engineering for Coastal Development, GEOCOAST 91, pp. 441-446.

Finn, W. D. L., Martin, G. R., and Lee, M. K. W. (1978). "Comparison of dynamic analysis of saturated sand," *Proc. of the ASCE Geotechnical Engineering Division of Specialty Conference on Earthquake Engineering and Soil Dynamics,* Pasadena, California, June, 472-491.

Halldorsson B and Papageorgiou, A. (2004). "Regional Specific Ground Motion Simulations Using The Specific Barrier Model," Engineering Seismology Laboratory Memorandum, July 14, 2004.

Hamada, M., and O'Rourke T. D. (1992). "Case Studies of Liquefaction and Lifeline Performance During Past Earthquakes," Technical Report, NCEER-92-0001, Volume 1.

Hamada, M., Isoyama, R. and Wakamatsu, K. (1996). "Liquefaction-induced ground displacement and its related damage to lifeline facilities," *Soils and Foundations*, Special Issue on Geotechnical Aspects of the January 17 1995 Hyogoken-Nanbu Earthquake, Japanese Geotechnical Society, pp. 81- 97.

Hamada, M., Towhata, T., Yashda, S., Isoyama, R. (1987). "Study of Permsnent Ground Displacement Induced by Seismic Liquefaction," Computer and Geo technics, Vol. 4, No. 4, Elsevier Applied Science Publishers, pp.197-220.

Hamada, M., Yasuda, S., Isoyama, R. and Emoto, K. (1986). "Study on Liquefaction induced permanent ground displacement*," Report for the Association for the Development of Earthquake Prediction.*

Hazırbaba, K. (2005) "Pore Pressure Generation Characteristics of Sands and Silty Sands: A Strain Approach", Ph.D Dissertation, The University of Texas at Austin**.**

Holzer T. L., Bennett, M. J., Ponti, D. J. and Tinsley, J. C. III. (1999). "Liquefaction and Soil Failure During 1994 Northridge Earthquake", *J. Geotech. and Geoenvir. Engrg.*, ASCE, 125(6), 438-452.

Holzer, T. L., Youd, T. L., and Hanks, T. C. (1989) "Dynamics of liquefaction during the Superstition Hills Earthquake s*M*=6.5d of November 24, 1987." Science, 244(7), 56–59.

Ishihara, K. and Okada, S. (1982). "Effects of large preshearing on cyclic behavior of sand", Soils and Foundations, 22(3): 109–125.

Ishihara, K., Yasuda, S., and Shinkawa, N. (1996). "Soil characteristics and ground damage." *Soils Found.*, Special Issue on Geotechnical Aspects of the Hyogoken-Nambu Earthquake, 109–119.

Itasca. (2005). "FLAC User's Manual".

Joyner, W. B. and Boore, D. W. (1981). "Peak Horizontal Acceleration and Velocity from Strong Motion Records Including Records from the 1979 Imperial Valley, California Earthquake," Bulletin of the Seismological Socoety of American, 71(6), 2011-2038.

Kachadoorian, R. (1968). "Effects of the Earthquake of March 27, 1964, on the Alaska Highway System," U. S. Geological Survey Professional Paper 545-C, 66 p.

Kramer, S. L. and Paulsen, S. B. (2004). "Practical Use of Geotechnical Site Response Models," *Proceedings*, International Workshop on Uncertainties in Nonlinear Soil Properties and their Impact on Modeling Dynamic Soil Response, University of California, Berkeley, 10 pp.

Kramer, S.L. (1996). "Geotechnical Earthquake Engineering," Prentice Hall International Series.

Lettis, W., Bachhuber, J., Witter, R., Barka, A., Bray, J., Page, W., Swan F., and Witter,R. (2000). "Surface Fault Rupture," Chapter 2 of the Kocaeli, Turkey Earthquake of August 17, 1999 Reconnaissance Report, *Earthquake Spectra*, Suppl. Vol. 16, pp. 11-53.

Li, X. S., Shen, C. K., and Wang, Z. L. (1998). "Fully Coupled Inelastic Site Reponse Analysis for 1986 Lotung Earthquake," J. J. Geotech. and Geoenv. Engrg., 124(7), 560-573.

Martin, G. R., Finn, W. D. L., and Seed, H. B. (1975). "Fundamentals of liquefaction under cyclic loading," Journal of the Geotechnical Engineering Division, ASCE, 101(GT5): 423–438.

Martin, G. R., Finn, W.D. L., and Seed, H. B. (1975) "Fundamentals of liquefaction under cyclic loading," Journal of the Geotechnical Engineering Division, ASCE, 101(GT5): 423–438.

McCulloch, D. S. and Bonilla, M. G. (1970). "Effects of the Earthquake of March 27, 1964, on the Alaska Railroad," U. S. Geological Survey Professional Paper 545-D, 161 p.

Mejia, L. H., Dawson, E. M. (2006). "Earthquake deconvolution for FLAC", 4th International FLAC Symposium on Numerical Modeling in Geomechanics, Itasca Consulting Group, pp.1-9.

Moriwaki, Y., Tan, P. and J, F. (1998). " Seismic Deformation of the Upper San Fernando Dam Under the 1971 San Fernando Earthquake," Geotechnical Earthquake Engineering and Soil Dynamics III, ASCE Geotechnical Special Publication No. 75, Vol. II, pp. 854-865.

O'Rourke T. D. and Hamada, M. (1992). "Case Studies of Liquefaction and Lifeline Performance During Past Earthquakes," Technical Report, NCEER-92-0001, Volume 2.

Olsen, P.T. (2008). "Shear Modulus Degradation of Liquefying Sand: Quantification and Modeling," MS thesis, Brigham Young University.

Olson, Scott M. and Stark, Timothy D. (2002). "Liquefied strength ratio from liquefaction flow failure case histories," Can. Geotech. J., 39(5): 629–647.

Papageorgiou, A. and Dong, G., (2004)." Strong Ground Motion Simulation Code for Eastern North American", http://civil.eng.buffalo.edu/EngSeisLab/index.htm.

ProShake User's Manual, (1998). Version 1.1, EduPro Civil Systems, Inc. Redmond Washington.

Puebla, H., Byrne, P.M. and Phillips, R. (1997). "Analysis of CANLEX liquefaction embankments: prototype and centrifuge models," Can. Geotech. Journal, 34(5), 641-657.

Pyke, R. (1979) "Nonlinear Soil Models for Irregular Cyclic Loadings," Journal of Geotechnical Engineering Division, ASCE, 105(GT6), 715-726.

Seed, H. B., Harder, L.F., and Jong, H.-L. (1988). "Re-Evaluation of the Slide in the Lower San Fernando Dam in the Earthquake of Feb. 9, 1971", University of California, Berkeley, Report No. ECB/EERC-88/04.

Seed, H. B., Harder, L.F. and Jong, H.-L. (1988). "Re-Evaluation of the Slide in the Lower San Fernando Dam in the Earthquake of Feb. 9, 1971", University of California, Berkeley, Report No. ECB/EERC-88/04.

Seed, H. B., and Idriss. I.M. (1969) "Influence of Soil Conditions on Ground Motion During Earthquakes," J. Soil Mech. Found., Div. ASCE, 95, 99-137

Seed, H. B., and Idriss. I.M. (1982) **"**Ground Motions and Soil Liquefaction during Earthquakes," Earthquake Engineering Research Institute Monograph MNO-5, 134 p.

Seed, H. B., Lee, K. L., Idriss, I. M. and Makdisi, F. (1973). "Analysis of the Slides in the San Fernando Dams During the Earthquake of February 9, 1971," University of California, Berkeley, Report No. EERC 73-2.

Seed, H. B., Wong, R. T., and Idriss. I.M. (1986) **"**Module and damping factors for dynamic analysis of cohesionless soils," Jounal of Geotechnical Engineering, Vol.112, No.11, November ,1986.

Seed, H.B. and Idriss, I.M. (1971) "Simplified procedure for evaluating soil liquefaction potential", Journal of the Soil Mechanics and Foundation Division, ASCE, 97(9), 1249-1273.

Seed, R. B., and Harder, L. F. (1990). "SPT-Based Analysis of Cyclic Pore Pressure generation and Undrained Residual Strength," Proceedings of H. Bolton Seed Memorial symposium, BiTech, Vancouver, B. C., Canada, Vol. 2, pp. 351 – 376, May 1990.

SeismoSignal Version 3.2, 2006, http://www.seismosoft.com/.

Tokimatsu, K., Mizumo, H., and Kakurai, **M.** (1996) "Building Damage Associatedwith Geotechnical Problems," Soils and Foundations, Special Issue on Geotechnical Aspects of the January 17 1995 Hyogoken-Nanbu Earthquake, Japanese Geotechnical Society, pp. 219-234.

Vucetic, M. and Dobry, R. (1991). "Effect of soil plasticity on cyclic response." *J. Geotech. and Geoenvir. Engrg.*, ASCE, 117(1), 89-107.

Wang Z. L. and Makdisi, F. I. (1999) "Implementing a Bounding Surface Hypoplasticity Model for Sand into the FLAC Program," Proceedings of the FLAC Symposium on Numerical Modeling in Geomechanics, Minneapolis, Minnesota, September 1-3, 1999.

Wang Z. L., Dafalias, Y. F., and Shen, C.K. (1990). "Bounding Surface hypoplasticity Model for Sand," ASCE, Journal of Engineering Mechanics, 116(5), 983-1001, 1990.

Wang Z. L., Egan J., Scheibel, L. and Makdisi, F. I. (2001). "Simulation of Earthquake Performance of a Waterfront Slope Using Fully Coupled Effective Stress Approach," Proceedings of the Second International FLAC Symposium, Lyon France, Oct. 29-31, 2001, published by A.A. Balkema Publishers.

Wijewickreme, D., Atukorala, U., and Fitzell, T. (1998). "Liquefaction-Induced Ground Displacement for Seismic Evaluation of Lifelines," Geotechnical Earthquake Engineering and Soil Dynamics III, ASCE Geotechnical Special Publication No. 75, Volume 1, pp. 434 – 445.

Youd, T. L. and Bartlett S. F. (1988). "Proceedings of First Japan—U.S. Workshop on Liquefaction, Large Ground Deformation and their Effects on Lifeline Facilities", November Tokyo, Japan

Youd, T. L. and Bartlett S. F. (1988), "US Case Histories of Liquefaction-Induced Ground Displacement," Proceeding of First Japan-US Workshop on Liquefaction, Large Deformation and Their Effects on Lifeline Facilities, November, Tokyo, Japan.

Youd, T. L. and Ben L. C. (2005). "Influence of Soil Softening and Liquefaction on Spectral Acceleration" *J. Geotech. and Geoenvir. Engrg.*, ASCE, 131(7), 811-825.

Youd, T. L. and Bennett, M. J. (1983). "Liquefaction Sites, Imperial Valley, California," *J. Geotech. and Geoenvir. Engrg.*, ASCE, 109(3), 440-457.

Youd, T. L. and Holzer, T. L. (1994). "Piezometer performance at the Wildlife liquefaction site", *J. Geotech. and Geoenvir. Engrg.*, ASCE, 120(6), 975-995.

Youd, T. L. and Hoose, S. N. (1978). "Historic ground failures in northern California triggered by earthquakes", U.S. Geological Survey Prof. Paper 993, 177 p.

Youd, T. L. and Perkins, D. M. (1987). "Mapping of Liquefaction Severity Index," *J. Geotech. and Geoenvir. Engrg.*, ASCE, 113(11),1374-1392.

Youd, T. L., 1978, "Major Cause of Earthquake Damage is ground Failure," *J. Geotech. and Geoenvir. Engrg.*, ASCE, 48(4), 47-51.

Youd, T. L., Hansen, C. M., and Bartlett, S. F. (2002). "Revised multilinear regression equations for prediction of lateral spread displacement." *J. Geotech. and Geoenvir. Engrg.*, ASCE, 128(12), 1007–1017.

Youd, T. L., Harp, E. L., Keefer, D. K. and Wilson, R. C. (1985). "The Borah Peak, Idaho Earthquake of October 29, l983—Liquefaction," Earthquake Spectra, Vol. 2, pp. 71-90.

Youd, T. L., Idriss, I.M., Andrus, R.D., Arango, G., Castro, G., Christian, J.T., Dobry, R., Finn, W.D.L., Harder Jr., L.F., Hynes, M. E., Ishihara, K., Koester, J.P., Liao, S.S.C., Marcuson III, W.F., Martin, G.R., Mitchell, J.M., Moriwaki, Y., Power, M.S., Robertson, P.K., Seed, R.B., and Stokoe II, K.H. (2001), "Liquefaction Resistance of Soils: Summary Report from the 1996 NCEER and 1998 NCEER/NSF Workshops on Evaluation of Liquefaction Resistance of Soils," *J. Geotech. and Geoenvir. Engrg.*, ASCE, 127(10), 817-833.

Zeghal, M. and Elgamal, A.-W. (1994). **"**Analysis of Site Liquefaction Using Earthquake Records," J. *Geotech. and Geoenvir. Engrg.*, ASCE, 120(6), 996-1017.